REGIONAL CLIMATE STUDIES

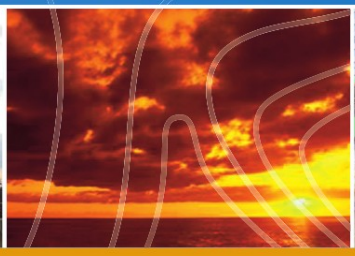

C. Fu · Z. Jiang · Z. Guan · J. He · Z. Xu (Eds.)

Regional Climate Studies of China

Springer

Regional Climate Studies

Series Editors: H.-J. Bolle, M. Menenti, I. Rasool

Congbin Fu · Zhihong Jiang · Zhaoyong Guan ·
Jinhai He · Zhongfeng Xu (Eds.)

Regional Climate Studies of China

With 164 Figures and 42 Tables

Springer

Editors
Prof. Congbin Fu

RCE-TEA
Institute of Atmospheric Physics
Chinese Academy of Sciences
100029 Beijing
P. R. China
fcb@tea.ac.cn

Prof. Jinhai He

Key Laboratory of Meteorological Disaster
Nanjing University of Information Science & Technology
114 Pangcheng New Street, Pukou District
210044 Nanjing
P. R. China
hejhnew@jsmail.com.cn

Prof. Zhihong Jiang

Key Laboratory of Meteorological Disaster
Nanjing University of Information Science & Technology
114 Pangcheng New Street, Pukou District
210044 Nanjing
P. R. China
zhjiang@nuist.edu.cn

Dr. Zhongfeng Xu

RCE-TEA
Institute of Atmospheric Physics
Chinese Academy of Sciences
100029 Beijing
P. R. China
xuzhf@tea.ac.cn

Prof. Zhaoyong Guan

Key Laboratory of Meteorological Disaster
Nanjing University of Information Science & Technology
114 Pangcheng New Street, Pukou District
210044 Nanjing
P. R. China
guanzy@nuist.edu.cn

ISBN 978-3-540-79241-3 e-ISBN 978-3-540-79242-0

Regional Climate Studies of China ISSN: pending

Library of Congress Control Number: 2008931311

© 2008 Springer-Verlag Berlin Heidelberg

This work is subject to copyright. All rights are reserved, whether the whole or part of the material is concerned, specifically the rights of translation, reprinting, reuse of illustrations, recitation, broadcasting, reproduction on microfilm or in any other way, and storage in data banks. Duplication of this publication or parts thereof is permitted only under the provisions of the German Copyright Law of September 9, 1965, in its current version, and permission for use must always be obtained from Springer. Violations are liable to prosecution under the German Copyright Law.

The use of general descriptive names, registered names, trademarks, etc. in this publication does not imply, even in the absence of a specific statement, that such names are exempt from the relevant protective laws and regulations and therefore free for general use.

Cover design: deblik, Berlin

Printed on acid-free paper

9 8 7 6 5 4 3 2 1

springer.com

Preface

China, located in East Asia, is characterized by monsoon climate, an unique climate type among various climate classification of the world.

There has been long history of regional climate study in China, beginning from late 1890s, represented by a number of scientists, such as Zhu, K. Z., Tu, C. W., Zhu, B. H., Yao, Z. S. and Zhang, B. K., etc. The introduction of modern atmospheric dynamics, synoptic meteorology and numerical modeling into the climate research has made further development of regional climatology in China (e. g. Ye, D. Z., Tao, S. Y., Chao, J. P., and Zeng, Q. C., etc).

In last several decades, the development of regional climate model, application of satellite information and information technique, implementation of continental scale experiments of energy/water balance of land surface and other advanced approaches have significantly promoted the progress of regional climate study in various parts of world.

As one volume of the book series of *Regional Climate Studies*, this book aims to summarize the progress of regional climate study of China mainly in last decade. It focuses on the physical and dynamic characteristics of climate of China based on current researches by applying these advanced approaches, rather than giving detail description of regional climate variables.

The volume consists of 11 chapters, beginning with the general introduction of monsoonal features of climate, followed by the paleo-climate (chapter 2), inter-decadal (chapter 3), interannual (chapter 4) climate variabilities and aridity trend of northern China as a specific regional climate issue (chapter 5). The effects of Tibetan Plateau, and soil moisture of land surface process on the regional climate of China are analyzed to understand the physical basis of climate variation in Chapter 6 and 7. To link with the impact of climate, the climate extremes and climate related disasters are presented in Chapter 8. Chapter 9 is a special one deal with the regional climate modeling. Finally, Chapter 10 and 11 present the projection of future climate and the assessment on impacts of climate variation on water resource and agriculture in China.

We would like to thank Drs Ichtiaque Rasool and Hans-Jurgen Bolle to invite us to make our contributions to the book series of Regional Climate

Studies. Thanks go also to the authors of all chapters for their contributions to the book.

A special thank goes to NUIST for partly support in the drafting process. Finally Dr Xu Z. F. has made great contributions in compiling the manuscripts and making the index of the book.

December, 2007

The Editors

Contents

Chapter 1 Climate of China and East Asian Monsoon 1
1.1 Introduction 1
1.2 Characteristics of the onset of Asian summer monsoon 5
1.2.1 The earliest onset of Asian summer monsoon and the regional characteristics 6
1.2.2 Large-scale characteristics of Asian summer monsoon onset . 10
1.2.3 The importance of Asian-Australian "land bridge" in the onset 16
1.3 Features of vertically integrated moisture transport 17
1.3.1 Seasonal distribution 18
1.3.2 Seasonal transition features 19
1.4 "Climate effect" of the Northeast Cold Vortex and its influence on Meiyu 27
1.4.1 Relationship between the Northeast Cold Vortex and Meiyu rainfall amount 29
1.4.2 Possible mechanisms of the influences of the Northeast Cold Vortex on Meiyu 30
1.4.3 Relationship between SST in the North Pacific and Northeast Cold Vortex 34
1.5 Droughts-floods coexistence (DFC) during the normal summer monsoons in the mid- and lower reaches of the Yangtze River 35
1.5.1 Precipitation distribution features of DFC summers 36
1.5.2 Circulation features of the strong DFC summers 38
1.5.3 SST features of the strong DFC summers 41
1.6 Conclusions and some outstanding issues 42
References 43

Chapter 2 Paleoclimate of China 49
2.1 Introduction 49
2.2 Reconstructed climate of China 50
2.2.1 Loess 52
2.2.2 Ice cores 53
2.2.3 Tree rings (Dendroclimatology) 54

2.2.4 Historical documents 54
2.2.5 Stalagmite 55
2.2.6 Pollen 55
2.2.7 Lake sediments 56
2.3 Climate simulation of the last 1000 years 56
2.3.1 Model description 57
2.3.2 Reconstruction data 57
2.3.3 Model and data comparison 58
2.4 Sensitive simulation of climate in LIA 61
2.4.1 Model description 61
2.4.2 Design of the simulation experiments 62
2.4.3 Analyses of simulation 62
2.5 Palaeoclimate simulations of mid-Holocene and LGM 68
2.5.1 The 6 ka BP climate simulations 70
2.5.2 The 21 ka BP climate simulations 80
2.6 Summary 87
References 89

Chapter 3 Interdecadal Climate Variability in China Associated with the Pacific Decadal Oscillation 97
3.1 Introduction 97
3.2 Interdecadal oceanic anomalies in the North Pacific 99
3.3 Interdecadal atmospheric anomalies in East Asia 101
3.3.1 Winter 101
3.3.2 Summer 103
3.4 Interdecadal climate anomalies in China 103
3.4.1 Winter 105
3.4.2 Summer 105
3.5 Interdecadal change of ENSO's impact on the climate of China . 107
3.5.1 In the developing phase of an ENSO event 107
3.5.2 In the decaying phase of an ENSO event 110
3.6 Summary 113
References 115

Chapter 4 Interannual Variability of Summer Climate of China in Association with ENSO and the Indian Ocean Dipole 119
4.1 Introduction 119
4.1.1 ENSO and its global impacts 119
4.1.2 Understanding the ENSO-China climate relations before 1995 120
4.1.3 Indian Ocean variabilities, especially the Indian Ocean dipole 121
4.1.4 Issues in the recent decades 121

4.2 Precipitation and temperature changes related to ENSO 122
4.2.1 Droughts and floods in China 122
4.2.2 Hot and cold summer climate in China 124
4.3 Circulation changes with ENSO 125
4.3.1 Western Pacific subtropical high 126
4.3.2 East Asian summer monsoon 127
4.3.3 South China Sea summer monsoon 128
4.3.4 Typhoons 129
4.4 Influence of IOD on the East Asian summer monsoon 129
4.4.1 IOD phenomenon 130
4.4.2 IOD teleconnections in the unusual summer of 1994 132
4.4.3 Individual influences of IOD and ENSO 139
4.4.4 Interference of IOD in the ENSO-EASM relation 143
4.5 Concluding Remarks 147
References 149

Chapter 5 Aridity Trend in Northern China 155
5.1 Introduction 155
5.2 Aridity trend on geological time scales 159
5.2.1 Formation of Asia inland arid/semi-arid regions as seen from Leoss deposition 159
5.2.2 Stepwise expansion of desert environment across northern China in the past 3.5 Ma and dry-wet oscillation on earth orbit time scale 163
5.2.3 Aridity trend in northwestern China during last 30 ka as seen from lake sediment records 169
5.3 Aridity trend in last hundred years 171
5.3.1 Dry-wet oscillation on centennial to decadal time scales 171
5.3.2 Evidences of aridity trend from historical documents and instrumental observations 173
5.3.3 Global aspects of aridity trend 176
5.3.4 Semi-arid region – the area with most significant aridity trend 177
5.4 Inter-decadal variability of atmospheric circulation in association with the aridity trend 180
5.4.1 Correlations between North Atlantic Oscillations (NAO) and eastern China wet/dry oscillation 180
5.4.2 Interdecadal variation of aridity trend in northern China associated with the Pacific Decadal Oscillation (PDO) 182
5.4.3 Interdecadal variability of Southern Oscillation and Walker Circulation and their relationships with Asian summer monsoon 184

5.5 Observation and model validation of land-atmospheric interaction in semi-arid region ... 185
5.5.1 Intensified field observation of water, energy and CO2 fluxes over semi-arid area of China ... 185
5.5.2 Validation of land surface model based on field observations over semi-arid area of China ... 194
5.6 Potential human impacts on aridity trend ... 198
5.6.1 Impacts of human activity on river runoff in the northern area of China ... 198
5.6.2 Impact of land surface degradation in northern China on regional climate ... 203
5.7 Conclusions ... 208
References ... 210

Chapter 6 Effects of the Tibetan Plateau on the Climate of China ... 219
6.1 Introduction ... 219
6.2 Climatic features of atmospheric heat source/sink over the TP ... 221
6.2.1 Computational methods of the atmospheric heat source/sink ... 221
6.2.2 Climatological distribution of the atmospheric heat source/sink ... 223
6.2.3 Temporal variation of atmospheric heat source/sink ... 224
6.3 Roles of the TP in Asian monsoon ... 226
6.3.1 Sensible heat driven air-pump (SHAP) over the TP ... 226
6.3.2 Simulation on the dynamic-thermodynamic effect of the TP ... 232
6.4 Plateau snow anomalies and its climate effects ... 236
6.4.1 Climatological features of the winter snow ... 237
6.4.2 Statistical relationship between snow anomaly and precipitation ... 238
6.4.3 Simulations of the effect of snow on precipitation ... 241
6.5 The nature of the South Asia High and its climate effects ... 247
6.5.1 Seasonal variation of SAH ... 248
6.5.2 Bimodality of the SAH in the seasonal cycle ... 249
6.5.3 Climate effects of SAH on the regional climate ... 252
6.6 Seasonal east-west movement of the EASWJ and its association with the diabatic heating over the TP ... 253
6.6.1 Seasonal east-west movement of the EASWJ core ... 253
6.6.2 Bimodality of the EASWJ core in midsummer ... 255
6.7 Stratus generated by the TP and its possible climate effects ... 256
6.7.1 Cloud–radiative forcing over East Asia ... 257
6.7.2 Formation of the nimbostratus and altostratus clouds ... 258
6.7.3 Stratus cloud–climate feedback over the lee side of the TP ... 259

6.7.4 Impacts of the Plateau stratus cloud deck on east China climate 261
6.8 Conclusions 263
References 266

Chapter 7 Soil Moisture Variations and Its Impact on the Regional Climatic Change in China 271
7.1 Introduction 271
7.2 In situ measured soil moisture in China 273
7.2.1 Soil moisture measurement in China 273
7.2.2 Temporal and spatial variation characteristics of soil moisture 274
7.3 Inversion of soil moisture from climate variables and remote sensing data 287
7.3.1 A scheme retrieving soil moisture with climatic variables in Eastern China and its application 287
7.3.2 Soil moisture retrieval from remote sensing data and its application 298
7.4 Relationship between soil moisture and regional climate variation in China 302
7.4.1 Soil moisture and climatic interannual variability 302
7.4.2 Correlation between area average soil moisture and climate variation 305
7.5 Summary and discussions 308
References 309

Chapter 8 Climate Extremes and Related Disasters in China 313
8.1 Introduction 313
8.2 Temperature extremes 314
8.2.1 Maximum and minimum temperatures 315
8.2.2 Warm days and cool days 316
8.2.3 Warm nights and cool nights 318
8.2.4 Hot days and frost days 318
8.3 Precipitation extremes 320
8.3.1 Total precipitation 320
8.3.2 Frequency and intensity of precipitation 321
8.3.3 Extreme precipitation 322
8.3.4 Wet spells 323
8.4 Cyclones 324
8.4.1 Tropical cyclones 324
8.4.2 Extra-tropical cyclones 327
8.5 Droughts 329
8.6 Dust storms 331

8.7 Changes in climate extreme in associated with the mean state..... 335
8.7.1 Changes in temperature extremes and mean temperature..... 336
8.7.2 Changes in extreme and total precipitation 337
8.8 Summary..... 338
References 339

Chapter 9 Regional Climate Modeling of China and East Asia 345
9.1 Introduction 345
9.2 Development of a regional climate model for Asia (RIEMS) and its validation..... 348
9.2.1 Framework of RIEMS 348
9.2.2 Validation of RIEMS..... 353
9.3 Simulation of climate of China and East Asia through inter-comparison of a set of regional climate models..... 355
9.3.1 Project Design 356
9.3.2 Phase one of RMIP..... 357
9.3.3 Phase two of RMIP..... 361
9.4 Study on multi-RCM ensemble of regional climate simulation for Asia 372
9.4.1 Ensemble Methods 372
9.4.2 Mean climate and biases..... 373
9.4.3 Cross validation of ensemble results 376
9.4.4 Conclusions 377
9.5 Effects of increasing greenhouse gases and aerosols on regional climate of East Asia..... 378
9.5.1 Future climate simulated by RIEMS-GOALS under the scenario of increased CO_2 emission 380
9.5.2 Impacts of aerosols on East Asia monsoon climate..... 383
9.6 Impact of human-induced large-scale land cover changes on the East Asian monsoon climate in RCM simulations 390
9.6.1 History of land-cover/-use changes over East Asia..... 391
9.6.2 Design of the numerical experiments 392
9.6.3 Changes of surface dynamic parameters under two vegetation coverages 393
9.6.4 Changes of the East Asia monsoon by human-induced land-cover changes 394
9.6.5 Conclusions 397
9.7 Summary..... 397
References 398

Chapter 10 Projection of Future Climate in China..... 409
10.1 Introduction 409

10.2 Projections of changes in temperature 411
10.2.1 Global climate modeling 411
10.2.2 Regional climate modeling 416
10.2.3 Statistical downscaling 418
10.3 Projections of changes in precipitation 421
10.3.1 Global climate modeling 421
10.3.2 Regional climate modeling 425
10.3.3 Statistical downscaling 427
10.4 Projection of extreme events 428
10.4.1 Extreme temperature 428
10.4.2 Rain and heavy rain days 432
10.4.3 Extreme climate indicators 432
10.4.4 Tropical cyclones 438
10.5 Conclusions and discussions 438
References 442

Chapter 11 Impacts of Climate Change on Water Resources and Agriculture in China 447
11.1 Introduction 447
11.2 Impacts of climate change on water cycle and water resources 447
11.2.1 Impact of climate change on runoff 448
11.2.2 Impact of climate change on evaporation 450
11.2.3 Impact of climate change on water supply-demand balance 451
11.3 Impacts of climate change on agriculture 452
11.3.1 Impact of climate change on cropping system 452
11.3.2 Impact of climate change on crop potential productivity 454
11.3.3 Impact of global warming on crop yield 455
11.3.4 Severe agrometeorological disasters caused by the climate change 456
11.3.5 Impact of climate warming on the crop diseases and insect pests 457
11.3.6 Adaptation to the climate change 459
11.4 Summary and prospect 460
References 462

Glossary (Acronyms) 465

Subject Index 472

Contributing Authors

Chen X.
Department of Atmospheric Sciences, Nanjing University
22 Hankou Road, Nanjing, 210093
China
xchen@nju.edu.cn

Fan L. J.
Institute of Atmospheric Physics, Chinese Academy of Sciences
P. O. Box 9804, Beijing, 100029
China
fanlj@tea.ac.cn

Feng J. M.
RCE-TEA
Institute of Atmospheric Physics, Chinese Academy of Sciences
P. O. Box 9804, Beijing, 100029
China
fengjm@tea.ac.cn

Fu C. B.
RCE-TEA
Institute of Atmospheric Physics
Chinese Academy of Sciences
100029 Beijing
P. R. China
fcb@tea.ac.cn

Guan Z. Y.
Key Laboratory of Meteorological Disaster
Nanjing University of Information Science & Technology
114 Pangcheng New Street
Pukou District, 210044 Nanjing
P. R. China
guanzy@nuist.edu.cn

Guo W. D.
RCE-TEA
Institute of Atmospheric Physics, Chinese Academy of Sciences
P. O. Box 9804, Beijing, 100029
China
guowd@tea.ac.cn

He J. H.
Key Laboratory of Meteorological Disaster
Nanjing University of Information Science & Technology
114 Pangcheng New Street
Pukou District, 210044 Nanjing
P. R. China
hejhnew@jsmail.com.cn

Jia W. J.
RCE-TEA
Institute of Atmospheric Physics, Chinese Academy of Sciences
P. O. Box 9804, Beijing, 100029
China
jiawj@tea.ac.cn

Jiang Z. H.
Key Laboratory of Meteorological Disaster
Nanjing University of Information Science & Technology
114 Pangcheng New Street
Pukou District, 210044 Nanjing
P. R. China
zhjiang@nuist.edu.cn

Li L. P.
KLME, NIM, Nanjing University of Information Science & Technology
114 Pangcheng New Street, Pukou District, Nanjing, 210044
China
liliping@nuist.edu.cn

Ma Z. G.
RCE-TEA
Institute of Atmospheric Physics, Chinese Academy of Sciences
P. O. Box 9804, Beijing, 100029
China
mazg@tea.ac.cn

Ning J. H.
College of Applied Meteorology, Nanjing University of Information Science & Technology
114 Pangcheng New Street, Pukou District, Nanjing, 210044
China

Shen S. H.
College of Applied Meteorology, Nanjing University of Information Science & Technology
114 Pangcheng New Street, Pukou District, Nanjing, 210044
China
yqzhr@nuist.edu.cn

Wang S. Y.
RCE-TEA
Institute of Atmospheric Physics, Chinese Academy of Sciences
P. O. Box 9804, Beijing, 100029
China
wsy@mail.tea.ac.cn

Wang Z. Y.
National Climate Center, China Meteorological Administration
46 Zhong Guan Cun Nan Dajie, Beijing, 100081
China
wangzunya_cma@163.com

Wu Z. W.
LASG, Institute of Atmospheric Physics, Chinese Academy of Sciences, P. O. Box 9804, Beijing, 100029
China
wzw@lasg.iap.ac.cn

Xu Z. F.
RCE-TEA
Institute of Atmospheric Physics
Chinese Academy of Sciences
100029 Beijing
P. R. China
xuzhf@tea.ac.cn

Yan Z. W.
RCE-TEA
Institute of Atmospheric Physics, Chinese Academy of Sciences
P. O. Box 9804, Beijing, 100029
China
yzw@mail.tea.ac.cn

Yang X. Q.
Department of Atmospheric Sciences, Nanjing University
22 Hankou Road, Nanjing, 210093
China
xqyang@nju.edu.cn

Zhai P. M.
Department of Forecasting Services and Disaster Mitigation, China Meteorological Administration
46 Zhong Guan Cun Nan Dajie, Beijing, 100081
China
pmzhai@cma.gov.cn

Zhang Y. C.
Department of Atmospheric Sciences, Nanjing University
22 Hankou Road, Nanjing, 210093
China
yczhang@nju.edu.cn

Zhao D. M.
RCE-TEA
Institute of Atmospheric Physics, Chinese Academy of Sciences
P. O. Box 9804, Beijing, 100029
China
zhaodm@tea.ac.cn

Zhao Z. C.
National Climate Center, China Meteorological Administration
46 Zhong Guan Cun Nan Dajie
Beijing, 100081
China
zhaozc@cma.gov.cn

Zhu Y. M.
Institute of Meteorology, PLA University of Science and Technology
60 Shuanglong Street, Nanjing 211101
China
yiminz@21cn.com

Zou X. K.
National Climate Center, China Meteorological Administration
46 Zhong Guan Cun Nan Dajie, Beijing, 100081
China

Chapter 1 Climate of China and East Asian Monsoon

1.1 Introduction

The East Asian monsoon is the principle component of the Asian monsoon system and plays an important part in the weather and climate in China. The regional flood and drought disasters in summer in China are closely related to the seasonal anomalies of the main rain belt whose progression is significantly influenced by the East Asian summer monsoon (Ding, 1992). The huge floods during Meiyu period in 1991 and 1998 are caused by the anomalies of East Asian summer monsoon, resulting in the property loss of around 100 billion and large casualty, and direct economic loss of 180 billion RMB, respectively (Ding, 1993; NCC, 1998). The East Asian winter monsoon works on the weather and climate in China in the form of cold air, of which the cold wave is the strongest and affects the widest areas, usually accompanying sudden temperature drop and blast and sometimes rain, snow, glitter ice or frost, even disasters when severe (Li, 1955). Therefore, the importance of East Asian monsoon is of self-evidence.

Tao and Chen (1987) provided the circulation model of the East Asian summer monsoon system, showing clearly the members and their allocation (Fig1.1). Circulations of East Asian monsoon and Indian monsoon are associated in some way, but the two systems are independent from each other. In the Indian monsoon system, the monsoonal current, namely southwesterly, comes from the Mascarene High in the Southern Hemisphere (SH), with Somalia jet traversing the equator and advancing from south to north, and the low-frequency waves in the equatorial Indian Ocean propagating from south to north as well. The Indian monsoon regions are influenced by both the tropical circulation and monsoon trough because of the barrier effect of the Qinghai-Tibet Plateau, indicating that the Indian summer monsoon system is a pure tropical circulation system. However, the origin of the monsoonal currents of the East Asian monsoon system is quite different. Seen from Fig1.1, the cross-equatorial southerly in 105°E–120°E from the SH converges with the westerly from the Indian

Ocean and the easterly from the south of the West Pacific subtropical high (WPSH) to form southwesterly which is tropical monsoonal current and southeasterly which is subtropical monsoonal current respectively, providing warm and moist southerly currents for the East Asian monsoon regions including the areas east of 100°E in the East Asian continent, Korea and Japan. These currents are primary water vapor sources of summer rainfalls in East China. The warm and moist currents advancing northward meet the cold air from the middle and high latitudes to form the Meiyu front (subtropical monsoon). The duration of Meiyu period and the total rainfall amounts are not only related to the position, intensity and water vapor transport of the circulation system in the south, but also limited by the circulation in the middle and high latitudes, which is the main difference between the circulations of the East Asian summer monsoon and Indian summer monsoon. That is, the circulation system in the middle and high latitudes has more impacts on the circulation and rainfalls in summer East-Asia (Zhang and Tao, 1998).

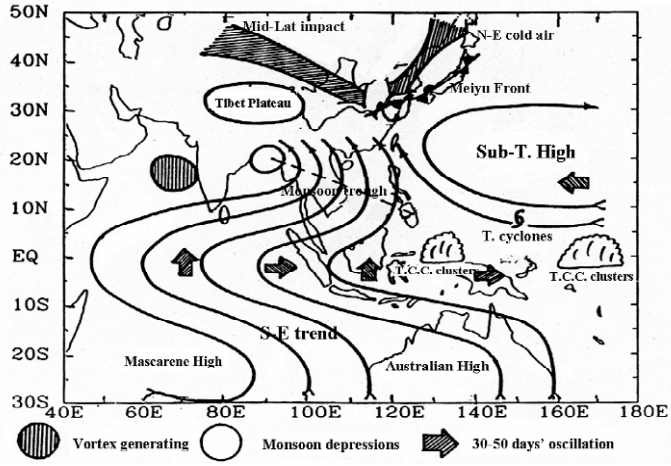

Fig. 1.1 A schematic map of members and circulation characters of Asian summer monsoon system (Zhang and Tao, 1998).

The northward advancement of summer monsoon in East Asia is closely associated with the variation of the WPSH whose intraseasonal oscillation (ISO) from April to July is represented by three mutation processes, corresponding in time to the onset of South China Sea (SCS) monsoon, the onset of Meiyu and the end of Meiyu, respectively.

When the ridge line of WPSH in summer is abnormally more southward or the ridge point is more westward, the circulation of East Asian summer

monsoon is weaker; with an anti-cyclonic circulation at 850 hPa over the tropical areas in East-Asia, a cyclonic circulation in the subtropical areas, the ascending motion at 500 hPa being weak over the tropical areas in East-Asia but strong in the Meiyu front areas, blocking high occurring at 500 hPa over the Okhotsk Sea in the high latitude of East-Asia and leading the cold air from the high latitude to the mid-latitude, and the disturbance in Meiyu front being strong and resulting in more rainfalls in Jiang-Huai Valley in the flood season. On the contrary, when the ridge line of WPSH in summer is abnormally more northward or the ridge point is more eastward, the circulation of East Asian summer monsoon is stronger and the atmospheric circulation systems in East-Asia show the opposite abnormal patterns, with less rainfalls in Jiang-Huai Valley in flooding seasons (Zhang and Tao, 2003).

On the seasonal scale, the intensity of WPSH, its west boundary position and the intensity of South Asian High (SAH) are all closely related to the intensity of the East Asian summer monsoon. Moreover, positions of the north boundary of WPSH and the blocking pattern in Ural are closely associated with rainfall amounts in summer East-Asia (Liu et al., 2004; Wu et al., 2006a,b,c).

In addition to the obvious seasonal variation, the East Asian summer monsoon also has prominent ISO which is related to the onset of summer monsoon (Wu et al., 2006d,e). The low-frequency westerly occurs 2d earlier than the onset of SCS summer monsoon. And its development and westward extension to the east of Philippine play a crucial role in the ISO in SCS, and trigger the outbreak of the summer monsoon (Li, 2004). ISO in the East Asian summer monsoon shows the pattern of wave-train along the coast and is represented by the monsoon surge propagating to the north, which consists of several ISO wet phases. The summer monsoon is established when the ISO wet phase is introduced or develops (Qian et al., 2000; Ju et al., 2005b).

The activities of the atmospheric ISO over SCS and its surrounding areas play an important part in the establishment of the strong East Asian summer monsoon (Li, 2004). When the SCS summer monsoon is strong, a strong ISO field is observed, with a strong cyclonic circulation being over SCS and West Pacific; on the contrary, the weak SCS summer monsoon corresponds to a weak ISO field, with a weak anti-cyclonic circulation being over SCS and West Pacific.

Two preferential modes (30–60d and 10–20d) may play a critical role in the modulation of summer monsoon activities in the East Asian monsoon region. Based on the case study of 1998, it is observed that the SCS summer monsoon is mainly controlled by the 30–60d mode, but it is modu-

lated by 10–20d mode (Ding, 2004; Ju et al., 2005b; Ju and Zhao, 2005). In years with strong East Asian monsoon surge, the impact of the quasi–30–60d oscillation is significant, resulting in more rainfalls in the mid- and lower reaches of Yangtze River; while in years with weak East Asian monsoon surge, the quasi–30–60d oscillation weakens and 10–20d oscillation becomes primary, resulting in droughts in the mid-lower reaches of Yangtze River.

ISO is significant in the Western North Pacific (WNP) monsoon region as well (Wang et al., 2005). Such climatological ISO consists mainly of 30–60d and 10–20d oscillations and the former is predominant. According to the phase-distribution of the convection and low-level westerly in the WNP, it is observed that the low-frequency convection and westerly in the WNP propagates westward and northward, and the convection and active-break cycle of westerly in the WNP are modulated by the low-frequency oscillations of 30–60d and 10–20d to a great extent.

The inter-annual variation of the intensity of East Asian summer monsoon has important impacts on rainfalls in China. There are more or normal Meiyu rainfalls in the mid-lower reaches of Yangtze River in weak SCS summer monsoon years; while there are normal or less Meiyu rainfalls in strong SCS summer monsoon years. And, the route and process of the water vapor transporting to the mid-lower reaches of Yangtze River are different in the early and late onset years of SCS summer monsoon. In the early onset years, the water vapor transports clockwise through Indo-China peninsula to the mid-lower reaches of Yangtze River, and returns to SCS, corresponding to more rainfalls (floods) in Yangtze River valley. While in the late onset years, the water vapor transports anticlockwise from SCS to South China, corresponding to less rainfalls (droughts) in the Yangtze River valley (Wu et al., 2003; Wu et al., 2006a).

The atmospheric circulation of East Asian monsoon and SST field exhibit interdecadal variation as well. East Asian summer monsoon has weakened since 1960s in the interdecadal scale, which has no obvious association with the global warming induced by human activities in the late 20^{th} century, and there are two abrupt changes in mid 1960s and in mid and late 1970s. The interdecadal variation of East Asian winter monsoon is significant as well. The prominent increase of temperature in the north of East-Asia since mid 1970s is directly influenced by the East Asian winter monsoon (Li and Zeng, 2002; Jiang and Wang, 2005; Wu, 2005; Zhao and Zhou, 2005; Zhao and Zhang, 2006).

The interdecadal variation of SCS summer monsoon in its maintenance period shows, divided by the year 1978, the SCS summer monsoon started later and ended earlier in the first twenty years, accompanied by less rain-

falls, weaker convection and weaker monsoon, while summer monsoon started later and ended later in the last twenty years, along with more rainfalls, stronger convection and stronger monsoon. Such variation is significantly influenced by the abrupt change of the atmospheric circulation in late 1970s. The intensity and position of WPSH also show obvious interdecadal variation in mid-1970s, after which the southwesterly influences the lower reaches of Yangtze River and South Korea in summer, producing less rainfalls and droughts in North China and more rainfalls in the Yangtze River and South Korea, and before which the southwesterly may reach North and Northeast China, causing more rainfalls in the north and less rainfalls in the Yangtze River (Dai et al., 2003; Qian, 2005).

1.2 Characteristics of the onset of Asian summer monsoon

The onset characteristics and the possible mechanisms have always been the highlight in the study of Asian summer monsoon (ASM). In particular, over where the earliest onset occurs has been the focus of investigations (Wang and LinHo, 2002), which is also one of the scientific goals of the South China Sea Monsoon Experiment (SCSMEX) (Ding et al., 2004). However, there is still no agreement as to this problem. Four major viewpoints are as follows: First, the ASM initially establishes in the SCS, and then advances northward and westward (Tao and Chen, 1987); second, in eastern Bay of Bengal (BOB) (Wu and Zhang, 1998); third, in Indo-China Peninsula (ICP) or its southern surrounding areas (He et al., 1996; Zhang et al., 2004; Lau and Yang, 1997; Matsumoto, 1997; Webster et al., 1998; Wang and Fan, 1999), and fourth, simultaneously over the whole areas of BOB, ICP and SCS. In a word, where on earth the ASM breaks out earliest needs further study.

The Asian summer (winter) monsoon and Australian winter (summer) monsoon are so closely associated with each other that they can be jointly called the Asian-Australian monsoon system. Therefore, the seasonal transition of the Asian monsoon, the interaction between the Northern and Southern Hemispheric atmospheres and the seasonal migration of the tropical convection are indivisible. The Maritime Continent (MC), including Sumatra and Kalimantan etc., has the strongest tropical convection in the world, and the seasonal migration of Sumatra convection is well related to the onset of summer monsoon in ICP (He et al., 1996). If ICP and MC are considered as Asian-Australian “land bridge” (He et al., 1996;

Chang et al., 2004; Wang et al., 2004), the seasonal migration of the Sumatra convection along the "land bridge" is exactly the manifestation of the primary driving forcing of summer monsoon. Therefore, it is of importance to fully comprehend the role of Asian-Australian "land bridge" in the onset of ASM.

1.2.1 The earliest onset of Asian summer monsoon and the regional characteristics

As the onset of summer monsoon is always accompanied with convective rainfalls, and, low TBB can figure convective clouds and rainfalls, TBB data are used to discuss the characteristics of seasonal transition in Asian-Australian monsoon region and the initial onset of ASM. Fig1.2 shows the horizontal distribution of the climatological TBB from March to June.

The distribution of TBB in March (Fig1.2a) is still the same as in January (figure omitted). There is a high TBB belt in the subtropics in Southern Hemisphere (SH) with the ridgeline at 25ºS and core in central Australia, corresponding to the austral subtropical high belt and the Australian high. There is also a high TBB belt in the boreal subtropics, with the ridgeline at 15º–20ºN and centers in West Pacific, SCS and northern BOB, corresponding to the boreal subtropical high belt and centers of discrete anti-cyclones. In between, a low TBB belt locates in the tropics, with low centers being in MC and the minimum in Sumatra. Moreover, a TBB trough extends from the New Guinea low center to North Australia, in correspondence with the summer monsoon there.

However, the characteristics change significantly in April (Fig1.2b): (1) the high TBB belt in the subtropics in Northern Hemisphere (NH) breaks in ICP (100ºE–110ºE, 10ºN–20ºN) (280K is the threshold), and an obvious trough extends from the low center in Sumatra to this region, connecting with the low TBB belt in the mid-latitude; (2) the high TBB in Australia moves northward notably (the axis moves to 20ºS), so the trough from New Guinea to northern Australia disappears. Those changes imply the northward movement of the entire circulation system, the first northward crush of the tropical convection into the subtropical high belt along ICP, and the disappearance of summer monsoon in Australia along with the seasonal change and the regional response to solar radiations, signifying the start of the seasonal transition of large-scale circulation in middle and low latitudes in the Asian-Australian monsoon region.

In May (Fig1.2c), it is noticeable that: (1) the eastern part of TBB high belt in the boreal subtropics retreats eastward rapidly, and the convection

from Philippine to SCS begins to flare up; (2) the low TBB center in Sumatra moves northwestward, strengthens and expands to occupy ICP, with the high center in North BOB shifting northwestward rapidly to the region around (80ºE, 25ºN). These changes indicate that the monsoonal convection has been fully established over ICP and BOB.

In June (Fig1.2d), the high TBB belt in West Pacific continues to retreat eastward along with the obvious jump of the ridge line to around 22ºN. There are two low centers in the low belt to the north of the high belt, lying in the lower reaches of Yangtze River and the southern Japan, respectively. They are in correspondence with Meiyu in China and Baiu in Japan, whose frontal structures and characteristics have been thoroughly studied (Gao et al., 2002a,b). The SCS-Philippine has been controlled by a strong low center, showing the summer monsoon has been fully established in SCS-West Pacific. The low center over Sumatra in winter has disappeared. A large strong low center appears in North BOB in place of the high center in winter, indicating that the summer monsoon has been fully established from BOB to India.

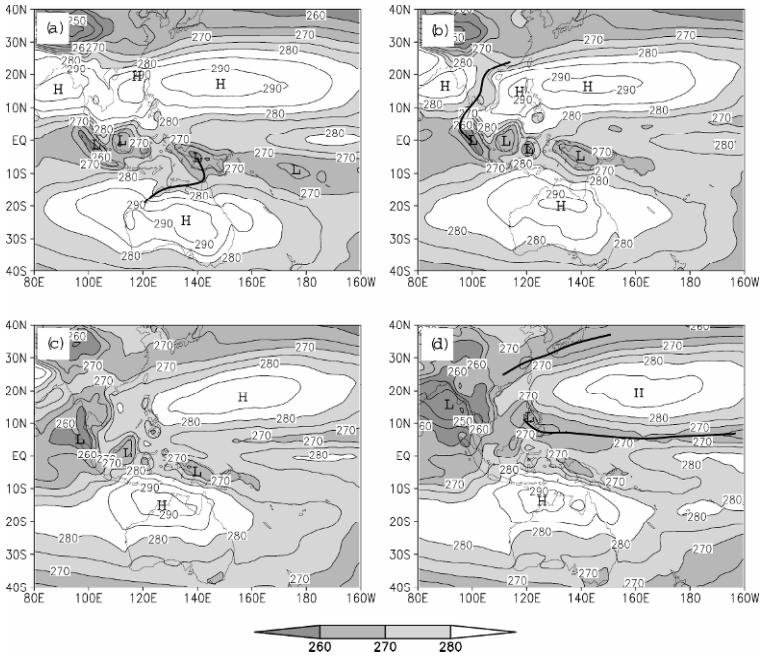

Fig. 1.2 Distributions of climatological TBB in (a) March, (b) April, (c) May, and (d) June. The thick solid line is the axis of low belt and areas of TBB<280K are shaded. (Units: K)

To sum up, it is the northward progression of the tropical convection in Sumatra that leads to the break of the high TBB belt in ICP and a series of succeeding events, resulting in the onset of ASM.

Fig. 1.3a shows the time-longitude section of TBB along (10ºN–20ºN). It can be seen that the convection illustrated by low TBB flares up initially over ICP, and then extends to the east and west. If TBB<275K (shaded areas) is taken as the sign of active convection, the onset of convection over eastern BOB (east of 90ºE) is one pentad earlier than in SCS. In Fig. 1.3b, the meridional temperature gradient overturns earliest over ICP (100º–110ºE), then over the eastern BOB and SCS, and last over the western BOB. Seen from Fig. 1.3c, the vertical shear of zonal wind reverses almost simultaneously over ICP and BOB, earlier than that over SCS. This course is in agreement with the development of BOB trough and the eastward extension of the southwesterly during the onset of the Southeast Asian summer monsoon. Above results indicating the simultaneous onset of summer monsoon over BOB, ICP and SCS in the 27^{th}-28^{th} pentad, claimed by Qian et al. (2004), coordinate the disputes on the earliest onset area.

According to above results, it is true that the convection first bursts out over ICP, which is closely associated with the seasonal migration of tropical convection over Sumatra along Asian-Australian “land bridge”. It will be further discussed in the following part.

In order to discuss the characteristics of the summer monsoon onset and their differences in various regions, the time-latitude sections of climatological TBB along 80ºE, 100ºE, 120ºE and 140ºE are computed (not shown), respectively.

The characteristic of the summer monsoon onset in East India (west of BOB) is that the low TBB belt propagates northward gradually from the equator in early May, and a low center is formed in East India in early and mid-June presenting the onset of Indian summer monsoon. East TP and Southeast Asia turns to be overlaid by low TBB belt from high TBB belt in early and mid-May, indicating that the onset of summer monsoon in Southeast Asia is one month earlier than in India. In addition, there is also a low belt from June to September in East TP (around 32ºN), separated from the low belt in Southeast Asia (15ºN) by a relatively high belt. This means the summer monsoon over East TP is relatively independent of that over Southeast Asia, unlike the summer monsoon over West TP which is the northward extension of Indian summer monsoon. The rapid transition from high TBB belt to low TBB belt in mid-May over SCS (12ºN) denotes the onset of summer monsoon over SCS. Furthermore, there is a low belt over East China in June, corresponding to the subtropical summer mon-

soon rain belt in China (Meiyu). The high belt between them corresponds to the West Pacific subtropical high. A strong low center appears around the equator from December to February, and extends southward to the west of North Australia, denoting the prevalence of Australian summer monsoon in SH. Along the longitude of Japan, West Pacific and the eastern part of North Australia, the subtropical high shows an obvious seasonal cycle of meridional fluctuation. There are low belts on both sides of the subtropical high, with the northern one corresponding to Baiu in Japan and the southern one to the West Pacific summer monsoon. A low belt controls North Australia from December to March, which embodies the prevalence of North Australian summer monsoon.

In general, three crucial features can be drawn as follows: (1) The summer monsoons over East India and Southeast Asia are established progressively along with the rapid northward migration of the low TBB belt at equator, reflecting the seasonal cycle of tropical convection. However, the onset of summer monsoon over SCS and West Pacific are quite different. The establishment of SCS summer monsoon is simultaneous in a wide range of 20 latitudes, that is, its abrupt behavior is much more obvious than India and Southeast Asia summer monsoons. This is directly associated with the rapid eastward retreat of the subtropical high belt after break (He et al., 2002). (2) Besides the low TBB belt over SCS-West Pacific, there is another low belt to the east of 100ºE, i.e. the subtropical monsoon rain belt in China-Japan (Meiyu in China and Baiu in Japan). The East Asian monsoon system includes not only tropical summer monsoon, but also subtropical monsoon (Zhu et al., 1986) and is more complex than Indian monsoon system. (3) The tropical summer monsoon is initially established in the longitude of ICP, and then advances eastward and westward, respectively. What processes and mechanisms result in such characteristics? Further discussion will be presented in the following section.

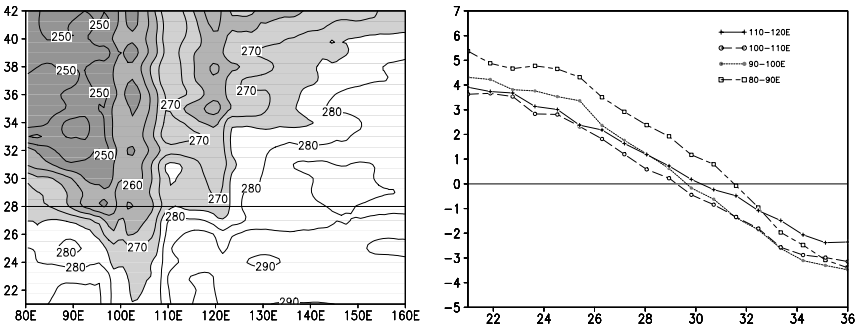

(a) (b)

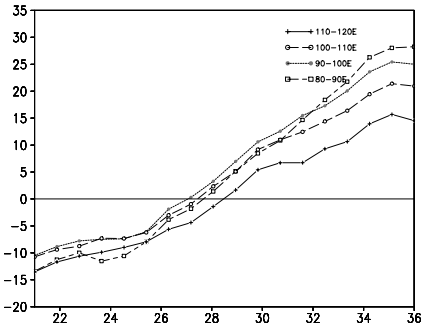

(c)

Fig. 1.3 (a) Time-longitude section of climatological TBB (10ºN–20ºN). Areas of TBB≤275K are shaded. (Units: K) (b) Climatological evolution of the meridional temperature difference (5ºS–5ºN minus 20ºN–30ºN) at 500 hPa. (Units: degC) (c) Climatological evolution of the zonal wind shear (850 hPa minus 200 hPa) in low-latitude (10ºN–20ºN). (Units: m s^{-1})

1.2.2 Large-scale characteristics of Asian summer monsoon onset

According to the study of Qian et al. (2004), the tropical Asian summer monsoon to the east of 90ºE bursts simultaneously and abruptly firstly over the whole area in BOB, ICP and SCS in the 27th–28th pentad. While to the west of 90ºE, the onset of summer monsoon over Indian peninsula and Arabian Sea is later, firstly to the south of 10ºN and proceeding northward gradually. Thereby, from a large-scale viewpoint, the onset of the tropical summer monsoon occurs earliest over SCS and its surrounding areas. After then, the large-scale circulation, water vapor transportation and convection over Asian-Australian monsoon regions have changed significantly (Ding, 2004). We have ever discussed the climatological characteristics of the onset of SCS summer monsoon (He et al., 2002), and further details will be provided below.

Fig. 1.4 shows the upper and lower circulation fields before the onset of SCS summer monsoon (4th pentad of April) and during the onset (4th pentad of May). The SAH center at 200 hPa lies in the ocean to the east of Philippine in the 4th pentad of April, and moves rapidly to southern ICP in the 6th pentad of April. It jumps from south of 15ºN to the north, and extends westward in the 2nd–4th pentad of May with the main body over SCS, ICP, BOB, Indian peninsula and Arabian Sea at 10ºN−25ºN. After the 5th pentad of May, the SAH continues to move northwestward to the north of 20ºN.

The subtropical high at 500 hPa distributes zonally along 15ºN with two centers in Philippine and West Arabian Sea, respectively (Fig. 1.4c), while the relatively low region is over BOB. The pattern changes on the 2nd pentad of May (Figure omitted), with the subtropical high belt tending to break, a closed cyclonic circulation (Sri Lanka vortex) appearing around (80ºE, 5ºN) and tending to extend northward, and the trough in northern BOB strengthening. In the 4th pentad of May, when SCS summer monsoon bursts out, Sri Lanka vortex combines with the trough over North BOB to form the well-known BOB trough (Fig. 1.4d). The subtropical high belt breaks completely with its eastern part retreating eastward and its western part controlling areas to the west of Arabian Sea, so India is controlled by northwesterly.

At 850 hPa (Fig. 1.4e, 1.4f), the splitting of the subtropical high belt, the rapidly eastward (westward) withdrawal of its eastern (western) part, and the formation and deepening of the BOB trough are similar to those at 500 hPa, but are more complex and a bit earlier. In particular, in mid-April, there is a cyclone in SH forming twin cyclone straddling the equator with the Sri Lanka vortex. In between, the equatorial westerly accelerates. In the 4th pentad of May, the Sri Lanka vortex moves northward into the BOB trough with the circulation center disappearing. The equatorial westerly between BOB trough and the cyclone in SH is much stronger, originated from mid-latitude northwesterly over Arabian Sea and cross-equator flow from Somali. And the westerly flows to ICP-SCS region and converges at SCS with the cross-equatorial current from North Australia and the returning current from the southern part of West Pacific subtropical high. Probably, it is the frame of three currents that leads to the complexity of the onset course of SCS summer monsoon, furthermore arises controversies.

The meridional temperature gradient and vertical shear of zonal wind in middle and low latitudes in Asia have also converted corresponding to changes of large-scale circulations (see Fig. 1.3). Therefore, it may be believed that the onset of SCS summer monsoon is not a local phenomenon, but a prominent large-scale event that occurs earliest during the seasonal transition of the Asian-Australian monsoon region and the onset course of Asian summer monsoon. In this sense, it is reasonable that the Asian summer monsoon is established earliest over SCS, as claimed by Tao and Chen (1987).

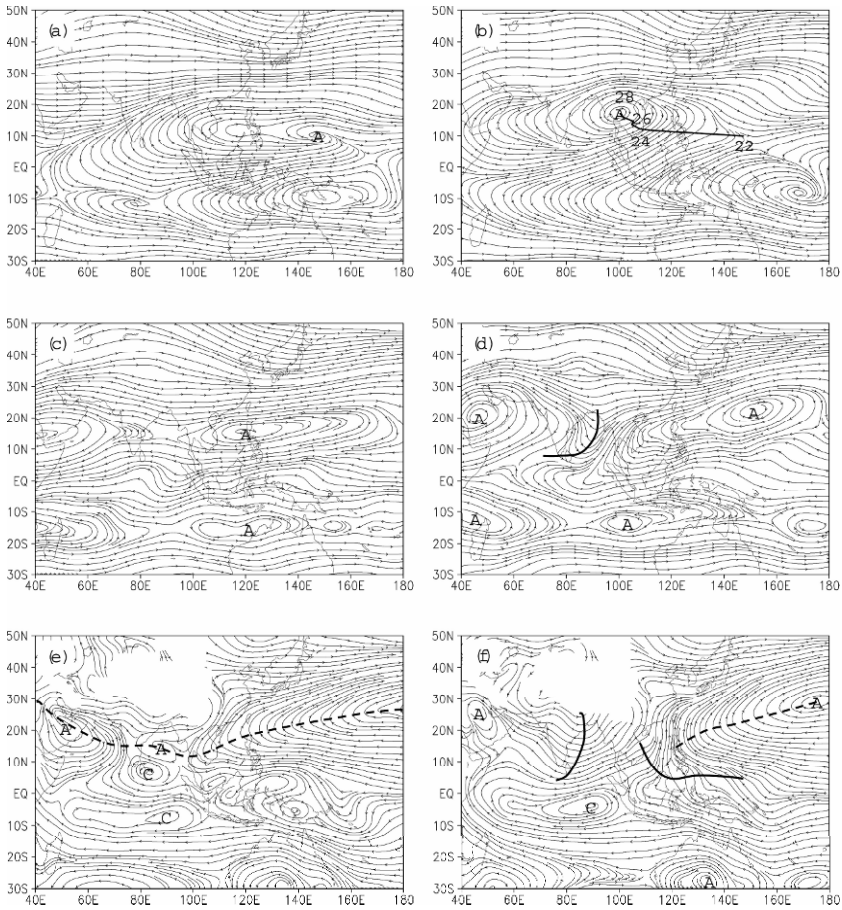

Fig. 1.4 Climatological circulation fields before and after the onset of South China Sea summer monsoon at (a),(b) 200 hPa, (c),(d) 500 hPa, and (e),(f) 850 hPa. (a), (c) and (e) for the 4th pentad of April; (b), (d) and (f) for the 4th pentad of May. The thick solid line in (b) denotes the movement of South Asia High center; the numbers on it is the pentad when the center is there. The thick solid lines in other figures are trough lines, and dash lines are the ridge line.

The relationship between the movement of SAH and the onset of ASM is widely accepted. Qian et al. (2004) especially emphasized the correlation between the position of SAH center and the onset date of ASM. It can be seen from Fig. 1.4 that the SAH advances westward rapidly to South ICP during the 4^{th}–6^{th} pentad of April, then moves northward, and summer monsoon is established over SCS afterwards. Then, why does the SAH advance westward rapidly? Why does it move northward along ICP?

Fig. 1.5 shows the variation of SAH at 150 hPa in the 5^{th} and 6^{th} pentad

of April and the vertical section of apparent heating ratio in the 5th pentad of April. The SAH disintegrates into two centers in the 5th pentad of April, lying over East and West Philippine, respectively. In the 6th pentad of April, the center in the east weakens and disappears, while the west one strengthens and moves westward to South ICP. Hence, the rapid westward progression of SAH during the 4th–6th pentad of April is actually a process of disintegration and reestablishment. It can be seen from Fig. 1.5c that there is a heating center (the apparent heating ratio is greater than 2 degK day^{-1}) at mid-upper troposphere above South ICP (7.5ºN–15ºN, 105ºE) in the 5th pentad of April. The SAH center at 150 hPa is located exactly above the heating center in the next pentad, implying the great attribution of the upper latent heating to the reestablishment or the rapid westward movement of SAH. It is noticed that the convection over Sumatra strengthens and proceeds northward rapidly in late April and early May. Therefore, we suppose with venture that there are some inner connections among the rapid northward progression of convection over Sumatra, the outbreak of convection over ICP and the rapid westward movement of SAH.

Fig. 1.6 presents the composite circulation at 850 hPa with the date when the subtropical high belt splits (Wen et al. 2004) as the reference point. Two pentads before the belt breaks, there is still a zonal subtropical high belt over South Asia, and twin cyclones on both sides of the equator near 80ºE. In the pentad when the subtropical high belt breaks (i.e. pentad 0), Sri Lanka vortex enters into the trough region and deepens the trough. The southwesterly in front of the trough arrives at ICP, but the summer monsoon has not yet been established over SCS where is still controlled by the WPSH. As the WPSH withdraws eastward rapidly to the east of Philippine two pentads later, the summer monsoon is fully established over SCS. It can be observed that a series of events, such as the appearance of twin cyclones, the northward movement of Sri Lanka vortex, the formation and development of BOB trough, the splitting of zonal subtropical high belt and the rapid eastward withdrawal of WPSH and so on, lead to the onset of summer monsoon over SCS. It is also clear that the onset of SCS summer monsoon is the process that the southwesterly advances from west to east rather than from south to north (at least it is the case in climatology), which helps to explain why SCS summer monsoon is established simultaneously in a wide range of 20 latitudes.

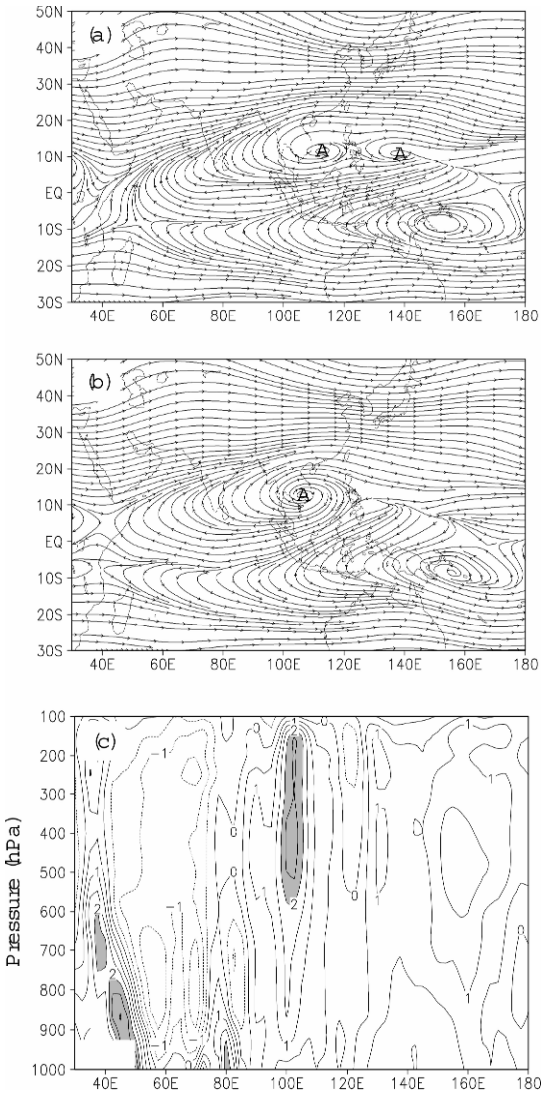

Fig. 1.5 Climatological circulation fields at 150 hPa in the (a) 5th pentad and (b) 6th pentad of April. (c) Vertical section of heating ratio in the 5th pentad of April averaged in (7.5ºN–15ºN), and areas of heating ratio greater than 3degK day^{-1} are shaded. (Units: degK day^{-1})

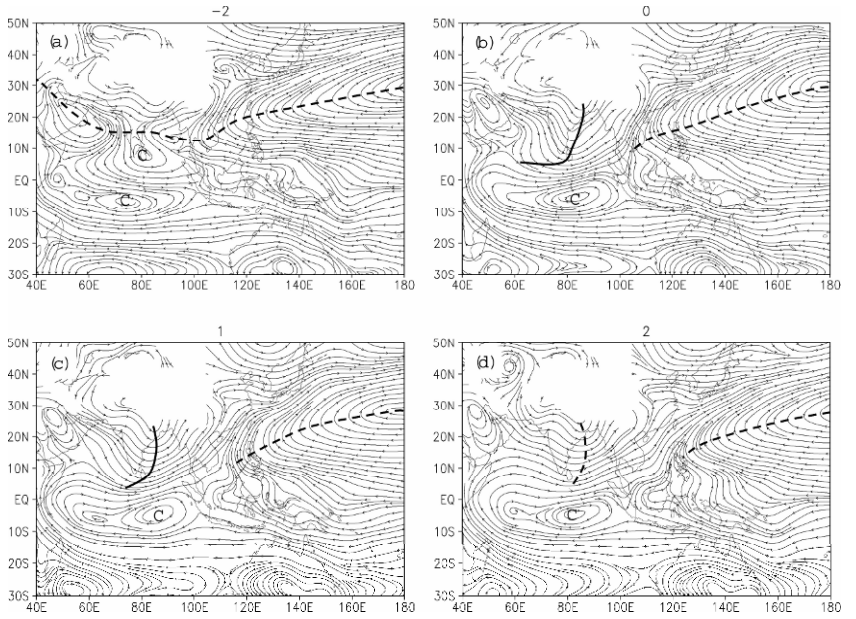

Fig. 1.6 Composite circulation fields at 850 hPa with the splitting dates of the subtropical high belt as reference point. (a) Pentad –2, (b) Pentad 0, (c) Pentad +1, and (d) Pentad +2. The dashed line is the ridgeline of the subtropical high, and the solid line is the trough line.

The composite time sections of the zonal wind at 850 hPa and OLR with the onset date of SCS summer monsoon as reference point are computed (not shown, He et al., 2003). Before (after) the onset of monsoon, the SCS is controlled by the easterly (westerly) and high (low) OLR, exactly accordant with the onset characteristics of summer monsoon. In addition, the westerly and low OLR propagate from the equatorial Indian Ocean (80ºE) to ICP and SCS, which are associated with the activating of the BOB trough and the strengthening of the westerly in the equatorial Indian Ocean. It is remarkable that the westerly and low OLR from South China propagate southward during the onset of monsoon, which might be the manifestation of the southward movement of South China stationary front triggering the onset of SCS summer monsoon (Chang and Chen, 1995). Liu et al. (2002) have stressed that the convective latent heat release may trigger two-dimensional asymmetric Rossby wave train after the onset of BOB summer monsoon. This Rossby wave train is also favorable for the southward movement of the South China stationary front. In a word, the interactions between mid-latitude and low latitude during the onset of SCS summer monsoon also attribute to the abrupt features in the SCS summer

monsoon onset.

1.2.3 The importance of Asian-Australian "land bridge" in the onset

We have discussed a series of processes including the northward progression of the tropical convection over Sumatra, the rapid westward movement of SAH to South ICP, the activating of convection over ICP and the subsequent splitting of subtropical high belt, the establishment and deepening of the BOB trough and the onset of SCS summer monsoon. How are they connected with each other? What is the possible mechanism? Then, we'll discuss them in this section.

Fig. 1.7 shows the time sections of climatological (1980–1997) low TBB and CMAP rainfalls along the Asian-Australian "land bridge". It can be seen that the low TBB over Sumatra (103ºE, 3ºS) in winter moves to 3ºN in April, proceeds northward rapidly in May–June, reaches its northernmost position in July–August, and retreats to near the equator in September. This seasonal cycle of the tropical convection is the manifestation of the primary driving forcing of monsoon. It is the movement of the convective center along "land bridge" from winter to summer that denotes the onset of summer monsoon over ICP, east of BOB, SCS and India afterwards.

The tropical convection over Sumatra proceeds northward rapidly and strengthens in late April and early May when the SAH advances westward rapidly to South ICP. Thereby, it is reasonable to take the rapid northward progression of convection over Sumatra as a critical event of the onset of ASM. Time series of the rapid northward shift of the tropical convection were determined to discuss its relationship with the activating of convection in ICP, the splitting of subtropical high belt and the onset of SCS summer monsoon (Wang et al., 2004). The interannual variation in the rapid northward shift of the tropical convection is in good agreement with that of the outbreak of convection over ICP, with the correlation coefficient between them being 0.5243. Additionally, in most years, the beginning date of the latter tends to lag behind that of the former. Consequently, the rapid northward shift of convection may influence the activating of convection in ICP. Furthermore, the activating of convection in ICP, the splitting of subtropical high belt and the onset of SCS summer monsoon are so well connected, with the coefficient of the former two being 0.7263 and the latter two 0.7206. It can be concluded that these events have some inner connections and temporal sequences, and the seasonal movement and rapid northward progression of tropical convection may be an important triggering mechanism.

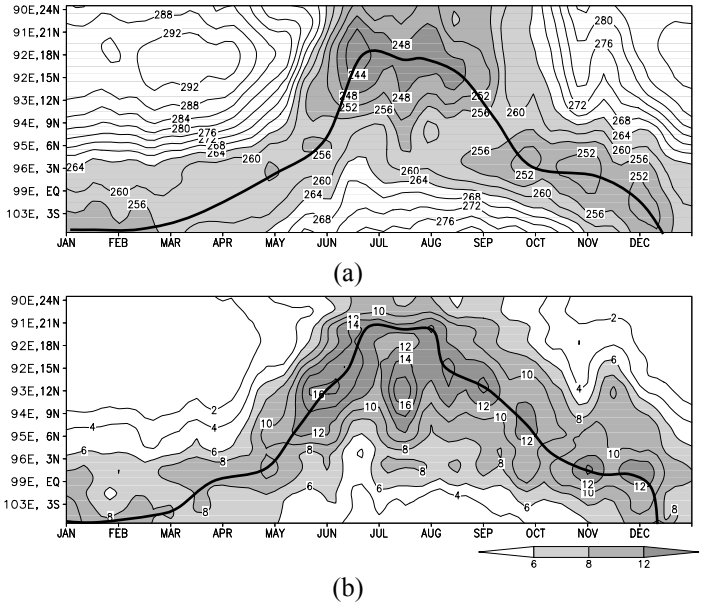

Fig. 1.7 Climatological (1980–1997) time sections of (a) TBB (units: K) and (b) rainfalls (units: mm day−1) along "Asian-Australian land bridge" from (105ºE, 5ºS) to (90ºE, 25ºN). In (a), areas of TBB≤265K are shaded, the thick solid line is the axis of low TBB. In (b), areas with rainfalls more than 6 mm day^{-1} are shaded, and the thick solid line is the axis of high rainfalls.(adopted from Wang et al., 2004)

1.3 Features of vertically integrated moisture transport

Moisture transport, especially the vertically integrated moisture transport (VIMT), is directly associated with monsoon rainfalls. The moisture carried by monsoon plays an important role in the moisture balance in the monsoon regions (Xu, 1958; Xie and Dai, 1959), therefore, investigations on moisture transport have always been in the highlight (He and Murakami, 1983; Tang et al., 1985; Wu, 1990; Ding 1995). Many recent studies have pointed out that the moisture transport by the southerly in summer monsoon influences greatly rainfalls in China (Huang et al., 1998; Zhang, 2001; Xie et al., 2001; Xu et al. 2002; Ding and Sun, 2002; Qiao, 2003). However, as

to moisture transport, some kinds of improper treatment may confuse the results. For example, some studies employ the moisture transport on only one level (e.g., 850 hPa level) or integrate it from 1000 hPa level. Actually, these methods contain serious errors over mountainous terrain, thus can not provide the true information (Zhou et al., 2004). Furthermore, instead of the daily data, some utilize monthly mean horizontal wind and specific humidity to calculate the monthly mean moisture flux, which may neglect the contribution of the transient components ($\overline{q'\tilde{V}'}$) that is also of importance sometimes. Therefore, this section calculates the daily VIMT integrated from the surface to 300 hPa, and the pentadly and monthly mean VIMT. Then on the basis of these data, the key periods, the key regions and the key symptoms in the seasonal transition of VIMT are discussed.

1.3.1 Seasonal distribution

The total vertically integrated water vapor flux vector Q can be expressed as:

$$Q = -\frac{1}{g}\int_{p_s}^{p} qU \, dp \tag{1.1}$$

Where g is the acceleration of gravity, P_s represents surface pressure, and P stands for top pressure which is 300 hPa here. The amount of specific humidity above 300 hPa is poorly known and therefore is not considered (Kalnay et al., 1996). In the tropics, specific humidity above 300 hPa is at least two orders smaller than that near the surface, and moisture transport is therefore of negligible influence to the calculation of total VIMT (Fasullo and Webster, 2003). q is specific humidity, U is horizontal wind vector, and the unit of Q is $kgm^{-1}s^{-1}$. Further, the pentadly and monthly values will be calculated using daily data. It should be kept in mind that the pentadly VIMT are constructed by the principle that the last pentad in any month always covers the period from the 26th to the end of the month, so it always contains 6 pentads for a calendar month (i.e. 72 pentads for a year), and it is quite convenient to confirm the month corresponding to the pentadly mean.

The climatologically seasonal distribution of VIMT is given in Fig. 1.8. The most prominent features in winter are four zonally oriented VIMT belts over the Asian-Australian monsoon region (Fig. 1.8a): (i) The easterly VIMT belt in the tropical area (5°N–10°N) is the strongest of the four. (ii) Another easterly one confined in the 15°S–25°S latitudinal band exhib-

its discontinuous feature. (iii) The westerly VIMT belt in the 5°S–10°S latitudinal band is associated with three significant inter-hemisphere VIMTs (around the 80°E, 105°E and 130°E, respectively). (iv) The last one which is the weakest is transported by the mid-latitude westerly from the northern Arabian Sea to West Pacific.

In summer (Fig. 1.8c), a 'great moisture river' (GMR) which originates from the Southern Hemisphere crosses the equator along the Somali coast, goes through the Arabian Sea, India and BOB, and then extends northeastward from SCS to East China, Korea, Japan and Western North Pacific (The distribution bears great similarity to that of Chen (1985), Park and Schubert (1997) and Simmonds et al. (1999)). This GMR pools together three moisture transport belts including the cross-equatorial one from the Southern Hemisphere and the southeasterly VIMT from the southern periphery of WPSH.

In the transitional seasons, the inter-hemisphere moisture exchanges are rather weak, which indicate weak coupling between the two hemispheres (Fig. 1.8b and 1.8d). Also noted are the asymmetric features between the two transitional seasons. For example, the mid-latitude westerly VIMT in the Northern Hemisphere is prominent in spring, but only exists in the central tropical Indian Ocean in autumn. And the southwesterly (northeasterly) VIMT prevails over the Indochina region in spring (autumn).

1.3.2 Seasonal transition features

It can be noted from Fig. 1.9 that the transitional process from boreal winter to summer contains several stages as follows: Before the 3rd pentad of Feb., the VIMT pattern in the Asian-Australian monsoon region has already reached its peak stage of winter pattern mainly characterized by the four pronounced southward cross-equatorial VIMTs along the Somali coast, 80°E, 105°E and 130°E (Fig. 1.9a). In the 4th (figure omitted) and 5th pentad of Feb. (Fig. 1.9b), the southward cross-equatorial VIMT nearly disappears along 80°E and the Somali coast, thus leading to serious weakness of the westerly VIMT over the tropical southern Indian Ocean (Fig. 1.9c). In the 3rd pentad of Mar., four dramatic changes occur simultaneously, heralding the collapse of winter pattern and the commencement of transition from winter to summer (see changes from Fig. 1.9c to Fig. 1.9d): the southerly VIMT exceeding 100kgm^{-1}s^{-1} appears over the Indochina Peninsula; the southward cross-equatorial VIMT weakens strikingly along 105°E and 130°E, and a continuous easterly VIMT belt forms in the 15°S–25°S latitudinal band. In late Mar. (Fig. 1.9e–f), the basic features of the spring transition have already been established (Fig. 1.8b), with en-

hancement of the southerly VIMT established over the Indochina region, disappearance of the southward cross-equatorial VIMT and the westerly VIMT over north of the Australian continent, and also splitting of the Asian tropical easterly VIMT belt over the Sri Lanka.

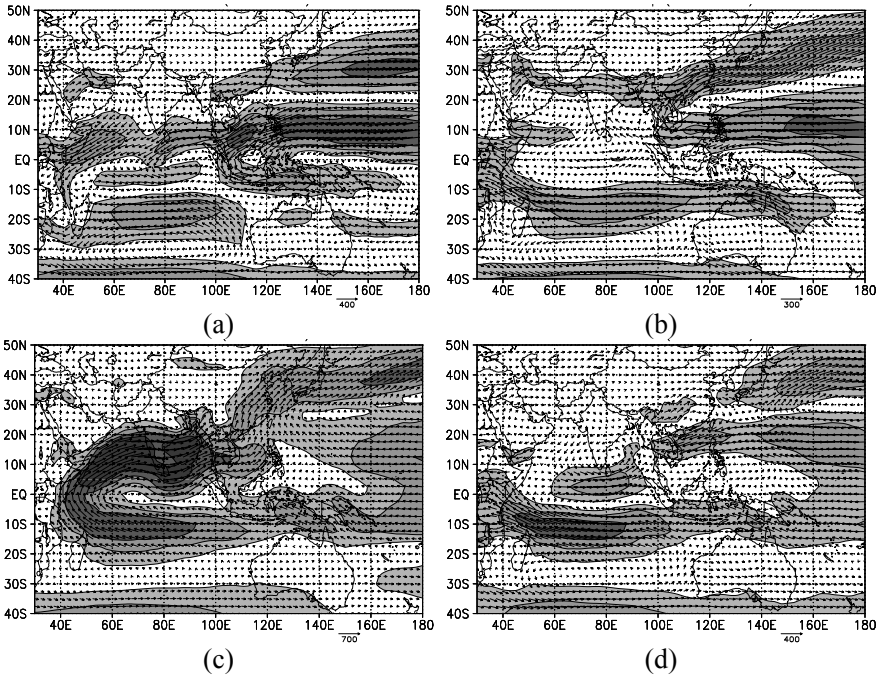

Fig. 1.8 Seasonal distribution of the VIMT ($Kgm^{-1}s^{-1}$) over the A-AM region in Jan (a), Apr (b), Jul (c) and Oct (d). The climatology for VIMT is based on NCEP/NCAR data from 1957 to 200l and the absolute value of VIMT>100Kg m^{-1} s^{-1} is shaded, and the shading interval is 100 Kg m^{-1} s^{-1}.

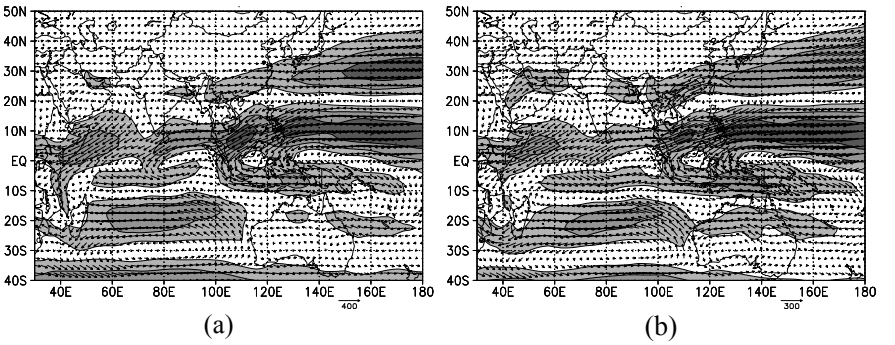

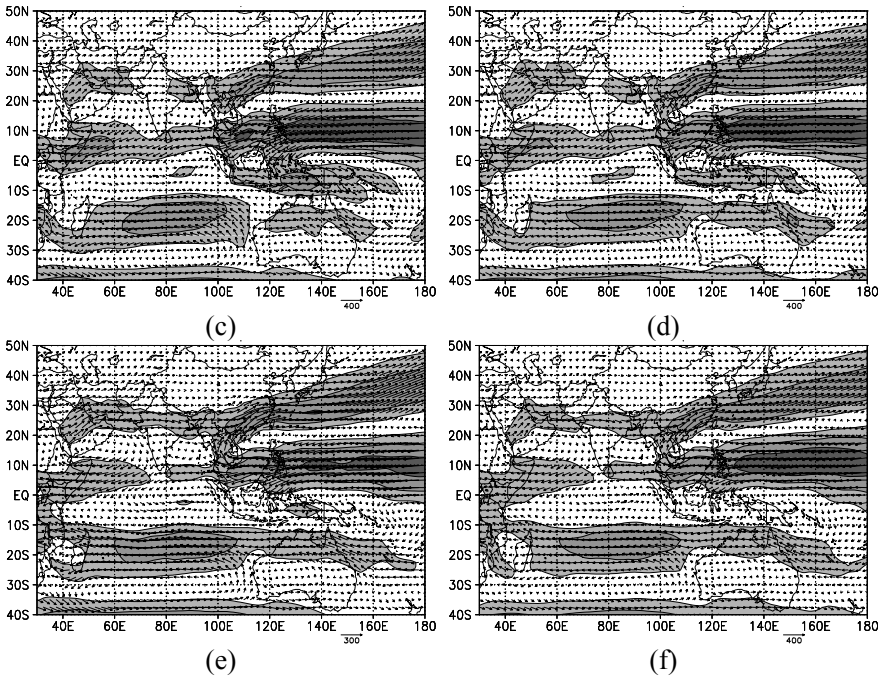

Fig. 1.9 The VIMT distribution in the seasonal migration from winter to summer. Figures from (a) to (e) exhibit the distribution in the 3rd pentad of Jan, the 5th pentad of Feb, the 2nd, 3rd, 5th and 6th pentad of Mar, respectively.

However, the ending date of Asian winter monsoon defined by the VIMT here is one pentad later than that by Matsumoto (1997). It is probably resulted from the different definition standard or covering period of datasets.

Base on the pentadly evolution of VIMT, the chain of remarkable events before the onset of SCS summer monsoon may be identified bellow: in late Apr. (Fig. 1.10a), a moisture low vortex around the Sri Lanka (hereafter referred to as the 'Sri Lanka low vortex') becomes active, which may greatly favor the acceleration and eastward propagation of the southwesterly VIMT in the tropical Indian Ocean. Around early and mid-May (Fig. 1.10b, c), with initiation of the northward cross-equatorial VIMT off the Somali coast (i.e. the Somali VIMT jet) and expansion and northward migration of the 'Sri Lanka low vortex', the southwesterly VIMT propagates further eastward through the Indochina region, the northern SCS and the Southern China, and merges with the other two VIMTs, namely, the mid-latitude westerly one and the southerly one flowing along southern periph-

ery of the WPSH from the Indochina region to the Southern China. However, the typical summertime features such as the establishment of the 'GMR' pattern are not integrated in this period when the westerly VIMT over the equatorial 50°E–60°E still keeps disconnected, the SCS region is under control of WPSH ridge and the SCS summer monsoon is not established yet. But one pentad later, in the 4th pentad of May (Fig1.10d), with rapid eastward retreat of the WPSH from SCS and domination of the southerly VIMT over the whole SCS, the 'GMR' transport pattern occurs and manifests an impressive onset feature of the SCS summer monsoon, though the inter-hemisphere VIMT near 105°E is still very weak.

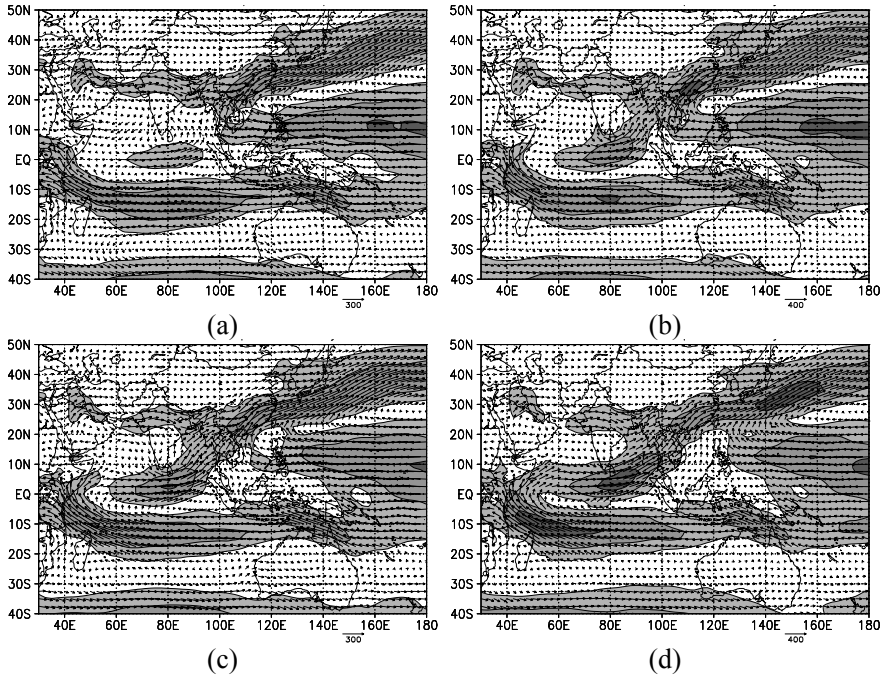

Fig. 1.10 Same as Figure 3.2, but for the period before the onset of the SCS summer monsoon. Figures from (a) to (d) exhibit the distribution in the 6th pentad of Apr, the 2nd , 3rd and 4th pentad of May, respectively.

As shown in Fig. 3.11, after the outbreak of the SCS summer monsoon, along with a rapid intensification of the Somali VIMT jet, the southwesterly VIMT in the tropical Indian Ocean undergoes considerable intensification and expansion along both northward and eastward routes to overcast the northern part of the Arabian Sea, the Indian Peninsular and the BOB around the 1st pentad of Jun. (Fig. 1.11a). Subsequently, with prominent re-

inforcement of the cross-equatorial VIMT around 105°E in mid-Jun., rapid expansion of the strong 'GMR' along northward and eastward routes simultaneously reaching the regions to the north of 50°N and east of 140°E, and enhancement of the cross-equatorial VIMT around 130°E in late Jul (Fig. 1.11d), the VIMT of the Asian summer and Australian winter monsoon gradually reach its peak phase. Five pentads later, Asian-Australian monsoon enters the decaying period: the strong 'GMR' suddenly moves from the Southeastern China to the West Pacific in the 4th pentad of Aug. (Fig. 1.11e), and the northward inter-hemisphere VIMT at approximately 130°E weakens strikingly manifested by the disappearance of VIMT belt exceeding 100kgm^{-1}s^{-1} (Fig. 1.11f).

In this period, two events that mark the commencement of the seasonal transition from summer to winter are the weakening of the inter-hemisphere VIMT around 130°E after mid-Aug. (Fig. 1.11e) and the outbreak of the monsoon southwesterly VIMT belt over the Northwestern Pacific in early Sep. (not shown). After these key periods, a series of changes lead to the establishment of the Asian winter and Australian summer VIMT stage: in the 2nd pentad of Sep., accompanied by the westward and southward retreat of the southwesterly VIMT and the westward expansion of the easterly VIMT along the southern periphery of WPSH, the westerly VIMT is replaced by the easterly one in the northern part of SCS (the similar phenomenon can be found in Matsumoto (1997) but for wind vector), which indicates that SCS summer monsoon transport commences its withdrawing process; after the 4th pentad of Sep. (not shown), the northward cross-equatorial VIMT around 105°E weakens remarkably, while the easterly VIMT along the southern periphery of WPSH further advances westward to reach the region west of 100°E; in mid-Oct., the former monsoon southwesterly VIMT retreats more westward and becomes rather weak marked by the decaying of the northward Somali VIMT Jet (not shown), thus the typical autumn VIMT situation is formed (as shown in Fig. 1.8d).

In the subsequent pentads, the transition of VIMT goes on to winter phase: in late Oct., with reactivity of the 'Sri Lanka low vortex', the easterly VIMT along the southern periphery of WPSH extends more westward, then the wintertime strong low-latitude easterly VIMT is established, indicating the end of Indian summer monsoon transport (not shown); accompanied by the intensifying of the aforementioned easterly VIMT, the decaying of 'Sri Lanka low vortex', and the splitting of the mid-latitude easterly VIMT belt over the northern Australian continent, a pronounced southward cross-equatorial VIMT is established in late Nov. at 105°E (not shown) and in early Dec. at 130°E (not shown), heralding the commencement of the austral summer monsoon. However, the sign of entering mature stage for the Asian winter and the austral summer monsoon transport

and the accomplishment of the seasonal transitions for VIMT in the Asian-Australian monsoon region are indicated by the establishment of the cross-equatorial VIMTs along the Somali Coast and 80°E in the 4th pentad of Dec. (not shown). In fact, the former one crosses the equator in late Nov., but does not extend southward to 10°S where VIMT is northerly.

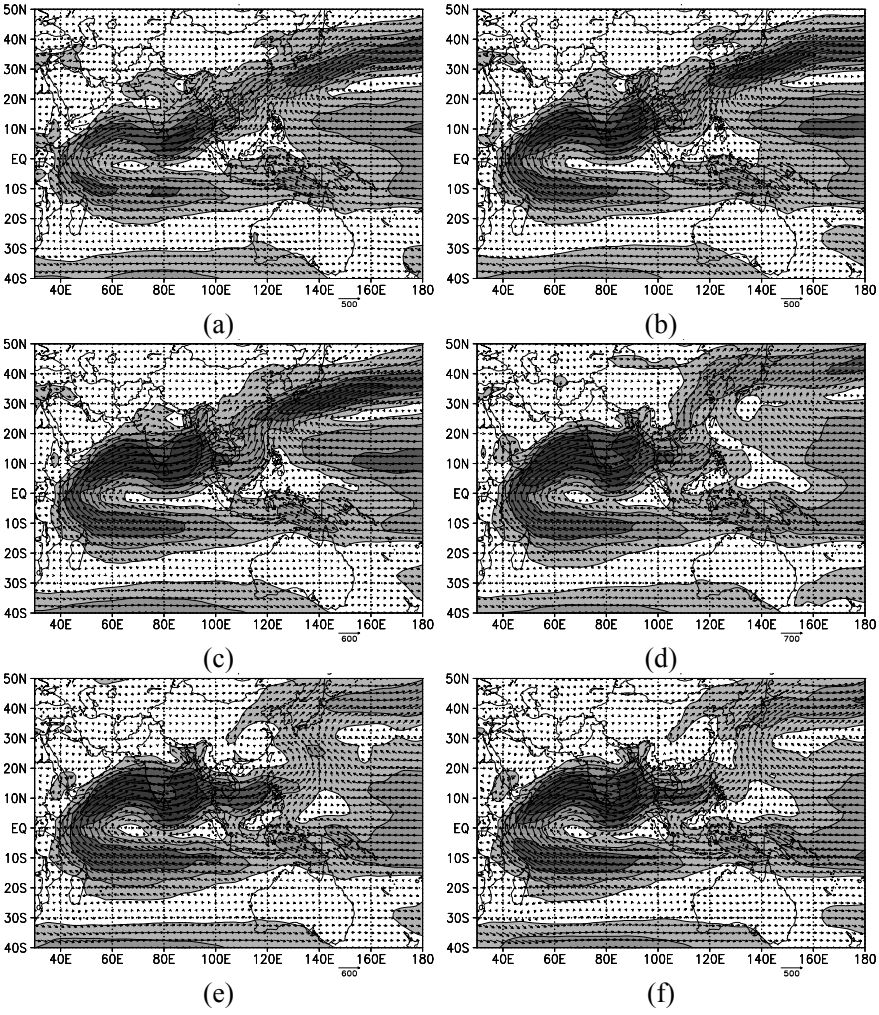

Fig. 1.11 Same as Fig. 1.9, but for the peak phase of Asian summer monsoon. Figures from (a) to (f) depict the distribution in the 1st, 3rd and 4th pentad of Jun, the 5th pentad of Jul, the 4th and 5th pentad of Aug, respectively.

In the western BOB region (80°E–90°E), the westerly VIMT from 5°S

starts its northward migration after 15th Pentad (mid-Mar.) and crosses the equator at 22nd Pentad (mid-Apr.). Therefore, before the 6th pentad of Apr. (P24), the easterly VIMT covers the western BOB while the westerly one dominates the north and south of it. After then, the VIMT reverses its direction from easterly to southwesterly and intensifies notably over the whole domain in the 1st pentad of Jun. (P31), which is in well consistency with the climatological onset date of the Indian summer monsoon. Around late Jul. (P40), the southwesterly VIMT gets to its maximum and expands to the northern-most latitude of 30°N. Hereafter, following southward retreat of the southwesterly VIMT, the easterly one occupies the northern part of the region again in early Oct. (around P55). However, the whole region is not covered by the easterly VIMT until the westerly VIMT retreats into Southern Hemisphere around late Oct. (P60). From the above transitional process, we may find that the onset of summer monsoon over the western BOB is closely related to the northward propagation of the equatorial westerly VIMT, although it seems to be resulted from a sudden eruption of southwesterly VIMT from a local point of view. In fact, when we investigate the evolving figures, we may find that the northward migration of westerly VIMT is closely associated with the northward march of the 'Sri Lanka low vortex' and the enhancement of the Somali northward cross-equatorial VIMT.

Compared to the western BOB region, in the eastern BOB region (90°E–100°E), the intensity of westerly VIMT belt is weaker, while the mid-latitude southwesterly VIMT is stronger and can expand more northward. The southerly VIMT is more evident and there is more westerly component after the onset of monsoon around early May (P26). Another noted feature is the occurrence of two maximal westerly VIMT centers in late Jun. when the southwesterly VIMT propagates to the north of 25°N and in mid-Aug.

In Indochina peninsula (100°E–110°E), the westerly VIMT from the Southern Hemisphere cannot migrate unceasingly northward across the equator during the transition from winter to summer. Before P15 (mid-Mar.), the northeasterly VIMT covers the 3°N–12°N latitudinal band, while strong westerly VIMT occupies the south and north of the band. Afterward, the southerly VIMT occurs at 15°N and then propagates northward, implying the dayspring of the seasonal transition from winter to summer in both the Indochina Peninsula and the whole Asian-Australian monsoon region. After mid-May (P27), due to the rapid eastward expansion of the tropical westerly VIMT from the eastern Indian Ocean (Ding and Sun, 2002 but for wind vectors), the southern Indochina region (south of 15°N) undergoes a striking change that the VIMT shifts from

southeasterly to southwesterly. In the same period, the notable mid-latitude westerly VIMT expands more northward to merge with the high-latitude westerly VIMT. However, the westerly VIMT does not expand to its northern edge of 35°N until summer monsoon reaches its prosperous epoch around P40 (late Jul.). Hereafter, with the withdrawal of the summer monsoon, the westerly VIMT also retreats gradually southward and eventually back into the Southern Hemisphere in early Nov.

The main feature in SCS (110°E–120°E) is exhibited by sudden arrival of the westerly VIMT in the 4th pentad of May (P28) when the SCS summer monsoon breaks out. In contrast, westerly VIMT propagates northward gradually in the BOB. On the other hand, the abrupt feature in SCS is also displayed by the pronounced increase of rainfall after P28 (Wang and LinHo, 2002). The above results may indicate that the arrival of monsoon rainfall in the SCS concurs with the sudden advent of the southwesterly VIMT. After then, with the expansion of the southwesterly VIMT, the rain band migrates suddenly from 23°N to 30°N, indicating the onset of Meiyu/Baiu season in East Asia (this feature is most obvious over the 130°E–140°E). After reaching peak phase (around P42), the westerly VIMT begins to retreat southward. Around 1st pentad of Sep. (P49), it withdraws from the northern SCS, thus the easterly VIMT is established again in the region (Matsumoto, 1997). In late Oct. (around P59), as the westerly VIMT returns to Southern Hemisphere, the rain belt also retreats to south of 5°N. The westerly VIMT and rain belt become vigorous again when they retreat to the 5°S–10°S latitudinal bands during the period of Jan. and Feb. in the subsequent year, corresponding to peak phase of Australian summer monsoon. Moreover, a remarkable invasion process from mid-latitude before the onset of SCS summer monsoon (as emphasized by Chan et al. 2000) can also be found in both rainfall and VIMT, i.e., both the mid-latitude westerly VIMT and rain belt marches southward before the onset of SCS summer monsoon. Thus, compared with the characteristics over the BOB region, the intrusion of mid-latitude events may contribute as a major factor to the SCS summer monsoon onset (Chang and Chen, 1995; Chan et al., 2000).

The longitudinal band between 130°E and 140°E is chosen as a representative zone of the WNP and Australian monsoon region. VIMT in this region shows a significantly asymmetric feature which is similar to that in the SCS region, but a more remarkable northeastward expansion after P32 near 30°N, which agrees with the northeastward migration of rain belt after the onset of Meiyu/Baiu season. After P33 from 5°N to the north, VIMT shifts gradually from easterly to westerly, which signifies that

summer monsoon is propagating northward. Hereafter, the WNP summer monsoon reaches peak phase around P45 then withdraws after P57 in agreement with the findings by LinHo and Wang (2002). Corresponding to the equatorward withdrawal of the WNP summer monsoon, VIMT in 10°S shifts from easterly to westerly around P68. However, the onset date of summer monsoon is around P1 in Australia, characterized by the sudden increase of the rainfall and enhancement of the westerly VIMT (as described by Matsumoto 1997 but for wind vectors). Around P6, it gets to peak stage with the occurrence of the maximal precipitation. After P18, the Australian summer westerly VIMT begins to retreat, and it does not disappear completely from Southern Hemisphere until P24, which is in coincidence with the findings by Murakami and Matsumoto (1994).

1.4 "Climate effect" of the Northeast Cold Vortex and its influence on Meiyu

Meiyu (i.e. Changma in Korea or Baiu in Japan), which is the product of the advancement of the East Asian summer monsoon (Zhu, 1934; Tu, 1944), occurs in June−July in boreal summer extending eastward from the mid-lower reaches of Yangtze River to Korea Peninsula and Japan. There are quantities of studies on Meiyu in many countries (Tao and Chen, 1987; Fu and Teng, 1988; Wu and Liu, 1995; Zhang, 2001; Zhang and Qian, 2002; Xu et al., 2002; Zhang et al., 2002; Huang et al., 2005), but affecting factors in the tropical regions are studied more particularly than the circulation systems in the middle and high latitudes. In fact, the atmospheric circulation in the middle and high latitudes plays an equally important role in the East Asian summer monsoon rainfall including Meiyu (Zhang and Tao, 1998; Li and Wang, 2003a,b; Ju et al., 2005a). It is well-known that the Northeast Cold Vortex (NECV) is a crucial component in the atmospheric circulation in middle and high latitudes in Asia. Generally, the life cycle of the NECV is 5−7 days, so it is a synoptic-scale system. However, spatially, besides influencing the weather and climate in Northeast China, NECV leads the cold air from the high latitude to the middle and low latitudes (Miao et al., 2006); temporally, the "climate effect" produced by the frequent activities of NECV influences not only the short-term and mid-term but also the long-term weather.

Sun (1997) showed that the most significant feature of the impacts of the NECV on summer weather is persistent low temperature and rainfalls in the affected regions, especially the former. When NECV acts more frequently, its intensity is stronger, and the low temperature events are more, thus the persistence of the low temperature is longer, leading to the season-

ally averaged lower temperature in the affected regions. On the contrary, when NECV acts less and its intensity is weaker, the seasonal mean temperature in the affected regions is higher. Then, we define the anomalous temperature and rainfalls caused by the anomalous NECV as its "climate effect". In order to describe quantitatively the influence of the "climate effect" on Meiyu in East Asia, we define a Northeast Cold Vortex Index (NECVI) in Meiyu period (June–July). Firstly, the average temperature at 1000 hPa in East Asia (100º~1145ºE, 20º~160ºN) during Meiyu period is analyzed by Rotated-EOF (Horel, 1981), with the principle component of the initial rotation being the first six principle components of EOF and the variance contribution of the first mode after rotation is 22.9% of the total variance (Fig. 1.12). It can be seen that the area of (127º~1145ºE, 37º~145ºN) is covered by a negative center (shaded areas in Fig. 1.12), being one of the active regions of NECV. Then, we define NECVI in Meiyu period as the contrary of the average temperature at 1000 hPa in June–July in the shaded regions. Here we use the contrary to conform the index to usual habits, i.e. the larger the index, the stronger the NECV; the smaller the index, the weaker the NECV. Years when the standardized NECVI is larger than 1 and smaller than −1 are defined as high NECVI years and low NECVI years in Meiyu period respectively (Table 1.1).

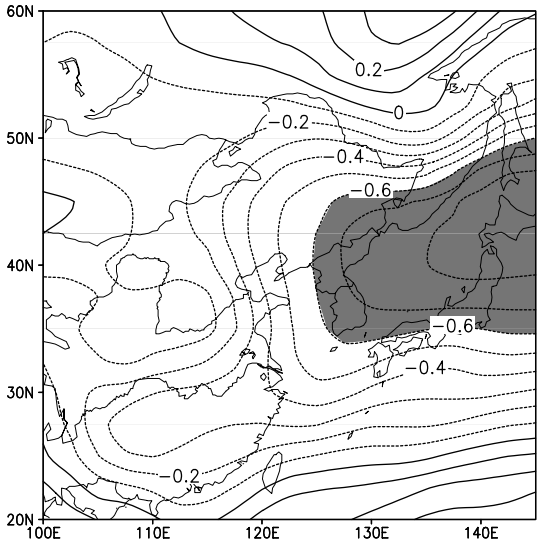

Fig. 1.12 The first mode of REOF of the temperature at 1000 hPa in East Asia (the absolute values exceeding 0.6 are shaded)

Table 1.1 Standardized NECVI in Meiyu Period from 1958 to 2002

year	NECVI	year	NECVI	year	NECVI	year	NECVI	year	NECVI
1958	–0.92	1967	–0.23	1976	0.57	1985	0.34	1994	–1.03
1959	–0.34	1968	0.00	1977	0.00	1986	2.06	1995	0.34
1960	–0.11	1969	0.46	1978	–2.06	1987	–0.34	1996	0.92
1961	–2.18	1970	0.00	1979	–0.34	1988	1.15	1997	–0.80
1962	–0.23	1971	0.57	1980	0.34	1989	0.92	1998	0.34
1963	0.00	1972	–0.92	1981	0.46	1990	–0.46	1999	–1.15
1964	0.46	1973	–0.34	1982	0.23	1991	–0.57	2000	–1.49
1965	0.46	1974	1.49	1983	2.64	1992	0.34	2001	–1.15
1966	1.03	1975	0.23	1984	–1.03	1993	2.18	2002	–0.34

1.4.1 Relationship between the Northeast Cold Vortex and Meiyu rainfall amount

Fig. 1.13 shows correlation coefficients of the NECVI and rainfall amounts during Meiyu period. The areas from the mid-lower reaches of Yangtze River to the Korea Peninsula and Japan are positively correlated, indicating that when NECVI is larger (i.e. NECV is stronger), there may be more rainfalls, but when NECVI is smaller (i.e. NECV is weaker), there may be less rainfalls in the Meiyu region in East Asia (Wu et al., 2006a). That is, the Meiyu rainfall amount may be more in strong NECV years and less in weak NECV years. Since the Meiyu rainfall is distributed on the skew rather than normally distributed, Z index (Wu et al., 2006a) is usually used to describe the variation of rainfalls. Specifically, based on the Meiyu region drawn by Wu et al. (2006a), the probability of γ distribution of the Meiyu rainfall amount is calculated, then the counter-accumulated distribution of the normal distribution is calculated and standardized to get Z index. The larger the Z index, the more the rainfall and the smaller the Z index the less the rainfall. Z index has the similar trend to the NECVI and that their correlation coefficient reaches 0.44 exceeding 99% significant test (not shown), indicating when NECVI is larger, Z index is likely larger and vice versa.

In a word, the NECV in Meiyu period and Meiyu rainfalls are significantly positively correlated, i.e. strong NECV corresponds to more Meiyu rainfalls, while weak NECV corresponds to less Meiyu rainfalls.

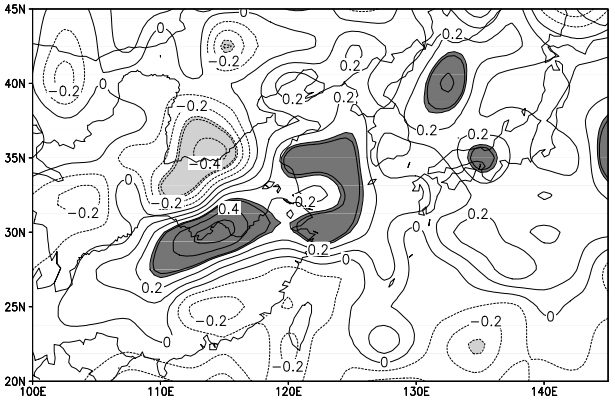

Fig. 1.13 Correlation coefficients between NECVI in Meiyu period and rainfall amount in East Asia from 1958 to 2002 (areas reaching 95% significant test are shaded, dark areas are significantly positively correlated, light areas are significantly negatively correlated).

1.4.2 Possible mechanisms of the influences of the Northeast Cold Vortex on Meiyu

Studies (Sun, 1997) showed that the NECV is reflected as a cold low center at the 500 hPa weather chart. In order to testify whether NECVI defined here can describe effectively the conceptual picture of NECV and its structure, the composite difference fields of geopotential height and temperature at 500 hPa between strong NECV (high NECVI) years and weak NECV (low NECVI) years in the First Flood Period are calculated (Fig. 1.14). It can be seen from the height field (Fig. 1.14a) that regions from North and Northeast China to the Korea Peninsula and Japan are significant low centers, indicating that low centers develop in the above areas in high NECVI years and that low centers fill or high centers develop in low NECVI years. As shown by the temperature field (Fig. 1.14b), such regions are covered by significant low centers, but the range is a bit smaller, indicating that cold centers develop in high NECVI years, but in low NECVI years, situations are just opposite. In conclusion, the NECVI defined here can basically reflect the primary features of the NECV; therefore, it can be used to describe the intensity of NECV quantitatively.

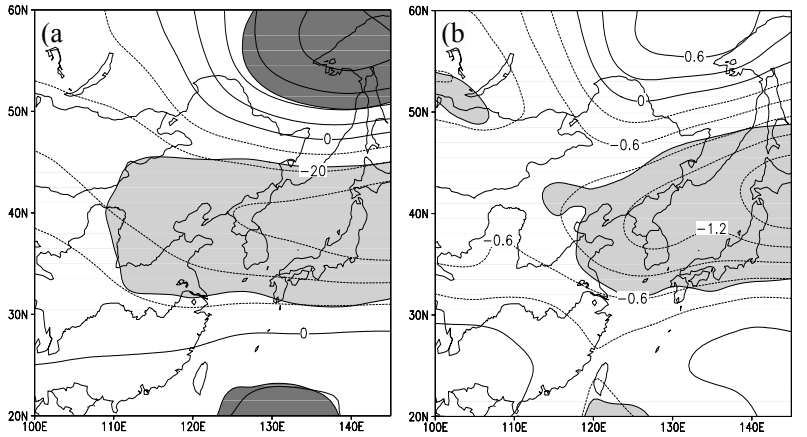

Fig. 1.14 The composite difference fields of geopotential height and temperature at 500 hPa between strong and weak NECV years (high NECVI years minus low NECVI years; areas reaching 95% significant test are shaded, light regions are significantly negative, dark regions are significantly positive) (a)geopotential height (unit: geopotential meter); (b)temperature (unit: 0.1℃).

Fig. 1.15 shows the correlation coefficients of NECVI during Meiyu period and the relative vorticity at 850 hPa and 100 hPa, respectively. It can be seen that areas from the eastern Inner Mongolia to the ocean to the east of Japan are significant positive correlations at both the lower (Fig. 1.15a) and the upper levels (Fig. 1.15b), indicating that the relative vorticity at both levels over regions with active NECV has the same trend. Therefore, the NECV is a deep system and has an equivalent barotropic structure. And the positive vorticity develops in high NECVI years, while the negative vorticity develops in low NECVI years. It is also noticed that at the lower-level there is significant positive correlation in the mid-lower reaches of Yangtze River and significant negative correlation to the south of the mid-lower reaches of Yellow River (Fig. 1.15a), but the situation is directly opposite at the upper-levels (Fig. 1.15b), indicating that the upper and lower relative vorticity in these regions has the reversed trend and the baroclinity increases. Such areas are located just at the bottom of the affected regions of the NECV, and belong to the active Meiyu belt. In addition, it is known that the positive (negative) vorticity accompanies the development of ascending (descending) motion. Therefore, in strong NECV years, there is the positive vorticity and ascending motion in the mid-lower reaches of Yangtze River and the negative vorticity and descending motion in regions to the south of the mid-lower reaches of Yellow River. Situations are just opposite in weak NECV years.

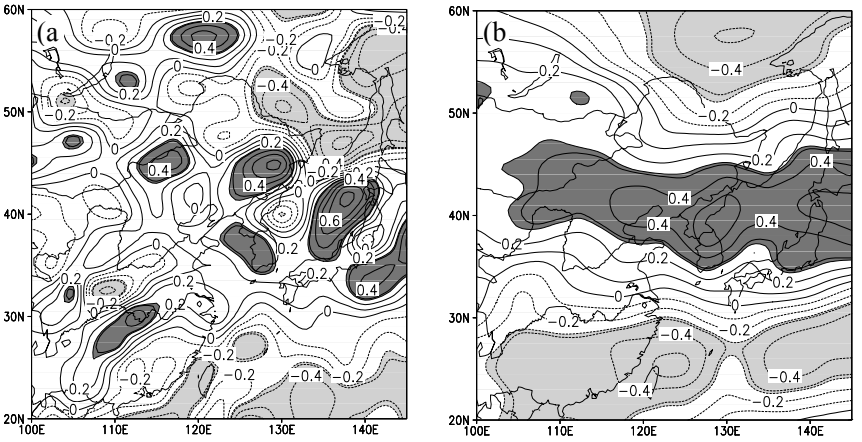

Fig. 1.15 The correlation coefficients between NECVI in Meiyu period and the relative vorticity field (areas reaching 95% significant test are shaded, light regions are significantly negative, dark regions are significantly positive) (a)850 hPa; (b)100 hPa.

The intensity of the water vapor transport plays a crucial role in the Meiyu rainfall amount (Xu et al., 2002). Next, we'll analyze the water vapor transport in the lower troposphere in Meiyu period in the anomalous NECV years. Fig. 1.16 shows the difference field of the composite water vapor transport at 850 hPa in the anomalous NECV years during Meiyu period. There is a convergence line from the mid-lower reaches of Yangtze River, Korea Peninsula to the ocean to the east of Japan (bold black line). To the south of the line, the significant west-southwest water vapor transport is observed, while to the north, the water vapor transport from the north is significant. In strong NECV years, the west-southwest water vapor transport to the south of the convergence line and the water vapor transport from north to the north of the line increase, resulting in the increase of the water vapor transport and convergence in the lower-levels and providing favorable conditions for the increase of Meiyu rainfall amount. It is very reverse in weak NECV years.

Stratification is another important factor affecting Meiyu rainfall (Tao et al., 1998). The correlation coefficients between NECVI in Meiyu period and relative humidity at 1000 hPa and 100 hPa are calculated respectively (not shown). In strong NECV years, Meiyu region (mid-lower reaches of Yangtze River-Korea Peninsula-ocean to the east of Japan) in the lower-levels is basically positively correlated, with centers lying in the mid-lower reaches of Yangtze River and its southern regions, Northeast China, Korea

Peninsula, and oceans in the southeast of Japan respectively, which indicates that the relative humidity in the lower-level in these areas increases. But in the upper-levels, a significant negative correlation band is observed at 30°~50°N, indicating that the relative humidity decreases in these areas. Thus an allocation of "upper dryness and lower wetness" is formed to aggravate the unstable stratification in Meiyu region, which is favorable to the increase of Meiyu rainfall amount. The situation is directly opposite in weak NECV years.

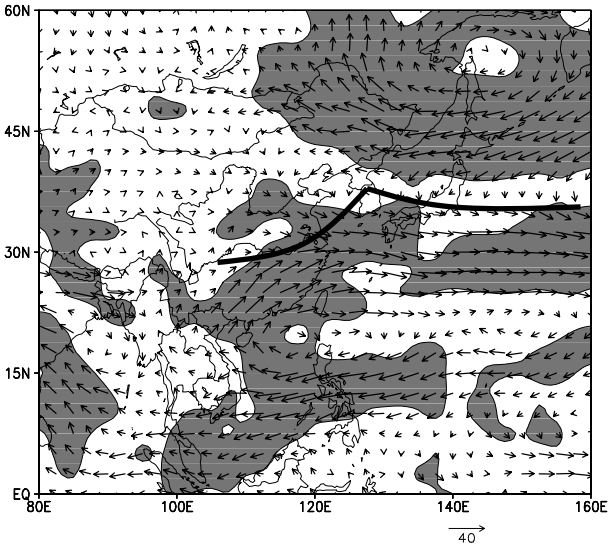

Fig. 1.16 The difference field of composite water vapor transport at 850 hPa in anomalous NECV years in Meiyu period (high NECVI years minus low NECVI years; unit: g/(cm*s); areas reaching 95% significant test are shaded; bold black line is the convergence line of water vapor transport).

In addition, ascending motion is also a primary factor affecting Meiyu rainfall. Here the streamline difference fields of the vertical sections along 120°E and 27.5°N respectively in the anomalous NECV years are computed (not shown). It is found from the longitudinal section that the troposphere in East Asia at 25°~30°N is mainly controlled by significant ascending air, while the troposphere at 30°~35°N mainly by the significant descending air. The latitudinal section shows that the lower troposphere (below 850 hPa) at 105°~135°E is mainly controlled by significant ascending air, while the upper troposphere (around 100 hPa) at 105°~135°E mainly by significant descending air. All of the above analyses indicate that in strong NECV years, ascending motion develops in the troposphere

in the area of (25°~30°N, 105°~135°E) and descending motion develops in the area of (30°~35°N, 105°~135°E). However, it is directly opposite in weak NECV years.

In conclusion, a possible mechanism of impacts of the NECV on Meiyu may be drawn as follows: in strong NECV years, the dry and cold air from the north is led by NECV to the south and converges with the low-level warm and wet southwesterly on the north verge of Meiyu region, thus forms an unstable stratification of "upper dryness and lower wetness". Triggered by ascending motion, the Meiyu rainfall amount is more than usual. It is on the contrary in weak NECV years.

1.4.3 Relationship between SST in the North Pacific and Northeast Cold Vortex

Given the close relationship between the anomalous atmospheric circulation and anomalous SST, we calculate the correlation between NECVI in Meiyu period and global SST in the preceding six months (from December of the preceding year to May of the present year) and in the corresponding period (June–July of the present year). It is found that NECVI is most significantly correlated with SST in the North Pacific (not shown). A small negative correlation area occurs in the central North Pacific in preceding December, then enlarges month by month, extends to northwest, and finally covers the entire Northwest Pacific in July with the center lying at 40°N–45°N, indicating that when the NECV in Meiyu period is stronger, SST in the above-mentioned region is usually significantly lower in the preceding or present year, which favors the development of the anomalous descending motion in this region. In the meantime, the thermodynamic property of the East Asian continent shifts from winter to summer (the East Asian continent is a cold source in winter and wind blows from land to sea; while it is a heat source in summer and wind blows from sea to land). Since the western North Pacific SST in summer is lower in strong NECV years and the land-sea thermodynamic difference between the western North Pacific and East Asian continent is mainly zonal, there is anomalous easterly in lower-levels between the western North Pacific and East Asian continent. The lower SST in the western North Pacific also increases the thermal difference between this region and middle and low latitudes in East Asia, thus strengthening the upper-level westerly jet. When NECV happens, an anomalous closed circulation is formed between the western North Pacific and middle and high latitudes in East Asia, which favors the further strengthening of NECV. Therefore, the anomalous SST in the North Pacific in the preceding year may be a factor resulting in the anomalous

NECV in Meiyu period.

It can be seen without effort that the land-sea thermal contrast facilitates NECV in summer, while that inhibits NECV in winter, which may be the reason why the NECV happens more frequently in summer than in other seasons.

1.5 Droughts-floods coexistence (DFC) during the normal summer monsoons in the mid- and lower reaches of the Yangtze River

Previous studies suggest that the summer rainfall in the mid-lower reaches of the Yangtze River valley (MLYRV) has close relationship with the advance and retreat of the East Asian Summer Monsoon (Tao and Chen, 1987; Ding, 1992; Wang, 1994; Chang and Chen, 1995; Lau and Yang, 1997). It is also found out that the severe summer droughts or floods in the MLYRV are associated with the singularities of the large-scale atmospheric circulation (Wang and Xu, 1997; He et al., 2001; Nan and Li, 2003). The majority of the previous literatures on severe droughts and floods put their emphasis on the seasonal mean rainfall (Simmonds et al., 1999; Webster et al., 1998; Barlow et al., 2002; Matsumoto, 1997), while few consider the sub-seasonal variation of rainfalls that are also of great importance. For instance, if precipitation of some summer is predicted to be normal, it might be misunderstood that there would be neither droughts nor floods in the summer. Nevertheless, if both droughts and floods happen within the summer, the seasonal precipitation may also be normal. Such a misunderstanding is due to the ignorance of the sub-seasonal variation of precipitation. As a result, the decision maker and the public may not be warned and prepared for severe floods and droughts in advance, which would cause disastrous loss of lives and property.

The summer droughts-floods coexistence (DFC) in the MLYRV is just such an occasion as extremely large rainfalls varying on the sub-seasonal scale, yet with a normal seasonal mean. The DFC refers to the occurrence of both droughts and floods during the normal summer monsoons. In order to describe the DFC phenomenon quantitatively, a DFC index (DFCI) is defined as follows:

$$DFCI = S_{STD} \cdot 10^{(0.5-|R_{STD}|)} \tag{1.2}$$

where S_{STD} and R_{STD} are, respectively, the normalized average summer no-

rain days and precipitation of the whole MLYRV. S_{STD} reflects the concentration intensity of the summer rainfall. The larger the S_{STD} is, the more concentrated the summer rainfall is, and *vice versa*. $10^{(0.5-|R_{STD}|)}$ is the weight coefficient which magnifies the weight of the normal-precipitation summers and reduces that of the severe floods or droughts summers. It should be emphasized that those indices over 0.5 and under –0.5 standard deviations are defined as the high DFCI (or strong DFC) and low DFCI (or weak DFC) summers, respectively. The absolute magnitude of the summer precipitation anomalies within 0.5 standard deviations is regarded as normal, while the anomalies over 0.5 and under –0.5 standard deviations are defined as floods and droughts, respectively.

1.5.1 Precipitation distribution features of DFC summers

To verify whether the DFCI is able to describe the occurrence of droughts and floods during the normal summer monsoons in the MLYRV, first we calculate the normalized precipitation and no-rain days of the high and low DFCI summers from 1957 to 2000 in the region (Table 1.2). It can be seen that among the 8 high DFCI summers, the absolute value of the precipitation anomaly is within 0.5 standard deviations in 5 summers, which indicates the precipitation of these 5 summers is normal, and there are 4 among these 5 summers having anomalously more no-rain days (no-rain days anomaly above 0.5 standard deviations). Although the precipitation anomalies of the other 3 summers are less than –0.5 standard deviations, their corresponding no-rain days anomalies are more than 1.5 standard deviations, much larger than the absolute value of the precipitation anomaly. All these indicate that the precipitation in the high DFCI summer is more concentrated than normal, which implies both droughts and floods occur. Among the 10 low DFCI summers, 8 summers have the normal precipitation and 9 summers have more rainy days (no-rain days anomaly less than –0.5 standard deviations), which indicates the precipitation in the low DFCI summer is more uniform. Therefore, in high DFCI summers both droughts and floods often occur in spite of the normal seasonal mean precipitation, and *vice versa*. Fig. 1.17a and Fig. 1.17b are the summer climatological pattern and the high DFCI summers composite pattern of Zeng-Li monsoon index (Li and Zeng, 2002). There is almost no difference between these two patterns, which illustrates that in spite of the occurrence of both droughts and floods, the high DFCI summers are of the same monsoon distribution as the summer climatological pattern. In other words, the high DFCI summers have the normal monsoons on seasonal timescale. So

do the low DFCI summer (not shown). Thus, DFCI might be regarded as a quantitative index describing the DFC phenomena during the normal summer monsoons in the MLYRV.

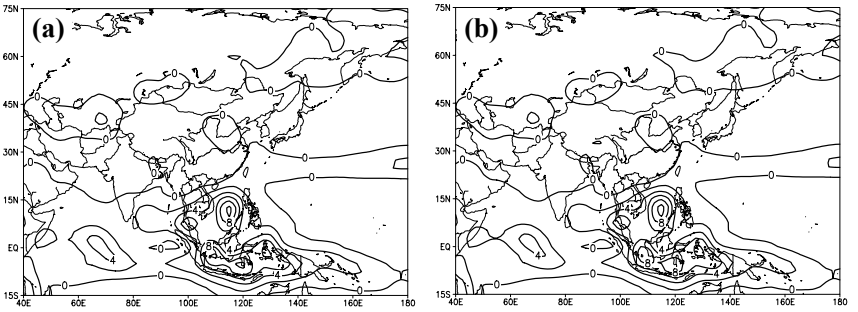

Fig. 1.17 (a) Summer climatological pattern and (b) high DFCI summers composite pattern of Zeng-Li monsoon indices.

Table 1.2 Normalized precipitation and no-rain days of the high and low DFCI summers in the MLYRV from 1957 to 2000

High DFCI Summers				Low DFCI Summers			
Year	DFCI	$\Delta R / \sigma_R$	$\Delta S / \sigma_S$	Year	DFCI	$\Delta R / \sigma_R$	$\Delta S / \sigma_S$
2000	2.70	–0.02	0.91	1977	–3.21	0.05	–1.23
1986	2.27	0.08	0.88	1975	–1.50	0.29	–1.03
1995	1.83	0.01	0.60	1993	–1.49	0.51	–1.70
1990	1.30	–0.59	1.58	1970	–1.44	0.15	–0.72
1997	0.94	–0.72	1.50	1965	–1.31	0.16	–0.67
1988	0.84	–0.44	0.69	1973	–1.04	–0.38	–0.90
1981	0.73	–0.93	1.84	1957	–0.85	0.38	–0.75
1971	0.67	–0.28	0.37	1974	–0.71	0.41	–0.68
				1963	–0.69	0.8	–1.63
				1989	–0.66	0.1	–0.31

where ΔR and ΔS refer to the summer precipitation anomaly and no-rain days anomaly, respectively, and σ_R and σ_S are the corresponding standard deviations.

Fig. 1.18 describes the temporal variation of the summer DFCI in the MLYRV from 1957 to 2000. The DFCI exhibits significant variability not only on inter-annual timescale, but also on decadal timescale. The poly-

nomial regression trend line illustrates that the summer DFCI has an increasing trend from 1957 to 2000, relatively lower before 1980s and higher after 1980s. It implies that the high DFCI summers have emerged more frequently in the MLYRV since 1980s, which is consistent with the result from Table 1.2 that 7 out of the 8 high DFCI summers are after 1980s and 8 out of the 10 low ones are before 1980s. It suggests that summer precipitation in the MLYRV is of larger sub-seasonal variation after 1980 than before 1980.

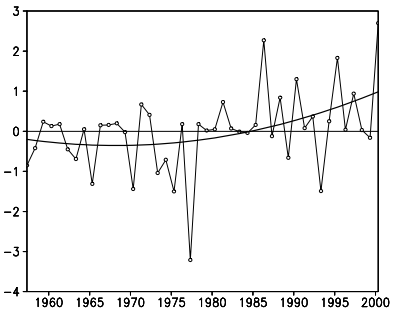

Fig. 1.18 The normalized summer DFCI time series (the thin line with open circles) in the MLYRV from 1957 to 2000 and its polynomial regression trend (the bold line).

1.5.2 Circulation features of the strong DFC summers

Fig. 1.19 displays the features of 500 hPa wind of the high DFCI summers. In May (Fig. 1.19a), the WPSH is centered at 20°N, 155°E, extending westward to the SCS; and its north and west sides are covered with significant anomalous areas over the western Pacific between 5° N−30°N. Another significant anomalous area is in the middle and high latitude regions in East-Asia. These features imply the WPSH is more southward than the climatological position and the intensity of the cold high over the East Asian continent is strong. In June, the WPSH has a northward shift (Fig. 1.19b) with its center at 25°N, 157°E, and the significant anomalous area is mainly on its north side. A large area of significant anomalies occur in the East Asian continent near 30°N in July (Fig. 1.19c), and the WPSH has a remarkable northwestward shift with its center at 30°N, 135°E. In August, the WPSH withdraws eastward (Fig. 1.19d), with its center at 30°N, 145°E, while the significant anomalies occurring in the western Pacific. According to the above analysis, the WPSH exhibits a wide range of spacial activities in the strong DFC

summers in the MLYRV, which implies that the anomalous sub-seasonal oscillation of the WPSH might be one factor contributing to the strong DFC in the MLYRV.

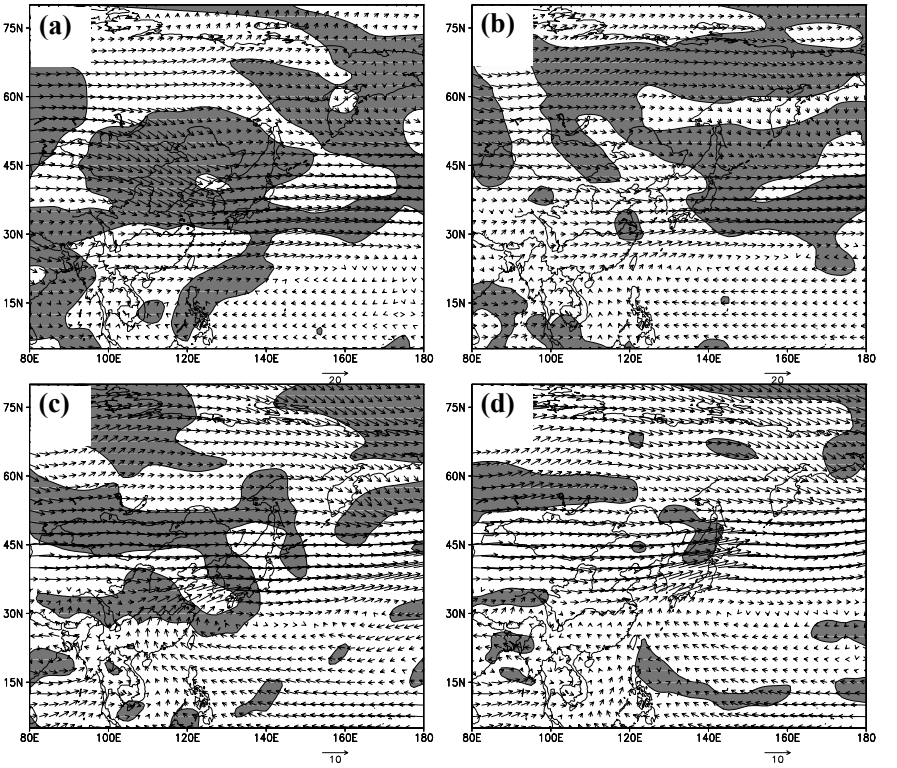

Fig. 1.19 The composite 500 hPa winds fields for (a) May, (b) June, (c) July, and (d) August of the high DFCI summers in the MLYRV. The winds anomalies (high DFCI summers minus summer climatological mean) in the shaded areas exceed the 95% confidence level based on the Student-*t* test.

Fig. 1.20 shows the correlation distribution of summer DFCI and simultaneous 850 hPa wind. Fig. 1.20a illustrates that there is a large positive area near the equator, which indicates that in the strong DFC summers, lower-level westerly wind anomalies often appear over the near-equatorial oceanic areas from Indian Ocean to the western Pacific, which provides necessary condition for the northward propagating of Rossby wave from the Southern Hemisphere (SH) to the Northern Hemisphere (NH) (Tomas and Webster, 1994). There are two regions with anomalous positive correlation: one near Sumatra and the other one near Somalia (Fig. 1.20b),

which demonstrates that the strong DFC summers usually corresponds to southerly winds anomalies in these two regions that reinforce the cross-equatorial flows from the SH (Tao and Chen, 1987).

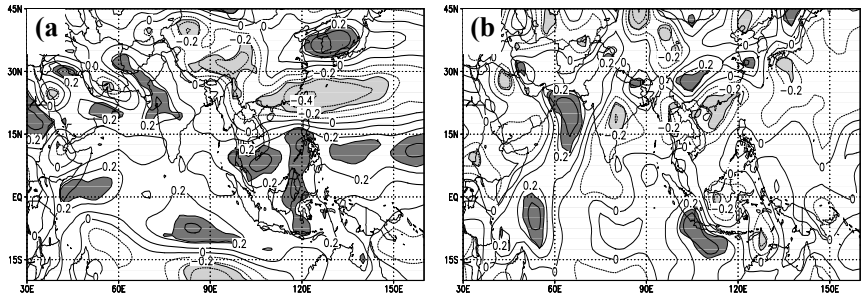

Fig. 1.20 Correlation coefficients between the summer DFCI and the summer 850 hPa (a) u, (b) v components of winds fields. The shaded areas exceed the 95% confidence level based on the Monte Carlo test.

In order to investigate the relationship between the summer DFC in the MLYRV and the preceding large-scale atmospheric circulation, the correlation coefficients between the DFCI and the Southern Hemisphere annual mode (SAM) index (Nan and Li, 2003), the Northern Hemisphere annual mode (NAM) index (Li and Wang, 2003a), the North Pacific Oscillation (NPO) index (Wallace and Gutzler, 1981) and the North Atlantic Oscillation (NAO) index (Li and Wang, 2003b) in the 6 preceding months (from the preceding November to April) are calculated respectively. The SAM in the preceding November, December and January (NDJ) are of the most significant relationship with the summer DFC in the MLYRV. Their correlation coefficients reach 0.35, 0.42 and 0.38, respectively, which exceed the 95% confidence level based on the Monte Carlo test. The correlation pattern between the summer DFCI and the composite SH sea level pressure of the preceding NDJ shows that the polar cap is covered by the significant negative correlation values and the mid-latitude is the significant positive correlation region (not shown), which means the higher the summer DFCI is, the larger the pressure gradient between the middle and high latitude regions in the SH is and the stronger the SAM is. Therefore, the preceding NDJ SAM might be regarded as a predictor for the following summer DFC in the MLYRV.

1.5.3 SST features of the strong DFC summers

The correlation coefficient map between the summer DFCI in the MLYRV and SST in the six preceding months (Fig. 1.21) illustrates that from the preceding November through April, anomalously positive correlation prevails over the oceanic areas including the western Pacific, the SCS, the Bay of Bengal, and the Arabian Sea, which indicates that the high DFCI summers in the MLYRV are usually accompanied by the preceding high SST in the above oceanic areas. In addition, it can be found that in the preceding November (Fig. 1.21a), significant positive correlation zones are observed in the equatorial central Pacific and the North Pacific, propagating eastward with time (not shown). Subsequently significant positive correlations appear in the oceanic areas from the West Coast of North America to the equatorial eastern Pacific and negative correlation prevails in the North Pacific in April (Fig. 1.21b). This correlation pattern implies that SST in the equatorial eastern Pacific has a tendency to increase in the preceding months of the strong DFC summers in the MLYRV.

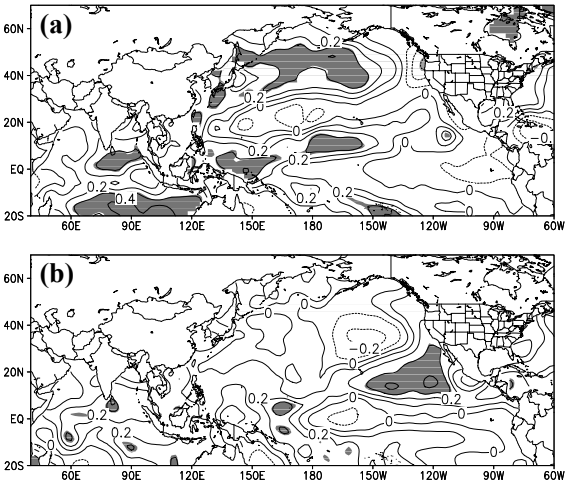

Fig. 1.21 The correlation coefficients between the DFCI in summer in the MLYRV and SST in the preceding (a) November and (b) April. Contour interval is 0.1. The shaded areas exceed the 95% confidence level based on the Monte Carlo test.

During the contemporary period, anomalously positive correlation prevails along the West Coast of North America and propagates from low to high latitude from May through August (not shown), which indicates that

the strong DFC summers are often related to the high SST propagating from the tropical eastern Pacific to extra-tropical eastern Pacific along the West Coast of North America continent. In fact, among the 8 high summer DFCI years in the MLYRV, 6 are El Niño years. Hence, the strong DFC summers in the MLYRV seem to be related to El Niño or the developing phase of El Niño.

1.6 Conclusions and some outstanding issues

Reviewing the previous researches, it is easy to find that studies on the onset of East Asian summer monsoon and the impact of its intra-seasonal, inter-annual and decadal variations on the climate in China have gained critical progress. In the meantime, the affecting factors and the physical processes are discussed as well. After such studies, the precise prediction of the seasonal variation of summer monsoon in China has been improved in a degree, and the predictability of the inter-annual and decadal variations of East Asian summer monsoon has been further comprehended. However, since the climate change of East Asian summer monsoon and its related physical mechanisms are complicated, many phenomena associated with the intra-seasonal, inter-annual and inter-decadal variations of East Asian summer monsoon in China and its surrounding areas, along with the affecting factors and physical processes, have not been revealed clearly enough. In addition, the atmospheric circulation model or the air-sea coupled model cannot simulate well the variation of summer monsoon rain belt in East Asia. Therefore, the following questions require further studies:

(1)Interactions between the monsoon activities in East Asia and the low frequency oscillation;

(2)Inner dynamic processes associated with the variability of East Asian monsoon;

(3)Physical mechanisms of the inter-annual variation of East Asian summer monsoon and its relationship with the East Asian winter monsoon in view of the annual cycle;

(4)Interactions between East Asian monsoon and ENSO cycle, and reproduction of this process by the air-sea coupled model;

(5)Simulation of East Asian summer monsoon, especially the rain belt;

(6)Causes of the inter-decadal variation of East Asian summer monsoon and its impacts on the inter-annual variation of summer monsoon;

As CLIVAR is pushed ahead step by step, the authors believe the above questions will be investigated in matters of observation, theory and simulation more comprehensively and more exhaustively in the future.

Acknowledgements. The authors would like to thank European Center for Medium-Range Weather Forecasts and National Meteorological Information Center of China Meteorological Administration for providing the related data and thank Doctor Wen Min, Chen Hua, Sun Chenghu, and Liu Yunyun for their suggestions and help in writing this chapter. This work is jointly supported by the National Natural Science Foundation of China under grants 40605022, 40221503 and 40375032.

References

Chan JCL, Wang Y, Xu J (2000) Dynamics and thermodynamics characteristics associated with the onset of the 1998 SCSSM. J Meteor Soc Japan 78: 367–380.

Chang CP, Chen GTJ (1995) Tropical circulations associated with southwest monsoon onset and westerly surges over the South China Sea. Mon Wea Rev 123: 3254–3267.

Chang CP, Harr PA, McBride J, et al. (2004) Maritime continent monsoon: annual cycle and boreal winter variability. In: Chang C p, ed. East Asian monsoon. Singapore: World Scientific Publishing Bo Pte Ltd, 107–152.

Dai XG, Wang P, Chou JF (2003) Multi- scale variations of rainfalls in North China and the interdecadal variation of summer monsoon. Chin Sci Bull 38(23): 2483–2487 (in Chinese).

Ding YH (1992) Summer monsoons rainfall in China. J Metero Soc Japan 70: 373—396.

Ding YH (1993) A study of persistent heavy rainfalls in Yangtze and Huaihe River valley in 1991, Meteorology Press, Beijing, 254–255 (in Chinese).

Ding YH (1995) The budget of the water vapor in monsoon regimes. In: Asian monsoon, Meteorology Press, Beijing, 105–113 (in Chinese).

Ding YH, Sun Y (2002) The seasonal advance and retreat and the water vapor transport of East Asian monsoon. Weather and Climate 1(1): 18—33 (in Chinese).

Ding YH (2004) Seasonal march of the East-Asia summer monsoon. In: C. P. Chang Eds, East Asian Monsoon, Singapore: World Scientific Publishing, 562–563.

Ding YH, Li CY, Li YJ (2004) Overview of the South China Sea Monsoon Experiment (SCSMEX). Adv Atmos Sci 21: 1–18.

Fasullo J, Webster PJ (2003) A hydrological definition of Indian Monsoon onset and withdrawal. J Climate 16: 3200–3211.

Fu CB, Teng XL (1988) The relationship between ENSO and the summer climate in China. Chinese Journal of Atmospheric Sciences, 133—141 (in Chinese).

Gao ST, Lei T, Zhou YS (2002a) Moist potential vorticity anomaly with heat and mass forcings in torrential rain systems. Chinese Phys Lett 19(6): 878–880.

Gao ST, Zhou YS, Lei T (2002b) Structural features of the Meiyu front system. Acta Meteorol Sin 16(2): 195–204.

He JH, Murakami T (1983) Water vapor flux over East and South Aisa during June of 1979. Journal of Nanjing Institute of Meteorology 6(2): 159─173 (in Chinese).

He JH, Zhu QG, Murakami M (1996) TBB data-revealed features of Asian-Australian monsoon seasonal transition and Asian summer monsoon establishment. Journal of Tropical Meteorology 12(1): 34─42 (in Chinese).

He JH, Zhou B, Wen M, et al. (2001) Vertical circulation structure, interannual variation features and variation mechanism of western Pacific subtropical high. Adv Atmos Sci 18(4): 497–510.

He JH, Wen M, Shi XH, et al. (2002) Splitting and eastern withdrawal of the subtropical high belt during the onset of the South China sea summer monsoon and their possible mechanism. Journal of Nanjing University (Natural Sciences) 38(3): 318─330 (in Chinese).

He JH, Yu JJ, Shen XY, et al. (2004) Research on mechanism and variability of East Asian monsoon. Journal of Tropical Meteorology 20(5): 439─459 (in Chinese).

Horel JD (1981) A rotated principal component analysis of the interannual variability of the Northern Hemisphere500 mb height field. Mon Wea Rev 2080–2092.

Huang RH, Gu L, Xu YH, et al. (2005) Characteristics of the interannual variations on onset and advance of the East Asian summer monsoon and their associations with thermal states of the tropical western pacific. Chinese Journal of Atmospheric Sciences 29(1): 20─36 (in Chinese).

Huang RH, Zhang ZZ, Huang G, et al (1998) Characteristics of the water vapor transport in East Asian monsoon region and its difference from that in South Asian monsoon region in summer. Chinese Journal of Atmospheric Sciences 22(4): 460─469 (in Chinese).

Jiang DB, Wang HJ (2005) Natural attribute of the interdecadal weakening of East Asian summer monsoon in late 20^{th} contrary. Chin Sci Bull 50(20): 2256─2262 (in Chinese).

Ju JH, Lu JM, Cao J, et al (2005a) Possible Impacts of the Arctic Oscillation on the Interdecadal Variation of Summer Monsoon Rainfall in East Asia. Adv Atmos Sci 22(1): 39–48.

Ju JH, Qian C, Cao J (2005b) The intraseasonal oscillation of East Asian summer monsoon. Chinese Journal of Atmospheric Sciences 29(2): 187─194 (in Chinese).

Ju JH, Zhao EX (2005) Impacts of the low frequency oscillation in East Asian summer monsoon on the drought and flooding in the middle and lower valley of the Yangtze River. Journal of Tropical Meteorology 21(2): 163─173 (in Chinese).

Kalnay E, Kanamitus R, Kistler R, et al. (1996) The NCEP/NCAR 40-year reanalysis project. Bull Amer Meteor Soc 77: 437–471.

Lau KM, Yang S (1997) Climatology and interannual variability of the Southeast Asian summer monsoon. Adv Atmos Sci 14(2): 141–162.

Li CY (2004) A review on intraseasonal oscillations. Natural Science Advances 14(7): 734─741 (in Chinese).

Li JP, Wang J (2003a) A modified zonal index and its physical sense. Geophys Res Lett 30(12): 1632–1635, doi:10.1029/2003GL017441.
Li JP, Wang J (2003b) On indices of the North Atlantic Oscillation. Adv Atmos Sci 20(5): 661–676.
Li JP, Zeng QC (2002) A unified monsoon index. Geophys Res Lett 29(8): 1151–1154.
Li XZ (1955) A study of cold waves in East Asia. In: Meteorology (1919~1949). Selected from Offprint of Scientific Works in Modern China. Science Press, Beijing, 35~117 (in Chinese).
Lin H, Wang B (2002) The time-space structure of the Asian-Pacific summer monsoon: A fast annual cycle view. J Climate 15(15): 2001–2019.
Liu CZ, Wang HJ, Jiang DB (2004) The configurable relationship between summer monsoon and precipitation over East Asia. Chinese Journal of Atmospheric Sciences 28(5): 700─712 (in Chinese).
Liu YM, Chan J, Mao JY, Wu GX (2002) The role of Bay of Bengal convection in the onset of the 1998 South China Sea summer monsoon. Mon Wea Rev 130: 2731–2744.
Matsumoto J (1997) Seasonal transition of summer rainy season over Indochina and adjacent monsoon region. Adv Atmos Sci 14(2): 231–245.
Murakami T, Matsumato J (1994) Summer monsoon over the Asian continent and WNP. J Meteor Soc Japan 72:719–745.
Miao CS, Wu ZW, He JH (2006) Characters of anomalies of cold vortex in Northeast China in recent 50 years and the relationship between the cold vortex and rainfalls in South China. Chinese Journal of Atmospheric Sciences (accepted, in Chinese).
Nan S, Li J (2003) The relationship between the summer precipitation in the Yangtze River valley and the foreal spring Southern Hemisphere annual mode. Geophys Res Lett 30(24), 2266, doi: 10.1029/2003GL01838/.
National Climate Center (1998) The heavy flooding and climate anomalies in 1998, Meteorology Press, Beijing, 138─139 (in Chinese).
Qian WH, Kang HS, Lee DK (2000) Seasonal march of Asian summer monsoon. Int J Climatol 20(11): 1371 –1378.
Qian WH (2005) Review of variations of the summer monsoon from seasonal to interannual and inter decadal scales. Journal of Tropical Meteorology 1(2): 199─206 (in Chinese).
Qiao YT (2003) Climatology, the intra-seasonal and the inter-decadal variations of the water vapor budget in Asian-Australian monsoon system. Meteorological doctoral degree paper of Zhongshan University (in Chinese).
Qian YF, Jiang J, Zhang Y, Yao Y, Xu Z (2004) The earliest onset of the tropical Asian summer monsoon and its mechanism. Acta Meteorologica Sinica 42(2): 129–139.
Smith TM, Reynolds RW (2004) Improved Extended Reconstruction of SST (1854-1997). J Climate 17: 2466–2477.
Sun L (1997) A study of the persistence activity of Northeast cold vortex in China. Chinese Journal of Atmospheric Sciences 21(3): 297─307 (in Chinese).
Tang DS, He JH, Wang JH (1985) A preliminary analysis of the vertical integrated water vapor transportation and the structure of the planetary-scale moist jet

stream in the low-latitudes. Journal of Tropical Meteorology 1(4): 307─314 (in Chinese).

Tao SY, Chen LX (1987) A review of recent research on the east Asian summer monsoon in China, Monsoon Meteorology[M]. C.-P. Chang and T. N. Krishnamurti, Eds., Oxford University Press, 60–92.

Tao SY, Zhao YJ, Chen XM (1998) The Meiyu of China. In: East Asian monsoon and heavy rainfalls in China ─ the corpus for celebrations of 80-year-birth of academician Tao Shiyan, Meteorology Press, Beijing, 3─46 (in Chinese).

Tomas A., Webster PJ (1994) Horizontal and vertical structure of cross-equatorial wave propagation. J Atmos Sci 51: 1417–1430.

Tu CW, Huang SS (1944) Advances and retreats of the summer monsoon in China. Acta Meteorologica Sinica 18: 1─20 (in Chinese).

Wang B (1994) on the annual cycle in the tropical eastern-central Pacific. J Climate 7: 1926-1942.

Wang B, Lin H (2002) Rainy season of the Asian~Pacific summer monsoon. J Climate 15(14): 386–39.

Wang B, Fan Z (1999) Choice of South Asian Summer monsoon indices. Bull Amer Meteor Sci 80: 629–638.

Wang B, Xu X (1997) Northern Hemisphere summer monsoon singularities and climatological intra-seasonal oscillation. J Climate 10: 1071–1085.

Wang H, Ding YH, He JH (2005) The climate research of summer monsoon over the western North Pacific. Acta Meteorologica Sinica 63(4): 418─430 (in Chinese).

Wang LJ, He JH, Guan ZY (2004) Characteristics of convection activities over Sumatra area and its relationship with SCS summer monsoon onset. Journal of Nanjing Institute of Meteorology 27(4): 451–460 (in Chinese).

Wallace JM, Gutzler DS (1981) Teleconnections in the geopotential height field during the Northern Hemisphere winter. Mon Weather Rev 109: 784–812.

Wen M, He JH, Xiao ZN (2004) Impact of the convection over the Indo-China peninsula on the onset of South China Sea summer monsoon. Chinese Journal of Atmospheric Sciences 28(6): 864─875 (in Chinese).

Webster PJ, Magana VO, Palmer TN, et al. (1998) Monsoons: Process, predictability, and the prospects for prediction. J Geophys Res 103: 14451–14510.

Wu BY (2005) Weakening of Indian Summer Monsoon in Recent Decades. Adv Atmos Sci 22(1): 21–29.

Wu GX (1990) Transport, budget and impacts on droughts in subtropical region of the water vapor in the atmosphere. Chinese Journal of Atmospheric Sciences 14(1): 53─63 (in Chinese).

Wu GX, Liu HZ (1995) Neighborhood response of rainfall to tropical sea surface temperature anomalies Part I: Numerical experiment. Chinese Journal of Atmospheric Sciences 19(4): 422─434 (in Chinese).

Wu GX, Zhang YS (1998) Tibetan Plateau forcing and the timing of the monsoon onset over South Asia and the South China Sea. Mon Wea Rev 126: 913–927.

Wu SS, Liang JY, Li CH (2003) Relationship between the intensity of South China Sea summer monsoon and the precipitation in raining seasons in China. Journal of Tropical Meteorology 19: 25-36 (in Chinese).

Wu ZW, He JH, Jiang ZH (2006a) The comparison analysis of flood and drought features among the first flood period in South China, Meiyu period in the Yangtze river and the Huaihe river valleys and rainy season in North China in the last 50 years. Chinese Journal of Atmospheric Sciences 30(3): 391─401 (in Chinese).

Wu ZW, He JH, Li JP, et al. (2006b) The summer drought – flood coexistence in the middle and lower reaches of the Yangtze river and analysis of its air-sea background feathers in anomalous years. Chinese Journal of Atmospheric Sciences 30(4): 570─577 (in Chinese).

Wu ZW, Li JP, He JH, et al. (2006c) The large-scale atmospheric singularities and the summer long-cycle droughts-floods abrupt alternation in the middle and lower reaches of the Yangtze River. Chin Sci Bull 51(14): 1717—1724 (in Chinese).

Wu ZW, Li JP, He JH, et al. (2006d) The occurrence of droughts and floods during the normal summer monsoons in the mid- and lower reaches of the Yangtze River. Geophys Res Lett 33, L05813, doi:10.1029/2005GL024487

Wu ZW, Li JP, He JH, et al. (2006e) The large-scale atmospheric singularities and the summer long-cycle droughts-floods abrupt alternation in the middle and lower reaches of the Yangtze River. Chin Sci Bull 51(16): 2027–2034.

Xie A, Song YY, Mao JY, et al. (2001) Climatological characteristics of moisture transport during summer monsoon over South China Sea. Climatic and Environmental Research 6(4): 425-434 (in Chinese).

Xie YB, Dai WJ (1959) A case study on the water vapor transport in summer East China. Acta Meteorologica Sinica 30(2): 171─185 (in Chinese).

Xu SY (1958) The balance and transport of the water vapor in China. Acta Meteorologica Sinica 29(1): 33─43 (in Chinese).

Xu XD, Tao SY, Wang JZ, et al. (2002) The relationship between water vapor transport features of Tibetan Plateau – monsoon "large triangle" affecting region and drought – flood abnormality of China. Acta Meteorologica Sinica 60(3): 257─267 (in Chinese).

Zhang Q, Wu GX, Qian YF (2002) The bimodality of the 100 hPa South Asia High and its relationship to the climate anomaly over East Asia in summer. J Meteor Soc Japan 80(4): 733–744.

Zhang RH, 2001: Relations of water vapor transport from Indian Monsoon with that over East Asia and the summer rainfall in China. Adv Atmos Sci 18(5): 1005–1017.

Zhang YC, Qian YF (2002) Mechanism of thermal features over the Indo-China peninsula and possible effects on the onset of the South China Sea monsoon. Adv Atmos Sci 19(5): 885–900.

Zhang ZQ, Chan J, Ding YH (2004) Characteristics, Evolution and Mechanisms of the summer monsoon onset over Southeast Asia. Inter J Climat 24: 1461–1482.

Zhang QY, Tao SY (1998) Influence of Asian mid- high latitude circulation on East Asian summer rainfall. Acta Meteorologica Sinica 56(2): 199─211 (in Chinese).

Zhang QY, Tao SY (2003) The anomalous subtropical anticyclone in western Pacific and their association with circulation over East Asia during summer. Chinese Journal of Atmospheric Sciences 27(3): 369─380 (in Chinese).

Zhao P, Zhang RH (2006) Relationship of interannual variation between an eastern Asia-Pacific dipole pressure pattern and East Asian monsoon. Chinese Journal of Atmospheric Sciences 30(2): 307─316 (in Chinese).

Zhao P, Zhou ZJ (2005) East Asian subtropical summer monsoon index and its relationship to rainfall. Acta Meteorologica Sinica 63(6): 933–941 (in Chinese).

Zhou YS, Gao ST, Shen S (2004) A diagnostic study of formation and structures of the Meiyu Front system over East Asia. J Meteor Soc Japan 82(6): 1565–1576.

Zhu KZ (1934) Southeast monsoon and rainfalls in China. Journal of Geographical Sciences 1(1): 1–27 (in Chinese).

Zhu QG, He JH, Wang PX (1986) A study of circulation differences between East Asian and Indian summer monsoon with their interaction. Adv Atmos Sci 3: 466–477.

Chapter 2 Paleoclimate of China

2.1 Introduction

The regional climate of China in the past can be studied by analyzing proxy data and modeling. In the last several decades, a plenty of proxy data, such as tree-rings, ice cores, stalagmite, peat, pollens, lake sediments, and historical documents were used by Chinese scientists to study climate changes of China. A longer perspective on climatic variability can be obtained by the study of natural evidences that are climate-dependent. Such evidences provide the proxy record of climate and are the foundation of paleoclimate studies. Thus, reconstructed paleoclimatic data from the proxy data provide the basis for studying the regional climate change of China at different time scales.

Many natural systems are dependent on climate; where evidence of such systems in the past still exists, it may be possible to derive paleoclimatic information from them. By definition, such proxy records of climate all contain a climatic signal, but the signal may be relatively weak, embedded in a great deal of extraneous "noise" arising from the effects of other (non-climatic) influences. The proxy material has acted as a filter, transforming climatic conditions at a point in time, or over a period, into a more or less permanent record, but the record is complex and incorporates other signals that may be irrelevant to the paleoclimatologist.

To extract the paleoclimatic signal from proxy data, we have to understand how, and to what extent, proxy materials are climate-dependent by using modern climatic records and proxy materials. Generally, we can assume that the modern relationships observed have operated, unchanged, throughout the period of interest (the principle of uniformitarianism). All paleoclimatic research, therefore, must build on studies of climate dependency in natural phenomena at the present. Dendroclimatic studies, for example, have benefited from a wealth of research into climate-tree growth relationships, which have enabled dendroclimatic models to be based on sound ecological principles. Significant advances have also been made in playnological research by improvements in our understanding of the relationships between modern climate and pollen rain. It is apparent, therefore,

that an adequate modern database and understanding of contemporary processes in the climate system are important prerequisites for reliable paleoclimatic reconstructions. However, not all environmental conditions in the past are represented in the period of modern experience. We must be aware of the possibility that erroneous paleoclimatic reconstructions may result from the use of modern climate-proxy data relationships when past conditions have no analog in the modern world.

For extending the climate series, calibration and assimilation are important in the reconstruction of the climate series for the past climate research in regional climate of China. The ice cores, tree-rings, stalagmite and documentary data have been used to estimate the regional temperature anomalies and precipitation to fill the gaps in observational series. As the Tibetan Plateau play a very important role in the climate of China, using more proxy data, mainly ice cores and tree rings from the Plateau, is necessary. A fundamental understanding of the climate change of China in the past is very valuable for understanding and detecting present and future climate change in China.

As a numerical tool, climate model has been used to estimate the spatial and temporal pattern of climate changes in the past. Models are used to test hypotheses about the causes of environmental changes in the past, to quantify the relative importance of one factor compared to another, and to examine the sensitivity of the climate system to different forcing mechanisms. Therefore, paleoclimatic modeling can provide the essential understanding of climate system variability, and its relation to both forcing mechanisms and feedbacks, which may amplify or reduce the direct consequences of particular forcing. Paleo-environmental data and modeling can help us to evaluate known climate changes in the past, and to comprehend the feedbacks and system responses that are of direct relevance to the understanding of the future impact of human activities.

2.2 Reconstructed climate of China

Chinese climatologist Zhu Kezhen, published the first paper “Climate change during the historical time in China” on the climate change in China in 1925. Then Zhu published “Preliminary study on climate change during the last five thousand years in China” in 1972. In the last 50 years, more paleoclimate studies based on the different kinds of proxy data, such as ice cores, tree-rings, lake sediments, and varve records, have been made and have greatly improved our understanding to the paleoclimate of China. By use of the proxy data we can reconstruct precipitation and temperature

time series with various resolutions for long time. From these reconstructions we have known more climate change of China in the past.

One of the hot points in paleoclimate is abrupt climate change. A great deal of the evidences showed that there were series of abrupt change events in China in the Holocene since Younger Dryas. The assorted evidences indicate that the most of the cold periods identified in China correspond to those of the world. Discrepancy in timing may relate to the uncertainty in those and the Chinese series.

Two typical cold periods were found as abrupt climate changes at 8.2 kaBP (Wang N L et al., 2002) and at 4.0 kaBP in the Holocene. The later one is possible related to the collapses of ancient civilization in the Nile Valley and the Mesopotamia and the alternation of the ancient cultures in China. (Wang S W et al, 2004). The results of studies indicate that the collapses of ancient civilization in the world were associated with an abrupt shift to a cold and drought climate (Group of experts, 2000). The changes of wetness in Qinghai Lake are related well to the reduction of precipitation at 4.0 kaBP.

The occurrence of MWP (Mediaeval Warm Period, AD 900~1300) in China is also an important topic in the studies of historical climate changes. Zhang De′er (1994) has shown that the 13th century was a warm period during the last millennium. Wang et al. (2001) reconstructed the temperature series for eastern and western China with 50-year time resolution. The mean temperature from AD 850 to 1300 was about 0.2°C higher than the mean during the whole period except in the 12th century in eastern China. However, no prolonged warm period was found in western China from AD 900 to AD 1300. Therefore, the MWP can probably be traced only in eastern but not in western China. Ge et al. (2002) have synthesized the pollen, varve, stalagmite and documentary data, and indicated that there was a warm period from 930 to 1310, but the climate of 1110-1190 was colder than that of 1951-1980. A recent study on the stalagmite record in Beijing supports the suggestion that there was a warm climate during AD 900-1300 while temperature was 0.5°C higher than the present (Tan et al. 2003).Yang et al. (2002) examined the temperatures over the Tibetan Plateau based on the lake sediment, ice cores, tree-rings, peat, and glacier data. They found that the warmest period appeared before AD 1000 over the northeastern, but no warm period before AD 1300 over the western Tibetan Plateau. The climate was warm during AD 1150-1350 over the southern Tibetan Plateau.

Lin et al. (1990, 1995) and Wang (1990) have extended the temperature series of China back to 1873 and 1880, respectively. Tu (1984) has constructed a homogeneous temperature series for China, in which monthly

mean temperature observations of 42 stations in eastern China are used. The gaps are filled with the aid of interpolation. Wang et al. (1998b) constructed an annual mean temperature series of China from AD 1880 to 2002.It indicates that temperature has increased in general for the last 120 years period. The great increments occurred from the end of 1900's to the middle of 1940's, and from the middle of 1980's to the end of the series. The warming trend is 0.58°C/100a according to the series of 1880-2002.

For the reconstruction of climate in the last 20ka, the lake status data of CLSDB show that the climate at 6ka BP was wetter than today in northeastern and northern China and most areas of western China. The lake records also suggest that southeastern China was drier than today. For 18ka BP(^{14}C), lake status data show wetter conditions than that of today in western China (west of 100°E) including the Tibetan Plateau and inland Xinjiang, but drier conditions in eastern China.

Quaternary climate records from South East Asia document large changes in environmental conditions during the Quaternary. The spatial pattern of these environmental changes provides insights into the changes in atmospheric circulation regimes that drive regional climates. The recognition of this fact has led to multiple attempts to synthesis and map the available palaeoenvironmental data from South East Asia (e.g. Winkler and Wang, 1993; Shi et al., 1993; Yu et al., 1998, 2000; Kohfeld and Harrison, 2003). These syntheses and interpretations are greatly supported by the existence of palaeoenvironmental databases (Kohfeld and Harrison, 2003), which provide comprehensive, well-documented and quality-controlled records from individual sites for continental-scale regions. There are three databases that provide such information for China: the Chinese Lake Status Database (CLSDB: Yu et al., 2001a, 2001b), the BIOME 6000 data sets for China (Yu et al., 1998, 2000), and the Chinese Loess database (Sun et al, 2000; Kohfeld and Harrison, 2003).

2.2.1 Loess

In the northwestern China, the loess plateau with maximum depth of 3000 m provides very important paleoclimate records (Ding *et al*., 1994) for the million years before present. Temperatures and precipitation in the Quaternary (2.4~2.5Ma BP to present) are reconstructed based on the analyses of magnetization and the size of particles of loess. The reconstruction from loess records show that there were about thirty-seven glacial-interglacial cycles in the past 2.5Ma and with different periodicities. The 100ka periodicity appeared in the period from 700~0 ka BP, and the

period reduced to about 41ka from 0.7 to 1.6MaBP. The loess record also suggested that temperature during the Last Glacial Maximum (LGM) (21ka BP) was 6°~7°C lower than that of present, and precipitation was about 50% of the present normal.

The Chinese Loess Plateau contains an extensive record of aeolian deposition through multiple glacial–interglacial cycles. Independent chronologies based on pedostratigraphy, magnetic susceptibility, radiocarbon and luminescence dating have been developed for 79 sites from the Loess Plateau and the surrounding region and used to estimate aeolian mass accumulation rates (MARs) for marine isotope stage (MIS) 1 through 5 (Sun et al., 2000; Kohfeld and Harrison, 2003).

High resolution records of loess accumulation during the Holocene show that accumulation rates were relatively high initially and fell to a minimum between ca 7000 and 3000 a B.P. Harrison and Kohfeld (2003) have suggested that these low accumulation rates during the mid-Holocene reflect an expansion of the Pacific monsoon resulting in wetter conditions on the Loess Plateau. The timing of the onset and cessation of reduced dust accumulation varies from site to site, and probably reflects spatial patterning in the timing of increased monsoonal rainfall.

2.2.2 Ice cores

Ice cores are another useful proxy for understanding past climate changes. Ice cores provide several hundred years to ten thousands years long proxy climate records with a high time resolution. The typical ice cores, such as from Dunde and Guliya drillings in Tibetan Plateau are 130m and 300m, respectively. The analyses of particles numbers and the $\delta^{18}O$ from Dunde ice core recorded the climate change during the last 40ka, especially for the Holocene. This record shows that the warmest period occurred from 3.6~2.6kaBP in the Holocene over Tibetan Plateau area. The unusual cold and dry event appeared at about 8.9~8.7kaBP, with temperature reduced 3.7k in 300a. Other typical climate periods, such as Little Ice Age (LIA), Medieval Warm Period (MWP) were also well determined from $\delta^{18}O$ of ice core in Dunde. Comparison of $\delta^{18}O$ from ice cores changes in Dunde and Greenland indicates significant stadial and interstadial alternations, and the evidence of abrupt climate change, such as the Younger Drays.

Guliya ice core provides longer climate records than that of Dunde. There are some ice cores from Dasuopu, Tanggula, Malan and other locations. Yao et al. compared $\delta^{18}O$ records from four ice cores in Dasuopu (south), Guliya (west), Dunde (north) and Purogangri (centrl), respectively.

They reconstructed annual mean temperature series of Tibetan Plateau in the last 100a and found that climate in the Plateau is warming in the last 100a.

2.2.3 Tree rings (Dendroclimatology)

The analyses of Qilian Mountain tree rings provide number of records for climate studies, which include winter and spring mean temperature in the last 1000a, tree ring width with 560a long, annual precipitation in the last 1100a, summer humidity index of 682a, Delingha 1000a precipitation, and precipitation in the 1437a in Zaidam . Tree rings collection from Tibetan Plateau include Dulan(1835a), Changdu (1000a), Wulan (824a). Besides these tree rings records, there are many records from Xinjiang, northeast China, and eastern China. Tree-ring data also provide information on precipitation variations in a relatively short time periods; one of the recent studies describe precipitation change in Qinghai for the last millennium (Shao *et al*., 2004). Synthesis work of the tree-ring studies has provided decadal mean precipitation anomaly maps of western China from the 1600s to the 1990′s (Wang *et al*., 1991; Kang et al., 1997, Wu et al.,1981; Wu et al., 1981; Yang et al., 2002).

2.2.4 Historical documents

Documentary data is one of the main proxy data in examining climate change in historical time. China has a long history and a plenty of historical document records. The historical documents most distributed in the eastern China, which including direct climate records about droughts, floods, rainfall, snow, freezing, frost, wind and fall dust. And also some of indirect records on climate are available, such as crop production, famine, population, insect diseases etc. Chinese historiographers and climatologists have done a lot work on the historical climate reconstruction for the last several thousand years, and set up the time series of climate changes in different regions. (Zhang Deer, 1981, 1997, Zhang Piyuan, 1996, Wang Shaowu, 1998b, Zheng Jingyun, 1993, Wu Xiangding et al., 1981). Zhu Kezhen is the first Chinese scientist who studied climate change during the last 5000 years in China. He confirmed the warm and wet period in the middle Holocene, and three cold periods within the Little Ice Age were identified too (Zhu, 1972). In the middle of the 1970s, Chinese scientists started a project to study the droughts and floods for the last 500 years and

published the “Droughts/floods maps for the last 500 years in China” in 1981 (CMI, 1981). After that time the series of records of droughts and floods extended to over a 1000 years (Zhang *et al*., 1997).

2.2.5 Stalagmite

In the present time current years, stalagmite as proxy data with high resolution is paid attention to and is used widely since it has a long time, accurate aging, and high resolution. Chinese scientists have been in the advance in the world due to their achievement on the paleoclimate studies by using stalagmite records. Their papers have been cited a lot. Tan Ming et al. (2003) disclosed the temperature variability in centennial scale and its spatial distribution by using integrated stalagmite and tree rings records. They found that the integrated climate record showed a temperature variation that is symmetrical like a “ V ” shape, not a “ Hockey Stick ” shape in the last 1000a in China. The minimum temperature was at “Spörer Minimum” and had the same pattern as climate in north Atlantic area. Therefore, this result confirmed that centennial variability of climate in eastern Asia and north Atlantic has the same phase in the last 1000a.

2.2.6 Pollen

Pollen data are widely used in the paleoclimate studies. From pollen analyses, many temperature anomaly series at different sites in China were reconstructed. The main shortcoming of the temperature anomaly series from pollen data is the low time resolution. Thus the pollen analysis is good for time averaged temperature in a period rather than for the single year or for high resolution study.

A typical case is the maximum temperature anomaly reconstruction of the Megathermal (mid-Holocene, ca 6ka BP, Shi, 1993). Temperature anomalies were also estimated according to the changes of vegetation (Zhang et al., 1993).

China is one of the first regions to be considered in the BIOME 6000 project (Yu et al., 1998) and there have been several subsequent attempts to improve the vegetation reconstructions (Yu et al., 2000). Tests with a set of 840 modern pollen samples spanning all biomes and regions show convincing agreement between reconstructed biomes and present natural vegetation types, both geographically and in terms of the elevation gradients in mountain regions of northeastern and southwestern China.

2.2.7 Lake sediments

Fluctuations in the water balance (precipitation minus evaporation: P-E) over the catchment of a lake are reflected in changes in lake area, level and volume, and can thus be reconstructed from geomorphic and stratigraphic records from the lake basin (Street-Perrott et al., 1989). Although such changes may be influenced by local non-climatic factors, regional-synchronous changes in lake area, level or volume (collectively referred to as lake status) are generally a response to climate. Thus, regional changes in lake status have been used to reconstruct regional palaeoclimates and the changes in atmospheric circulation patterns that gave rise to them (Harrison et al., 1996). Continental-scale reconstructions of changes in lake status have also been used as a benchmark to evaluate model simulations of changes in P-E (e.g. COHMAP, 1988; Qin et al., 1998).

The Global Lake Status Data Base (GLSDB: Qin et al., 1998) is an effort to compile the geomorphic and biostratigraphic data for changes in lake status for individual lake basins, in order to document changes in regional water balance during the last 40,000 years. The Chinese Lake Status Data Base (CLSDB: Yu et al., 2001a, 2001b) is a component of the GLSDB. Version 1 of the CLSDB contains 42 lakes (Yu et al., 2001a) and a further 26 lakes are included in an updated version of the data set (Yu et al., 2001b).

2.3 Climate simulation of the last 1000 years

Historical climate simulation through long time integration is undergoing a rapid development phase. The numerical model simulation plays a vital role in understanding the causes and physical mechanisms of climate change on centennial time scale. In this section the temperature over the last millennium simulated by the global climate model ECHO-G is used to compare with the reconstructed temperature anomalies in the eastern China. The purposes are to test the skill of the model in simulating regional climate of China, and to understand the causes and mechanisms of the past climate changes in China (Liu et al., 2005). The present study may help improving our comprehensive understanding of the historical climate change, enhancing the forecast reliability for predicting the tendency of future climate change.

2.3.1 Model description

The climate model ECHO-G consists of the spectral atmospheric model ECHAM4 and the global ocean circulation model HOPE-G, both were implemented and developed at the Max-Planck-Institute of Meteorology (MPI) in Hamburg. ECHAM4 is a fourth generation of atmospheric general circulation model, which is based on primitive equations with a mixed p-σ coordinate system. The horizontal resolution of the model is T30, or approximately 3.75°×3.75°, and the vertical resolution is 19 levels with five upper levels being located above 200hpa. The horizontal resolution of the ocean model HOPE-G is about 2.8°×2.8° with a grid refinement in the tropical regions, where the meridional grid point separation reaches 0.5°. The ocean model has 20 vertical levels. The model ECHO-G has been used in a number of simulations for the present and past climates.

Two 1000-year integrations with the ECHO-G model have been carried out at MPI. One is a control simulation, in which the external forcing is kept at constant values of the present climate. This experiment can simulate annual, inter annual and decadal climate oscillations that are determined by the internal dynamics of the coupled climate system, but cannot simulate the climate change caused by external forcing, such as the Medieval Warm Period and the Little Ice Age. Another experiment is externally forced simulation, in which the model ECHO-G was driven by three external forcing factors: solar variability, greenhouse gas concentrations in the atmosphere (including CO_2 and CH_4) and an estimation of radiative effects of stratospheric volcanic aerosols, for the period of 1000 to 1990 A.D. Further details of the simulations can be found in Storch et al. 2004. The result from the forced simulation is used for comparison with the reconstructed sequences in this section.

2.3.2 Reconstruction data

Abundant historical, documentary records on phonological events of cold/warm and dry/wet climate are available in China as described in last section. Numerous studies on reconstructing the historical climate change have been done by Chinese scientists using these documentary records. In recent years, Ge et al. conferred with and developed Zhu's method of deducing climate change for the past 5000 years using phonological records in China. They reconstructed winter half-year (October to April) temperature anomalies for the past 2000 years in the central region of eastern China (25°–40°N, east of 105°E) at 10–30 years resolutions. Their reconstructed temperature anomalies since 1000 A.D. at a 30-year resolution are

used here.

The study of climate change since Little Ice Age (LIA, 1550-1850AD) has been received extensive concern in China. Widely spread and severe famine and serious social turmoil have taken place in China during LIA (Xu, 1997). Because of this broad interest, the climate of China during the last 2000 years has been reconstructed by Chinese scientists, in particular temperature and precipitation since LIA with a variety of proxy data, such historical documents, tree rings, ice cores, lake warves, archaeological materials, etc. (Wang et al., 1998; Wang and Gong, 2000; Zheng and Zheng, 1993; Yao et al., 1996).

2.3.3 Model and data comparison

The simulated temperature anomalies from the externally forced simulation with ECHO-G are first compared with 120-year observed data in eastern China (25°–40°N, east of 105°E) in order to test the model's performance. Fig.2.1 compares the simulated and the observed variations of the winter-half year temperature anomalies in the eastern China since 1870. It can be seen that the increasing trends of temperature fluctuations in the eastern China are evident and consistent for both model output and observations. There is a statistically significant correlation between them at 99.5% confidence level, although the simulated mean temperature is about 0.15°C lower than the observed one. The uncertainty in Jones' observed data is of the same order, suggesting that the model results and Jones' data may be considerably consistent with each other.

To be compatible in temporal resolution, we first compiled the winter-half year temperature anomalies in the eastern China (25°–40°N, 105°–123.75°E, 20 grid points) from the externally forced simulation, and then calculated 30-year mean temperature anomalies. Finally, the simulated results are compared with reconstructed winter-half year temperature anomalies (at a 30-year resolution) of the eastern China. Figure 2.2 shows these two time series along with their corresponding polynomial fitting curves.

Figure 2.2 indicates that the reconstructed and the simulated results exhibit similar low-frequency variations and long-term trends. The range of the simulated temperature is from –0.70°C to 0.92°C, and that of reconstructed is –1.1°C to 0.9°C. The amplitude of the simulated temperature anomalies is about 1.62°C, slightly less than that of reconstructed (2.0°C). The correlation coefficient of the two time series is 0.37 that is significant

at 97.5% confidence level. Overall, both simulation and reconstruction show the Medieval Warm Period from 1000 to 1300, the Little Ice Age from 1300 to 1850, and the modern warming period since 1900. The anomalies from simulation and reconstruction in the Little Ice Age (1300–1850) and warming since 1900 are particularly consistent. Especially, both simulated and reconstructed temperatures reached their minimum values without phase difference during the Maunder Minimum of sunspots from 1670 to 1710. However, for the Medieval Warm Period of 1000-1300, the simulation and reconstruction show some phase differences: The reconstruction displays two peaks with one valley in between, whereas the simulation shows three peaks with two valleys in between.

It can be seen from Fig.2.1 that after 1500 the phases and amplitudes of the reconstruction and the simulation match better than those in the period prior to 1500 A. D. This may be related to the fact that less amount of data sites were used for climate reconstruction in the earlier period. Of also notable is that the difference between the simulation and reconstruction becomes large in the last 100 years. The simulation shows a faster increasing trend and higher than reconstructed temperature. The possible cause for this discrepancy may be partially due to the exclusion of the aerosol forcing in the forced experiment. The effects of aerosol have been thought to be a forcing factor that can offset the warming. It is conceivable that the regional cooling effect of aerosols could reduce the warming if they were included in the model, especially in the 20^{th} century.

It is worthy to point out that the simulated temperature anomaly in the 20th century is higher than that in the Medieval Warm Period, while the reconstructed temperature in the 20th century is lower, albeit close to that of the Medieval Warm Period (Fig. 2.1). These two different results provide two different interpretations regarding the nature and amplitude of the recent global warming. One is that the 20th century warming has exceeded the normal range of the climate change, and it will result in catastrophic impact on human beings if warming continues going up. The other is that the current climate change has not yet exceeded the range of natural climate change in the past millennium. The final answer for this problem calls for both the improvement of the fidelity of the climate models in their long-term climate simulation and more profound work on quantitative reconstruction of paleo-climatological data. The latter requires reconstructing historical climate change sequences with higher resolution, precision, and reliability.

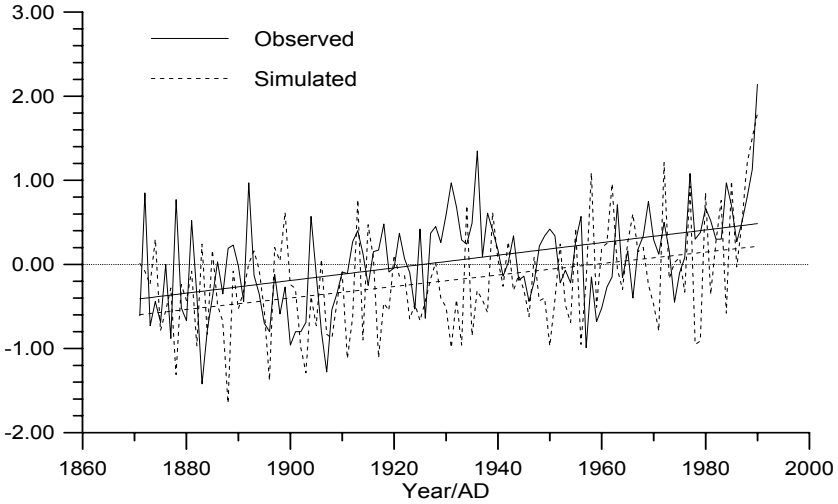

Fig. 2.1 Comparison of model-simulated and the observed winter half-year temperature anomalies (Jones, 1998) in the eastern China. The anomalies are calculated with reference to the 1951–1980 mean temperature as shown by the dotted line.

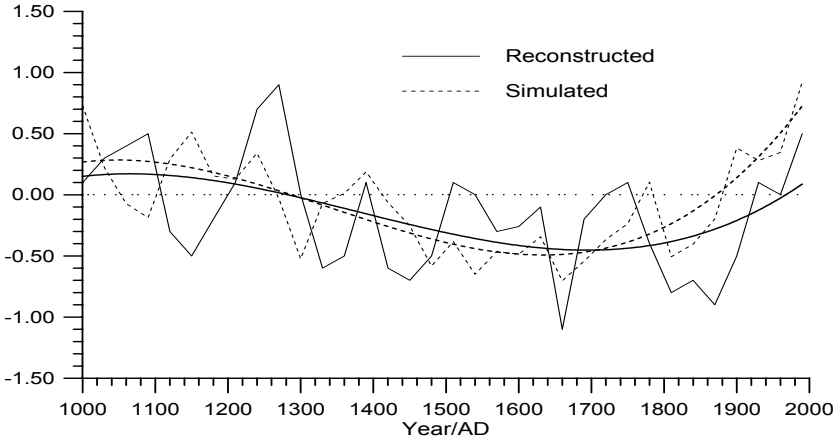

Fig. 2.2 Comparison of simulated and reconstructed winter half-year temperature anomalies in the eastern China. Detailed explanation is referred to the text.

2.4 Sensitive simulation of climate in LIA

Promoted by the international research projects of PAGES and CLIVAR, the studies on climatic and environmental changes in the past 2000 years have drawn the attention of geologists and palaeoclimatologists all over the world. Among them the cold event of the Little Ice Age (LIA) is particularly the most attractive one, which is the nearest typical cold period in the global range from modern age, and had a profound impact upon human society. Additionally, more knowledge about the causes of origin and dynamic mechanisms of LIA may enrich and improve the theory of climatic changes on century scale, which can be used to predict the future tendency of climatic changes, and evaluate the possibility of cold vibrations on the global warming background.

There has been a half-century history of the LIA study abroad. Recently, based on the high-resolution and multi-environmental proxies from ice cores, tree rings, historical documents, lake sediments, corals and stalagmites, scientists have deeply known about the age, internal fluctuations and the characteristics of the climate and environment in LIA. Subsequently, setting out from the climatic control factors, the cause of LIA formation was effectively explained, by using the changes of those parameters, such as sequences of ^{14}C in tree ring (related to solar activity), acidity of ice core (related to volcanic activity), and concentration of green house gases in ice core bubbles. Owing to the continual progresses in methods and techniques of climatic simulation, scientists have carried out the simulation experiments of LIA, and have made obvious progresses.

Studies on lots of historical documents, archaeological datum and kinds of climatic proxies (tree ring, ice core, lake sediment), Chinese scientists have worked hard and carefully on several aspects, including the main climatic characteristics and stages of LIA in China and the effect of LIA on Chinese social ecology and people's livelihood. The results mentioned above indicate an evident regional difference in origin, amplitude and duration of the change in temperature and precipitation. This part is about LIA simulations on the mechanisms of climatic changes during LIA by using a GCM (Liu et al., 2002).

2.4.1 Model description

A global model (AGCM + SSiB) is used which includes the terrestrial processes. The AGCM model is an improved nine-layer and fifteen-spectrum model, with horizontal resolution of $7.5^{o} \times 4.5^{o}$. The SSiB model is a simplified version of the simple biosphere model, in which

there is one vegetation layer with twelve vegetation types and three soil layers. After the calculation of SSiB, diagnostic variables are obtained, such as soil temperature and humidity in each layer, the temperature and moisture storage of the vegetation crown and ground temperature and snow amount, and SSiB and AGCM are coupled finally. Ever since the 1990s, Chinese climate modelers have made improvements in many aspects of the model.

2.4.2 Design of the simulation experiments

During LIA the solar radiation was 0.5% less than the average of modern time, the average optic depth of stratosphere volcanic dust is 0.15 and the vegetation of the underlain surface is slightly changed by human activities. We therefore design seven simulation experiments (Table 2.1).

In all the LIA simulation experiments (Table 2.1), atmospheric CO_2 level, sea surface temperature, background and preliminary field of atmospheric aerosol have consistent values. The integration time of the model is 15 years, taking the average result of the last 10 years as the equilibriums of these simulations. Running the experiments involved above, we can compare the effects and mechanisms caused by changes of solar radiation, optic depth of stratosphere volcanic dust, underlain surface vegetation and CO_2 content in the formation of LIA.

2.4.3 Analyses of simulation

Temperature

(1) Characteristics of the temperature change forced by a single factor. The differences between Exp.1 and Exp.2 reflect the possible effect of the decrease in solar radiation output by 0.5%, taking Exp.1 as the comparative standard experiment (control run). Fig. 2.3 shows the difference distribution of annual mean temperature, summer temperature and winter temperature in Eurasian continent between Exp.1 and Exp.2, respectively. The difference of annual mean temperature of the whole Eurasia is abnormally negative (Fig.2.3 (a)), except for the small region of Middle East and the Siberian high-latitude region. And the most remarkable temperature decrease appears in northeastern China and northern Africa, the mean maximum decrease may reach up to 0.6°C, mostly exceeding over 0.2°C. The summer temperature decrease is larger than that of winter. The whole Eurasia of the Eastern Hemisphere suffered from temperature decrease by over 0.2°C, the maximum is up to 1°C (Fig. 2.3 (b)). Compared with that

of summer, the temperature decrease of winter is smaller both in region and extent. Temperature still decreases in Northeastern China, whereas the increase occurs in the mid and west part of China. All the results above indicate that the reduced solar radiation, as the forcing mechanism of temperature decrease during LIA, has different effects on the seasonal temperature decrease; the temperature decrease is more evident in summer than in winter. Meanwhile, because of other feedback mechanisms, there is a large regional difference in the winter temperature change. However, the annual mean temperature decrease is the most obvious characteristic.

Table 2.1 Characteristics of LIA simulation experiments

Expt.	Solar radiation (w/m^2)	Optic depth of volcanic dust	Type of underlain surface vegetation	CO_2 (ppm)	Remark
1	Modern value (1367.04)	Modern value	Modern	345	Control experiment
2	-0.5% (1360.165)	Modern value	Modern	345	Single-factor sensitivity experiment
3	Modern value (1367.04)	+0.15	Modern	345	Single-factor sensitivity experiment
4	Modern value (1367.04)	Modern value	Ante- Industrial-Revolution	345	Single-factor sensitivity experiment
5	-0.5% (1360.165)	+0.15	Modern	345	Double-factor sensitivity experiment
6	-0.5% (1360.165)	+0.15	Ante- Industrial-Revolution	345	Tri-factor sensitivity experiment
7	-0.5% (1360.165)	+0.15	Ante- Industrial-Revolution	280	Typical LIA experiment

Fig.2.4 gives the distribution of temperature difference between Exp.3 and Exp.1, which represents the temperature change effect after increasing the optic depth of stratospheric volcanic dust. The temperature decrease effected by volcanic dust is obvious, and the annual mean value is between 0~0.4°C, with the maximum of 0.4°C being in Northeastern China (Fig.2.4

(a)). The temperature decrease is slightly smaller than that of Exp.2 in both region and extent. Compared with the figure about annual mean, summer mean, and winter mean change of temperature (Fig.2.4), the amplitudes of summer and winter mean change are apparently larger than that of annual mean. Additionally, the change in winter is more remarkable than in summer. The summer temperature decrease in most parts of China is between 0~0.6°C, while that is 0.2~0.8°C in winter, the maximum in the Siberian region is above 1.2°C. The results indicate that volcanic dust plays an important role in the winter temperature decrease. This decrease is opposite to the effect of temperature decrease caused by solar radiation. Moreover, comparing Fig.2.3 with Fig.2.4, the effect of temperature decrease arising from the change of volcanic dust is smaller than that from the reduction of solar radiation, however, their spatial distribution has some similarity.

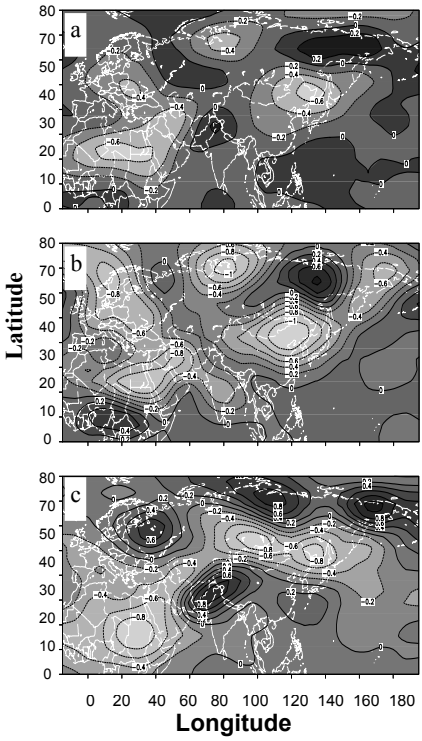

Fig. 2.3 The distribution of temperature difference between Exp.1 and Exp.2. (a) Annual mean; (b) summer mean; (c) winter mean.

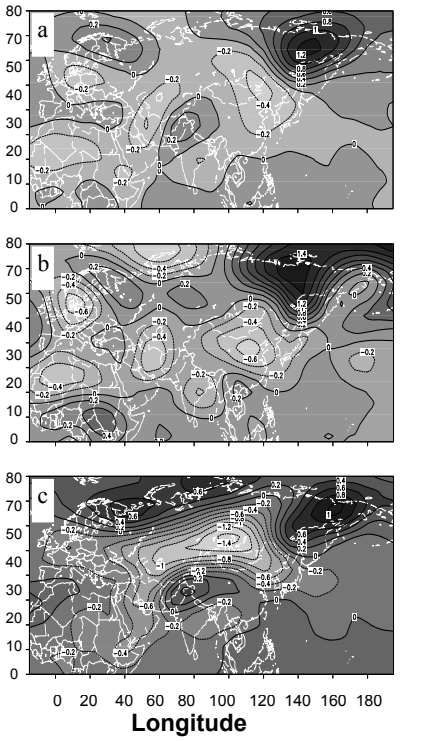

Fig. 2.4 The distribution of temperature difference between Exp.1 and Exp.3.(a) Annual mean; (b) summer mean; (c) winter mean.

(2) Characteristics of the temperature change forced by double factors. Fig.2.5 shows the temperature effect after reducing the solar radiation and increasing the optic depth of stratospheric volcanic dust. In these maps, annual mean temperature in Eurasia still decreases. The annual mean temperature decrease in China is between 0.2~0.4°C, and that in Europe and most parts of North Africa is above 0.2°C (Fig.2.5 (a)). Comparing with Fig.2.3(a) and Fig.2.4(a), the region of maximum temperature decrease above 0.4°C in Fig.2.5 (a) extends, which reflects that the synchronous function caused by the reduction of solar radiation and the increase of optic depth of volcanic dust has a superposed strengthening effect on the temperature decrease in large regions. The main regions of summer temperature decrease include the whole Eurasia, especially in East China, whose central part is North China, with an amplitude of 0.2~1.0°C. The range of summer temperature decrease is still larger than that of the annual average. In winter the center of temperature decrease in Eurasia moves to the west, the center of maximum temperature decrease approximately above 1°C. And the east part of China turns into an uneven decrease region. The most remarkable temperature decrease occurs in North East and South China, while the slight temperature increase appears in West China.

In the analysis of the results of simulation experiments mentioned above, both the reduction of solar radiation and the increase of the optic depth of stratospheric volcanic dust can result in the air temperature decrease of land surface, but because the mechanism of decrease in temperature and the background of atmospheric circulation are different, the extent of the decrease and the regional distribution are not the same. However, the integrated effect is to decrease the temperature, to make the distribution more even, and to strengthen the average extent of temperature decrease.

(3)Temperature effect resulting from the change of vegetation and CO_2 concentration is another important topic in the LIA climate change. Many research and simulation experiments indicate that the change of vegetation plays an important role in the air temperature of land surface in the certain time scale and climatic background. When performing the LIA climate simulation experiments, two types of vegetation are chosen for making comparison, modern vegetation and vegetation before Industrial Revolution. As a whole, the latter has a larger rate of natural vegetation coverage than that of the former. The result of Exp.4 indicates that the change of vegetation field engenders different tendency in temperature change, i.e. the annual mean temperature increased in East Asia, while that of North Africa decreased significantly (figure omitted). Thus the promotion of the vegetation coverage profits the increase of temperature, and the decrease of vegetation coverage contributes to the decrease in temperature of the land surface. Because the LIA climate turned cold, the vegetation coverage

in some regions of China became smaller. So, from this point of view the vegetation status has played a certain role in the formation of LIA climate. For lack of the more completed vegetation status in LIA, the simulation experiments with real vegetation coverage in LIA did not perform.

Precipitation

(1) Precipitation effect caused by the reduction of solar radiation is shown in Fig.2.6 and Fig. 2.7. Fig.2.7(a) shows the difference of precipitation distribution between Exp.2 and Exp.1. It can be seen that there is no evident change of annual precipitation in the whole Eurasia, while precipitation increases significantly in the West Pacific Region. The increase in annual precipitation in the West Pacific Region and the South East China is above 0.3 mm/d, and that in North West and Mid of China is about 0~0.3 mm/d, approximately 100 mm/a or so. Precipitation in other regions slightly decreases or remains as usual. While in summer the precipitation changes evidently, increasing in East Asia, South Asia and Indian region. In the most parts of China, except the littoral region in South China, the precipitation variation is positive abnormally, especially in east part of China, with an increase about 0.5~1.0 mm/d, which amounts to 50~100 mm in the three months of summer. Meanwhile, precipitation also increases in the equator TCZ, South Asia, Northwestern Pacific Ocean and Indian Ocean, but decreases in the South China Sea and Bengal Bay. The change of winter precipitation is similar to that of the annual precipitation. Except the South China Sea and the West Pacific Ocean with an increase of 0.5~1.5 mm/d, there is nearly no change in the mainland of China. These characteristics of precipitation uncover that summer monsoon circulation and precipitation change in East Asia with the change of solar radiation, that is, certain decrease in insolation will profit increase in precipitation of summer monsoon in East Asia.

(2) Precipitation change caused by effect of volcanic dust is shown in Fig.2.7. Fig.2.7 (a) indicates that the increase in the optic depth of volcanic dust does not affect the annual precipitation in most parts of the Eurasian continent, while precipitation increases slightly in the region of China and India in East Asia. Furthermore, there is still a significant increase in precipitation in the region of the Western Pacific Ocean. The change of annual precipitation is less than 50 mm, or even unchanged in most parts of China. Meanwhile, precipitation changes insignificantly in the region near the equator. This tendency is strengthened in summer, and precipitation increases evidently in the middle of China. The increase range in the Indian subcontinent is approximate to that in the region of East Asia. In China from southeast littoral to inland, the increase range is between 0~1 mm/d,

which means that the maximum change in summer precipitation can reach about 50~100 mm. The significant decrease in precipitation still occurs in the South China Sea. There is an evident increase in precipitation in the Western Pacific Ocean and equator TCZ, with the maximum value of 2.5 mm/d. This phenomenon probably implies that the increase in the optic depth of volcanic dust can intensify the precipitation caused by Southwestern Monsoon and South western Air current, while in other non-monsoon regions the effect of volcanic dust is not significant (Fig.2.7 (b)). The fact that the winter precipitation decreases in South Asia and slightly increases in Mid-Asia may indicate its relationship with the activity of southern branch of westerly (Fig.2.7(c)).

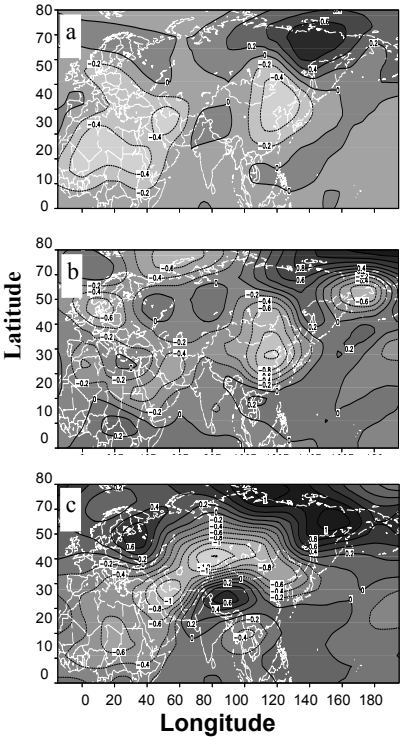

Fig. 2.5. The distribution of temperature difference between Exp.1 and Exp.5. (a) Annual mean; (b) summer mean; (c) winter mean.

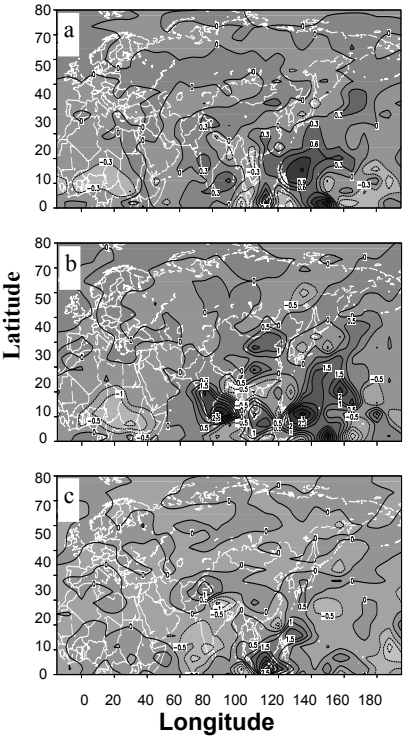

Fig. 2.6. The distribution of precipitation difference between Exp.1 and Exp.2. (a) Annual mean; (b) summer mean; (c) winter mean.

(3) Precipitation change affected by double factors. Fig.2.8 shows the precipitation change caused by both the reduction of insolation and the increase in the optic depth of stratosphere volcanic dust. The composite effects of the two forcing factors cause the increase in annual precipitation in East Asia, especially in East China. The maximum of that is 0.3 mm/d, equal to about 100 mm/a, while the decreases in annual precipitation in both Southeast Asian and Indian region. The spatial distribution pattern of summer precipitation is similar to that of annual precipitation, but the ranges of increase and decrease become larger; and the summer precipitation increases by above 0.5 mm/d (approximately 46 mm in the season) in East China; the maximum is more than 90 mm, while the summer precipitation decreases by above 1 mm/d (90 mm) in South Asia; the maximum exceeds 180 mm. The winter precipitation does not change evidently in the whole Eurasia, but there is a maximum center in Mid-Asia where the precipitation increases over 40 mm. The conclusion is that the composite effects of both factors are to promote the precipitation of summer monsoon in East China, and to reduce the southwestern monsoon precipitation in South Asia.

Precipitation change affected by the change of vegetation. After changing the status of vegetation (Exp.4), the annual precipitation increases significantly in East Asia, and the precipitation of summer monsoon also increases by 46~160 mm. Meanwhile, there is evident precipitation increase in India and Southeast Asia, while precipitation decreases in Mid-Africa. Winter precipitation does not change significantly. It is suggested from these analyses that, after coupling with vegetation component, precipitation increases where the vegetation coverage increased (e.g. East Asia); when the vegetation coverage reduces (e.g. North Africa), the precipitation decreases, too.

2.5 Palaeoclimate simulations of mid-Holocene and LGM

Reconstructions from proxy data, including pollen, lake-level, and loess records, have been providing a picture of regional climate changes of China during the Quaternary. The General Circulation Models (GCMs) has been used to explore the mechanisms of observed regional and global climate in the past decades. By use of GCMs, we can simulate the atmospheric response to the external forcing in LGM (21ka B.P.) and mid-Holocene (6ka B.P.). Some model simulations have demonstrated the importance of land-surface and ocean feedbacks for regional climates. Here we introduce the results of equilibrium climate simulation for the East Asia

by using prescribed vegetation coverage corresponding to the observed changes in vegetation patterns for these two periods. Comparisons of model simulations with palaeoclimate data from China show how far we can explain past climate changes and the confidence that can be placed in current state-of-the-art models.

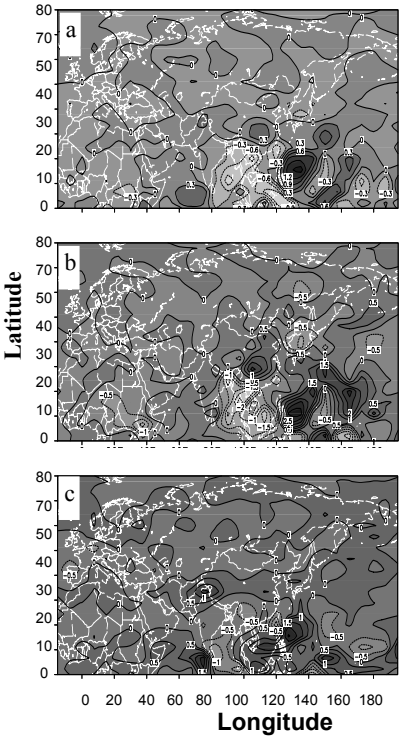

Fig. 2.7. The distribution of precipitation difference between Exp.1 and Exp.3. (a) Annual mean; (b) summer mean; (c) winter mean.

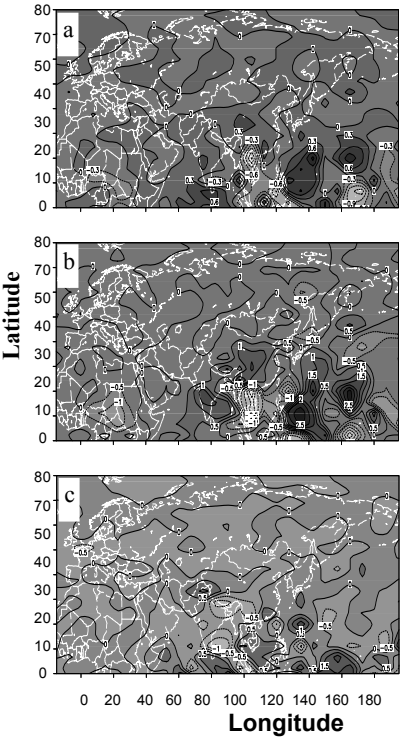

Fig. 2.8 The distribution of precipitation difference between Exp.1 and Exp.5. (a) Annual mean; (b) summer mean; (c) winter mean.

As we known that the Palaeoclimate Modelling Intercomparison Project (PMIP: Joussaume and Taylor, 1995; Joussaume and Taylor, 1999) has examined how the northern hemisphere monsoons responded to changes in climatic forcing at the last glacial maximum (LGM, ca 21 ka BP. equivalent to ca 18 ^{14}C ka BP.) and during the mid-Holocene (Pinot et al., 1996; Joussaume et al., 1999). These two intervals represent two climate extremes.

The model used here is the same as that used in LIA simulation, AGCM+SSiB to simulate climate changes in the Asian region at 6 ka BP and 21 ka BP. The experimental design for the 6 ka BP and 21 ka BP. experiments followed the PMIP protocol (Joussaume and Taylor, 1995) and some changes are made according to the reconstructed vegetation data in order to investigate the importance of vegetation feedbacks on regional climates over Asia.

The BIOME 6000 vegetation data sets for 6 ka BP and 21 ka BP. (Version 4.0: Prentice et al., 1996; Yu et al., 1998; Yu et al., 2000) were used as the basis for the derived land-surface characteristics. The pollen-based reconstructions at each site in the BIOME 6000 data set were interpolated to the grid of the climate model; grid cells containing multiple pollen sites were attributed to the modal vegetation type, and no change was made to grid cells lacking pollen sites.

2.5.1 The 6 ka BP climate simulations

It is important for us to understand a similar impact of climate warming in response to the increased atmospheric carbon dioxide in the future, and climate warming in response to one likely consequence of the changes in radiation forcing in the mid-Holocene (6 kaBP), which has become one of hot topics in international community of Global Changes.

An international project for paleoclimate modeling at 6 kaBP (PMIP: Paleaoclimate Modeling Intercomparison Project) was launched in 1990s and has made great progresses. However, some important issues have not resolved so far. The PMIP designed a program for AGCM (Atmospheric General Circulation Model) simulations in which variations of solar radiation is considered as a major dynamic force for 6 kaBP climate. As the solar radiation variation played a unique role in the simulations, consequently most of the AGCMs have simulated the paleoclimate of 6ka BP with a general pattern of a warm summer and a cold winter over the major continents of the world.

However, synthesized studies from Quaternary data indicate that winter temperature at 6 kaBP was 2.5°C warmer in the east and 3-4°C warmer in the west of China than that at the present. This warm climate condition was recorded not only in China, but also in northern America. These facts do not agree with the modeling results that were only driven by solar radiation. Therefore, there would be other control factors that contributed to the warm climate at 6 ka BP, especially to the winter warming. It is necessary

for us to explore the causes of winter warming in the mid-Holocene in the East Asia.

Studies from TEMPO Program have revealed that, after introducing the feedback of surface albedo with a coupled climate-biome model, a northward-shift climate zone in northern Africa can be simulated. Chinese scientists also did modeling experiments to test the impact of vegetation on the monsoon precipitation. Claussen et al., (1996) found that the influence of changed orbital geometry of the Earth has been amplified in the climate change in subtropical climate zone because of the feedback of atmosphere and vegetation. It is likely believed that changes in the regional and global vegetation have strong feedbacks on climates of the mid-Holocene.

Although the above studies have suggested that the climate at 6kaBP was directly or indirectly controlled by a feedback between climate and land surface, the simulations of PMIP before 1999 did not include the forcing from an active land surface in the boundary conditions of the modeling experiments. This caused that modeling results disagreed with observed data from the East Asia, especially they produced a contrary result for winter temperature in China.

In this section, an AGCM plus SSiB was used to simulate climate at 6 ka BP. As an improved dynamical factor, land surface conditions of vegetation at 6 ka BP were reconstructed from geological records and input into the climate model in order to simulate more realistic features of paleoclimate (Chen et al., 2002).

Forcing conditions

Forcing conditions for control test (0 kaBP) are based on modern climate, including orbital geometry of the earth (1950 AD), atmospheric CO_2 concentration (345ppm), sea surface temperature (SST), vegetation distribution, and ice or snow coverage.

The paleoclimate simulation is designed in two experiments. The forcing conditions for Experiment One of 6 kaBP climate (Exp. 1) are prescribed according to a standard prescription from the PMIP. The orbital geometry of the Earth is from Berger's studies. CO_2 is set to 280 ppm. SST, vegetation, and ice or snow coverage are prescribed as the present-day conditions. In Experiment Two of 6 kaBP climate (Exp. 2), solar radiation, SST, ice or snow coverage and CO_2 are the same as Exp. 1, but we used paleovegetation at 6 ka BP instead of a prescribed one from modern vegetation. The vegetation distribution at 6 kaBP is reconstructed from pollen data over major continents by using biomization method. This method is good at translating pollen data into vegetation types. Yu (1998) introduced

how to translate pollen data of 6 kaBP into vegetation types in detail. We interpolated the point-type vegetation data into grid data by 4.5°×7.5°grids in order to match the resolution of the AGCM. Forcing conditions of control test (0 kaBP) and 6 kaBP simulations are listed in Table **2.2.**

Table 2.2 Forcing conditions used in the simulation experiments

Forcing condition		0 kaBP	6 kaBP
Orbital parameter (Berger)	Obliquity	23.446	24.105
	Eccentricity	0.016724	0.018682
	Perihelion	282.04	180.87
Topography		present	Same as 0 kaBP
SST		present	Same as 0 kaBP
Sea ice		present	Same as 0 kaBP
Ice sheet		present	Same as 0 kaBP
CO_2 concentration		345 ppm	280 ppm
Vegetation		present	Based on pollen data

Results and Analysis of the Simulations at 6 kaBP

11-year model run was made under the forcing conditions for 6 kaBP simulations. The average of the last 10 years was treated as mean climate condition.

Temperature simulation in Exp. 1

Fig.2.9 plotted the differences of simulated temperature between 6 kaPB and 0 kaBP. In the west of Eurasia, annual temperature at 6 kaBP was 0-0.5°C warmer than that in the present in the south of 50°N, and colder than present in the north of 50°N (Fig.2.9a). In the East Asia, summer temperature was about 2.0°C warmer at 6 kaBP than the present in the south of 40°N (Fig.2.9b), and winter temperature decreased about 2.0°C (Fig.2.9c) at 6 kaBP comparing with the present. This result agrees with those of PMIP climate simulations at 6ka BP.

PMIP standard simulations at 6 kaBP revealed a typical Post-glacial climate when Quaternary ice sheets were melted in the Northern Hemisphere. In views of climate dynamical mechanisms, solar radiation is the fundamental basic forcing that causes changes in climate warming globally and extensions of African and Indian monsoons regionally. Similar to all of the PMIP simulations at 6 kaBP, the Exp. 1 also showed annual and summer temperature about 1°C increases and significant decrease in winter

temperature in the low and middle latitudes (20-50°N) of Eurasian continent.

During the Holocene, the summer solar radiation reached the maximum at 9 kaBP (11 kaBP in calendar year) in the Northern Hemisphere, and was 7-8% greater in summer and 2-3% less in winter than present in middle and low latitude area (south of 50°N). This abnormal pattern had continued to the mid-Holocene (6 kaBP) and becomes a key reason why the PMIP climate simulations and the Exp. 1 modeled the cold temperatures in winter at 6 kaBP.

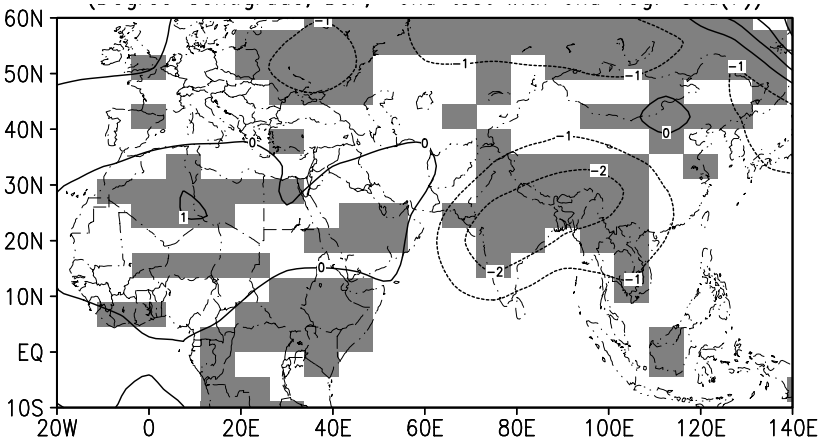

(a)

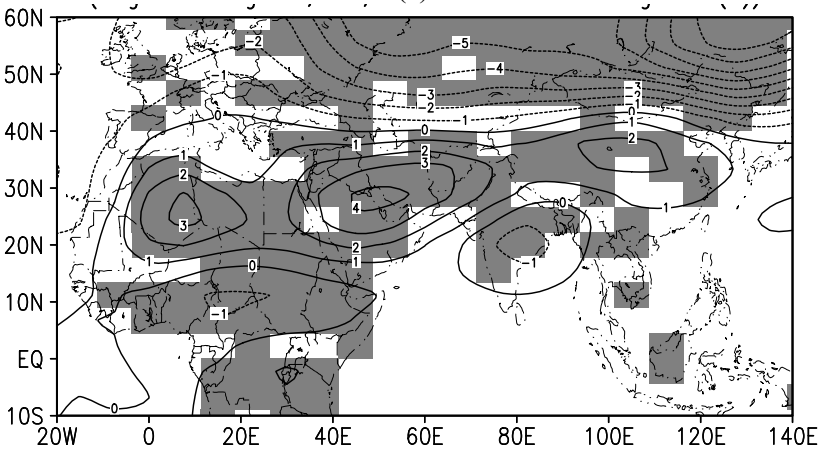

(b)

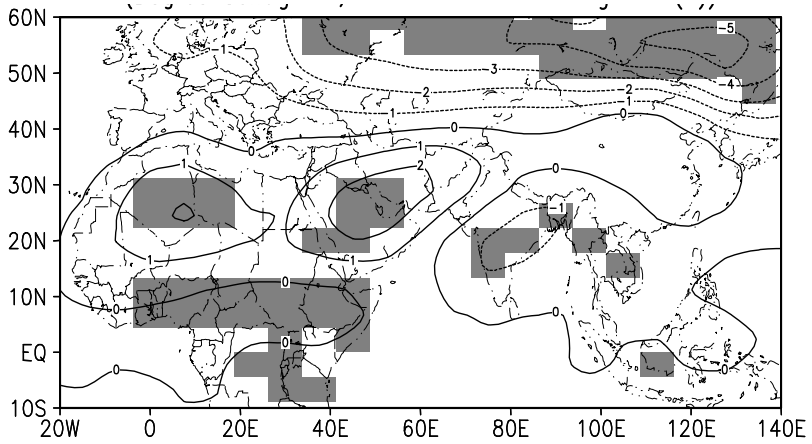

(c)

Fig. 2.9 Differences of simulated temperatures between 6ka BP (Exp. 1) and 0ka BP, (a) Difference of annual temperature (°C), (b) Difference of summer temperature (°C), (c) Difference of winter temperature (°C)

Temperature simulation in Exp. 2

In the Exp.2, the vegetation distribution at 6 kaBP is used as land surface coverage in the modeling. The differences of temperature between Exp. 2 and control test (Figs not given) in the East Asia indicate ca 1-2°C warmer in summer and ca 0.5-1.0°C warmer in winter at 6 kaBP than the present. The annual temperature at 6 kaBP increased about 0.5-1.5°C over all of the East Asia. The results imply that Exp. 2 has much more improvement in temperature simulation of 6 kaBP than Exp. 1. To compare the temperature simulations between the two experiments, we computed the temperature differences between Exp. 2 and Exp. 1 in order to understand the net effect of the vegetation on the temperature changes (Fig.2.10a, b and c). The index was shown in Fig. 2.10.

Simulated annual temperature in Exp. 2 was higher than that in Exp. 1 in the north of 50°N in Europe, but it was slightly lower in Exp. 2 than Exp. 1 in Siberian area. In the south of 50°N, annual temperature was about 1-2°C higher than that in Exp. 1 in the eastern and northern China. There was no significant change of summer temperature between Exps. 1 and 2 (Fig.2.10b). However, winter temperature in Exp. 2 was 1°C higher than Exp. 1 in the middle and eastern parts of China in the south of 50°N (Fig. 2.10c)

Exp. 2 did not show a significant temperature change in Tibetan Plateau at 6 kaBP. It was 1-2°C lower in winter in the central Plateau and 1°C

warmer in summer of north plateau than those in Exp. 1. Modern summer warming in the plateau is mainly due to increased solar radiation, which the summer heating is a major contribution to the annual temperature increase due to the specific geographical position and atmospheric optical characteristics of the plateau. Thus the warming effects should not mainly come from the vegetation changes in the plateau region. However, it is necessary to further study the causes of temperature change in the plateau in terms of the specific horizontal and vertical structures, the independent pressure system, and the planetary westerly over the Tibetan Plateau, e.g. using coupled climate-vegetation model to explore the possible mechanisms of climate at 6 kaBP.

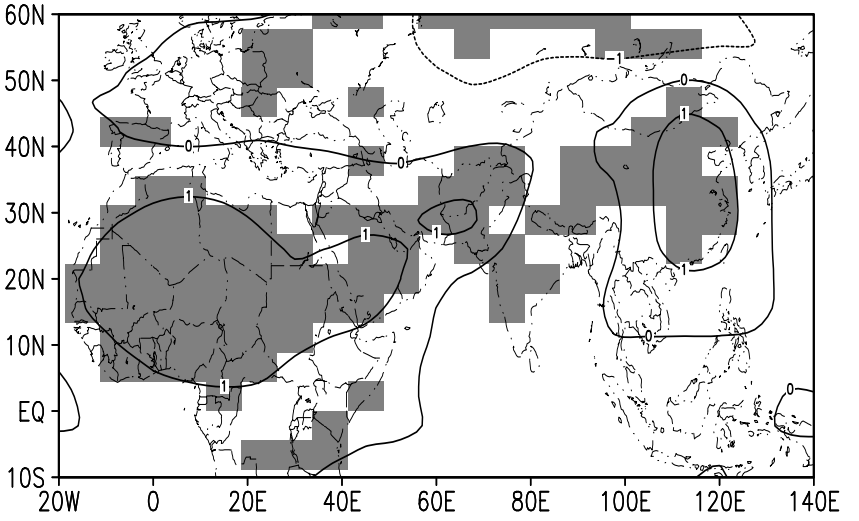

(a)

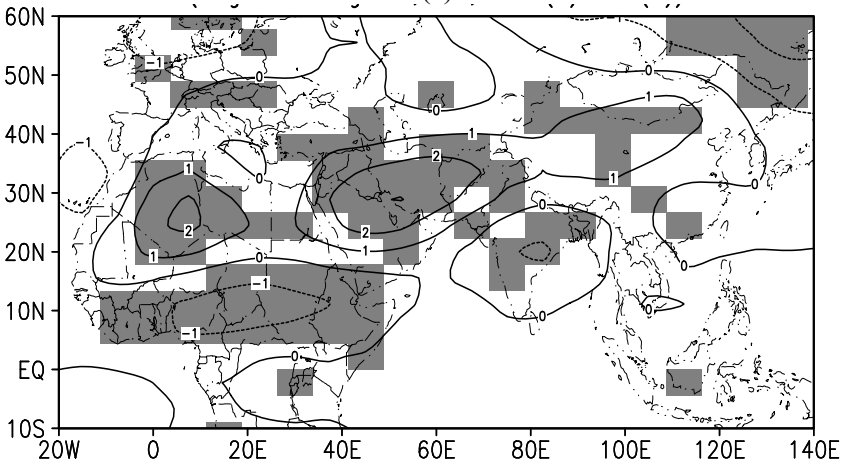

(b)

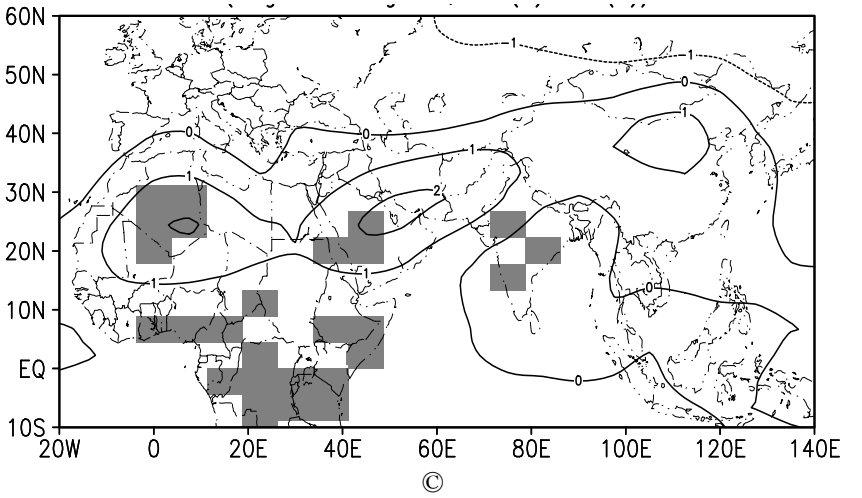

Fig. 2.10 Differences of simulated temperature at 6 kaBP between Exp. 2 and Exp.1, (a) Difference of annual temperature (°C), (b) Difference of summer temperature (°C), (c) Difference of winter temperature (°C)

Significant test of simulations

From above analysis we can see that changes of solar radiation and vegetation in the mid-Holocene (6 kaBP) have played very important roles in the climate changes. Here we give the results of significant test for these simulation changes. By using T-student test at 95% confidence limit, two pairs of experiments (0 ka BP and 6 ka BP in Exp. 1, 6ka BP in Exp. 1 and 6 ka BP in Exp. 2) have been performed by T-test processes. Significant areas for each pair of parameters are shadowed in Fig.2.9 and Fig.2.10. In Exp. 1, when solar radiation is considered as a unique forcing factor, both summer warming and winter cooling in the East Asia are significant. The simulation of winter temperature by vegetation forcing in Exp. 2 has the largest significant areas in the east parts of China, and also larger significant area in the subtropics area (western Asia and northern Africa). Significant test showed that increases in annual and summer precipitation are significant in the middle latitude of the East Asia (30°N –50°N), northern Africa, and western China (Figs not shown).

Data and model comparison of climate at 6 ka BP

Paleaoclimate records can provide a reconstructed climate in the mid-Holocene in China, on basis of studies in Quaternary sciences, paleoclimatology and paleoenvironmeatal sciences. Records from pollen, fossil plants

and animals, paleosoils, lakes, ice cores, and the Neolithic archaeological evidences have reconstructed that annual mean temperature was higher than the present in China in the mid-Holocene. Researchers used various proxy indices to reconstruct qualitatively climate change (such as warm and wet, hot and dry, cool and mild, etc.) and to transform quantitatively temperature estimates. Pollen data indicate that paleovegetation belts shifted northward in latitude and upward in altitude. Records of macrofossils of animals and plants have estimated temperature of the mid-Holocene on basis of animal groups immigrated northward to a large extent. The paleosoils development and anthropological traces (traces of ancient human) in loess series, the change of oxygen isotope in ice core, historical documents and archaeological evidence of animal distributions all indicated a warm condition in the mid-Holocene. Based on these studies we estimated quantitatively mean temperature of annual, summer, and winter at 6 kaBP.

The annual mean temperature (from 43 sites), summer temperature (from 7 sites), and winter temperature (from 12 sites) are presented by differences of temperature between 6kaBP and 0ka BP in each geological site. In climatological studies, summer temperature infers to the mean temperature of June, July and August. In the geological studies, the definition of summer temperature is not accurate since some people used three months of June, July and August, but others may use the warmest month (July), so did the definitions in winter. Here, we included both climatological and geological definitions as semi-quantitative climate parameters. Result shows that annual mean temperature at 6 kaBP was about 1-5°C higher in the western China and about 3-4°C higher in the North China than the present. Exp. 1 has simulated about 0.5°C warmer in this area, but Exp. 2 showed 1-2°C warmer, suggesting that Exp. 2 has made great improvement comparing with the geological data. The winter temperature at 6 kaBP was about 3°C higher than the present in China. Exp. 2 simulated about 1-2°C higher in winter in this region, which agreed with extents of temperature changes from estimate of geological data. Summer temperature change at 6 ka BP was smaller than winter, about 1-2°C. The Exps. 1 and 2 have simulated similar summer temperatures to the geological data.

Improved surface condition in Exp. 2 has produced a better climate simulation with increased winter temperature at 6 kaBP. This simulation revealed the potential effects of both solar radiation and vegetation on the climate change, because the simulated winter warming is very much approaching to the reconstructed climate from geological data at 6 kaBP. Our climate simulation of 6 kaBP has also improved PMIP simulation of 6 kaBP. It should be pointed out that the pollen data could respond to the mean status of annual temperature and the plants growing season in spring-

summer. To improve the comparisons, more proxy data and the analyses are necessary.

Mechanisms of vegetation effects on climate change

The simulations suggested that increased solar radiation in the mid-Holocene played a major role in global warming, and increases in regional precipitation were mainly controlled by feedback of vegetation forcing. Foley et al., (1994) pointed out that the main cause of 6 kaBP warming in the high latitudes (60-90°N) of North Hemisphere is due to the decrease in the surface albedo because forests were extending northward and replacing tundra. Claussen et al (1999) discussed the sensitivities of vegetation and climate change over northern Africa in the mid-Holocene, suggesting that the regions with more vegetation coverage could not only absorb more solar radiation on the surface, but also increase surface evaporation, which could enhance greenhouse effect and lead to warm and wet climate comparing with bare surface conditions. TEMPO members (1996) found that the position of the northern border of forests in the mid-Holocene was related with temperature increases, especially the changes in vegetation could caused warming in summer (July), ca. 1.5°C to 4.0°C higher than that in 0 kaBP. Bonan et al., (1992) suggested that winter and summer temperature in the high latitudes (60-90°N) would increase when forests replaced tundra because of significantly reduced surface albedo. Studies of paleovegetation in the mid-Holocene showed that in the east part of China (east of 100°E), tropical broadleaf-evergreen trees extended northward and the large area covered by forests that replaced groundcover and desert in Inner Mongolia. At the same time, forests in Tibetan Plateau were extended upward at the high altitude. Therefore, the change and extension of vegetation coverage in large-scale would result in the spatial variation of the earth surface albedos. According to the vegetation distribution used in present simulation, needle leaved evergreen trees in mid-Holocene extended to the areas of modern tundra in the north part of Eurasia continent. Modern deciduous needle leaved trees forest in the high latitude of eastern Eurasia area was covered by needle leaved evergreen forest in the mid-Holocene. There were broadleaf-evergreen trees that shifted northward in the east part of China. Broadleaf trees and groundcover in northern Africa in subtropical latitudes covered deserts in the mid-Holocene. These evidences suggested: (1) When deciduous-trees was replaced by evergreen trees, the surface albedo in winter was reduced from 0.14 to 0.12 and annual average surface albedo kept same values 0.12 as today. (2) When desert and bare soil were replaced by groundcover, surface albedo decreased either. (3) When tundra in high latitudes replaced by coniferous-evergreen trees, the average sur-

face albedo changed from 0.16-0.17 to 0.10-0.12. Because of decrease in surface albedo, especially the winter albedo, it can create a warmer effect on climate in the mid-Holocene. Decreases in winter surface albedo, as a consequence of vegetation changes in the south part of China, would be equivalent to increases in surface net radiation and lead to increase in winter temperature.

According to the heat balance on the earth surface, changes in the surface albedo would lead to the differences of the thermal contrast between land and ocean, and lead to variations of monsoon circulation in the Eastern Asia. From the seasonal sea level pressure differences between Exp. 1 and Exp. 2 (Figs. Not shown), there is an enhanced low-pressure system over the East Asia and a subtropical high-pressure over Northwestern Pacific Ocean in the summer. As a result, difference between land and ocean would cause a strong summer monsoon circulation. In winter, high-pressure system over the East Asian continent and pressure system over northwest Pacific all became weaker in the mid-Holocene. The possible cause of this monsoon circulation change is likely that the tundra in high latitude area retreated to polar area, and coniferous leaved trees extended northward in a large-scale. Changes in the surface vegetation cover in the high latitude would increase earth surface thermo capacity, reduced cooling in high latitude, and weaken the cold high-pressure system over the continent. Thus, weakened winter monsoon circulation in the Eastern Asia would reduce the winter cooling, although there was an cooling effect of solar radiation decrease in the middle and low latitude areas (0-40°N). Furthermore, variation of the earth surface albedo from vegetation change in the mid-Holocene led to differences of seasonal thermo contrast between land surface of the East Asia and sea surface of northwest Pacific Ocean. As a result, summer monsoon circulation in the mid-Holocene became stronger than the present and wetter climate is formed.

Discussion

Based on two sets of boundary conditions, i.e. PMIP setting at 6 kaBP (Exp. 1) and paleovegetation setting (Expt. 2), the climate at 6 kaBP was simulated by using AGCM+SsiB. Exp. 1 simulated about 1-2°C increase in annual mean temperature and about 2°C decrease in high latitudes in the East Asia. Exp. 1 revealed solar radiation driving and responded to the change of orbital geometry of the Earth in the mid-Holocene. This result is similar to those of most PMIP climate simulations at 6 kaBP in the late of 1990s.

Simulation of Exp. 2 explored the warming effects of vegetation under solar radiation forcing in the mid-Holocene. Annual mean temperature was

about 1-2°C warmer and winter temperature was 2-4°C warmer in the Eastern Asia. This fact revealed the vegetation effects on the climate warming through reducing surface albedo. Even though there are some discrepancies with geological records, results of Exp. 2 made a great improvement for winter temperature simulation in the mid-Holocene, suggesting that surface vegetation plays a very important role in changes of the seasonal and regional climate at 6 kaBP.

The comparison of simulation experiments shows that surface albedo variation due to vegetation change can produce the seasonal change in the thermodynamic differences between land surface in the Eastern Asia and sea surface over western Pacific Ocean in the mid-Holocene. On the other hand, forest extending in high latitude regions has increased the thermal capacity on the surface and reduced the cooling effects. As a result, the winter monsoon circulation was weakened and cold air activity was limited, leading to the winter temperature increased. Next work will need, in paleoclimate modeling, especially developing simulation experiments with coupled climate-biome models to improve simulation so that we can fully understand the physical processes and mechanisms of the paleaoclimate change.

2.5.2 The 21 ka BP climate simulations

Last Glacial Maximum (21ka BP) is another hot topic in the field of paleoclimate study. Recently, a lot of research results from data analysis of palaeoclimate and numerical simulation reveal that global climate at 21ka is very different from that in the present due to the existence of north-hemispheric icesheets, low concentration of CO_2, different sea surface temperatures (SSTs), and orbital-forcing insolation anomalies (CLIMAP Members, 1981; COHMAP Members, 1988; Harrison et al., 1996; Kotlia et al., 1997; Street-Perrott et al., 1989;Tarasov et al., 1994; Wright et al., 1993). Quaternary researches in China reveal very different climate patterns at 21ka BP comparing with present in China. They are unique and special in the world (Chen et al., 1990; Li et al., 1988; Li et al., 1994; Li et al., 1995; Liew et al., 1998; Qin and Yu, 1998; Sun et al., 1995; Wang et al., 1990; Yao et al., 1994). The palaeoclimate at 21ka BP in China has been reconstructed and the results indicated that there were very different dry and wet climate patterns in the east and the west, and a dramatically decreases in temperature in this area. But the dynamical mechanisms and atmospheric circulation background of the climate anomalies at 21ka BP are not very clear. Some experiments to reproduce this condition at 21ka BP have been conducted just for the global climate at 21ka BP (Dong

et al., 1996; Joussaume and Taylor, 1995; Kutzhach et al., 1998). But so far no good simulation results of paleoclimate experiments have been reported about the climate change in China at last glacial maximum, especially the explanations of mechanism of East Asian monsoon variations.

In this section, based on the analysis of different sources of paleoclimatological records, by using a general atmospheric circulation model (AGCM) coupled with a simplified land processes model (SSiB) (e.g. AGCM+SSiB) and the forcing conditions, climate conditions at 21ka BP in China are reproduced and the possible dynamical mechanisms are explored. By comparing reconstructed climate from various proxy indices with atmospheric circulation features from the model, the major characteristics associated with the potential mechanisms of climate change at 21ka BP in China are addressed preliminarily (Chen et al., 2000, 2001; Yu et al., 2001).

Forcing conditions

The experiments are designed according to Paleo-climate Modeling Inter-comparison Project (PMIP). It is used to determine the model predicted equilibrium climate that is consistent with certain imposed changes in boundary condition characteristics of the period under study. Here, the boundary conditions indicate various prescribed conditions (including orbital parameters which determining the insolation pattern, atmospheric CO_2, glacial ice distribution and sea surface temperatures), which are considered to be external to the components of the climate system for typical GCMs. By considering equilibrium climate states, the study limits the kinds of issues that can be addressed concerning the evolution of climate from the state to another. For the last glacial maximum (LGM), two experiments are designed in PMIP. In one experiment SSTs are prescribed, while in the other experiment, SSTs are created by ocean model. In this study, the first method is used and the massive ice sheets covering North America and Scandanavia have been prescribed according to reconstruction by Peltier (1994). It is very important that the last glacial maximum climate is characterized by large changes in the surface boundary conditions (ice sheet extent and elevation, sea surface temperatures (SSTs), and surface albedo) and atmospheric carbon dioxide concentration, but only minor changes in the insolation pattern. This period (21ka BP) is very important for understanding how ice sheets and lowered CO_2 levels influence the climate. Among the climate features of interest in this experiment are only the simulated changes in the Northern Hemisphere jet stream location and associated changes in the storm tracks (Gates, 1976; Valdes and Hall, 1994; Manabe and Broccoli, 1985; Rind, 1987; Kutzbach and Guetter,

1993; Joussamue, 1993). To our knowledge, there is no numerical simulation study focusing on Asia monsoon climate features in China at 21ka BP. Therefore, in this study, we design the experiment and attempt to simulate the climate at 21ka BP in East Asia and China.

Design of simulation

In this experiment 21ka BP simulation is driven by two kinds of forcing conditions. One is associated with solar radiation, e.g. earth orbital parameters (perihelion, eccentricity and obliquity). The other is associated with the earth surface conditions, including sea surface temperatures (SSTs), snow and ice coverage, atmospheric CO_2 concentration and vegetation. In order to identify the climate change at 21ka BP from the present, we run both 0ka and 21ka BP experiments. In the 0ka (control) test, SST is present data with 10-year variation. Snow and sea ice coverage with seasonal variation, vegetation distribution and earth orbital parameters are same as present. CO_2 concentration is 280ppm. In the 21ka BP experiment, SSTs, sea ice, snow cover and ice sheet are determined based on PMIP document. CO_2 concentration is 200ppm, and earth orbital parameters are estimated according to Berger (1978). Some researches indicated that interaction between vegetation and atmosphere is very important in climate simulation (Foley et al., 1994; Martin et al., 1999; Winkler and Wang, 1993). In this study vegetation distribution at 21ka in Eastern Asia are prescribed according to pollen data (Yu et al., 2000). All forcing conditions are summarized in Table 2.3. For both 21ka BP and control experiments, 11 modeling years simulation was run, and averages of last 10 years were treated as mean equilibrium climate conditions. Here, 10-year average is used as a typical period of climate status at 21ka BP and to be compared with modern climate.

Table 2.3 Earth orbital parameters and boundary conditions for simulation experiments

Parameters	The earth orbital parameters			Boundary conditions
	Eccentricity	Perihelion	Obliquity	
Present (0ka)	0.0167	282.04	23.446	280ppm CO2 concentration, 10-year SST, present snow and sea ice cover, present vegetation distribution
21ka BP	0.0187	294.42	22.949	200ppm CO2 concentration, SST from CLIMAP, snow and ice sheet from PMIP, vegetation distribution changed over Eurasia from geological data

Simulation Results

(1) Modeled climate features at 21ka BP in China

The simulated surface temperature, precipitation and effective precipitation P-E at 21ka in the area of China are shown in Fig.2.11 (a), (b) and (c). The annual mean surface temperatures (shown in Fig.2.11(a)) are from 20°C to –20°C with the region from Hainan Island, southern China, to northeastern China. Annual mean surface temperature in Tibetan Plateau is about –5°C to –10°C, the one of the coldest regions by the model simulation, and the another one is northeastern China. It can be seen from Fig.2.11 (b) that there is high annual precipitation in the Tibetan Plateau region. The maximum of that is more than 2.5mm/d, and the most of the Plateau is covered by area of 1.5mm/d. There is the region covered by 2.5mm/d in the north of China. On the contrary, precipitation in eastern and southeastern China is less than 2.5mm/d. Index representing dry and wet conditions (annual effective precipitation P-E), is mapped in Fig.2.11 (c). The pattern of P-E distribution is very similar to that of precipitation. The maximum of that is in Tibetan Plateau. In the middle and south of the Plateau, P-E is greater than 1.5mm/d, and maximum is about 2mm/d. As a contrast, P-E is less than 1mm/d in the eastern China, which is much less than that in the Plateau. This distribution shows that there was humid climate in Tibetan Plateau and dryer climate in the east of China at 21ka BP.

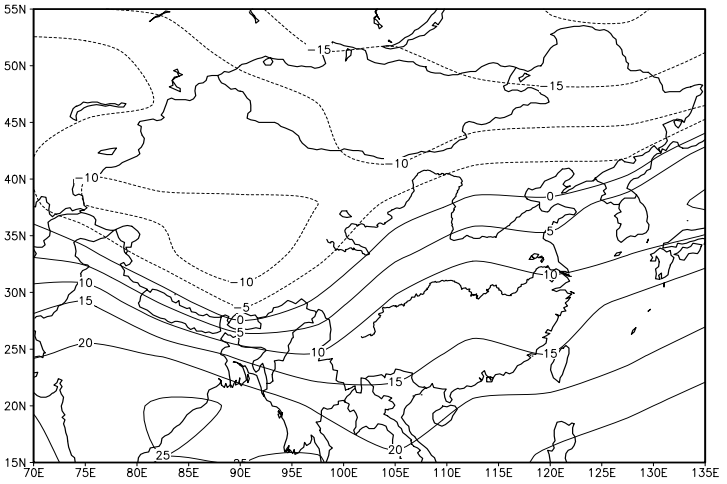

(a)

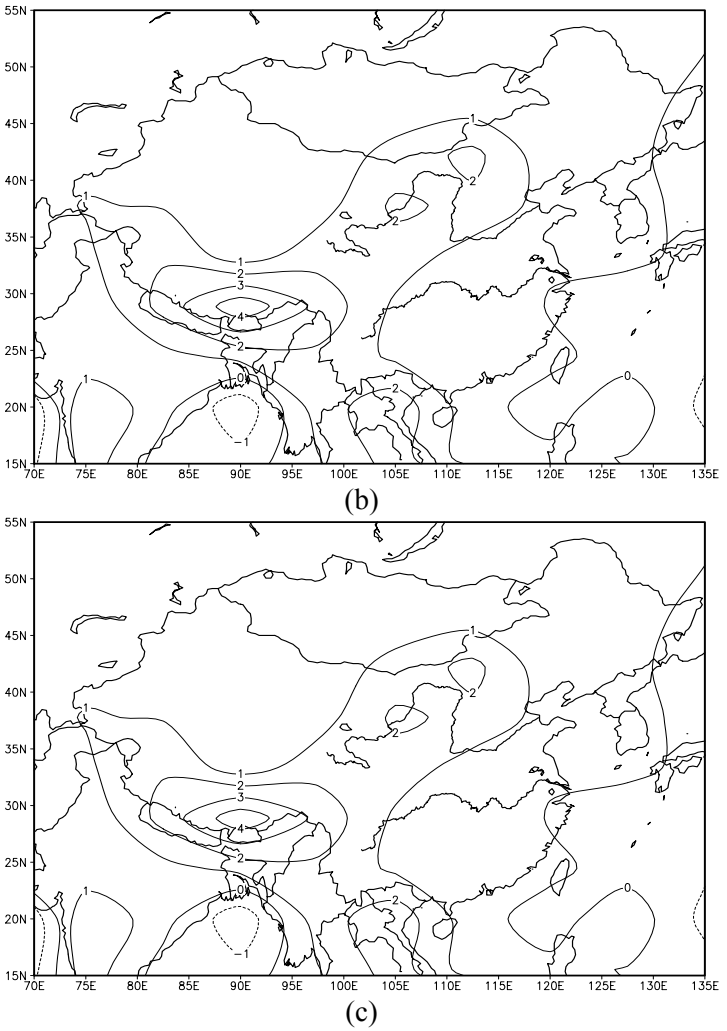

Fig. 2.11. Simulated surface temperature, precipitation and effective precipitation P-E at 21 ka BP (a) Annual surface temperature(°C), (b) Annual precipitation(mm d^{-1}); (c) Annual effective precipitation P-E（mm d^{-1}）

From above results we can find the main climate features at 21ka BP in China are that it was colder and wetter in the Tibetan Plateau and warmer and drier in eastern China compared with the Plateau. The differences of the climate between 21ka BP and present are shown in Fig.2.12 (a), (b) and (c). From the differences of annual mean temperature (Fig.2.12 (a)), it can be seen that decreases in temperature ranged between 1°C to 10°C at 21ka

BP. In the Plateau, temperature decreasing in summer is less than that in winter. This indicates that climate was warm in summer half year in Tibetan Plateau. The anomalies of annual precipitation at 21ka BP (Fig.2.12 (b)) shows that the positives located at Tibetan Plateau, northwest of Xinjiang, north and northeast of China. The differences of annual precipitation are negative in the regions where precipitation is plentiful at present, such as the east and the southeast of China. Especially in the up and middle basins of Yangtze River, the decrease in precipitation is more than 1mm/day. It means that these areas are short of precipitation at 21ka BP. The distributions of difference of annual effective precipitation (P-E) are almost the same as that of annual precipitation (Fig. 2.12 (c)).

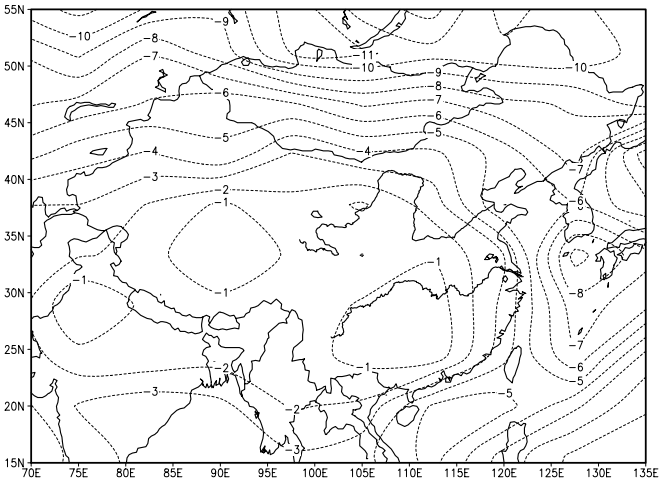

(a)

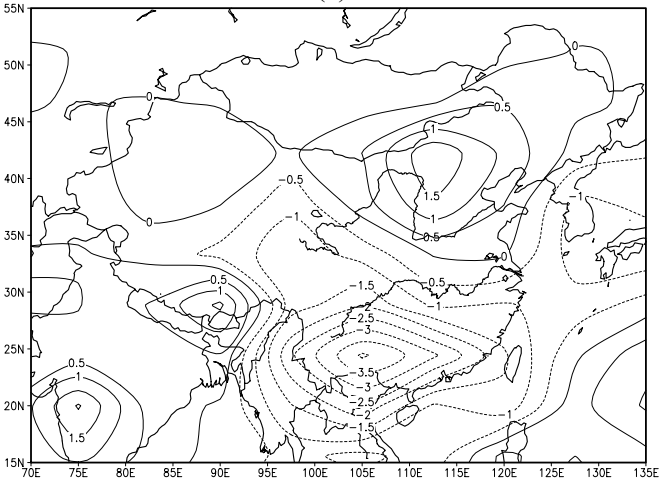

(b)

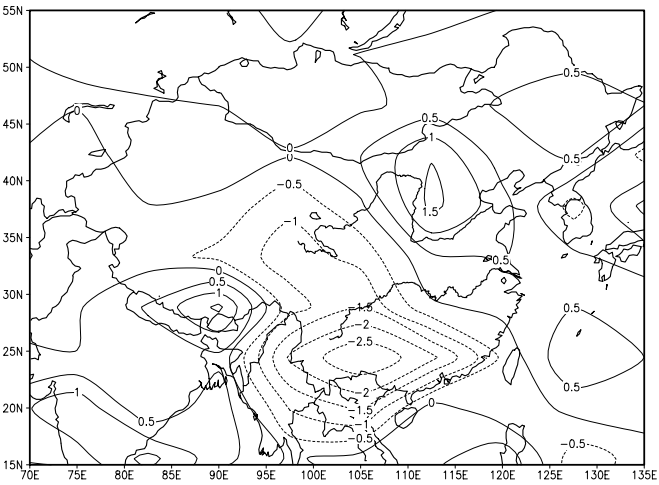

(c)

Fig. 2.12. Differences of simulated temperature at 21 ka BP and present (a) Difference of annual temperature (in °C); (b) Difference of Annual precipitation (in mm d^{-1}); (c) Difference of Annual effective precipitation P-E (in mm d^{-1})

From the simulation of 21ka BP conditions, we can find that it is colder in China at 21ka BP than present, and the humidity spatial patterns are almost inverse between 21ka BP and present, e.g., it is wetter in the west and drier in the east of China at 21ka BP.

(2) Comparison between the simulation and paleoclimate evidence of 21ka BP

The simulation of climate at 21ka BP is validated by palaeoclimatical evidence. Reconstructed lake status and vegetation pattern at 21ka BP in China from paleo-lake -status database and pollen database can be used as indices of the climate conditions, are compared with the model simulation results.

The lake records show that lake-water levels are low at present in the northwest, north and northeast of China, and they are high in southern and southeastern China today. The conditions registered by lake-status match the precipitation distribution in the present China. The data of 21ka BP show high lake water levels in Tibetan Plateau and northwestern China and the low levels in the eastern China. These reconstructed climate features at 21ka BP were wet in the west and dry in the east of China. The distribution of vegetation patterns shows that the cold and humid conditions are in the northeast of China. As a comparison, modern vegetation patterns in the

southeast of China is indicating warm and wet condition, the steppe and desert vegetation responding to dry condition in the northeast and northwest of China, while the tundra in eastern Tibetan Plateau controlled by alpine cold and wet conditions. In these regions climate is colder and drier. While at 21 ka BP in China, the vegetation in the most eastern China, except for the coastal zone of southeast, was characterized by the steppe and deserts. There were some vegetation adjusting to humid climate in Tibetan Plateau and the northeast of China. Therefore the climate in these regions was cold and humid, and consistent with the distributions of modeled precipitation and effective precipitation shown in Fig.2.12.

Discussion

The preliminary simulation results of climate at 21ka BP in China discussed above give the typical climate conditions that have been addressed by a lot of geological data. The simulation of AGCM+SSiB model to climate at 21ka BP in China is fare consistent with reconstructed paleoclimate. Before then there were some simulation experiments by using CCMs and UGAMP, but these experiments could not give realistic Eastern Asia monsoon system signal and precipitation field. In our study, modeled Eastern Asia monsoon system is better and 21ka BP simulation is agreed with geological evidences.

Based on the comparison between model output and data analysis, we can obtain preliminary conclusions as follows:

(1) The modeled results of AGCM+SSiB with 21ka BP boundary conditions and changed vegetation distribution experiment simulated complete different conditions at 21ka BP from the present in China, as dry conditions in the eastern China and humid conditions in Tibetan Plateau. This result is consistent with paleoclimate evidences and it shows different climate at 21ka BP comparing with present. This is the first successful simulation that captured the climate features in China at 21ka.

(2) Decreases in temperature at 21ka BP in China were significant. The range of temperature decrease is from 1°C to 10°C.

(3) The changes of eastern Asia monsoon circulation are dramatic in summer at 21ka BP. The weaker summer monsoon is associated with the decreasing of pressure differences between land and sea, while in Tibetan Plateau summer monsoon was strengthened.

2.6 Summary

In this chapter, the studies on regional paleoclimate of China by proxy

data and climate models are presented. The research results of that give a brief picture of paleoclimate in the past. The most reliable and high resolution proxy data can be used to reconstruct climate time series up to more than ten thousands years. Therefore, in the last 20ka, especially in the Holocene, the climate of China is studied more sufficient both in the proxy data analysis and in the modeling. From these results we can know and understand some features of climate change since the LGM in China. Paleaoclimate records can provide a reconstructed climate in the mid-Holocene in China, on basis of studies in Quaternary sciences, paleoclimatology and paleoenvironmeatal sciences. Records from pollen, fossil plants and animals, paleosoils, lakes, ice cores, and the Neolithic archaeological evidences have reconstructed that annual mean temperature was higher than the present in China in the mid-Holocene.

The temperature over the last millennium simulated by the global climate model ECHO-G is used to compare with the reconstructed temperature anomalies in the eastern China. By this simulated regional climate of China, we examined the possible causes and mechanisms of the past climate changes in China. A global atmospheric circulation model (AGCM + SSiB) is also used to make sensitive simulation of LIA climate, and found that the volcanic eruption, solar constant, and vegetation changes are the key factors for the climate change in LIA. Both the reduction of solar radiation and the increase of the optic depth of stratospheric volcanic dust can result in the temperature decrease over the land surface. Two types of vegetation, modern vegetation and vegetation before the Industrialization, were used to test the sensitivity in LIA climate change. As a whole, the latter has a larger rate of natural vegetation coverage than that of the former. The result indicates that the change of vegetation field engenders different tendency in temperature change, i.e. the annual mean temperature increased in East Asia, while that decreased in North Africa. Thus the promotion of the vegetation rate profits the increase of temperature, and the decrease of vegetation rate contributes to the decrease of land temperature.

Simulations suggested that increased solar radiation in the mid-Holocene played a major role in global warming, and increases of regional precipitation were mainly controlled by feedback of vegetation forcing. The comparison of simulation experiments shows that variation of the surface albedo due to vegetation change can produce the seasonal change in the thermal differences between land surface in the Eastern Asia and sea surface over western Pacific Ocean in the mid-Holocene. The forest extending in high latitude regions increased the thermal capacity of the land surface and reduced the cooling effects. As a result, the winter monsoon circulation was weakened and cold air activities were reduced, and leading to an increased winter temperature.

The model simulation shows that the main climate features at 21ka BP in China was colder and wetter in the Tibetan Plateau and warmer and drier in eastern China compared with the Plateau. The differences of annual precipitation are negative in the regions where precipitation is plentiful at present, such as the east and the southeast of China. It means that these areas are short of precipitation at 21ka BP, especially in the upper and middle reaches of Yangtze River. The simulation results are validated by lake-status of 21ka BP that shows high lake water levels in Tibetan Plateau and northwestern China and the low levels in the eastern China. That means wet climate in the west and dry in the east of China at 21ka BP.

Proxy data studies and climate modeling studies can help us understand the mechanisms of paleoclimate changes in China in great details. Also, these studies provide us an opportunity to link the climate changes in China to those in the rest of the world.

References

An Zhisheng, Wu Xihao, Lu Yanchou et al. (1990) A preliminary study on the paleoenvironment change of China during the last 20,000 years, Loess, Quaternary geology and global change (Part II) (in Chinese) (ed. Liu Dongsheng), Beijing: Science Press, 1-26.

Berger, AL (1978) Long-term variations of daily insolation and Quaternary climatic changes, J. Atmos. Sci., 35: 2362-2367.

Bonan, GB, Pollard, D, Thompson, SL (1992) Effects of boreal forest vegetation on global climate, Nature, 359: 716-718.

Cao JT, Wang SM, Shen J (2000) Primary study of paleoclimate changes during the past millennium in Daihai lake, Inner-Mongolia, Marine Geology & Quaternary Geology, 20(2), 15-20 (in Chinese)

Central Meteorological Institute of Chinese Meteorological Administration et al., (eds), 1981: The Drought and flood Charts in China for the Last 500 years. China Atlas Press, Beijing, 332 pp

Chen JY (1988) Preliminary studies to the several questions about lichen of glacier change in the Holocene in Wulumuqi River of Tianshan Mountain. Science in China, (1), 95-104

Chen K, Bower J, Kelts K (1990) Changes in climate on Qinghai-Xizang plateau during the last 40000 years, Quaternary Sciences, (1): 21-30.

Chen Xing, Yu Ge, Liu Jian (2000) A preliminary simulation of climate at 21 ka BP in China, Journal of Lake Sciences (in Chinese), 12(2): 154-164.

Chen, X. et al. (2001) An AGCM+SSiB simulating changes in paleomonsoon climate at 21ka in China. Acta Meteorologica Sinica, 15(3): 333.

Chen, X. et al. (2002) Mid-Holocene climate simulation and discussion on the mechanism on temperature change. Science in China (in Chinese), 32(4): 335.

Chen Xing, Liu Jian, Wang Sumin (2002) Climate simulation of Little Ice Age over eastern Asia, SCIENTIA METEOROLOGICA SINICA, 25(1): 1-8

Claussen, M (1996) Variability of global biome patterns as a function of initial and boundary conditions in a climate model, Climate Dynamics, 12: 371-379.

CLIMAP Members Seasonal reconstructions of the Earth's surface at the Last Glacial Maximum, Geological Society of America Map Chart Series 36. 1981

COHMAP Members, Climatic changes of the last 18,000 years: observations and model simulations, Science, 1988, 241: 1043-1052.

Cubasch U et al (1997) Simulation of the influence of solar radiation variations on the global climate with an ocean-atmosphere general circulation model. Climate Dynamics, 13: 757.

Ding ZL, Yu ZW, Rutter NW et al (1994) Towards an orbital time scale for Chinese loess deposits. Quarter. Sci. Rev., 13, 39-70

Dong B, Valdes P, Hall N (1996) The changes of monsoonal climates due to earth's orbital perturbations and ice age boundary conditions, Palaeoclimates, 1:203-240.

Du Naiqiu, Kong Zhaochen, Shan Fashou (1989) A preliminary investigation on the palaeoclimate and palaeoenvironment based on pollen analysis in core QH85-14C, Acta Botanica Sinica (in Chinese), 31: 803-814.

Etheridge D et al (1996) Morgan natural and anthropogenic changes in atmospheric CO_2 over the last 1000 years from air in Antarctic ice and firn. J. Geophys. Res,' 101: 4115.

Foley JA, Kutzbach JE, Coe MT et al (1994) Feedbacks between climate and boreal forests during the Holocene epoch, Nature, 371: 52-54.

Gates WL (1976) The numerical simulation of ice-age climate with a global general circulation model. J.Atmos.Sci., 33: 1844-1873.

Ge QS, Zheng JY, Man ZM et al (2002) Reconstruction and analysis on the series of winter-half-year temperature changes over the past 3000 years in eastern China. Earth Science Frontiers, 9(1), 69-181 (in Chinese)

Group of Experts (2002) Project of Chronology Studies on the Xia, Shang and Zhou Dynasties-Report of 1996-2000: Simplified Version. World Book Press, Beijing, pp86−88 (in Chinese)

Harrison SP, Yu G, Tarasov P (1996) Late Quaternary lake-level records from northern Eurasia, Quaternary Research, 45: 138～159.

Hong Yetang, Liu Dongsheng, Jiang Hongbo et a (2000), Evidence for solar forcing of climate variation from $\delta^{18}O$ of peat cellulose, Sciences in China, series D, 43(2): 217-224.

Jones PD, Mann ME (2004) Climate over past millennia. Rev. Geophys., 42, R 2002, 1-42

Joussaume S, Taylor KE, Braconnot JF et al (1999) Monsoon changes for 6000 years ago: Results of 18 simulations from the Paleoclimate Modeling Intercomparison Project (PMIP), Geography Research Letters, 26(7): 859-862.

Joussaume S, Taylor KE, (1995) Status of the Paleoclimate Modeling Intercomparison Project (PMIP), In: Proceedings of the First International AMIP Scientific Conference (Monterey, California, USA, 15～19 May 1995), WCRP Report, 92: 425～430.

Kang XC, Graumlich LJ, Sheppard P (1997) The last 1835 year Climatic changes inferred from tree-ring records in Dulan Region, Qinghai. China Quaternary Sciences, (1), 70-75 (in Chinese)

Kohfeld KE, Harrison SP (2003) Glacial-interglacial changes in dust deposition on the Chinese Loess Plateau, Quaternary Science Reviews, 21: 1859-1878.

Kong Zhaochen, Du Naiqiu, Zhang Yijun et al (1991) Discovery of Helicia fossil floral and sporopollen assemblage of Baohuashan in Jurong county and its climatic and botanical significance, Quaternary Sciences (in Chinese), 326-335.

Kotlia BS, Bhalla MS, Sharma C et al (1997) Palaeoclimatic conditions in the upper Pleistocene and Holocene Bhimtal-Naukuchiatal lake basin in south-central Kumaum, North India, Palaeogeography, Palaeoclimatology, Palaeoecology, 130: 307-322.

Kutzbach, JE, Gallimore R, Harrison SP et al (1998) Climate and biome simulation for the past 21,000 years, Quaternary Science Reviews, 17: 473-506.

Kutzbach JE, Guetter PJ, Behling P et al (1993) Simulated climatic changes: Results of the COHMAP climate-model experiments, Global Climates since the Last Glacial Maximum, ed. Wright, Jr. H. E., Kutzbach, J. E., Webb, III. T., et al., University of Minnesota Press, Minneapolis, 24-93.

Kutzbach JE, Guetter PJ (1986) The influence of changing orbital parameters and surface boundary conditions on climate simulation for the past 18,000 years. J. Atmos. Sci., 43: 1726-1759.

Li B, Cai B, Liang Q (1988) Sedimentary characteristics of Aiding Lake, Tulufan Basin, Chinese Science Bulletin, 33（8）: 608-610.

Li B, Li Y, Kong Z et al (1994) Environmental changes during last 20ka in the Gounongcuo Regions, Kekexili, Tibet, Chinese Science Bulletin, 39（18: 1727-1728.

Li JJ (1986) Tibetan Glacier. China Sciences Press, Beijing, pp 37-66 (in Chinese)

Li Y, Zhang Q, Li B (1995) Ostracode and its environmental evolution during late Pleistocene in the west Tibet, In: Committee of Tibet Research of China (Editor), Collections paper for meeting of Tibetan Plateau and global changes, Beijing: Meteorology Press, pp. 52～61.

Liew P, Kuo C, Huang S et al (1998) Vegetation change and terrestrial carbon storage in eastern Asia during the Last Glacial Maximum as indicated by a new pollen record from central Taiwan, Global and Planetary Change, 1998,16-17: 85-95.

Lin XC, Yu SQ (1990) Climatic trend in China for the last 40 years. Meteor. Monthly, 10, 16-21 (in Chinese)

Lin XC, Yu SQ, Tang GL (1995) Series of average air temperature over China for the last 1009year period. Chinese J. Atoms. Sci., 19, 525-534 (in Chinese)

Liu GY, Wang YX, Zhang XG (1984) Dendro-climatology of tree-ring in Qilian Mountain during the last millennium and its reflection on the glacier. Collected Papers of Institute of Glacier and Permafrost in Lanzhou, No. 5. pp.97-108,Chinese Science Press, Beijing (in Chinese)

Liu Hui, Wu Guoxiong (1997) Impacts of land surface on climate of July and onset of summer monsoon: a study with an AGCM plus SSiB. Advances in Atmospheric Sciences, 14(3): 290-308.

Liu H, Wu G. (1995) Description for a 9-layer Spectral Climate Model (L9R15), LASG Technical Report No. 3.

Liu Jian, Storch H , Chen Xing, Zorita E, Zheng Jingyun, Wang Sumin (2005) Comparison of simulated and reconstructed temperature in eastern China during the last 1000 years. *Chinese Science Bulletin*, 50 (24): 2872-2877

Liu J et al (2002) Sensitivity experiment of climate change in Eastern Asia during the Little Ice Age by changing solar radiation and volcanic dust. Journal of Lake Science (in Chinese), 14(2): 97.

Lou JY, Chen CT (1997)Paleo-climatological and paleo-environmental records since 4,000 a BP in sediments of alpine lakes in Taiwan. Science in China (D), 40(4), 424-461

Man ZM, Zhang W (1996) Chapter 7. Temperature changes in eastern China since Xia and Shang Dynasties in *Climate Change in China during Historical Times*，edited by Shi Y. E. and P. Y. Zhang, pp.293-300, Shandong Science and Technology Press, Jinan (in Chinese)

Manabe S, Broccoli AJ (1985) The influence of continetal ice sheets on the climate of an ice age. J. Geophys. Res., 90:2167-2190.

Martin C, Kubatzki C, Brovkin V et al (1999) Simulation of an abrupt change in Sahara vegetation in the mid-Holocene, Geophysical Research Letters, 26:2037-2040

McAvaney BJ, Bourke W, Puri K (1978) A global spectral model for simulation of the general circulation, Journal of Atmospheric Sciences, 35: 1557-1583.

PAGES/IGBP, CLIVAR/WCRP. The PAGES/CLIVAR Intersection, Report of a Joint IGBP-WCRP Workshop, Venice, Italy, 1994.

Peltier WR (1994), Ice age paleotopography, Science, 265: 195-201.

Prentice IC, Guiot J, Huntley B et al (1996) Reconstructing biomes from palaeoecological data: a general method and its application to European pollen data at 0 and 6 ka, Climate Dynamics, 12: 185-194.

Qin B, Yu G. (1998), Implications of lake level fluctuations at 6ka and 18ka in mainland Asia, Global and Planetary Change, 18: 59-72.

Qiu SH, Chen TM Cai LZ (eds), ^{14}C Chronological Research in China. China Science Press, 1990，Beijing, 366 pp (in Chinese)

Qin XG., Tan M, Liu DS et al (2000) Characteristics of annual laminae gray level variations in a stalagmite from Shihua Cave, Beijing and its climatic significance (II). Science in China (D). 43(5): 521-533

Ren GY, Zhang LS (1997) Late Holocene vegetation in Maili Region, Northeast China, as inferred from a high-resolution pollen record. Acta Boranica Sinica, 39(4), 353-362 (in Chinese)

Rind D (1987) Components of ice age circulation. J. Geophys. Res., 92: 4241-4281.

Ruddiman WF, Mix AC (1993) The north and equatorial Atlantic at 9000 and 6000 yr BP, Global climates since the Last Glacial Maximum, ed. Wright, Jr. H. E., Kutzbach, J. E., Webb, III, T,, et al., University of Minnesota Press, Minneapolis, 94-124.

Sellers PJ, Mintz Y, Sud YC et al (1986) A simple biosphere model (SiB) for use within general circulation models, J. Atmos. Sci., 43: 505-531.

Shao XM, Huang L, Lin HB *et al* (2004) Precipitation changes recorded in tree-ring data during the last millennium in Delinha region, Qinghai, Science in China (Series D), 2004, 34 (2): 145-153

Shi YF, Kong SC (1993) The climate and environment of China during the Megathermal of the Holocene, Ocean Press, Beijing, 212pp (in Chinese)

Shi YF, Kong SC, Wang SM et al (1992) General characteristics of climate and environment of China during the Megathermal of the Holocene. In *The Climate and Environment of China during the Megathermal of the Holocene*, edited by Shi and Kong, pp.1-18,Ocean Press, Beijing (in Chinese)

Shi YF, Zhang PY (1996) Historical Climate Changes in China. Shandong Science and Technology Press, Jinan, 538 pp（in Chinese）

Shi Yafeng, Li Jijun, Li Bingyuan, Qingzang Plateau bulge and environmental change in the late Cenozoic Era (in Chinese), Guangzhou: Guangdong Technical and Sciences Press, 1998, 249-295.

Street-Perrott FA, Marchand DS, Roberts N et al (1989) Global lake-level variations from 18,000 to 0 years ago: a palaeoclimatic analysis, Washington：U.S. DOE/ER/60304-H1 TR046. U.S. Department of Energy, Technical Report, 230.

Sun J, Ke M, Zhao J et al (1995) Vegetation and climate of the Loess Plateau in China during the late Pleistocene, Scientia Geologica Sinica, Supplementary Issure, (1): 91-103.

Sun Lan, Wu Guoxiong, Sun Shufen (2000) Numerical simulations of effects of land surface processes on climate: implementing of SSiB in IAP/LASG AGCM L9R15 and its performace, Acta Meteorologica Sinica (in Chinese), 58(2): 179-193.

Tan M, Liu TS, Hou JZ et al (2003) Cyclic rapid warming on centennial-scale reveals by a 2650-year stalagmite record of warm season temperature. Geophys. Res. Lett., 30(12), 19-1-4

Tang Mocang, Guo Weidong (2000) The Great Ice Age cycles associated with the variation of the atmospheric heat engine efficiency, Sciences in China, Series D, 43(3): 284-288.

TEMPO Members (1996) Potential role of vegetation feedback in the climate sensitivity of high-latitude regions: A case study at 6000 years B.P., Global Biogechemical Cycles, 10(4): 727-736.

Tarasov PE, Harrison SP, Saarse L et al (1994) Lake status records from the former Soviet Union and Mongolia: Data base documentation, Boulder: NOAA Palaeoclimatology Publications Series Report 2, 27.

Tong G.B, Zhang JP, Fan SX et al (1996) Environmental change at the top of Taibai Mountain, Qinling since 1ka ago. Marine Geology & Quaternary Geology, 16(4), 95-104 (in Chinese)

Tu QP (1984) Trend and periodicity in air temperature variations during the last one hundred years. J, Nanjing Institute of Meteorology, 1984, 7: 151-161 (in Chinese)

Valdes PJ, Hall NMJ (1994) Mid-latitude depressions during the last ice-age. In Long-Term Climate Variations - Data and Modeling. Edited by J.-C. Duplessey and M._T. Spyridakis, NATO ASI Series I, 22: 510-532.

Wang NL, Yao TD (2002) Evidence of ice core record in Guliya on the severe cold event in early Holocene. Chinese Sci. Bull., 47 (17), 1,422-1,427

Wang Huijun (1999) Role of vegetation and soil in the Holocene megathermal climate over China. Journal of Geophysical Research, 104(D8): 9361-9367.

Wang SM et al (1991) Lacustrine sediments— An indicator of historical climatic variation: the case of Qinghai lake and Daihai lake. Chinese Science Bulletin, 36(16):1364.

Wang SM (1990) The environmental change and paleoclimate in Daihai since the last ice age, Quaternary Research, (3), 223-232 (in Chinese)

Wang SW, Zhao ZC, Chen ZH et al (1987) Drought/flood variations for the last two thousand years in China and comparison with global climatic change. In: Ye DZ et al (eds) *The Climate of China and Global Climate*, China Ocean Press, Beijing, pp.20-29

Wang SW (1990) Trend in temperature variations in China and around the world for the last one hundred years. Meteor. Monthly, 16, 11-15 (in Chinese)

Wang SW (1991) Reconstruction of palaeo-temperature series in China From the 1380s to the 1980s. Würzburger Geographische Arbeiten, Heft 80, 1-19

Wang SW, Ye JL, Gong DY (1998a) Climate in China during the Little Ice Age. Quaternary Sciences, (1), 54-64 (in Chinese)

Wang SW, Ye JL, Gong DY, Zhu JH, Yao TD (1998b) Construction of mean annual temperature series for the last hundred years in China. Quart. J. App1. Meteor., 9, 392-401 (in Chinese)

Wang SW, Gong DY, Ye JL, Chen ZH (2000) Seasonal precipitation series over China since 1880. Acta Geographica Sinica, 55, 281-293 (in Chinese)

Wang SW, Zhou TJ, Cai JN et al (2004) Abrupt climate change at 4ka BP: Role of THC as indicated by a GCM experiment. Adv. Atmos. Sci., 21(2), 291-295

Wang ZT (1991) The Little Ice Age of Northwest China. Journal of Arid Land Resources and Environment, 5(3): 64 (in Chinese)

Winkler MG., Wang P (1993) The late-Quaternary vegetation and climate of China, In: Wright, H.E., Kutzbach, J.E., Webb, III T., et al. (Editors), Global Climates since the Last Glacial Maximum, Minnesota: University of Minnesota Press, pp. 221-261.

Wright JrHE, Kutzbach JE, Webb, III T et al (1993) Global climates since the Last Glacial Maximum, Minneapolis, University of Minnesoda Press, 468-513.

Wu XD, Lin ZY (1981) Preliminary study of climate change of Qinghai-Tibetan Plateau during the last two thousand years. In "*Proceedings of National Conference on Climatic Change Studies*, edited by Central Meteorological Institute, Chinese Science Press, Beijing, pp18-25 (in Chinese)

Xia YM, Wang PF (2000) Peat record of climate change since 3,000 years in Yangmu, Mishan Region. Geographical Research, 19(1), 53-59 (in Chinese)

Xu G.C (1997) Climate Change in Arid and Semi-Arid Zone. Meteorology Press, Beijing, 101 pp (in Chinese)

Xue Yongkang, Sellers PJ, Kinter JL et al (1991) A simplified biosphere model for global climate studies, J. Climate, 4: 345-364.

Yang B, Braenning A, Johnson KR et al (2002) General characteristics of temperature variation in China during the last two millennia. Geophys. Res. Lett., 29(9), 38-1-4

Yang B, Braenning A, Shi YF (2003) Late Holocene temperature fluctuations on the Tibetan plateau. Quarter. Sci. Rev., 22, 2335-2344

Yang B et al (2000) Decadal climatic variations indicated by Dulan tree-ring and the comparison with temperature proxy data from other regions of China during the last 2000 years. Scientia Geographica Sinica(in Chinese), 20(5): 397.

Yang XD et al (1995) Polynological evidence of climatic change during past 2000 years in middle reaches of Huaihe River. Memoirs of Nanjing Institute of Geography and Limnology Academia Sinica(in Chinese), 13: 20.

Yao TD et al (1996) Variation in temperature and precipitation in the past 2000a on Xizang(Tibet) plateau-Guliya ice core record. Science in China, Ser.D, 39(4): 459.

Yao TD, Xie ZC, Wu XL (1990) Little Ice Age climate record in Dande ice cap. Science in China (B), (11),1, 196-1,201

Yao TD, Shi YE (1992) Climatic change of the Holocene in the ice core records of Dunde in the Qiliandhan Mountain in *The climate and Environment of China during the Megathermal of the Holocene* , edited by Shi Y. F. and S. C. Kong, Ocean Press, Beijing, pp.206-211 (in Chinese)

Yao TD, Yang ZH, Huang CL (1996) Preliminary research on the climatic and environmental changes by using of the 2ka Guliya ice core data. China Science Bulletin, 41, 1103-1106

Yao T, Jiao K, Zhang X (1994) Climatic and environmental records from Guliya cap, China Science (D), 24: 766-773.

Yu G., Harrison SP (1995) Lake status records from Europe: Data base documentation, Boulder: NOAA Paleoclimatology Publications Series Report 3, pp. 451.

Yu G et al (1999) Lake records and LGM climate in China, Chinese Science Bulletin, 45(13): 1158-1164.

Yu Ge (1998) Preliminary study on pollen-based biomization and Chinese biome mapping of 6000 a BP, Acta Botanica Sinica (in Chinese), 40(7): 665-674.

Yu Ge, Chen Xing, Liu Jian et al (2001) Preliminary study on LGM climate simulation and the diagnosis for East Asia, Chinese Science Bulletin, 46(5): 364-368.

Yu G., Harrison S.P., Xue B, (2001a) Lake Status Records from China. Data Base Documentation. Technical Report in Max-Planck-Institute for Biogeochemistry, No.4 Jena. Germany, pp 243.

Yu G., Xue B, Liu J *et al* (2001b) Lake Records in China and the Palaeoclimate Dynamics. China Meteorological Press, Beijing , pp 196 (in Chinese)

Yu Ge, Chen Xudong, Ni Jian et al (2000) Palaeovegetation of China: a pollen data-based synthesis for the mid-Holocene and last glacial maximum, Journal of Biogeography, 27: 635-664.

Zhang De′er and Zhu SL (1981) Preliminary analysis of winter temperature conditions of south China during the last 500 years. In *Proceedings of National Conference of Climate Change*, edited by Weather and Climate Institute, Science Press, Beijing, pp.64-70 (in Chinese)

Zhang De′ er (1994) Evidence for the existence of the Medieval Warm Period in China. Climatic Change, 26 (2-3), 289-297

Zhang DE et al (1998) Paleoclimate inferred from the Chinese historical records of the northern boundary of migratory locust. Quaternary Sciences, 1: 12 (in Chinese)

Zhang DE (1995) Paleoclimate and environmental records available from Chinese historical documents. In: Proceedings of the 1995 Nagoya IGBP-PAGES/PEP-II Symposium. Nagoya: Nagoya University, 20.

Zhang DE, Liu CZ, Jiang JM (1997) Reconstruction of wetness series of six regions in east China during the last 1000 years and abrupt climate change. China Quaternary Research, (1), 1-11 (in Chinese)

Zhang LS, Fang XC, Ren GY (2000) Global Change, High-education Press, Beijing, 341 pp (in Chinese)

Zhang Lansheng (1993) Study on historical change and law of subsisting environment in China (Part I), Ocean Press, Beijing (in Chinese)

Zhang PY, Kong SC, Gong GF et al (1996), Climate change in China during the Historical Times. Shandon Science and Technology Press, Jinan,533 pp (in Chinese)

Zhang PY et al (1994) The stages of climate change in recent 2000 years. Science in China, Ser.B, 24(9): 998.

Zhang, W.Q. et al (2000) The Little Ice Age and its environmental effects in the tropical zone of China. Acta Geography Sinica(in Chinese), 55(6): 744.

Zhang XG., Li XQ (1982) Some characteristics of temperature variation in China in the present century. Acta. Meteor. Sinica, 40: 198-208 (in Chinese)

Zhang XH et al (2000) IAP Global Ocean-Atmosphere-Land System Model. Beijing: Science Press, 8-50.

Zhang Y, Wang WC (1993) Air temperature field near the ground in mid-Holocene in China. In Zhang Y. et al (eds) *Climate Change and its Impact*, pp91-107, Meteorology Press, Beijing (in Chinese)

Zhang ZK et al (1999) Climatic changes of Little Ice age and its social effects in China. Exploration of Nature(in Chinese), 18(1): 66.

Zhang ZK et al (2000) Lacustrine records of climatic change and human activities in the catchment of Erhai lake, Yunnan Province since the past 1800 years. Journal of Lake Science(in Chinese), 2(4): 297.

Zheng JY et al (1993) An analysis on cold/wet in Shandong Provience during historical times. Acta Geographica Sinica(in Chinese), 48(4): 348.

Zhong K (1997) The lacustrine sediment records of the environmental changes since the Little Ice Age (LIA) in the northern parts of East Xingjian. Journal of Xingjiang University, Natural Science Edition(in Chinese), 14(2): 78.

Zhu KZ (1972) Preliminary study on the climate change in China during the last 5000 years. Acta Archeological Sinica, 2(1), 15-38 (in Chinese)

Zhu KZ (1973) Preliminary study on the climatic fluctuations during the last 5000 years in China. Scientia Sinica, 16(2): 226.

Chapter 3 Interdecadal Climate Variability in China Associated with the Pacific Decadal Oscillation

3.1 Introduction

Observational evidence for the interdecadal variability of the ocean-atmosphere system in the North Pacific has attracted more and more attentions over the past decade. A number of earlier studies have revealed a regime shift around 1976/77 in the North Pacific (Namias et al., 1988; Nitta and Yamada, 1989; Trenberth, 1990; Trenberth and Hurrell, 1994; Graham, 1994; Miller et al., 1994; Hare and Mantua, 2000; Miller and Schneider, 2000). Such a regime shift is characterized by a surface cooling in the Kuroshio/Oyashio Extension (KOE, hereinafter) and midlatitude North Pacific and a surface warming in the central and eastern tropical Pacific. Associated with the cooling in the central North Pacific, the Aleutian low was enhanced and the midlatitude surface westerly was thus increased. The climate variability relevant to the North Pacific regime shift has been analyzed with nearly century-long oceanic and atmospheric data records (Zhang et al., 1997; Mantua et al., 1997; Nakamura et al., 1997; Zhu and Yang, 2003a). It is shown that the regime shift in 1976/77 is not unique during the past century. Similar regime transitions occurred also in 1920s and 1940s. This indicates the existence of prominent interdecadal variability in the North Pacific. Mantua et al. (1997) called the variability as the Pacific Decadal Oscillation (PDO). Distinguished from the interannual El Niño and Southern Oscillation (ENSO) variability, the signature of PDO is most visible in the midlatitude North Pacific while secondary in the tropics, whereas the opposite is true for the ENSO.

The impact of the PDO on the interdecadal climate variability in those regions surrounding the Pacific has been increasingly documented. Several studies have found evidence for the direct impact of the PDO on the North American climate (Latif and Barnett, 1994, 1996; Zhang et al., 1997; Mantua et al., 1997). It is also found that the PDO-related interdecadal variability could provide a slowly-varying background to modulate the ENSO properties (Wang, 1995) and the ENSO-related interannual variabilities in

North America and Australia (Minobe and Mantua, 1999; Gershunov and Barnett, 1998; Power et al., 1999). The climate of China has experienced significant variabilities on the decadal-to-interdecadal timescales over the past century (Wang, 1994; Shi et al., 1995; Chen et al., 1998; Li et al., 1999), and most of those variabilities are associated with the East Asian monsoon (Li and Li, 2000; Wang, 2001; 2002; Xue, 2001; Zhu and Wang, 2001). Some previous studies have implicitly described a possible relationship between the climate variations in China and the PDO-related SST anomaly in the Pacific (Wang and Zhao, 1979; Yu and Lin, 1997; Huang et al., 1999; Li and He, 2000). The ENSO is the strongest interannual signature in the Pacific and has significant impact on the East Asian summer monsoon and associated precipitation in China (Zhang et al., 1999). The impact of an ENSO event on the climate of China strongly depends on the phase of the event (Huang and Wu, 1989). Some studies have shown that the ENSO-monsoon relation is not robust over the past half century (Xu and Zhu, 1999; Wang, 2002), implicitly implying the role of the PDO in modulating interannual ENSO-monsoon relation.

Recently, the relationships between the climate variations in China and the PDO have been explicitly examined (Yang et al., 2002; Zhu and Yang, 2003b; Yang et. al. 2004). This chapter aims to summarize the main results from those studies, with emphasis on describing typical spatial-temporal structure of the climate variabilities in China associated with the PDO and especially with the North Pacific regime shift in 1976/77. The chapter is organized as follows. In Section 2, the regressed patterns upon the PDO index are shown for describing the oceanic features of PDO. The direct impact of PDO on the climate anomalies in East Asia and China is presented in Sections 3 and 4, respectively. Interdecadal change of interannual relationship between ENSO and summer climate variability in China is depicted in Section 5. Final section is devoted to conclusions.

The datasets used in the study described in this chapter include: the PDO index (PDOI) for 1900-2000 defined as the leading principal component from an EOF decomposition of monthly SST anomalies northward of 20^{o}N in the North Pacific (Zhang et al., 1997; Mantua et al., 1997), the NCEP/NCAR monthly mean reanalysis data on a resolution of $2.5^{o}\times2.5^{o}$ (Kalnay et al., 1996), the monthly precipitation and surface air temperature records for 160 stations in China compiled by China Meteorological Administration, the SST and upper-ocean (500m) heat content data from Maryland Simple Ocean Data Assimilation (SODA) analysis (Carton et al., 2000a, b), and the monthly SST data taken from the $1^{o}\times1^{o}$ gridded global ice and sea surface temperature (GISST) dataset (Parker et al. 1995; Rayner et al. 1996). All of those data are used for the common period 1951~1998, during which the North Pacific regime shift in 1976/77 is

prominent. Similar to those defined for an ENSO event, the extreme phase of a PDO event can be defined as either a warm or a cool phase with SST anomalies in the Pacific. When SST is anomalously cool in the central North Pacific and warm in the tropical Pacific, the PDO is said to be at its warm phase and the PDO index has positive value; and vice versa.

A linear regression method is used to examine the interdecadal climate anomalies in East Asia and China associated with the North Pacific regime shift in 1976/77, in which the typical oceanic and atmospheric patterns are regressed upon the PDO index and an *F*-test is adopted to check the significance of regression coefficients. Before the regression analysis is applied, the linear trend and the components with timescales less than 8a are filtered to isolate the decadal-to-interdecadal components. A sliding correlation analysis method is used to denote the interdecadal change of relationship between the ENSO and the climate anomaly in China. The ENSO is represented by a standardized SST anomaly index, i.e. an averaged SST anomaly over Nino-3 region (5^oS-5^oN，90^oW-150^oW). The sliding correlation is computed in a moving window with a 21-year width. Moreover, the composite analysis is used to depict the contrast of the ENSO-related summer atmospheric circulation anomalies over East Asia between the warm and cool PDO phases, and the student *t*-test is used to check the significance.

3.2 Interdecadal oceanic anomalies in the North Pacific

The PDO is a coherent ocean-atmosphere signature in the North Pacific on the interdecadal timescales. The fingerprint of the PDO is visible both in the atmosphere and ocean. The typical PDO patterns can be illustrated by regressing the SST and upper-ocean (500m) heat content anomalies upon the PDO index.

Fig 3.1a shows the temporal variation of the PDO index during 1900-2000, which is calculated with the GISST dataset. A remarkable feature of this index is its tendency for multiyear and multidecadal persistence indicating the significant interdecadal variations and with a few instances of abrupt changes beginning in 1925, 1947 and 1977 which have been called as the regime shifts in previous studies (Zhang et al. 1997, Mantua et al. 1997 and Minobe 1997). To be coincided with atmospheric variables from the NCEP/NCAR reanalysis, we select this index from 1951 to 1998.

The regressed spatial pattern of the PDO-related SST interdecadal variability upon the PDO index for 1951-1998 is shown in Fig. 3.1b. During a warm PDO phase (say, after 1976/77), the SST in the central-to-western

North Pacific is significantly cooler than normal while it is warmer in the central-to-eastern tropical Pacific and along the western coast of North and South America. The largest negative SST anomaly occurs between 25°N-45°N and 170°E-150°W in the central North Pacific. The similar negative SST anomalies are also found in the central South Pacific but the amplitude is much weaker. In contrast, the centers of positive SST anomalies appear to be in the vicinity of the Californian and Alaskan Gulf. The positive SST anomalies from the Californian Gulf and the South American coast extend both toward the central-to-eastern equatorial Pacific. For the pan-Pacific basin, the distribution of spatial pattern seems to be roughly north-south symmetric about the equator.

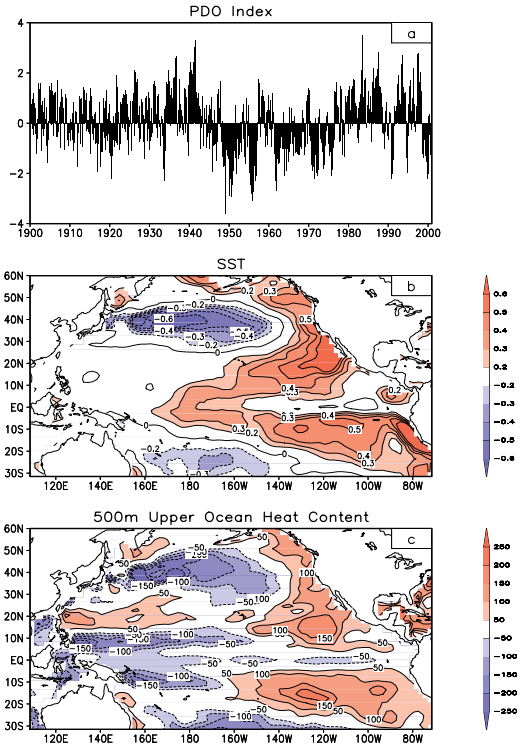

Fig. 3.1 (a) Pacific Decadal Oscillation (PDO) index during 1900-2000 and the regressions of (b) sea surface temperature anomaly and (c) upper-ocean heat content anomaly upon the PDO index for the period 1951-1998.

The regressed pattern of the PDO-related interdecadal variability for the

upper-ocean (500m) heat content (HC500) anomalies upon the PDO index is shown in Fig. 3.1c. The interdecadal anomalies of the HC500 are generally characterized by a similar pattern to that of the SST anomalies. The largest PDO-related HC500 anomaly is found in the central North Pacific with opposite signal in the eastern equatorial Pacific and along the coasts of North and South Americas. Moreover, the interdecadal HC500 anomaly is quite large in the western equatorial Pacific. However, the interdecadal SST anomaly is rather weak here. This could be related to the interdecadal variation of the ENSO cycle.

3.3 Interdecadal atmospheric anomalies in East Asia

A number of previous studies described the relationship between the PDO and the climate anomalies in North Pacific and North America. However, the impact of the PDO on atmospheric circulation anomalies in East Asia has not been well realized. To address this question, the interdecadal anomalies for some selected atmospheric variables, such as sea level pressure (SLP), geopotential height, temperature and wind, over the East Asia and Pacific sector, are regressed upon the PDO index. An *F*-test is made for the regression to verify statistical significance. Although the pattern of SST anomalies associated with the PDO is observed year-round (see Fig. 3.1), the atmospheric response in the extratropics is known to vary from season to season (Zhang et al. 1997). Therefore, the climate anomalies in East Asia associated with the PDO will be discussed for winter (DJF) and summer (JJA), respectively.

3.3.1 Winter

The regression of the wintertime sea level pressure (SLP) anomaly upon the PDO index for 1951-1998 is shown in Fig. 3.2. It is illustrated that, during a warm PDO phase, the Aleutian low tends to be enhanced and the pressure in northwestern North America is higher than normal while the subtropical high moves southeastward. The pressure is higher than normal in the western tropical Pacific and lower in the southeastern tropical Pacific, inducing an interdecadal decrease of the Southern Oscillation index (SOI). Another intriguing feature as seen from Fig. 3.2 is that the Mongolian high appears much stronger (but the Siberian high is weaker) when the Aleutian low is intensified, indicating a striking interdecadal “seesaw” pattern between the two pressure systems. It is suggested from this pattern that the winter monsoon tends to be stronger over Northeast Asia. Thus,

the simultaneous variation between the Aleutian low and the Mongolian high could be an important way by which the PDO exerts its impact on the atmospheric circulation over East Asia.

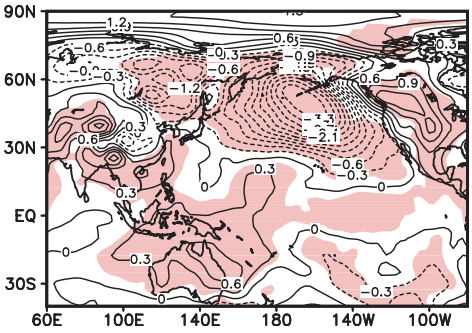

Fig. 3.2 Regression of the sea level pressure anomalies upon the PDO index in winter for the period 1951-1998. Regions over 0.05 confidence level are shaded.

The regressed wintertime geopotential height anomaly at 500hPa upon the PDO index is shown in Fig. 3.3a. Corresponding to the cooling in the central North Pacific as seen in Fig. 3.1a and the enhanced Aleutian low as seen in Fig. 3.2, there are considerable negative geopotential height anomalies at 500hPa over the central North Pacific, suggesting a local air-sea relationship, i.e., the cool SST versus the trough, with equivalent barotropic atmospheric vertical structure. Besides the local air-sea structure in the central North Pacific, it is noteworthy that the 500hPa geopotential height anomalies between the Aleutian and Mongolian regions also appear to be a "seesaw" pattern similar to that in SLP anomalies. The 500hPa geopotential height anomaly is also characterized by the PNA pattern, suggesting a possible tropics-midlatitude interaction through so-called "atmospheric bridge" mechanism and an approach through which the PDO impacts on the North American climate.

The regressed wintertime temperature and wind anomalies at 850hPa upon the PDO index are shown in Fig. 3.3b and Fig. 3.3c, respectively. It is evident in Fig. 3.3b that the 850hPa temperature over the central North Pacific anomalously drops in accordance with the cooling of underlying SST. In contrast, the temperatures are higher in the western and eastern tropical Pacific as well as in Indian Ocean. As for the East Asian sector, the higher temperature covers Siberia while the lower temperature is dominant in Mongolian and Tibetan Plateau. It is interesting that a warmer temperature ridge stretches from northeastern China to northern China with a maxi-

mum warmer center over northern China. As seen from Fig. 3.3c, for the 850hPa wind, an anomalous cyclone significantly appears in the North Pacific corresponding to the intensified Aleutian low while an anomalous anti-cyclone is formed over northwestern China in concomitance with the strengthened Mongolian high. Resultantly, the northerly anomaly prevails east of the anti-cyclone, inducing a stronger East Asian winter monsoon over northeast Asia. Meanwhile, in the tropical Pacific the trade wind is weakened while the equatorial westerly anomaly is enhanced.

3.3.2 Summer

The regressed summertime atmospheric circulation anomalies in East Asia upon the PDO index are shown in Figs. 3.3d~f. Similar to that during winter, during a PDO warm phase (i.e., after 1976/77), the negative SLP anomalies exist in the North Pacific while the positive ones in East Asia. In the tropical Pacific, the SLP anomalies are positive in the western tropical Pacific and eastern Australia while negative in the southeastern tropical Pacific. Similar negative 500hPa geopotential height anomalies can be seen in the western and central North Pacific with much less intensity and extent compared to the winter. The location of western Pacific subtropical high (WPSH) tends to be more southward. In East Asian continent, significant positive 500hPa geopotential height anomalies are centered in the vicinity of Balkhash Lake and Baikal Lake, indicating a weakening of the trough there (Fig. 3.3d). The 850hPa temperature is anomalously lower in the central-to-eastern North Pacific while higher in most of the tropical Pacific. Over the East Asian continent, the temperature is warmer in Siberian region but cooler in a broad region of southern Balkhash Lake and Baikal Lake. It is also warmer over the region from Indian peninsula and Indochina peninsula to southern China (Fig. 3.3e). As seen from Fig. 3.3f, there are double anomalous cyclones over the North Pacific, while in the tropical Pacific the trade wind is weakened and the equatorial westerly anomaly is enhanced with stronger amplitude than that in winter. Meanwhile, a strong anomalous anticyclone is centered south of Baikal Lake, causing a northerly anomaly prevailing over East Asia continent. Consequently, the East Asian summer monsoon (EASM) is weakened.

3.4 Interdecadal climate anomalies in China

To reveal the PDO-related interdecadal climate variations in China, observed records of precipitation and surface air temperature at 160 stations

in China for 1951-1998 are used. Similar to those done in the above section, the regressions are performed upon the PDO index to express interdecadal anomalies for the two variables. These regressions are depicted in Fig. 3.4 for winter and summer, respectively.

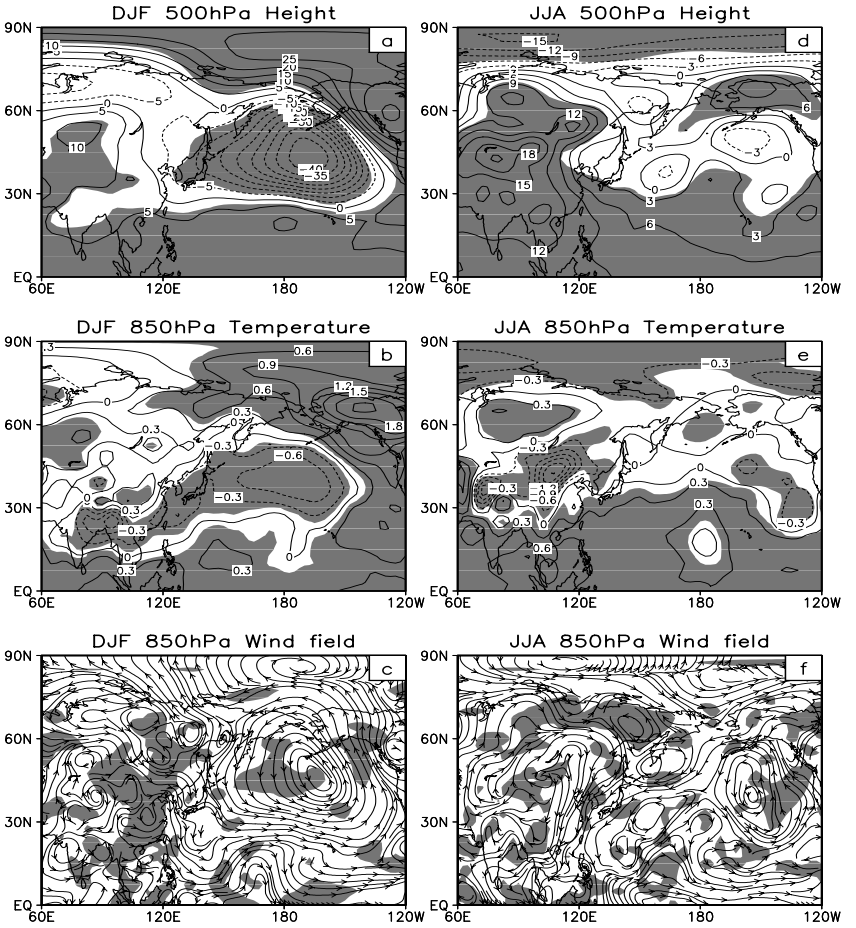

Fig. 3.3 Regressions of (a, d) the 500hPa geopotential height, (b, e) 850hPa air temperature and (c, f) 850hPa wind anomalies upon the PDO index for the period 1951-1998 in winter (a~c) and summer (d~f), respectively. Regions over 0.05 confidence level are shaded.

3.4.1 Winter

The regression coefficients for the wintertime precipitation and air temperature in China are shown in Figs. 3.4a,b. It can be seen from Fig. 3.4a that during a warm PDO phase the precipitation is less than normal in most of China, especially in northeastern, northern China and along Yangtze River valley. This can be attributed to the deepening and southward moving of Aleutian low and the strengthening of winter monsoon in East Asia. On the interdecadal timescale, there is a significant northwesterly anomaly along the coastal regions, which is not in favor of precipitation.

The temperature is significantly warmer than normal in the northeastern, northwestern and northern China while cooler than normal in the southwestern and southeastern China (Fig. 3.4b). A variety of studies have shown that over the past two decades the temperature anomalously rises in northern part of China, and the "warming winter" phenomenon occurred successively. However, this is not true for the southwestern and southeastern China where the surface is cooling. As shown in Fig. 3.3b, similar cooling can be seen at 850hPa. Thus, the "northern warming versus southern cooling" pattern is a typical feature for the interdecadal variations of winter temperature in China, which is closely associated with the PDO.

3.4.2 Summer

The regressed interdecadal anomaly pattern for the summer precipitation is shown in Fig. 3.4c. It is striking that more precipitation is observed along Yangtze River valley as well as in northeastern and northwestern China and in part region of southern China, while less precipitation is in northern China. This "southern flood versus northern drought" spatial pattern is similar to that of the linear trend of precipitation for the past decades, which is a major concern of China (Huang et al., 1999; Yan, 1999). A lot of previous studies attribute the pattern to the consequence of human activity such as emissions of carbon dioxide and aerosols. Current study suggests that the PDO-related ocean-atmosphere interaction could make comparable contribution to anomalous precipitation pattern in China.

The summertime precipitation anomaly is closely related to the PDO-related atmospheric circulation anomaly. As described in previous section (Fig. 3.3d and Fig. 3.3f), the western Pacific subtropical high is weakened and moves southeastward, the 500hPa geopotential height is increased in Mongolia and northwestern China, and therefore the significant northerly anomaly at 850hPa prevails over China. All of these PDO-related anomalies are in favor of the weakening of the East Asian summer monsoon.

Consequently, water vapor from the Bay of Bengal, South China Sea and western Pacific is more transported to southern China and Yangtze River valley while less to northern China, inducing an increase of precipitation in Yangtze River valley and an opposite situation in northern China.

As for the summertime temperature anomaly pattern, it is evident as shown in Fig. 3.4d that the anomalous cooling is in northwestern China and in a broad region along Yangtze River valley, while the warming is in northeastern, northern and southern China. The spatial pattern of temperature is roughly opposite to that of precipitation with a cool/wet or warm/dry relation, except for those in northeastern China and in part region of southern China where more precipitation corresponds to higher temperature.

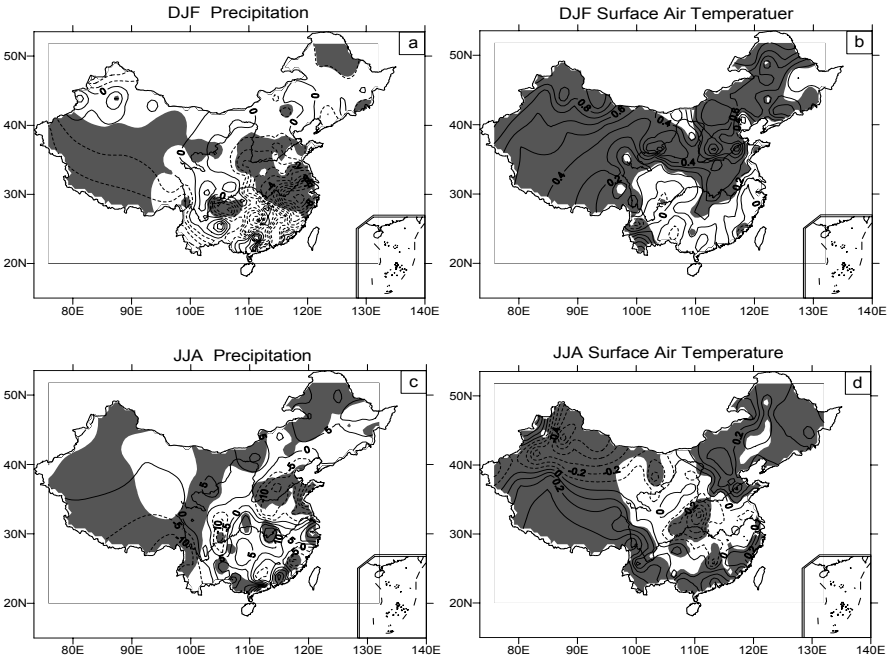

Fig. 3.4 Regressed precipitation (a, c) and surface air temperature (b, d) anomalies in China upon the PDO index for the period 1951-98 in winter (a, b) and summer (c, d), respectively. Regions over 0.05 confidence level are shaded.

3.5 Interdecadal change of ENSO's impact on the climate of China

Previous sections have presented the direct impact of the PDO on the interdecadal climate variability in East Asia and China. Besides this direct impact, the PDO also could provide a slowly-varying background for the interannual variability to modulate it and its impact. As mentioned in introduction, the ENSO as the strongest interannual signature in the tropical ocean-atmosphere system has significant impact on climate anomalies in China, and this impact depends on the phase of the ENSO cycle itself. However, the relationship between the ENSO and the climate anomalies in China is not robust and could change interdecadally. Such kind of change will be described in this section with insight into a possible modulation role of the PDO. Since the ENSO's impact on the summertime climate in China is of our particular interest, the interannual relationship between the ENSO and the summertime (JJA) climate anomaly in China will be presented below. Note that the fact that the evolution of an ENSO event tends to be phase-locked to season, with developing in summer, maturing in winter and decaying in next summer. Therefore, when the ENSO's impact on the summer climate anomaly is examined, one needs to distinguish the phase of an ENSO event. The developing phase of an ENSO event is defined as the summer prior to a winter (DJF) when an ENSO event is matured, and its decaying phase the summer just after the winter.

In order to further understand possible physical mechanism responsible for the ENSO-related climate anomalies in China for different interdecadal epochs, the composites of the ENSO-related atmospheric circulation anomalies in East Asia during different PDO phases are made. Eleven El Niño events in total for the period 1951-1998 are categorized. There are seven El Niño events (1953, 1957, 1963, 1965, 1968, 1972 and 1976) during the cool PDO phase and four El Niño events (1982, 1987, 1991 and 1997) during the warm PDO phase.

3.5.1 In the developing phase of an ENSO event

As we know, the PDO reversed from cool phase to warm phase around 1976/77. Associated with the phase reversal, the interannual relationship between ENSO and summertime climate variability in China may have interdecadal change. Fig 3.5 shows the correlations between the Nino-3 SST anomalies during winter (DJF) when an ENSO event is matured and the precipitation and surface air temperature anomalies during preceding summer (JJA) when the event is developing for two epochs, 1951-1976

and 1977-1998, respectively. Dramatic change in correlation pattern can be clearly seen between two epochs. During the cool PDO phase (Figs. 3.5a,b), a developing El Niño event is related to less summer precipitation in northern and southern China, more precipitation (Fig. 3.5a) and lower temperature (Fig. 3.5b) in northeastern China. However, during the warm PDO phase (Figs. 3.5c,d), a developing El Niño event is associated with less precipitation (Fig. 3.5c) and higher temperature (Fig. 3.5d) during summer in northern, northeastern and northwestern China and opposite situations in southern China.

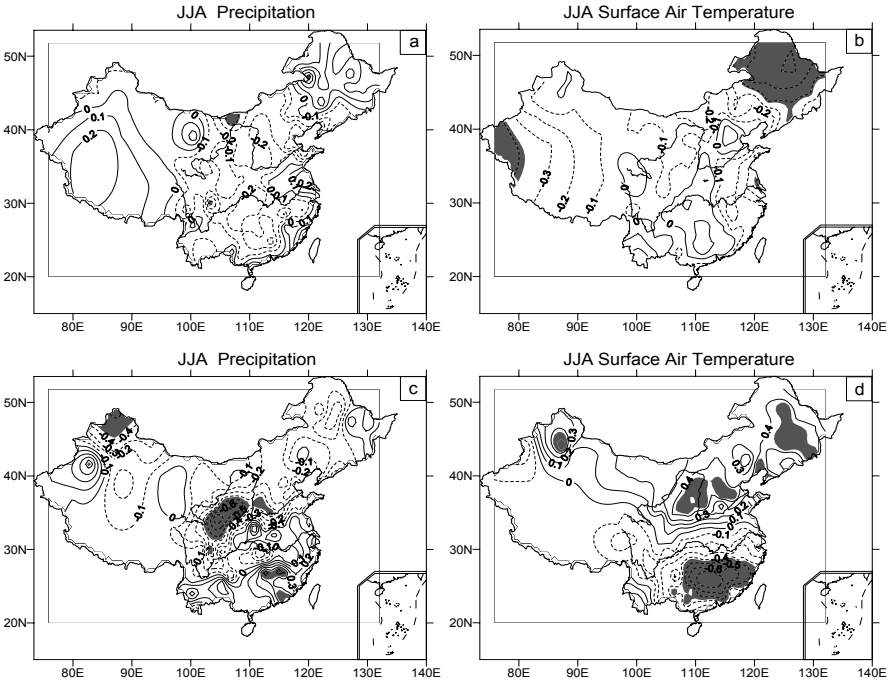

Fig. 3.5 Correlations of the preceding summer precipitation (a, c) and surface air temperature (b, d) anomalies with winter Nino-3 SSTA during (a, b) cool PDO phase and (c, d) warm PDO phase.

To further validate the above change, the temporal evolution of correlations between the winter Nino-3 SST index and the preceding summer precipitation anomaly for four selected regions are shown in Fig. 3.6. These correlations are computed with a sliding correlation analysis with a 21-year sliding window. As seen from Fig. 3.6, most of these correlations have a dramatic shift occurring around the mid-1970s, except for in northern

China (Fig. 3.6a) where there is a persistent negative correlation over the last five decades corresponding to less summer precipitation in the developing phase of El Niño. There is an obvious change from significant positive correlation to negative one in the late 1970s for southern China (Fig. 3.6b), and opposite situations for northeastern China (Fig. 3.6c) and for the lower reach of Huaihe River (Fig. 3.6d).

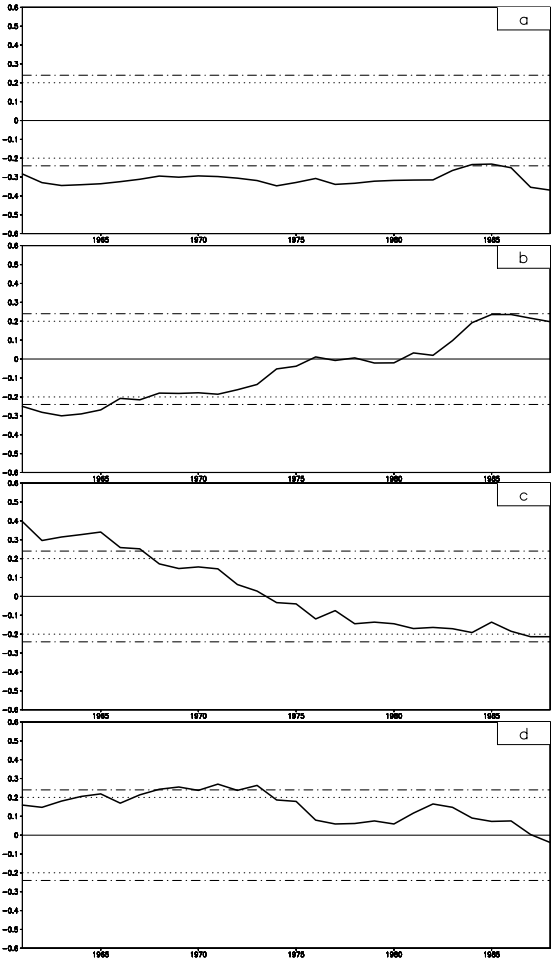

Fig. 3.6 Sliding correlations of area-averaged preceding summer precipitation anomalies with winter Nino-3 SSTA with a 21-yr window for (a) northern China, (b) southern China, (c) northeastern China, and (d) Huaihe River valley. The dashed and dashdotted horizontal lines denote 0.1 and 0.05 confidence levels, respectively.

As shown in Figs. 3.9a,b, in the developing phase of an El Niño event the composite 850hPa wind anomaly patterns during summer for two interdecadal epochs are similar in the lower latitudes with increased equatorial westerly and weakened western Pacific subtropical high while almost reversed in the midlatitudes. During the cool PDO phase (Fig. 3.9a), a developing El Niño event is related to a southerly anomaly extending from central China to northeastern China, favoring more precipitation in northeastern China (as seen in Fig. 3.5a) through enhancing northern summer monsoon and associated moisture transport. In contrast, during the warm PDO phase (Fig. 3.9b), a developing El Niño event is associated with a considerably large northerly anomaly from northeastern China through southern China, inducing a weaker northern summer monsoon and thus reducing precipitation in northeastern and northern China and increasing precipitation in southern China (as seen in Fig. 3.5c).

3.5.2 In the decaying phase of an ENSO event

Similar to Fig. 3.5, Figure 3.7 shows the correlations between the winter Nino-3 SST anomalies and the following summer precipitation and surface air temperature for the two epochs, respectively. During the cool PDO phase, a decaying El Niño event induces more summer precipitation in Yangtze River valley and in northern China while less along Huaihe River (Fig. 3.7a). During the warm PDO phase, a decaying El Niño event induces more summer precipitation in Yangtze River valley as well as in Huaihe River valley while less precipitation in northern China (Fig. 3.7c). Obviously, the impact of a decaying ENSO event on the summer precipitation has an interdecadal shift in northern China and in Huaihe River valley. However, such an impact is robust along Yangtze River valley. Accordingly, the interdecadal change for summer temperature is characterized by warming in northeastern China and cooling in northern and southern China during the cool PDO phase (Fig. 3.7b) while opposite situations during the warm PDO phase (Fig. 3.7d), corresponding to a decaying El Niño event.

Similarly, a sliding correlation analysis is made to examine the temporal evolution of the impact of a decaying El Niño event on the summer precipitation at some selected regions. As seen in Fig. 3.8a, the following summer precipitation in Yangtze River valley has robust significant positive correlations over last five decades with winter Nino-3 index. However, in northern China there is an outstanding change from significant positive correlations to negative ones in the late 1970s (Fig. 3.8b), while in Huaihe River valley there are significant negative correlations before the mid-1970s while an obvious weakening of the correlation after the late 1970s

(Fig. 3.8c).

Overall, above results clearly show that the interannual relationships between summer climate variability in China and the ENSO either in its developing phase or in its decaying phase are not robust and have experienced remarkable change, concurrently associated with the phase reversal of PDO in the late 1970s. Therefore, besides its direct impact, the PDO has modulation role in the impact of ENSO on summer climate variability in China.

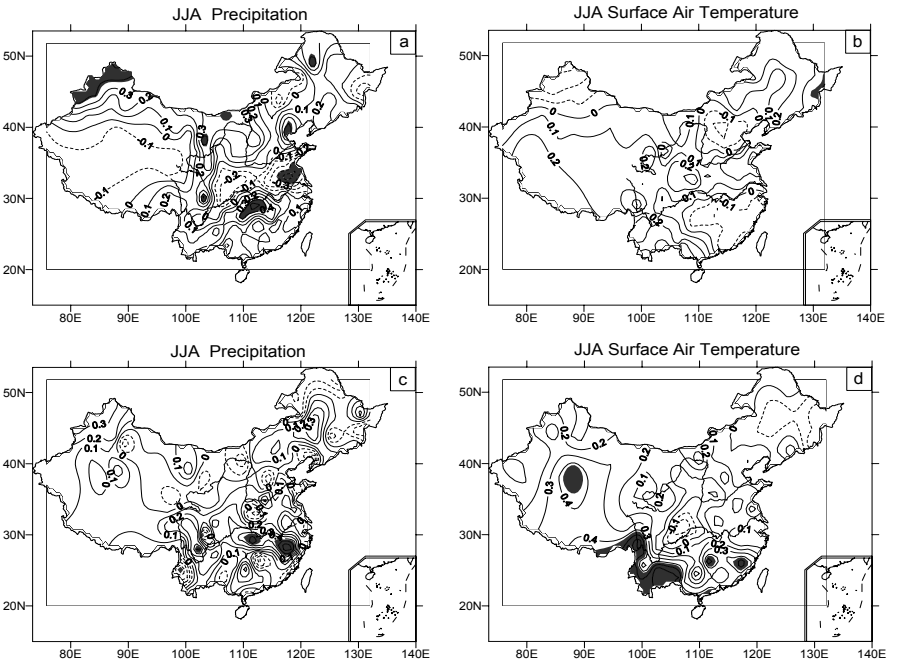

Fig. 3.7 Correlations of the following summer precipitation (a, c) and surface air temperature (b, d) anomalies with winter Nino-3 SSTA during (a, b) cool PDO cool phase and (c, d) warm PDO phase.

As shown in Figs. 3.9c,d, in the decaying phase of an El Niño event the composite 850hPa wind anomaly patterns during summer for two interdecadal epochs are similar in the lower latitudes with decreased equatorial westerly and enhanced western Pacific subtropical high while quite different in the midlatitudes. During the cool PDO phase (Fig. 3.9c), ENSO's impact is only characterized by a weaker anomalous anticyclone over the Philippine sea which induces a southerly anomaly in southern China, enhancing southern summer monsoon and favoring more precipitation along

Yangtze River valley and less one in Huaihe River valley (as seen in Fig. 3.7a). During the warm PDO phase (Fig. 3.9d), ENSO's impact is characterized by a stronger anomalous anticyclone over the Philippine sea together with a Pacific-Japan (PJ) wavetrain extending into the midlatitudes, inducing a strong northerly anomaly over northeastern-northern China which leads to a weaker northern summer monsoon and thus more precipitation along Yangtze River and Huaihe River valleys and less one in northern China (as seen in Fig. 3.7c).

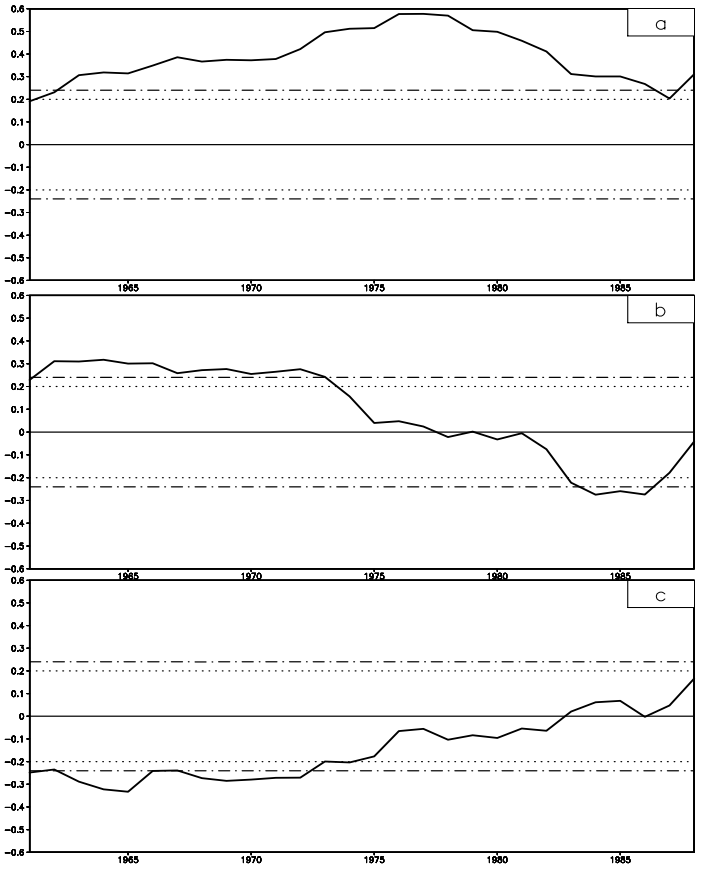

Fig. 3.8 Sliding correlations of area-averaged following summer precipitation anomalies with winter Nino-3 SSTA with a 21-yr window for (a) Yangtze River valley, (b) northern China, and (c) Huaihe River valley. The dashed and dashdotted horizontal lines denote 0.1 and 0.05 confidence levels, respectively.

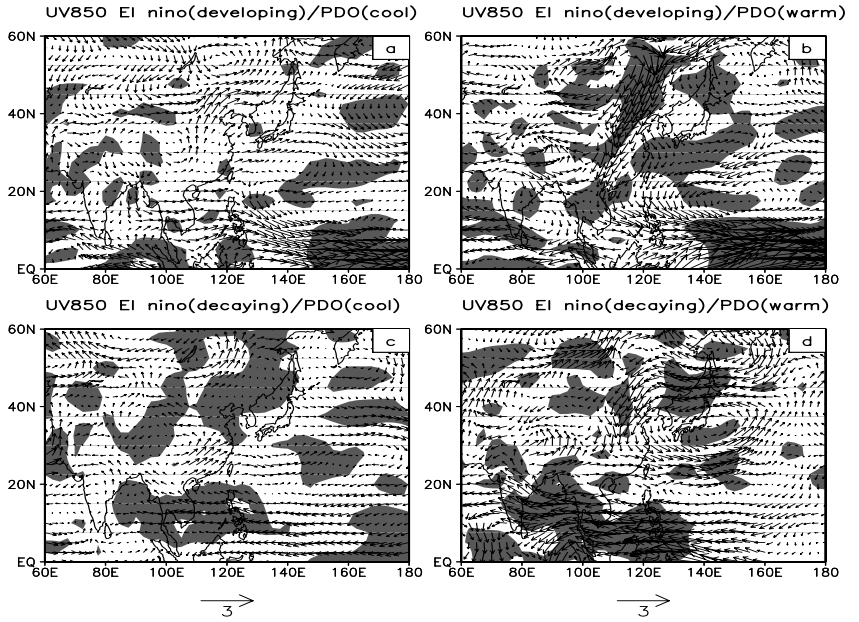

Fig. 3.9 Composite summer (JJA) 850hPa wind anomalies in the developing phase of an El Niño event (a, b) and in the decaying phase of an El Niño event (c, d) during cool PDO phase (a, d) and warm PDO phase (b, c), respectively. The shaded areas indicate regions where the differences are statistically significant at 0.05 confidence level by student ***t*** test.

3.6 Summary

The oceanic features of the Pacific Decadal Oscillation (PDO) and the associated interdecadal climate anomalies in East Asia and China are described in this chapter with NCEP/NCAR reanalysis data and station records for 1951-1998 by using regression analysis. The interdecadal change of the impact of ENSO on the summertime climate anomaly in China and corresponding atmospheric circulation anomaly in East China are also investigated with insight into the modulation role of PDO by using sliding correlation analysis.

The PDO is characterized by principal SST anomalies in the central North Pacific and secondary opposite SST anomalies in the tropical Pacific. The associated upper-ocean heat content anomalies generally have a similar pattern to that of the SST anomalies, except in the western equatorial

Pacific where the heat content anomaly is also quite large but the SST anomaly is rather weak. Over the past half century, the PDO has featured an interdecadal shift occurred in the mid-1970s with a considerably large cooling in the central North Pacific.

Regression analyses show that the PDO-associated atmospheric circulation anomalies in East Asia and climate anomalies in China are significantly remarkable. During winter, corresponding to the cooling shift of the central North Pacific in 1976/77, the Pacific/North American (PNA) pattern is in its positive phase and the Aleutian Low tends to be stronger. In East Asia, the Mongolian High is enhanced while the Siberian High is weakened. There is an interdecadal seesaw-like oscillation between the Aleutian Low and the Mongolian High. Associated with this, the air temperature is lower in Mongolian and Tibetan Plateaus and southern China and higher in northwestern, northeastern and northern China, indicating a "northern warming versus southern cooling" pattern in China. At this time, less precipitation is observed in most of China, especially in northeastern, northern China and Yangtze River valley.

During summer, corresponding to the cooling shift of the central North Pacific in 1976/77, the western Pacific subtropical high is weakened and moves southeastward, the 500hPa geopotential height is increased in Mongolia and northwestern China, and a significant northerly anomaly at 850hPa prevails over China, and therefore the East Asian summer monsoon is greatly weakened. Resultantly, more precipitation is observed in Yangtze River valley and less in northern China. Meanwhile, the anomalous cooling is in northwestern China and in a broad region along Yangtze River valley, while the warming is in northeastern, northern and southern China. The spatial pattern of temperature is roughly opposite to that of precipitation with a cool/wet or warm/dry relation, except for those in northeastern China and in part region of southern China where more precipitation corresponds to higher temperature.

Sliding correlation analyses exhibit a significant interdecadal change around mid-1970s in the relationship between the ENSO and the summertime climate anomalies in China, showing the PDO's modulation role in the ENSO's impact. During the cool PDO phase (1951-1976), a developing El Niño event tends to dry/warm southern China and cool/wet northeastern China, while a decaying El Niño event acts to wet/cool northern and southern China and dry/warm Huaihe River valley. During the warm PDO phase (1977-1998), however, a developing El Niño event tends to wet/cool southern China and dry/warm northern, northeastern and northwestern China, while a decaying El Niño event acts to dry/warm northern and southern China and normalize Huaihe River valley. It is interesting that the fact that a decaying El Niño event induces increased precipitation

along Yangtze River valley is robust without any interdecadal change. This is a valuable signature for the seasonal prediction of precipitation.

Further composite analyses show that the interdecadal change of ENSO-related atmospheric circulation anomalies is responsible for the change of relationship between the ENSO and precipitation anomalies in China. For two interdecadal epochs, ENSO-related atmospheric anomalies are similar in the lower latitudes but quite different in midlatitudes. Concurrent with the phase reversal of PDO in 1976/77, the summer monsoon throughout China is weakened instead of an enhanced northern summer monsoon in the developing phase of an El Niño event, while the northern summer monsoon is reduced instead of a slightly enhanced southern summer monsoon in the decaying phase of an El Niño event.

Overall, this study suggests that the PDO which is the strongest interdecadal signature in the North Pacific ocean-atmosphere system has not only direct impact on the interdecadal climate variabilities in East Asia and China but is able to modulate interannual variabilities (say, ENSO's impact). However, this study only presents a bunch of evidence without exploring deep mechanisms for those facts which are of major concerns to be investigated in the future studies.

References

Carton JA, Chepurin G, Cao J (2000a) A simple ocean data assimilation analysis of the global upper ocean 1950-95. Part I: Methodology. *J. Phys. Oceanogr.*, **30**, 294~310.

Carton JA, Chepurin G, Cao J (2000b) A simple ocean data assimilation analysis of the global upper ocean 1950-95. Part II: Results. *J. Phys. Oceanogr.*, **30**, 311~326.

Chen Longxun, Zhu Wenqin, Wang Wen, Zhou Xiuji, Li Weiliang (1998) Studies on climate change in China in recent 45 years. *Acta Meteorologica Sinica*, **56,** 257~271 (in Chinese).

Gershunov A, Barnett TP (1998) Interdecadal modulation of ENSO teleconnection, *Bull. Amer. Meteor. Soc.*, **79**, 2715~2725.

Graham NE (1994) Decadal scale variability in the 1970s and 1980s: observations and model results. *Climate Dynamics*, **10**, 135~162.

Hare SR, Mantua NJ (2000) Empirical evidence for North Pacific regime shifts in 1977 and 1989. *Progress in Oceanography*, **47**, 103~145.

Huang Ronghui, Wu Yifang (1989) The influence of ENSO on the summer climate change in China and its mechanism. *Advances in Atmospheric Sciences*, **6(1)**, 21-32.

Huang Ronghui, Xu Yuhong, Zhou Liantong (1999) The Interdecadal variation of summer precipitations in China and the drought trend in North China. *Plateau Meteorology*, **18**, 465~475 (in Chinese).

Kalnay E, Coauthors (1996) The NCEP/NCAR 40-year reanalysis project. *Bull. Amer. Meteoro. Soc.*, **77**, 437~471.

Latif M, Barnett TP (1994) Causes of decadal climate variability over the North Pacific and North America. *Science*, **266**, 634~637.

Latif M, Barnett TP (1996) Decadal climate variability over the North Pacific and North America: dynamics and predictability. *J. Climate*, **9**, 2407~2423.

Li Congyin, Li Guilong, Long ZhenXia (1999) Comparing Analyses of atmospheric circulation for interdecadal climate variation in China. *Quarterly Journal of Applied Meteorology*, **10**, 1~8 (in Chinese).

Li Chongyin and Li Guilong (2000) The NPO/NAO and interdecadal climate variation in China. *Advances in Atmospheric Sciences*, **17(4)**, 555~561.

Li Feng and He Jinhai (2000) The decadal change of the interaction between North Pacific SSTA and East Asian Summer Monsoon. *Journal of Tropical Meteorology*, **16(3),** 260~271 (in Chinese).

Mantua NJ, Hare SR, Zhang Y, Wallace JM, Francis RC (1997) A Pacific interdecadal climate oscillation with impacts on salmon production. *Bull. Amer. Meteor. Soc.*, **78**, 1069~1079.

Miller AJ, Cayan DR, Barnett TP, Graham NE, Oberhuber JM (1994) The 1976–1977 climate shift of the Pacific Ocean. *Oceanography*, **7**, 21~26.

Miller AJ, Schneider N (2000) Interdecadal climate regime dynamics in the North Pacific Ocean: theories, observations and ecosystem impacts. *Progress in Oceanography*, **47**, 355~379.

Minobe S (1997) A 50–70 year climatic oscillation over the North Pacific and North America. *Geophysical Research Letters*, **24**, 683~686.

Minobe S, Mantua NJ (1999) Interdecadal modulation of interannual atmospheric and oceanic variability over the North Pacific. *Progress in Oceanography*, **43**, 163~192.

Nakamura H, Lin G, Yamagata T (1997) Decadal climate variability in the North Pacific during the recent decades. *Bull. Amer. Meteor. Soc.*, **98**, 2215~2225.

Namias J, Yuan X, Cayan DR (1988) Persistence of North Pacific sea surface temperature and atmospheric flow patterns. *J. Climate*, **1**, 682~703.

Nitta T,Yamada S (1989) Recent warming of tropical sea surface temperature and its relationship to the Northern Hemisphere circulation. *J. Meteor. Soc. Japan*, **67**, 375~383.

Parker DE, Folland CK, Jackson M (1995) Marine surface temperature: Observed variations and data requirements. *Clim. Change*, **31**, 559~600.

Power S, Casey T, Folland C, Colman A, Mehta V (1999) Interdecadal modulation of the impact of ENSO on Australia. *Climate Dynamics*, **15**, 319~324.

Rayner NA, Horton EB, Parker DE, Folland CK, Hackett RB (1996) Version 2.2 of the global sea-ice and sea surface temperature data set, 1903-1994. *Clim. Res. Tech. Note,* 74, 1–21.

Shi Neng, Chen Jiaqi, Pu Qitu (1995) 4-Phase climate change features in the last 100 years over China. *Acta Meteorologica Sinica*, **53,** 431~439 (in Chinese).

Trenberth, KE (1990) Recent observed interdecadal climate changes in the Northern Hemisphere. *Bull. Amer. Meteor. Soc.*, **71**, 988~993.

Trenberth KE, Hurrell JW (1994) Decadal atmosphere–ocean variations in the Pa-

cific. *Climate Dynamics*, **9**, 303~319.
Wang Bin (1995) Interdecadal changes in El Niño onset in the last four decades. *J. Climate*, **8**, 267~285.
Wang Huijun (2001) The weakening of the Asian Monsoon Circulation after the end of 1970's. *Advances in Atmospheric Sciences*, **18(3)**, 374~386.
Wang Huijun (2002) The instability of the East Asian Summer Monsoon-ENSO relations. *Advances in Atmospheric Sciences*, **19(1)**, 1~11.
Wang Shaowu, Zhao Zongci (1979) The 36a flooding and drought fluctuation in East China. *Acta Meteorologica Sinica*, **37(1),** 64~73 (in Chinese).
Wang Shaowu (1994) Diagnostic studies on the climate change and variability for the period of 1880-1990. *Acta Meteorologica Sinica*, **52(3),** 261~273 (in Chinese).
Xu Jianjun, Zhu Qiangen (1999) The numerical study of the effect of ENSO and its interdecadal variation on the global and Asian Monsoon precipitation. *Acta Meteorologica Sinica*, **57,** 301~315 (in Chinese).
Xue Feng (2001) Interannual to interdecadal variation of East Asian Summer Monsoon and its association with the global atmospheric circulation and sea surface temperature. *Advances in Atmospheric Sciences*, **18(4)**, 567~575.
Yan Zhongwei (1999) Interdecadal oscillations of precipitation in North China and its relation with global Temperature Change. *Quarterly Journal of Applied Meteorology*, **10**, 16~22 (in Chinese).
Yang Xiuqun, Guo Yanjuan, Xu Guiyu, Ren Xuejuan (2002) A comparison of spatio-temporal structures between interannual and interdecadal variabilities, *Journal of Nanjing University*, 38(3), 308-317 (in Chinese).
Yang Xiuqun, Zhu Yimin, Xie Qian, Ren Xuejuan, Xu Guiyu (2004) Advances in studies of the Pacific Decadal Oscillation, *Acta Atmospherica Sinica*, 28(6), 979-992 (in Chinese).
Yu Shuqiu and Lin Xuechun (1997) Climatic jump of North Pacific SST and its effect on precipitation of floods season in China. *Journal of Tropical Meteorology*, **13(3),** 265~275 (in Chinese).
Zhang Y, Wallace JM, Battisti DS (1997) ENSO-like interdecadal variability: 1900-93. *J. Climate*, **10**, 1004~1020.
Zhu Yimin, Yang Xiuqun (2003a) Joint propagating patterns of SST and SLP anomalies in the North Pacific on bidecadal and pentadecadal timescales. *Advances in Atmospheric Sciences*, **20(5)**, 694~710.
Zhu Yimin, Yang Xiuqun (2003b) Relationships between Pacific Decadal Oscillation (PDO) and Climate variabilities in China, *Acta Meteorologica Sinica*, **61(6),** 641~654 (in Chinese).
Zhu Jinhong, Wang Shaowu (2001) 80a-Oscillation of summer rainfall over the east part of China and East-Asian Summer Monsoon. *Advances in Atmospheric Sciences*, **18(5)**, 1043~1051.
Zhang Renhe, Akimasa Sumi, Masahide Kimoto (1999) A diagnostic study of the impact of El Niño on the precipitation in China. *Advances in Atmospheric Sciences*, **16(2)**, 229~241.

Chapter 4 Interannual Variability of Summer Climate of China in Association with ENSO and the Indian Ocean Dipole

4.1 Introduction

4.1.1 ENSO and its global impacts

The El Niño/Southern Oscillation (ENSO) is the strongest signal in the ocean-atmosphere system on the interannual time-scales. Its warm and cold episodes appear alternatively, with periodicities of 3-7 years (e.g., Trenberth, 1997; Torrence and Webster, 1999). When an ENSO event occurs, the climate in many parts of the world changes largely in precipitation, temperature, and other climate variables. In different regions of the world, ENSO tends to have different climate impacts (e.g., Ropelewski, et al, 1987 ; Fu and Teng, 1988; Kiladis et al.,1989; Wang et al, 2000; Kawamura, et al, 2001; Lau and Wu, 2001). During an El Niño, less rainfall is received in Indonesia, northern part of Australia, and India. Meanwhile, air temperature tends to be higher than normal in these regions. In Korean peninsula and Japan islands, higher temperatures are also observed during El Niño events. The rainfall in Africa, North and South Americas can also be influenced by ENSO more or less. The climate of China is dominated by the Asian monsoon activities and the circulation changes in middle and high latitudes. However, summertime climate conditions in China are also significantly influenced by ENSO, as reported in many studies (e.g., Fu and Teng, 1988; Wang et al, 2000; Lau and Wu, 2001). To understand what and how the ENSO influences Summer climate of China (SCC), we present readers first in this chapter a brief overview of the results as obtained mainly in China in the period before 1995. Following it is the brief summary of the studies after 1995 on the ENSO-China climate relations. Because the Indian Ocean variabilities (IOV), particularly the Indian Ocean dipole (IOD) (Saji, et al, 1999; Webster et al., 1999) merge as a very important factor that influences the summer climate of China, we present readers some results related to the topics of the IOD and Asian summer monsoon variations.

4.1.2 Understanding the ENSO-China climate relations before 1995

ENSO influences summer climate of China significantly. Shi et al. (1983) shows based on a statistical study that more summertime rainfall is received in Yangtze River (or Changjiang, the longest river in China) valley in El Niño years while less rainfall in the southern China. However, in the year following an El Niño event, less summertime rainfall is received in Yangtze River Valley whereas more rainfall in the southern part of China. These results seem to be very different from the conclusions by Fu(1987), who claimed that the summertime rainfall is much less in most part of China, particularly in Yangtze River valley in the year when an El Niño sets up. However, in the year after an El Niño sets up, Rainfall in Yangtze River valley tends to be significantly more. Some other authors attempt to find more convincible results by dividing ENSO events into different types in terms of the starting time of the ENSO events. Zhao(1990) found that, if an El Niño event begins in fall or winter season in a year, precipitation during Meiyu/Baiu period in Yangtze river valley tends to be more in this or the following year. On the other hand, if an El Niño starts in spring or summer season in a year, precipitation during Meiyu period tends to be significantly less in both the El Niño starting and its following years. By defining the 'Eastern' and 'Central' Pacific as two types of El Niño, Lin et al (1993) suggested that less rainfall occurs in Yangtze river valley while more rainfall in both northern China and the region south of Yangtze river before both the two types of El Niño reach their peak phases. In the decaying phase of the two types of El Niño, pattern of the anomalous summertime rainfall shows just the opposite signature. Furthermore, some results, as given by Wang in 1992 using a relatively longer historical data (500 years), suggested that more than 58% of the drought events in the northern part of China are related to the warming events occurred in the central and eastern equatorial Pacific.

Temperatures in some parts of China during boreal summer can be influenced by ENSO events. In an El Niño year, weak summer monsoon prevails over China, causing the rain belt anomalously stretching along Yangtze River or south of this River. The summer climate in northern part of China is thus hotter and drier than normal. In the northeastern part of China, temperature is lower than normal during an El Niño year. Six extremely cold summer events in years including 1954, 1957, 1964, 1969, 1972, and 1976 are observed; most of them occur in El Niño years (Wang and Zhu, 1985). In La Niña years, climate of the northeastern part of China including Shenyang, Changchun, and Harbin tends to be warmer than normal in summer seasons.

4.1.3 Indian Ocean variabilities, especially the Indian Ocean dipole

More and more attention has been paid to the Indian Ocean variabilities (IOV) in recent years. Two leading modes of IOV on the interannual timescales, as observed in sea surface temperature anomalies (SSTA), have been found. The one is the basin wide mono-polar mode, and the other the dipole mode. The mono-polar mode is ENSO related (Cadet, 1985; Saji, et al, 1999; Wu et al., 2000; Zhou, et al, 2001; Alexander et al, 2002; Ashok et al, 2003); the SSTA changes with 3 months lag to ENSO (Klein, et al, 1999; Ashok et al, 2003). The Indian Ocean dipole mode (IODM), discovered in 1999 (Saji et al, 1999;Webster et al, 1999), is believed to be a local air-sea interaction phenomenon. It usually starts in April, and peaks in October. Both the mono-polar mode and the IODM can influence the Asian summer monsoon and henceforth the summer climate of China (Behera, et al, 1999; Guan and Yamagata, 2003; Saji and Yamagata, 2003a).

4.1.4 Issues in the recent decades

ENSO has profound impacts on summer climate of China as mentioned above. However, where and how much the summertime rainfall in China is influenced by ENSO has not been well clarified because results as reported before 1995 from different study groups are not so well consistent with each other. Those arguments may be due to (1) the reliability of the available data and shorter length of data time series in earlier decades of 20^{th} century (In some studies, only are fewer ENSO cases involved, causing the results different from one study group to another.), (2) the long term trends which were not effectively dealt with, and (3) a lot of factors that can affect precipitation variability on interannual time scales, such as monsoon activities, circulation changes in mid and high latitudes, air-sea-land interactions, etc. In recent years, scientists have found that IOV, especially the IODM can affect summer climate of China (e.g., Guan and Yamagata, 2003). As some IOD events co-occur with ENSO events, the IOD makes people feel more difficult to understand exactly the ENSO's influences on summer climate of China.

Therefore, to better understand the influences of ENSO on summer climate of China we here present readers a new summary of the results on regional climate of China as reported from year 1996 then on.

4.2 Precipitation and temperature changes related to ENSO

There are regional differences in influences of ENSO on the Summertime rainfall and air temperature variations in China. We therefore will focus on the summer climate variations in regions in the southern China, Reaches of Yangtze River and Huaihe River, Reaches of Yellow River, and the northeastern China.

4.2.1 Droughts and floods in China

In Reaches of Yangtze and Huaihe Rivers

Most of the flood/drought events in the eastern part of China are due to the anomalous Meiyu precipitation in June and July in reaches of Yangtze and Huaihe rivers. Meiyu is known as a phenomena designated by a rain belt that elongates in zonal and moves in a quasi-stationary way in meridional. This rain belt is always related to some fronts with sometime the strong convections around them. Meiyu can be influenced by ENSO. In different stages of El Niño events, rainfall in the eastern part of China shows its different statistics (Ye, 1996; Jin et al, 1999; Wang, 1992). Generally, the flood/drought events occur usually in the developing or decaying period of the El Niño/La Niña events. In the developing stage of the El Niño events a rain belt stretches steadily in reaches of the Yangtze and Huaihe rivers, and in regions of South Korea and Japan, causing more rainfall in these regions. Meanwhile, less than normal rainfall is received in the northern part of China and in areas south of Yangtze River. In the decaying stage of the El Niño events, much less rainfall, even the drought events are observed in reaches of Yangtze and Huaihe rivers and in regions of South Korea. In areas south of Yangtze River, especially in regions of Dongting and Panyang lakes, flood events are observed. However, during the La Niña events, the scenarios of the rainfall anomalies as mentioned above seem to be oppositely signed in those regions.

It seems that there are some lagging influences of ENSO on the summer rainfall in China. If the El Niño events develop in fall and winter seasons, the precipitation in the following summer tends to be more in reaches of Yangtze and Huaihe rivers. If the El Niño events develop in spring and summer seasons, the rainfall in the following summer tends to be less there (Li, et al, 2000). The ENSO occurred in 1997/1998 could be an example case. The 1997/1998 El Niño was the strongest ENSO event in the 20^{th} century. It had strong impacts on the summer climate of China. Ob-

servational studies (Tao et al, 1998; Huang, et al, 1998; Yan, 1998) show that the occurrences of the extraordinary flood events in Yangtze River Valley in 1998 and the drought event in the northern part of China in 1997 are closely related to the 1997/1998 El Niño event.

These lagging influences could be related to the ENSO effects on Indian Ocean variabilities. Some studies (Wu, 1996; Sun, et al, 2003) suggested that the Meiyu rainfall should be more (less) when the anomalously higher (lower) temperatures were observed in both the central and eastern equatorial Pacific and the tropical Indian Ocean, along with the anomalously lower (higher) temperature in the western Pacific.

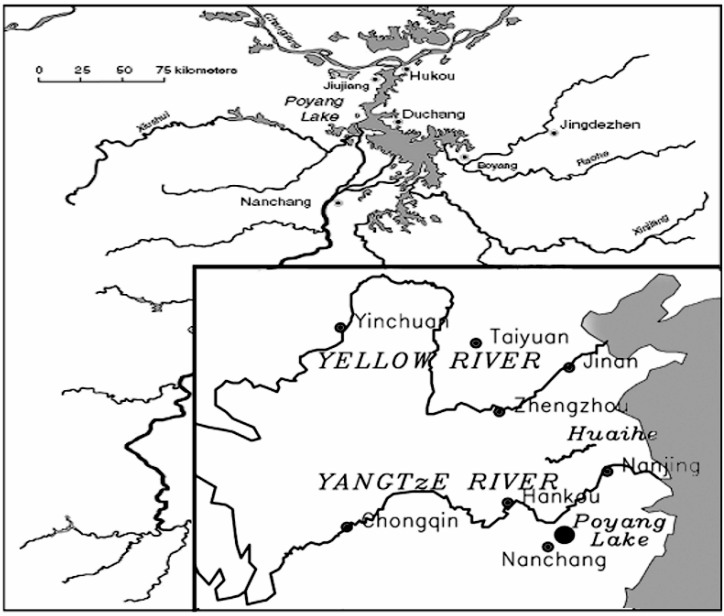

Fig. 4.1 Map of the Poyang Lake drainage basin and Reaches of Yangtze, Huaihe, and Yellow Rivers. See also Shankman et al. (2006).

In Poyang Lake Area

A good hydrological indicator that indicates the influences of ENSO on the summertime rainfall near the Yangtze River is the lake stage of the Poyang Lake. Poyang Lake is the largest lake in China, locating in Jiangxi Province, covering about 4000 km^2 during high water levels (Fig.4.1), draining though some narrow outlets into the Yangtze River and other several rivers. The area immediately surrounding Poyang Lake consists of

low-lying alluvial plains prone to floods that regularly occur in summer season. The most severe floods in this region occur when a high discharge from the rivers in Jiangxi occurs later than normal in summer months while the level of the Yangtze River is simultaneously high. Shankman et al. (2006) investigated the relationships between the lake stage and El Niño events using the hydrological data available from the Jiangxi Provincial Government Bureau of Hydrology. From 1950 through to 1998, there were seven years identified as severe flood years in Poyang Lake region (lake stage >20.5 m); all the seven flood events occurred during or immediately following El Niño events. The largest flood ever recorded was during 1998 when the lake and river stages exceeded historic highs for several consecutive weeks.

In reaches of Yellow River

The interannual variabilities of the precipitation in Reaches of Yellow River are possibly influenced by the El Niño events. In 1972, known as a strong El Niño year, there occurred a severe drought event in Yellow river region, causing a drying-up(zero-flow) event in some parts of the River (Bao and Xiang, 2000). From 1972 through to 2000, there occurred 22 drying-up events. Interestingly, 11 times out of these 22 events occurred in El Niño years. Particularly, a record breaking severe dry-up event was recorded in 1997(Long and Li, 1999), in which year the strongest El Niño events in 20th century was observed. Studies on the runoff–ENSO relations well agree with the above results (Chen, 2002).

4.2.2 Hot and cold summer climate in China

In Reaches of Yangtze and Huaihe Rivers

The summer climate conditions in reaches of Yangtze and Huaihe rivers are affected by ENSO. In an El Niño or its following year, the weak summer monsoon in China is usually observed. The monsoonal rain belt locates steadily in reaches of Yangtze River or south of it, inducing a colder and flood summer in this region, and a hot and drought summer in the northern part of China (Chen et al., 2000;Tao and Zhang, 1998ab; Huang, 2001). For instance, the severe drought and hot summer climate conditions were observed in the northern part of China in 1997 while a severe flood in middle and lower reaches of Yangtze and Huaihe rivers in the year following 1997.

In Northeastern China

The air temperature near the earth surface in the northeastern China is strongly influenced by ENSO events. In an El Niño year, the colder than normal air temperature is observed in the northeastern, especially the central and northern parts of the northeastern China(Lu and Zhang, 1995). The 6 extremely cold summers including years 1954, 1957, 1964, 1969, 1972, and 1976, as identified by Wang and Zhu (1985) using the historical records, are found to be interestingly related to El Niño events. In a La Niña year, the oppositely scenario is observed. The hotter than normal summer climate is usually observed in Shenyang, Changchun, and Harbin in the northeastern part of China.

However, results from some other studies (Zhu and Chen, 2003) that take global warming into account have demonstrated that the frequency of occurrence of severe cold summer events in the northeastern China have been decreasing since 1980's in 20^{th} century although the El Niño event occurs more frequently than before during that overlapping period of time.

4.3 Circulation changes with ENSO

The summer climate over China and East Asia is dominated by the activities of the East Asian summer monsoon system. The anomalous changes in the Summer monsoon circulation can lead to some extremely hot or cool and dry or humid summer climate conditions in this region. It was reported that the East Asian countries including China, Korea, and Japan experienced a record breaking hot and drought summer climate in 1994 (Park and Schubert, 1997). Similar extraordinarily anomalous hot or cool and drought or flood summer monsoon climate conditions have also been recorded in these countries frequently since late 1970s (cf. Kawamura et al., 1998; Ye and Huang, 1996). To understand and predict such an Interannual variability of the East Asian summer climate (EASC) is very important to the East Asian countries.

The East Asian summer monsoon system is one of the subsystems in the Asian monsoon regime (cf. Wang and Fan, 1999; Wang et al, 2001). It interacts with the other subsystems such as the Indian summer monsoon via the tropospheric jets, Tibetan high, and even the westerly jet stream at about 40^{o}N in the upper troposphere (e.g., Liang and Wang, 1998; Rodwell and Hoskins, 1996). The interannual variations of the East Asian summer monsoon climate are strongly influenced by low frequency variabilities from both the tropics and mid-latitudes in the ocean-land-atmosphere system. When the circulation over tropical Pacific, South Asia, and Eurasia

regions changes anomalously, it is reasonable to expect that the anomalous changes in the summer monsoon circulation over East Asia will also take place.

4.3.1 Western Pacific subtropical high

The summertime rainfall in China and the East Asian monsoon activities are strongly influenced by the western Pacific subtropical high (WPSH). The WPSH, particularly its location changes on seasonal and interannual timescales are strongly affected by both the ENSO-related thermodynamics in the tropical western Pacific and the convection activities in this region. When the west Pacific is in its warmer episode during the developing phase of a La Niña event, the convections around the Philippine Sea intensify. These intensified convections cause the location of the WPSH to be more northern and eastern via the Hadley cell and PJ pattern (Nitta, 1987; Huang, 1992), leading to less summer rainfall in reaches of the Yangtze and Huaihe Rivers in China, and in regions of South Korea and Japan. When the west Pacific is in its colder episode during the El Niño phase, convections around Philippine Sea weaken, resulting in the location of WPSH to be more southern and western, and henceforth causing more summer rainfall even floods in reaches of Yangtze and Huaihe rivers, and regions of South Korea and Japan. Because of the importance of the convections around Philippine, some studies have focused on influences of these convective activities on the east-westward migration of the WPSH (cf. Huang et al., 2001), showing that those anomalous convections facilitate the formation of an anomalous anticyclonic circulation near Philippine Sea.

Chang et al. (1999) examined the relationships of the East Asian summer monsoon (EASM) variations on interannual timescales with the SSTA in tropical Pacific. It is found that if the positive SSTA are found in the eastern equatorial Pacific in the winter season before a wet EASM, the negative SSTA will be found there in the fall season following the wet EASM. In a year of a wet EASM, because of the positive feedback between Hadley and Walker cells, a Rossby wave is generated as a response of the atmosphere to both the cooling and the evaporation-wind feedbacks in the west Pacific. This Rossby wave strengthens the WPSH over South China Sea (SCS) and tropical western Pacific. The ridge of WPSH stretches westward with time from the winter through to the coming fall, inducing an anomalous anticyclone at 850hPa near the coasts of the southern part of China. This anomalous anticyclone plays an important role in Meiyu rainfall processes. Firstly, it prevent the front from moving south-

ward before and during the Meiyu period, causing the Meiyu front to locate steadily in reaches of Yangtze and Huaihe rivers for longer period of time. Secondly, it leads to intensifying the Meiyu front due to the stronger pressure gradients in the northwest flank of the WPSH. Thirdly, this anomalous anticyclone can intensify the air decent in South China Sea, inducing the SST to increase there and henceforth to facilitate more water vapor to be transported from SCS northward into the precipitation area.

4.3.2 East Asian summer monsoon

In the mature phase of the El Niño events, convections are usually more vigorous in the central and eastern equatorial Pacific while they are less vigorous in the western Pacific region. These convection anomalies induce the southwest wind anomalies in the tropical western Pacific, and north wind anomalies in the subtropical region of the central Pacific north of equator (Zhang et al., 1996). These wind anomalies are found to appear around an anomalous anticyclonic circulation in the regions of the South China Sea and the western Pacific. This anomalous anticyclonic circulation facilitates the intensification of the Meiyu-related monsoonal circulations and the northward transport of water vapor, causing more Meiyu rainfall in reaches of Yangtze and Huaihe rivers. On the other hand, weak Indian summer monsoon in El Niño years (Kumar, et al., 1999) weakens the water vapor transports from Bay of Bengal towards China and other East Asian countries, causing less rainfall in the northern part of China. In the decaying phase of an El Niño event and the developing phase of a La Niña event, the EASM transports water vapor northward from Bay of Bengal, South China Sea, and tropical west Pacific. The water vapor converges in Reaches of Yangtze and Huaihe rivers, Korea, and Japan, inducing severe floods in these regions (Zhang et al., 1999a; 1999b).

Some lag influences of ENSO on the East Asian summer monsoon are investigated (Wang et al., 2001). When the El Niño event matures in the wintertime, a pattern of an anomalous anticyclonic circulation in the western Pacific is maintained in the following summer, being similar to the pattern of the aforementioned circulation changes. If the El Niño develops into its mature stage during boreal winter, the anomalous convections will occur in the tropical western Pacific and regions around maritime continents, inducing a tropospheric Rossby wave as a result of the atmospheric response to the anomalous forcing due to the anomalous convections, and henceforth resulting in an anomalous anticyclone near the Philippine Sea (Fig.4.2). This scenario is recognized as a Teleconnection that links East Asia summer climate to the SSTA in east equatorial Pacific (Zhang and

Huang, 1998; Wang et al., 2000; Huang and Chen, 2002). This teleconnection characterizes with an anomalous anticyclone around Philippine Sea in the lower troposphere, due to the atmospheric response to both the forcing of the colder sea surface in the northwestern part of the tropical Pacific and that of the warmer sea surface in the central equatorial Pacific.

4.3.3 South China Sea summer monsoon

The South China Sea summer monsoon (SCSSM) varies with periodicities from intra-seasonal to inter-decadal. On the inter-annual time scales, onset of the South China Sea summer monsoon is possibly linked to the ENSO-related SSTA in tropical Pacific (Zhou, et al., 2005; Zhou and Chan, 2007). Usually, the zonal wind component in the central part (110°-120°E, 5°-15°N) of SCS is used to define the monsoon onset date (MOD). The MOD is found to change with ENSO from a year to another. Studies on MOD variations have demonstrated that the SCSSM will onset normally or earlier than normal, and then normally or later than normal, when the ENSO cycle changes from a La Niña year to an El Niño year. Those years, for instance are 1956-58, 1971-73, 1974-78, 1984-87, and 1995-98. However, the onset dates of the SCSSM will be in a reversed order as compared to the MOD in years from a La Niña to an El Niño when the cycle phase changes from an El Niño year to a La Niña year. These years are, for instance, including 1968-71, 1982-85, 1986-89, 1991-96, and 1997-2001. Therefore, the MOD changes inter-annually with ENSO. It seems that the Western Pacific subtropical high dominates the inter-annual variations of the onset dates of South China Sea summer monsoon. Hence the factors that cause the WPSH to vary in its intensity are expected to influence the activities of the SCSSM.

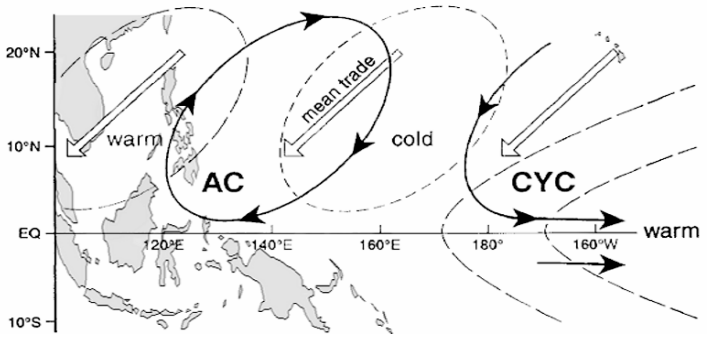

Fig. 4.2 Illustration of circulation features in the western North Pacific in El Niño years. The double arrows denote the mean trade winds. The heavy lines

with black arrows show the anomalous winds. The long (short) dashed lines indicate contours of positive (negative) SST anomalies. See also Wang et al. (2000).

4.3.4 Typhoons

Typhoons have large societal and economical impacts in many Asian countries. Most of the landfall typhoons in Asia hit China year by year. From July to September, most of the typhoons including the tropical cyclones generate in the western Pacific and South China Sea (e.g., Li, 1987; He, et al., 1999; Chan, 2000; Camargo and Sobel, 2005; Xu,et al., 2005). Historical records show that 347 out of 753 landfall typhoons (more than 40%) in summer months from July to September in years from 1949 through to 1997 landed China, causing tremendous damages in this country (Xu, et al., 2005). Guangdong (Canton) is the place where more strong typhoons are prone to landing on, as compared to the quantities and intensities of typhoons that land on other provincial regions such as Hainan, Taiwan, and Fujian.

During boreal summer, fewer typhoons occur during El Niño episodes whereas more typhoons during La Niña episodes. In the past century, people witnessed several strongest ENSO events. In 1980s and 1990s, air-sea interactions are found strongest in central equatorial Pacific. Interestingly, fewer typhoons occurred in the El Niño years of those two decades. In fact, number of landfall typhoons is related to the SST in the regions where the typhoons generate. In an El Niño year, lower SSTA appear in the western Pacific, causing convections there less active than normal. Locations of both the WPSH and the monsoon trough (the ITCZ in tropical part of East Asia) are observed more southern, which facilitates occurrences of typhoons to be fewer and number of landfall typhoons to be smaller in the El Niño episodes. In an El Niño year, the averaged number of typhoon occurrences, and that of typhoons landing China are 26.1 and 6.7, respectively, which are fewer than normal in a year. However, in a La Niña year, those averages are respectively 30.5 and 9.3, larger than normal in a year.

4.4 Influence of IOD on the East Asian summer monsoon

The Indian summer monsoon system interacts with the tropical Indian Ocean. The East Asian summer monsoon interacts with the Indian summer monsoon via the tropospheric jets, Tibetan high, and even the westerly jet

stream at about 40°N in the upper troposphere (e.g. Lau and Li, 1984; Liang and Wang, 1998; Webster et al., 1998; Wang and Fan, 1999; Wang et al, 2001; Lu et al, 2002; Enomoto et al, 2002). When the circulation over South Asia changes anomalously, it is reasonable to expect that the Summer monsoon circulation over East Asia will also change anomalously. We here discuss what and how the EASM circulation was influenced by the IOD events.

4.4.1 IOD phenomenon

The Indian Ocean dipole (IOD) is a manifestation of the Indian Ocean Variability (IOV) on the interannual timescale (Saji et al., 1999). It explains about 12% of the total variance of anomalous Indian Ocean Sea Surface Temperatures (SST). The Indian Ocean Dipole Mode Index (IODMI) is defined as "the difference in SST anomaly between the tropical western Indian Ocean (50°E-70°E, -10°S-10°N, named as Box A) and the southeastern Indian Ocean (90°E- 110°E, 10°S- equator, named as Box B)". To describe the IOD more clearly, we show in Fig.4.3a a time-longitude diagram of SSTA averaged over [-10°S-10°N] during June-July-August-September (JJAS). Shown in Fig.4.3b are the time evolution of JJAS mean SST anomalies (SSTA) at different locations on a 5°×5° mesh in the tropical eastern Indian Ocean region (90°E- 110°E, -10°S-10°N) (solid lines), and that outside of that region (40°E- 90°E, -10°S-10°N) (dotted lines). The areas described by Boxes A and B are identified, along with some features of the dipole SSTA, in Fig.4.3c, 4.3d, and 4.3e. It is clearly seen from Fig.4.3a that the SST anomalies are oppositely signed in the western and the eastern regions of Indian Ocean during some years; when the negative (positive) SSTA prevails in the eastern Indian Ocean, the positive (negative) SSTA prevails in the western Indian Ocean. This tendency is also seen in Fig.4.3b, with an out-of-phase relation between SSTA in the eastern Indian Ocean, and the SSTA in the western Indian Ocean during years such as 1961, 1963, 1972, 1977, 1982, and 1994. These are the positive dipole (pDM) years. Similarly, the opposite phase relationship between these SSTA is noticeable during the negative dipole years such as 1958, 1959, 1960, 1969, 1970, 1989, and 1992. Fig.4.3c displays the composite feature of pDM that is similar to the results obtained by Saji et al. (1999). The time-series of IODMI, along with the time-series of SSTA averaged over Box A and over Box B, is displayed in Fig.4.3e. The time-variations are consistent with the results in Saji et al.(1999). Figs.4.3a-4.3e demonstrate that, the IOD SSTA pattern indeed exists during JJAS season of aforementioned dipole years, and the Boxes A and B reasonably repre-

sent the two different poles of the IOD.

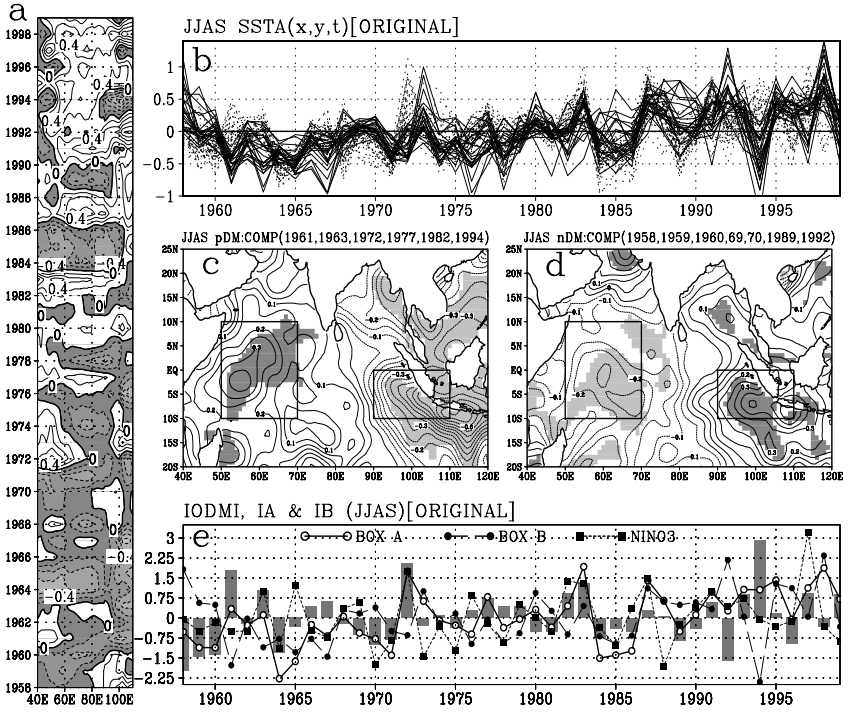

Fig. 4.3 (a) JJAS mean longitude-time diagram of SSTA averaged over (-10°S-10°N). The contours with shading are for negative values. (b) The time-series of SSTA at 5°×5° grid-point in equatorial Indian Ocean. The solid lines are for the time-series in area (90°E-110°E,-10°S-10°N); the dotted ones are for the SSTA in area (40°E-89°E, -10°S-10°N). (c) Composite JJAS mean SSTA of positive IOD events. The shaded areas denote that the composite mean of SSTA is significant above 90% level of confidence, obtained from a 2-tailed t-test. (d) Same as in 4.3c but for the negative IOD events. (e) Normalized time series of SSTA averaged over Box A (solid line with open circle), Box B (dashed with closed circle), NINO3 region (dotted with closed square), and the IOD mode index (bars). Units are in °C. From Guan et al. (2003).

Study of some recent dipole events suggests that IOD is an air-sea interaction phenomenon (Behera et al., 1999; Saji et al., 1999; Webster,et al., 1999). When the IODMI is positive, it may lead to droughts over the Indonesian region, while simultaneously causing heavy rains and floods over the East Africa. When the phase of the IOD is reversed, the associated anomalous fluctuations in rainfall also shift to the opposite phase. It is ob-

served that the relationship between ENSO and Indian summer monsoon rainfall has been weakened since 1980's (Krishna Kumar, et al, 1999; Chang, et al, 2001). This is explained as a result due to some different reasons such as the influence of the climate change in the Atlantic circulation (Chang, et al, 2001), and the westward shifting of ENSO induced subsidence from Indian continent (Krishna Kumar, et al, 1999). However, Ashok et al. (2001) showed that the IODMI has a positive correlation with rainfall over the Indian region. They proved that frequent occurrence of the intense IOD events has caused the recently observed fall in correlations between the ENSO and Indian summer monsoon rainfall. They demonstrated that the IOD could modulate the Indian summer monsoon rainfall using an AGCM.

Literature on the atmospheric response to the anomalous thermal forcing from Indian Ocean is available (e.g., Kumar and Hoerling, 1998). Because of the importance of the IOD in modulating the rainfall over the regions around the equatorial Indian Ocean, Guan et al. (2003) studied in detail the response of the tropical atmosphere to the Indian Ocean Dipole SST anomalies by using an AGCM, along with some of the available observational datasets.

Several sensitivity experiments using the AGCM have been carried out to understand the response of the atmosphere to the imposed IOD SSTA in JJAS (Guan et al., 2003). The response of the tropical atmosphere to the IOD SSTA forcing is of a distinct dipole structure in the distributions of many atmospheric variables. The anomalous circulation shows a baroclinic structure in tropics, which is consistent with the results obtained by Webster (1981). The observed stronger anomalous divergence (convergence) of wind fields is well simulated over the anomalously cold (warm) pole in lower troposphere. This pattern is reversed in the upper troposphere. The anomalous convergence (divergence) centre of water vapor is over the anomalously warmer (colder) region. An anomalous Walker cell is hence produced, influencing the circulation change even over the dipole region. More rainfall is received in the warmer pole and its surrounding area during the dipole episode. At the same time, an anomalous circulation in meridional-vertical plane from the eastern pole of the dipole towards India and Bay of Bengal is simulated. This anomalous Hadley circulation affects the Indian summer monsoon rainfall, as observed.

4.4.2 IOD teleconnections in the unusual summer of 1994

In 1994, East Asian countries suffered from the record-breaking hot and drought summer climate. Park and Schubert (1997) examined the nature of

this year using some assimilated data from 1985 through 1994. Their conclusion is that "the anomalous circulation is primarily the result of an orographic forcing associated with zonal wind changes over Tibet". However, different work by Guan and Yamagata (2003) has shown that the abnormal 1994 East Asian summer conditions are related to the Indian Ocean Dipole (IOD).

Using the SST data (GISST2.3b) from 1979 through 1999 (Parker et al., 1995), Guan and Yamagata (2003) showed in Table 4.1 the SSTA for June-July-August (JJA) and its standard deviation (σ) for three different tropical regions and the IODMI. The IODMI in 1994 shows the variance reaching about 2.6σ, which indicates that a very strong positive IOD event occurred in the summer of 1994. Note that the NIÑO3 region (5°S-5°N, 150°W-90°W) showed the weak negative SST anomaly during the same period.

The Indian summer monsoon is significantly influenced by the IOD (Ashok et al, 2001; Guan et al., 2003). Using the 'All Indian Rainfall' derived from the *in situ* observations (Parthasarathy et al., 1995), it is actually found that India received good monsoon rainfall during June-July-August of 1994; it amounts to 265mm per month by 19% above the mean climatological value. Moreover, our earlier study using both the observational data and an atmospheric general circulation model (AGCM) suggests that the well-known negative correlation between Indian summer monsoon rainfall and El Niño can be interfered in during decades of active IOD events (Ashok, et al, 2001).

Table 4.1 Averaged JJA SSTA in 1994 and the standard deviation from 1979 through 1999 for different tropical regions. From Guan and Yamagata (2003)

Regions	IODMI	Box A	Box B	NIÑO3
SSTA	0.90	0.24	-0.65	-0.21
σ	0.35	0.32	0.31	0.85

Circulation changes have been examined, using the NCEP/NCAR reanalysis data (Kalnay, et al., 1996) from 1979 through 2001 and the CMAP precipitation data from 1979 through 1999 (Xie and Arkin, 1996). Circulation anomalies during the summer months (JJA) of 1994 have been plotted in Figs. 4.4 and 4.5. Large positive air temperature anomalies are found over the northeastern and eastern China, Korea, and Japan in 1994 summer (Fig.4.4a). Some positive anomalies are also found above the Kuroshio Extension in the northwestern Pacific. The anomaly of thickness between 200hPa and 850hPa isobaric surfaces is also positive (not shown), indicating that the temperature of the air column is anomalously high. The region is associated with the strong negative precipitation anomalies (Fig.4.4b). The water vapor anomalously diverges from this region, lead-

ing to a severe drought condition. This agrees well with those in Park and Schubert (1997). It is known that this northeastern part of Asia was covered during the summer of 1994 by an anomalous anticyclonic circulation in the lower troposphere. The anomalous circulation can also be found in the upper troposphere over this region (Fig.4.5a), showing its equivalent barotropic structure. On the other hand, we find an anomalous cyclonic circulation elongating westward from the tropical western Pacific to the southern part of China (Fig.4.4a). This circulation facilitates the surplus rainfall in this region (Fig.4.4b) but it weakens the moist monsoonal southerly wind that blows northward from the Bay of Bengal and the South China Sea to the eastern part of China, Korea and Japan.

The above anomalous cyclonic circulation along with the intensified monsoon trough over India appears to be linked directly with the tropical IOD event. As seen in Fig.4.4b, the distinctive IOD structure over the tropical Indian Ocean is manifested in rainfall anomalies (Fig.4.4b) and also in the velocity potential field (Fig.4.5b). The water vapor converges into the western Indian Ocean (Fig.4.4b), while it diverges in the southeastern Indian Ocean. An anomalous meridional circulation associated with the IOD connects the anomalous decent branch over the southeastern Indian Ocean and the anomalous ascent branch at about 20°N, as simulated by Ashok et al. (2001). More precisely, the anomalous northwestward low-level winds from the eastern pole of IOD reaches the Peninsula of India and then turns eastward (Fig.4.4a). Since just the opposite winds are seen in the upper troposphere (Fig.4.5a, b), the wind field in the tropics has a baroclinic structure. These results are in agreement with other results obtained from both data analysis and AGCM studies (Behera, et al., 1999; Ashok, et al., 2001; Guan et al., 2003).

Teleconnection mechanisms have been put forward. The precipitation over India and the southern part of China is enhanced during the positive IOD event (Fig.4.4b). This fact is also reported in Ashok et al (2001). The northward branch of the meridional circulation excited by the eastern pole of the positive IOD leads to the anomalous updraft and the associated divergent flow in the upper troposphere over the Tibetan Plateau (Fig.4.5). This divergent flow emanating from India, the Bay of Bengal and the southern part of China acts as anomalous vorticity source in the upper troposphere (Fig.4.5b). To the northwest of this vorticity source region at 150hPa, we observe an anticyclonic circulation (Fig.4.5a), which is generated as a result of the atmospheric response to the anomalous vorticity source as discussed by Sardeshmukh and Hoskins (1988) using a simple model.

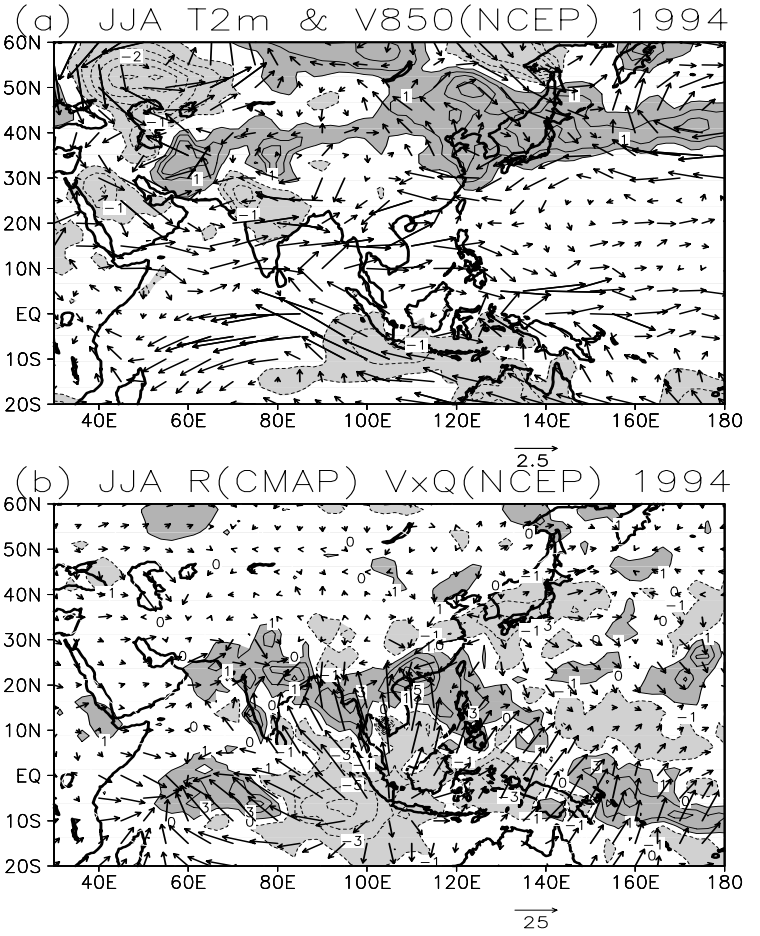

Fig. 4.4 (a) The JJA mean anomalous air temperature at 2m above the earth surface (°C) along with the wind at 850hPa (in $m \cdot s^{-1}$) during 1994. (b) The anomalous precipitation (in $mm \cdot d^{-1}$) and the anomalous water vapor flux (in $Kg \cdot m^{-1} \cdot s^{-1}$) which is vertically integrated from the earth surface up to 300hPa (shown with vectors). From Guan and Yamagata (2003).

An anomalous cyclonic circulation to the east of the vorticity source region is also found (Fig.4.5a). A Rossby wave train is excited by the vorticity source (the divergent flow), propagating northeastward from the southern China. This pattern looks similar to the Pacific-Japan (PJ) teleconnection pattern as put forward by Nitta (1987) but the location is a little shifted westward in the 1994 case.

The IOD-induced divergent flow in the upper troposphere near India also progresses westward and converges over the Mediterranean/Sahara region (Fig.4.5b). The zonal section averaged between 25°N and 35°N captures the vertical circulation (Fig.4.5c); the anomalous convection over India, which is induced by the IOD SSTA, is amazingly linked to the anomalous decent in the Mediterranean/Sahara region, as expected by Rodwell and Hoskins (1996) in a somewhat different context.

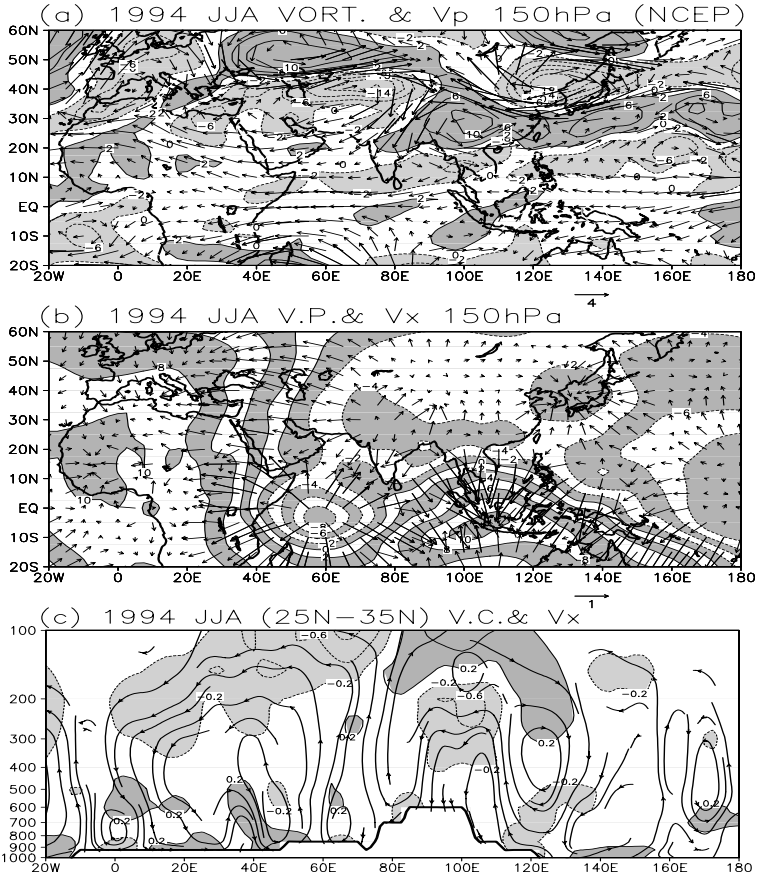

Fig. 4.5 (a) JJA mean anomalous vorticity (to be multiplied by 1×10^{-6} s^{-1}) along with the rotational wind ($m\cdot s^{-1}$) at 150hPa in 1994. (b) JJA mean velocity potential along with the divergent wind ($m\cdot s^{-1}$) at 150hPa in 1994. The contour interval is $4\times10^{-5}m^2\cdot s^{-1}$. (c) JJA mean zonal-vertical circulation averaged over (25°N-35°N). The contours denote the zonal component of the divergent wind with contour interval of $0.2m\cdot s^{-1}$. From Guan and Yamagata (2003).

To examine mechanisms behind the above circulation changes in more detail, it is shown in Fig.4.6 the heat budget anomalies during the summer of 1994 in terms of thermodynamic equation. Over the northern as well as eastern part of China, the anomalous diabatic heating is responsible for the abnormally hot summer (Fig.4.5c). Over Japan and Korea, the dynamic heating due to the anomalous descent of air is dominant, which cancels the anomalous negative horizontal advection of temperature. Around the Sea of Okhotsk, however, the anomalous positive horizontal advection of temperature balances the dynamic cooling (Fig.4.5b). These differences imply, from the viewpoint of the heat budget, that there are different mechanisms of the hot summer over land and sea. Furthermore, these results, in agreement with Park and Schubert (1997), indicate that the strong positive SSTA around Japan in 1994 (not shown) is not the cause of the hot summer. Rather, it is the result of the hot and dry summer condition.

Over India and the Bay of Bengal, the net anomalous diabatic heating is found (Fig.4.6c), which balances the negative anomalies of dynamic cooling due to the anomalous upward motion (Fig.4.6b). On the other hand, the net diabatic cooling is found over the Mediterranean/Sahara region (Fig.4.6c). The negative anomalies of the horizontal advection of temperature are also found in this region (Fig.4.6a). Both the diabatic and dynamic cooling are compensated by the anomalous dynamic heating due to the decent of air. Based on this heat budget diagnosis along with the vertical circulation shown in Fig.4.5c, the relationship between the IOD/monsoon and the anomalous circulation changes over the Mediterranean/Sahara region can be established. The present view confirms the monsoon-desert mechanism put forward by Rodwell and Hoskins(1996); they suggested that the diabatic heating due to convective activities in the Indian region could induce an anticyclonic Rossby wave pattern that covers west Asia and northern part of Africa. The adiabatic decent induced by the remote thermal forcing from the Asian summer monsoon intensifies the decent induced by radiative cooling over the Mediterranean/Sahara region.

The IOD-induced dynamic warming due to the decent of the air over the Mediterranean/Sahara region and its vicinity must steadily perturb the mid-latitude westerly. The lateral adiabatic cooling as manifested by the Maestro and Etesian may also generate disturbances. Since the mid-latitude westerly acts as a Rossby waveguide (Hoskins and Ambrizzi, 1993), the wave energy propagates along the westerly eastward to East Asia, periodically intensifying the aforementioned anomalous anticyclonic and cyclonic circulations around East Asia and the Western Pacific (Fig.4.5a). This scenario can be properly checked by examining the wave activity flux (WAF) introduced by Plumb (1986). The wave activity fluxes

at 200hPa are much larger along the Asian westerly jet than those over other regions (not shown). The WAF converges around the Sea of Japan, indicating the accumulation of wave energy in this area. The longitude-height cross-section (not shown) shows that the anomalous wave energy propagates upward into the upper troposphere around the regions of the Mediterranean Sea, the Caspian Sea, and the East Asia along the westerly jet stream. To the north of the Asian jet, we observe very weak Rossby wave propagation; this suggests that the 1994 East Asian summer climate is not directly related to variations in higher latitudes. The upward propagating wave energy in the eastern flank of the Tibetan Plateau suggests that orographic forcing also plays an important role in 1994, as suggested by Park and Schubert (1997).

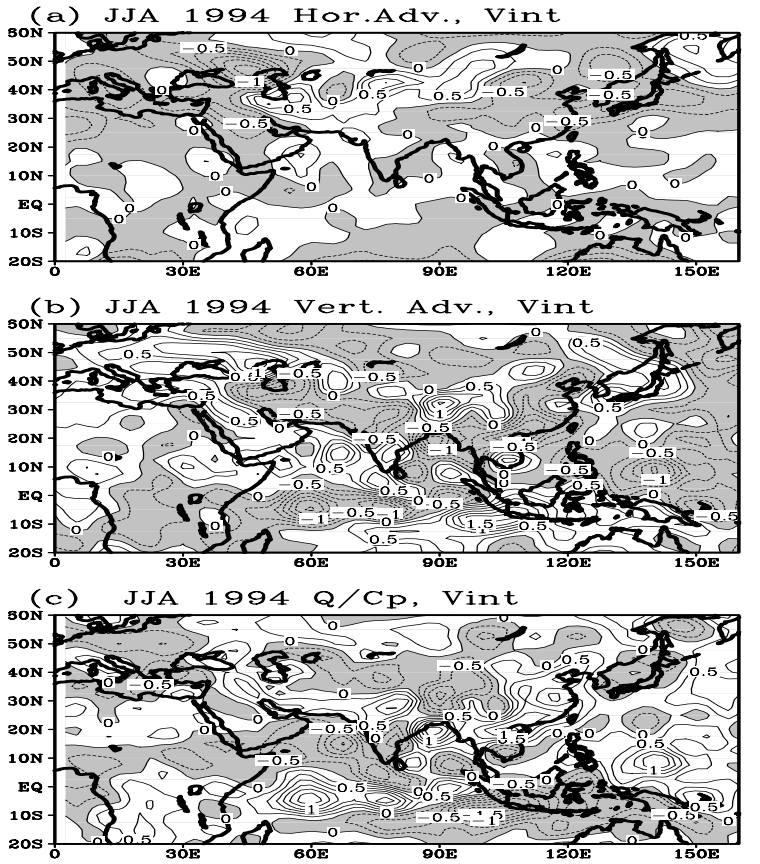

Fig. 4.6 JJA mean vertically integrated quantities for 1994. (a) The anomalous horizontal advection of temperature, (b) the anomalous vertical advection of po-

tential temperature, and (c) the anomalous diabatic heating rate. All these quantities are vertically averaged over pressure from surface to 100hPa. The unit is $^{o}C \cdot d^{-1}$. From Guan and Yamagata (2003).

4.4.3 Individual influences of IOD and ENSO

People nowadays have been paying more and more attention to the IOD impacts on the EASC (e.g., Behera et al., 1999;Ashok et al., 2001; Guan and Yamagata, 2003; Saji and Yamagata, 2003; Xiao et al., 2000). Without having the ENSO influences removed, the significant correlation is found between the IOD and variables including winds in South Asia, Tibetan High, and WPSH (Li and Mu, 2001). However, because some positive (negative) IOD events co-occurred with El Niño (La Niña), it is obviously very necessary for us to examine the individual and combined influences of IOD and ENSO on the EASC.

Data used in this part include the Ncep-Ncar reanalysis (Kalnay and co-authors, 1996), HADISST with 1°×1° grid mesh from British Atmospheric Data Center (http://badc.nerc.ac.uk/data/hadisst/), and in situ 160 station precipitation and air temperature from China Meteorological Administration. Time series used in the present section has a length of 42 years from 1958 through to 1999. All time series have been preprocessed by having the long term 'linear' trends removed using a linear regression.

Table 4.2 Years of ENSO and IOD identified in the present study. Year number with superscription of star represents the 'pure' year. See also Rao et al. (2002).

Positive IOD year	Negative IOD year	El Niño year	La Niña year
1961*	1958*	1963	1964
1963	1960*	1965*	1967*
1967*	1964	1969*	1970*
1972	1971	1972	1971
1977*	1974*	1976*	1973*
1982	1975	1982	1975
1983*	1989*	1986*	1978*
1994*	1992*	1987*	1984*
1997	1993*	1997	1985*
	1996		1988*
			1996

Two indices including Niño3 and IODMI are respectively used as two

indicators of ENSO and IOD phenomenon. Niño3 index is defined by averaging the SSTA over region (150°-90°W, 5°S-5°N) as usual, while IODM index is defined as 'the difference of SSTA averaged over area (50°-70°E, 10°S-10°N) from the SSTA averaged over area (90°-110°E, 10°S-0°)', identical to the definition given by Saji et al.(1999). To separate the influences of IOD from those of ENSO, we define "pure" events for both IOD and ENSO with no co-occurrence of positive (negative) IOD with El Niño (La Niña). Thus, the "pure event years" are identified, which are presented in Table 4.2.

Impacts of 'pure' ENSO events on Summer climate of China

Many scientists have examined the ENSO impacts on summer monsoon variations in China in recent decades, as mentioned in section 4.1-4.3 in this Chapter. However, they had never linked the IOD with summer climate conditions of China before the IOD was discovered. To understand more clearly the ENSO impacts on China climate, it must be helpful to have the IOD signals removed from the data before analyzing the ENSO influences. In some studies (e.g., Ashok et al., 2001; Saji and Yamagata, 2003b; Guan et al., 2003), the partial correlations are employed to assess the individual influences of IOD and ENSO. Here, we do the composites instead to analyze the individual influences for showing magnitudes of the anomalies of the climate variables.

The differences of composite variables in 'pure' El Niño years from those in 'pure' La Niña years are plotted in Fig.4.7. In 'pure' El Niño years, more rainfall is received in reaches of Yangtze River (Fig.4.7a) whereas less rainfall in reaches of Yellow River. Vertically integrated water vapor or precipitable water (Fig.4.7b) is significantly less than normal in the northern and northeastern parts of China, India, and western part of north Pacific, but it is relatively more in reaches of Yangtze River and the southern part of China. This distribution of water vapor anomalies facilitates more rainfall in this region. Vertically integrated water vapor transports (Fig.4.7c) show clearly the convergence of water vapor in Reaches of Yangtze River whereas divergence in the northern part of China, South China Sea, the western North Pacific, and Indian continent, being consistent with the anomalous rainfall pattern as shown in Fig.4.7a. Usually, more clouds are expected where more rainfall is received, which hence induces less shortwave radiation at the earth surface, and possibly more evaporation at a wetter surface in this area. These lead to significant air temperature changes as seen in Fig.4.7d and lower temperatures appear in Reaches of Yangtze River and the northeastern part of China.

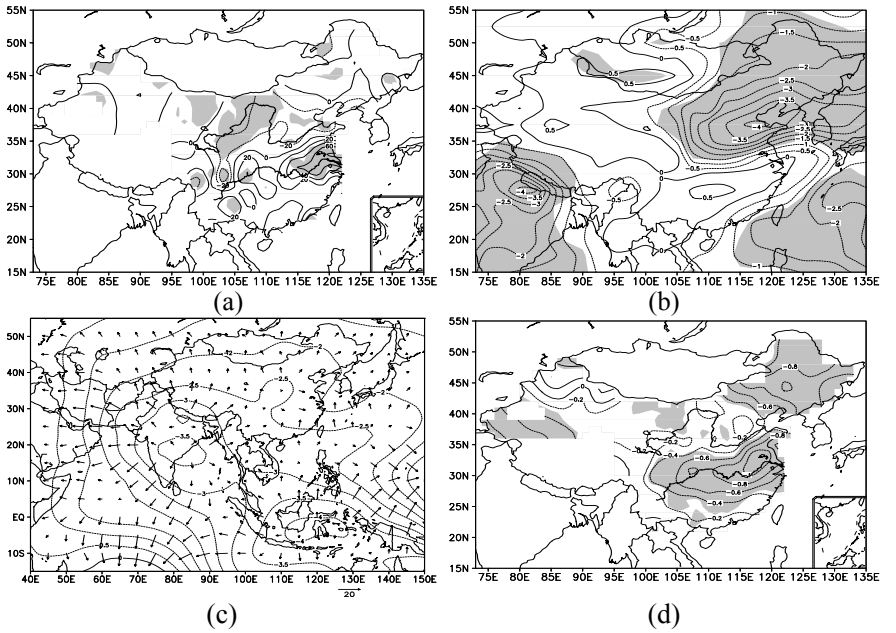

Fig. 4.7 JJA mean differences of composite anomalies of physical quantities between "pure" El Niño years and "pure" La Niña years. Values above 90% level of confidence are shaded using the Student's *t* test. (a) The rainfall (in mm·month^{-1}), (b) the moisture content (in kg) which is vertically integrated from the earth surface up to 300hPa, (c) the velocity potential of the moisture flux (in 10^7kg.s^{-1}), and (d) the air temperature (in °C). From Yang et al. (2007).

These results above have reconfirmed that the ENSO events indeed have significantly simultaneous influences on the Summer climate of China. The anomalous rainfall pattern looks similar to the pattern occurred in a developing stage of El Niño events as discussed in section 4.2.1. This reconfirmation is very convincing and encouraging. Those results are helpful for predicting and understanding variabilities of the summer climate in China on inter-annual time scales as long as the cases of IOD-ENSO co-occurrence are kicked out.

Impacts of 'pure' IOD on the Summer climate of China.

To reconfirm the influences of IOD on summer climate of China, it is necessary to remove ENSO signals from variations of climate variables. Fig.4.8 displays the differences of composite quantities in positive 'pure' IOD years from those in negative IOD years. During positive IOD years,

precipitation tends to be less than normal in reaches of Yangtze and Huaihe Rivers while it tends to be more in northern part of China and in regions around Guangxi and Guangdong provinces (Fig.4.8a). This pattern looks quite different from the impacts of ENSO on summer climate of China, as compared to anomalous rainfall pattern shown in Fig.4.7a. Distribution of the vertically integrated water vapor from the earth surface up to the isobaric surface at 300hPa as displayed in Fig.4.8b indicates that more precipitable water exists in the troposphere over northern part of China. This anomalous accumulation of water vapor there comes partly from western North Pacific and East China Sea, and partly from the region east of Tibetan plateau, which relates to the East Asian summer monsoon circulation changes in this region. Water vapor diverges anomalously from the eastern pole of the IOD in the Indian Ocean directly into South China Sea and regions north of SCS (Fig.4.8c), leading to more precipitation there (Fig.4.8a). The air temperature anomalies are intrinsically determined by the atmospheric thermodynamics including the interactions among clouds, radiation, evaporation, and so on. The pattern of anomalous air temperatures corresponding to the anomalous rainfall distributions display the hotter summer climate conditions in regions of Yangtze, Huaihe and Yellow rivers, and in the northeastern part of China (Fig.4.8d). This agree well with Guan and Yamagata(2003), and Saji and Yamagata (2003a).

By comparing the individual influences of IOD and ENSO with each other, one can find that the IOD cancels the influences of ENSO on summer climate in the eastern China. This cancellation is very amazing. Scientists have to be fully aware of the existence of this cancellation in predicting summer climate variations when they use the ENSO other than IOD as a predictor otherwise the prediction fails.

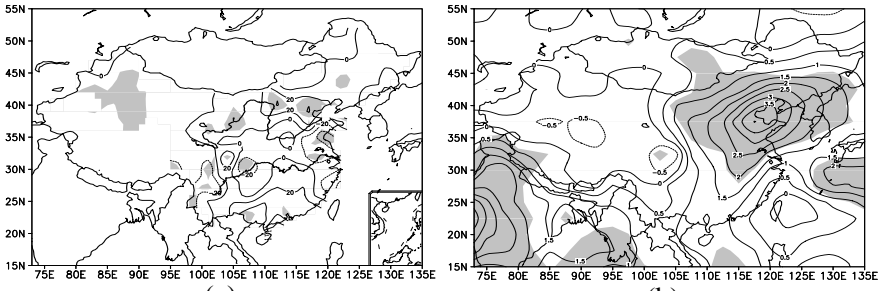

(a) (b)

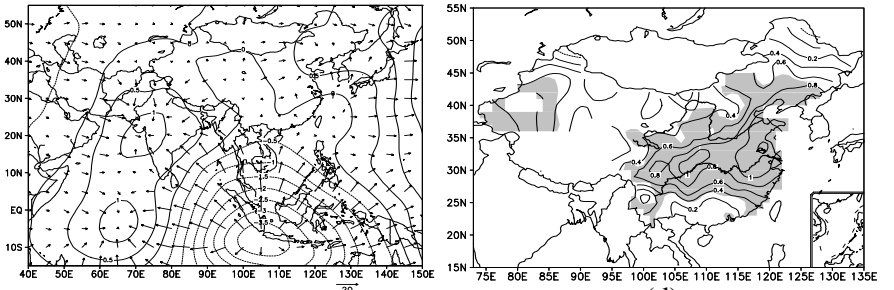

(c) (d)

Fig. 4.8 JJA mean differences of composite anomalies of physical quantities between "pure" positive IOD years and "pure" negative IOD years. Values above 90% level of confidence are shaded using the Student's ***t*** test. (a) The rainfall (units in mm·month^{-1}), (b) the moisture content (units in kg) which is vertically integrated from the earth surface up to 300hPa, (c) the velocity potential of the moisture flux (units in 10^7kg.s^{-1}), and (d) the air temperature (units in °C). From Yang et al. (2007).

4.4.4 Interference of IOD in the ENSO-EASM relation

The 'Pure' ENSO and 'Pure' IOD events have quite different impacts on Summer climate of China as discussed above. However, when an ENSO event co-occurs with an IOD event, what influences of ENSO will be on the summer climate of China? Ashok et al. (2004) examined using an AGCM the individual and combined influences of ENSO and the Indian Ocean dipole on the Indian summer monsoon, who found that the IOD can induce more Indian summer monsoon rainfall. Fig.4.9 displays the composite differences of climate quantities in years when El Niño events co-occur with positive IOD events (El-pIOD year hereafter) from those in years when La Niña events co-occur with negative IOD events (La-nIOD year hereafter). Apparently, rainfall is received more than normal in regions near the southeastern coastline of China whereas it is received less in reaches of Yangtze and Yellow Rivers (Fig.4.9a). The troposphere is relatively drier over most part of China but around the southeastern coastline (Fig.4.9b). Water vapor diverges from the east pole of the IOD, and from reaches of Yangtze and Yellow Rivers towards regions including the southeastern coastline of China and tropical west Pacific (Fig.4.9c). The air temperature is almost higher everywhere except for the southeastern part of China (Fig.4.9d). These features of the ENSO-IOD combined impacts on the summer climate of China look very different from the 'pure'

ENSO's impacts and also very different from the 'pure' IOD's impacts. This kind of combined or mixed impacts of both ENSO and IOD drove climate investigators into troubles because they felt sometime very difficult to well predict the summer climate conditions of China using ENSO as a predictor in the past decades.

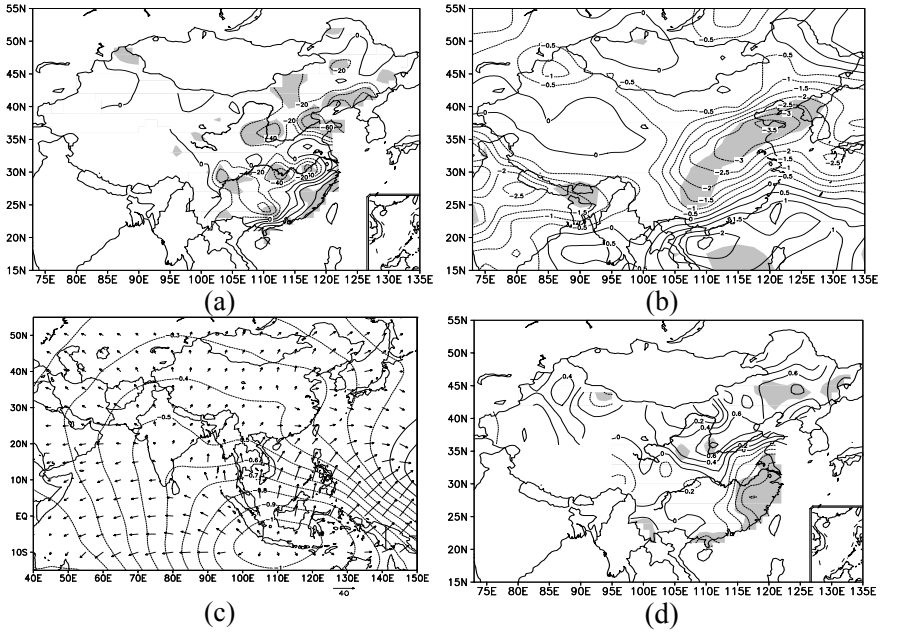

Fig. 4.9 JJA mean differences of composite anomalies of physical quantities in El-PIOD years from those in La-nIOD years. Values above 90% level of confidence are shaded using the Student's ***t*** test). (a) The rainfall (in mm·month^{-1}), (b) the moisture content (in kg) which is vertically integrated from the earth surface up to 300hPa, (c) the velocity potential of the moisture flux (in 10^8kg.s^{-1}), and (d) the air temperature (in °C). From Yang et al. (2007).

To clarify the possible interferences of IOD in relations between the ENSO and summer climate of China, some plots have been prepared here (Fig.4.10 and 4.11) to display the differences of composite climate variables in El-pIOD (La-nIOD) years from those in 'pure' El Niño ('pure' La Niña) years. As the samples used in Figs.4.10-4.11 are not large enough, these differences of composites are employed to indicate just the possible interferences of IOD in the ENSO-China climate relations. In the El-pIOD years, the positive IOD events tend to induce more rainfall in southern part of China, and in a relatively small area between Yangtze and Yellow rivers

(Fig.4.10a). Apparently less rainfall is induced by positive IOD events in regions along Yangtze River, and in the northeastern part of China (Fig.4.10a). Consistently, the air temperature is increased everywhere but in the southeastern part of China (Fig.4.10c). As we know that the 'pure' El Niño tends to induce lower than normal air temperatures (even cold summer events) in the northeastern part of China, the co-occurrence of positive IOD with El Niño events are interestingly to reduce the 'low temperature hazards' there. In La-nIOD years (Fig.4.10b and 4.10d), scenarios seem to be oppositely signed as compared to those in El-pIOD years. Similarly, in years of La Niña events co-occurred with negative IOD events, the role of negative IOD tends to cancel the influences of La Niña on the summer climate by decreasing the air temperatures in regions including reaches of Yangtze River, northern, and northeastern parts of China, where the temperatures usually increase anomalously in the La Niña years.

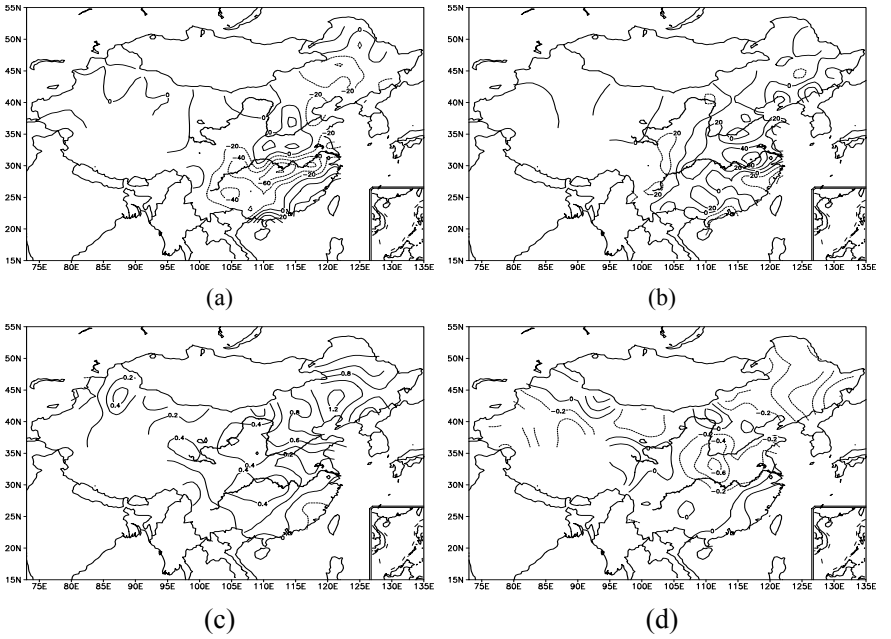

Fig. 4.10 (a) Differences of composite rainfall anomalies (in mm·month^{-1}) in El-pIOD years from those in pure El Niño years, and (b) of those in La-nIOD years from those in the pure La Niña years. (c) Differences of composite temperature anomalies (in °C) in El-pIOD years from those in pure El Niño years, and (d) of those in La-nIOD years from those in the pure La Niña years. From Yang et al. (2007).

To understand how the IOD interferes in ENSO-SCC relation, differences of composite anomalies of both streamfunction and velocity potential have been plotted in Fig.4.11. In the summer of El-pIOD years, the IOD events disturb the atmosphere, exciting a PJ-like teleconnection pattern (Nitta, 1987; Guan and Yamagata, 2003) in the lower troposphere from South China Sea northeastward to place east of Japan (Fig.4.11a). An anomalous cyclonic circulation as a node of this Teleconnection pattern at 850hPa appears in the eastern part of China, weakening the monsoonal south wind, and henceforth weakening the northward transports of water vapor from SCS and Bay of Bengal. Correspondingly, a divergence center can be found in the lower troposphere in China, along with another divergence center locates at the east pole of the Indian Ocean dipole. Some convergence is seen in regions around the southeast coastline where more rainfall, and lower than normal air temperature are induced in El-pIOD years (Fig.4.11b). Fig.4.11c and 4.11d shows largely opposite scenarios in La-nIOD years, as compared to those in El-pIOD years (Fig.4.11a and 4.11b).

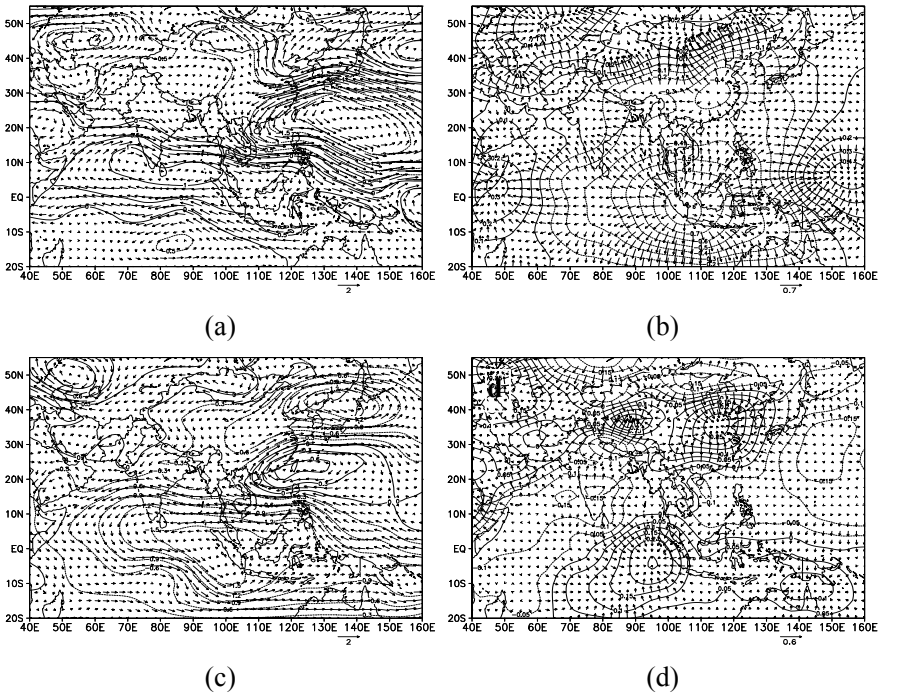

Fig. 4.11 (a) Differences of composite stream function anomalies (in $10^6 m^2 \cdot s^{-1}$) and anomalous rotational wind (in $m \cdot s^{-1}$) at 850hPa in El-pIOD years from those

in pure El Niño years, and (b) same as in (a) except for velocity potential anomalies (in $10^6 m^2 \cdot s^{-1}$). (c) Differences of composite stream function anomalies and anomalous rotational wind at 850hPa in La-nIOD years from those in pure La Niña years, and (d) same as in (c) except for velocity potential anomalies. From Yang et al. (2007).

4.5 Concluding Remarks

Interannual variabilities of the summer climate of China in association with ENSO and IOD have been examined in the present chapter. Results as briefly summarized from studies by different research groups in China, Japan, and US in the past decade have demonstrated that Summer climate of China is significantly influenced by both the ENSO and IOD.

Whether flood or drought events occur in reaches of Yangtze River is ENSO-phase dependent. During the developing phase of the El Niño events, surplus rainfall is received in reaches of Yangtze and Huaihe Rivers whereas deficit rainfall in the northern part of China and in regions south of Yangtze River. The anomalous air temperature tends to be lower than normal in place where more rainfall is received, especially in reaches of Yangtze and Huaihe Rivers and in the northeastern China. Scenarios are oppositely signed during decaying phase of the El Niño events. There are lag influences of ENSO on summer climate of China, which is related to the processes of the atmosphere-ocean coupling as well as the persistence of SSTA variations.

The EASM circulation is influenced by ENSO. Two teleconnections link the EASM to the SSTA in tropical Pacific. The one is a Rossby wave related anomalous anticyclone in the western North Pacific along with the anomalous Walker circulation in equatorial Pacific region, which is generated as a response of the atmosphere to the SSTA forcing (El Niño). Another is the PJ-like pattern in the lower troposphere that links the perturbations in the tropics northeastward to place east of Japan. The anomalous anticyclone near Philippine Sea is the key system that transports water vapor northward to China during El Niño phase, inducing rainfall anomalies in China in boreal summer.

Because of the discovery of IOD, the East Asian summer climate in association with SSTA in tropical oceans has been further investigated to clarify the individual and combined influences of ENSO and IOD. Results have shown that the ‘pure’ ENSO events affect the summer climate of China significantly, inducing more rainfall in Reaches of Yangtze River. However, in the northern part of China, deficit rainfall in ‘pure’ El Niño

years is found. The air temperature in most part of China during ‘pure’ El Niño episodes tends to be lower than normal especially in northeastern China and reaches of Yangtze River. On the other hand, IOD events have opposite influences on the summer climate of China; it tends to cancel the influences of ENSO events. In the southern China, rainfall tends to be more during JJA of ‘pure’ positive IOD years whereas the rainfall tends to be less in Reaches of Yangtze River. The air temperature is observed significantly higher than normal in eastern part of China. The patterns of the combined influences of ENSO and IOD on summer climate are very different from the patterns of individual influences of ‘pure’ ENSO and ‘pure’ IOD. These results suggest that it be very necessary to examine the different impacts of ENSO and IOD for our better understanding and predicting the summer climate in China.

The possible mechanisms on IOD’s impacts on the East Asian summer climate can be put forward from a case study on 1994 which is known as a typical positive IOD year. In summer of 1994, people in East Asia experienced an extraordinarily hot and dry summer. It is found that an anomalous anticyclonic circulation over the eastern as well as northeastern part of China in the lower troposphere induces the higher than normal temperatures there. The anomalous cyclonic circulation over the southern part of China and the western Pacific weakens the monsoonal northward wind from the Bay of Bengal, the South China Sea, and the tropical Western Pacific, preventing the subtropical East Asia from receiving the normal water vapor from the tropical regions. The anomalously hot summer climate over East Asia including China, Korea, and Japan is explained as a result from the anomalous dynamic heating around Japan, and diabatic heating over the northeastern as well as eastern part of China (Guan and Yamagata, 2003).

The IOD induced the circulation changes over East Asia during the summer of 1994 at least in two ways. One is that a Rossby wavetrain was excited in the upper troposphere by the IOD-induced vorticity source (the divergent flow) over India, the Bay of Bengal, and the southern China. The wavetrain propagates northeastward from the southern part of China. This pattern looks similar to the PJ teleconnection pattern. Another is that the IOD-induced diabatic heating around India and the Bay of Bengal excited a Rossby wave pattern to the west of the heating. Through the Monsoon-desert mechanism, the circulation change over the Mediterranean/Sahara region is linked to the IOD/monsoon variations. The westerly jet acts as a wave-guide to link this circulation change around the Mediterranean Sea with the anomalous circulation change over East Asia.

Acknowledgments: The first author is supported partly by the "NSFC pro-

ject (No.40475028)" as well as the "National Key Programme for Developing Basic Sciences, G2006CB403602". Reanalysis data are provided by the NOAA-CIRES Climate Diagnostics Center through the web site at http://www.cdc.noaa.gov/. The GrADS software is used to draw figures in this chapter.

References

Alexander MA, Bladé I, Newman M, Lanzante JR, Lau NC, Scott JD (2002) The atmospheric bridge: the influence of ENSO teleconnections on air-sea interaction over global oceans. *J. Climate* 15: 2205-2231.

Ashok K, Guan ZY, Yamagata T (2001) Impact of the Indian Ocean dipole on the relationship between the Indian monsoon rainfall and ENSO. *Geophys. Res. Lett.* 28: 4499-4502.

Ashok K, Guan ZY, Yamagata T (2003) A look at the relationship between the ENSO and the Indian Ocean dipole. *J. Meteor. Soc. Japan* 81: 41-56.

Ashok, K., Guan ZY, Saji N.H. and Yamagata T., Individual and Combined Influences of ENSO and the Indian Ocean Dipole on the Indian Summer Monsoon, *J. Climate,* 17, 3141-3155.

Behera SK, Krishnan R, Yamagata T (1999) Unusual Ocean-Atmosphere conditions in the tropical Indian Ocean during 1994. *Geophys. Res. Lett.* 26: 3001–3004.

Bao CL, Xiang YZ (2000) Impact of El Niño event on human society. *Scientia Meteorologica Sinica* 20: 277~283. (in Chinese)

Cadet DL (1985) The southern Oscillation over the Indian Ocean. *J. Climatol*. 5: 189-212.

Camargo SJ, Sobel AH (2005) Western North Pacific tropical cyclone intensity and ENSO. *J. Climate* 18: 2996–3006.

Chang CP, Harr P, Ju JH (2001) Possible roles of Atlantic circulations on the weakening Indian monsoon rainfall-ENSO relationship. *J. Climate* 14: 2376-2380.

Chang CP, Zhang YS, Li T (2000) Interannual and Interdecadal Variations of the East Asian Summer Monsoon and Tropical Pacific SSTs. Part I: Roles of the Subtropical Ridge. *J. Climate* 13: 4310-4325.

Chan JC (2000) Tropical cyclone activity over the western North Pacific associated with El Niño and La Niña events. *J. Climate* 13: 2960–2972.

Chen W (2002) Impacts of El Niño and La Niña on the cycle of the East Asian winter and summer monsoon. *Chinese J. Atmos. Sci.* 26: 595-610.

Chen W, Graf H, Huang RH (2000) The interannual variability of East Asian winter monsoon and its relation to the summer monsoon. *Adv. Atmos. Sci*. 17: 48-60.

Fu C (1987) A review of study on El Niño/Southern Oscillation associated with the interannual climate variability. *Scientia Atmospherica Sinica* 11: 209-220. (in Chinese)

Fu C, Teng X (1988) The relationship between ENSO and climate anomaly in China during the summer time. *Scientia Atmospherica Sinica*, Special Issue: 133–141. (in Chinese)

Enomoto T, Hoskins BJ, Matsuda Y (2003) The formation of the Bonin high in August. *Q. J. R. Meteorol. Soc* 129: 157-178.

Guan ZY, Ashok K, Yamagata T (2003) Summertime response of the tropical atmosphere to the Indian Ocean dipole sea surface temperature anomalies. *J. Meteor. Soc. Japan* 81: 533-561.

Guan ZY, Yamagata T (2003) The unusual summer of 1994 in East Asia: IOD teleconnections, *Geophys. Res. Lett*. 30, 1544, doi:10.1029/2002GL016831

He M, Song WL, Chen XF (1999) Typhoon activity in the northwest pacif ic in relation to El Niño/La Niña events. *J. Tropical Meteorol.* 15: 17-25.

Hoskins BJ, Ambrizzi T (1993) Rossby wave propagation on a realistic longitudinally varying flow. *J. Atmos. Sci.* 38: 1179-1196.

Huang RH (2001) Progress in the research on the formation mechanism and prediction theory of severe climatic disasters in China. *China Basic Science* 8: 4-8. (in Chinese)

Huang RH (1992) The East Asia/Pacific teleconnection Pattern of summer circulation and Climate Anomaly in East Asia. *Acta Meterologica Sinica* 6: 25-37.

Huang RH, Chen W (2002) Recent Progresses in the Research on the Interaction between Asian Monsoon and ENSO Cycle. *Climatic and Environmental Research* 7:146-159. (in Chinese)

Huang RH, Zhang Z, Huang G, Ren B (1998) Characteristics of the Water Vapor Transport in East Asian Monsoon Region and Its Difference from that in South Asian Monsoon Region in Summer. *Scientia Atmospherica Sinica* 22: 460-469.

Jin Z, Tao SY (1999) A Study on the Relationships between ENSO Cycle and Rainfalls during Summer and Winter in Eastern China. *Scientia Atmospherica Sinica* 23: 663-672.

Kalnay E, coauthors (1996) The NCEP/NCAR 40 year Reanalysis Project, *Bull. Amer. Meteorol. Soc.* 77: 437-471.

Kawamura RT, Matsuura, Satoshi I (2001b) Interannual atmosphere–ocean variations in the tropical western North Pacific relevant to the Asian summer monsoon–ENSO coupling. *J. Meteor. Soc. Japan* 79: 883–898.

Kawamura RM, Kayahara ST, Sato N (1998) Recent extraordinary cool and hot summers in East Asia simulated by an ensemble climate experiment. *J. Meteor. Soc. Japan* 76*:* 597-617.

Kiladis GN, Diaz HF (1989) Global climatic anomalies associated with extremes in the Southern Oscillation. *J. Climate* 2: 1069–1090.

Klein SA, Soden BJ, Lau NC (1999) Remote sea surface temperature varaitions during ENSO: evidence for a tropical atmospheric bridge. *J. Climate* 12: 917-932.

Kumar KK, Rajagopalan B, Cane MA (1999) On the weakening relationship between the Indian monsoon and ENSO. *Science* 284: 2156–2159.

Lau KM, Li MT (1984) The monsoon of East Asia and its global associations-A survey. *Bull. Amer. Meteorol. Soc.* 65: 114-125.

Lau KM, Wu HT (2001) Principal modes of rainfall-SST variability of the Asian summer monsoon: A reassessment of the monsoon–ENSO relationship. *J. Climate* 14: 2880–2895.

Li CY (1987) A study on the influence of El Niño upon typhoon action over western Pacific. *Acta Meteorologica Sinica* 45: 229-235. (in Chinese)

Li CY, Mu MQ (2001) The Dipole in the Equatorial Indian Ocean and Its Impacts on Climate. *Chinese J. Atmos. Sci.* 25: 433-443.

Li S, Shou S (2000) Equatorial eastern pacific SST and analysis on causes of summer floods/droughts in the Changjiang and Huaihe river basin. *Quart. J. Appl. Meteorol.* 11:331-338. (in Chinese)

Liang XZ, Wang WC (1998) Associations between China monsoon rainfall and tropospheric jets. *Q. J. R. Meteorol. Soc*. 124: 2597-2623.

Lin XC, Yu SQ (1993) El Niño and rainfall during the flood season (June-August) in China. *Acta Meteorologica Sinica* 51: 434-441. (in Chinese)

Long ZX, Li CY (1999) Numerical simulation of the ENDO influences on east-Asian monsoon activities afterwards. *Acta Meteorologica Sinica* 57: 651-662.(in Chinese)

Lu DJ, Zhang XG. The response of precipitation and temperature in China to ENSO. *Quart. J. Appl. Meteorol.* 6: 118-123. (in Chinese)

Lu RY, D BW (2001) Westward extension of North Pacific subtropical high in summer. *J. Meteor. Soc. Japan* 79: 1229-1241.

Lu RY, OH JH, Kim BJ (2002)A teleconnection pattern in upper-level meridional wind over the North African and Eurasian continent in summer. *Tellus* 54A: 44-55.

Nitta T (1987) Convective activities in the tropical Western Pacific and their impact on the Northern Hemisphere summer circulation. *J. Meteor. Soc. Japan* 65: 373-390.

Park CK, Schubert SD (1997) On the nature of the 1994 East Asian summer drought. *J. Climate* 10: 1056-1070.

Parker DE, Folland CK, Jackson M (1995) Marine surface temperature: observed variations and data requirements. *Climate Change* 31: 559-600.

Parthasarathy B, Munot AA, Kotawale DR (1995) Monthly and seasonal rainfall series for all-India homogeneous regions and Meteorological sub-divisions: 1871-1994. *Res.Rep.* No. **65** (Indian Institute of Tropical Meteorology, Pune, India, 1995)

Plumb RA (1986) Three-dimensional propagation of transient quasi-geostrophic eddies and its relationship with the eddy forcing of the time-mean flow. *J. Atmos. Sci*. 43: 1657-1678.

Rao SA, Behera SK, Matsumoto Y, Yamagata T (2002) Interannual subsurface variability in the tropical Inidan Ocean with a special emphasis on the Indian Ocean dipole. *Deep Sea Res*. II 49: 1549-1572.

Rodwell MJ, Hoskins BJ (1996) Monsoons and the dynamics of deserts. *Q. J. R. Meteorol. Soc.* 122: 1385-1404.

Ropelewski CF, Halpert MS (1987) Global and regional scale precipitation patterns associated with the El Nin˜o/Southern Oscillation. *Mon. Wea. Rev*. 115: 1606–1626.

Sardeshmukh PD, Hoskins BJ (1988) The generation of global rotational flow by steady idealized tropical divergence. *J.Atmos.Sci.* 45: 1228-1251.

Saji NH, Goswami BN, Vinayachandran PN, Yamagata T (1999) A dipole mode in the tropical Indian Ocean. *Nature* 401: 360-363.

Saji NH, Yamagata T (2003a) Possible impacts of Indian Ocean dipole mode events on global climate. *Climate Research* 25: 151-169.

Saji NH, Yamagata T (2003b) Structure of SST and Surface Wind Variability during Indian Ocean Dipole Mode Events: COADS Observations. *J. Climate* 2735-2751.

Shankman BD, Kelm, Jie S (2006) Flood Frequency in China's Poyang lake region: trends and teleconnections. *Int. J. Climatol* 26: 1255–1266 .

Shi J, Lin XC, Zhou Qf (1983) Relationships of the El Niño phenomenon with June-July-August precipitation in China. *Meteorological Monthly* 4: 2-5. (in Chinese)

Sun SQ, Ma SJ (2003) Analysis and Numerical Experiment on the Relationship between the 1998 Summer Monsoon Activities and SSTA in Tropical Regions. *Chinese J. Atmos. Sci.* 27:36-51. (in Chinese)

Tao SY, Zhang QY, Zhang SL (1998) The Great Floods in the Changjiang River Valley in 1998. *Climatic and Environmental Research* 3: 290-299. (in Chinese)

Tao SY, Zhang QY (1998) Response of the Asian Winter and Summer Monsoon to ENSO Events. *Scientia Atmospherica Sinica* 22: 399-407. (in Chinese)

Torrence C, Webster PJ (1999) Interdecadal changes in the ENSO-monsoon system. *J. Climate* 12**:** 2679-2690.

Trenberth KE (1997) The definition of El Niño. *Bull. Amer. Meteor. Soc.* 78: 2771–2777.

Trenberth KE, Caron JM, David PS, Steve W (2002) Evolution of El Nin˜o–Southern Oscillation and global atmospheric surface temperatures. *J. Geophys. Res*. 107-D8, 10.1029/2000JD000298.

Wang BZ, Fan (1999) Choice of South Asian summer monsoon indices. *Bull. Amer. Meteorol. Soc*. 80: 629-638.

Wang B, Wu R, Fu X (2000) Pacific–East Asian teleconnection: How does ENSO affect East Asian climate? *J. Climate* 13: 1517–1536.

Wang B, Wu R, Lau KM (2001) Interannual Variability of the Asian Summer Monsoon: Contrasts between the Indian and the Western North Pacific–East Asian Monsoons. *J. Climate* 14: 4073-4090.

Wang SW (1992) Reconstruction of El Niño events chronology for the last 600 year period. *Acta Meteorologica, Sinica* 6: 47-57.

Wang SW, Hong Z (1985) Summertime extraordinarily low air temperature over East Asia in association with El Niño events. *Chinese Science Bulletin* 30: 1323-1325. (in Chinese)

Webster PJ (1981) Mechanism determining the atmospheric response to sea surface temperature anomalies, *J. Atmos. Sci*., 38: 554-571.

Webster PJ, Magana VO, Palmer TN, Shukla J, Tomas RA, Yanai M, Yasunari T (1998) Monsoons: Processes, predictability, and the prospects of prediction. *J. Geophys. Res.* 103: 14451-14510.

Webster PJ, Moore A, Loschnigg J, Leban M (1999) Coupled ocean-atmosphere

dynamics in the Indian Ocean during 1997-98. *Nature* 40: 356-360.
Wu GX, Liu P, Liu YM, Li WP (2000) Impacts of the sea surface temperature anomaly in the Indian ocean on the subtropical anticyclone over the western Pacific two-stage thermal adaptation in the atmosphere. *Acta Meteorologica Sinica* 58: 513-522. (in Chinese)
Wu RG (1996) Summer rainfall in middle and lower Reaches of Yangtze River in association with planetary atmospheric circulation and the SST in tropical regions, Processes of climate disasters and their diagnoses (Ed: R.-H. Huang). Meteorological Press, Beijing, 23-30pp.(in Chinese)
Xiao Z, Sun JH, Li CY (2000) Influence of the Indian Ocean SSTA on Asian Climate during an ENSO Period. *Scientia Atmospherica Sinica* 24: 461-469.
Xie P, Arkin PA (1996) Analyses of global monthly precipitation using gauge observations, satellite estimates and numerical model predictions. *J.Climate* 9: 840-858.
Xu WC, Ma JS, Wang W (2005) A review of studys on the influence of ENSO events on the climate in China. *Scientia Meteorologica Sinica* 25: 212-220. (in Chinese)
Yamagata T, Behera SK, Rao SA, Guan Z, Ashok K, Saji HN (2002) The Indian Ocean dipole: a physical entity. *CLIVAR EXCHANGES* 24: 1-6.
Yan H (1998) Analysis on the Weather and Climate Features and Causes of the Extraordinary Flood Disaster over China in 1998 and the Relevant Meteorological Prediction Services. *Climatic and Environmental Research* 3: 323-334. (in Chinese)
Yang X, Guan ZY, Zhu BL (2007) Role of Indian Ocean dipole events in the influence of ENSO on the summer rainfall and temperature in China. *J. Nanjing Institute of Meteorol.* 30:170-177. (in Chinese)
Ye DZ, Huang RH (1996) On variations of droughts and floods in Reaches of Yangtze and Yellow Rivers. Academic Press of Shandong, Jinan, 222-236pp. (in Chinese)
Zhao HG, Zhang XG, Ding YH (1990) The El Niño events and the anomalous climate of China (Collection of papers on long range weather forecasting). Meteorological Press, Beijing, 108-118pp. (in Chinese)
Zhang RH, Sumi A, Kimoto M (1996) Impact of El Nin˜o on the East Asian monsoon: A diagnostic study of the ’86/87 and ’91/92 events. *J. Meteor. Soc. Japan* 74: 49–62.
Zhang RH (1999) The role of indian summer monsoon water vapor transportation on the summer rainfall anomalies in the northern part of China during the El Niño mature phase. *Plateau Meteorology* 18: 567-574. (in Chinese)
Zhang RH, Sumi A, Kimoto M (1999b) A diagnostic study of the impact of El Niño on the precipitation in China. *Adv. Atmos. Sci*. 16: 229-241.
Zhang RH, Huang RH (1998) Dynamical role of zonal windstresses over the tropical Pacific on the occurring and vanishing of El Niño, Part I: diagnostic and theoretical analysis. *Scientia Atmospherica Sinica* 22: 587-599. (in Chinese)
Zhou T, Yu R, Li W, Zhang X (2001) On the variability of the indian ocean during the 20th century. *Acta Meteorologica Sinica* 59: 257-272. (in Chinese)

Zhou W, Chan JC (2007) ENSO and the South China Sea summer monsoon onset. *Int. J. Climatol*. 27: 157-167.

Zhou W, Chan JC, Li CY (2005) South China Sea Summer Monsoon onset in relation to the off-equatorial ITCZ. *Adv. Atmos. Sci.* 22: 665–676.

Zhu YF, Chen LX, Yu RC (2003) Analysis of the relationship between the China anomalous climate variation and ENSO cycle on the quasi-four-year scale. *J. Trop. Meteorol*. 19: 345-356. (in Chinese)

Chapter 5 Aridity Trend in Northern China

5.1 Introduction

As a natural process of earth evolution, huge arid and semi-arid regions formed over northern part of China, occupy nearly 40% of China terrestrial area (Fig. 5.1) (Liu Tungsheng and Ding Zhongli, 1999; An et al., 2001; Zhang Jiacheng, 1991). The landscape of these areas are featured largely by desert, semi-desert and grassland and characterized by dry climate, low nutrition content and low capacity of water conservation of the soil (Fu and Wen, 2002; Zhu Zhenda, 1985; Dong Guangrong, 1997). The land surface processes in the arid and semi-arid regions are significantly different from those in humid areas, especially the hydrological process in the soil, which arises big challenges for the existed land surface process models (Dickinson, 1986; Sellers, 1986).

These areas are also major sources of dust storms, transporting huge amount of dust particles all way to downstream, which have significant influence on the human health, the regional and global climate(Yeh, et al., 2000; Wang Tao et al., 2001). Researches have also evaluated the correlation between increasing dust frequency and decreasing rainfall in the Sahelian region of Africa and proposed potential interaction between dust aerosols and the hydrological cycle (Brooks,2000).

Aridity trend is one of the most severe living environmental problems in northern China, which greatly impacts the social and economic development of the region. In recent years, the aridity trend has been further aggravated partly because of regional climate change related to global warming as well as the anthropogenic effects of the rapid development of social economy and the expansion of urbanization (Qian, 2003; Zhai, 2003; Ma, 2003).

Aridity trend over northern China is not an isolated regional phenomenon, but has strong global background (Nicholson et al., 1998; Steffen et al., 2004). Recent research indicates the area of global extreme arid region has been expanded by more than two times since the late 1970s. Such a tendency is more significant after the 1980s (Dai, 2004). As one of the key issues of global change, the study of aridity trend has been included in a

series of large international research projects, such as Global Land Project (GLP, http://www.globallandproject.org/), Global Water System Project (GWSP, http://www.gwsp.org/), Integrated Land Ecosystem Atmosphere Processes Study (iLEAPS, http://www.atm.helsinki.fi/ILEAPS/) and Monsoon Asia Integrated Regional Study Programs (MAIRS), etc.

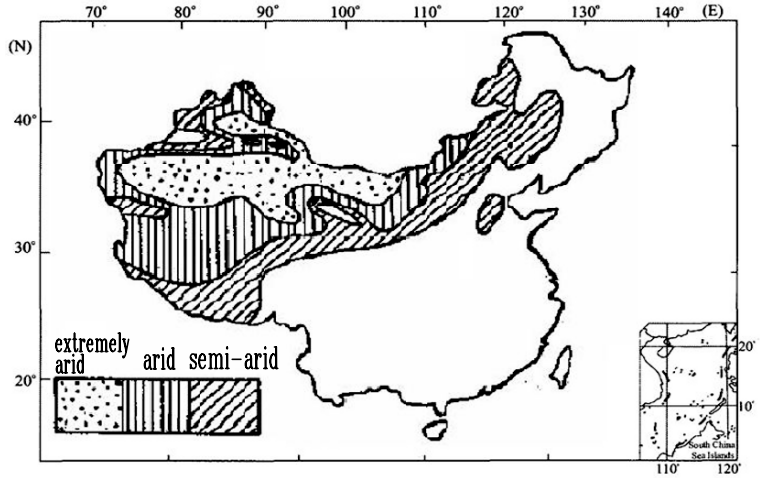

Fig. 5.1 Distribution of arid and semi-arid region in China based on drought index. (Blue cover book of science and technology in China, No.5-Climate, 1990)

Because of long history of human civilizations, aridity trend over northern China has its own characteristics that short-term effect and long-term accumulated effect coexist, global effect and regional effect coexist. The development of aridity trend over northern China is a kind of integrated behavior of environment system, including increasing air temperature and surface evaporation; decreasing precipitation, runoff and soil moisture; degradation of ecosystem and so on, probably represents the regional response to global change. Therefore, aridity trend over northern China should be studied as an issue of crossing scientific disciplines (Fu and An, 2002).

Based on rich environmental information in China, a sets of time series of proxy data to represent East Asian peleo-Monsoon climate and environmental variation at time scales from multimillion to thousand years are established. Their variability at different time scales, the abrupt and transitional features of changes have long been a major subject in climate research of China (Zhu kezhen, 1973; An Zhisheng, 1990; Shi Yafeng and Zhang Piyuan, 1996; Shi Yafeng, 1992; Wang Sumin, 1991; Zhang Der,

1983; Shi Yafeng, 1993; Zhang Piyuan et al., 1994; Wu Xiangding et al., 1990; Shao Xuemei, 1997; Yu Ge et al., 2001; Yu Ge, 2000). The main findings in current researches including: (1) The inland arid Asia formed in about 2.6Myr ago when the Tibetan plateau was expanded and uplifted rapidly. It is also the time of the East Asian monsoon establishment (An et al., 2001); (2) The records also provide a significant 20 ka period oscillation between the backspin period of the latest two glacial periods with the wet phase in interglacial period and dry phase in glacial period. (3) There was an aridity trend beginning from 4000-3000 BP (Ding et al., 2000; Shen Ji and Wang Sumin et al., 2001; Zhou Weijian et al., 2002; Yang Xiaoping et al., 2003; Li Xiaoqiang et al., 2003). It is approved by using of reconstructed temperature curve in past 2650 years based on stalagmite records. (Tan et al., 2003; Hou Juzhi et al., 2003); (4) Considering the effect of both natural and human factors, the current distribution of loess plateau is perhaps reflects the desert expanding induced mainly by human activities in historical periods (Li Xiaoqiang et al., 2003).

Studies on climate and environment variations on 10-100yr timescale have been another area of climate researches in China (Fu, 1991,1994; Peng, 2003; Qian and Zhu, 2001; Qian et al., 2003a). Relationships between aridity trend over northern China, changes of monsoon climate and global warming are revealed. It was found that the abrupt change of south Asian monsoon occurred simultaneously with the global papid warming in the 1920s (Fu et al., 1991,1994); Around the same time, China transit rapidly from a relatively wet period into a dry period (Fu,1994). The reconstructed 160 years precipitation index over inner-Mongolia from April to early July based on examples of tree-rings shows also an transition from wet to dry in 1920s and further dry after the 1950s(Liu Yu, 2003). The integrated analysis of air temperature, precipitation, soil moisture and drought index show that there exist quai-20yr and 70yr oscillations in air temperature and precipitation records over east China (Qian et al., 2003b). The decreasing precipitation and increasing temperature occurred in most areas of northern China, enhanced the trend of aridity trend all over northern China in recent 50 years (Zhai and Pan, 2003); aridity trend mainly happens in the east of northern China, especially in North China plain and the east of northwest China (Ma and Fu, 2003).

Inter-decadal variability of atmospheric circulation in association with the aridity trend over northern China has been studied (Tao Shiyan, and Chen Longxun, 1987; Huang Ronghui et al., 1999; Li Chongyin and Li Guilong, 1999; Zhang Qingyun, et al, 2003; Wang Huijun, 2000; Xue Feng, 2001). The results show that there was a wet period during 1951~1964 and a dry period during 1980~1997 in northern China. The decadal drought pattern during 1980~1997 at 500 hPa was the anomalous

height located at the middle latitude of Eurasia continent. Recently Yang (2005) suggested the Pacific inter Decadal Oscillation (PDO) plays an important role in occurrence of the decadal-to-interdecadal drought or flood in North China. During the drought period , the sea surface temperature anomaly is positive in the tropical eastern Pacific but negative in the extratropical North Pacific, indicating a warm PDO phase, and vice versa. Accompanying the warm PDO phase, the sea level pressure anomaly is negative over eastern Siberia and north of Japan but positive over most of Southern China, which generates an anomalous northwesterly over North China and reduces gain of the water vapor from oceans.

The semi-arid Asia located at nearly the northern edge of Asia summer monsoon is a transitive zone between arid continent climate and humid monsoon climate, which is very sensitive to the climate and human perturbation. The variation of climate and water cycle in this area are highly correlated with the high variability of the Asia monsoon system. This leads to the high frequency of extreme events and climate disasters over there. (Fu, 1992; Zhang Xinshi, 1995). Researches have shown that the semi-arid region has experienced the most severe aridity trend in last 50 years (Fu et al, 2001, 2005).

These areas are the most vulnerable in response to both human perturbation and global environmental change. Under the development of human society, these areas had experienced the most significant change of land cover (Deng, 1983). The human-induced land cover changes over these regions, particularly along the edge of the regions, the semi-arid areas, have brought about further land degradation, the expansion of the desertificated land and the increase of intensity and frequency of dust storm and so on (Ge quansheng, 2004; Liu Jiyuan et al., 2003). The further deterioration of environment over these regions has become a critical issue in the sustainable development of the world (Sun Honglie, et al., 2004).

In the past 3000 years, more than 60% of the region has been affected by conversion of various categories of natural vegetation into farmland, conversion of grassland into semi desert and widespread land degradation (Deng, 1983). Such human-induced land cover changes result in significant changes of surface dynamic parameters, such as albedo, surface roughness, leaf area index and fractional vegetation coverage, etc. The results of a pair of numerical experiments have shown that by altering the complex exchanges of water and energy fluxes from surface to atmosphere, the changes in land cover have brought about significant changes to the East Asian monsoon (Fu and Yuan, 2001; Fu, 2003; Zhang et al., 2005). These include weakening of the summer monsoon and enhancement of winter monsoon over the region and a commensurate increase in anomalous northerly flow. These changes result in the reduction of all components of

surface water balance such as precipitation, runoff, and soil water content. The consequent diminution of northward and inland moisture transfer may be a significant factor in explaining the decreasing of atmospheric and soil humidity and thus the trend in aridity in many parts of the region, particularly over Northern China during last 3000 years. It is very likely that the anthropogenic modification of monsoon system would have been occurred in the long history of civilization.

To understand the nature of the aridity trend over arid/semi-arid northern China, the atmospheric, land surface processes, and their interaction with human activities in arid/semi-arid region, the intensive field observation and integrated analysis of remote sensing information and model simulation are conducted over the different patterns of land cover and land use (Fu and An, 1999; Lu Daren, 2002). The research results includ the exchanges of fluxes of energy, water and other material, land surface energy budget and water balances and structure of near surface layer over different patterns of land cover and land use; validation of several land surface schemes applied for this region, etc.

5.2 Aridity trend on geological time scales

5.2.1 Formation of Asia inland arid/semi-arid regions as seen from Leoss deposition

Late Miocene–Pliocene aridification history of the Asian interior

The climates of Asia are affected significantly by the extent and height of the Himalayan Mountains and the Tibetan plateau. Uplift of this region began about 50Myr ago, and further significant increases in altitude of the Tibetan plateau are thought to have occurred about 10±8Myr ago, or more recently (An Zhisheng, et al., 2001).

The deserts of northern China, covering an area of about 1.5×10^6 km^2, together make up the world's largest mid-latitude, temperate, continental interior desert. The location of this desert zone is thought to be closely associated with the uplift of the Tibetan Plateau during the late Cenozoic, a process that progressively hindered northward penetration of moisture-laden air from the Indian Ocean. Another forcing mechanism leading to dryland environmental change is the variation in the strength of the East-Asian summer monsoon (see Fig. 5.2).

Based on continuous aeolian deposits covering the interval from 22 to 6.2 million years ago, on the basis of palaeomagnetic measurements and fossil evidence. A total of 231 visually definable aeolian layers occur as

brownish loesses interbedded with reddish soils. The new evidence indicates that the eolian dust deposited in the middle reaches of the Yellow River (Huang He) mainly originated from the desert lands in Asia, including those in northern and northwestern China (Liu, 1985). The existence of dry lands in Asia is thus one of the necessary conditions for eolian dust deposition in the Loess Plateau region. The Miocene loess-soil sequences in the western Loess Plateau indicate the onset of desertification in the Asian interior by 22 Ma ago (Guo et al., 2002).

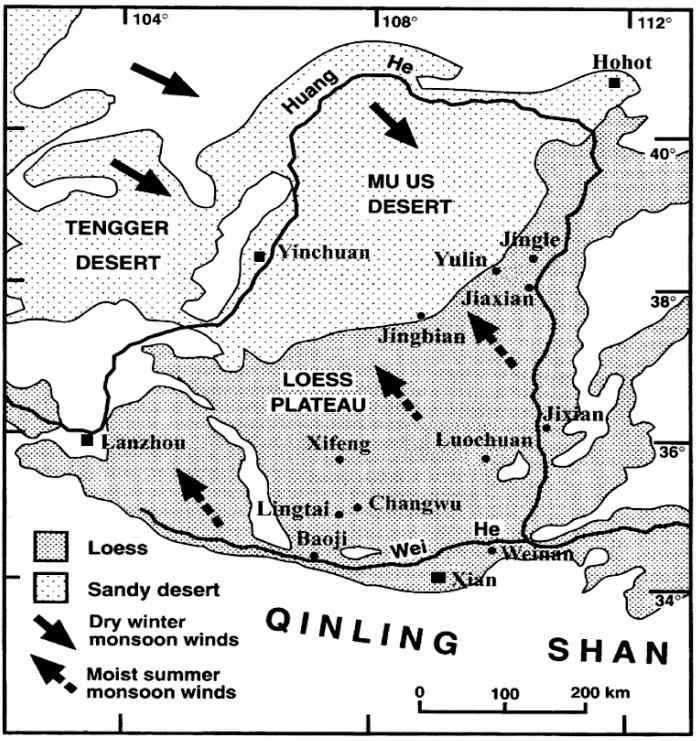

Fig. 5.2 Map showing the Loess Plateau in northern China, the locations of the Cenozoic sedimentary sites in Loess Plateau, and the modern East-Asian summer and winter monsoon circulations (modified after An and Porter, 1997)

The eolian deposits younger than 6.2 Ma, as recorded in the Xifeng section, indicate that the desert lands in Asia, which were able to provide a significant amount of eolian dust, must have been constantly maintained during Late Miocene–Pliocene time. However, the finer texture and the

generally lower accumulation rate of the Red-Earth compared with the overlying loess of the last 2.6 Ma suggest smaller desert extent and weaker wind strength.

Eolian dust accumulated at a high rate from ~6.2 to ~5 Ma BP in both Loess Plateau region and North Pacific, associated with coarser eolian grain size in China. These suggest stronger continental aridity in the source regions. According to the grain-size data of the Red-Earth and the eolian mass accumulation rate in the North Pacific (Rea et al., 1998), this drier period lasted until ~5.4 Ma BP. From ~5 – 5.4 to ~3.6 Ma BP, eolian accumulation rates in China and in the North Pacific and eolian grain-size of the Red-Earth coherently dropped to a lower level, indicating less dry conditions in the interior of Asia. Drastic increases of eolian accumulation rate and eolian grain-size at ~3.6 Ma BP are obvious for all the records, indicating a significant strengthening of the Asian continental aridity. Another increase of the aridity occurred at ~2.6 Ma BP, as is shown by both the eolian accumulation in China and in the North Pacific, the median grain size (Md) and the SiO2/Al2O3 ratio of the Red-Earth.

A seasonal atmospheric circulation sufficiently energetic across the drylands is necessary to transport dust particles to the depositional site. It is generally agreed that the loess deposits were mainly brought to the Loess Plateau by the northwesterly winds, the so called Asian winter monsoon related to a high-pressure cell over Siberia (Liu, 1985; An and Porter, 1997). The high degree of similarity between the geochemical properties of the Red-Earth and loess samples (Guo et al., 2001) suggests rather similar source areas and comparable dust-transporting trajectories. Thus, the Asian winter monsoon circulation was always the main dust-carrier during Late Miocene– Pliocene time.

Links with the Tibetan uplift and the ice build-up in the northern hemisphere

Two main factors may be invoked to explain the desertification in the interior of Asia in the Late Miocene–Pliocene time. Climate models suggest that the uplift of the Tibetan Plateau may have played an important role in Asian aridification through modulating the atmospheric circulation and its barrier effect to moisture (Ruddiman and Kutzbach, 1989; Manabe and Broccoli, 1990; An et al., 2001). Another factor is the ongoing global cooling and the expansion of Arctic ice-sheet, which is likely to have had a major impact on the intensity of the winter Siberian highpressure cell, resulting in higher continental aridity in Asia (Ruddiman and Kutzbach, 1989).

Although the timing of the Tibetan uplift is still controversial (Sun and Zheng, 1998), the available data (e.g. Li et al., 1997; Sun and Zheng, 1998) suggest that an uplift of portions of the Plateau occurred at ~3.6 Ma BP, which is synchronous with a major increase in Asian continental aridity. Another strengthening of the Asian aridification occurred at ~2.6 Ma BP indicates a major uplift of the Tibetan Plateau at that time. These suggest that other factors have also played a major role on the development of Asian desertification.

Although ice-rafting history near the Arctic region may be traced back to ~12 Ma BP, a real icesheet in the Arctic region appeared at ~6 – 7 Ma BP in Greenland (Jansen and Sjoholm, 1991). The high Asian continental aridity from ~6.2 to ~5 Ma BP is correlative with intense icerafting events in the Arctic region, and with a cooler events indicated by the marine δ 18O record. The lower aridity from ~5.0 to ~3.6 Ma BP correlates with the lower intensity of ice-rafting events and warmer conditions. The strong aridification at ~2.6 Ma BP, indicated by the intense eolian deposition (the lower boundary of the loess-soil sequence) in northern China is synchronous with a sudden increase in the amount of ice-rafted debris.

The aridification history in the Late Miocene and Pliocene in East Asia is therefore highly consistent with the ongoing cooling and the development of the Arctic ice-sheet. The stepwise increases of loess accumulation rate at ~1.8 and ~0.9 Ma BP as recorded by the loess of the last 2.6 Ma also strongly support this interpretation. This suggests that the development of the northern hemispheric icesheets had played an important role in driving the Asian aridification over the past 6 Ma. The ~0.9 Ma age boundary would also be consistent with another uplift phase of the Himalayas–Tibetan complexes (Amano and Taira, 1992; Sun and Zheng, 1998; Lu et al., 2001).

The links between the Asian aridification and northern hemisphere cooling are likely to be explainable by two mechanisms. First, ocean cooling would provide less moisture to the continents, and thus lead to drier conditions in Asia. Second, cooler high latitudes, extended sea-ice and icesheets in the arctic region strengthened the Siberian high-pressure cell, which in turn, significantly intensify the continental aridity in the interior of Asia (Ruddiman and Kutzbach, 1989).

Both the Tibetan uplift and the ongoing global cooling/arctic icebuilding processes have played major role on the aridification in the interior of Asia during the in the late Cenozoic. Their roles are not mutually exclusive.

5.2.2 Stepwise expansion of desert environment across northern China in the past 3.5 Ma and dry-wet oscillation on earth orbit time scale

Desert migrations during the past 3.5 Ma

The long-term evolution of the deserts of northern China remains poorly understood because of the sparseness of directly extractable geological evidence of suitable type and quality to be found within them. Given that the loess deposits making up the Loess Plateau of China lie immediately south and southeast of these deserts, and so are largely a product of winds from these dryland sources, it is considered that well-dated, semi-continuous loess records may provide valuable insights into the recent history of the deserts and their margins.

In this study, a thick eolian loess–red clay sequence at Jingbian near the Mu Us desert were sampled and analyzed, The aim was to use spatial changes in loess particle size to establish a semi-quantitative relation between particle size and desert margin location, and to reconstruct shifts in desert margins since the late Pliocene.

The Jingbian section (37°40'N, 108°31'E), at 1370 m above sea level, lies on the summit of the Baiyu Mountains. It is located only 12 km south of the present margin of the Mu Us Desert. No local sources of sand, such as river channels, are present in this area. The section is composed of a 252 m thick Pleistocene loess-soil sequence resting on a 30 m Pliocene red clay deposit, making a total thickness of 282 m. A previous magnetic polarity study showed that this sequence has a basal age of 3.5 Ma. Field observations have demonstrated that the development of the paleosols within both the Pleistocene and Pliocene eolian deposits is much weaker at Jingbian than in the main body of the Loess Plateau series, and that the Pleistocene

loess-soil stratigraphy correlates well with the classic loess sections. To the best of our knowledge, the Jingbian section is the only desert margin eolian sequence known to cover the whole Pleistocene and the late Pliocene. Its proximity to the dust source region makes it ideal for the study of long-term desert changes.

In the field, samples were taken at 5–10 cm intervals, making up a total of 3440 samples. The magnetic susceptibility values at Jingbian are 2–4 times higher in paleosols than in loess horizons, and grain sizes are much coarser in loess than in soils. Both the susceptibility and grain-size records further support our field observation that this eolian sequence is a well preserved and almost complete record, making it possible to develop a time scale for this sequence by correlating its loess-soil unit succession to the Chinese Loess Particle Time Scale (Chiloparts). The Chiloparts record was

developed by stacking five individual loess grain-size records that were tuned to the obliquity and precession records of the Earth's orbits. The Jingbian magnetic susceptibility and grain-size records, plotted on the Chiloparts time scale, are shown in Fig. 5.3, together with a composite marine oxygen isotope record.

The > 63 and > 125 μm (%) records at Jingbian show four stepped increases in sand-sized particle content. The late Pliocene red clay (below L33) contains few sand particles, indicating that the dust was transported in suspension, mainly from a remote source. From 2.6 to 1.2 Ma, sand content in interglacial soils remains low, whereas it varies generally between 18% and 25% in glacial loess except for the case of L15 and L16. This suggests that, during glacial periods, the desert environment advanced to a location no more than 200 km from the present northern margin of the Loess Plateau. In the part of the section deposited between 1.2 and 0.7 Ma,

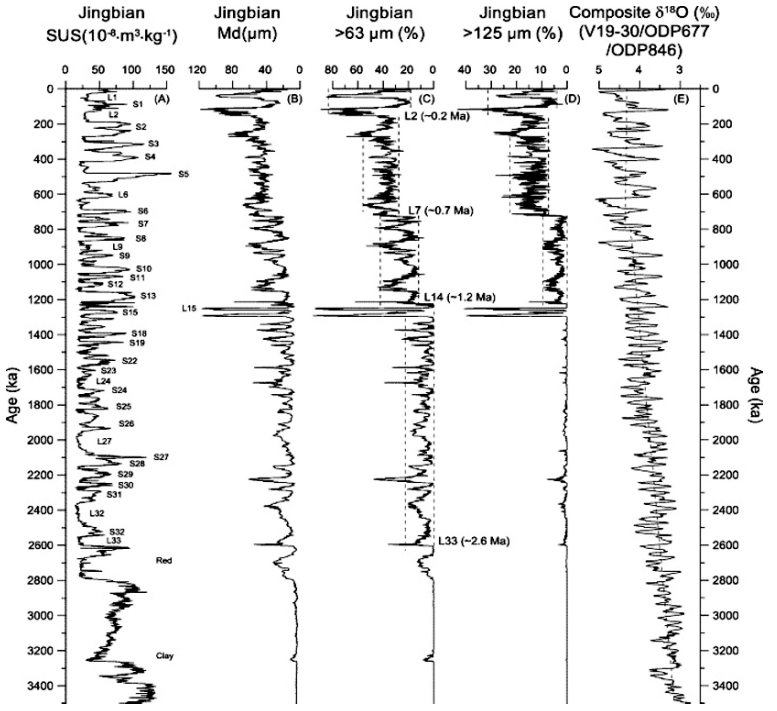

Fig. 5.3 Changes in magnetic susceptibility (A) and grain-size data (B, C, D) at Jingbian, and correlation with a stacked marine δ 18O record (E). The time scale of the Jingbian section was developed by correlating the loess-soil units with the Chiloparts record (modified after Ding et al., 2005).

sand content increases to 12% in soils and to 43% in loess with a substantial increase in > 125 μm particles, implying a large-scale advance of the desert margin during both glacial and interglacial times. Throughout material deposited in the interval 0.7–0.2 Ma, > 63 μm particles range from 30% in soils and 55% in loess units, with the > 125 μm particles exceeding 8%. This suggests that the distance between the Loess Plateau and the present desert margin was less than 100 km. During the last two glacial periods, eolian sand was directly deposited at Jingbian, indicating a further southward desert shift.

The Jingbian sand-sized particle record clearly demonstrates that, superimposed on the glacial–interglacial oscillations, the deserts in northern China experienced significant expansion at 2.6, 1.2, 0.7 and 0.2 Ma, directly implying a stepwise southward retreat of the monsoon rainfall belt, associated with a complementary reduction in summer monsoon strength, in the past 3.5 Ma.

Temporal variation of the paleomonsoon and dry-wet oscillation on earth orbital time scales

In recent years, several new loess sections have been discovered and studied during an investigation for clearly defined soils within the Wucheng Loess. Among them, the most important could be the Baoji, Weinan, Xian, and Lingtai sections situated in the southern part of the Loess Plateau. Observations of these sections demonstrate that there are about 18 paleosols in the Wucheng Loess. They are named S15 to S32. Each of the soils is also underlain by a loess bed with varying thickness.

Fig. 5.4 shows the loess-soil stratigraphy and paleomagnetic polarity of the Baoji loess section (Liu et al 1989). Paleomagnetic dating results show that the Matuyama/Gauss magnetic reversals occurred within the oldest loess unit, L33. Therefore, a basal age of about 2.5 Ma is estimated for the Chinese loess deposits (Zheng et al 1991, Ding et al 1992). According to the new paleomagnetic polarity time scale (Cande & Kent 1992), the age of the contact between the red clay and loess should be about 2.6 Ma.

Great efforts have been made to characterize the time-dependent evolution of periodicities and other aspects of monsoonal changes in the last 2.5 Ma. Since the magnetic susceptibility and grain-size records can correlate well with each other at Baoji loess section, even in details. Hence, discussion here of the long-term monsoon climate evolution is based on the Baoji grain-size record obtained by Ding and coworkers (1992). The Baoji grain-size record has been tuned to an orbital target (Ding et al 1994) with the same procedure as that developed by Imbrie and coworkers (1984) in tun-

ing the marine SPECMAP record. Each monsoon event recognized can therefore be constrained by this orbital time scale.

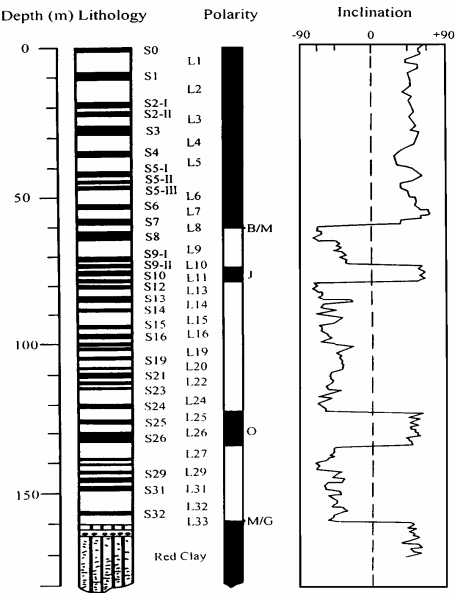

Fig. 5.4 Lithology and paleomagnetic results of the Baoji loess section. The thickness of the loess-soil sequence in Baoji is about 160 m, underlain by red clay sediments. The soils (black horizons) are labeled as Si and the loess layers (white horizons) as Li. The Bruhnes/Matuyama magnetic reversal occurred within L8, Jaramillo subchron between L10 and L12, Olduvai subchron from L25 to the base of S26, and the Matuyama/Gauss boundary within L33 (from Liu et al 1989).

Fig. 5.5 shows the Baoji grain-size time series in the last 2.5 Ma. The grain-size ratio is defined as the proportion of the grain size that is <2 μm (%) to that >10μm (%), with high values corresponding to interglacial paleosols and low values to glacial loess. It is evident that the history of winter monsoonal winds exhibits an oscillatory pattern during the Quaternary, being intensified in glacial periods and weakened in interglacial periods. This pattern shows a negative correlation with that of the summer monsoon variations. The summer monsoon is much stronger during interglacial periods than in glacial periods, as indicated by the susceptibility records. Within some major soil and loess units particularly in the upper part of the loess sections, short climatic pulses are identifiable in the grain-size record. For example, each of the loess units L1, L2, L5, L6, and L9 can be divided into five parts. Also within the soils S1, S2, S3, S5, etc, further di-

vision is possible (Fig. 5.5). Events of these kinds represent second-order monsoonal oscillations superimposed on major glacialinterglacial monsoon cycles.

Ding et al. (1994) have divided the Baoji grain-size record into 166 numbered events (Fig. 5.5). For the purpose of a ready correlation among loess sections in different localities, we maintain the L-S system used in designating major loess soil horizons (Liu 1985).

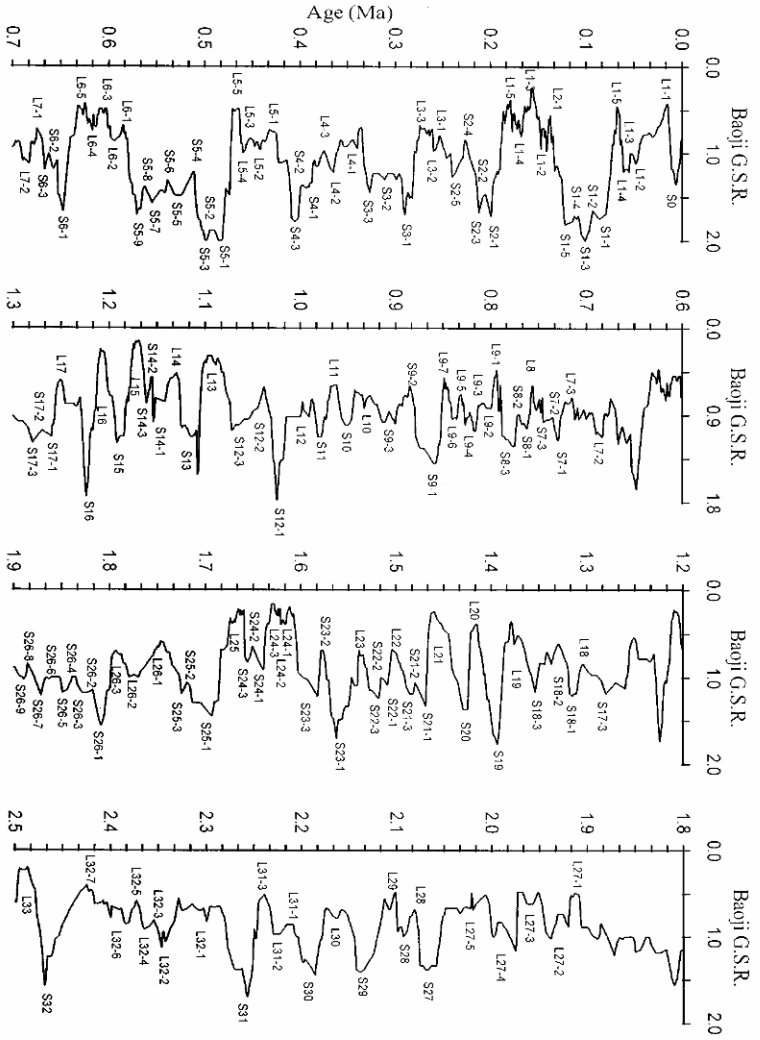

Fig. 5.5 Subdivision of the winter monsoon events recognized in the Baoji grain-size time series. The grain-size record is from Ding and coworkers (1994).

Ding et al. (1994) have analyzed the time-dependent evolution of paleomonsoon periodicities on the basis of the Baoji grain-size time series. As shown in Fig. 5.6, monsoonal changes have strong periods corresponding to the variations in the orbital parameters of the Earth. However, the dominant monsoon period differs over different time intervals. It appears that the cyclic changes of the winter monsoon intensity in the past 2.5 Ma can be subdivided into three time intervals. From 2.5 to about 1.6 Ma, the monsoonal variation has relatively strong periods centered on 400- and 55-ka and weak 23- and 19-ka periods. Between 1.6 and about 0.6 Ma, a predominant 41-ka period is observed. At about 1.0 Ma, a 100-ka period occurred and culminated at about 0.6 Ma.

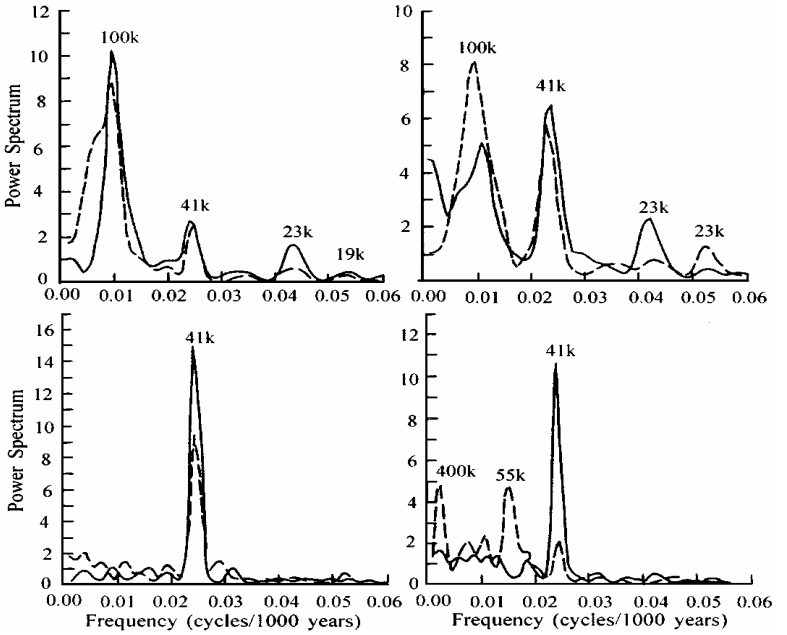

Fig. 5.6 Comparison of the spectra of the Baoji grain-size record (dashed line) with those of the Deep-Sea Drilling Project site 607 δ 18O record (solid line) over four different time intervals. The δ 18O data are from Ruddiman et al (1989) and Raymo et al (1989). The Baoji grain-size data are from Ding and coworkers (1994).

As shown in Fig 5.6, the Baoji grain-size record has documented two major shifts in climate modes over the past 2.5 Ma, one occurring at about 1.6 Ma and the other at about 1.0–0.6 Ma. The 1.6-Ma shift is character-

ized by a rather abrupt transition from various monsoon periodicities to dominant 41-ka cycles, while the 1.0 – 0.6 Ma event shows a relatively gradual transition from constant 41- to 100-ka cycles (Fig. 6.6).Compared with the deep-sea δ 18O records (Ruddiman et al 1989, Raymo et al 1989, Shackleton et al 1990), the 1.0–0.6 Ma loess/soil record shift matches well, whereas the 1.6-Ma shift seems to be a regional event, as it is absent in global ice volume records.

5.2.3 Aridity trend in northwestern China during last 30 ka as seen from lake sediment records

As a natural comprehensive unnit which is relatively isolated from the surrounding environment in the continent, lake has been resulted from the interaction among land, atmosphere, water body, and ecosystem in a certain region. The lake level, lake area, water depth and water salinity are therefore used as the indices to reflect the environmental evolution of the region. Lake sediment record is characterized by its rich information, wide distribution and high consistency, which makes it an important component in studying the terrestrial environment history.

Yu et al. (2001) have systematically summarized the studies of lake sediment records in China, and compiled the Chinese lake status database. The lake level, lake area, water depth and water salinity in the database are based on a consensus interpretation of multiple lines of evidence, including palaeolake shorelines, changes in lacustrine sedimentation, assemblages of aquatic pollen, geochemistry and archaeological records, etc. The sites chosen for the database have been screened to exclude records or parts of records where lake status appeared to have been influenced by non-climatic factors, such a tectonism or fluvial influence, or by factors where the climatic influence is indirect, such as sea-level changes or glacier fluctuations, in order to obtain the information of fluctuations of lake status responding to changes in water balance of precipitation minus evaporation over a catchment. Chronology of changes in lake status at individual sites is based on radiometric dating (given as 14C years before the present) and TL dating. This database is regarded as one of the important sources of the international paleolake database.

From the database, Yu et al. derived the lake status data from 42 lake sediment records which are capable of reflecting the climate change since 30 Ka BP. The period of 30-40 Ka BP corresponds to the later phase of marine oxygen isotope stage 3, or to the mega-interstadial of the last glacial period. Spatial and temporal charactristics of lake status change are

analysed based on these data and many important conclusions are drawn. Among them, one of the most significant findings is the obvious aridity trend in northwestern China over this period. For example, from 30 to 27 Ka BP, the lakes in western China are basicly featured by high lake level, low water salinity, and high water depth (Fig. 5.7, Shi Y. F. et al., 2001); the area and the extent of high lake level began to experience a remarkable decrease since 24 Ka BP, especially in Xin Jiang atonomous region where the dominant lake level is medium.

During the Last Glacial Maximum (LGM, 18 ka BP), the medium depth lake were widely distributed in Xin Jiang and western Tibet. A case in point is the Qinghai Lake. However, these lakes are still marked with higher lake level, larger lake area, lower water salinity compared with the modern time. The late LGM started from 15 Ka BP when the main features of lakes in western China remain unchanged (Yu, et al., 2000). Similar pattern were found in these lakes dated to 9 Ka BP. Further decrease trend of the lake level appeared around 6 Ka BP, the latest warm epoch before present. The aridity trend in western China was distinct in 3 Ka BP, a new glacial period, demonstrated by a notable increase of the proportion of low water level lakes (Fig. 5.7).

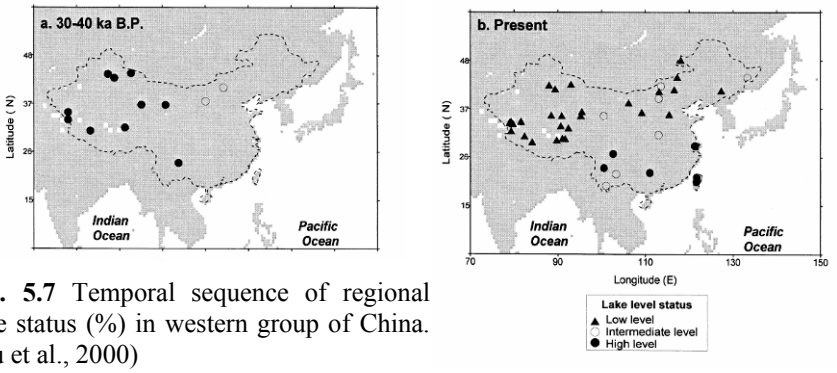

Fig. 5.7 Temporal sequence of regional lake status (%) in western group of China. (Yu et al., 2000)

Fig. 5.8 indicates the lake temporary sequence in changes of each 500 year interval in western China since 30 Ka BP. The figure covers 22 lakes from the Xizang-Qinghai Plateau, Xinjiang inlands and western Inner Mongolian Plateau. The temporal sequence identifies three periods, pre 28 ka, 21-17 ka and 7-6 ka characterized by the high lake level. Compared with three high lake level intervals, the highest lake level appeared pre 28 ka, while the second highest lake level between 21-17 ka, and lowest high lake level between 7-6 ka. Generally speaking, the proportion of high lake level became less and less. As far as pre 28 Ka BP is concerned, the pro-

portion of high lake level is 85%, and it is 15% for medium lake level, while for the second highest lake level between 21-17 ka, these two percentages are the same, 50%. The proportion of high lake level is only 40% in the third highest lake level between 7-6 ka BP. In contrast, the proportions are 35% and 25% respectively for medium and low lake levels. High lake level has begun to disappear since 3 ka BP. Medium lake level only takes 20% in this period while the low lake level shares the rest proportion.

All these evidences from lake sediment records indicate an evident long-term aridity trend in northwestern China since 30 ka BP characterized by the stepwise decrease in lake level and area.

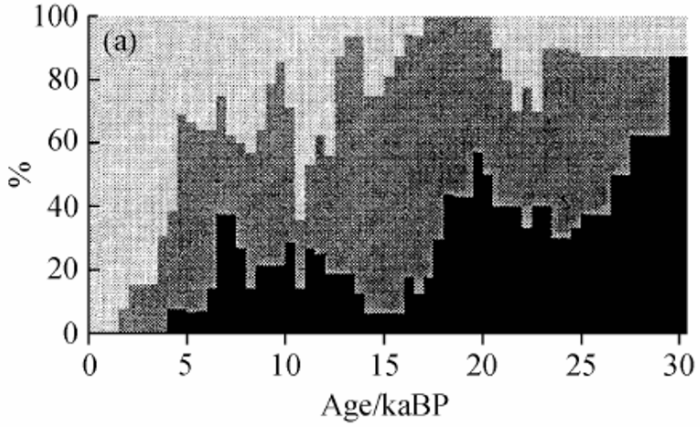

Fig. 5.8 Temporal sequence of regional lake status (%) in western group of China. (Yu et al., 2000)

5.3 Aridity trend in last hundred years

5.3.1 Dry-wet oscillation on centennial to decadal time scales

Since the 1970s, Chinese climatologists have collaborated in an effort to extract climatic information from over 2000 historical documentary records for the last 530 years beginning in 1470. These records included the government weather book ‘‘Clear and rain records’’ and local government drought/flood reports and private diaries. A product of this effort is the yearly charts of dryness/wetness in China for the last 500 years (Central Meteorological Bureau, 1981). The summer season climate (May–

September) was categorized into dry and wet intensity (DWI) on a scale of 1 to 5, from very wet (flood, 1), wet (2), normal (3), dry (4), and very dry (drought, 5), for each summer in the 530 years from 1470 to 1999 for 120 sites in China.

Qian et al. (2003) combined DWI with three independent long-term climatic data and modern observations into one cohesive set to describe the spatial and temporal patterns of variability of dry and wet periods in East Asia over the past one thousand years and to examine physical causes of the pattern variations. The data include the 220-year observed precipitation in Seoul, South Korea, and other two independent chronologies of dryness-wetness grades in the past millennium in eastern China based on instrumental observations and historical documents. Geographic distribution of the 100 sites selected in eastern China is shown in Fig. 5.9. Various analysis methods including wavelet transform and rotated empirical orthogonal function were used in revealing climate variations from these datasets.

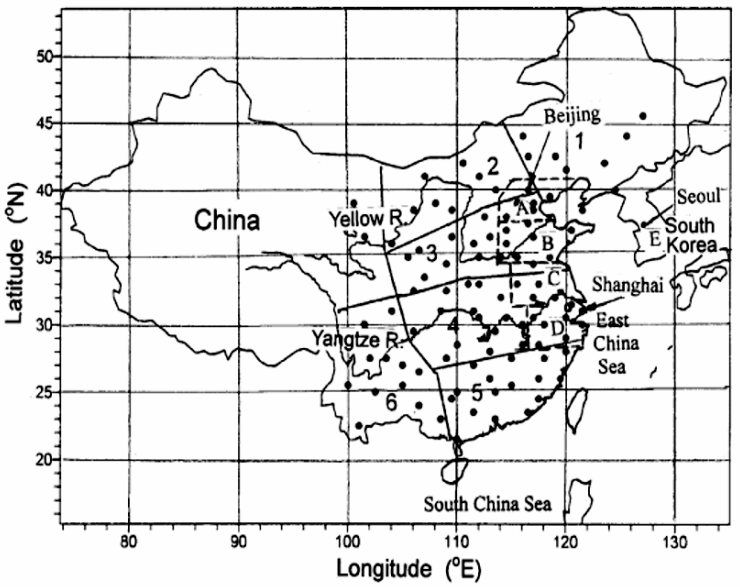

Fig. 5.9 Geographic distribution of the 100 sites selected in eastern China. Geographical location of the six study regions: 1 is northeast China, 2 is northern north China, 3 is the mid- and lower Yellow River, 4 is the mid- and lower Yangtze River, 5 is south China, and 6 is southwest China. The lettered regions, A, B, C, D, and indicate four regions divided by the dashed lines in east China and E is South Korea. The Yellow River and the Yangtze River are labeled (Qian et al., 2003)

Major results show that the dry and wet anomalies initially appeared in the north part of eastern China and then migrated southward to affect south China. This process is repeated about every 70 years. However, in contrast in the last two decades of the twentieth century a dry situation appeared in north China and a wet climate predominated in the south part of the country.

The multidecadal variations of the monsoon circulation in East Asia and the thermal contrast between inland Asia and its surrounding oceans may contribute to the dry-wet phase alternation or the migration of dry-wet anomalies. In regional scale variations, a consistent dry or wet pattern was observed spreading from the lower Yangtze River valley to South Korea. Frequencies of severe dry-wet situations were low in the eighteenth and nineteenth century and they were higher in the twentieth century. The recent increasing trend in frequencies of severe dry-wet chances occurred along with global warming and regional climatic changes in China.

5.3.2 Evidences of aridity trend from historical documents and instrumental observations

A distinct aridity trend in northern China in last 100 years

A distinct aridity trend in northern China in last 100 years is presented by applying a linear fitting to both the climate records and the hydrological records which is supported by evidence of environmental changes (Fu et al., 1993). In detecting the trend, a linear fitting is applied to the drought and flood indices of China since 1887.

Here the drought and flood indices are defined by

Id =n4+5 / N,

Iw=n1+2 / N,

where N is the total number of stations ; n4+5 is the number of stations with precipitation grades of 4 and 5; n1+2 is the number of stations with precipitation grades of 1 and 2.

The amount of precipitation is classified into five grades based on the following criteria,

grade 5: △R / R<-50%

grade 4: -50% <△R/ R<-25%

grade 3: -25%<△R/ R<+25%

grade 2: +25% < △R / R< +50%

grade 1: +5O%<△R / R

where △R / R is percentage of the precipitation departures in the rainy season (May to September).

The drought and flood indices of China is calculated by using 100 stations data, but there are no stations to the west of 100°E, because no long-term records are available in that region. In calculating the indices, some proxy data are also included in classification of precipitation for the stations which have no instrumentation records during the early period. These data are taken from the Atlas of Drought and Flood Distribution of China (1470-1979) (State Meteorological Administration of China, 1980).

From 10 years running means of drought and flood indices of northern China and its linear fitting since 1880, a significant increasing trend is shown in drought indices. The drought index has increased by more than 10 percent in the past 108 years. On the other hand, the wet index shows a decreasing trend, although its slopes is much less than the drought index. That means a distinct aridity trend appeared in northern China in the last 100 years. Superimposed on this long-term trend, there is an oscillation with the period of about 36 years, the so-called "Brucker period" which is supposed to be related to the solar activities.

More evidence of aridity trend in China is the decrease of summer monsoon rainfall in East China from 1350 mm to 1050 mm in 100 years. In past 40 years, the desertification occurred mainly in the semi-arid zone of northwestern part of the country. It is estimated that the desertification land was expanding at the rate of 1560 km^2 per year (Dong, 1989). Additional evidence of an aridity trend in China is a decrease in the underground water level, etc. (Climate, No.5, Blue Book of Science and Technology of China, 1990).Although there should be many anthropogenic factors involved in the environmental changes, the decreasing trend of precipitation is still a major factor in the development of aridity trend.

Variation trend of extreme drought during 1951—2004

Extreme drought always brings about severer natural disasters, and threatens much the agricultural production and human's daily life. Lots of statistical results show the rapid increase of the damage caused by extreme drought. Thus it is necessary to study the frequency and variation trend of extreme drought. Here, the variation trend of extreme drought over China during 1951—2004 was analyzed (Ma and Fu, 2003).

The method is to calculate the month-to-month Palmer Drought Severity Index (PDSI) of each station in 54 years, if PDSI≤-3.0, this month is considered as an extreme drought month and counts for one. The number of extreme drought month every year is the extreme drought frequency. For the contrast analysis, the frequency distribution of monthly PDSI<0 is

shown as well, to better study the evolution characteristics of extreme drought through temporal variation study of frequency.

The variation trend of frequency for monthly PDSI<0 (drought) and monthly PDSI≤-3.0 (extreme drought) in the latest 54 years presents the increasing frequency of monthly PDSI<0 in eastern China and the areas to north of 30°N, indicating that the drought occurrence frequency is increasing yearly. The significant increasing regions are located in the central part of North China, the eastern part of Northwest China, the central and the southern parts of Northeast China, nearly corresponding to the regions of obviously decreasing precipitation. The similar spatial variation trend of the occurrence frequency between drought and extreme drought was found. The occurrence frequency of extreme drought in the area to east of 100°E and north of 30°N shows the increasing trend, but the scope of significant trend is slightly smaller. The extreme drought frequency decreases in the western part of Northwest China and the areas to the south of Yangtze River, and the most prominent occurs in the western part of Northwest China.

The analysis results show that the frequency of drought (monthly PDSI<0) is increasing in the eastern part of Northwest China, the central part of North China and Northeast China, and the frequency of extreme drought also shows an increasing trend. In the late 1990s, the number of extreme drought in the eastern part of Northwest China and Northeast China increased sharply by two times or more, especially in Northeast China, the average was 6 times/year during 2001－2004. The increase number in the central part of North China occurred in the 1980s, earlier than that of the eastern part of Northwest China and Northeast China. The extreme drought frequency in the western part of Northwest China varies little and stabilizes at about 1. The analysis above shows the warming beginning around the 1980s and the obvious increase after the mid 1980s, which may be one of the important reasons for the significant drying trend in northern China during the latest 20 years.

The analysis indicates a rapid increase of extreme drought frequency in northern China and the areas to east of 100°E during the latest 54 years. Despite the different starting time in the eastern part of Northwest China, the central part of North China and Northeast China, a sharp increase in latest 10 years is the common characteristic in the three subregions, which is closely related to the significant warming in recent years.

5.3.3 Global aspects of aridity trend

Palmer Drought Severity Index for 1870–2002

Aridity trend over northern China is not an isolated phenomenon, but with significant worldwide linkage. The Palmer Drought Severity Index (PDSI) is the most prominent index of meteorological drought used in the United States (Heim 2002). The PDSI was created by Palmer (1965) with the intent to measure the cumulative departure (relative to local mean conditions) in atmospheric moisture supply and demand at the surface. A monthly dataset of Palmer Drought Severity Index (PDSI) from 1870 to 2002 is derived by Dai et al. (2004) using historical precipitation and temperature data for global land areas on a 2.5°grid.

Over Illinois, Mongolia, and parts of China and the former Soviet Union, where soil moisture data are available, the PDSI is significantly correlated (r=0.5 to 0.7) with observed soil moisture content within the top 1-m depth during warm-season months. The strongest correlation is in late summer and autumn, and the weakest correlation is in spring, when snowmelt plays an important role. Basin-averaged annual PDSI covary closely (r= 0.6 to 0.8) with streamflow for seven of world's largest rivers and several smaller rivers examined. The results suggest that the PDSI is a good proxy of both surface moisture conditions and streamflow. An empirical orthogonal function (EOF) analysis of the PDSI reveals a fairly linear trend resulting from trends in precipitation and surface temperature and an El Nino – Southern Oscillation (ENSO)-induced mode of mostly interannual variations as the two leading patterns. The global very dry areas, defined as PDSI<-3.0, have more than doubled since the 1970s, with a large jump in the early 1980s due to an ENSO-induced precipitation decrease and a subsequent expansion primarily due to surface warming, while global very wet areas (PDSI>+3.0) declined slightly during the 1980s. Together, the global land areas in either very dry or very wet conditions have increased from ~20% to 38% since 1972, with surface warming as the primary cause after the mid-1980s. These results provide observational evidence for the increasing risk of droughts as anthropogenic global warming progresses and produces both increased temperatures and increased drying.

Global aridity trend in the second half of the 20th century

The variation of global dry/wet trend in 1951-2002 was analyzed by Ma et al. (2007a) through the surface wetness index (SWI), which was derived from using global grided monthly precipitation and monthly mean surface

air temperature datasets from Climatic Research Unit (CRU) from 1951-2002 over global land. Its basic mechanism is to consider two main factors affecting surface drying- wetting variation: changes in precipitation and surface potential evaporation. More precipitation conduces to a wetter surface, while it increases in surface potential evaporation to a drier surface.

The characteristics of the SWI dry/wet variation and its discrepancy in the global continents, such as North America, South America, Eurasia, Africa, and Australia, were inter-compared as shown in Fig. 5.10. The results show that the SWI variation has the distinct regional differences in the second half of the 20th century under the global warming background. The drying trend in the last 52 years mainly occurred in Africa, Eurasia, Australia and South America, most obviously in Africa and Eurasia. On the contrary, North America shows a wetting trend after 1976. A 30-year period of drying/wetting oscillation is found in South America and Australia. The results also pointed out that global warming has changed the drying-/wetting pattern of the global land environment, indicating that the increases in surface air temperature can not be ignored for the aridity detection.

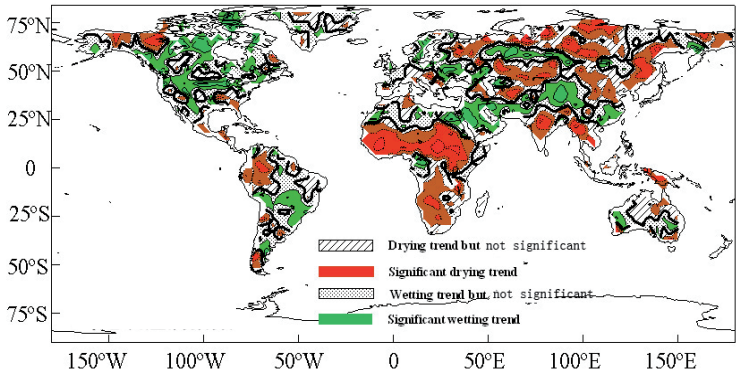

Fig. 5.10 Global variation trend of SWI (shaded areas mean passed the significant level of 95%).

5.3.4 Semi-arid region—the area with most significant aridity trend

As a natural process of earth evolution, the huge arid and semi-arid regions formed at the Asia continent at the time of rapid uplifting of Tibetan

plateau in about 3.6-2.6 million years B.P. (An et al, 2003). Based on the Koppen classification of climate (Henry Kendall et al, 1976), The geographic location of semi-arid regions covers central Asia as well as some part of India sub-continent, where the potential evaporation excess the precipitation on annual average and the landscapes are characterized by dry climate, low vegetation cover, low nutrition content and low capacity of water conservation of the soil. These areas are most vulnerable in global environmental change.

These areas are also known as the major source of dust aerosols, which not only directly causes serious damage to human health, agriculture and economics in regions, but also to other regions through long distance transport of huge amount of dust particles across the Pacific ocean and even North America. The dust aerosols also have significant influence on the regional and global climate through their radiative forcing. Upon deposited in the ocean, aeolian mineral dust is important to many biogeochemical cycles, including the growth of phytoplankton, which will influence the carbon cycle in the ocean. Researches have also proposed an interaction process between dust aerosols and the hydrological cycle (Ramanathan,V., P.J. Crutzen, J.T.Kiehl and D.Rosenfeild, 2001).

The semi-arid region of East Asia is located nearly at the northern edge where the summer monsoon can reach. It is a transitive zone between arid continent climate and humid monsoon climate, which is very sensitive to the climate and human perturbation. The variation of climate and water cycle in this area are highly correlated with the high variability of the Asia monsoon system. This leads to the high frequency of extreme events and climate disasters over there. Both the observation and numerical modeling have shown that an aridity trend is occurring and will occur most significantly in the semi-arid regions in terms of precipitation, soil moisture, and the frequency of drought events under the global warming (Fu et al, 2000, Dai, 2003, Ma and Fu, 2005).

On the other hand, the semi-arid region is also the one with most significant change of land cover under the development by humans. The human-induced land cover changes in this region have brought about further land degradation, the expansion of land under desertification, loss of groundwater reservoirs and the increase of dust storm frequency and so on. The large-scale destruction of natural vegetation by human activities would also influence the intensity of the summer monsoon and reduce the moisture transfer into the continent, which would enhance the aridity even more over the semi-arid regions (Fu and Yuan, 1999; Fu, 2003).

Decadal variations of arid and semi-arid boundary in China during last 100 years have been analyzed by using Thornthwaite's method. The results indicate that, during the last 50 years, there is a distinguished periodic

variation of arid and semi-arid boundary in their locations in the middle part of northeast China and northern part of North China, and an obvious trend moving to the east. In the southern part of Shannxi province and North China, the boundaries between arid and semi-arid areas have been moving to the south, with a periodic variation for the locations, and the boundary of semi-arid area reaches the largest extent to the south at present. During the last 100 years, there is a trend of the boundaries moving to the south or east, namely, the area of semi-arid region has expanded. And in the southern part of North China and the central part of northeast China in the 1920s, the range of arid and semi-arid area was the largest and the intensity was the severest. The location variation of arid and semi-arid boundaries is closely related to regional warming and precipitation reduction.

Fig. 5.11a presents the dry-wet variation in the recent 50 years in China tested by using Mann-Kendall method. The red regions represent remarkable aridity trend (drying), and the green means remarkable humidification (wetting). Fig. 5.11b shows the 10-year mean value of the 1990s minus the previous 40 years average, and the meaning of the red and green region is the same as Fig. 5.11a. Compared with Fig. 5.1, we know that most parts of semi-arid area in China are located in the regions with obvious aridity trend, which shows that the aridity extension is closely related to the local drying trend. The aridity extension is not only resulted from precipitation change, but also induced by the temperature increase. This can explain further that the semi-arid boundaries moving southward and eastward result in the spacious drying trend. Under global warming, the quantity of precipitation is no longer an object index to evaluate the drying or wetting of a region.

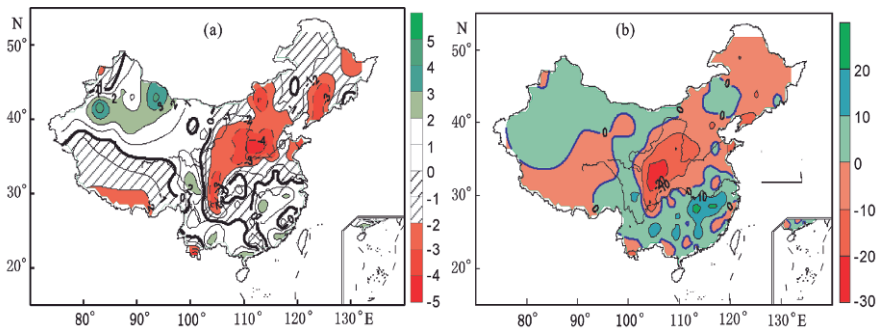

Fig. 5.11 Trend of dry/wet change in China from 1951 to 2000 (Ma Zhuguo, 2007b)

5.4 Inter-decadal variability of atmospheric circulation in association with the aridity trend

5.4.1 Correlations between North Atlantic Oscillations (NAO) and eastern China wet/dry oscillation

The North Atlantic Oscillation (NAO), North Pacific Oscillation (NPO), Southern Oscillation (SO) and Antarctic Oscillation are known as four oscillations to present the major special characteristics of global atmospheric pressure field. Walker et al. (1932) discovered the out of phase variation tendency of surface pressure between Greenland and the area from Azor islands to southwestern Europe in 1930's. This is the well-known North Atlantic Oscillation. Researches in early days believed that NAO had less impact on global or hemispheric weather and climate than El Nino/Southern Oscillation (ENSO), because it is usually regarded as a significant regional phenomenon. However, recent studies have paid more attention to the variations of NAO and NPO, as well as their impacts on regional and global climates.

The impact of NAO on regional and global precipitation is not so significant as on temperature, since the precipitation is affected, to a large extent, by those local factors and has more complex relationship with atmospheric circulation.

Fewer studies, so far, have paid attention to the relationship between the long-term variations of NAO and the flood/drought in summer China. Considering that the atmospheric circulation patterns associated with NAO are located at the upstream of China territory, the changes of atmospheric circulation related to NAO may have important influences on the weather and climate in China. Hence, study on the relationship between NAO and food/drought in China may provide useful information for the ultra-long term prediction of rainfall in summer China.

The Flood Drought Index (FDI) data of 100 stations in eastern China, i.e. east of 100°E, from 1470 to 1999 were used (Zhu, 2003). Data are categorized into 5 classes: flood, wet, normal, slight drought and drought, which labeled from 1 to 5, respectively. The time series of NAOI used in this research was based on those mean values in winter months (from December to the next February) from 1429 to 1983 and reconstructed by Glueck and Stockton (GS) (2001), and calibrated by the instrumental series of NAOI at Lisbon and Stykkisholmur of Iceland (LISJHI) from 1863 to 1983. In order to fit the time interval of FDI data used in this study, the NAOI data are cut off from 1470 to 1983

The mean value in northern China is defined by 40 stations mean scattered on the area of north of 35N and east of 100E, including North China,

Northeast China, Ningxia and Inner-Mongolia Autonomous regions, Shaanxi and Gansu Provinces. The lag correlation coefficients between the mean FDIs in various areas and those NAOIs of original 10 and 20 years running mean, with formers lagging 1-3 years behind respectively found that there are positive correlations between NAOI and FDIs of northern China. In terms of the original time series, the positive correlation coefficient between FDI and NAOI, with FDI lagging 2 years behind, reaches to 0.134 at confidence level above 0.005. And the confidence level of correlation coefficient reaches to 0.05 for the case of NAOI 2-3 years ahead of FDI.

The results mentioned above indicate that when NAOI is positive (negative) and high in the winter, a slight drought (wet) would appear in summer in eastern China and, specially, in northern China in the next three years. This coincides with our examinations of the rainfall data in recent decades in summer China. For examples, when NAOI was positive and high in 1994/1995 winter, the temperature was higher and a serious drought occurred in eastern China and, specially, in northern China in summer of 1997; when NAOI in 1995/1996 winter dropped to its lowest value of several decades, a heavy flood disaster occurred in summer of 1998 in Northeast China, Inner-Mongolia and Yangtze River valley; when NAOIs were positive and high in 1998/1999 and 1999/2000 winters, almost all the area in northern China was in drought and less rainfall since 1998, especially in 1999. Checking the extreme high and low values of NAOI in winters of 1960's-1980's, it is found that to a large extent, it has high correlation with the flood/droughts a few years later in northern China. The rainfall has been reducing since 1980's, especially in North China and the strength of drought has been increasing since the mid 1970's. Ma et al. (2003) pointed out that Northeast China and North China are in the period of high frequency of extreme drought since 1980's and especially in last decade, the frequency of extreme drought increased obviously. Also, they pointed out that it may be related to the positive and high phases of NAOI occurring frequently since 1970' and especially, it persisted in last decade.

All three time series of NAOI in winter and mean FDIs in eastern China and northern China in summer had the oscillations with a period of about 10 years, and a decadal variation was shown clearly after applying 10-year running mean. It could be seen that there were more years with positive value than those with negative values before 1650 in both series of FDI and NAOI, but both series show high variability of amplitudes. These features indicated the high frequency of drought and light drought events in eastern China. In later several hundred years, all three series showed small amplitudes oscillation near the zero line, with more negatives than posi-

tives. It indicated that the rainfall in eastern China was slightly more than normal.

It is found from the above analysis that the mean FDI in eastern China, especially in northern China, has positive correlation with NAOI. The correlation coefficients between NAOI and 1-3 years lagged FDI are 0.106, 0.097 and 0.134, and reached to significance level of 0.01-0.001, respectively. For 10 and 20 years running series, the confidence level of correlation in northern China reached to above 0.001.

5.4.2 Interdecadal variation of aridity trend in northern China associated with the Pacific Decadal Oscillation (PDO)

Recently, the relationships between the climate variations in China and the PDO have been explicitly examined (Yang et al., 2002; Zhu and Yang, 2003b; Yang et. al. 2004; Ma et al., 2006).

The oceanic features of the Pacific Decadal Oscillation (PDO) and the associated interdecadal climate anomalies in East Asia and China are described with NCEP/NCAR reanalysis data and station records for 1951-1998 by using regression analysis. The interdecadal change of the impact of ENSO on the summertime climate anomaly in China and corresponding atmospheric circulation anomaly in East China is also investigated with insight into the modulation role of PDO by using sliding correlation analysis.

The PDO is characterized by principal SST anomalies in the central North Pacific and secondary opposite SST anomalies in the tropical Pacific. The associated upper-ocean heat content anomalies generally have a similar pattern to that of the SST anomalies, except in the western equatorial Pacific where the heat content anomaly is also quite large but the SST anomaly is rather weak. Over the past half century, the PDO has featured an interdecadal shift occurred in the mid-1970s with a considerably large cooling in the central North Pacific.

Regression analyses show that the PDO-associated atmospheric circulation anomalies in East Asia and climate anomalies in China are significantly remarkable. For instance, Ma (2007b) have reported the close spatial correlation between annual PDO index and the Surface Wetness Index (SWI, Ma et al., 2007a) as shown in Fig. 5.12.

During winter, corresponding to the cooling shift of the central North Pacific in 1976/77, the Pacific/North American (PNA) pattern is in its positive phase and the Aleutian Low tends to be stronger. In East Asia, the Mongolian High is enhanced while the Siberian High is weakened. There is an interdecadal seesaw-like oscillation between the Aleutian Low and the Mongolian High. Associated with this, the air temperature is lower in

Mongolian and Tibetan Plateaus and southern China and higher in northwestern, northeastern and northern China, indicating a "northern warming versus southern cooling" pattern in China. At this time, less precipitation is observed in most of China, especially in northeastern and North China.

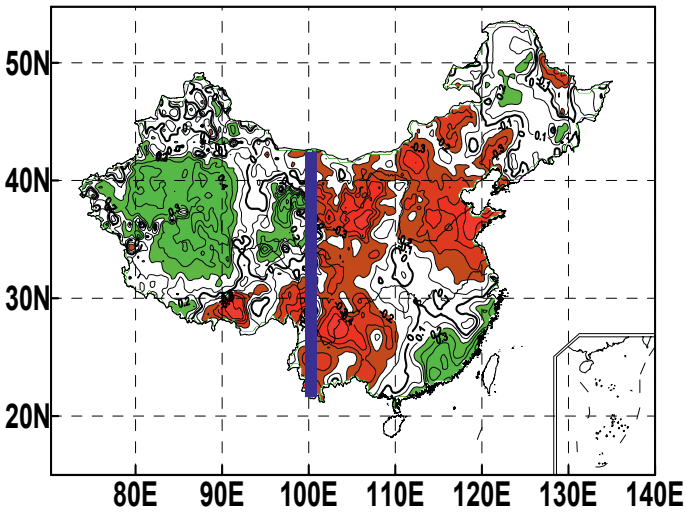

Fig. 5.12 Spatial distribution of the correlation between annual PDO and SWI (red region indicates significant negative correlation, green region indicates significant positive correlation) (Ma, 2007b)

During summer, corresponding to the cooling shift of the central North Pacific in 1976/77, the western Pacific subtropical high is weakened and moves southeastward, the 500hPa geopotential height is increased in Mongolia and northwestern China, and a significant northerly anomaly at 850hPa prevails over China, and therefore the East Asian summer monsoon is greatly weakened. Resultantly, more precipitation is observed in Yangtze River valley and less in northern China. Meanwhile, the anomalous cooling is in northwestern China and in a broad region along Yangtze River valley, while the warming is in northeastern, northern and southern China. The spatial pattern of temperature is roughly opposite to that of precipitation with a cool/wet or warm/dry relation, except for those in northeastern China and in part region of southern China where more precipitation corresponds to higher temperature.

Sliding correlation analyses exhibit a significant interdecadal change around mid-1970s in the relationship between the ENSO and the summer-

time climate anomalies in China, showing the PDO's modulation role in the ENSO's impact. During the cool PDO phase (1951-1976), a developing El Niño event tends to dry/warm southern China and cool/wet northeastern China, while a decaying El Niño event acts to wet/cool northern and southern China and dry/warm Huaihe River valley. During the warm PDO phase (1977-1998), however, a developing El Niño event tends to wet/cool southern China and dry/warm northern, northeastern and northwestern China, while a decaying El Niño event acts to dry/warm northern and southern China and normalize Huaihe River valley. It is interesting that the fact that a decaying El Niño event induces increased precipitation along Yangtze River valley is robust without any interdecadal change. This is a valuable signature for the seasonal prediction of precipitation.

Further composite analyses show that the interdecadal change of ENSO-related atmospheric circulation anomalies is responsible for the change of relationship between the ENSO and precipitation anomalies in China. For two interdecadal epochs, ENSO-related atmospheric anomalies are similar in the lower latitudes but quite different in midlatitudes. Concurrent with the phase reversal of PDO in 1976/77, the summer monsoon throughout China is weakened instead of an enhanced northern summer monsoon in the developing phase of an El Niño event, while the northern summer monsoon is reduced instead of a slightly enhanced southern summer monsoon in the decaying phase of an El Niño event.

These studies suggest that the PDO which is the strongest interdecadal signature in the North Pacific ocean-atmosphere system has not only direct impact on the interdecadal climate variabilities in East Asia and China but is able to modulate interannual variabilities (say, ENSO's impact).

5.4.3 Interdecadal variability of Southern Oscillation and Walker Circulation and their relationships with Asian summer monsoon

Based on the observational sea surface pressure (SLP) data (1866~2002), it was found the SLP at Darwin keeps on increasing and that at Tahiti decreasing from the late 1970's. This phenomenon indicates the significant weakening of tropical Walker Circulation. In the same period, the intensity of Asian summer monsoon becomes weakening too. Depending on the composite analysis from 1978 to 1997(1958~1977), the summer precipitation is above (below) normal at Yangtze River Valley, and below (above) normal at central China and southern China. This distribution of precipitation over China is related to the weakening (strengthening) of Walker Circulation. After late 1970's, while the SLP over tropical western

Pacific (10ºS~0º,130º~150ºE) keeps on increasing, that over subtropical western Pacific area (20º~30ºN,130º~150ºE) keeps on decreasing in same time. The Decreasing of SLP over subtropical western Pacific area is related to the strengthening of convective activities at Yangtze River Valley and strengthening of aridity trend in northern China.

At interdecadal timescale, the variability of tropical Walker circulation can influence the distribution of precipitation of East Asian summer monsoon through the meridional circulation. During the weak period of Walker circulation (1978-1997), the weakened convective activity was found over tropical western Pacific, and the strengthened convective activity was near 30ºN of East Asian area. Thus, the summer precipitation is above normal at Yangtze River Valley, and below normal at central China and southern China. The period of strong Walker circulation (1958-1977) is on the contrast to the weak period.

5.5 Observation and model validation of land-atmospheric interaction in semi-arid region

5.5.1 Intensified field observation of water, energy and CO2 fluxes over semi-arid area of China

Arid and semi-arid areas comprise about 40% of China's territory. Most of them are located in Northern China. These areas are important on the land -atmosphere interaction process because of their unique energy budget and hydrological processes, increasing aridity and desertification trend (Fu et al., 2002b; Huenneke et al., 2002). In addition, as mentioned in section 7.3.3, the semi-arid areas are more sensitive to climate change and land use and the extent and distribution of arid and semi-arid areas are subject to modification because of land use and water utility(Fu et al.,2002b). Higher albedo because of deforestation and desertification has been shown to cause a reduction in precipitation and evapotranspiration (ET) regionally. Changes in climate and climate variability will likely have a significant impact on these regions.

From the 1980s, land surface process studies have been important research areas in atmospheric sciences. There are many comprehensive field experiments conducted over the world in different climate areas. Some field experiments have been carried out over the arid and semi-arid region of China in recent 30 years, for example, HEIFE (Hu, et al., 1994a, 1994b), IMGRASS (Lu, et al., 2002, 2005), NWC-ALIEX (Huang, 2004, Zhang and Huang, et al., 2005, Bao and Lu, 2006), dust aerosol observations in Dunhuang (Iwasaka and Shi, et al., 2003, 2004), surface layer tur-

bulent flux observations over Naiman (Zhang, et al., 2001; Liu, et al., 2002) in which a great deal of observation data and research achievements were gained.

However, eddy covariance measurements of the turbulent flux in the surface layer were conducted only in the summer during intensive observation period for one or two months in most of these experiments.

Eddy covariance methods to measure directly the turbulent fluxes between the land surface and the atmosphere have been used since the late 1950s and early 1960s. Yet, only recently has the technology been available to make continuous flux measurements. There are more than 10 years continuous flux data for some sites in Ameriflux and Euroflux (Baldochi, et al., 2001). However, continuous flux measurements with the eddy covariance method began in China only in 2002 (www.chinaflux.net). Few studies have investigated year-round eddy covariance measurements of energy fluxes in semi-arid ecosystems.

Long-term field observation at Tongyu, a Reference Site of CEOP program in semi-arid region of China

From 2002, long-term intensified CO2, sensible and latent heat fluxes were measured continuously in the semi-arid cropland and degraded grassland surfaces in Tongyu, Northeastern China. The Tongyu observation site is also one the reference sites of the international CEOP program (Coordinate Water and Energy cycle Observation Project, Bosilovich et al., 2002). The main objectives of this long-term observation are the following (Liu HZ et al., 2004):

- investigate the effects of the land use on the aridification in North of China;
- obtain the nature and mechanisms of the water vapour, CO2 and heat flux transfer over different ecosystems in semi-arid areas with long-term observations;
- compare the different transfer process over different land surface.

The long term observations will be continued until the end of the Phase II of CEOP (www.ceop.net).

The climate in Tongyu is a semi-arid terrestrial climate in the mid-temperature zone. The mean annual precipitation measured from 1961 to 2000 in Tongyu County, which is about 30km northeast of the site, is 388.2 mm. The annual mean air temperature measured from1961 to 2000 in Tongyu County is 5.7ºC. Approximately 80% of the annual precipitation occurs between the May and September. Winter precipitation is mainly the solid precipitation in from of snow. The annual total precipitation is variable and has interannual variations. It was 333mm in 2003 and 215mm in 2004. Climate variability has the potential to affect energy parti-

tioning and CO2 exchange between the land surface and the atmosphere. The more serious drought in 2004 and a little less than climate average total annual precipitation (the mean annual precipitation is 388.2mm from 1961 to 2000) in 2003 provided an excellent opportunity to investigate the impact of climate variability on seasonal and diurnal variations of the CO2, sensible and latent heat fluxes in the semi-arid cropland and degraded grassland surfaces.

1) Site description

The observation site is located in Tongyu (44°N25', 122°E52'), in a semi-arid area of the Jinlin province, Northeastern China. At the site, there have two observation sites at a cropland and a degraded grassland surfaces, where the distance departure between two stations is about 5km or so. The terrain at this area is fairly open and flat with terrain slope less than 10 in all directions. The vegetation at the grassland site is dominated by C3 plants, and it height is usually less than 10 cm. The vegetation cover percent is less than 70% in summer in the degraded grassland ecosystem, and the grass is grazed by sheep and cow every summer with a stocking rate about 3 yak ha^{-1}. The main crop is corn mixed with sunflower within 1000m of the measurement location in the cropland ecosystem during the growing season, while in winter there is bare soil. The maximum height of the corn and sunflower is near 2 m in the growing season. The soils in this area are mainly sandy soil, slight chernozem, salty alkaline soil, and meadow soil.

2) Observation items

The main observation includes the eddy covariance to measure the turbulent fluxes, the normal meteorological observation tower in the surface layer and the radiation flux observation system, the soil temperature and the soil humidity measuring system. The observation content is the same over two different land surfaces.

20-meter tower was constructed at each station as the observation platform. Meteorological parameters such as temperature, humidity, wind speed and direction were measured at heights of 2, 4, 8, 12 and 17m above the surface in the tower. Radiation components such as incoming and outgoing solar radiation, incoming and outgoing long wave radiation are measured at the height of 2m over the degrade-grassland surface, and 3m over the cropland surface on a mast separated from the tower structure by 15m and 20m respectively. Soil temperature was measured at the surface and depths of 0.02, 0.05, 0.10, 0.20, 0.50 and 0.80 m in the soil near the mast. The soil volumetric moisture content was measured at depths of 0.05, 0.10, 0.20, 0.40, 0.80m, and 1.6m. Soil heat flux was measured at two depths (0.05, 0.10m) using flux plates. Fig. 5.13 shows some instruments at Tongyu station over the degraded grassland.

Fig. 5.13 Some instruments at Tongyu station over the degraded grassland (Liu HZ et al., 2004)

3) Data analysis

More than five years (Oct. 2002 to Dec., 2007) continuous observational data has been obtained on the water and energy budget over different land surface in the semi-arid area. Based on 3 years of the eddy covariance (EC) observation (2003-2005) in the semi-arid area of Tongyu, over degraded grassland and cropland surfaces, the seasonal and diurnal variations of the exchange of the water vapor and have been investigated.

3.1) Energy balance in the surface layer

The maximum value of half-hour average global solar radiation (W/m^2) was near 1100 during the growing season (July, 2004), with maximum being less during the non-growing season (790, March 2004) in the cropland. The partitioning of the available energy differs dramatically in the two seasons (Fig. 5.14). During the growing season, both sensible (W/m^2) and latent heat fluxes (W/m^2) showed a linear dependence on, with tending to be slightly higher than in the cropland. However, in the non-growing season, never rose above about 50 Wm-2, with almost all available energy at high being dissipated as the sensible, rather than latent heat flux.

In general, the surface energy imbalance was approximately 20% and 25 % in the cropland and degraded grassland surfaces respectively in 2004,

while the imbalance energy was 22% and 28% in the cropland and degraded grassland surfaces respectively in 2003 and 2005 (Fig. 5.15).

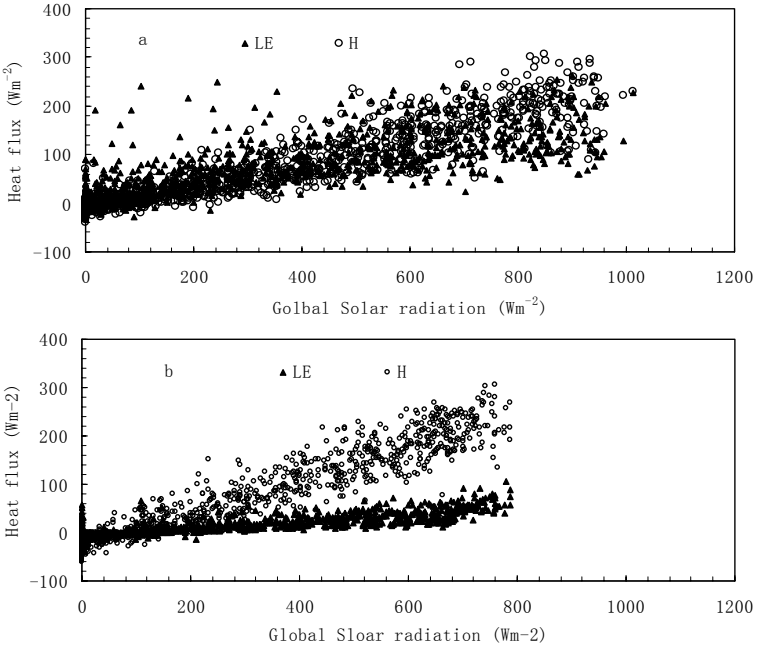

Fig. 5.14 (a) Global Solar radiation (R_s), latent and sensible heat flux (*LH*, *H*) in the wet season of July, 2004 in the cropland; (b) Global Solar radiation (R_s), latent and sensible heat flux (*LH*, *H*) in the dry season of March, 2004 in the cropland. (Liu HZ et al., 2004)

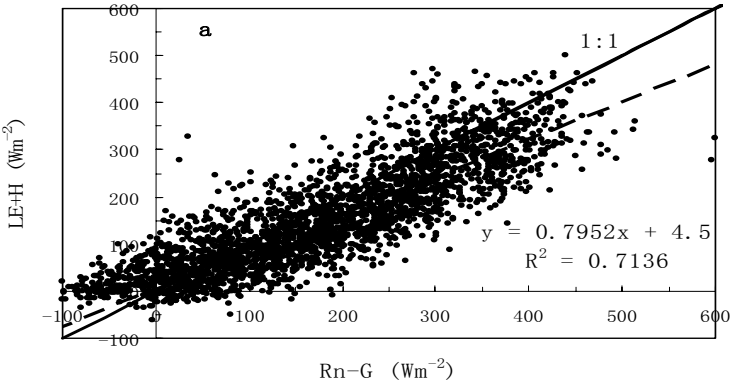

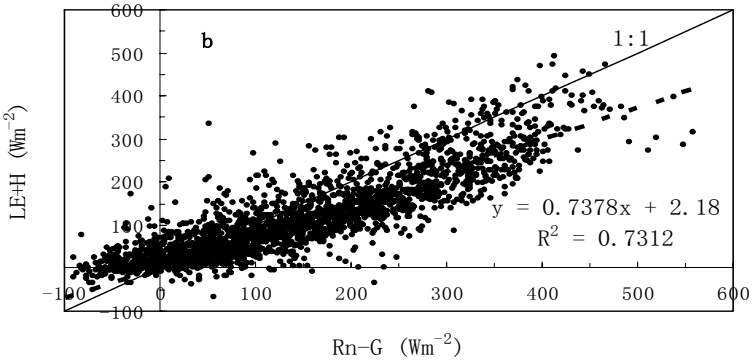

Fig. 5.15 Energy closure in daytime in the surface layer over cropland and degrade grassland at 2004 with 30-min average fluxes, while the soil heat flux includes the correction of the energy storage between the surface and the 5cm soil. (a) over the cropland surface, (b) over the degraded grassland surface. (Liu HZ et al., 2004)

3.2) Seasonal patterns of energy fluxes

Seasonal variation of the daily mean net radiation (R_n), sensible and latent heat (H, LH), soil heat fluxes (G_s) over the cropland and degraded grassland surfaces at 2003-2005 are shown in Fig. 5.16. The latent heat flux is larger over the cropland surface than that over degraded land surface in the growing season, while in the non-growing season their difference is very few. The soil heat flux is usually very small except in the growing season. During the growing season, as rain wets the surface, latent heat flux increase to a value about the same as sensible heat flux. During three years cycle, we can find the daily mean latent heat flux in the growing season in 2004 is less than that in 2003 in the two land surfaces, while the daily sensible heat flux is larger in the growing season in 2004 than that in 2003 and 2005.

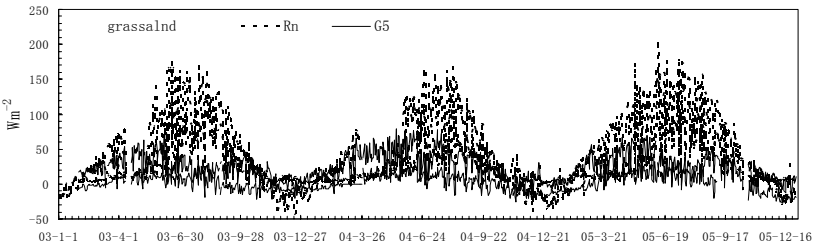

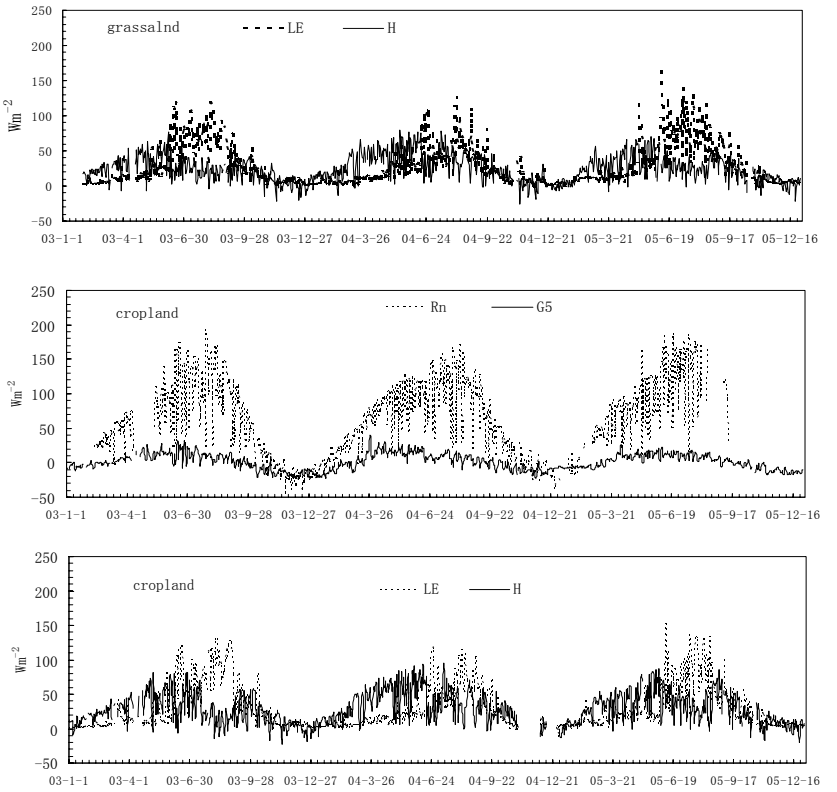

Fig. 5.16 Seasonal variation of the daily mean net radiation (R_n), sensible and latent heat (H, LH), soil heat fluxes (G_s) over the cropland and degraded grassland surfaces during 2003 – 2005. (Liu HZ et al., 2004)

3.3) Monthly average of diurnal patterns for fluxes during the wet and dry seasons

Fig. 5.17 shows the monthly average diurnal patterns for energy fluxes in the wet and dry seasons in the cropland. The monthly average diurnal patterns for energy fluxes in the degrade grassland are also the same with that in the cropland. The sensible heat flux and the soil heat flux were not in phase in wet and dry seasons. The net radiation has very small difference in two years. In wet season the latent heat flux is the main part of the available energy, while the sensible heat flux is the main part of that in dry season. Compared the diurnal variation in 2004 with that in 2003, we can find that the sensible heat flux is larger in 2004 than that in 2003 in wet

season, while the latent heat flux in 2004 is less than that in 2003. The diurnal variation in 2005 is similar with that in 2003.

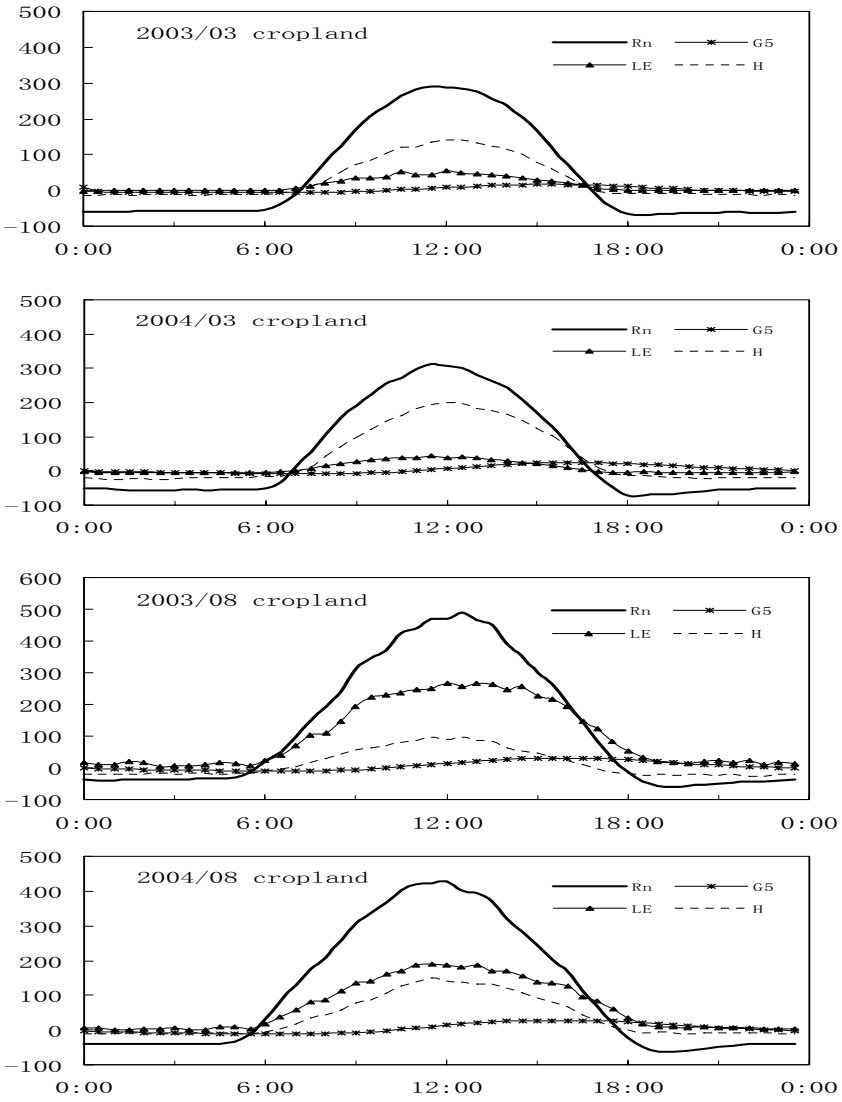

Fig. 5.17 monthly average diurnal variation of the energy fluxes in the cropland surface in dry and wet seasons.

3.4) CO_2 flux

Comparing the monthly mean diurnal variation of daily total CO_2 flux in growing season (August) in the two different land surfaces in two years (2003-2004), daily total CO_2 flux in the daytime in 2004 is less than that in 2003 in the two land surfaces., while the respiration in the night in 2004 is also less that in 2003 (Fig. 5.18). The CO_2 uptake and the daily total CO_2 flux in the grassland is less than that in the cropland in the growing season, while the difference is very small during the non-growing season. The diurnal variation daily total CO_2 flux in growing season (August) in 2005 was similar as that in 2003.

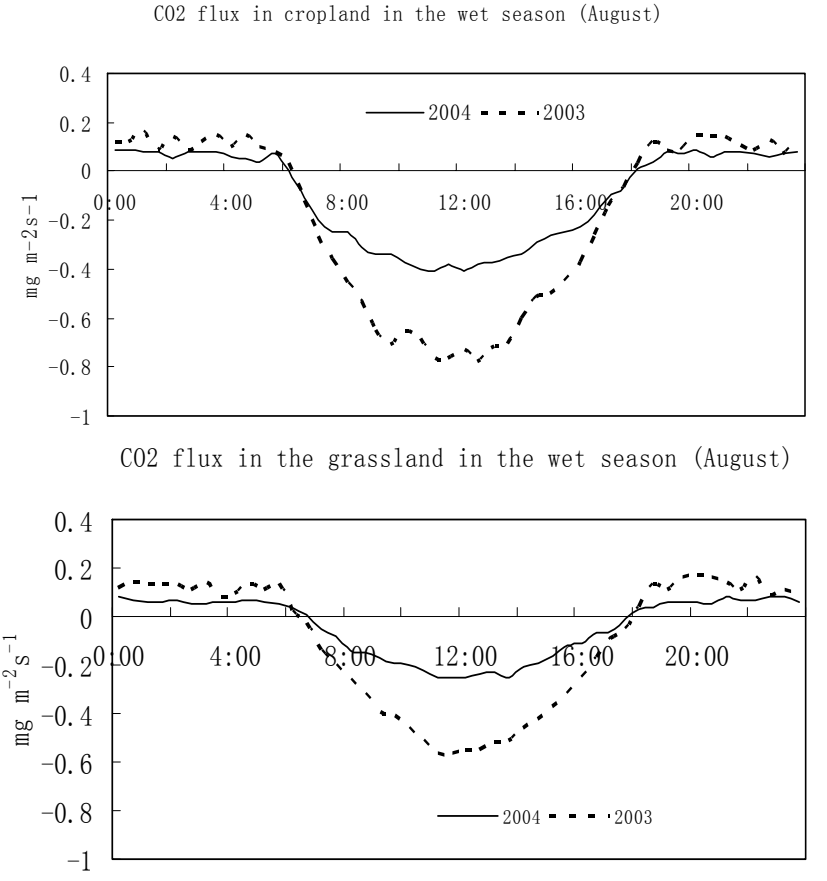

Fig. 5.18 Monthly average diurnal variation of the CO2 flux in the cropland and degraded grassland surfaces in the wet season.

Field observation at Lanzhou, another Reference Site of CEOP program over Loess Plateau

Another CEOP Reference Site, the Semi-Arid Climate & Environment Observatory of Lanzhou University (SACOL) has been established since 2005. The topography around the site is characterized by loess plateau, the largest arid and semi-arid zone and one of the dust aerosol sources in China. SACOL is specifically designed to assess dust aerosol effect on local climate as well as global climate.

The major SACOL scientific objectives are to provide monitoring of long term tendencies in semi-arid climate changes, monitoring of the aerosol effect on water cycle, studies of interaction between land surface and atmosphere, improving the land surface and climate model, and validation of space-borne observations. Further details will not be discussed in this section.

5.5.2 Validation of land surface model based on field observations over semi-arid area of China

The terrestrial biosphere is an integral part of both the global carbon and hydrological cycles. Every year about 14% of the carbon in the atmospheric is exchanged with the terrestrial biosphere, and about 20% of the water added to the atmosphere annually derives from evapotranspiration from the land (Wesfall and Stumm, 1980; Friend 1997). Researches on carbon and hydrological cycles of the terrestrial ecosystem have been one of the main issues in the global change science. For the purpose of predicting the developing trends of global change in the future and seeking the effective ways to regulate carbon and hydrological cycles of the earth ecosystem, it is necessary to have an acquaintance with each process and feedback mechanisms of these two cycles in the terrestrial ecosystem.

Dynamic land surface models that coupled carbon and hydrological cycles have been developed primarily to fulfill this need, for example, BATS (Dickinson 1986), FOREST-BGC (Running 1988), BIOME-BGC (Running 1993), AVIM (Ji, 1995), IBIS (Foley 1996), SIB2 (Sellers 1996), TEM (McGuire 1997; 2000) , CoLM (Dai et al., 2001), NCAR CLM (Dickinson, 2005; Bonan 2001), and so on.

At present, these models have been widely applied in the researches on carbon and water fluxes exchange between land surface and atmosphere. However, the verification and validation of models based on field observations in different temporal and spatial scales are greatly needed, and as a result, scientists and researchers should still pay enough attention to these aspects. It should be pointed out particularly that current climate models

have shown the highest bias error of simulated precipitation in summer over the arid and semi-arid Asia. (Fu et al, 2005). It is perhaps mainly due to lack of knowledge of land surface process, especially of the hydrological process over arid and semi-arid regions in the land surface model. Currently the most hydrological modules in land surface model are developed and calibrated for use in humid areas.

Up to now, a number of land surface model including NCAR-CLM3, Common Land Model, SiB2, BIOME3, and so on have been calibrated in the semi-arid region of China based on the field observations as mentions in the previous section. Here, we show an example by using a sophisticated model, the Integrated Biosphere Simulator (IBIS), in simulating CO_2 and sensible/latent heat fluxes exchanges between land furface and atmosphere based on dynamic vegetation schemes.

In this study, we apply a new version of the integrated biosphere simulator(or IBIS) of Foley (1996) and Delire (1999), which has improved representations of land surface physics, plant physiology, canopy phenology, plant functional type differences and carbon allocation (Kucharik 2000). For the purpose of evaluating the ability of IBIS in reproducing the main biophysical processes occurring at the land surface, we present model simulations of net exchange of CO_2, latent and sensible heat fluxes at Tongyu, and make a comparison with the CEOP reference site observations through year 2003 and 2004.

IBIS (version 2.6) is a fairly comprehensive model of terrestrial biosphere processes and includes four modules of (1) land surface processes, (2) vegetation phenology, (3) terrestrial carbon cycling, and (4) vegetation dynamics (Foley 1996).

The land surface module uses a two-layer vegetation, six-layer soil scheme to simulate the surface energy, water, carbon, and momentum balance of the soil-vegetation-atmosphere system on a relatively short time step (Delire 1999). This module borrows much of its basic structure from the LSX land surface package (Thompson and Pollard 1995a; 1995b). Physiologically based formations of canopy photosynthesis (Farquhar 1980; Farquhar and Sharkey 1982), stomatal conductance (Collatz 1991; 1992) and respiration (Amthor 1984) are used to simulate canopy gas exchange processes. The above processes are organized in a hierarchical framework and operate at different time steps, ranging from 60 min to 1 year. And this approach allows for explicit coupling among ecological, biophysical, and physiological processes occurring on different timescales. More details of the IBIS model are described and given by Foley (1996) and Kucharik (2000).

Simulations of surface fluxes for the whole 2003 output by IBIS are presented and a comparison between model results and the observed data at the Tongyu site was made, so as to evaluate the performance of the model.

The eddy correlation measurements include the item of NEE, which is used to test the simulation of the physiological processes linked to photosynthesis and respiration in the model. Because the photosynthetic process mainly controls the stomatal conductance, NEE provides an independent way of assessing the transpiration simulated by the model (Delire and Foley 1999). Simulated versus observed NEE of the grassland and cropland indicate that at the Tongyu site the two kinds of ecosystems serve as weak carbon sinks, with minus NEE almost all the year. And simulated NEE in growing seasons (mainly from April to September) are bigger than those in the other period. From the comparison analysis between simulated and observed NEE, we can know that they two show fair agreement with the correlation coefficients (R^2) 0.41 in grassland and 0.49 in cropland.

On average, the simulated monthly mean NEE of the grassland and the cropland ecosystems at Tongyu site in 2003 are bigger than these of observed and they all reach the maximum in August. Meanwhile, the simulated and observed NEE have some discrepancy from May to August, especially at the cropland. In general, the simulated NEE of the whole 2003 year accumulates up to -443.33gC m^{-2} a^{-1} at the grassland and -581.32 gC m^{-2} a^{-1} at the cropland, overestimated by 23.21% and 27.43%, respectively.

The trend of monthly variations of simulated and observed sensible heat flux for simulation and observation are generally in agreement (Fig. 5.19). At the degraded grassland the simulations of monthly mean sensible heat flux are mostly larger than observations (overestimated by 9.90% for the whole 2003); while at the cropland the two are basically in accordance with each other except from July to August and November to December, and as a result the accumulation of simulated sensible heat flux reach as 10234.05 W m^{-2}, overestimated by 11.98% compared with the observation of 9138.39 W m^{-2}. This might be due to the inaccurate simulation for the growth process of maize at the cropland ecosystem.

The agreement between simulated and observed latent heat flux is quite reasonable although the maximum latent heat flux is often underestimated from July to August (Fig. 5.20). The squared correlation coefficients for the grassland and cropland are 0.82 and 0.84, respectively. Meanwhile, the maximum of simulated latent heat flux at the cropland is about twice that at the degraded grassland, and this might be resulted from the partition between grassland and cropland in the IBIS model. And the latent heat flux, which is related to evapotranspiration, only has diurnal variation both at the grassland and cropland during the growing season. While in the non-

growing season for both the two underlying surfaces are covered with bare soil, the latent heat flux is usually less than 30W m^{-2}.

From the comparison of the monthly mean latent heat flux, it can be found that the simulation is very close to the observation except in June and September. In general, the accumulations of simulated latent heat flux for the whole 2003 at the grassland and cropland reach as 9325.62W m^{-2} and 10161.41W m^{-2}, while the corresponding values of observation are 9778.16 W m^{-2} and 10527.51 W m^{-2}, underestimated by 4.63% and 3.48%, respectively.

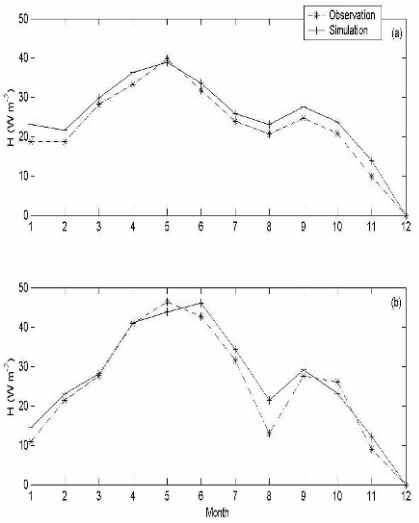

Fig. 5.19 Monthly variation of simulated and observed sensible heat flux in Tongyu Observation Station in 2003: (a) grassland ecosystem and (b) cropland ecosystem.

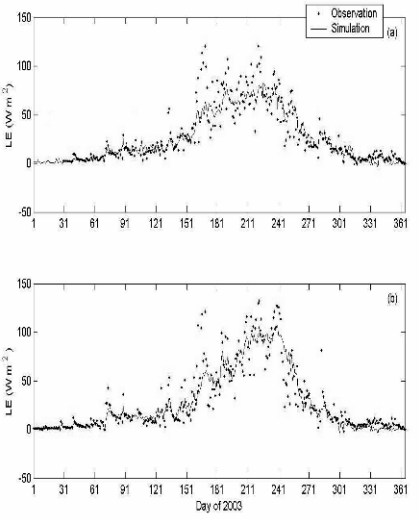

Fig. 5.20 Daily average of simulated and observed latent heat flux (LE): (a) denotes the grassland ecosystem and (b) the cropland ecosystem. The observed flux data of grassland from 1 to 29 January are missing.

Analyses mentioned above indicate that the IBIS could reproduce NEE, sensible and latent heat fluxes reasonably, as indicated by correlation coefficients exceeding the significant level of 0.05. Generally speaking, the model overestimated the annual NEE (by 23.21% at the grassland and 27.43% at the cropland) and sensible heat flux (with corresponding percentage of 9.90% and 11.98%), and underestimated the annual latent heat flux by 4.63% and 3.48%, respectively.

One possible reason for the above mentioned inconsistence between model outputs and the direct measurements is the uncertainties in long term observation, which is resulted at least partly from eddy covariance technique. The model biases are also resulted from physical limitation of instrumentation, two and three dimensional air flow motion effects, methods of data processing, and underestimation of nighttime fluxes, etc. On the other hand, it also indicated several aspects of improvements for the IBIS model, especially for its application in China's Semi-arid region, such as classification of vegetation types, verification of model parameters setting and so on.

5.6 Potential human impacts on aridity trend

5.6.1 Impacts of human activity on river runoff in the northern area of China

Global environment has changed very much with human activity. There is no exception to hydrological regimes (Conway, 2001; Garcia, et al., 1998). In fact, due to agricultural, industrial, urban development, such as irrigation and drainage, hydraulic structure across a river, the elements of hydrological cycle have changed in terms of quantity and quality, both in time and in space. In this section, an attempt is made to analyze quantitatively the effect of human activity on river runoff in different spatiotemporal scales including daily, monthly, annual, inter-decade, inter-century variations, according to long-term observation data (Ren et al., 2005). The driving force of annual runoff change in a river will be analyzed also. In this section, natural flow means runoff generated without the impacts of the human activity. It is derived from the summation of measured runoff plus water amount both stored in the reservoirs and taken directly from river course for various kinds of utilization during the computed period.

The following basins are taken as case study areas: the Yellow River, the Haihe River, the Luanhe River, the Songhuajiang River, and the Liaohe River in the northern area of China, covering Bejing, Tianjin, Ningxia, Shanxi, Hebei, Liaoning, Jilin, Hailongjiang Provinces, and partial area of Shaanxi, Gansu, Qinghai Provinces and Inner Mongolia Autonomous Region, as shown in Table 5.1 and in Fig. 5.21. The total area is almost 2 million km^2.

On one hand, the total amount of water use has been increasing within the study area since 1949. Capitation amount of water use came up to 450 m^3 at the beginning of the 1980's, and has been kept as this value in China to the end of the 20th century. Although annual growth rate of water use

decreases from 7.1% in 1959 to 1.8% in 1997, the total amount of water use increases because of economic development especially along the coast in China.

On the other hand, water-use structure has been changing. The percentage of industrial and municipal use in total amount of water use grows at a great rate. The percentage of agricultural use in total amount of water use decreases with time. The ratios of agricultural, industrial, and municipal use in total amount were 88.2%, 10.3%, and 1.5% in 1980; 69.2%, 20.7%, and 10.1% all over the country in 1999, respectively. The annual growth rate of agricultural, industrial, and municipal use was –0.058%, 8.1%, and 38.5% respectively in China from 1980 to 1999. The water-use structure has changed as well with the development of industry, agriculture and urbanization from the 1980's to the 1990's. The ratios of agricultural, industrial, and municipal use in total amount were 77.3%, 16.8%, and 5.9% in Beijing; 90.6%, 7.2%, and 2.2% in Hailongjiang Province; 90.5%, 8.4%, and 1.1% in Shanxi Province in 1988, respectively. However, they were 44.2%, 25.3%, and 30.5% in Beijing; 65.2%, 28.9%, and 5.9% in Hailongjiang Province; 62.6%, 23.5%, and 13.9% in Shanxi Province in 1999, respectively. As remarked above, water use outside of river increases rapidly. And river discharge decreases. Such case has become more and more serious. Some evidences are given as follows. Analyses will be made on the change of daily, monthly, annual, inter-decade, inter-century runoff due to human activity.

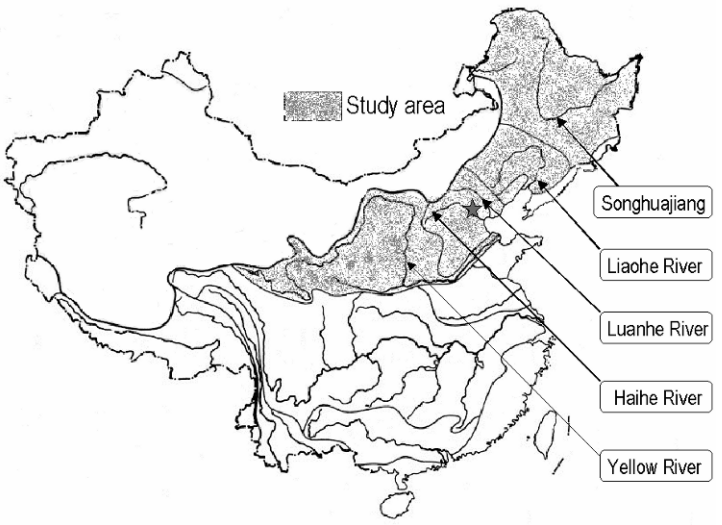

Fig. 5.21 Location of study area in China map (Ren et al., 2005)

Table 5.1 Outline of rivers in the study area

Name of River	Total length(km)	Total Area (km^2)	Annual runoff (10^9 m^3)
Yellow River	5,464	752,444	59.2
Luanhe River	1,090	263,631	22.8
Haihe River	877	44,100	4.8
Liaohe River	1,390	228,960	14.8
Songhuajiang River	2,308	557,180	74.2

- Effect on order of daily discharge

Since the 1990's, the number of days in which daily discharge is more than 3,000 m^3/s, is no more than 4 days on the average at Huayuankou Station controlling the area of 730,037 km^2 in the lower reach of the Yellow River. Fig. 5.22 shows statistical characteristics of daily discharge data series measured at Huayuankou Station from 1946 to 1998.

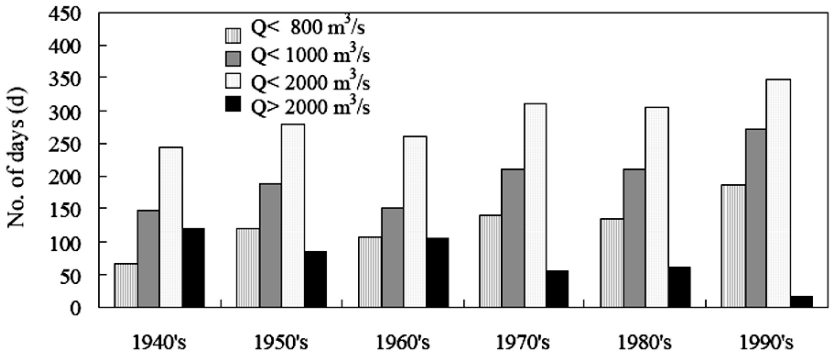

Fig. 5.22 Statistical characteristics of daily discharge series observed at Huayuankou Station from the 1940's to the 1990's (After Zhu, et al., 1999)

The number of days in which daily discharge was more than 2000 m^3/s, decreased from 86 days in the 1950's to 17 days in the 1990's. However the number of days in which daily discharge at Huayuankou Station was less than 3000 m^3/s, increased from 300 days in the 1940's to 361 days in the 1990's, and the occupying percentage in total number of days during the whole year increased from 82% in the 1940's to 99% in the 1990's correspondingly. That's to say, minor daily discharge, measured at a specific

downstream site, occurs more often than before. The reason is that upstream runoff is retained and stored in reservoirs, perhaps flowing lately in the coming year, or that upstream runoff is taken from river course for agricultural irrigation (consumed by plant transpiration), industrial and municipal consumptions. Daily discharge at downstream is becoming less and less. More serious situation has occurred, i.e. river flow cutoff in the lower reaches of the Yellow River Basin. In 1972, river flow was cut for 19 days, beginning on April 23rd; and the length of flow cutoff was about 310 km. In 1998, flow was cut for 142 days, beginning on January 1st; and the length of flow cutoff expanded for about 515 km. The decrease of discharge, even flow cutoff, could cause four serious results: (1) to deteriorate aquatic ecological environment in the lower reaches of the Yellow River Basin; (2) to aggravate deposition of sediment, so as to raise the risk of floods; (3) to make water supply difficult for domestic, agricultural, and industrial use in the Yellow River Delta; (4) to aggravate intrusion of sea water in the outlet.

- Effect on monthly runoff

The human activity such as the construction of reservoirs across a river would make the distribution of monthly runoff in one year changed. For instance, the proportion of runoff during rainy season in the annual runoff decreases, while the proportion of runoff during dry season in the annual runoff increases. And the ratio of the maximum to the minimum of monthly runoff decreases further. For example, the differences between natural and observed monthly runoff data at Fuyu Station controlling 71,783 km2 in the Songhuajiang River and at Wangben Station controlling 10,418 km2 in the east upper area of the Liaohe River in 1994 are almost the same as above. Owing to irrigation in the growth period of crops, observed monthly runoff decreased by 83.8% at Wangben Station, 67.2% at Fuyu Station, respectively with respect to natural runoff in June of 1994.

- Effect on annual runoff

Fig. 5.23 represents the variation of annual precipitation, observed runoff, and runoff coefficient series in the upstream of Xiaoheyan Station, controlling the area of 18,599 km^2 over the Laohahe River Catchment, from 1955 to 1998. The Laohahe River lies in the west upper reach of the Liaohe River Basin. It could be seen from Fig. 5.18 that there is no a trend towards decrease in the series of annual precipitation from 1955 through 1998. However, there is a tendency towards decrease in the series of annual runoff observed as well as in the series of annual runoff coefficient from 1955 through 1998. That's to say, the same order of precipitation produced less runoff in the Laohahe River Cachment in the 1980's than that in the 1950's.

The differences between natural and observed runoff within the area of 72,875 km^2 in the upper reach of the Songhuajiang River Basin, and within the area of 10228 km^2 in the east upper reach of the Liaohe River Basin are larger in 1990 and in 1994 than the other. Anyhow, there exists the same phenomenon that observed runoff is less than natural runoff.

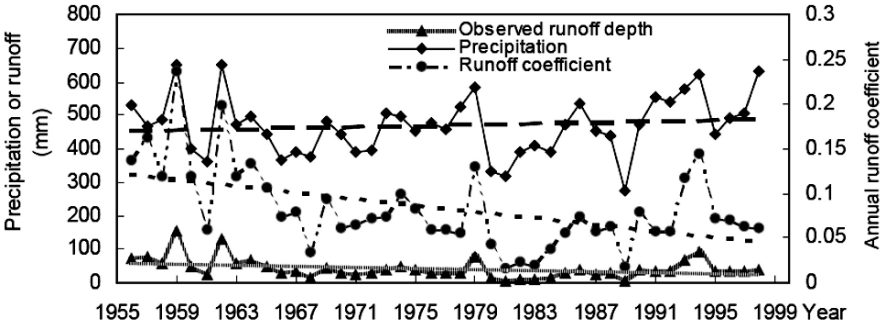

Fig. 5.23 Variation of annual precipitation, observed runoff, and runoff coefficient series at Xiaoheyan Station controlling the area of 18, 599 km^2 in the Laohahe River Catchment from 1955 to 1998 (Ren et al., 2005)

- Driving force analysis

In general, there are three aspects of reasons in the reduction of river runoff. Firstly, the amount of precipitation becomes less. Secondly, water is artificially drawn out from river channel. It contains the inter-basin transfer of water quantity as well, which could show up in the flow regime in the coming days. And groundwater is overexploited. That makes underground water table decrease. Finally, climate variability or climate change induced by human activity has influence over water resources.

The decrease in natural precipitation is the principal, main and direct cause of runoff reduction. But more or less of natural precipitation varies in space. Precipitation does not decrease in all the northern area of China. The main reason of runoff reduction is the growth of population, the enlargement of the scales of agricultural and industrial production, as well as urban development within Jilin Province, which consume a large amount of river flow and groundwater.

The annual growth rate of population was 1.59%, and the amount of water use increased by 12.5% in the whole basin of the Yellow River in 1999 than that in 1980. 3380 reservoirs, with the total storage capacity of 27.37 billions m^3, had been built before 1985. Also effective irrigation area had reached 43.8 thousands km^2 before 1985. Those are the main rea-

son why measured runoff decreases. As regards the influence of climate variability/change on water resources, it does not look very obvious. The same situation appeared in the Chaobaihe River (Li, et al., 2000) having 19,354 km^2 of area, the tributary of the Haihe River, nearby Beijing. According to statistics, total storage capacity of reservoirs reaches 4.8 billions meters, and real irrigation area is more than 2,500 km^2. With socioeconomic development, the utilization ratio of water resources becomes larger and larger, so that river flow cutoff began to occur in the Chaobaihe River in 1972. Moreover, stream flow had cut off for 276 days from February through December within the year of 1984. The utilization ratio of water resources, which has been increasing continuously beyond the limited ratio of 40%, makes it tend to be a seasonal river. The general hydrological regime is changed fundamentally. The local ecological landscape is difficult to be rehabilitated. The decrease of annual runoff is mainly caused by human activity rather than under the impact of climate change, though the climatic condition serves as the background of runoff change.

5.6.2 Impact of land surface degradation in northern China on regional climate

The climatic and environmental effect of land use/cover change has always been considered as one important aspect of global change study, and is also one of focuses of four international global environmental change research programs (IGBP, IHDP, WCRP, and DIVERSATE). But up to now, the studies of land-atmosphere interaction especially the feedback effects of vegetation cover on climate have mostly focused on the tropic region, where the impact of thermodynamic forcing is large and the impact of nonlinear dynamical instabilities is relatively small. Among them the impacts of Amazon deforestation and Sahel desertification have been widely investigated.

Fu (2001) investigated the potential impacts of human-induced land cover change on East Asia monsoon. As one major performance of anthropogenic activities, human-induced land use and land cover changes in East Asia have been one of the largest regions in the world. In the past 3000 years, more than 60% of the region has been affected by conversion of various categories of natural vegetation into farmland, conversion of grassland into semidesert and widespread land degradation. Such human-induced land cover changes result in significant changes of surface dynamic parameters, such as albedo, surface roughness, leaf area index and fractional vegetation coverage, etc. The results of a pair of numerical experiments have shown that by altering the complex exchanges of water and

energy from surface to atmosphere, the changes in land cover have brought about significant changes to the East Asian monsoon. These include weakening of the summer monsoon and enhancement of winter monsoon over the region and a commensurate increase in anomalous northerly flow. These changes result in the reduction of all components of surface water balance such as precipitation, runoff, and soil water content. The consequent diminution of northward and inland moisture transfer may be a significant factor in explaining the decreasing of atmospheric and soil humidity and thus the trend in aridification observed in many parts of the region, particularly over Northern China during last 3000 years. The variation of East Asia monsoon in his study is the result of land cover changes only. It is very likely that the anthropogenic modification of monsoon system would have been occurred in the long history of civilization.

Jiang Jin et al. have conducted a series of numerical experiments to study the impacts of recovering natural vegetation on local environment and climate. The experiments are based on NCAR RegCM2 (Giorgi, 1993a, b) with a land surface scheme-BATS1e (Dickinson, 1993), in which the heat/water vapor fluxes exchanges between soil-vegetation-atmosphere are considered in detail. The model is centered at 115°E, 37°N, with 61 grid points in east-west direction and 55 grid points in south-north direction at a spatial resolution of 60 km. The selected area covers western part of Northeast China, eastern Inner Mongolia, and some parts of North China. This area mainly consists of semi-arid region which acts as both ecosystem and climate transitional zone.

Four sets of experiments are designed in this study. The land cover was changed from cropland into potential natural vegetation (forest or grassland) with a proportion of 25%, 50%, 75%, and 100% respectively. For each set of experiment, a continuous 10-year integration was carried out. The results show that the aridity trend in selected region could be alleviated effectively by recovering the potential natural vegetation. More than that, it is noticeable that the soil wetness in upper layers and precipitation has a gradual increase trend along with the increase of the recovered vegetation, especially in southern part of the area. In terms of soil moisture, the annual value has an increase trend with time. Meanwhile, a larger increase was found corresponding to a higher percentage of the recovered vegetation.

Over the last five decades, northern China in the middle latitudes has experienced dramatic interdecadal climate change in conjunction with land degradation in large area. North China experienced a relatively wet period from 1950s to 1964, and has suffered a severe drought since the end of 1970s. The interdecadal precipitation variation over South China is identical to that in North China, but the situations over Central China and North-

east China are opposite to those over North and South China. The expanding rate of desertification land over northern China was 1560 km^2 per year from the 1950s to 1975, and 2100 km^2 per year from 1975 to 1987, and had increased to 3600 km^2 per year from 1987 to 2000.

Furthermore, the expansion in other kinds of land degradation has been accelerated during the late five decades. Land degradation mostly occurred over the transitional climate and ecology zone over northern China, and statistical analysis based on the observed data proved that vegetation cover change over the transitional zone has more significant effect on summer precipitation over China. Xue(1996) explored the role of desertification over the Mongolian and the Inner Mongolian grassland in an atmospheric general circulation model, and found that desertification could bring significant influence on surface climate over China. Similar results were produced based on regional climate model simulations according to Wei et al. (1998) and Zheng et al. (2002).

Zhang et al. (2005) estimated the contribution of land-use change to surface warming by comparing NCEP/NCAR Reanalysis data with station data, because the NCEP/ NCAR Reanalysis is not sensitive to land surface change as it does not assimilate surface observations such as temperature, moisture, and wind (Kalnay et al., 1996; Kalnay and Cai, 2003). The NCEP/NCAR surface temperature data are linearly interpolated to each site of the climatic stations, and the monthly mean is obtained by averaging the daily data, then the 40-a mean annual cycle for each site is removed, finally the annual anomalies are obtained by averaging the monthly mean anomalies. Considering the impacts of topography and changes in the observing system, we get the decadal trends by 1990—1999 minus 1980—1989 for the sites east of 110°E. The differences of decadal trends between observation and NCEP/NCAR data may represent the contribution of land use change to surface temperature.

The results indicate that land use change tends to increase the temperature over northern and southern China, and decrease that over lower Yellow River Valley. The significant increases in temperature occur over northern China with a mean of 0.4°C/decade, which are mostly caused by land surface degradation such as deforestation and desertification.

Based on the statistical results mentioned above, a high-resolution regional integrated environmental model system (RIEMS) is employed to investigate the effects of land surface degradation over the transitional zone and its surrounding areas (northern China and southern Mongolia) on the regional climate. The regional integrated environmental model system (RIEMS) has been employed, of which the dynamical component of RIEMS is the same as that of PSU/NCAR meso-scale model MM5, and is coupled with BATS1e land surface scheme and CCM3 radiation package.

Validation of the RIEMS performance has shown that it has reasonably good capacity to simulate the regional climate in East Asia.

Two experiments were conducted, one is control run (referred to as CASE C) with current vegetation derived from the International Satellite Land Surface Climatology Project (ISLSCP) gridded on 1° boxes, where the 15 vegetation types in ISILSCP are aggregated to 18 types in BATS; the other is desertification experiment (CASE D) where the semi-desert, grassland, cropland and forest are replaced by desert over the area from 108°E to 121°E, 40°N to 48°N, according to the areas of slight, moderate and severe desertification land and the acceleration of desertification expansion (Zhu et al., 1989; Dong et al., 1995).

Fig 5.24 demonstrates model domain, current vegetation, and desertification area. The two experiments are identical to each other for all the conditions except for vegetation cover, including the initial and lateral boundary conditions, the parameters of the physical processes. The Kuo-Anthes culumus parameterization, Holtslag planetary boundary layer formulation, CCM3 radiation package, land surface scheme BATS, and the linear relaxation scheme are used in the two experiments. The RIEMS is integrated from February 1 to November 30 for the three years of 1992, 1994 and 1996.

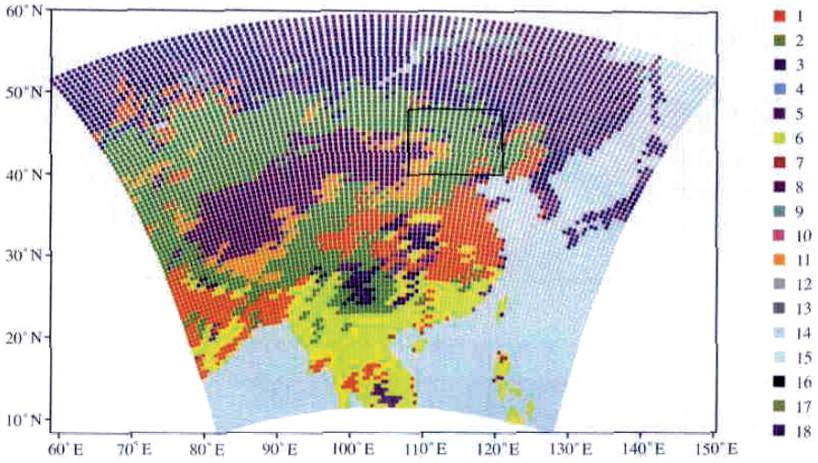

Fig. 5.24 Model domain, current vegetation, and desertification area. 1, Crop/mixed farming; 2, short grass; 3, evergreen needleleaf tree; 4, deciduous needleleaf tree; 5, deciduous broadleaf tree; 6, evergreen broadleaf tree; 7, tall grass; 8, desert; 9, tundra; 10, irrigated crop; 11, semi-desert; 12, ice cap/glacier; 13, bog or marsh; 14, inland water; 15, ocean; 16, evergreen shrub; 17, deciduous shrub; 18, mixed woodland. (Zhang et al., 2005)

The Willmott et al.'s dataset (Willmott et al., 2002) which represents the long-term surface observations at 0.5°×0.5°, and the wind and geopotential height components of NCEP/NCAR Reanalysis data are used for comparison. The comparison of the results in CASE C with observation shows clearly that the RIEMS generally simulates the principal features and regional details of the precipitation.

Comparing the observed summer (June, July and August) precipitation differences between 1978 – 1999 means and 1956 – 1977 means, and the simulated differences between CASE D and CASE C averaged for the three years., the land degradation tends to decrease the precipitation over the area from North China to Central Mongolia, with the mean amplitude of about 0.5 mm/d, and increase the precipitation over Central China, also with a mean value of about 0.5 mm/d, which is consistent with the observed differences. The negative precipitation anomalies occur over South and Southwest China, but the mean decreased value is smaller than the observation. There exists a negative-positive-negative pattern of rainfall anomalies from south to north over China, which is consistent with the observation.

The temperature changes in relatively small areas with a mean warming of 1°C over vegetation cover change area, and a cooling over central China, which are similar to the observed anomalies.

To gain insight to the impacts on summer atmospheric circulation, they evaluated the summer geopotential height and wind differences between NCEP 1978 – 1999 means and 1956 – 1977 means, and the simulated differences between CASE D and CASE C averaged for the three years. Overall, the land degradation causes similar geopotential height anomalies to observed interdecadal anomalies, with a decrease in 200 hPa and an increase in 850 hPa over the transitional zone and its surrounding areas, which enhance rising motion. Corresponding to the geopotential height anomalies, there is a strong anomalies anticyclone in 850 hPa and a strong anomalies cyclone in 200 hPa over northern China for both observation and simulation, and the southerly flow in 850 hPa is enhanced over eastern China after land degradation, and these provide base circulations leading to the changes in surface climate.

The RIEMS simulates the seasonal march of precipitation from spring to autumn. The northward traveling rainfall occurs from June in the Yangtze River valley to August in North China, and the autumn rainy season is noted from mid-August to September. The differences between CASE D and CASE C show that the strong precipitation anomalies emerge in June, July and August, with two negative anomalous centers over the transitional

zone and its surrounding areas, and southern China, respectively, and a positive anomalous center in between, but the precipitation anomalies over southern China are weaker. Furthermore, land degradation also plays an important role in seasonal changes in 500 hPa geopotential height.

5.7 Conclusions

Aridity trend is one of the most severe living environmental problems in northern China. In recent years, the aridity trend has been further aggravated partly because of regional climate change related to global warming as well as the anthropogenic effects of the rapid development of social economy and the expansion of urbanization.

Aridity trend over northern China is not an isolated phenomenon, but with significant worldwide linkage. However, due to its unique natural landscape and the long history of human development, it has its own characteristics in time and space.

Based on abundant environmental proxy data, aridity trend at different timescales in northern China are studied. It is found that the Asian desertification was started by 22 Ma ago. Sizeable desert lands in East Asia must have been maintained during Late Miocene – Pliocene time, and were able to provide a significant amount of eolian dust. The continental aridity was stronger from ~6.2 to ~5 Ma BP, weaker from ~5 to ~3.6 Ma and then strengthened at ~3.6, and more significantly at ~2.6 Ma BP. The most important aridification event at ~3.6 Ma BP corresponds to an uplift of portions of the Tibetan Plateau. Both the Tibetan uplift and the ongoing global cooling/arctic ice-building processes have played major role on the aridification in the interior of Asia during Late Miocene and Pliocene time. The record also reveals an obvious 20 ka oscillation with the wet phase in interglacial period and dry phase in glacial period. Aridity trend has further developed from 4000-3000 BP during the Holocene Epoch. The integrated analysis of air temperature, precipitation, soil moisture and drought index show that there exist quai-20yr and 70yr oscillations. In last 50 years, the decreasing precipitation and increasing temperature occurred in most areas of northern China, which result in the further enhancement of the aridity trend.

The semi-arid region of East Asia is located nearly at the northern edge where the summer monsoon can reach. It is a transitional zone between arid continent climate and humid monsoon climate, which is very sensitive to the climate and human perturbation. The variation of climate and water cycle in this area are highly correlated with the high variability of the Asia

monsoon system. This leads to the high frequency of extreme events and climate disasters over there. On the other hand, the semi-arid region is also the one with most significant change of land cover under the development by humans. The studies have shown that the semi-region has experienced the most severe aridity trend in last 50 years.

The aridity trend in northern China is also closely associated with the inter-decadal variability of atmospheric circulation. The area-mean Flood/Drought Index (FDI) in northern China share almost the same oscillation periods with winter North Atlantic Oscillation Index (NAOI) on the inter-annual, decadal and centurial scales. The maximum positive correlation coefficients between NAOI and area-mean FDI in northern China lagging 2-3 years reach to 0.001 significance level. The long term correlation between FDI and NAOI is time-dependent. Analyses also show that the correlation between Pacific Decadal Oscillation (PDO)-associated atmospheric circulation anomalies in East Asia and climate anomalies in China are significantly high. Corresponding to the cooling of the central North Pacific in and after 1976/77, less precipitation are observed in China, while the East Asian summer monsoon is weakened which acts to wet/cool Yangtze River valley and dry/warm northern China. Composite analyses show that the inter-decadal variation of ENSO-related atmospheric circulation anomalies may be responsible for the change of relationship between the ENSO and precipitation anomalies in China.

Land surface processes are extremely important in understanding the mechanism of aridity trend in northern China where the land-atmosphere coupling is strong, and the energy and water cycles are unique. To better understand the nature of aridity trend over northern China, the intensified field observations of land surface processes are conducted over the different types of land cover and land use areas. Based on available data obtained from Tongyu, a reference site of International Coordinated Energy and water cycle observations Project (CEOP) located in semi-arid region of China, the diurnal and seasonal variations of exchanges of energy, water and other material between soil, vegetation and atmosphere are analyzed preliminarily. Several land surface models are validated based on the field observations. Generally speaking, the models are able to reproduce the basic features of energy and water vapor exchanges between land-surface and atmosphere, which lays a solid foundation for the studies of aridity mechanism and optimization of model parameters, as well as the improvement of coupled climate models in the long run.

Concurrent with the natural variability, human impact is another very important factor contributing to the aridity trend in northern China, especially in context of global change. Impacts of human activity on river runoff in the northern area of China over past half century are analyzed quan-

titatively on different spatiotemporal scales. Besides climatic change, the increase of the amount of water taken from river course is the direct cause why observed runoff decreases in the northern part of China. Annual mean runoff generated from the same order of precipitation in 1980's and 1990's decreases by 20% ~ 50% as compared in 1950's and 1960's. The impact of human activity on river discharge is more in arid or semi-arid area than that in humid area.

At the same time, human-induced land cover changes in East Asia result in significant changes of surface dynamic parameters, such as albedo, surface roughness, leaf area index and fractional vegetation coverage, etc. Comparison of reanalysis data with station data also demonstrates that land use changes such as desertification and deforestation may have obviously contributed to the significant increases in temperature over northern China. The results of numerical experiments have shown that land use changes such as desertification and deforestation may have obviously contributed to the significant increases in temperature over northern China by altering the complex exchanges of water and energy from surface to atmosphere. Land degradation could produce a negative-positive-negative anomalous precipitation pattern from south to north over China, transfer less moisture to and enhance rising motions over northern China. Therefore, changes in land cover have brought about significant changes in the East Asian monsoon and contributed to the aridity trend over northern China.

References

Alley RB, Mayewski PA, Sowers T, Stuiver M, Taylor KC, Clark TU. 1997. Holocene climate instability: aprominent, widespread event 8200 years ago. Geology 25:483–6.

An ZS, Kukla G, Porter SC, Xiao JL, (1991) Magnetic susceptibility evidence of monsoon variation on the Loess Plateau of central China during the last 130,000 years. Quaternary Research 36, 29-36.

An ZS, Thompson, LG (1998) Paleoclimatic change of monsoonal China linked to global change. In: Galloway, J.N. (Ed.), Proceedings of Global Change. Cambridge University Press, London, pp. 18-41.

An ZS, Kutzbach JE, Prell WL et al (2001) Evolution of Asian monsoons and phased uplift of the Himalaya-Tibetan plateau since Late Miocene times. Nature, 411:62-66

An ZS, Wu XH, Lu YC (1990) A preliminary study on the environmental change in China since 20 ka. Liu D S. Loess. Quaternary Geology, Global Change, Beijing: Science Press, 91-101

Blue Book of Science and Technology in China, No.5 Climate. National Committee of Science and Technology. Scientific and Technical Documents Publishing House, 1990.

Brooks N (2000) Dust-climate interactions in the Sahel-Sahara zone of northern Africa, with particular reference to late twentieth century Sahelian drought. Climatic Research Unit, University of East Anglia, Norwich.

Cao Z. 1986. History of the population of Shaanxi Province. Xi'an: San Qin Press. p 28–31.

Central Meteorological Bureau, 1981, Atlas of flood and drought in China in the last 500 years. Meteorological Press, Beijing, China, p 332

Cho H-K, Na I-S (1979) Changes in climate in Korea during the eighteenth century-centering on rainfall amount (in Korean). J Korean Studies 22: 83–103

Dai AG, Kevin ET, Qian TT (2004) A Global Dataset of Palmer Drought Severity Index for 1870–2002: Relationship with Soil Moisture and Effects of Surface Warming. Journal of Hydrometeorology, 5(6): 1117–1130

Deng JZ et al (1983) General view of agriculture geography of China. Science Press, Beijing, p. 334. (in Chinese)

Dickinson RE, Henderson-Sellers A, Kennedy PJ, Wilson MF (1986) Biosphere-Atmosphere Transfer Scheme (BATS) for the NCAR community climate model. NCAR Tech. Rop. NCAR/TN275+STR. Boulder (Colorado): NCAR, 69pp.

Dickinson RE, Henderson-Sellers, A, Kennedy, P.J. 1993. Biosphere-Atmosphere Transfer Scheme (BATS) version 1e as coupled to the NCAR Community Climate Model. Technical Note NCAR/TN-387+STR, NCAR, Boulder, CO.

Ding Z.L., E. Derbyshireb, S.L. Yang, J.M. Sun, and T.S. Liu (2005), Stepwise expansion of desert environment across northern China in the past 3.5 Ma and implications for monsoon evolution, Earth and Planetary Science Letters, 237: 45-55

Ding ZL, Yu ZW, Yang SL et al (2000) Coeval changes in grain size and sedimentation rate of eolian loess, the Chinese Loess Plateau. Geophysical Letters, 28:2097-2100

Dong GR, Chen HZ, Wang GY, Li XZ, Shao YJ, Jin J (1997) The evolution of deserts with climatic changes in China since 150 ka B.P. Science in China, Ser.D, 40(4), 370-382

Du NQ, Kong ZC, Shan FS. 1989. Spore pollen analysis from Lake Qing Hai core QH85-14C and the discussion of its paleoclimate and environment. Acta Botanic Sinica 31:803–14.

Fu CB, Diaz H, Dong DF et al (1999) The changes of atmospheric circulation over Northern Hemispheric oceans associated with the global rapid warming of the 1920s. International Journal of Climatology，19: 581-606.

Fu CB, An ZS (2002a) Study of aridization in northern China-a global change issue facing directly the demand of nation. Earth Science Frontiers, 9(2): 271-275.

Fu CB, Wen G (2002b) Several issues on aridization in the northern China. Climatic and environmental research, 7(1): 22-29

Fu CB, Wen G (1999) Variation of ecosystems in East Asia in association with the seasonal, interannual and decadal monsoon climate variability. Climatic Change, 43:477-494

Fu CB (2003) Potential impacts of human-induced land cover change on East Asia monsoon. Global and Planetary Change, 37:219-229

Fu CB (2002) Monsoon Asia: Climate, humans and the environment, IGBP Newsletter, 62:4-7

Fu CB, Yuan HL (2001) An virtual numerical experiment to understand the impacts of recovering natural vegetation on the summer climate and environmental conditions in East Asia. Chinese Science Bulletin, 46(14):1199-1203

Fu, C.B., Zheng, Z.M., 1998. Monsoon regions: the highest rate of precipitation changes observed from global data. Chinese Science Bulletin 43 (8), 662-666.

Fu CB, Wang SY, Xiong Z et al (2005) Regional Climate Model Inter-comparison Project for Asia. Bulletin of American Meteorological Society, 86(2):257-266

Gao Y. 1962. Maximum summer monsoon frequency –Problems related to the East Asian Monsoon. Beijing: Science Press. p 51–9.

Ge QS, Dai JH, He FN, et al (2004) Spatiotemporal dynamics of reclamation and cultivation and its driving factors in parts of China during the last three centuries. Progress in Natural Science. 14(7): 605-613.

Giorgi, F., Marinucci, M.R., Bates, G.T., 1993a. Development of a second generation regional climate model (RegCM2). Part I: Boundary-layer and radiative transfer processes. Monthly Weather Review 121, 2794-2813.

Giorgi, F., Marinucci, M.R., Bates, G.T., Canio, G.D., 1993b. Development of a second generation regional climate model (RegCM2). Part II: Convective processes and assimilation of lateral boundary conditions. Monthly Weather Review 121, 2814-2822.

Glueck, M. F., Stockton, C. W., Reconstruction of the North Atlantic Oscillation, 1429-1983. Int. J. Climatology, 2001, 21(12): 1453-1465.

Guo WD, Fu CB, Su BK et al (2005) An integrated predictive study on the evolution of aridization over northern China in early 21 century. Abstracts of IAMAS Assembly, (Session C2), Aug. 2-11, Beijing, China

Guo Z. T., William F. Ruddiman, Q. Z. Hao, et al., Onset of Asian desertification by 22 Myr ago inferred from loess deposits in China, Nature, 416, 159-163

Guo Z. T., Shuzhen Peng, Qingzhen Hao, et al., Late Miocene–Pliocene development of Asian aridification as recorded in the Red-Earth Formation in northern China, Global and Planetary Change, 41 (2004), 135–145

Huang RH, Xu YH, Zhou LT (1999) The Interdecadal Variation of Summer Precipitations in China and the Drought Trend in North China. Plateau Meteorology, 18(4), 465-476.

Hou JZ, Tan M, Cheng H, Liu TS (2003) Stable isotope records of plant cover change and monsoon variation in the past 2200 years: evidence from laminated stalagmites in Beijing, China. Boreas, 32:304-313.

Ju JH, Lv JM, REN JZ (2006) The Effect of Interdecadal Variations of Arctic Oscillation on Aridization in North China, Plateau Meteorology, 25(1): 74-81 (in Chinese)

Kalnay, E., and Coauthors, 1996: The NCEP/NCAR 40-year reanalysis project. Bullet. Amer. Meteorol. Soc., 77, 437-471.

Kalnay, E., and M. Cai, 2003: Impact of urbanization and land –use change on climate, Nature, 423(6939), 528-531.

Li CY, Li GL (1999) The evolutions of the North Atlantic Oscillation and North Pacific Oscillation and climatic abrupt change during 1960's. Chinese Science Bulletin, 44, 1765-1769

Li XQ, Zhou J, Dodson J (2003) The vegetation characteristics of the "Yuan" area at Yaoxian on the Loess Plateau in China over the last 12000 years. Review of Palaeobotany & Palynology, 124:1-7

Li XQ, Zhou WJ, An ZS, Dodson J (2003) The vegetation and monsoon variations at the desert-loess transition belt at Midiwan in northern China for the last 13ka. The Holocene, 13:779-784.

Lin Q. 1985. Study on ecological-economic problems. Shanghai: People's Press. p 193–209.

Liu HZ, Dong WJ, Fu CB, Shi LQ (2004) The Long-Term Field Experiment on Aridification and the Ordered Human Activity in Semi-Arid Area at Tongyu, Northeast China. Climatic and Environmental Research, 9(2): 378-389

Liu HN, Jiang WM (2004) A preliminary study on the heterogeneous chemical processes on the dust surface and their effect on climate. Chinese J. Geophys. (in Chinese), 47(3): 417-422

Liu JY, Zhuang DF, Luo D, Xiao X (2003) Land-cover Classification of China: Integrated Analysis of AVHRR Imagery and Geophysical Data. Int. J. Remote Sensing, 24(12): 2485-2500.

Liu Tungsheng and Zhongli Ding, Chinese Loess and the plleomonsoon, Annu. Rev. Earth Planet. Sci., 1998. 26:111–145

Liu TS and Ding ZL (1999) Project introduction: Dynamic changes of the environment in arid and semi-arid regions of China during the past 150 Ka and its developing trend in the future, Science Foundation in China, 1: 39-41

Liu Y, Won-Kyu Part, Cai QF, et al (2003) Variation of summer monsoon precipitation over East Asia since 1840 AD-Taking the tree ring samples in China and Korea as examples. Science in China (Series D), 33(6): 543-549 (in Chinese)

Luo ZX et al (2005) An introduction to the dynamics of drought climate over Northwest China, Beijing: Meteorological Press. 232pp. (in Chinese)

Lv DR et al (2002) Composite study on Innermongolia Semi-arid Grassland Soil-vegetation-atmosphere Interaction (IMGRASS), Earth Science Frontiers, 9(2): 295-306

Ma ZG, Fu CB (2003) Interannual characteristics of the surface hydrological variables over the arid and semi-arid areas of northern China. Global and Planetary Change, 37: 189-200

Ma ZG, Shao LJ (2006) Relationship between dry/wet variation and the Pacific Decade Oscillation (PDO) in North China during the last 100 years. Chinese Journal of Atmospheric Sciences (in Chinese), 30(3): 464-474

Ma Zhuguo, Fu Congbin, 2007a, Evidences of Drying Trend in the Global During the later Half of 20th Century and Their Relationship with Large-Scale Climate Background, Science in China (Series D-Earth Sciences),50(5): 776~788

Ma Zhuguo,2007b, The interdecadal dry/wet trend and shift of North China and their relationship to the Pacific Decadal Oscillation (PDO), Chinese Science Bulletin，52（15）：2130~2139

Nicholson SE, Tucker CJ, Ba MB (1998) Desertification, drought and surface vegetation, Bull. Am. Meteorol. Soc., 79: 818-829

Peng ZC, Chen TG, Nie BF et al (2003) Coral δ18O records as an indicator of winter monsoon intensity in the South China Sea. Quaternary Research, 59:285-292

Porter, S.C., An, Z.S., 1995. Correlation between climate events in the North Atlantic and China during the last glaciation. Nature 375, 305-308.

Qian WH, Chen D, Zhu Y, Shen HY (2003a) Temporal and spatial variability of dryness/wetness in China during the last 530 years. Theoretical and Applied Climatology, 76: 13-29

Qian WH, Hu Q, Zhu YF et al (2003b) Centennial-scale dry-wet variations in East Asia. Climate Dynamics, 21:77-89

Qian WH, Zhu YF (2001) Climate change in China from 1880 to 1998 and its impact on the environmental condition. Climatic Change, 50:419-444.

Qin DH (2002) Assessment for Evolution of Environment in Western China, Beijing: Science Press

Ren Liliang, Meirong Wang, Chunhong Li, Wei Zhang, Impacts of human activity on river runoff in the northern area of China, Journal of Hydrology, 2005

Rind, D., Russell, G., Ruddiman, W.F., 1997. The effects of uplift on ocean-atmosphere circulations. In: Ruddiman, W.F. (Ed.), Tectonic Uplift and climate Change. Plenum Press, New York, pp. 121-147.

Ruddiman, W.F., Kutzbach, J.E., 1989. Forcing of late Cenozoic Northern Hemisphere climate by Plateau uplift in southern Asia and the America West. Journal of Geophysical Research 94, 18409-18427.

Sellers PJ, Mintz Y, Sud YC, Dalcher A (1986) A simple biosphere model (SiB) for use within general circulation models. J. Atmos. Sci., 43, 505-531.

Shao XM (1997) Advancements in Dendrochronology. Quaternary Sciences, 3, 265-271

Shen J, Ryo Matsumoto, Wang SM, Zhu YX (2002) Quantitative reconstruction of the Lake water paleotemperature of Daihai Lake, Inner Mongolia, China and its significance in paleoclimate. Since in China (Series D), 45(9): 792-800。

Shi PJ, Yi Y, He CY et al (2004) Land Use Pattern Adjustment under Ecological Security: Look for Secure Land Use Pattern in China. Geographical Review of Japan, 77(12):282-298

Shi YF, Zhang PY (1996) The Current and Influence of Climatic and Sea-Level Changes in China: The Historical Climate of China (Vol 1). Jinan: Shandong Science and Technology Press, 533pp

Shi YF, Kong ZC, Wang SM et al (1993) Mid-Holocene climate and environments in China, Global and Planetary Change, 7: 219-233

Shi YF, Kong ZC (1992) The Climates and Environments of Holocene Megathermal in China. Beijing: China Ocean Press, 1-211

Shi Yafeng, Yu Ge, Liu Xiaodong, Li Bingyuan, Yao Tandong (2001) Reconstruction of the 30-40 Ka BP enhanced Indian monsoon climate based on geological records from the Tibetan Plateau, Palaeogeography, Palaeoclimatology, Palaeoecology, 169: 69-83

Steffen W, Sanderson A, Tyson PD et al (2004) Global Change and The Earth System: A planet under pressure. Springer-Verlag, Berlin, 638pp

Sun DH., Wu XH, Liu TS (1996) Evolution of the summer monsoon regime over the Loess Plateau of the last 150 ka. Science in China, Series D 39 (5), 503-511.

Sun DH, Liu TS, Cheng MY., An ZS, Shaw J (1997) Magnetostratigraphy and paleoclimate of Red Clay sequences from the Chinese Loess Plateau. Science in China, Series D 40, 337-343.

Sun DH, Shaw J, An ZS, Cheng MY, Yue LP (1998) Magnetostratigraphy and paleoclimatic interpretation of a continuous 7.2 Ma Late Cenozoic eolian sediments from the Chinese Loess Plateau. Geophysical Research Letters 25 (1), 85-88.

Sun HL, et al., Theory and practice of environmental construction in China, Scientific Press, 2004

Tan M, Liu TS, Hou JZ et al (2003) Cyclic rapid warming on centennial-scale revealed by a 2650-year stalagmite record of warm season temperature. Geophysical Research Letters, 30(12): 1617-1620

Tao SY, and Chen LX (1987) A review of recent research on the East Asian summer monsoon in China, Monsoon Meteorology , Edited by C. P. Chang, and T. N. Krishnarmurti, Oxford University Press, 60-72.

Walker, G..T, Bliss, E. W., 'World Weather V', Mem. Roy. Meteorol, Soc., 1932, 4, 53-84.

Wang HJ (2000) The interannual variability of the East Asian monsoon and its relation with SST in a coupled atmosphere-ocean-land climate model. Advances in Atmospheric Sciences, 17: 31-47

Wang SW, Zhao ZC, Chen ZH, Tang ZG (1987) Drought/flood variations for the last two thousand years in China and comparison with global climatic change. In: Ye DZ, Fu CB, Chao JP, Yoshino M (eds) The climate of China and global climate. China Ocean Press, Springer Berlin Heidelberg New York, pp 20–29

Wang SW, Zhu JH, Cai JN (2004) Interdecadal Variability of Temperature and Precipitation in China since 1880. 21(3): 307-313

Wang SM, Feng M (1991) Environmental change recorded in the Daihai Lake and its relationship with the change in strength of the southeast monsoon. Science in China (Series B), 21(7): 759-768

Wang SM, Ji L (1995) Lake Hulun: study on paleolimnology. Hefei. University of Science and Technology Press, China. p 87–93.

Wang T, Chen GT, Qian ZA, Yang GS, Li DL (2001) The Situation of Dust Storms and its Strategy in North China. Bulletin of the Chinese Academy of Sciences, 5: 343-348

Wu XD (1990) Tree Ring and Climate change. Beijing: Meteorology Press
Xue F (2001) Interannual to Interdecadal Variation of East Asian Summer Monsoon and its Association with the Global Atmospheric Circulation and Sea Surface Temperature. Advances in Atmospheric Sciences, 18(4): 567-575
Yang SL, Ding ZL (2003) Color reflectance of Chinese loess and its implications for climate gradient changes during the last two glacial-interglacial cycles. Geophysical Research Letters, 30:61-64
Yang XP, Williams MAJ (2003) The ion chemistry of lakes and late Holocene desiccation in the Badain Jaran Desert, Inner Mongolia, China. Catena, 51:45-60.
Yang XQ, Zhu YM (2006) Interdecadal Climate Anomalies in East Asia and China Associated with the Pacific Decadal Oscillation, submitted to Adv. Atmos. Sci.
Yang XQ, Xie Q, Zhu YM et al (2005) Decadal-to-interdecadal variability of precipitation in North China and associated atmospheric and oceanic anomaly patterns. Chinese Journal of Geophysics, 48: 789-797
Ye DZ, Chou JF, Liu JY et al (2000) Causes of Sand-stormy Weather in Northern China and Countermeasures, ACTA GEOGRAPHICA SINICA, Vo l. 55, No. 5, 513-521
YU Ge, XUE Bin, WANG Sumin & LIU Jian, Lake records and LGM climate in China, Chinese Science Bulletin Vol. 45 No. 13 July 2000, 1158-1164
Yu G., Xue B, Liu J et al, Lake Records from China and the Palaeoclimate Dynamics (in Chinese), Beijing: China Meteorology Press, 2001. 196pp
Zhai PM, Pan XH (2003) Trends in temperature extremes during 1951-1999 in China. Geophysical Research Letters, 30(17): 1913, doi: 10.1029
Zhang DE (1983) The variation of drought/flood for different regions and their relationship to winter temperature during the last 500 years in China. In: Collected Papers of Meteorological Science and Technology (IV). Beijing: Chinese Meteorological Press, 40-46
Zhang'D (1988) The method for reconstruction of the dryness/wetness series in China for the last 500 years and its reliability. In: Zhang J (ed) The reconstruction of climate in China for historical times. Science Press, Beijing, China, pp 18–30
Zhang JY, DONG Wenjie, FU Congbin, et al (2005) Impact of land surface degradation in northern China and southern Mongolia on regional climate, Chinese Science Bulletin. 50(1): 75—81
Zhang JC (1991). Climate of China. Beijing: China Meteorological Press
Zhang PY, Wang Z, Liu XL, Zhang SH (1994) The modes of climate change for the. past 2000 years in China. Sci. China (Ser. B), 24, 998-1008.
Zhang QY, Wei J, Tao SY (2003) The Decadal and Interannual Variations of Drought in the Northern China and Association with the Circulations. Climatic and Environmental Research, 8(3): 307-318
Zhang XS, Yang DA (1995) Allocation and Study on Global Change Transects in China. Quaternary Sciences, 1, 43-52

Zhou WJ, Dodson J, Head MJ, Li BS, Hou YJ, Lu XF, Donahue DJ, Jull AJT (2002) Environmental variability within the Chinese desert-loess transition zone over the last 20000 years. The Holocene, 12:107-112.

Zhou, W.J., Donahue, D.J., Porter, S.C., Jull, A.J.T., Li, X.Q., Stuiver, M., An, Z.S., Matsumoto, E., Dong, G.R., (1996) Variability of monsoon climate in East Asia at the end of the Last Glaciation. Quaternary Research 46, 219-229.

Zhou, W.J., An, Z.S., Porter, S.C., Donahue, D.J., Jull, A.J.T., (1997) Correlation of climatic events between East Asia and Norwegian Sea during the last deglaciation. Science in China, Series D 40, 496-501.

Zhou Weijian et al., (2001) Environmental and climatic changes as recorded in geological sediments from the arid to semi-arid zone of China, Radiocarbon, 43(2B), 619-627

Zhu KZ (1973) A preliminary study on the climate fluctuations during the past 5000 years in China. Science in China, 2: 291-296

Zhu, Y. F., (2003) The regional division of dryness/wetness over eastern China and variations of dryness/wetness in northern China during the last 530 years. Acta Geographica Sinica (in Chinese), 58(Supplement): 100-107.

Zhu ZD, Wang T. (1992) The theory and practice of Chinese desert research. Quaternary Sciences 5: 97–106.

Zhu ZD (1985) Status and trend of desertification in northern China, Journal of desert research, 5(3), 3-11 (in Chinese).

Chapter 6 Effects of the Tibetan Plateau on the Climate of China

6.1 Introduction

Tibetan Plateau (TP), the highest Plateau in the world, covers nearly 2.5 million km^2, and its height reaches up to the middle of the troposphere. Such a huge block will evidently affect atmospheric motions. Since the end of the 1940's, a series of studies have been carrying out, aiming at the dynamic and thermodynamic effects of the TP on the general circulation, and many important findings have been made. In the period prior to the middle 1950's, studies on the plateau meteorology were mainly focused on its dynamical effects. Charney and Eliassen (1949), Bolin (1950) and Yeh (1950) studied the dynamic effects of the Plateau in the winter half-year. It had been found that the excitation of the quasi-stationary ultra-long waves in winter, the maintenance of the East Asian trough, and the formation of the Aleutian high in the stratosphere are all related to the existence of the Plateau. Qian et al (1988) performed a series of numerical experiments to investigate the dynamic effects of the TP. Their results indicated that the air flow tends to go around the TP rather than go over it; as for the Rocky Mountains, the flow tends to go over rather than go around it. These results coincide with Trenberth and Chen's theoretical research (1988). However, in the middle of 1950's, it was found that the TP is a huge heat source in summer (Koo and Ye, 1955; Yeh et al., 1957; Flohn, 1957). Thereafter Chinese scientists have been carrying out many studies on the effects of this heat source on atmospheric general circulation (Ye et al., 1974; Ye et al., 1979; Ye, 1982; Fu and Fletcher, 1985; Wu et al, 1997b; Wu and Zhang 1998; Zhang et al, 2002; Qian et al, 2003; Zhang et al, 2006; Xu and Qian, 2006, etc). Some of these studies are presented in the following sections.

In the 1970's, several cooperative researches were organized in China. It was found that the TP area not only exhibits particular features in synoptic meteorology and climate, but also plays different roles in the global general circulation during different seasons. A systematic summary of the studies performed from 1960's to 1970's was published in the book

The Meteorology of the Qinghai-Xizang (Tibet) Plateau by Ye, Gao, and their colleagues in 1979. Considering the importance of TP in modulating the regional and global climate, two scientific experiments on the TP meteorology have been organized by Chinese scientists during the past 30 years. The first Qinghai-Xizang Plateau Meteorological Experiment (QXPMEX) was launched during the summer of 1979. It was the first time that various valuable intensive observational data over the TP were obtained. The second Tibetan Plateau Experiment (TIPEX) program was conducted during May to August 1998, which mainly focused on the monitoring of the planetary boundary layer (PBL) over the TP using more sophisticated sounding techniques. Many advanced instruments had been employed, such as wind profilers, 6-7 level gradient observing towers (20 m), Bowen ratio systems, ultrasonic anemometers/thermometers, fluctuating hygrothermoscopes, infrared thermometers, digital Doppler acoustic radars, tethersonde profilers, low-level radiosondes, optical raingages and various radiometers etc. During two periods of the TP field experiments, many intensive atmospheric observational data and reliable PBL data had been obtained at plateau observation stations. TIPEX observations show that there exists apparent humidity inversion phenomenon in the plateau PBL, strong solar radiation related to the distribution of cumulus and its radiative effect which seldom found in other areas, heat imbalance phenomenon, strong mesoscale convection and rapidly developed unstable stratification after the sunrise. With the efforts of meteorologists, the material has been subjected to careful analysis using advanced techniques, and many new results have been obtained. This greatly increased our knowledge of the Plateau's meteorology, especially in summer season. The observational results and the associated analyses are summarized in several books (Zhang et al., 1988; Tao et al., 2000a, 2000b, 2000c).

In addition to observational studies, numerical modeling is also an effective method to investigate the effect of the TP. Hahn and Manabe (1975) revealed the important effect of the TP on South Asian monsoon circulation by using climate model. Many other numerical experiments have also been conducted by using climate models during the past years to understand the mechanism of the mechanical and thermal forcing of the Plateau on the climate variability. Kuo and Qian (1982) investigated the relative importance of radiative heating, deep cumulus condensation, orography, and initial conditions for the development of the mean monsoon circulation from June to July. The climatic effects of the TP uplift have been investigated by Kutzbach et al (1989, 1993), Ruddiman and Kutzbach (1989), Broccoli and Manabe (1992), Zhang and Qian (1999), Chen et al (1999), Liu and Yin (2002) and Manabu et al (2004). They found that the Plateau uplift has significant impact on the Asian monsoon climate, midlatitude

Northern Hemisphere dry climate and Pacific sea temperature. On the other hand, many studies have been focused on the thermal and hydrological characteristics of the TP, snow cover on the TP and their climatic effects (Yanai and Li, 1994; Yatagai, 2001; Tsujimura et al, 2001; Zhao and Chen, 2000a, b; Zhao and Chen, 2001; Qian et al, 2002; Qian et al, 2003; Wu and Qian, 2003; Qian et al, 2005; Qin et al, 2006).

In this chapter, we will summarize and report the recent studies made by Chinese scientists about the effects of the TP on regional climate, especially on China climate anomaly. The thermal characteristics of the TP are given in section 2. The effects of the TP on the Asian monsoon are discussed in section 3. Snow anomalies over the TP and its climatic effects are presented in section 4. This is followed by a discussion in section 5 and 6 on the South Asian High (SAH) and East Asian subtropical westerly jet (EASWJ), two components of Asian monsoon which are closely related to the heating effect of the TP. All above sections (section 2 to section 6) mainly focus on the thermal effects of the TP. Section 7, however, focuses on the role of the mechanical forcing of the TP in the formation of East Asian continental stratus clouds.

6.2 Climatic features of atmospheric heat source/sink over the TP

In the mid-1950's, Yet et al. (1957) and Flohn (1957) found independently that a huge heat source exists over the TP in summer. At that time none of them found this phenomenon through direct observations. With the increase of observational data, some quantitative analysis of the heat source over the Plateau appeared to be possible (Yeh et al, 1979; Chen et al, 1985; Yanai et al, 1992). However, the long time series of the heat regime over the TP had not been obtained. Recently, Zhao and Chen (2001) calculated the 35-year atmospheric heat source/sink over the TP by using the 1961-1995 monthly averaged meteorological data from 148 surface stations on the TP and its surrounding areas. Their results are presented as follows.

6.2.1 Computational methods of the atmospheric heat source/sink

The heat source/sink for a given air column is defined as:

$$< Q_1 >= SH + R_{net} + LP \tag{6.1}$$

where *SH* is the sensible heat flux at the surface; R_{net} the radiation in the atmosphere and *LP* the condensation-released latent heat; they are defined as follows:

$$SH = C_p \rho C_h V(t_s - t_a) \tag{6.2}$$

$$LP = \rho C_q V(q_s(t_s) - q_a) \tag{6.3}$$

$$R_{net} = S_0 \downarrow (1 - A_P) - S \downarrow (1 - A) + R_e - R_\infty \tag{6.4}$$

where C_p denotes the specific heat constant of air at constant pressure; ρ the surface air density; C_h the turbulent heat exchange coefficient; $V = \sqrt{u^2 + v^2}$ the surface scalar wind; t_a the temperature at screen height; t_s the soil temperature at 0 cm; q_s the saturation specific humidity of surface air at t_s; q_a the specific humidity of surface air; C_q the vapor turbulent exchange coefficient at surface; $S_0\downarrow$ the solar radiation arriving at top of the atmosphere; $S\downarrow$ the total radiation at the surface; A_p the planetary albedo; A the surface albedo, R_∞ the outgoing longwave radiation at top of the atmosphere; R_e the effective radiation at the surface. It is difficult to estimate C_h and C_q in a direct manner. For climatic study Williamson et al. (1987) assumed C_q to take as the form

$$C_q = D_w C_h$$

where D_w is a rectification factor related to soil humidity with $0 \le D_w \le 1$. Referring to Williamson et al. (1987), the TP underlying surface is divided into three classes. The corresponding value of D_w is given as follows.

$$D_w = \begin{cases} 0.1 & for \quad grassland, \quad bush \\ 0.05 & for \quad wildness \\ 0.25 & for \quad others \end{cases}$$

The C_h is computed by multivariate stepwise regression scheme for surface air temperature, wind, relative humidity and total cloudiness as follows:

$$C_h = a_1 t_0 + a_2 v + a_3 q + a_4 c_l + a_5$$

More details about the computation of above parameters can be found in Yeh et al. (1979) and Zhao et al (2000a, 2000b).

6.2.2 Climatological distribution of the atmospheric heat source/sink

Fig.6.1 illustrates the monthly distributions of the $<Q_1>$ values averaged over 1961~1990. It is seen from Fig.6.1a that the $<Q_1>$ values are negative all over the TP in January, which means that the air column over the TP loses energy and becomes a cold source. There are several centers with larger values around 35°N, 93°E, 34°N, 98°E and 29°N, 101°E. In February, $<Q_1>$ values over the TP begin to increase and some parts of the southern TP change to heat source. In March, the high-value centers still locate the southern parts of the TP around Cona (28°N, 92°E) and Gongshan County (27.7°N, 98.6°E). In April (Fig.6.1b), the heating center at Cona shifts noticeably westward to Lhaze (29.1°N, 87.6°E) with its value increasing to 81 $W \cdot m^{-2}$ and the heating center in the Gongshan county still remains there with the value of 126 $W \cdot m^{-2}$ that is the annual maximum. In May, the positive $<Q_1>$ cover the TP. The strongest heating center in the southwestern TP still appears around Lhaze. In the eastern TP, however, the heating center around the Gongshan County greatly reduces, indicating that the heating center moves westward. In June, due to the release of latent heat associated with convection development, the maximal heating center appears at Jiulong County (29°N, 101.3°E) with the value of 160 $W \cdot m^{-2}$. In the meantime, the heating center in the southwest part moves westward further from Lhaze to Burang (30.5°N, 81.4°E) with its central value increasing to 130 $W \cdot m^{-2}$, which is the annual maximum in the southwest part of the TP. This is the second westward obvious movement of the heating center in the southwestern TP. After the Asian summer monsoon onset, the heat source in the southwest part of the TP starts to be weakened in July (Fig.6.1c). Its heating center retreats eastward to 85°E and then remains there till October with the central value diminishing gradually. On the contrary, the heat source over the eastern TP continues to increase in July. Since August the atmospheric heat sources over the whole TP start to be weakened and to October the atmosphere acts as a cold source over the majority of the TP (Fig.6.1d).

Since the variation of atmospheric heat source in the eastern Plateau is different from that in the western Plateau, Table 6.1 gives the monthly values of various type of heating for the southwest and east part of the TP and the whole TP. ETP denotes the area to the east of 90°E with the elevation above 3000m. SWTP denotes the area to the west of 90°E and south of 33°N, with the elevation above 3000m, and the whole TP is the sum of ETP and SWTP. It is seen from Table 6.1 that the whole TP atmosphere acts as a heat source from April to September with its peak value of 78 $W \cdot m^{-2}$ in July and as a cold source in the other months with its peak value

of -72 $W \cdot m^{-2}$ in December. Both surface sensible heat and latent heat of condensation are positive all year around, which indicates that the TP is a heat source in comparison with the atmosphere over the TP all year around, whereas the atmospheric net radiation results in the atmospheric cooling. In winter, the sensible heat and latent heat are too weak to compensate for the heat loss due to the radiation, thereby generating an atmospheric cold source. In spring, with the increase of the sensible and latent heat, the atmospheric column over the TP becomes a heat source and the heat source strengthens gradually. In the southwest part of the TP, the change of heating is mainly due to the remarkable increase of the sensible heat in spring because the latent heat is weaker in this season. In July and August, although latent heat grows rapidly, the atmospheric net radiation and sensible heat are obviously reduced, which is responsible for the great decrease of the heat source in the southwest TP in this period. Different from southwestern TP, the sensible heat over the eastern TP is weaker and increases slowly. Nevertheless, the sensible heat is still a main factor responsible for the $<Q_1>$ increase in the east part from late winter to spring. In summer the latent heat intensifies noticeably over east of the TP while the sensible heat decreases there. Thus latent heat acts as a main factor that makes the heat source in the east part continue increasing during summer.

6.2.3 Temporal variation of atmospheric heat source/sink

The analysis on the temporal variation of seasonal and annual mean $<Q_1>$ values of the whole TP during 1961~1995 indicates that the $<Q_1>$ value of winter ranges from -65 to -40 $W \cdot m^{-2}$ (figure not shown). It exhibits a greatly decreasing trend in 1960s and early 1970s with the minimum value of -66 $W \cdot m^{-2}$ in 1977 and a noticeable rise from 1978 to 1983 with the sub-maximum value of -48 $W \cdot m^{-2}$ in 1983. In spring, the $<Q_1>$ values are positive, which indicates a heat source, and show a decreasing trend in the 1960s with the minimum of 3 $W \cdot m^{-2}$ in 1969. A significantly rising trend is observed from the 1970s to the middle 1990s, peaking at 27 $W \cdot m^{-2}$ in 1989. In summer, the $<Q_1>$ value is 50~80 $W \cdot m^{-2}$ and displays a decreasing trend from 1961 to 1977 with a minimum of 53 $W \cdot m^{-2}$ in 1977 and oscillations in later years. It is noticed that the $<Q_1>$ values in summers of 1962, 1974, 1980, 1984, 1987 and 1993 exceed 70 $W \cdot m^{-2}$ with a maximum in 1962, corresponding to the relatively strong heat source over the TP, and in the summers of 1967, 1972, 1975, 1977 and 1978 are below 60 $W \cdot m^{-2}$ with the minimum in 1977, corresponding to the relatively weak heat source. In autumn, the $<Q_1>$ value varies between -15 and -35 $W \cdot m^{-2}$. It shows a conspicuous decreasing trend from 1971 to 1976 and then an in-

creasing trend till the end of the 1980s and again a decreasing trend in the 1990s. Additionally, the $<Q_1>$ values experience more remarkable interdecadal variation in winter, spring and autumn. All values of these four seasons have the minimums or sub-minimums around 1976~1977. This feature is also seen from the temporal curve of the annual mean $<Q_1>$ values over the TP (Figure not shown). The annual mean $<Q_1>$ value exhibits a decreasing trend in the 1960s and an increasing trend in late 1970s and early 1980s. The obvious interdecadal change occurs around 1977. The annual mean $<Q_1>$ averaged over the periods of 1967~1976 and 1978~1987 are -3.6 and 1.6 $W \cdot m^{-2}$, respectively. The analysis using the moving *t*-test method for these two means shows that the difference between them is remarkable (at a significance level of 0.001) and maximizes in this case.

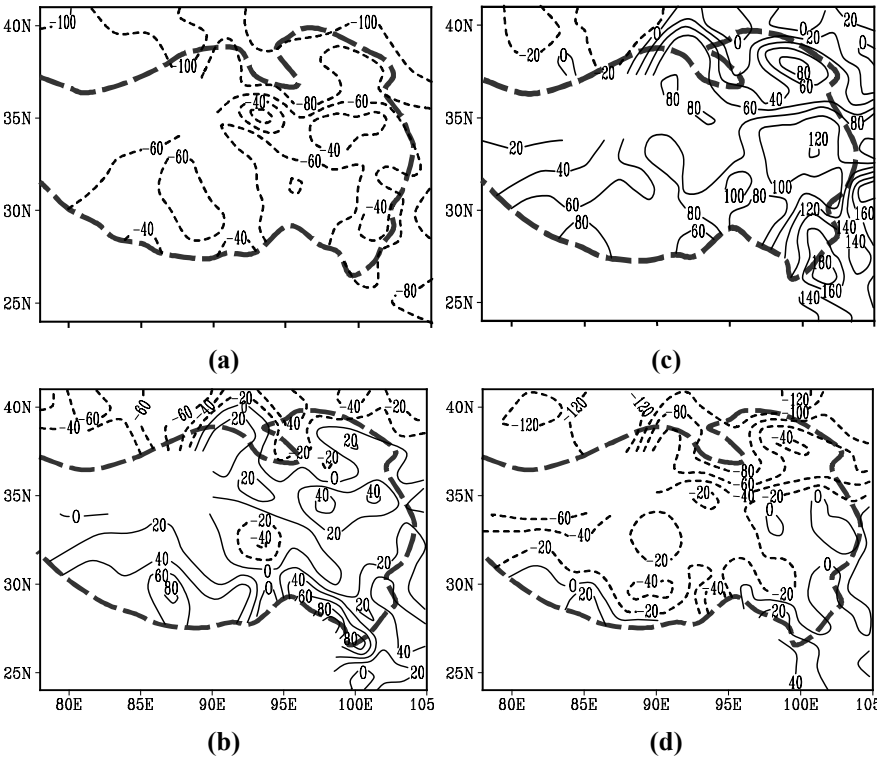

Fig. 6.1 Climatological distribution of $<Q_1>$ for **(a)** January, **(b)** April, **(c)** July, **(d)** November. The thick dashed line is the 3000m contour of topography (Zhao and Chen, 2001)

Table 6.1 The climatological mean monthly *SH*, R_{net}, *LP* and $<Q_1>$ for the southwest and east parts of the TP and the whole TP. units: $W \cdot m^{-2}$ (Zhao and Chen, 2001)

Month		Jan	Feb	Mar	Apr	May	Jun	Jul	Aug	Sep	Oct	Nov	Dec	Annual mean
SWTP	SH	6	31	62	88	100	99	73	61	54	36	15	1	52
	Rnet	-68	-58	-59	-58	-54	-53	-79	-83	-74	-63	-71	-79	-67
	LP	3	5	6	5	12	29	64	67	31	9	3	3	20
	$<Q_1>$	-59	-22	10	36	57	75	58	45	11	-18	-54	-75	5
ETP	SH	9	22	39	55	64	58	50	44	33	24	14	6	32
	Rnet	-73	-67	-68	-63	-56	-56	-60	-68	-78	-77	-77	-80	-69
	LP	3	5	11	20	39	76	91	77	63	23	5	3	35
	$<Q_1>$	-60	-40	-19	12	47	79	81	53	19	-30	-58	-71	1
TP	SH	9	24	45	63	73	69	56	48	38	27	14	5	39
	Rnet	-72	-64	-66	-62	-55	-55	-65	-72	-77	-74	-75	-80	-69
	LP	3	5	9	17	32	64	84	75	55	20	4	3	31
	$<Q_1>$	-60	-34	-12	18	50	78	75	51	17	-27	-57	-72	2

6.3 Roles of the TP in Asian monsoon

6.3.1 Sensible heat driven air-pump (SHAP) over the TP

The TP has a large impact on the atmospheric circulation because of its size, height and latitudinal position. Firstly the Plateau is situated in the subtropical belt where the prevailing current is weak in summer, thus the heating to the atmosphere there will not be carried away quickly. Secondly, the heat produced there is directly added to the middle troposphere and used only to heat half of the atmosphere. Furthermore, the strong convergence near the surface and divergence in the upper troposphere act as important vorticity source near the surface and sink in the upper troposphere in summer (Ye and Wu, 1998). Numerical experiment of Hahn and Manabe (1975) showed that without the presence of the TP in a GCM, there should be no occurrence of the present-day Asian monsoon, and the main rain band over Asia should shift southward. As seen from the former section, the sensible heat over the TP has a dramatic increase in spring (Mar, Apr, and May) and reaches its maximum in May. The elevated heat source will have a remarkable effect on the general circulation. So it can be deduced that the disappearance of elevated heat source, comparing with the mechanical forcing of the TP, should be mainly responsible for the disappearance of

the Asian monsoon and the southward retreat of main rain belt. This deduction can be confirmed by two numerical experiments (Wu et al. 1997) which is presented in the following texts.

The model and the experimental schemes

The model used is the atmospheric component of the global ocean-atmosphere-land coupled GCM (GOALS) developed at the Institute of Atmospheric Physics of Chinese Academy of Sciences (Wu et al., 1997a). The GOALS (R15L9) is a spectral model with rhomboidal truncation at wave-number 15. It has 9 vertical layers with σ coordinate. The lowest σ level is about 70 m from the earth surface. The prescribed monthly means of sea surface temperature (SST) and sea ice are interpolated to Gaussian grid by using the Atmospheric Model Intercomparison Project II (AMIP II) data. The vegetation is also prescribed according to observation. In order to investigate the effects of sensible heat on the monsoon circulation, two experiments are designed. One is the control experiment (CON) which is integrated from the January 1st 1979 to December 31st 1998 with AMIP II SST and sea ice data. Another is the no sensible heating experiment (NSH) in which the TP is kept unchanged but the surface sensible heating was removed from the atmospheric thermodynamic equation. Namely, the NSH is the same with CON except no sensible heating over the TP. The output variables of two experiments are saved as monthly mean quantities.

The influence of SHAP on low level circulation

In the control experiment (CON) in which the sensible heat on the Plateau is kept, the simulated stream field is close to the observed climate (Figure not shown). By using the 10-year outputs of the CON, the annual mean low level stream field was subtracted from the monthly mean stream field to obtain the seasonal departure from the annual mean. Comparing January departure with July one, it can be seen that the winter circulation pattern are almost opposite to summer pattern at middle-low latitudes. The surface air always flows from the winter hemispherical continents, passes through the oceans, crosses the equator, to the summer hemispherical continents. The major convergence/divergence centers of Northern Hemisphere are located in the North Africa-Arabian peninsula, TP, central part of North Pacific and Latin America. However, the southern hemispheric ones are located in the southern part of Africa, Australia and Bolivia Plateau. The low latitude monsoons are the dominant wind systems which shuttle between these convergence and divergence centers. According to the configuration of these convergence and divergence centers, the wind systems

can be divided into five monsoon systems: South America-North Africa monsoon system, South America-Latin America monsoon system, Australia-West Pacific monsoon system, Australia-TP monsoon system (East Asian monsoon) and South Asia-South Africa monsoon system (South Asian monsoon).

Another notable characteristic in the departure field is the difference of large scale vertical motion over the TP between January and July. No matter in January or July, the TP and its vicinities are the strongest departure center of vertical motion by comparing with other areas in the world. The strongest departure of downdraft and updraft appears in January and July, respectively. Computation indicated that the TP cools the atmosphere at a rate of 1°C/d (50 $W \cdot m^{-2}$) in January and warms the atmosphere at a rate of 2°C/d (80$W \cdot m^{-2}$) in July (Wu et al., 1996). It is the sensible heat exchange between the surface of the TP and atmosphere that cools/warms the atmosphere and produces downdraft/updraft like a drain/inspiratory pump in January/July. As a result, the SHAP regulates the direction of mass exchange not only between the TP and the semipermanent atmospheric action center over north Pacific but also the other three monsoon regions except the South Africa-North America and Latin America. The TP SHAP transports the continental air to the southern hemisphere along three paths: (1) the continental air originates from the hinterland of the TP, flows southward along the Arabian Sea-Somali coast, passes the South Indian Ocean, and then converges in the southern part of Africa; (2) the continental air originates from the South China, flows southward along the South China Sea-Bay of Bengal, traverses the equatorial central Indian Ocean to Australia; (3) the continental air originates from Mongolia and Northeast China, flows through Japan and arrives the central part of Northern Pacific, traverses the equator to South Pacific, and then converges with the air flowing to Australia. In July, however, these three air currents flow back to the hinterland of the TP along the opposite directions from that in January. So the TP SHAP, South Africa Pump and Australia Pump form three driving sources of low level atmosphere and dominate the seasonal variation of general circulation over these regions from West Pacific, East Asia and South Asia to Southeast Africa, South Indian Ocean and Australia.

In the NSH run, the ascending motions are remarkably weakened due to switching off the SHAP on the TP with elevation above 3000m in July. The difference of divergence (NSH-CON) at 0.991 σ level shows that a strong differential divergent center appears just over the TP surrounded by several convergent centers (Figure not shown). The difference of vorticity is well matched with that of divergence. The notable anticyclonic anomaly appears over the TP, and the cyclonic anomalies cover the South China,

Indochina and Indian peninsula at 0.991 σ level. As a result, precipitation is decreased over the TP and North China and increased over the South China, Indochina and Indian peninsula. In general, SHAP has most significant influences on low level circulation over the TP and its south and east parts. With the appearance of SHAP, the East Asian Monsoon extends northward to North China and the strong precipitation belt shifts toward the TP.

The influence of SHAP on upper level circulation

In the CON run, the 200hPa mean stream field in July exhibits two wave characteristics at the Northern low-middle latitudes, with two anticyclonic centers over the TP and Mexico and two troughs in the northeast-southwest direction over the Pacific and Atlantic Ocean, respectively. The simulated 200hPa stream field is close to the observation in July. In the NSH run, a ridge is found over Ural; the trough of Northeast Asia disappears; a trough appears over Bering Strait and the Baffin Bay. However, the most significant change is that the SAH disappears over the TP; the anticyclone center appears over South China-South China Sea instead. The cross-equatorial flow originally located in the Western Pacific disappears. The pattern of East Asian summer circulation in the NSH run is similar to the observational pattern in early spring. Thus it can be concluded that the maintenance of SAH is closely related to sensible heating over the TP. When the surface sensible heating over the Plateau is removed, the differential field between the CON run and the NSH run shows that a strong anticyclonic center appears just over the Plateau, and a Rossby wave ray with zonal wave number 2 is generated over the globe (Figure not shown). The wave ray emanating from the Plateau propagates eastward. It bends southward over the Northern Pacific, enters the tropics through the westerlies at the bottom of the tropical upper-tropospheric trough, and then propagates into the southern hemisphere. This wave ray splits over the Northern Pacific. The northern branch propagates further eastward. It passes over Alaska and Baffin Bay, then bends southward over the North Atlantic, and disappears over the north of Cap Verde due to the obstruction of the axis of the subtropical high (where $u = 0$) and the easterlies to its south. Wherever this wave reaches, the distribution of troughs and ridges in the stream field is disturbed (figures not shown). Therefore, the above results suggest that the influence of the anomalous elevated surface heating of the TP on climate can be global.

Comparing with the CON run, the NSH run exhibits a notable positive anomaly of 200hPa vorticity over the TP with its intensity over $+2\times10^{-5}s^{-1}$, and negative anomalies around South China, Indochina peninsula and South

Asia (Figure not shown). The pattern of 200hPa circulation anomaly is well matched with that of low level circulation. The upper tropospheric convergence and positive vorticity anomaly correspond to low tropospheric divergence and negative vorticity anomaly, which results in less precipitation in the NSH run, and vice versa. At the middle-high latitudes, the positive vorticity anomalies over TP emanate from the TP to the globe by virtue of Rossby wave and its propagation paths are consistent with that of the anomaly of stream filed. The temperature section along 33.3°N shows that switching off SHAP exerts a global scale influence (Figure not shown). The global tropospheric temperature becomes cooler than normal except Atlantic Ocean. Whereas, the sharpest change of temperature appears over the TP and its vicinities. The averaged tropospheric temperature decrease is more than 1°C along 60°E~120°E. The sharpest decrease approaches 6°C near the surface of the TP. Contrarily, the maximum increase of stratospheric temperature is more than 5°C over the TP, indicating that the tropopause height decreases and anomalous descending motion prevails over the TP. The anomalous zonal wind section (Figure not shown) illustrates a large difference along 10°~50°N. An easterly anomaly is located in the south of the TP and weak westerly anomaly is located in the north of the TP below 500hPa, but a contrary distribution appears above the 500hPa level. As a result, there is an anticyclonic anomaly at low troposphere and a cyclonic anomaly at upper troposphere. The vertical section of differential circulation between NSH and CON along the same longitude also indicates that the anomalous descending motion appears over the TP accompanied by anomalous upper tropospheric convergence and low tropospheric divergence (figure not shown).

It can be concluded that the closure of SHAP gives an impact on general circulation mainly through two mechanisms: firstly, the closure of SHAP induces a convergence at upper troposphere and descending motion over the TP which in turn results in a divergence at low troposphere and precipitation anomaly in its vicinities; secondly, the closure of SHAP induces a sharp cooling of low tropospheric atmosphere which will induce a positive upper tropospheric vorticity anomaly due to the direct proportional relationship between the local variation of vorticity and variation of the heating rate with height. Thus, the upper tropospheric vorticity is significantly strengthened and affects the global climate by virtue of the frequency dispersion of Rossby wave.

The influence of SHAP on seasonal variation and Asian monsoon

In the 1950's Ye et al. (1959) found that the seasonal transition from winter to summer of the atmospheric circulation over South Asia is abrupt:

within a few days the mid-latitude westerly jet, the axis of the subtropical anticyclone, and the tropical easterlies all shift northward abruptly by 5 to 10 degrees of latitude. The seasonal variation of zonal wind and the ridge of subtropical high in the CON run also indicate the abrupt seasonal transition (Figure not shown). In the CON run, easterlies are maintained near the equator, a westerly jet, at 35°N and the axis of the subtropical anticyclone (u = 0) at 10°N during the period from winter to early spring. At the end of May and the beginning of June, however, the axis of the subtropical anticyclone suddenly shifts northward from 10° to 27°N and the westerly jet moves correspondingly from 35° to 45°N. These results agree fairly well with those obtained by Ye et al. (1959), and indicate that the model is capable of simulating the mean climate state. On the other hand, in the NSH run, the axis of the subtropical anticyclone shifts from 10°N in May to 20°N in July in two months and varying smoothly. This then suggests that the abrupt seasonal change of such Asian circulation system may be mainly attributed to the elevated surface heating of the TP.

Following Li and Yanai (1996), Wu et al. (1997b) adopted the difference between 30° and 5°N of the mean temperature averaged from 200 to 500hPa (ΔT) to represent the thermal characteristics of the upper troposphere along the tropical and subtropical zones. A positive ΔT can be used to indicate the Asian summer monsoon period. By using the NCEP/NCAR monthly mean reanalysis data from 1982 to 1995, the monsoon period is estimated to persist from the middle of May to September (Fig.6.2a). By using the model output of the CON run, the simulated monsoon period is from the middle of May to the middle of September (Fig.6.2b), fairly close to the analysis based on the reanalysis data shown in Fig.6.2a. In the NSH run, however, the monsoon does not start until early June, and ends as early as in the middle of August (Fig.6.2c). The summer monsoon period is shortened by half in the NSH run compared to that in the CON run and in the "observations". In addition, the most persistent longitude of the monsoon period also shifts from the Plateau region in the CON run to about 120°E in the NSH run. These results imply that the elevated surface heating of the TP is very important for the location and persistence of the Asian monsoon.

The SHAP is driven by the sensible heat exchange between the plateau surface and the atmosphere over the TP. Since the sensible heat occurs at the middle-low troposphere about 3 kilometers high, the elevated heating source can effectively regulate the seasonal variation of atmosphere. In winter, the cooling effect of the plateau surface pumps the upper tropospheric air toward the TP and causes the descending motion, in turn pumps the air out of the TP. In summer, the heating effect of the plateau pumps the low tropospheric air toward the TP and, consequently, causes the as-

cending motion and divergence at upper troposphere. SHAP effectively regulate the Asian winter monsoon and summer monsoon by virtue of the cycle of pumping into air and pumping out air.

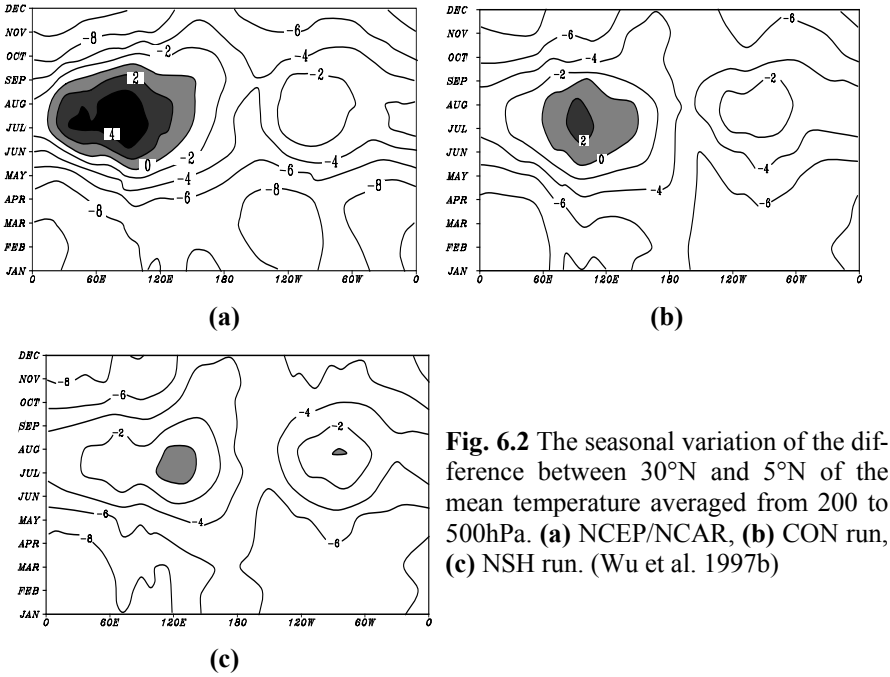

Fig. 6.2 The seasonal variation of the difference between 30°N and 5°N of the mean temperature averaged from 200 to 500hPa. **(a)** NCEP/NCAR, **(b)** CON run, **(c)** NSH run. (Wu et al. 1997b)

6.3.2 Simulation on the dynamic-thermodynamic effect of the TP

It is known that large-scale orography, especially the TP, exerts considerable influence on atmospheric circulation through its dynamic and thermodynamic effects. On the other hand, it has been long believed that the land-sea heating contrast is the fundamental mechanism driving monsoon circulation. In this subsection, we investigate the relative influences of land-sea distribution and Asian large-scale orography on East Asian monsoon. A series of numerical experiments have been carried out with various land-sea distributions and orographies using the NCAR Community Climate Model (CCM3). Table 6.2 provides a summary of the main experiments discussed in this subsection.

Table 6.2 experimental designs

Categories	Cases	Underlying surface of the model
Aqua-plant	AP	The whole planet is covered by Ocean except the south of 78°S covered by sea ice
latitudinal land-sea distribution (LatD)	LO21	The same with the AP case except that the north of 21°N is covered by land with global elevation 1 m, no orography
longitudinal land-sea distribution (LonD)	POAO	Both the Pacific Ocean and the Atlantic Ocean are included based on the LO21 case
Tropical continents (TpC)	AfrSAm	Both the African and south American continents are included based on the POAO case
No Mountain	NM	The present-day land-sea distribution but no orography
Large-scale orography within Asian and African monsoon region	MAsia	The Asian large-scale plateaus (Tibetan, Iranian and Mongolian plateau) are included based on the NM case
	MAfr	The whole African and Arabian peninsular orography are included based on the NM case
	MAsiaAfr	Both the Asian and African orography are included based on the NM
All mountains	M	The present-day orography and land-sea distribution.

In order to accentuate the effects of land-sea distribution and orography, all experiments are integrated with globally uniform vegetation type, soil color and soil texture. We take the most extensive 'warm grassland' which covers the largest area of land surface among others, as the prescribed surface type, and 4 as the parameter of soil color which is also the most extensive one. The global average fraction of sand (50.6%), silt (25.7%) and clay (23.7%) is taken as the soil texture. To remove the information of the present-day land-sea distribution in the external forcing and the initial fields, the prescribed zonal averaged climatological SST and zonal averaged initial fields are used. Each experiment is integrated for twelve years with monthly SST forcing periodically. The pentad mean results from the last ten years are analyzed for this study.

It is known that the summer pattern of the difference of land-sea pressure is opposite to the winter pattern due to the land-sea thermal difference. Hereby, Guo (1983) developed an East Asian summer monsoon intensity index by using the difference between 110°E and 160°E of sea level pressure (SLP). Following Guo, but with a little modification, we adopt the difference of SLP, which is smaller/larger than -5hPa/5hPa summed from 20° to 40°N, to represent the intensity of East Asian summer/winter monsoon (EAMI). It is seen that the absolute value of EAMI in nine cases compose

"three stairs" with distinct height (Fig. 6.3). "The first stair" includes the AP and the LO21 cases, and there is no monsoon in East Asia because of the absence of longitudinal land-sea distribution (LonD). "The second stair" includes the POAO, the AfrSAm, the NM and the MAfr cases. In these cases, the East Asian monsoon (EAM) appears with the inclusion of LonD. However, the EAMI has little change among the AfrSAm, the NM and the MAfr cases. Thus, the occurrence of EAM can be attributed to the existence of the broad-scale LonD in the middle-high latitudes. Comparing with LonD, the tropical continents and African orography have little impact on EAM. "The third stair" includes the MAsia, the MAsiaAfr and the M cases. In these cases, no matter in winter or summer, the East Asian monsoon appears to be remarkably strengthened after the Asian large-scale orography is included. However, no evident change of EAMI is found when the other mountains are included such as African, American and Antarctic mountains etc. That suggests it is the Asian large-scale orography, not the others, that is responsible for the remarkable enhancement of EAMI. In fact, we also conduct another experiment which only includes the TP, and the result is quite similar with that of the MAsia case, especially in summer. That means the enhancement of EAMI is mainly attributed to the effect of the TP. A notable phenomenon in Fig. 6.3 is that the summer EAMIs are roughly equal to the winter ones among the cases of the second stair; however, the winter EAMIs are distinctly larger than the summer ones among the cases of the third stair. That means the EAMI induced by the LonD in winter is equivalent to that in summer, however, the influence of Asian large-scale orography on the EAMI in winter is stronger than that in summer.

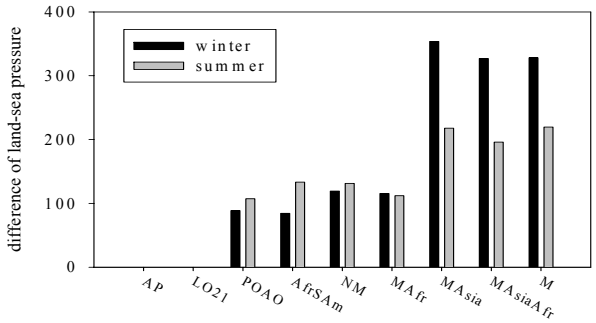

Fig. 6.3 The absolute value of EAMI for winter and summer in various cases. The EAMI is defined by the absolute values of the difference between 110°E and 160°E of sea surface pressure summed from 20°N to 40°N.

To further detail the influence of Asian large-scale orography on EAM, Fig. 6.4 illustrates the longitude-pressure cross-section of the difference of temperature between the MAsia and the NM case along 35°N. The shaded areas represent the difference of average temperature between the MAsia and the NM case reaches the significance level of 0.01. With the inclusion of Asian large-scale orography, the temperature is significantly decreased from 300hPa to the sea surface level over East Asia to the west of 145°E in winter (Fig. 6.4a). The maximum decreasing amplitude is more than 4°C over the TP and its eastern vicinities, whereas there is a significant warming at 250hPa over the western Pacific Ocean. In summer (Fig. 6.4b), the significant warming mainly appears between 600hPa and 200hPa over East Asia and western Pacific. The maximum increasing amplitude is more than 7°C at 400hPa over the TP, whereas, the temperature is significantly decreased above 150hPa over East Asia. Comparing Fig. 6.4a with b, it is found that almost the whole tropospheric air is cooled over East Asia in winter because of the inclusion of the Asian large-scale orography, whereas, only the air between 600 and 200hPa is warmed in summer. The influence of the Asian large-scale orography on the low level air temperature is not significant in summer. This explains why the Asian large-scale orography has stronger influence on the difference of land-sea pressure in winter than in summer. The atmospheric pressure can be expressed as the weight of the air above that surface per unit area. In winter, almost the whole tropospheric atmosphere is cooled over East Asia (Fig. 6.4a), especially for the low level atmosphere, which evidently increases the weight of the whole air column due to the increase of air density and in turn produces much more additional pressure. In summer, only the middle-upper troposphere is warmed (Fig. 6.4b) which induces a relative less decrease of the weight of the whole air column due to the thinner thickness of warmed air and low density at middle-upper level troposphere. So the change of SLP induced by Asian large-scale orography in winter is larger than that in summer over East Asia. On the other hand, it also can be seen that the cooling induced by Asian large-scale orography is confined to the west of 145°N in winter (Fig. 6.4a). However, in summer, the influence of plateau on mid-upper tropospheric temperature can spread far more east to 180°, which is not in favor of the enhancement of land-sea pressure gradient. This is another reason why the winter difference of SLP between 110°E and 160°E is larger than the summer one.

Apparently, the occurrence of the East Asian subtropical monsoon depends on the existence of LonD, however, the TP also plays a very important role. With the occurrence of the TP, the East Asian monsoon is significantly strengthened. In fact, it can been found that the TP has significant

impact on the extension of EAM by comparing the 925hPa wind field in the MAsia case with that in the NM case (figure now shown). In the NM case, the ridge of winter continental high-pressure system is located in 35°N, therefore, northeasterly wind prevails to the south of 35°N over East Asia. In summer, the southerly wind can reach the latitude of 50°N over East Asia. If we take the areas with seasonal reversal of wind as monsoon region, the East Asian monsoon only occurs to the south of 35°N in the NM case. In the MAsia case, the summer pattern of wind field over East Asia is similar to that in the NM case, however, in winter, the northeasterly wind extends northwardly to 45°N with the winter continental high-pressure system northward shift. That means the monsoon region extends northward from 35°N in the NM case to 45°N in the MAsia case. More discussions on the effects of land-sea distribution and orography on Asian monsoon can be found in Xu and Qian (2006)

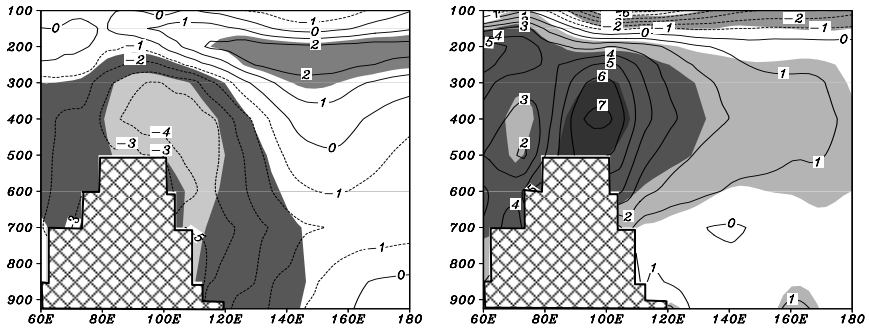

(a) **(b)**

Fig. 6.4 The longitude-pressure cross-section of the difference of temperature between MAsia and NM case along 35°N in **(a)** winter and **(b)** summer. Meshed area denotes the TP. The shaded areas represent difference of average temperature at the significance level of 0.01.

6.4 Plateau snow anomalies and its climate effects

The snow anomaly over the TP will change its thermal forcing remarkably and, consequently, influence the developing process of the Asian monsoon, resulting in large-scale floods or droughts in China (Qian et al., 1988, 2001). This section is focused on the effects of the snow anomalies over the TP on climate variability in China. Special attention will be paid to

which parameter, the snow depth or the snow cover, is more important, and in which season, in winter or in spring, is the effect of snow anomaly more influential. At first, the climatological features of the winter snow depth over the TP are presented. Then, the statistical relationship between plateau snow depth and precipitation anomalies will be diagnosed by SVD technique in section 4.2. To investigate the mechanism of plateau snow effects on precipitation anomalies, several numerical simulations will be followed in section 4.3. Due to lack of snow cover observation from the 78 snow stations, its relationships with precipitation in China are not diagnosed, but will be simulated by a numerical model in section 4.3

6.4.1 Climatological features of the winter snow

Spatial pattern of snow depth over TP

Fig. 6.5 shows the spatial pattern of averaged snow depth (cm) during the winter snow maxima (January and February) between 1978 and 1987, estimated by Scanning Multichannel Microwave Radiometer (SMMR). Obviously, the snow cover occurs mainly in the high altitude regions with elevation above 3000m, however, its geographical distribution is uneven. It was about 59% snow covered in winter. Only in the peripheries of the TP, particularly in the eastern and western peripheries, including the Himalayas, Pamirs, Nyainqentanglha, and eastern Tanggula Mountains, is there heavy snow cover present. In the vast interior, such as the Qaidam basin, Yarlung Zangbo Valley, snow cover is rare, and in the north of the TP snow cover is thin and of a short duration. In addition, the heavy snow also occurs in Tianshan Mountains.

Annual cycle of snow cover

Over the TP snow season normally begins in mid-September (Figure not shown). Snow cover growth is rapid in the first half of winter, with the maximum occurring in January. This is followed by a slow decline until June. The long snow season, early snow peak, rapid snow growth, and slow snow decay are evident. Of all snow seasons, winter (December, January, and February) has the greatest snow storage. The winter, spring (March, April and May), and autumn (September, October and November) are represented by 45.2%, 28.0%, and 21.2% of the annual snow storage, respectively. The largest variability of peak snow amount is the most striking feature with great differences of as much as $300\times10^8 m^3$ between the heavy snow winter and the light snow winter. Such a significant interannual variability of snow storage must have notable influence on general

circulation.

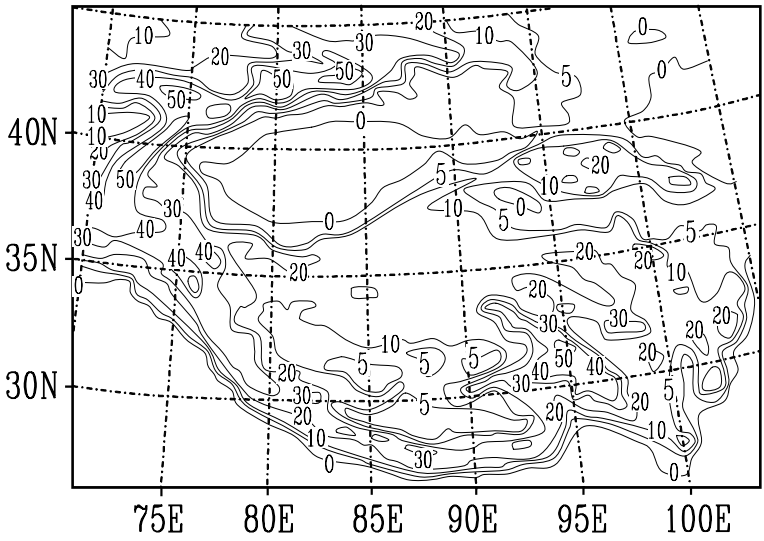

Fig. 6.5 Spatial pattern of average snow depth (cm) during the winter snow maxima between 1978 and 1987 estimated by SMMR over the TP. (Qin et al. 2006)

6.4.2 Statistical relationship between snow anomaly and precipitation

To diagnose the relationship between snow depth anomaly and precipitation, the satellite data are still far from sufficient length. Ground station data could provide longer time series of snow depth data. In this section, the monthly mean snow depth data from 78 stations over the TP and its vicinities and monthly precipitation data from 160 stations in China during the 42 years from 1957 to 1998 are used. The geographical locations of the snow depth stations are indicated with crosses (+) and the precipitation stations with dots (•) are shown in Fig.6.6. Some key areas are also shown, including the TP with the area higher than 3000m shaded, the Tianshan Mountains, the Xinjiang Basin, Sichuan Basin, the Yellow River, the Yangtze River, the Huaihe River basin and the Bay of Bengal. The eastern TP, east of 90°E, and the western TP are also denoted. Using SVD technique, four pairs of snow depth and precipitation anomalies were analyzed (Qian et al., 2003). The first pair contained anomalies of the winter snow depth

and the spring precipitation. The second contained anomalies of the winter snow depth and the summer precipitation. The third and the fourth were the same as the first and the second, but the left field was the spring snow depth. The results show that the snow depth anomaly, especially in winter, is one of the factors influencing precipitation in China, and the winter snow anomaly is more important than the spring one. Only the result of SVD analysis between winter snow anomaly and precipitation over China is presented here.

Before the SVD analysis, both the data for the snow depth (taken as the left field) and the precipitation (taken as the right field) are standardized with unit variances. The first mode of the winter snow depth explains 22.7% of the total variance and that of the spring precipitation explains 39.7%. It is seen clearly that the positive anomalies of snow depth over the eastern TP, between 90° and 102°E along 30°N, are positively correlated with the spring precipitation in eastern China south of the Yangtze River and northeastern China north of 45°N, and are negatively correlated with that of a large area in between (Figure not shown). This means that if the winter snow depth over the eastern TP is deeper than normal, then the spring precipitation to the south of the Yangtze River and northeastern China will be heavier than normal and in between it is less than normal, and vice versa. The SVD analysis on winter snow depth and summer precipitation anomalies shows the first mode of the winter snow depth explains 27.4% of the total variance and that of the summer precipitation explains 32.1%. The positive snow depth anomalies over the eastern TP between 90° and 103°E along 35°N are positively correlated with the summer precipitation in the Yangtze River and the Huaihe River basins and northeastern China, and are negatively correlated with the summer precipitation in southern China and northern China. Therefore, when the winter snow depth over the eastern TP is deeper than normal, the summer precipitation in the Yellow River basin, northern China and southern China will be less than normal, whereas in the Yangtze River and the Huaihe River basins it will be more than normal. It is also found that for precipitation in different seasons, the key areas of the winter snow depth anomalies are somewhat different. For the spring precipitation anomalies in China, the snow depth anomalies over the south of the eastern TP are more important than those over other areas. For the summer precipitation, the snow depth anomalies over the north of the eastern TP are more important. Moreover, the snow depth anomalies over different areas also have different effects on precipitation. Nevertheless, the responses of spring and summer precipitation to snow depth anomalies over the whole eastern TP are roughly similar.

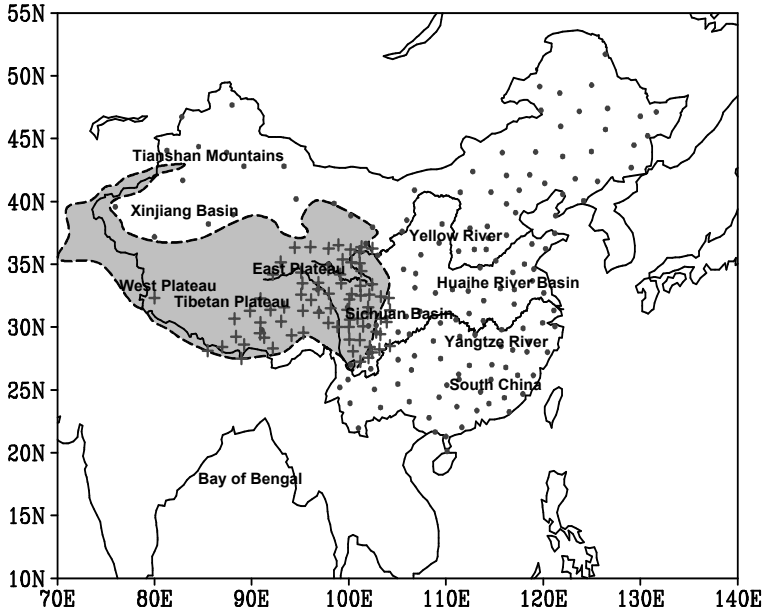

Fig. 6.6 Geographical distributions of some key regions in East Asia and the 78 snow stations (+) and the 160 rainfall stations (●) in China. Topography higher than 3000m is shaded

In order to verify the above results obtained from the discussions of the first SVD modes, the combined relationships between the winter and the spring snow anomalies over the eastern TP, east of 90°E, and the spring (represented by the rainfall in May) and the summer rainfall anomalies in China are also diagnosed by calculating their correlation coefficients. The results are shown in Table 6.3, in which the absolute values of the correlation coefficients greater than 0.2 and 0.3 are given in italics and bold respectively, in order to accentuate their higher coefficient coefficients. It is found from Table 6.3 that, in May, the anomalies of both the winter and the spring snow depth are negatively correlated with precipitation in the Yangtze and the Huaihe River basins, the eastern Sichuan Province and northern China, whereas they are positively correlated with precipitation in northeastern China and southern China. In summer, the correlation between the snow depth and the rainfall anomaly does not change in eastern Sichuan Province, northern China and northeastern China; however, in the Yangtze and Huaihe River basins and southern China the relationship alters its sign. It is further seen from Table 6.3 that the winter snow depth anomaly has a relatively large influence on precipitation in southern China and northeast-

ern China in May and in southern China and the Yangtze and Huaihe River basins in summer, and that the spring snow depth anomaly has relatively more impact on precipitation in the Yangtze and Huaihe River basins and eastern Sichuan Province in May and in the Yangtze and Huaihe River basins and northern China in summer. Both the spring and the winter snow anomalies have the greatest impact on the summer precipitation in the Yangtze and Huaihe River basins. However, whether in May or in summer, the absolute correlation coefficients are not large enough. Only the correlation coefficient between the winter snow depth and the spring snow depth and the summer precipitation in the Yangtze and Huaihe River basins reaches the significance levels of 0.05 and 0.1 respectively. So, the snow depth anomaly, especially in winter, is one of many factors influencing the summer precipitation in China; however, it is perhaps not the only one and even not the most important one. Nevertheless, it is proved that the winter snow anomaly over the TP is relatively more important than the spring one to the regional precipitation in China. These conclusions will be further examined by several numerical experiments in order to further investigate their mechanisms. Moreover, the results obtained from Table 6.3 are moderately consistent with those obtained from aforementioned results of SVD analysis.

Table 6.3 Correlation coefficients between precipitation and snow depth anomaly.

	Precipitation									
	May					Summer (JJA)				
	SC	YH	ES	NC	NEC	SC	YH	ES	NC	NEC
Winter snow	*0.20*	-0.17	-0.12	-0.17	**0.28**	*-0.22*	**0.38**	-0.18	-0.12	0.18
Spring snow	0.14	*-0.20*	*-0.22*	-0.19	0.13	-0.02	**0.312**	-0.17	*-0.22*	0.15

Note: Abbreviations are *SC* for South China, *YH* for the Yangtze River and the Huaihe River basins, *ES* for the eastern Sichuan Province, *NC* for North China, and *NEC* for Northeast China. The absolute values of coefficients equal to and greater than 0.2 and 0.3 are given in italics and bold respectively to express higher coefficients. (Qian et al. 2003)

6.4.3 Simulations of the effect of snow on precipitation

In order to simulate the influences of the TP snow anomalies on the re-

gional climate in China, the second version of the NCAR (National Center for Atmospheric Research) regional climate model (RegCM2) is used with the model domain containing the TP and the horizontal resolution being 120 km with 11 levels in the vertical. The turbulence kinetic energy (TKE) scheme and a new computational scheme of boundary layer tops with much better effectiveness of simulation are incorporated to replace the original ones in the model (Zheng et al., 1999). The following six experimental schemes are designed.

1. The control experiment (hereafter termed CN). In the CN, the NCEP/NCAR reanalysis 10 year monthly mean fields of meteorological variables, snow depth and snow cover in January from 1986 to 1995 are used as the model's initial data. The time integration starts from 1 January 00:00UTC and ends at 31 August 24:00UTC for 8 months. The nesting values of boundary variables and the sea surface temperatures (SSTs) are also taken from the same period using monthly mean data, interpolated to each day and changed day by day. By using the 10 year monthly mean fields the influences of the background large-scale circulation conditions are removed and the effects of snow are easier to discuss and compare. The model outputs are stored every day; in particular, the model-produced snow depth and snow cover fields are stored every 12 h for later use in other experiments. The purpose of the CN is to check the model performance in simulating the regional climate features and its results are taken as the climatological base for comparisons with other sensitivity experiments.

2. The deeper February snow depth experiment (hereafter termed DL). In the DL, every 12 h in February the snow depth is set to be deeper than that in the CN by a factor of 20~50%, but the snow area is the same as in the CN. Owing to the fact that in the eastern TP the snow depth anomalies have the most evident impacts on precipitation, the snow depth anomalies there are assumed to be the deepest. The other variables are the same as in the CN. By comparing the DL results with those in the CN the effect of the positive winter snow depth anomaly on spring and summer precipitation will be found.

3. The deeper March snow depth experiment (hereafter termed DL2). The DL2 is the same as the DL, but the forcing due to the snow depth anomaly is added in March. By comparing the DL2 with the CN we may find the effect of the positive spring snow depth anomaly on spring and summer precipitation.

4. The shallower February snow depth experiment (hereafter termed DS). In the DS, every 12 h in February the snow depth is set to be shallower than that in the CN by a factor of 20~50% at different grid points over the

TP. The spatial pattern of the snow depth anomaly is the same as in the DL but with about 25% of the amount. By comparing the DS with the CN we may find the effect of the negative snow depth anomaly in winter on precipitation in spring and summer.

5. The larger February snow cover experiment (hereafter termed CL). In the CL, every 12 h in February the snow cover is forced to be larger than that in the CN by expanding the CN-produced snow cover boundary one grid outwards. The other variables are the same as in the DL. By comparing the CL with the CN we may find the effect of the positive snow cover anomaly in winter on precipitation in spring and summer. Then by comparing the CL with the DL, we may find the relative importance of snow cover and snow depth anomalies.

6. The boundary forcing experiment (hereafter termed BN). The BN is designed to study the effect of the background circulation condition at the model boundaries on the interior regional climate and to compare the relative functions of the snow anomaly and the boundary forcing. The boundary variables are taken from the observed ones in the South China Sea Monsoon Experiment (SCSMEX) from 1 May to 31 August in 1998.

In February (Figure not shown), it is clearly seen the simulated snow in the CN occur mainly over the Tianshan Mountains and TP with heavy snow concentrating in the peripheries of TP, particularly in the eastern and western Plateau. Such an essential distribution is fairly coincident with observations (Fig.6.5). In May, the snow mostly melts away due to the temperature rises except over the Tianshan Mountains and the southeastern plateau. It is also shows that the largest time variation of snow and snow depth anomaly take place in the east Plateau.

The peak value of snow depth in the CN appears in February both in the west and the east parts of the plateau. In the DL, it appears in March with a delay of one more month compared to the CN. From the beginning of February the difference in snow depth between the DL and the CN becomes larger and larger, reaching a maximum at the end of the month. From early March the difference gets smaller and smaller and disappears finally at the end of May. The above features of time variations are basically in agreement with the observed ones. The simulated area mean snow depth in the CN is not very much different in both the west and the east of the plateau, while in the DL the snow is much deeper in the east than in the west owing to the different percentage of incorporated snow forcing in the two areas. Therefore the forcing of snow depth anomaly not only influences the difference of snow depth between the two experiments, but also increases the difference of snow depth between the east and the west parts of the plateau,

which may enhance the thermal contrast between the west and the east of the TP and therefore influence circulation patterns over the plateau.

Fig.6.7a and b are the differences of precipitation (in mm day^{-1}) between the DL and the CN in May and in summer. It is seen that due to the increased snow depth over the TP in February, the precipitation in May is remarkably reduced in the region south of the Yangtze River. The precipitation in summer is increased roughly between 30°N and 40°N while decreased both south and north of the area. So, the increase of winter snow depth reduces precipitation in the South China area both in May and in summer as well as in the north part of China in summer, while it increases precipitation in the mid and the lower Yangtze River basins in summer. Precipitation over the Bay of Bengal is even more severely influenced by the snow depth anomaly and largely reduced when the snow depth over the plateau increases in winter. Fig.6.7c and d are the same as Fig.6.7a and b but for the BN case. It can be found that the basic patterns of precipitation differences between the BN and the CN are similar to those between the DL and the CN but with much bigger values. The negative anomalies in May in the south of the Yangtze River and South China are more evident and the domain is much larger. The positive anomalies in summer occupy a much larger area between 30°N and 40°N, so that the whole region between the Yangtze River and the Huaihe River becomes an area with more precipitation. Therefore, the background circulation reflected in the boundary forcing conditions has an in-phase effect with the deeper winter snow, though it may be more important to the summer precipitation anomaly. Fig.6.7e and 6.7f show the precipitation differences between the CL and the CN. It is found that the spatial patterns of the differences in May and in summer are somewhat similar to those between the DL and the CN. However, precipitation anomalies are much smaller both in May and in summer except for the Bay of Bengal area in summer where the anomalies are as large as those in Fig.6.7b and even larger than those in Fig.6.7d. Therefore, it may be inferred that the anomalies of snow depth and snow cover are equally important for the summer precipitation in the Bay of Bengal area and more important than that of the background conditions. However, the snow cover anomaly is relatively less important than that of snow depth for the floods over the Yangtze River and the Huaihe River basins in summer. Moreover, the comparison of Fig.6.7 with the previous result of SVD analysis indicates the similarity of the anomaly patterns of summer precipitation in all three experiments to those in the SVD analysis, though with some discrepancies in area and value.

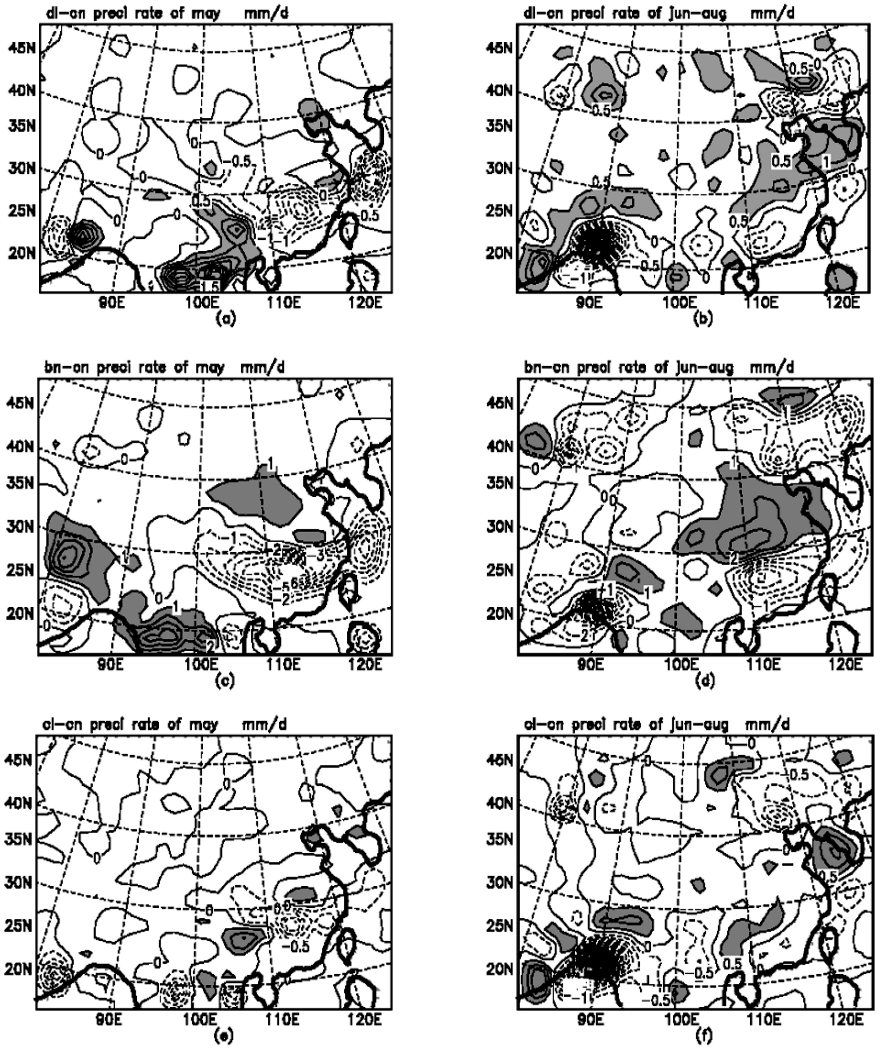

Fig. 6.7 Differences of precipitation rate (in mm day^{-1}) between the DL and the CN in May (a) and in summer (b); (c) and (d) the same but between the BN and the CN; (e) and (f) between the CL and the CN. (Qian et al. 2003)

The surface energy budget equation can be written as follows (Vernekar et al., 1995):

$$F_{S\downarrow}(1-\alpha_S)-\varepsilon\sigma T_S^4+F_{lW\downarrow}-F_{sh\uparrow}-F_{lh\uparrow}-F_{g\downarrow}-F_m=0 \tag{6.5}$$

where $F_{S\downarrow}$ is the downward shortwave radiation flux density at the surface, α_S the surface reflectivity, ε the surface longwave radiation emissivity, σ the Stefan–Boltzmann constant, T_S the surface temperature, $F_{lW\downarrow}$ the downward atmospheric longwave radiation flux density at the surface, $F_{sh\uparrow}$ the upward surface sensible heat flux density, $F_{lh\uparrow}$ the upward surface latent heat flux density, $F_{g\downarrow}$ the sensible heat flux density to soil, which may be neglected due to its smaller value than the other terms, and F_m the energy loss due to melting of snow.

Comparisons of DL and CN show that the surface absorbed short wave radiation flux $F_{S\downarrow}(1-\alpha_S)$ averaged from March to May in the areas of snow depth anomaly decrease, and it does so along a northwest to southeast zone with the snow anomaly area in February as the centre. However, to the east of the TP at 100°E and in the northwest of the plateau the absorbed solar radiation increases. The net longwave radiation $(-\varepsilon\sigma T_S^4 + F_{lW\downarrow})$ emitted at the surface in the eastern TP near 32°N and 100°E in the DL is less than that in the CN. The latent heat $F_{lh\uparrow}$ distributions are quite similar to that of the shortwave radiation, especially in the mid-latitude belt but with a much smaller amount. The sensible heat flux $F_{sh\uparrow}$ is influenced remarkably, due to the deeper snow depth resulting in a large decrease, but the pattern is also somewhat similar to that of the shortwave radiation (figure not shown). The contribution of latent heat flux and net longwave radiation flux is less than the net shortwave radiation and the sensible heat fluxes. Therefore, it seems that the deeper snow depth over the TP influences the surface absorbed shortwave radiation first, and consequently the surface temperature changes, altering the surface heat fluxes. As the residual of the above four flux terms, the difference of the F_m term can be positive or negative. When the F_m difference is positive, the snow will melt more and faster, and hence the surface water content will be higher than that in the CN and *vice versa*.

The above discussion is made only for the averaged flux differences from March to May. However, the surface flux densities and other model variables, such as the surface temperature and the soil water content, are always changing with time and space. In order to reveal the mechanism more clearly, the seasonal cycles of the 10-day mean flux differences averaged over the western and the eastern TP are further analyzed too (figures not shown). It is found that in March and May the decrease of the shortwave radiation flux is less than the sum of the decreases of the other three

fluxes, indicating that there is a greater energy surplus at the surface in the DL than in the CN. This greater energy surplus may be used to increase the surface temperature or the melting speed of snow. If it is used to increase the surface temperature, the sensible heat and the upward longwave radiation fluxes should increase to offset the surplus. If it is used for melting of snow, the land surface temperature may not increase and may even decrease, and the water content will increase. In order to check which case takes place, the seasonal cycles of the 10-day mean surface water content and temperature differences between the DL and the CN and between the CL and the CN are also analyzed. It is found that in both the western and the eastern TP the water content difference between the DL and the CN increases with time before June, and is much faster in the east than in the west. The surface temperature differences in both areas are basically negative, especially in the eastern part of the TP. The water content and the surface temperature differences between the CL and the CN have the same seasonal cycles; however, with larger amplitudes before late March, and from April to May they are in opposite phase both in the east and the west. Therefore, the energy surplus in the DL is used for the melting of snow rather than for increasing surface temperature. Barnett *et al*. (1989) has pointed out that the increased water content enhances the soil heat capacity, the surface longwave emissivity and water evaporation from the surface. Therefore, the lower surface temperature can persist for a long time, influencing the atmospheric circulation patterns and precipitation in different regions. However, in these experiments, such a mechanism seems only partly correct. In fact, the lower surface temperature in the DL comes from the energy consumption for melting of snow and results in both decreases of the latent and the sensible heat fluxes, and the enhancement of the surface longwave emissivity increases the upward longwave radiation flux only a little due to the lower surface temperature.

6.5 The nature of the South Asia High and its climate effects

Each summer, there is one semi-permanent anticyclonic circulation in lower stratosphere over the TP called “the Tibetan High”, which is the strongest at l00hPa. The High’s center at l00hPa is also frequently located over the Iranian Plateau. In winter, there is an anticyclonic circulation over the ocean, moving northwestward gradually with the change of season and forming a high center. In summer, the anticyclonic circulation reaches the TP and the Iranian Plateau, completing an annual cycle. Therefore, both of

the winter anticyclonic circulation over ocean and the summer one over land are defined as SAH. The heating of the TP has been believed to play an important role in the development and movement of SAH. In this section, the seasonal variation characteristic of SAH and its climate effects will be presented by using the NCEP/NCAR monthly mean reanalysis data from January 1958 to May 1998 and pentad mean reanalysis data from 1980 to 1994.

6.5.1 Seasonal variation of SAH

The center of the SAH is defined at the point with the largest geopotential height and is expressed by its longitude and latitude. The area of the SAH is computed by counting the points at which the geopotential height should be equal to or larger than the characteristic height of 1660 gpdm. Therefore, the area is expressed as the number of total points counted and designated with *A*s. Three kinds of the SAH intensity indices are defined, the center intensity I_1 which is the geopotential height at the center, the absolute intensity I_2 which is the sum of differences between the geopotential height at each point and the characteristic one in the SAH area, and the mean intensity I_3 which is the ratio between I_2 and *A*s.

There is an evident seasonal migration of the center of SAH. The center is located in tropical regions to the south of 15°N before April, then jumps abruptly northward to the north of 20°N in May, moves northward largely again in June with the center near 30°N, reaches to the northernmost positions north of 30°N in July and August, retreats southward continuously after September, and returns to tropical regions by December. The center of SAH also has evident longitudinal migration accompanying its latitudinal migration. There are two evident sudden changes, one in spring (February to April) and the other in autumn (September to November). In spring, the SAH advances westward suddenly to the Indo-China Peninsula (ICP) from the ocean, and in autumn, it retreats eastward rapidly. Combined with the time variation of the center latitude, it is found that the SAH center remains in the tropical region when advancing in spring, while it retreats southeastward from the TP along a different path when withdrawing in autumn.

Three SAH intensity indices and *A*s have quite similar and notable seasonal variation. They are the smallest in winter, increase gradually after, and reach a maximum in July and August. It is also found that the northwestward advance of the SAH center is more abrupt than southeastward withdrawal, while the area and the intensities of SAH change more rapidly during their southeastward withdrawal.

6.5.2 Bimodality of the SAH in the seasonal cycle

Fig.6.8 shows the geographic distributions of the SAH centers with longitude during 1958-1997. It is seen that there are two steady modes of the SAH along longitude. In winter, the SAH centers are usually located over ocean while in summer over land. The summer mode can be further divided into two sub-modes with one over the Iranian Plateau, the Iranian High (IH), in 50~70°E and the other over the TP, the Tibetan High (TH), in 80~l00°E. In China, some meteorologists defined the two sub-modes as the west pattern and the east pattern of the TH. However, they have different thermal structures. It is found from Fig.6.8 that the SAH tends to stay over the TP in May, June, and September (designated with "○"), over the west TP and the east Iranian Plateau in July and August in midsummer (with"●"), over the Pacific Ocean between l40°E and l70°W in winter from December to April (with"+"), while over the western Pacific between l40°E and l60°E in October and November, the transition season from autumn to winter(with"×").

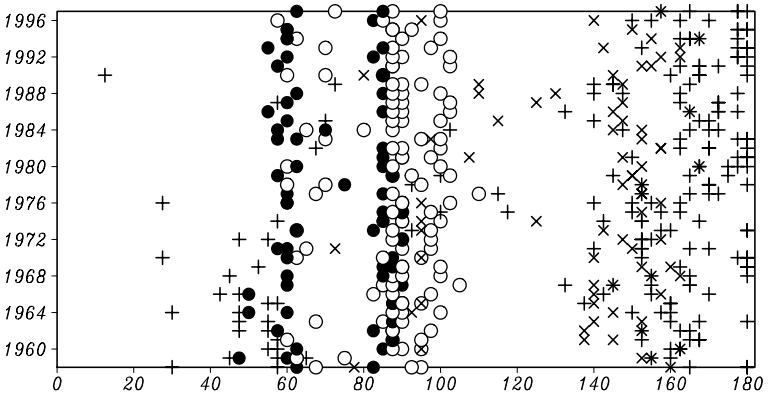

Fig. 6.8 The geographic (b) distributions of the SAH center with longitude. symbol "+" represents the SAH center position in December to April, "○"in May, June and September, "●"in July and August of mid summer, "×"in October and November.

The midsummer mean SAH which is centered over the TP and its neighborhood exhibits as a huge system covering most part of the subtropics in northern Hemisphere. Another high system lies over the Rocky Mountains with a much smaller scale. Such a distribution may imply that in summer the high system in the upper level is related to the large scale topography, and their thermal features may be deduced from such a mor-

phological character. The activities of the SAH in summer are examined in detail by the NCEP/NCAR individual pentad data. The period considered for the statistics is July and August, which means that there are 12 pentads in each midsummer, totally 180 pentads during 1980~1994. Quite similar to that of the monthly mean data (Fig.6.8), the SAH centers possess two preferable locations corresponding to the location of the TP to the east and Iranian Plateau to the west, but scarcely appear near 70~80°E, where the centered region of the climatological mean SAH is located. Statistically, among the total 180 pentads there are 77 pentads for TH (42.8%), and 62 pentads for IH (34.4%).

To understand the thermal and dynamical features of the bimodality of SAH in summer, composite analyses for the two modes are presented in the following (figure not shown). It can be found that the TH corresponds to the anomalous strong ascending motion over the central TP, which enhances the original ascending motion over the TP, and is accompanied by the anomalous warm column. In the case of the IH, the anomalous ascending motions are observed over the Iranian Plateau, which weakens the original descending motion over the Iranian Plateau, and is also accompanied by the anomalous warm column. It is also found that contrasting to the tropospheric warm column, the SAH center at 100hPa exhibits as a cold one. The above vertical structures show that in both the TH and the IH case, the cold SAH center at 100hPa corresponds to the tropospheric anomalous ascending motions and the anomalous warm column. In the other words, the SAH has the feature of warm preference. It may suggest that the anomalous warm column is related to the SAH center via the anomalous ascending motion in the column. The anomalous ascending motions enhance the divergence at upper level, thus increase the negative vorticity at the region, and result in the maintenance of the anticyclone center over the region. Such a warm preference feature of the SAH is also demonstrated by the meridional section composites (figure not shown).

To further examine the thermal characteristics of the bimodality of SAH and the possible reason of the SAH's warm preference, the each term in the thermodynamic equation (6.6) is calculated.

$$\frac{\partial T}{\partial t} = -\vec{V} \cdot \nabla T - \left(\frac{P}{P_0}\right)^{\kappa} \omega \frac{\partial \theta}{\partial p} + \frac{Q_1}{Cp} \tag{6.6}$$

where T is temperature, θ potential temperature, $\vec{V}$ horizontal wind, ω vertical p-velocity, $\kappa = R/C_P$, Q_1 diabatic heating, Cp the specific heat at constant pressure of dry air, P_0=1000hPa. Fig.6.9 shows the pressure-longitude cross sections of the terms of Eq. (6.6) along the SAH ridge line latitude for the TH. It is found that the obvious warming occurs over the TP up to

200hPa. Fig.6.9d indicates that such a warming results from the diabatic heating over the TP, while the strong cooling due to ascent over the Plateau shown in Fig.6.9c compensates the diabatic heating to a large extent. The horizontal advection shown in Fig.6.9b contributes only a small part to the warming. Therefore, the contribution of the diabatic heating of the TP is much important to the maintenance of the TH. It can be found from the similar pressure-longitude cross sections for the IH that the warming center over the Iranian Plateau is located in the lower and middle troposphere, acting as a warm background for the IH, and also illustrating the warm preference of the SAH (Figure not shown). Similar to the case of the TH, such a warming over the Iranian Plateau in the lower troposphere is mainly due to the in situ surface heating. However, unlike the case shown in Fig.6.9d, the warming in the middle troposphere centered at 400hPa over the Iranian Plateau is mainly due to the in situ adiabatic heating, compensated by the horizontal advection and diabatic cooling. It is indicated that the center of the SAH tends to stay over the warm air column. For the TH, such a warming is mainly due to the diabatic heating over the TP; whereas for the IH, besides the diabatic heating in the lower troposphere, the adiabatic heating associated with descent in the middle troposphere over the Iranian Plateau is more important. Therefore, the maintenance of the SAH over the certain region mostly depends on the thermal effect of the atmosphere over the region.

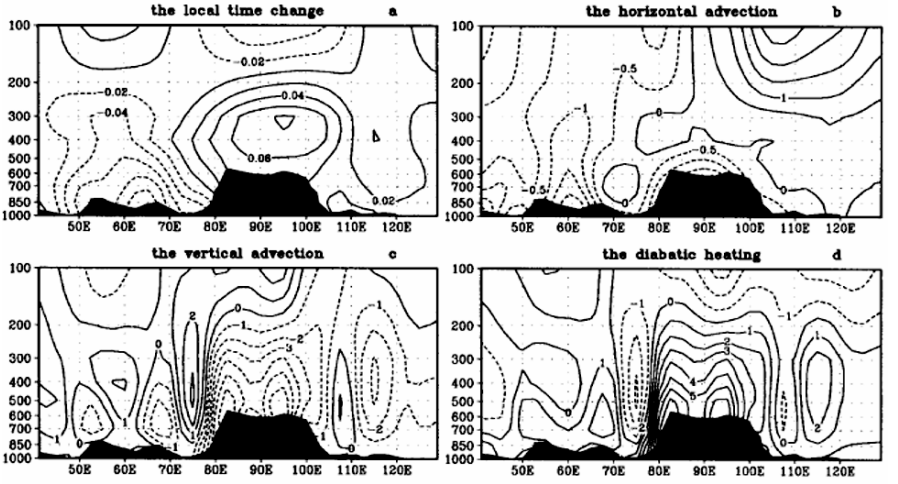

Fig. 6.9 The pressure-longitude cross sections composed for the terms in Eq. 6.6 along 30°N for the TH, unit is K/day. (a) Local time change, (b) horizontal advection, (c) vertical advection, and (d) diabatic heating. 77 TH cases and 62 IH cases are included in July-August from 1980 to 1994. (Zhang et al. 2002)

The South Asian High, even as viewed from its seasonal variation, also has the property of heat preference. The center of SAH usually locates over or moves to an area with relatively larger heating rates (Qian,et al., 2002).

6.5.3 Climate effects of SAH on the regional climate

It has been found that the temporal variation of SAH has a close relationship with the onset of tropical Asian summer monsoon (Qian et al, 2005). Namely, when the SAH center advances to north of 20°N, the South China Sea (SCS) summer monsoon onsets, and to north of 25°N, the Indian summer monsoon onsets at its south end. Comparison between the monsoon onset time determined by SAH and that with other methodologies shows fair consistency in the SCS area and some differences in the Iranian Plateau area. In addition, a special study on the relation between the SAH and the precipitation in North China is also carried out using the monthly NCEP/NCAR reanalysis data and observational precipitation from 160 stations in China during the period from 1958 to 1997 (Huang and Qian, 2003). It is found that the interannual variations of the SAH and North China precipitation are closely correlated to each other, especially the correlation between the longitudes of the SAH in June and precipitation in summer (Figure not shown). The precipitation in North China in summer does not have a strong relationship to the SAH intensities in the previous June. However, they are well related to each other after 1974. There are 10 years (namely 1959, 1966, 1970, 1971, 1973, 1977, 1978, 1984, 1994, and 1996) with both the further east SAH center and the less North China precipitation, and 16 years (namely 1965, 1968, 1969, 1972, 1979, 1981, 1982, 1983, 1985, 1986, 1987, 1988, 1989, 1991, 1992, and 1997) with both the further west SAH center and the more North China precipitation. This indicates that in most years during 1958~1997, the negative correlation between the longitude of the SAH center and the North China summer precipitation is relatively robust. Furthermore, the composites of the 100hPa flow fields in June for more and less precipitation in North China show that in years with more precipitation in North China the SAH center shifts more westward and northward and opposite in years with less precipitation; the differential flow center between the two cases is located over 35~40°N and 60°E (figures not shown).

6.6 Seasonal east-west movement of the EASWJ and its association with the diabatic heating over the TP

In the upper troposphere and lower stratosphere, there exists a narrow and strong westerly belt with strong horizontal and vertical wind shears over the subtropical East Asia, which is referred to the EASWJ. The EASWJ exhibits robust seasonal evolutions in the intensity and location. The axis and center of the EASWJ are located at 200 hPa and reach the southernmost position in March and the northernmost in August. The central intensity of the EASWJ is about 70 m s^{-1} in winter and 35 m s^{-1} in summer. From winter to summer, the axis experiences two northward jumps. Previous studies on EASWJ were mainly focused on the meridional shift of the westerly jet and its effect on eastern Asian weather and climate [Yin, 1949; Yeh et al., 1958; Tao et al., 1958]. The EASWJ also experiences obvious longitudinal migration with season, which might be related to the land-sea thermal contrast in the longitudinal direction. In this section, the seasonal evolution of the subtropical westerly jet core in east-west direction and its association with the diabatic heating over the TP is presented.

6.6.1 Seasonal east-west movement of the EASWJ core

The location of the EASWJ core is represented by the position of the maximum westerly over East Asia. The seasonal evolution of the EASWJ core is shown in Fig.6.10. From Fig.6.10a, it is seen that the core of the EASWJ is located near 140°E before 35th pentad and near 90°E around 42nd pentad, indicating a rapid seasonal east-west displacement of the EASWJ core from 140°E to 90°E between the 35th and 39th pentad. From Fig.6.10b, it can be seen that the core of EASWJ is located near 33°N before 18th pentad, and then begins to move northward, reaches its northernmost position around 42nd pentad with twice abrupt northward jump around 25th and 37th pentad, and thereafter retreats southward. Obviously, the second northward jump of EASWJ core is almost simultaneous with its westward jump (Fig.6.10a, b). In general, the northward (southward) displacement of EASWJ core is companied by the decrease (increase) to zonal wind speed (Fig.6.10b, c). The EASWJ core reaches its westernmost position to the west of 90°E, northernmost position to the north of 45°N and minimum zonal wind speed at the same time (Fig.6.10a, b, c). Further analysis on the longitude-press cross section of the pentad mean zonal wind indicates that the location change of the EASWJ core actually reflects the relative intensity change of the different EASWJ centers. There are three centers over 200hPa during 36th~37th pentads (figure not shown).

All the three centers exhibit little changes in their position during 36th~37th pentads. In contrast, the relative intensity of the centers displays some change during pentads 35~40, which results in the location change of the EASWJ core. It is well known that the plum rain season in China starts after pentad 33 or 34 and ends after pentad 38 climatologically; this coincidence is of significance for the determination of the rainy season beginning and ending date in East Asia. To further examine the reliability of the subseasonal change of the EASWJ core, the occurrence number of the EASWJ core in the region of (30°~45°N, 60°~180°E) from pentad 32 to pentad 43 is counted. The result shows the EASWJ core occurs most frequently to the east of 140°E before pentad 35, then the large occurrence numbers oscillates between 140°~160°E and 85°~110°E during 36~39th pentads, and after pentad 39, the EASWJ core shifts to the west of 100°E, having occurrence numbers centralized steadily at 90°E.

Based on the principle of thermal wind:

$$\frac{\partial u}{\partial p} = \left(\frac{R}{fp}\right)\frac{\partial T}{\partial y} \tag{6.7}$$

The variation of zonal wind with altitude depends on the meridional gradient of air temperature. If the air temperature is decreased poleward, the westerly increases or the easterly decreases with altitude; on the contrary, if the air temperature is increased poleward, the westerly weakens or the easterly intensifies. Therefore, strong zonal winds normally appear over the frontal area of the troposphere, and the intensity of zonal winds is directly proportional to the intensity of the meridional gradient of air temperature. In fact the 200hPa westerly jet is well matched with the horizontal meridional temperature gradient which is calculated by the air temperature averaged from surface to 200hPa in the south minus that in the north with 2.5° latitude interval (Figure not shown). Thus the 200hPa westerly jet always follows the larger meridional temperature gradient.

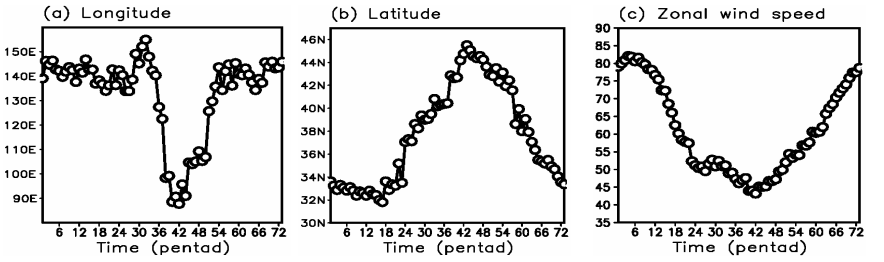

Fig. 6.10 Seasonal evolutions of the pentad mean longitude position of the EAWSJ core.

The diabatic heating has a strong impact on the atmospheric temperature change. To unravel the contribution of the diabatic heating to the temperature change in the lower-upper troposphere, and to the westerly jet core shift at 200hPa, the total diabatic heating rate is diagnosed by using the NCEP/NCAR reanalysis data. The time-longitude variation of the diabatic heating rate averaged between 30°N and 45°N, from surface to 200hPa, are shown in Fig.6.11. The diabatic heating includes turbulent heating, condensation latent heating and radiative heating. The strong heating is located to the east of 130°E before pentad 24, and the westerly jet core occurs over this area coincidently. With the enhancement of the diabatic heating from 80°E to 100°E, the jet core approaches to this area. Meanwhile, the diabatic heating to the east of 120°E weakens. Thus the diabatic heating is responsible for the intensity change and location shift of the westerly jet core at the upper troposphere. Moreover, the evolution of the diabatic heating rate shown in Fig.6.11 represents the longitudinal thermal contrast, which is also related to the longitudinal change of the EASWJ core.

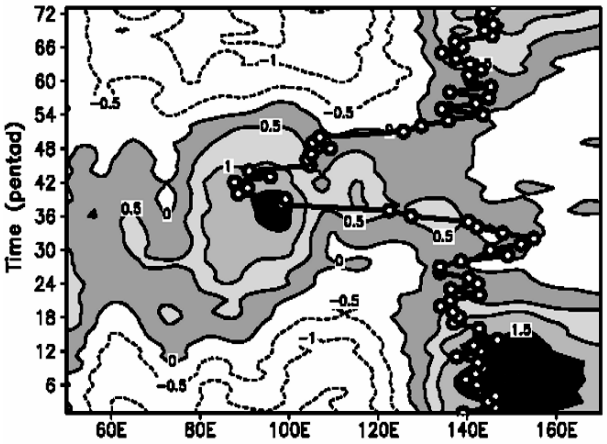

Fig. 6.11 The longitude-temporal variation of diabatic heating rate averaged between 30°N and 45°N (unit: °C day^{-1}). The bold line with open circles represents the westerly jet core locations

6.6.2 Bimodality of the EASWJ core in midsummer

As mentioned in section 5, the SAH shows the bimodality feature during

boreal summer. In terms of the dynamic relation between pressure and wind, the wind field matches well with the variation of the pressure field, leading to the formation of the westerly jet. In midsummer, the major westerly jet centers occur frequently at two positions, which correspond to the TP to the east from 85ºE to 100ºE and the Iranian Plateau to the west from 45ºE to 60ºE. According to the preferable locations, the westerly jet can be classified into the TP Jet mode (TJM) with the major center over the region to the east of 80ºE and the Iranian Plateau jet mode (IJM) with the major center over the region to the west of 60ºE. There are 211 TJM and 211 IJM cases in total 480 cases from 37th to 48th pentad in forty years (1961-2000). Thus, there are two westerly centers over the northern TP and the northern Iranian Plateau in midsummer, the bimodality feature of the jet core is found over East Asia, similar to SAH. Clearly this bimodality of the jet core is related to the elevated topography i.e. the TP and the Iranian plateau.

Corresponding to the bimodality of the westerly jet core in midsummer, there exist obvious differences in geopotential height fields, air temperatures and circulations, as a result, the related climate anomalies are possibly apparent. The composite maps of surface air temperature and precipitation at 518 stations in China (Figure not shown) show that most regions in China experience negative temperature anomaly except the South China in TJM, and the opposite situation occurs in IJM. This implies that TJM corresponds to a lower surface air temperature and the situation is opposite in IJM. As to the rainfall anomaly distribution, a positive anomaly area is located at the south of the TP and the lower reaches of the Yangtze River valley while the South China and the North China are the less precipitation areas, and the distribution in IJM is opposite. The rain-belt is somewhat southward (northward) corresponding to the ascending flow area due to the southward (northward) shift of jet axis in TJM (IJM).

6.7 Stratus generated by the TP and its possible climate effects

Stratus in the southeast China is very common during the winter and early spring season, with stratus cloud amounts near 50% during DJF and MAM. Klein and Hartmann (1993) noticed that all of the regions with a significant fraction of stratus clouds are located over cold oceans except over China. Distinctive from low marine stratus clouds, the stratus clouds over eastern China are primarily middle clouds (Yu et al. 2001). In this section, special attention will be paid to the radiative characteristics of the

middle stratus clouds downstream of the TP and its climatic impacts (Yu et al, 2004). The effect of clouds on radiation budget is measured by cloud radiative forcing (CRF), which represents the difference between cloud-free radiative fluxes and the average of all-sky observations (Ramanathan et al. 1989). The net CRF at the top of atmosphere (TOA) depends on the balance between the cloud albedo and greenhouse effects.

6.7.1 Cloud–radiative forcing over East Asia

Based on the International Satellite Cloud Climatology Project (ISCCP) data from 1991 to 2000, it can been found that the maximum cloud optical depth in the global tropics and middle latitudes between 60°S and 60°N is located eastern China, the downstream of the TP. The annual mean total amount of clouds over eastern China is less than those over western Pacific warm pool (where deep cumulus/anvil clouds prevail) and over the eastern Pacific (where marine stratus persists); both are about 75%. Why is the cloud optical depth over the eastern flank of the TP the largest? It is found that the largest cloud optical depth downstream of the plateau is primarily attributed to its cloud properties (Yu et al. 2004). In fact, the fractional coverage of nimbostratus and altostratus clouds reaches a maximum just east to the TP. The longitudinal cross sections of cloud fraction for different cloud types (figure not shown) also illustrates that along 29°N and to the east of the TP, especially over the Sichuan basin (103°~108°E), the amount of nimbostratus and altostratus clouds exceeds the amounts of all other types of clouds that have large optical thickness (e.g., deep convective, low-level stratus, and stratocumulus clouds). In contrast, along the equator the marine stratus (stratus and stratocumulus) dominates in the eastern Pacific, whereas the cirrus and cirrostratus clouds prevail in the western Pacific. The nimbostratus and altostratus clouds are responsible for the extremely large cloud optical thickness of the TP stratus cloud deck. This proposition is further confirmed by comparing zonal variations of cloud optical depth and nimbostratus–altostratus cloud amount along 29°N from 100° to 120°E (Fig.6.12). Obviously, the nimbostratus and altostratus clouds dominate the zonal variation of cloud optical depth. Over the Sichuan basin (27°~32°N, 103°~108°E), the annual variation of the thick stratus cloud amount is in tandem with that of the cloud optical thickness (Fig.6.12b), confirming that the nimbostratus and altostratus clouds are major contributors to the large cloud optical thickness. The correlation coefficient between annual-mean variations of the nimbostratus–altostratus cloud amount and the cloud optical thickness in Sichuan basin is 0.674 from 1984 to 2000.

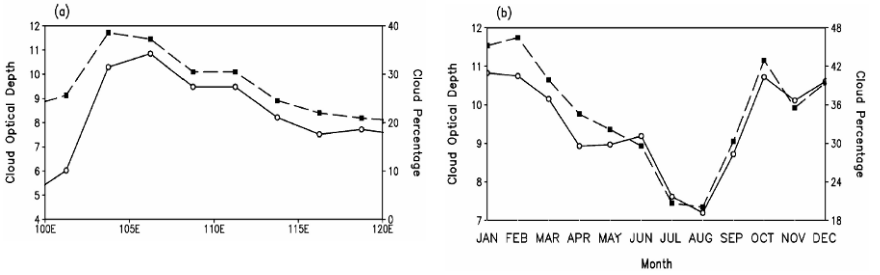

Fig. 6.12 (a) Longitudinal cross section of cloud optical thickness (solid) and the percentage of nimbostratus and altostratus cloud amount (dashed) along 29°N from 100° to 120°E; **(b)** annual cycles of the averaged cloud optical thickness (solid), and the percentage of the nimbostratus and altostratus clouds (dashed) averaged over the Sichuan basin (27°–32°N, 103°–108°E) from 1991 to 2000. The data are derived from the monthly ISCCP data. (Yu et al. 2004)

6.7.2 Formation of the nimbostratus and altostratus clouds

Nimbostratus and altostratus clouds generally cover a vast area and have a bulky vertical extent. The nimbostratus is sometimes thick enough to block out entirely the direct solar beam. The nimbostratus clouds have low cloud base and considerable vertical development, bringing the tops into the middle tropospheric level. The nimbostratus and altostratus often form when stably stratified moist air is forced by steady mechanical lifting over a large area. This often happens at a warm or cold front with gentle slope, occlusion, or in the presence of other large-scale forcing. Usually the atmosphere is stably stratified, and turbulence mixing in the clouds is weak. Yu et al. (2004) put forward that the persistent nimbostratus and altostratus clouds over subtropical East Asia result from the blocking and frictional effects of the TP. During most time of the year, particularly from November to May, the TP is continuously exposed to tropospheric westerlies. The elevated plateau bifurcates upstream low-level westerly flows and forces the surrounding flows to converge downstream. Meanwhile, the plateau also slows down the mid-tropospheric westerlies that flow over its mountainous surface, resulting in downstream mid-level divergence. The low-level convergence sustains large-scale steady lifting, while the mid-tropospheric divergence confines the lifting to the lower troposphere. To validate this opinion, Fig.6.13 shows the 1991~2000 annual mean westerly speed at 500hPa and winds at 850hPa. It is clear that the westerly flow is considerably slowed down when flowing over the TP, which induces a

strong divergence in the middle troposphere leeward of the plateau. The 850hPa surrounding flows converge downstream of the plateau. The 1991~2000 annual-mean vertical profile of divergence averaging in the region (27°~32°N, 103°~118°E) is shown in Fig.6.13b, which clearly displays the low-level convergence and middle and high tropospheric divergence downstream of the TP. Fig.6.13c shows the relationships among the total amount of nimbostratus and altostratus clouds and the mid-level divergence. Both variables are presented in terms of their mean annual cycles and averaged over the lee side of the plateau (27°~32°N, 103°~108°E). The mid-tropospheric divergence coincides very well with the amount of nimbostratus and altostratus clouds throughout the year. Results shown in Fig.6.13 suggest that mechanical forcing by the plateau provides a favorable large-scale environment for the formation of deep stratus clouds. Fig.6.12b and 6.13c also indicate that the cloud optical thickness and nimbostratus–altostratus cloud amount reach their extremes in the cold season when the westerlies are strongest.

In addition to the mechanical forcing by the plateau, the southern branch of the low-level westerly flows (Fig.6.13a) is recharged with moisture due to their trajectories passing across the warm Indian subcontinent and the Bay of Bengal. The moist, southern branch of the low-level westerly is constantly uplifted by the Yun-Gui Plateau, a highland extending from the southeast corner of the TP to Indochina. The sustained ascent, increased moisture transport, and stable stratification on the lee side of the plateau, together provide a suitable large-scale condition for the maintenance of nimbostratus and altostratus clouds.

6.7.3 Stratus cloud–climate feedback over the lee side of the TP

Over subtropical eastern China, the cloud amount and surface temperature exhibits a pronounced negative correlation. The spatial pattern of the correlation coefficients between the observed anomalous monthly cloud fractions and the anomalous surface temperatures shows that the most significant negative correlation is found along the Yangtze River valley (Figure not shown). Over the Sichuan basin (27°~32°N, 103°~108°E) where the cloud–radiative forcing is strongest, the correlation coefficient of annual mean cloud amounts and surface temperatures reaches -0.62 from 1951 to 2000. The 10-yr running mean surface temperature and cloud fraction for the Sichuan basin from 1956 to 1995 shows that the surface temperature variation has a strong opposite tendency from that of the total cloudiness on monthly to decadal time scales over the Sichuan basin (and the southeastern China in general). The negative correlation between the

surface temperature and stratus cloud amount suggests a coupling between the surface temperature and the cloud radiative forcing. It is well understood that the clouds can affect surface temperature through changing CRF (Chen et al. 2003). How does surface temperature affect the continental stratus clouds?

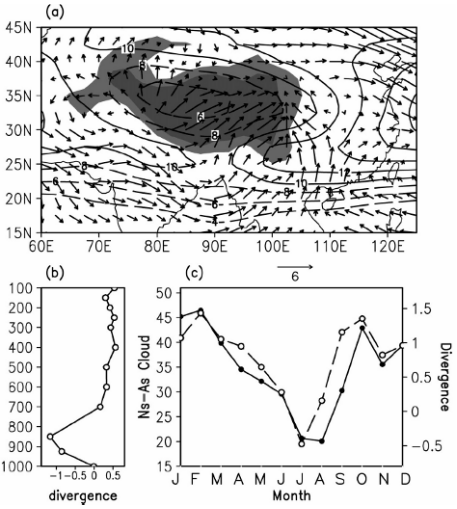

Fig. 6.13 (a) The 1991~2000 annual-mean westerly wind speed at 500hPa (contour interval is 2m s^{-1}) and the winds at 850hPa (vectors with maximal length for 6m s^{-1}). The dashed contours denote wind speed below 10m s^{-1}. The shading denotes mountain heights, and the edges of light and dark shading denote the contours of 2000 and 3500m, respectively. (b) 1991~2000 annual mean vertical profile of horizontal divergence averaging in the region (27°~32°N, 103°~118°E) in units of $10^6 s^{-1}$. (c) 1991~2000 mean annual cycles on the lee side of the plateau (27°~32°N, 103°~108°E), including nimbostratus–altostratus cloud amount (percentage) (solid), which is derived from the monthly ISCCP data, and the divergence in the midlevel (600~500hPa) in units of 10^6 s^{-1} (dashed). The circulation data are derived from the NCEP/NCAR reanalysis dataset. (Yu et al. 2004)

Analysis of the NCEP/NCAR reanalysis data and Chinese surface station data reveals that the surface temperature is highly correlated with the temperature below 850hPa (correlation coefficient reaches 0.72 from 1963 to 2000), but is nearly uncorrelated to the temperature above 600hPa. This implies that a surface warming would destabilize the low troposphere and reduce the relative humidity in the boundary layer because the increase of water vapor in the air is slower than the increase of the saturation vapor over most of the land area.

The above analyses lead to two hypothetically positive feedback processes between the cloud physics and large-scale dynamics, that is, the stratus–surface temperature feedbacks through changing stability and relative humidity. When surface temperature rises, the reduced relative humidity would reduce stratus cloud fraction, allowing more radiative fluxes into the earth system and resulting in further surface warming. Meanwhile, the surface warming would also reduce the lower-tropospheric static stability, which in turn reduces the potential for stratus cloud formation and favors further surface warming. In addition, the reduction in static stability could stimulate stronger mixing with drier air above and could further induce the reduction in low level humidity, which could enhance the feedback.

To confirm the proposed positive cloud feedback mechanisms, the interannual variations are examined. For the period from 1963 to 2000, the correlation coefficient between the surface temperature and the mean relative humidity in the layer between 925 and 700hPa is -0.48; the correlation coefficient between the surface temperature and 500~850-hPa differential potential temperatures is -0.42. The annual mean total cloudiness is positively correlated with the mean relative humidity and the differential potential temperature (stability) with the correlation coefficients being 0.73 and 0.50, respectively.

The10-yr running mean surface temperatures, relative humidity and the differential potential temperature indicates that a significant negative (positive) correlation between the surface temperature (total cloud amount) and lower-troposphere relative humidity or static stability exists on decadal time scales (Figure not shown). The strong coupling among the surface temperature, clouds, relative humidity, and static stability indicates the important contributions of the stratus cloud feedback (through changing relative humidity and static stability) to the climate variations on the lee side of the plateau.

6.7.4 Impacts of the Plateau stratus cloud deck on east China climate

Impacts on mean climate

The negative net CRF of the plateau continental stratus exhibits a maximum that is comparable with that of marine stratus clouds over the southeastern Pacific (figure not shown). This is expected from the radiative properties of the nimbostratus and altostratus clouds. Corresponding to the largest cloud optical depth, the TP stratus deck produces strongest shortwave CRF at the TOA (figure not shown). Although the corresponding long wave CRF is more than twice larger than that of the marine stratus, the net

CRF at the eastern flank of the plateau remains to be dominated by the shortwave CRF. Under the clear sky condition, the annual mean net downward radiative fluxes in this region are around 40W·m^{-2}. The all-sky net downward radiative fluxes are negative with a minimum below -20W·m^{-2}, which is located at the Sichuan basin. Therefore, the clouds produce more than 60 W·m^{-2} radiative cooling. The zonal variation of shortwave CRF and the net CRF along the Yangtze River coincides well with the zonal variations in nimbostratus–altostratus clouds and the cloud optical thickness. Their annual cycles also match each other quite well (figure not shown), indicating that both the strongest shortwave CRF and net CRF are over the Sichuan basin, especially during the cold season. The extremely strong negative CRF of the plateau stratus deck has prominent impacts on the climate in eastern China. It affects profoundly the local energy balance. To compensate the radiative cooling induced by the negative net CRF at the TOA, the atmospheric column there must gain energy from the moist static energy convergence. Therefore, eastern China becomes an area of energy sink. This is in sharp contrast to other subtropical regions where the atmosphere exports moist static energy (Yu et al. 1999).

Impacts on the surface temperature variation

The positive feedback between the surface temperature and the TP stratus deck may help to explain the climate variation downstream of the plateau. It is conceivable that the cloud radiative feedback during the surface cooling period could be more robust than that in the warming period. When the surface cools, the increased static stability favors stratus cloud formation while it restrains deep convection and related cirrus cloud formation, which results in more intensified solar radiative cooling that dominates the cloud-induced greenhouse warming. However, when the surface warms, the induced unstable stratification might, in part, favor cumulus convective clouds that could weaken the positive cloud feedback.

The case study indicates more robust positive cloud feedback in the cooling period. During the warming period from 1986 to 1987, the surface temperature increased 0.78°C; the net cloud radiative forcing increased by 6 W·m^{-2} (the total cloud fraction decreased by 1%, and the stratus cloud amount decreased by 3.3%). Therefore, the cloud radiative feedback is only 7.7 W·m^{-2}·K^{-1} if changes in cloud are entirely related to the changes in surface temperature. On the other hand, during the cooling period from 1987 to 1989, the surface temperature decreased 0.78°C, and the net cloud radiative forcing decreased by 13 W·m^{-2} (the total cloud fraction increased by 5.5% and stratus clouds increased by 6.2%). Thus, the cloud radiative feedback amounts to 16.7 W·m^{-2}·K^{-1} if changes in cloud are entirely related

to the changes in surface temperature. Based on this estimation, the positive cloud radiative feedback during the cooling period is obviously stronger than that during a warming period. The relatively weak cloud radiative feedback during the warming period could be due to the nonstratus cloud formation. During the warming period of 1986~87, 70% of the stratus cloud decrease is balanced by nonstratus clouds, while during the cooling period 1987~89, only 11% of stratus cloud increase is offset by nonstratus clouds. Thus the change of stratus clouds during the cooling period more effectively dominates the total cloudiness variation than that during a warming period.

6.8 Conclusions

In this chapter, we present recent achievements made by Chinese scientists on the TP meteorology. It is seen that the formation and evolution of the Asian Monsoon, East Asian subtropical westerly jet, South Asian High and the continental stratus cloud over eastern China are closely linked to the thermal and mechanical forcing of the TP. The elevated heat source of TP can more effectively heat up the atmosphere aloft. The intensity, distribution and seasonal variation of the atmospheric heat source/sink over TP are presented in section 2. It is seen that the TP atmosphere acts as a heat source from April to September, and as a cold source in the other months. The sensible heat of the surface increases remarkably over the southwest of the TP, causing the obvious increase of $<Q_1>$ there in February and March, which makes a center of the atmospheric heat source appear over the north slope of the Himalayas. Afterwards, this center continues to intensify and experiences noticeable migration westwards twice, separately occurring in April and June. In summer, the latent heat of condensation becomes a heating factor as important as the sensible heat and is also a main factor that makes the atmospheric heat source over the east part of the TP continue growing. On the interdecadal time scale, $<Q_1>$ of the TP shows an abrupt change in 1977 and a remarkable increase after 1977.

The plateau sensible heat is an important part of $<Q_1>$ and plays a significant role in regulating general circulation. Wu et al (1997) put forward the concept of sensible heat driven air-pump (SHAP) and investigated its effects on the monsoon circulation and the seasonal transition of general circulation. It is found that SHAP gives an impact on general circulation mainly through two mechanisms: firstly, the closure of SHAP induces a convergence at upper troposphere and descending motion over the TP which in turn results in divergence at low troposphere and precipitation

anomaly in its vicinities; secondly, the closure of SHAP induces a sharp cooling of low tropospheric atmosphere which will induce a positive upper tropospheric vorticity anomaly due to the direct proportional relationship between the local variation of vorticity and variation of heating rate with height. Thus, the upper tropospheric vorticity increases significantly and affects the global climate by virtue of the frequency dispersion of Rossby wave. In addition, the seasonal variation of general circulation near the TP is also closely linked to the TP SHAP. The numerical experiments show that without the SHAP, the simulated monsoon period is shortened and the most persistent longitude of the monsoon period also shifts from the Plateau region in the CON run to about 120°E in the NSH run. To explore the effect of the TP in East Asian monsoon, a series of numerical simulations have been carried out with various land-sea distributions and orography. The result shows the occurrence of East Asian subtropical monsoon is dependent on the existence of longitudinal large-scale land-sea distribution. However, the inclusion of the TP markedly strengthens the intensity of East Asian monsoon and extents the monsoon region northward.

The plateau sensible heat is influenced by snow to a large extent. Section 4 shows that snow anomalies over the TP change the soil moisture and the surface temperature through the snowmelt process at first, and subsequently alter heat, moisture and radiation fluxes from the surface to the atmosphere. SVD analysis shows that the snow depth anomaly, especially in winter, is one of the factors influencing precipitation in China; however, it is perhaps not the only one, and even not the most important one. Nevertheless, it is proved that the winter snow anomaly over the TP is relatively more important than that in spring for the regional precipitation in China. Results of numerical simulations show that the snow anomaly over the plateau has evident effects on China's summer monsoon climate. The increase of both snow cover and snow depth can delay the onset and weaken the intensity of the summer monsoon obviously, resulting in a decrease in precipitation in southern China and an increase in the Yangtze and Huaihe River basins. The influence of the winter snow depth is more substantial than that of both the winter snow cover and the spring snow depth. The mechanism of how the plateau snow anomaly influences the regional monsoon climate shows that abnormal circulation conditions induced by changes of surface fluxes may affect the underlying surface properties in turn. Such a long-term interaction between the wetland and the atmosphere is the key process resulting in later climatic changes.

The South Asian High (SAH), the strongest, largest, and most stable anticyclonic circulation system at 100hPa in the Northern Hemisphere, also results from the heating effect of TP (Mason and Anderson, 1958; Flohn, 1960). The SAH has two seasonal steady modes, one of which is the conti-

nental high in summer and the other the ocean high in winter. The continental high can be divided into two patterns as well, that is the Tibetan high and the Iranian high. The diagnosis based on the thermodynamic equation reveals that the TH is closely related to the diabatic heating of the TP, whereas the IH is more associated with the adiabatic heating in the free atmosphere, as well as the diabatic heating near the surface. It is found that the interannual variations of the SAH and precipitation are closely correlated to each other, especially the correlation between the longitudes of the SAH in June and precipitation in summer. Furthermore, the composites of the 100hPa flow fields in June for more and less precipitation in North China show that the SAH center shifts more westward and northward in years with more precipitation, whereas the opposite situation is found in years with less precipitation.

Analysis on the location of the westerly jet core at upper troposphere in June and July by using the NCEP/NCAR reanalysis data shows that the location of the westerly jet core shifts rapidly from 140ºE to 90ºE during 35th–39th pentads, which corresponds to the plum rain period over East Asia. The meridional temperature contrast in the troposphere is associated with the rapid location change of the jet core. The diabatic heating changes are the primary factor determining the seasonal evolution of the westerly jet core over East Asia. In the boreal midsummer the major westerly jet centers occur frequently at two positions, which correspond to the TP to the east from 85ºE to 100ºE and the Iranian Plateau to the west from 45ºE to 60ºE. Thus, the bimodality feature of the jet core is found over East Asia, similar to that of the SAH. Clearly this bimodality of the jet core is related to the elevated topography i.e. the TP and the Iranian plateau. Corresponding to the bimodality of the westerly jet core in midsummer, there exist obvious differences in geopotential height fields, air temperatures and circulations, as a result, the related climate anomalies are possibly apparent. The composites of surface air temperature and precipitation at 518 stations in China show that most regions in China experience negative temperature anomaly except the South China in TJM, and the opposite situation occurs in IJM. This implies that TJM corresponds to a lower surface air temperature and the situation is opposite in IJM. As to the rainfall anomaly distribution, a positive anomaly area is located at the south of the TP and the lower reaches of the Yangtze River valley while the South China and the North China are the less precipitation areas, and the distribution in IJM is opposite.

The formation of continental status cloud located on the leeside of the TP is linked to the mechanical forcing of the TP. This largest cloud optical depth is produced by persistent deep stratus clouds (primarily the nimbostratus and altostratus) during winter and spring. These deep stratus clouds

are generated and maintained by the frictional and blocking effects of the TP. The plateau slows down the overflow, inducing downstream midlevel divergence; meanwhile it forces the low-level flows to converge downstream, generating sustained large-scale lifting and stable stratification that maintain the thick stratus clouds. These stratus clouds produce extremely strong cloud radiative forcing at the top of the atmosphere, which fundamentally influences the local energy balance and climate change. Analysis of the long-term meteorological station observations reveals that the monthly mean anomalous cloudiness and surface temperature vary in tandem. In addition, the surface warming leads to destabilization and desaturation in the boundary layer. This evidence suggests a positive feedback between the continental stratus clouds and surface temperature through changing lower-tropospheric relative humidity and stratification. It is shown that the positive feedback mechanism is more robust during the period of the surface cooling than during the surface warming. It is suggested that the positive climate feedback of the continental stratus cloud may be instrumental in understanding the long-term climatic trend and variations over East Asia.

Numerical models have been an important tool for climate research and operational prediction after extensive model developments and verifications. Whereas, the significant deviations of simulation from the observation still exist, especially in East Asia. One important reason is the existence of the TP. Since the East Asian weather and climate is closely related to the effects of the TP, it is worth to pay more attention to how to develop the suitable parameterization for Asian climate modeling with well considering the aforementioned dynamical and thermodynamic effects of TP in future studies.

References

Barnett TP, Dumenil L, Schiese V, Roeckner E, Latif M (1989) The effect of Eurasian snow cover on regional and global climate variations. J. Atmos. Sci. 46: 661-685

Bolin B (1950) On the influence of the earth's orography on the westerlies. Tellus 2: 184-195

Broccoli AJ, Manabe S (1992) The Effects of Orography on Midlatitude Northern Hemisphere Dry Climates. J. Climate 5: 1181-1201

Charney JG, Eliassen A (1949) A numerical method for predicting the perturbations of the middle latitude westerlies. Tellus 1: 38-54

Chen B, Chao WC, Liu X (2003) Enhanced climatic warming in the TP due to doubling CO2: A model study. Climate Dyn. 20: 401–413

Chen LX, Reiter ER, Feng ZQ (1985) The atmospheric heat source over the TP: May-August 1979, Mon.Wea. Rev. 113(10): 1771-1790

Chen LX, Liu JP, Zhou XJ, Wang PX (1999) Imapct of uplift of Qiinghai-Xizang Plateau and change of land-ocean distribution on climate over Asia. Quaternary Sciences 4: 314-329 (in Chinese)

Flohn H (1957) Large-scale aspects of the "summer monsoon" in South and East Asia. J. Meteor. Soc. Japan (75th Ann. vol.): 180-186

Flohn H (1960) Recent investigation on the mechanism of the ‘summer monsoon’of southern and eastern Asia. Proc. Symp. Monsoon of the World, New Delhi. Hind Union Press, 75-88

Guo QY (1983) The summer monsoon Intensity index in East Asian and its variation. Acta Geographica Sinca 38(3): 207-217 (in Chinese)

Fu C, Fletcher JO (1985) The relationship between Tibet-tropical ocean thermal contrast and interannual variability of Indian monsoon rainfall. J. Climate Appl. Meteorol. 24: 841-847

Hahn DG, Manabe S (1975) The role of mountain in the south Asia monsoon. J. Atmos. Sci. 32: 1515-1541.

Huang Y, Qian YF (2003) Relationships between South Asian High and summer rainfall in north China. Plateau Meteorology 22(6): 602-607 (in Chinese)

Klein SA, Hartmann DL (1993) The seasonal cycle of low stratiform clouds. J. Climate 6: 1587-1606.

Koo CC, Yeh TC (1955) Some calculations of the influence of the large-scale topography on the climate of China. Acta Meteorologica Sinica 26: 167-182 (in Chinese)

Kuo HL, Qian YF (1982) Numerical simulation of the development of mean monsoon circulation in July, Mon. Wea. Rev. 110(12): 1879-1897

Kutzbach JE, Guetter PJ, Ruddiman WF, Prell WL (1989) Sensitivity of Climate to Late Cenozoic Uplift in Southern Asia and the American West: Numerical Experiments. J. Geophys. Res. 94(D15): 18393-18407

Kutzbach JE, Prell WL, Ruddiman WF (1993) Sensitivity of Eurasian climate to surface uplift of the TP. J. Geology 101: 177-190

Li C, Yanai M (1996) The onset and internnual variability of the Asian summer monsoon in relation to land-sea thermal contrast. J. Climate 9: 358-375.

Liu XD, Yin ZY (2002) Sensitivity of East Asian monsoon climate to the uplift of the TP. Palaeogeography, Palaeoclimatology, Palaeoecology 183: 223-245

Manabu ABE, Yasunari T, Kitoh A (2004) Effects of Large-scale Orography on the Coupled Atmosphere-Ocean System in the Tropical Indian and Pacific Oceans in Boreal Summer. J. Meteor. Soc. Japan 82(2): 745-759

Mason RB, Anderson CE (1958) The development and decay of the 100mb summertime anticyclone over southern Asia. Mon. Wea. Rev. 91: 3-12

Qian YF (1988) Numerical simulations of the dynamic effects of the TP. In: Qian YF, Yan H, Wang QQ, Wang AY (eds) Numerical studies of orographic effects in the planetary atmosphere, Science Press, Beijing, pp 103-118 (in Chinese).

Qian YF, Wang SY, Shao H (2001) A possible mechanism effecting the earlier onset of the South China Sea southwesterly summer monsoon compared to that of the Indian monsoon. Meteorol. Atmos. Phys. 76: 237-249.

Qian YF, Zhang Q, Yao YH, Zhang XH (2002) Seasonal Variation and Heat Preference of the South Asia High. Adv. Atmos. Sci. 19(5): 821-836

Qian YF, Zheng YQ, Zhang Y, Miao MQ (2003) Responses of China's summer monsoon climate to snow anomaly over the TP. Int. J. Climatol. 23: 593-613

Qian YF, Zhang Y, Jiang J, Yao YH and Xu ZF (2005) The earliest onset areas and mechanism of the tropical Asian summer monsoon. Acta Meteorologica Sinca 19(2): 129-142

Qin DH, Liu SY, Li PJ (2006) Snow Cover Distribution, Variability, and Response to Climate Change in Western China. J. Climate 19: 1820-1833

Ramanathan, VR. Cess D, Harrison EF, Minnis P Barkstrom BR, Ahmad E, Hartmann D (1989) Cloud radiative forcing and climate: Results from the Earth Radiation Budget Experiment. Science 243: 57-63.

Ruddiman WF, Kutzbach JE (1989) Forcing of Late Cenozoic Northern Hemisphere Climate by Plateau Uplift in Southern Asia and the American West. J. Geophys. Res. 94(D15): 18409-18427

Tao SY, Zhao YJ, Chen XM (1958), The association between Mei-yu in East Asia and seasonal variation of the general circulation of atmosphere over Asia, Acta Meteorologica Sinica 29(2), 119-134 (in Chinese)

Tao SY, Chen LS , Xu XD, Xiao YS (2000a) Progresses of Theoretical Study in the Second TP Atmosphere Scientific Experiment (Part I). China Meteorological Press, Beijing, 348pp. (in Chinese)

Tao SY , Chen LS , Xu XD, Xiao YS (2000b) Progresses of Theoretical Study in the Second TP Atmosphere Scientific Experiment (Part II). China Meteorological Press, Beijing, 396pp. (in Chinese)

Tao SY , Chen LS , Xu XD, Xiao YS (2000c) Progresses of Theoretical Study in the Second TP Atmosphere Scientific Experiment (Part III). China Meteorological Press, Beijing, 203pp. (in Chinese)

Trenberth KE, Chen SC (1988) Planetary waves kinematically forced by Himalayan orography. J. Atmos. Sci. 45: 2934-2948.

Tsujimura Maki, Atusi Numaguti, Lide Tian, Shigemasa Hashimoto, Atsuko Sugimoto and Masayoshi Nakawo, 2001: Behavior of Subsurface Water Revealed by Stable Isotope and Tensiometric Observation in the TP. J. Meteor. Soc. Japan 79, 599-605

Vernekar AD, Zhou J, Shukla J (1995) The effect of Eurasian snow cover on the Indian monsoon. J. Climate 8: 248-266.

Williamson DL, Keihl JT, Ramanathan V, Dickinson RE, Hack JJ (1987) Description of NCAR community climate model (CCM1), NCAR Tech. Note, Ncar/TN-285+STR, National Center for Atmospheric Research, Boulder, Colo., pp 10-15.

Wu GX, Zhang YS (1998) TP forcing and the Timing of the monsoon onset over South Asia and South China Sea. Mon Wea. Rev. 126 (4): 913-927.

Wu GX, Zhu BZ, Gao DY (1996) The impact of Tibetan Plateau on local and regional climate. From Atmospheric Circulation to Global Change. Ed Institute of Atmospheric Physics, CAS, China Meteor. Press. 425-440 (in Chinese)

Wu GX, Zhang XH, Liu H, Yu YQ, Jin XZ, Guo YF, Sun SF, Li WP, Wang B, Shi GY (1997a) Global ocean-atmosphere-land system model of lasg(goals/lasg) and its performance in simulation study. Quarterly Journal of Applied Meteorology 8 (Suppl):15-28 (in Chinese)

Wu GX, Li WP, Guo H, Liu H (1997b) Sensible heat-driving air pump of the TP and the Asian summer monsoon. In: Ye DZ (eds) Momorial Volume of Prof. Zhao Jiuzhang, Chinese Science Press, Beijing, pp 116-126. (in Chinese)

Wu TW, Qian ZA (2003) The Relation between the Tibetan Winter Snow and the Asian Summer Monsoon and Rainfall: An Observational Investigation. J. Climate 16: 2038-2051

Xu ZF, Qian YF (2006) Land-sea Distribution, Orography and Asian Monsoon. Doctoral dissertation of Nanjing University, pp 24-82. (in Chinese)

Yanai M, Li C (1994) Mechanism of heating and the boundary layer over the TP. Mon. Wea. Rev. 122: 305-323

Yanai M, Li C, Song ZS (1992) Seasonal heating of the TP and its effects on the evolution of the Asian summer monsoon, J. Meteor. Soc. Japan 70(1): 319-350.

Yatagai A (2001) Estimation of precipitable water and relative humidity over the TP from GMS-5 water vapor channel data. J. Meteor. Soc. Japan 79: 589-598

Yeh TC (1950) The circulation of the high troposphere over China in the winter of 1945-1946. Tellus 2: 173-183.

Ye DZ (Yeh, TC) (1982) Some aspects of the thermal influences of the Qinghai-TP on the atmospheric circulation. Arch. Meteor. Geophys. Bioclim, Series A 31(1): 205-220.

Ye DZ, Change CC (1974) A preliminary experimental simulation of the heating effect of the TP on the general circulation over East Asia in the summer. Scientia Sinica (Science in China) 12: 397-420.

Ye DZ, Wu GX, (1998) The Role of The Heat Source of the TP in the General Circulation. Meteorol. Atmos. Phys. 67: 181-198

Yeh TC, Lo SW, Chu PC (1957) On the heat balance and circulation structure in the troposphere over the TP and this vicinity. Acta Meteorologica Sinica 28: 108-121 (in Chinese)

Yeh DZ, Tao SY, Li MC (1958) The abrupt change of circulation over Northern Hemisphere during June and October, Acta Meteorologica Sinica 29(4), 250-263 (in Chinese)

Ye DZ, Tao SY, Li MC (1959) The abrupt change of circulation over the Northern hemisphere in June and October. In: Bolin B (eds) The Atmosphere and the Sea in Motion. Scientific Contributions to the Rossby Memorial Volume, The Rokce Seller Institute Press and Oxford University Press, 249-267.

Ye DZ, Gao YX et al. (1979) Meteorology of the Qinghai-Xizang Plateau. Beijing: Science Press (in Chinese)

Yin MT (1949) A synoptic-aerological study of the onset of the summer monsoon over India and Burma, J. Meteorol. 6, 393-400

Yu RC, Zhang M, Cess RD (1999) Analysis of the atmospheric energy budget: A consistency study of available data sets. J. Geophys. Res. 104: 9655-9661.

Yu RC, Yu YQ, Zhang MH (2001) Comparing cloud radiative properties between the eastern China and the Indian monsoon region. Adv. Atmos. Sci. 18, 1090-1102.

Yu RC, Wang B, Zhou TJ (2004) Climate Effects of the Deep Continental Stratus Clouds Generated by the TP. J. Climate 17: 2702-2713.

Zhang YC, Qian YF (1999) Numerical study on the uplift of TP effects on the critical height of atmosphere. Acta Meteorologica Sinica 57(2): 157-167 (in Chinese)

Zhang JJ, Zhu BZ, Zhu FK, Weng DM, Sun GW, Lu JN, Peng YQ, Wang YZ (1988) The Qinghai-Xizang Plateau Meteorological Experiment (1979) and Research. In: Zhang JJ (eds) Advances in the Qinghai-Xizang Plateau Meteorology. Science Press, Beijing, 268 pp. (in Chinese).

Zhang Q, Wu GX, Qian YF (2002) The Bimodality of the 100hPa South Asia High and its Relationship to the Climate Anomaly over East Asia in Summer. Journal of Meteorological Society of Japan 80(4): 733-744.

Zhang YC, Kuang XY, Guo WD and Zhou TJ (2006) Seasonal evolution of the upper-tropospheric westerly jet core over East Asia. Geophysical Research Letters 33, L11708, doi:10.1029/2006GL026377

Zhao P, Chen LX (2000a) The climate characteristics of surface turbulent exchange coefficients and surface heat source over the Qinghai-TP, Acta Meteorologica Sinica 14(1): 13-29.

Zhao P, Chen, LX, (2000b) The calculation of solar albedo and radiation balance and the analysis of their climate characteristics over the Qinghai-TP, Advances in Atmospheric Sciences 17(1): 140-156.

Zhao P, Chen, LX, (2001) Climatic features of atmospheric heat source/sink over the Qinghai-Xizang Plateau in 35 years and its relation to rainfall in China, Science in China. Ser. D, 44(9): 858-864

Zheng YQ, Miao MQ, Qian YF, 1999: Application of the turbulent kinetic energy scheme in the RegCM2 climate model. Acta Meteorologica Sinica 57: 641–650. (in Chinese)

Chapter 7 Soil Moisture Variations and Its Impact on the Regional Climatic Change in China

7.1 Introduction

Namias (1958) was among the first in the meteorological community to address the influence of surface soil moisture anomalies on the atmospheric circulations at the seasonal scales. However, the advanced development of the soil moisture effect to climatic change was from middle 1970s. Charney (1975) pointed out that soil moisture can greatly affect surface albedo and evaporation during his research on biophysical feedback between land and atmosphere in the Sahel. Numerical simulations disclosed that the influence of soil moisture on surface fluxes is more important than those of surface albedo, soil structure and types (Mccumber, 1981). Sensitivity tests by Zhang et al. (1982) showed that the daytime planetary boundary layer structure us most sensitive to moisture availability, roughness length, albedo and thermal capacity, in that order. Several studies also showed that soil moisture had effect on not only local circulation in which anomaly exists, but also regions nearby (Rind, 1982; Rowntree et al., 1983; Yeh et al., 1984). Researches (Ookouchi et al., 1984; Avissar et al., 1989; Mahfouf et al., 1987; Pinty et al., 1989; Avissar et al., 1994) further pointed out that horizontal uniformity of soil moisture can induce local circulation and may contribute to the formation of strong synoptic system (Lanicci et al., 1987; Chang et al., 1991).

Comparisons between dry and wet soil affection on regional climate with numerical model by Shukla et al. (1982) showed that the precipitation in July in major continent from dry soil is 40-50% weaker than that from wet soil, which means the contribution of land evaporation to precipitation is unelectable, and more sensible heat flux from dry soil can lead to stronger convection precipitation with abundant vapor transport in the region. In main monsoon regions such as India subcontinent where monsoon circulation is dominant, the precipitation from dry soil is stronger than that from the wet soil, which may be explained as the monsoon precipitation is controlled by water vapor transport from monsoon circulation rather than inland evaporation. Meanwhile, surface temperature at dry surface is 2-3°C

higher than that of the wet one; however, the pressure at dry surface is lower than that if the wet one. Sensitive test by Walker et al. (1978) also showed that dry soil can lead to the rise of temperature with stronger precipitation and wet soil is helpful to the duration of the precipitation. Yeh et al. (1984) investigated the effect of irrigated soil to the climate with GFDL GCM and pointed out that the increased soil moisture can lead to the greater precipitation and lower temperature. A study by a coupled vegetation-climate model to perform comparisons of different surface conditions in Sahel by Xue (1990) showed that surface condition changes have strong feedback on the precipitation and cloud amount but also the temperature can be affected therefore regional climate change.

Wang (1991) studied the influence from soil moisture anomaly with IAP-GCM (Institute of Atmospheric Physics) and also found that positive soil moisture anomaly leads to increased precipitation and humidity, lower temperature and higher pressure. However, the effect is weak 20 days later. Similar to other studies, his study shows the impact of soil moisture anomaly can propagate outside the region. One mechanism that soil moisture affecting climate change is through changing surface heat and hydrology process, therefore the feedback on flux transport between surface and the atmosphere.

It was well expressed the importance of soil moisture to the climatic change, especially in the areas of continental climate. However, due to the lack of in situ soil moisture observation data, numerical simulation is the mostly used and convenient tool in present studies. With current observation dataset few diagnosis and analysis on the relationship between soil moisture and climatic change can be performed, excepting for some field observation experiment, which are not long enough to detect long term climatic variation at large scale. Further comprehension on the mechanism between soil moisture and long term climatic change interaction at large scale is necessary though difficult for climatic change research at present.

Global distributions of soil moisture gauge stations are shown by Fig. 7.1. Comparing to observation at global scale, there is advancement in regional scales. For instance, in situ soil moisture data from former Soviet union and China agricultural meteorological gauge stations are available from 1980s (Robock et al., 2000). Originally serving agricultural meteorology, in situ soil moisture measurement, such as soil moisture, is of great importance in studies of climate change and land surface process interaction.

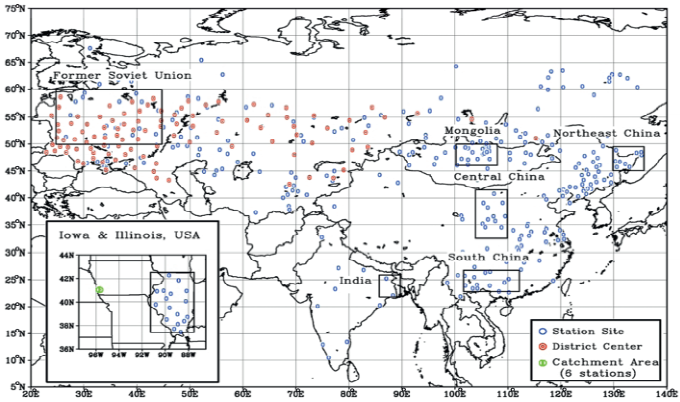

Fig. 7.1 Global distributions of soil moisture gauge stations (Robock et al., 2000)

7.2 In situ measured soil moisture in China

7.2.1 Soil moisture measurement in China

In China, soil moisture measurement started from 1980s (mostly from 1981), which aimed to serve the purpose of research and application of agricultural meteorology. Soil water condition (in-situ soil moisture) is the main observation element.

There are two techniques for soil moisture measurement at agricultural meteorology stations: the gravimetric method, and neutron probes. The gravimetric method is also called the thermostat-weight technique. Soil samples are taken using coring devices or augers at required depths and locations. The sample is weighed, oven-dried, and weighed again. The difference in mass gives the total soil moisture in the sample, which is converted to volumetric units with the density of the soil. The neutron probes method is to install a probe with a fast neutron source on the surface or lower soil in an access tube (transparent to the neutrons), and the backscattered flux of slow neutrons are measured, which is proportional to the density of hydrogen atoms. Because water is the major source of hydrogen atoms that changes with time, the neutron probe can provide a good measurement of soil water content. Calibration of slow neutron counts with gravimetric samples of soil moisture content and bulk densities yields a relationship to estimate the volumetric soil moisture content.

The in-situ soil moisture is measured at 11 layers of 0-5cm, 5-10cm, 10-20cm, 20-30cm, 30-40cm, 40-50cm, 50-60cm, 60-70cm, 70-80cm, 80-90cm and 90-100cm and on 8th, 18th and 28th days every month, except for winter time in northern China where soil is frozen. Detailed information can be found in the observational method and criterion (National meteorological administration, 1993). There are 178 gauge stations available at present with 76 new gauge stations established in the west, and distributions are shown in Fig. 7.2.

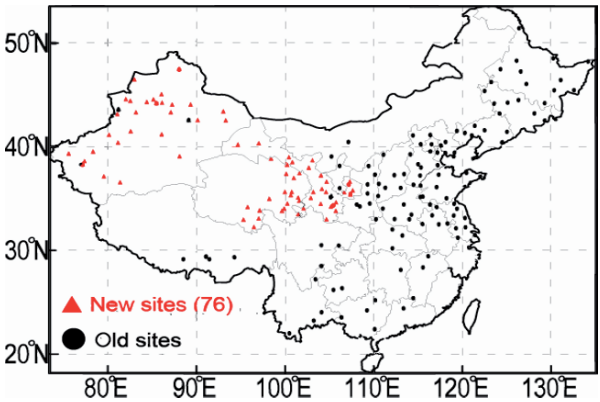

Fig. 7.2 Distributions of gauge stations for soil moisture measurement in China

7.2.2 Temporal and spatial variation characteristics of soil moisture

The temporal and spatial variations of soil moisture are analyzed using in-situ soil moisture data from 98 agricultural meteorological gauge stations in Eastern China for the years 1981－1991. The data includes gravimetric soil moisture, field capacity, bulk density of soil and wilting level. Distributions of gauge stations for soil moisture measurement are shown by Fig. 7.3, in which F represents non irrigation and T for irrigation. Irrigation stations will not be used in analysis in order to remove the influence of human activity. Soil types of gauge stations are mainly loamy and sandy loamy soils (as shown in Fig. 7.4,). 12 sub-regions were divided in Eastern China according to soil and soil moisture characteristics (Table 7.1). Field capacity, bulk density and wilting level were regarded as constant in each region.

Table 7.1 12 small regions

No.	Latitude and longitude
1	$lat \geq 44^\circ$ N， $lon \geq 126^\circ$ E
2	40° N $\leq lat < 44^\circ$ N , $lon \geq 124^\circ$ E
3	$lat \geq 44^\circ$ N , $lon < 126^\circ$ E
4	40° N $\leq lat < 44^\circ$ N , 114° E $\leq$ lon $< 124^\circ$ E
5	$lat \geq 36^\circ$ N , 100° E $\leq$ lon $< 114^\circ$ E
6	28° N $\leq$ lat $< 36^\circ$ N , 100° E $\leq$ lon $< 106^\circ$ E
7	$lat < 28^\circ$ N , 100° E $\leq$ lon $< 104^\circ$ E
8	30° N $\leq$ lat $< 40^\circ$ N , $lon \geq 114^\circ$ E
9	28° N $\leq$ lat $< 36^\circ$ N , 106° E $\leq$ lon $< 114^\circ$ E
10	$lat < 28^\circ$ N , 104° E $\leq$ lon $< 110^\circ$ E
11	$lat < 30^\circ$ N , $lon \geq 114^\circ$ E
12	$lat < 28^\circ$ N , 110° E $\leq$ lon $< 114^\circ$ E

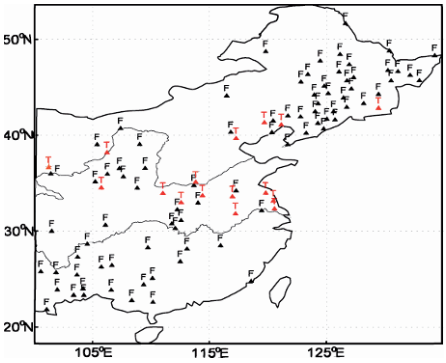

Fig. 7.3 Distributions of gauge stations for soil moisture measurement in Eastern China (F represents non irrigation and T for irrigation)

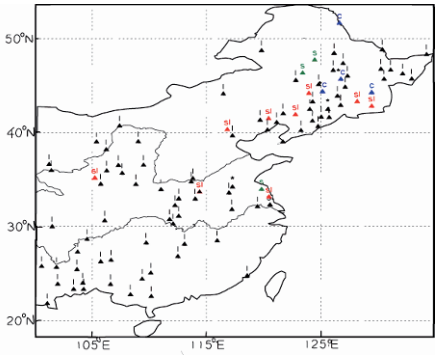

Fig. 7.4 Soil types of gauge stations(c: clay, l: loam, s: sand, sl: sandy loam)

Data and methodology

Soil moisture represents water content stored in the soil, which can be expressed by gravimetric soil moisture, volumetric soil moisture, stored water content and efficient water content.

Commonly used soil moisture parameters are defined as follows:

Gravimetric soil moisture (w, unit: g g^{-1}):

$$w = \frac{g_w}{g_s} \tag{7.1}$$

g_w is the weight of water stored in unit volume (unit: g) and g_s is the weight of dry soil in unit volume (unit: g).

Volumetric soil moisture (q, unit: $cm^3\ cm^{-3}$)

$$q = w \times \rho \tag{7.2}$$

ρ is bulk density of soil moisture (unit: $g\ cm^{-3}$).

Relative moisture of the soil (unit: %)

$$r = \frac{w}{f_c} \times 100\% \tag{7.3}$$

f_c is field capacity and w is gravimetric soil moisture.

Total water content (η, unit: mm)

$$\eta = \rho \times h \times w \times 10 \tag{7.4}$$

h is the depth of the soil layer (cm), and w is gravimetric soil moisture.

Efficient water content (η_v, unit: mm)

$$\eta_v = \rho \times h \times (w - w_k) \times 10 \tag{7.5}$$

w_k is wilting level.

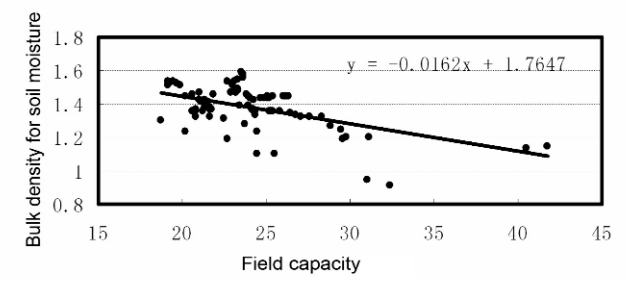

Fig. 7.5 The relationship between field capacity and bulk density for soil moisture

These soil parameters have different physical meanings. Volumetric soil moisture, efficient water content and total water content are usually used in land surface model. Relative moisture of the soil is a useful

parameter that is comparable among different soil characteristics. Efficient water content is widely used in agricultural meteorology.

Fig. 7.5 shows the linear relationship between field capacity and bulk density for soil moisture. Accordingly a formula can be written as

$$y=-0.062x+1.7647 \tag{7.6}$$

in which x is field capacity, y is bulk density. Bulk density can therefore be determined when observation is scarce.

The temporal variation characteristics of soil moisture

Soil moisture variations are controlled by those of precipitation, surface evaporation and runoff, and evaporation and runoff is determined by soil types and vegetations.

Three latitude belts can be obtained according to annual variation of the climate: northern belt (to the north of 40°N), including areas No.1-4; middle latitude belt (30°N~40°N) including areas No.5-9; and the southern belt (to the south of 30°N) including areas No.7-12. The corresponding annual variations of soil moisture will be discussed here.

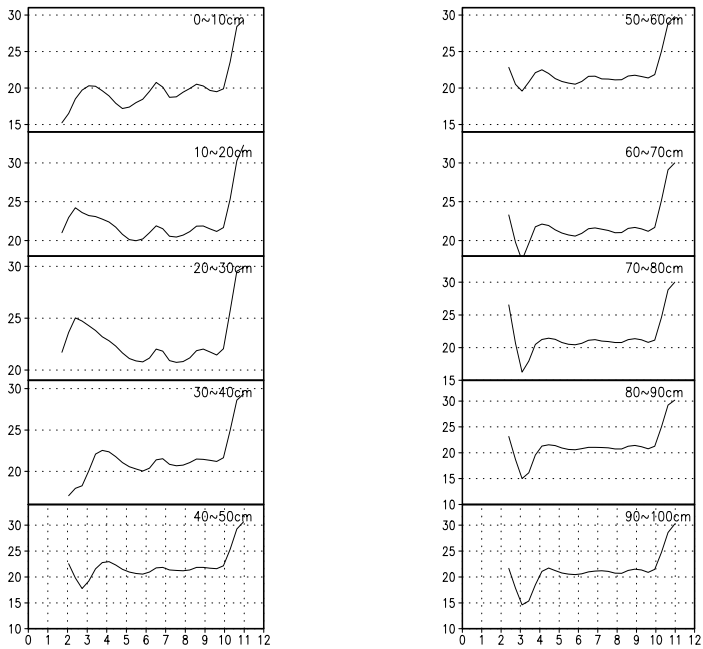

Fig. 7.6 Seasonal variations of volumetric soil moisture at different layers in No.3 region (unit: %)

North of Eastern China

Significant annual variations can be found at both surface and lower layers. Seasonal variations of volumetric soil moisture at different layers in region No.3 are shown in Fig. 7.6. At surface layer (less than 30~40cm), soil moisture increases from early March and reach maximum in late March, then decreases and reaches minimum in late May or June. Less variation can be found from July to October. The variance is about 5% at surface layer and 2% at the deeper layer. One significant difference of seasonal variations between upper layers (<= 30~40cm) and lower layers (>= 30~40cm） is the opposite change tendency in March. In lower layers the minimal variation is in March, which is only the half of yearly maximum in magnitude (about 15%).

The difference in soil moisture between surface and deep layers mainly results from snow melting in spring. With the rise of temperature in spring, melted snow can increase soil water content, meanwhile soil temperature remains low at lower levels, leading to low evapotranspiration and little water content loss. Omitting the effect of runoff, the formula for calculating soil moisture can be written as:

$$\frac{\partial w}{\partial t} = p_s - E \tag{7.7}$$

where P_s is snow melting rate and E is evaporation rate.

When the air temperature increases with time, the soil temperature will rise and lead to greater evapotranspiration. The available melting snow will reduce, and soil moisture will decline after later march due to less precipitation when dry season begins. As raining season comes the precipitation provides an abundance of soil water content, which also contributes to less variation of soil moisture during raining season (from May to October). Soil moisture increases rapidly in early November, benefiting from low temperature and less evapotranspiration. Fig. 7.6 also shows that only surface soil moisture can be affected by snow melting in spring. Soil moisture variations at surface and deep layer are uniform in summer and autumn, which means that the precipitation in summer and autumn can have influence on soil moisture distributions up to 100cm.

Middle latitude of Eastern China

In region No.5, seasonal variations of soil moisture, which is connected with snow pack in winter, are similar to those in the North China (Figure

not shown here). However, significant seasonal variations can be found below surface layer, which magnitudes increase with increasing depth.

There are obvious differences for soil moisture seasonal variations between No.5 and No.6 regions (Fig. 7.7). For region 6, soil moisture is low at layers of 40~50cm in spring and summer with minimum in the middle May, and it reaches minimum in middle June at layers below 40-50cm. It is worthwhile noticing that during middle June to late August the variations for soil moisture from 60-70cm layer are double comparing to minimum. Soil moisture increases from early September and reaches maximum in late December.

It can be seen that the regional differences are obvious for seasonal variations of soil moisture. The difference between No.9 and No.6 demonstrates that there are two peaks at each layer above 40~50cm for the seasonal variations of soil moisture, which appears in late May and August. However, below 40~50cm layers variations show one-peak character, which is related to seasonal variations of local precipitation and temperature and will be discussed in the following sections.

As shown in Fig 7.8, seasonal variations of soil moisture at each layer have minimal values in late May. The maximal variations occur in winter, with second maximum in summer and autumn.

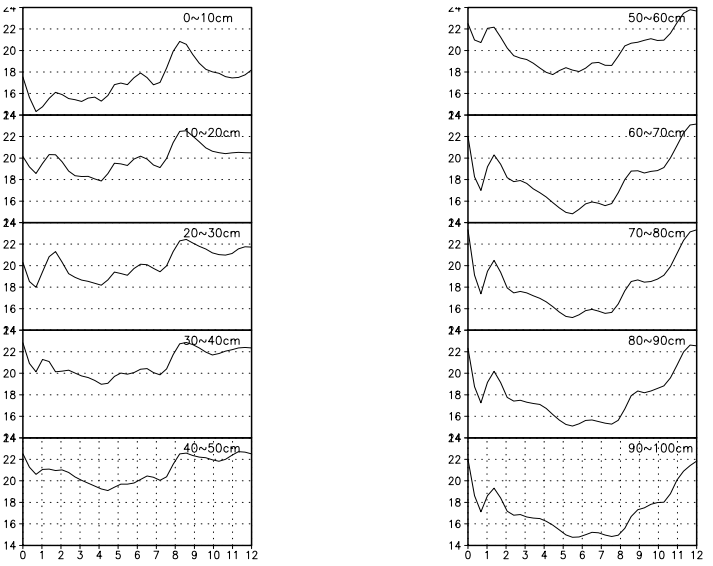

Fig. 7.7 Seasonal variations of volumetric soil moisture at different layers in No.6 region (other illustrations as Fig.6)

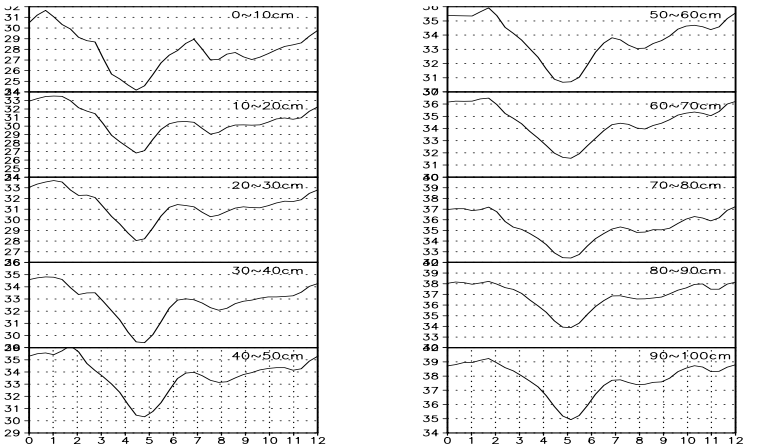

Fig. 7.8 Seasonal variations of volumetric soil moisture at different layers in No.8 region (other illustrations as Fig.6)

In the south of Eastern China

It is similar for seasonal variation of soil moisture to the east of 110°E (No.11and No.12), also regions No.7 and No.10 to the west of 110°E share similar seasonal variation. Therefore, they will be discussed separately.

Regions 11 and 12 have similar seasonal variations. In the region to the east of 110°E (Fig. 7.9), soil moisture increases from January and reaches maximum in middle March, then decreases from early May and reaches minimum in early October. Variations at different layers show the similar seasonal cycle. So do regions 7 and 10. We will discuss their variations in two groups.

For regions 7 and 10, which locate to the west of 110°E (Fig. 7.10), seasonal variations of soil moisture are of the opposite phase comparing to those of regions to the east of 110°E, in which soil moisture decreases form early January and reaches minimum in late April, then increases and reaches maximum in late November.

The maximal value of soil moisture content propagates downward with the increasing depth, with the time lag about a dekad. The different variation patterns between east and west 110°E may result from the controlling climate systems.

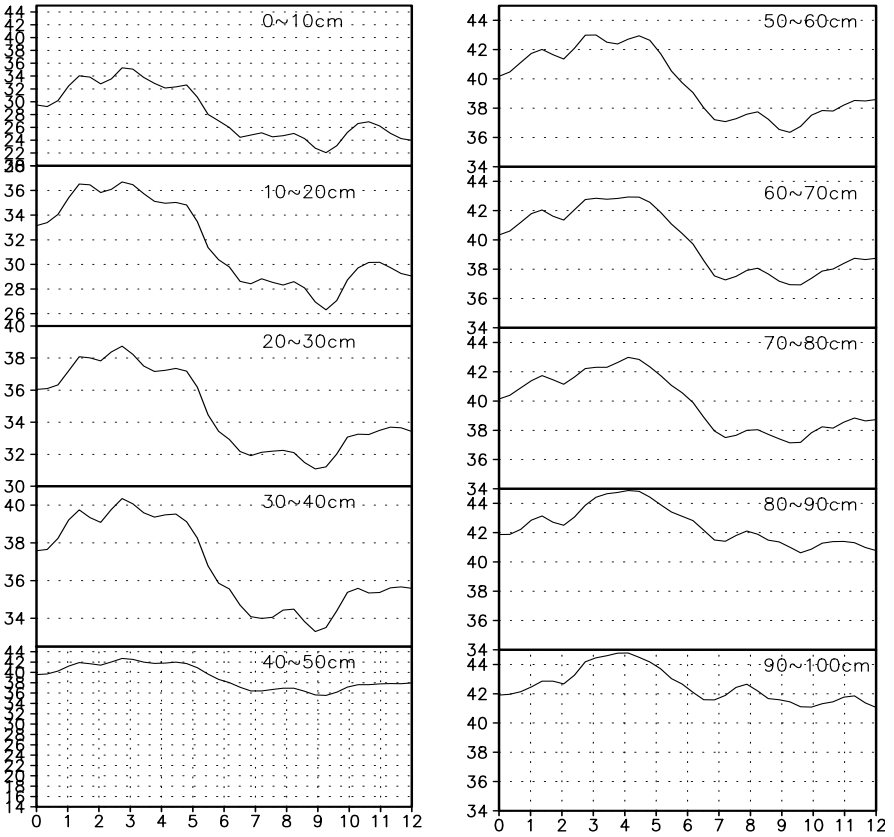

Fig. 7.9 Seasonal variations of volumetric soil moisture at different layers in No.12 region (other illustrations as Fig.6)

In general, it is greater for seasonal variability amplitude (difference between maximum and minimum during the whole year) of soil moisture at surface layer than that of deep layer. (Usually the annual soil moisture variation range at the surface is larger than that of lower layers.) However, seasonal variability amplitude at representative gauge stations in different latitudes shows different vertical profile characteristics, which reaches maximum at 10~20cm layer, shown by Fig 7.11. Also the maximum seasonal variability amplitude layer is connected with the latitude belt, which is deeper in the northern and shallower in the southern and middle latitude. This may result from different root distributions of the vegetation.

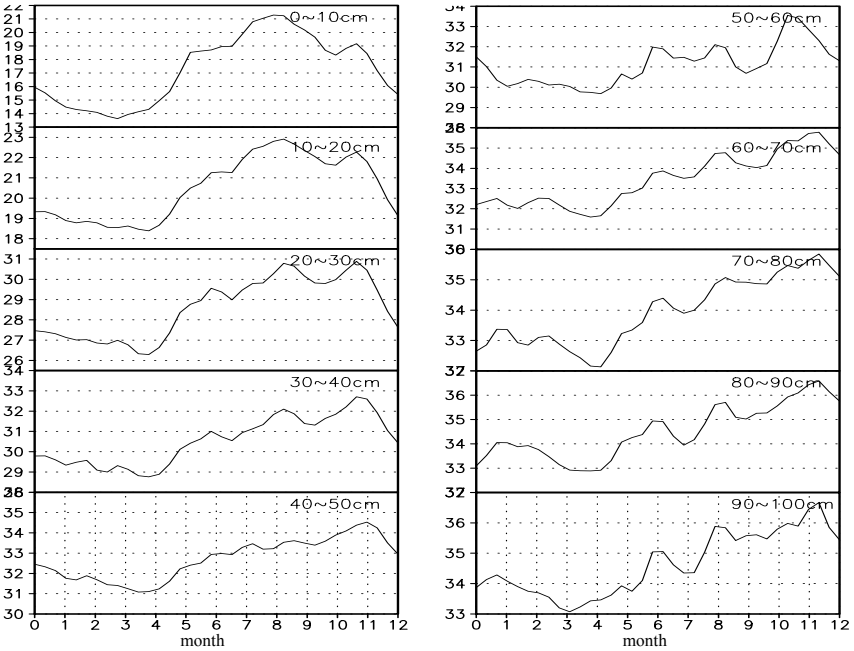

Fig. 7.10 Seasonal variations of volumetric soil moisture at different layers in No.7 region (other illustrations as Fig.6)

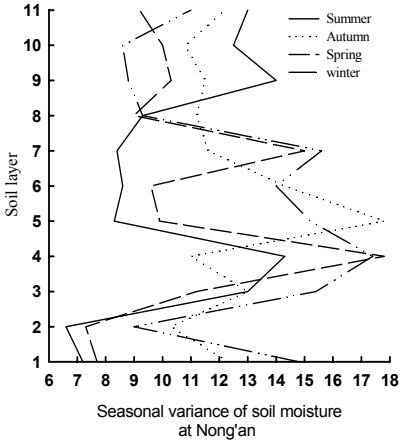

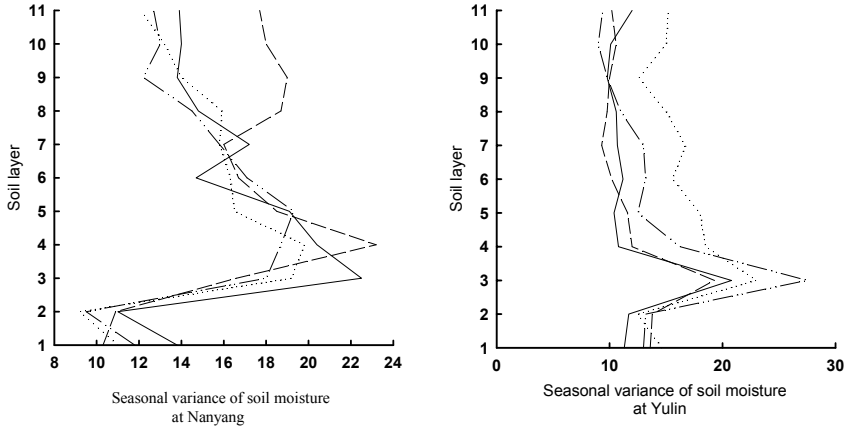

Fig. 7.11 The vertical profile of soil moisture seasonal variability at representative stations in different latitudes

The analysis on continuous effect of soil moisture anomaly

Correlation analysis was carried out to detect the temporal variation of soil moisture. The analysis shows that previous soil moisture anomaly continues when it is positive; however, there is no duration for the anomaly in case of negative correlation coefficient. Similar research was done by Liu (1990), although the study was only focus on Zhengzhou and Jinan stations.

Statistic method

The original soil moisture dataset was standardized to form a new time series. As said before the observation is taken 3 times per month, the sample number therefore is 396(from 1981 to 1991). From this new time series the lag-cross correlation was calculated.

$$y_n = \frac{x_n - \bar{x}_n}{s_{nx}} \tag{7.8}$$

x_n is the new series and $\bar{x}_n$ is average value of x_n, y_n is a standardized x_n, s_{nx} is standard deviation

$$s_{nx} = \sqrt{\frac{1}{n}\sum_{i=1}^{n}\left(x_{ni} - \bar{x}_n\right)} \tag{7.9}$$

$$R_l = \frac{1}{n-m}\sum_{i=1}^{n-m} y_{n(i)} \times y_{n(i+m)} \tag{7.10}$$

Here m is lagged time step, which is ten days. R_l is the lag cross-correlation coefficient.

Results

Analysis shows that in the Northern China (No.1-4), the durations of soil moisture can range from 1 to 12 dekads with the average of 6 dekads, and in lower levels the durations can have the increasement of 2 dekads comparing to surface level. In middle latitude (No.5-8), durations of soil moisture anomaly are 3-13 dekads, and similar to Northern China, the durations in deeper soil level would be longer.

Comparing to other two latitude zones, soil moisture durations for Southern China in vertical direction are not uniformly distributed. For example, the persistent time of soil moisture anomaly in certain regions decreases with the depth (No.11). And the durations of soil moisture anomaly shows larger variation with persistent time varies from one to 36 dekads.

To further demonstrate the regional durations of soil moisture anomaly, soil moisture distributions at surface layer (0~5cm) and deep layer (90~100cm) was analyzed (Fig. 7.12). Durations of soil moisture anomaly at surface show little spatial heterogeneity, with the length of averaged persistent time about 2 months. It is not significant for the increasement of soil moisture duration with the soil depth increasing. It is about 2-3 dekads in the northeast China; however, it is over 18 dekads in majority regions to the south of 40°N with maximum 36 dekads in deep layer. Meanwhile, it is longer for duration at deep layer in the southern China than that of other two regions. Therefore, it is about 6 dekads at surface layer and above 18 dekads at deep layer. The duration time at lower soil level is much longer than that of surface, and shows more spatial heterogeneity: in northeast China, the increasement is limited to 2-3 dekads, and in the area south of 40N, the anomaly can last up to 18 dekads (6 months) with maximal value of 36 dekads.

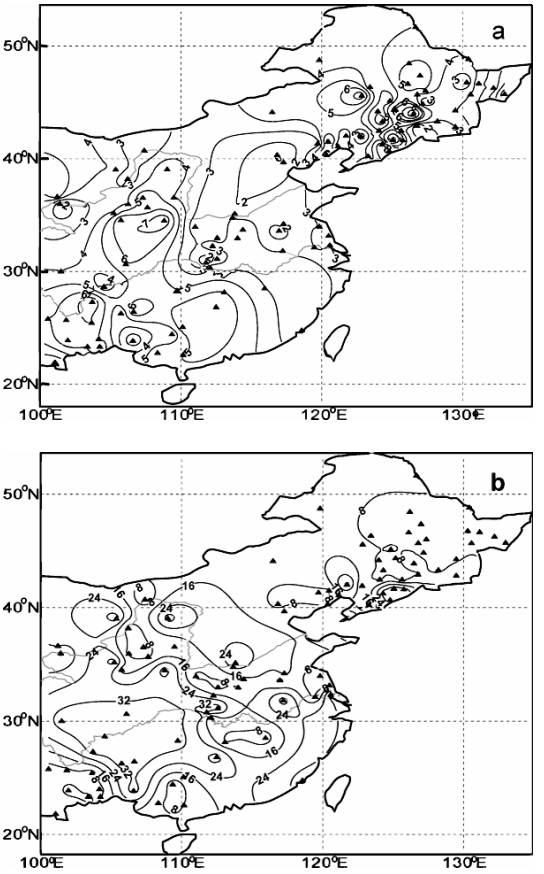

Fig. 7.12 Geographic distributions of soil moisture duration (the dekads of lag cross-correlation coefficient continued > 0.135) (a: 0-5 cm, b: 90-100cm)

In general, obvious seasonal variations and spatial heterogeneity for soil moisture anomaly exist. At surface the soil moisture anomaly could last 2 months and in deeper soil level up to 6 months. As a result, in land-surface study it is necessary to take the significant difference of soil moisture anomaly at different layer into consideration; to achieve that, the model needs higher resolution in vertical, which is about two months at surface layer and six months at deep layer.

The spatial variation of soil moisture

Spatial distribution

Geography distributions of accumulated water storage at 100cm is not homogeneous in space (showed in Fig. 7.13), with storage ranging from 130mm to 400mm. The water storage shows clear east-west gradient in Northeast China and mid-latitude area, and for the region to the south of 30°N，from west boundary, the distribution follows pattern of high-low-high-low value centers, with highest value center locating at area around 110°E.

Soil moisture variations with depth

Fig. 7.14 demonstrates the variations of volumetric soil water for all 12 sub-regions with the soil depth on 4 typical dekads (second dekads of January, April, July and October), representing four seasons respectively (winter, spring, summer and winter). In three regions of the northern China (No.1-3), in spring soil moisture shows an increasing with the depth at upper soil layers (10-20cm), and decreasing below this layer, which is the result of snow melting.

In the south China and middle latitude area, the soil moisture increases with the depth in all four seasons, except for regions No.6 and No.10. For region No.6, a high water content layer forms at 40-50cm soil level, except for the first dekad of January. In region No.10, similar high soil water content layers can be found at the depth of 30-60cm for all four seasons. Further investigation is required to identify the mechanism of the formation of the high water content layers.

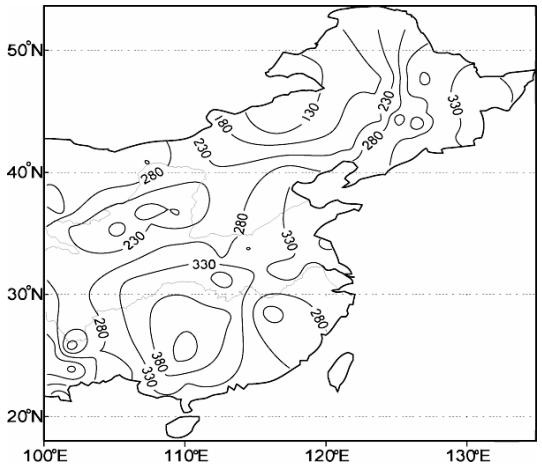

Fig. 7.13. Geography distributions of 0-100cm total stored water (unit: mm)

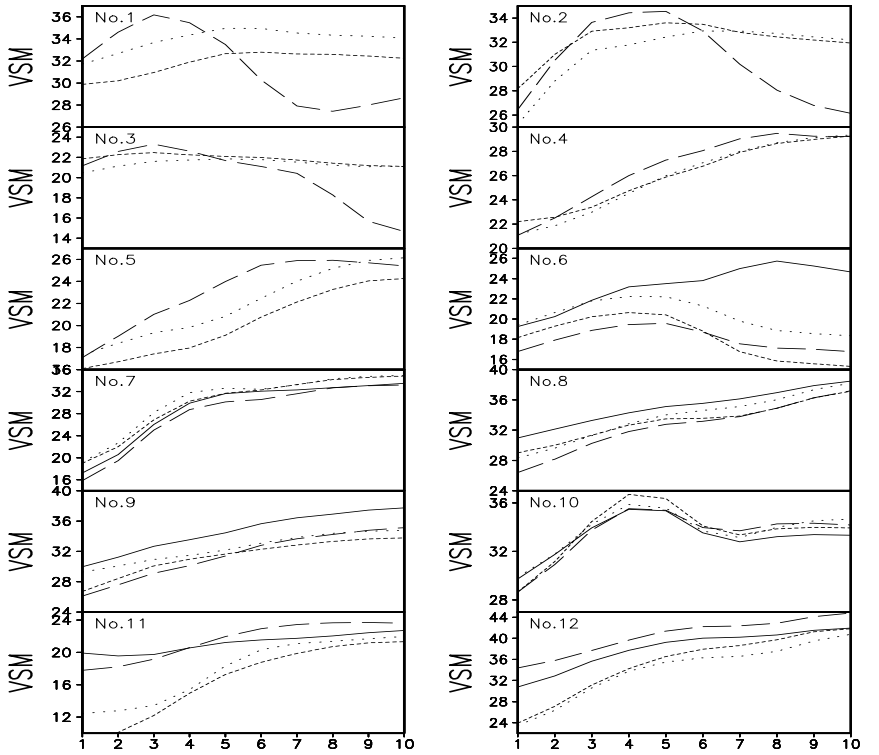

Fig. 7.14 Variation of soil moisture with the depths (real line: first dekad of Jan.; long dashed line: middle dekad of Apr.; short dashed line: middle dekad of Jul.; dotted line: middle dekad of Oct.) (Lateral axis represents layers: 1, 0~10cm; 2, 10~20cm; 3, 20~30cm; 4, 30~40cm; 5, 40~50cm; 6, 50~60cm; 7, 60~70cm; 8, 70~80cm; 9, 80~90cm; 10, 90~100cm; unit: %)

7.3 Inversion of soil moisture from climate variables and remote sensing data

7.3.1 A scheme retrieving soil moisture with climatic variables in Eastern China and its application

A scheme retrieving soil moisture with climatic variables in Eastern China

Basic concept

Based on the theoretic and statistical and analyses of soil moisture variation and its relationship with regional climate change(Ma et al., 2000), a new variable Surface Wetness Index is constructed using operational climate observation such temperature and precipitation, which can represent the soil moisture budget. With Surface Wetness Index a Soil Moisture Retrieving Scheme then was developed to obtain spatially and temporally high resolution soil moisture. The new scheme can greatly improve the soil moisture initialization in climate model, which is one of the critical issues the climate modeling community is concerning about. The scheme is computively affordable and its input is easy to obtain. The problem for soil moisture initial values in climate simulations, we hope to find a physical parameter, which can qualitatively represent soil moisture budget with routine precipitation and temperature data from meteorological gauge stations. A scheme, which can be calculated only depending less climate variables and is easy to get, will be established to retrieve soil moisture in eastern China and can be used as initial conditions of soil moisture to simulate regional climatic change.

Fig. 7.15 shows a simplified schematic diagram of soil water budget, which components include precipitation, runoff, percolation, evapotranspiration, horizontal drainage from unsaturated flow, and vertical drainage through the lower scheme boundary. Soil moisture at surface layer is mainly controlled by precipitation and evaporation (bare soil) or evapotranspiration (vegetable covered ground) (Manabe et al., 1981). A Soil Moisture Retrieving Scheme must have the ability to represent these two processes correctly. Taking this into consideration, Surface Humidity Index will be constructed which can combine the effects of two parameters.

According to Hulme et al (1992), Surface humidity index can be defined as:

$$H_i = \frac{P}{P_e} \tag{7.11}$$

H_i is surface humidity index, P is the precipitation and P_e is potential evapotranspiration(mm). Maximum Potential Evapotranspiration P_e is essential in soil water budget but its estimation cannot be done with simple method. It is possible to have Maximum Potential Evapotranspiration utilizing meteorological data which are continuously collected; however, Project for Intercomparison of Land surface Parameterization Schemes (PILPS) summarized that the estimated potential evapotranspiration from current land surface models show great difference (Henderson-Sellers, 1996). Shao et al. (1996)‘s review provides the detailed summary and de-

scription of most commonly used schemes to calculate potential evapotranspiration and draw similar conclusion to that of PILPS. Most of these schemes require perfect surface observed data, which is the difficult in reality. Therefore, more efforts are needed to apply the operational observation data, as well as the empirical and semi-theory and semi-experience methods, to compute potential evapotranspiration. Thornthwaite's scheme (1948) was original in using surface temperature to estimate potential evapotranspiration, which is still widely used in climate studies. The scheme developed here is a revised version on the base of Thornthwaite scheme.

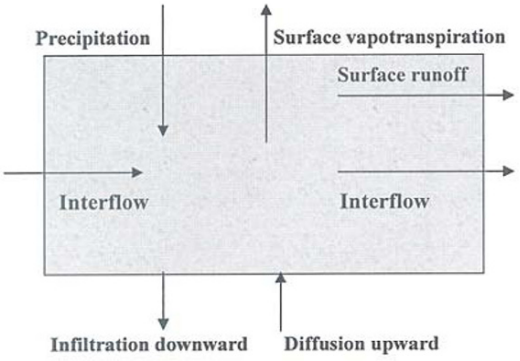

Fig. 7.15 Simplified schematic diagram of soil water budget

The potential evapotranspiration

The primeval purpose of this retrieval scheme is to provide object initial soil moisture conditions using routine meteorological observation for climate model. The scheme is characteristic of using least inputs to produce realistic soil moisture initial field.

According to Thornthwaite scheme, potential evapotranspiration can be calculated as following:

$$pe_x = \begin{cases} 0 & T_x \le 0°C \\ 1.6d_x(10T_x / I_m)^a & 0°C < T_x \le 26.5°C \\ -415.8547 + 32.2441T_x - 0.4325T_x^2 & T_x > 26.5°C \end{cases} \quad (7.12)$$

where pe_x is potential evapotranspiration

$d_x = d/3$， d is days in each month divided by 30

T_x is dekad mean temperature

$a = 0.49239 + 1.792(10)^{-2} I - 7.71(10)^{-5} I^2 + 6.75(10)^{-7} I^3$

$I_m = \sum_{1}^{12} i$ is total monthly mean heat index

$i = \left(T_m / 5 \right)^{1.514}$ is monthly mean heat index

T_m is monthly mean temperature

Surface humidity index scheme

As mentioned before, Surface Humidity Index (SHI) can depict the soil water budget qualitatively. The concept here is to find the relationship between soil moisture and SHI, and based on which a scheme to retrieve soil moisture can be constructed.

When air temperatures below 0℃, no evaportranspiration can occur and the potential evapotranspiration is zero. Then (7.11) can be written as $H_i = \frac{p}{pe} \to \infty$ when surface air temperature is below 0℃. Assuming that no snow is melted when mean air temperature below 0℃, efficient precipitation infiltrated into the soil P is close to 0, and $H_i = \frac{P}{Pe} \to 1$. As a result, surface humidity index can be written as:

$$H_i = \begin{cases} 1 & T \le 0°C \\ \dfrac{P}{P_e} & T > 0°C \end{cases} \tag{7.13}$$

It is known that the soil moisture budget in winter time is the balance of snowmelt water and sublimation from snow surface, which is negligible. Under the assumption of no snowmelt in wintertime when air temperature below freezing point, the soil moisture can be considered as a constant. With the spring snowmelt, soil water content increases rapidly. As a result, the effect of snowmelt on soil water balance is of great importance, and must be taken into consideration in soil moisture retrieve scheme.

Supposing snowmelt begins when surface air temperature is greater than 0℃, the influence of snow melting on soil moisture can be assumed to follow normal-school distribution.

Defining P_m as accumulated snow amount, then

$$P_m = \alpha_1 P_m + \alpha_2 P_m + \alpha_3 P_m + \alpha_4 P_m + \alpha_5 P_m \tag{7.14}$$

where α_1 - α_5 are weighing coefficients for the first five dekads. The weighting coefficients are latitude dependent as shown in Table 7.2. When temperature is higher than 0°C, effective precipitation that can influence soil moisture can be written as:

Table 7.2 Weighing coefficients in the different latitude zone

	α_1	α_2	α_3	α_4	α_5
lat<30ºC	0	0	0	0	0
30-40ºC	0.3	0.4	0.3	0	0
lat>40ºC	0.1	0.2	0.4	0.2	0.1

$$P_{a\mathrm{a}} = P + \alpha_1 P_m \tag{7.15}$$

P is the dekad total precipitation. If weighting coefficient α equals to zero, $P_a = P$. And Equation 7.13 can be re-written as:

$$H_i = \begin{cases} 1 & T \le 0^\circ C \\ \dfrac{P_a}{Pe} & T > 0^\circ C \end{cases} \tag{7.16}$$

The Scheme for Retrieving Soil Moisture (SRSM)

The scheme has 11 layers in vertical (Fig. 7.16), which is same to that of the observation. It could be convenient to validate the simulation results from scheme with observed soil moisture. The surface soil moisture will be retrieved first, and soil moisture for deeper soil layer will be calculated

based on the understanding of the relationship between surface soil moisture and that of deeper soil layers.

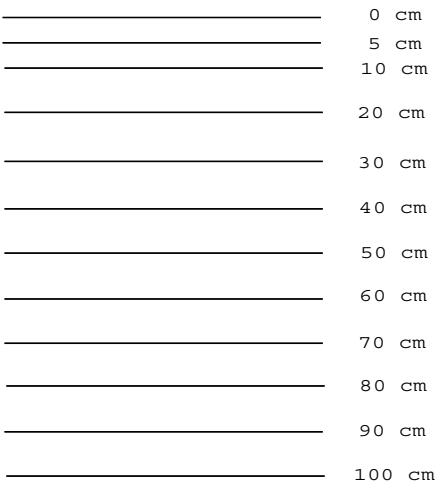

Fig. 7.16 Vertical distribution of each layers of soil moisture observation

Soil moisture retrieval at surface layer

Based on the analyses of spatial distribution of multi-year averaged gravimetric soil water content at surface layer (0-5cm), four subregions can be defined in Eastern China. Each subregion is characteristic of its own soil moisture variation. Empirical scheme to retrieve soil moisture in different subregions can be written as follows:

$$s_m = c_0 + c_1 H_i + c_2 H_i^{\,2} + c_3 \log H_i \tag{7.17}$$

where H_i is Surface Humidity Index, c_0 , c_1 , c_2 are empirical constants, s_m is gravimetric soil moisture. All the empirical constants are region-dependent.

Soil moisture retrieval at deep layer

Analysis shows that the surface soil moisture is linearly related to that of deeper soil layers. Therefore, soil moisture at deeper soil layers can be defined based on following hypothesis:

$$S_m = k_{m0} + k_{m1} S_{m-1} \tag{7.18}$$

k_{m0} and k_{m1} are empirical constants, which are determined by the relationship of soil moistures between at different layers.

Equations (7.12)-(7.18) are the basic of the Scheme for Retrieving Soil Moisture. The validation of retrieved results with in situ soil moisture will be described in the following sections.

The validation of retrieved soil moisture

The validation data are dekad soil moisture collected from 98 agricultural meteorological gauge stations in Eastern China observed from 1981-1991. The observation has 11 layers in vertical (0-5cm, 5-10cm,10-20cm, 20-30cm, 30-40cm, 40-50cm, 50-60cm, 60-70cm, 70-80cm, 80-90cm, 90-100cm), and is taken 3 times per month (8th, 18th and 28th days of each month).

Comparison of geography distributions between retrieval and observational soil moisture

Retrieved and observed soil moistures at 0-5cm on 8th July 1981 are shown in Fig. 7.17. They are in good agreement with each other, for example the high soil moisture centers in the Northeast and Southwest China, low value center in the Yangtze River-Huai River Valley and to the south of Yangtze River Valley.

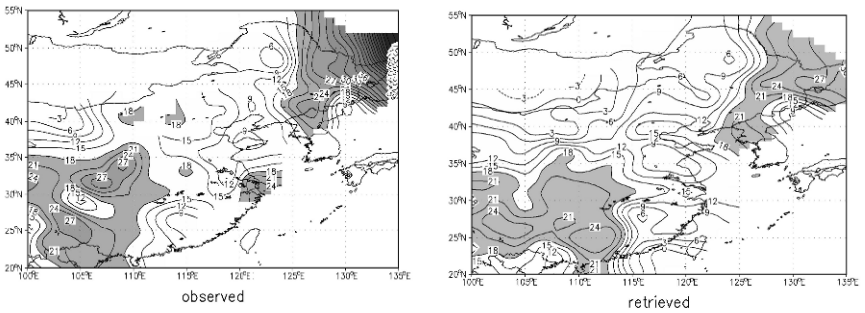

Fig. 7.17 Retrieved and in situ soil moisture at 0-5cm on 8th July 1981

The regional climate change is not only affected by surface soil moisture anomaly, but that of deeper soil layers, though their effects are at dif-

ferent time scales. It's essential for the retrieving scheme to provide accurate soil moisture at different soil levels.

The spatial correlation between retrieved and observed soil moisture fields at different levels are shown in Fig. 7.18. At upper soil layers (up to 50cm) observation and retrieval results of SRSM are significantly correlated in most area at the significant level of 0.01 (shaded area in Fig. 7.18).

Correlation analysis of 42 stations shows that at upper soil level the retrieved soil moisture agrees better with observation. At deeper levels observed and retrieval soil moistures have similar spatial distribution, though their correlation coefficients are not as high as those at upper levels.

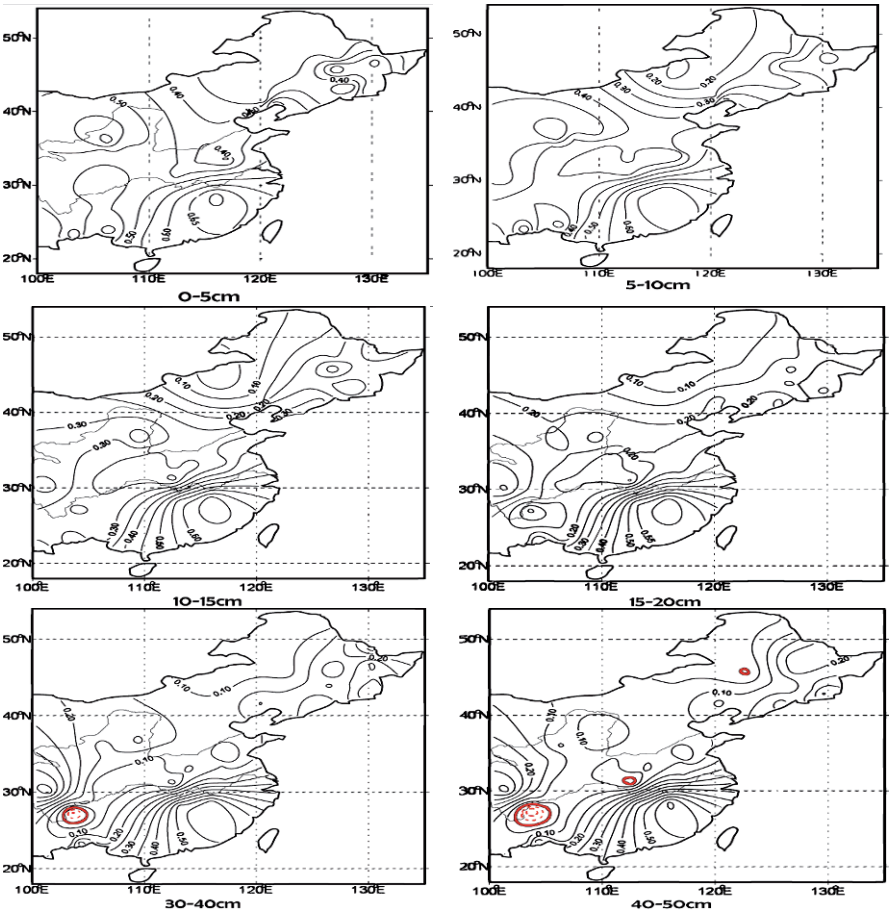

Fig. 7.18 The distributions of correlation coefficients between retrieved and oserved soil moisture at different layers

Comparison of seasonal variations of observed and retrieval soil moistures

The correlation analysis of retrieved and observed soil moisture at 42 stations also shows that, at first three levels (0-10cm), the correlation coefficients of all 42 stations are significant with significant level of 99%; for 10-20cm soil levels, the percentage of stations that can pass the significant test drops to 98%, at 20-30cm to 83%, at 30-40cm to 62% and 40-50cm to 43%. The results indicate that SRSM is reliable in retrieving soil moisture's seasonal variations above 50cm layer, especially for summertime. For spring and autumn, the temporal variations of observation and retrieval results are different in magnitude. Time series of retrieved and in situ soil moisture at Nanchong are shown by Fig. 7.19.

Above analysis shows that SRSM has ability to reproduce the spatial distribution and temporal variation of soil moisture in Eastern China. It is proved to be reliable and feasible, and can be used to produce the replacement the observation when it is scarce. SRSM can also be used to generate initial soil moisture field for regional climate simulation in Eastern China, and credible data for land surface model validation. The scheme is efficient replacement and supplement for physical models which at present still can not provide objective soil moisture. The analysis also demonstrates that further efforts should be made to improve SRSM's ability, especially the treatment of underground soil water.

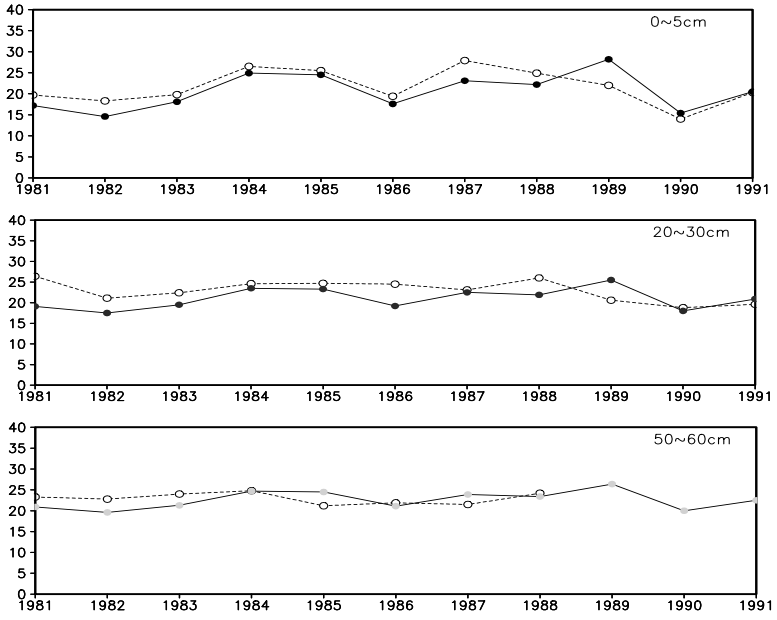

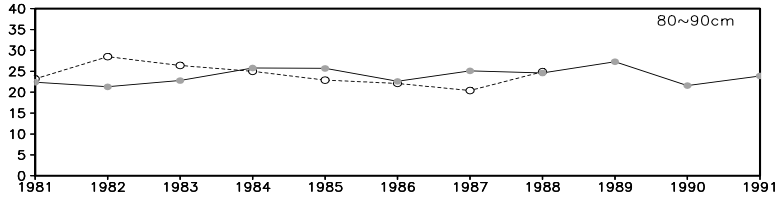

Fig. 7.19 Interannual variation of retrieved and observed soil moisture at Nanchong in the first dekad of July (dotted line: observed; real line: retrieved)

The application of SRSM in drought study

The detection of dry-wet variation (Ma et al., 2006)

The time series of 55 years (1951-2005) soil moisture in East China is generated by SRSM. The data then used to analyze the dry/wet trend in Eastern China, and the results are compared with commonly used drought-wetness indexes such as precipitation, surface humidity index and Palmer drought index (PDSI).

The trends of precipitation, Surface Humidity Index (SHI), PDSI and retrieved soil moisture at 50-60cm from 1951 to 2004 are analyzed with M-K method, and the results are shown in Fig. 7.20.

The spatial distributions of four trends are similar in Eastern China. But the location and scope of the most arid area generated by SRSM is different from those of other three indexes. The significant drying trends from precipitation, SHI and PSDI are likely to continue in Northeastern China, and trend from SRSM shows less prominent in the same area. For SRSM, the most significant drying trend region locates at the transition belt in Northern China, which the precipitation's been decreasing, though not significantly. The inconsistency of soil moisture and precipitation trends might be the results of surface air temperature rising, which causes the increase of potential evaporation at surface and further reduce the surface soil moisture. The severe dryness extends downward and induces the significant deeper soil drying. In center-south part of Northern China, which also shows notable regional warming, the decreasing precipitation is associated with deeper soil moisture reduction. The mechanisms controlling interactions between precipitation and soil moisture in different regions are complicated and need to be further analyzed with coupled climate and hydrology model.

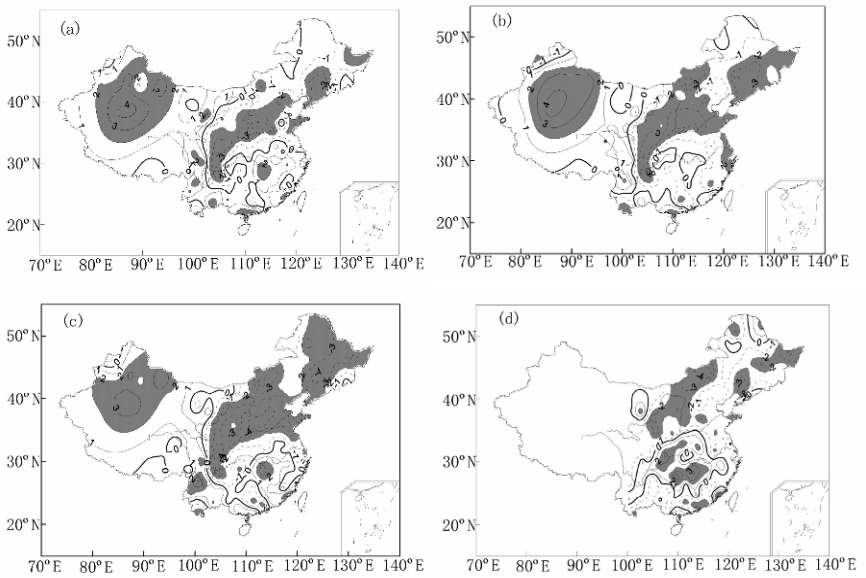

Fig. 7.20 Tendencies of a) precipitation, b) surface humidity index, c) PDSI, and d) soil moisture in China ($U_{(d_k)}$: positive value represents increase trend, and negative value means decrease trend which express with diagonals; for precipitation: negative value means decreasing tendency, and positive value means increasing tendency; and for other three indexes: negative value means drying tendency, and positive value means wetting tendency; and the shaded parts reach 95% level significance test.)

The application of SRSM retrieved soil moisture as an initial scheme in RIEMS (Regional Integrated Environment Modeling System) (Wang 2002)

The retrieved soil moisture by SRSM (Ma, 1999） is used as the 'real' soil moisture to Regional Integrated Environment Modeling System (RIEMS) to study the impacts of the initial soil moisture anomaly on East Asia climate. The results indicate that initial soil moisture anomaly affects surface energy budget obviously, with a strong effect on the resulting surface temperature changing. The response of surface water budget, however, is more complicated due the interaction and feedback between the local land surface-atmosphere energy, moisture exchanges and large-scale circulation. The study also shows that the arid, semi-arid area in North China is more sensitive to initial soil moisture changes. The retrieved soil

moisture is used to investigate the role of initial soil moisture in simulating extreme climate events. Two extreme cases are selected: warm and drought summer in 1997 and heavy rainfall in 1998. The results show that, though the 'real' soil moisture can not modify model-simulated location and scope of high-temperature center, it reduces its intensity and to some degree improves model performance in simulation of extreme hot summer. Similar conclusions can be drawn for 1998 heavy rainfall. Therefore, initial soil moisture from SRSM retrieved results can modify the simulated results with RIEMS.

7.3.2 Soil moisture retrieval from remote sensing data and its application

Remote sensing in soil moisture retrieval

Soil moisture is critical for the applications such as weather forecasting assimilation (four-dimensional data assimilation (4DDA) models), crop and drought monitoring, initial conditions in flood forecasting, and global water budget quantification. It is also characteristic of large variations in both space and time, and its observation in large scale is one of the most attractive and critical target for hydrology, meteorology and climate researches. Due to the fact that in site soil moisture observation is highly limited in space coverage and temporal resolution (Schulin et al. 1992, Georgakakos and Baumer, 1996; Fennessy and Shukla, 1999; Dirmeyer et al. 2004), model output for soil moisture is usually used to perform research in large scale (Robock et al., 2000), a lot of efforts have been devoted to develop alternative methods for soil moisture observation (Engman and Chauhan, 1995). In last twenty years, the maturing of satellite remote sensing techniques, especially microwave remote sensing, offers a direct way to assess soil water content (Njoku et al., 1996; Moran et al., 2000; Engman and Chauhan 1995). The advantage of remote sensing measurement is that it can provide estimates of spatial scales ranging from a few meters to thousands of kilometers. And there is no need to infer area averages from point data as the remotely sensed data directly come as area averages. One disadvantage of microwave remote sensing is that it can not provide soil moisture information when the soil is frozen or snow covered.

The global soil moisture of 1992-2000 was derived from European Remote Sensing Satellite (ERS) scatterometer data (Wagner et al. 2003). The data is available at http://www.ipf.tuwien.ac.at/radar. This dataset comprises the retrieved surface soil moisture data and Soil Water Index (SWI) which is a measurement of the soil moisture profile obtained by filtering

the surface soil moisture time series with an exponential function (Wagner et al. 1999b).

The Soil Water Indexes (s_{wi}) from satellite remote sensing and in situ soil moisture from agricultural meteorological stations in Eastern China are used to retrieve soil moisture. s_{wi} is a trend indicator ranging between 0 (dry) and 100% (wet). For the conversion from relative to absolute units in volume (θ_{swi}), the wilting level w_l, the field capacity f_c and the porosity t_{wc} are used, shown by (7.19) (Wagner et al., 1999a)

$$\theta_{swi}(t) = w_l + s_{wi}(t) \cdot \left(\frac{f_c + t_{wc}}{2} - w_l \right) \tag{7.19}$$

The wilting level w_l is the soil moisture content at which soil suction is too great for plant to pull remaining water defined as soil moisture content at which the suction to remove the soil water is too great for plants to exert. The field capacity f_c is soil moisture content when deep percolation has nearly stopped after the soil has been thoroughly wetted by heavy rainfall or irrigation, and is measured in field. The porosity t_{wc} is the relative pore volume of the soil and is equal to the total water capacity of the soil when it is supposed that all pores can be filled with water. The subscript in θ_{swi} indicates that soil moisture data are derived from scatterometer data. Here θ_{swi} is a measure of the profile soil moisture for the first 100cm layer.

In situ soil moisture data, provided by Climatic Data Center of Chinese National Meteorological Administration, include relative soil moisture (θ_f), field capacity (f_c) and bulk density of soil (ρ). The data were collected from agricultural meteorological gauge stations in China at 5 vertical levels (10cm, 20cm, 50cm, 70cm and 100cm), and the samples were taken on 8th, 18th and 28th of each month for year of 1992-2000. Detailed observational method and criterion was summarized by the National Meteorological Administration (1993). Volumetric soil moisture θ hen can be computed from relative moisture θ_f of the soil following Eq. (7.20).

$$\theta = \rho \times \theta_f \times f_c \tag{7.20}$$

Most of agricultural meteorological gauge stations locate to North of 32°N in China. Because of the scarcity of in situ soil moisture in most regions of China, it is of great importance to use remote sensing data to reflect soil moisture distribution.

A retrieval method by Zhao et al. (2006) can be summarized as follows: (1). For the volumetric soil moisture at 10cm: in situ soil moisture θ at 10cm, which is computed by formula (7.19) and the corresponding parameters θ_{swi}, s_{wi}, f_c, t_{wc} and w_l, which are regarded as x_i (i=1,5) are used to find the possible coefficients $a_i \sim g_i$ (i=1,5) in equation (7.21) with Matlab.

$$\theta_{010} = \sum_{i=1}^{k}(a_i x_i + b_i x_i^2 + c_i x_i^3) + \sum_{i=1}^{k-1} d_i x_i x_{i+1} + \sum_{i=1}^{k} e_i \sqrt{x_i} + \sum_{i=1}^{k} f_i \log x_i + \sum_{i=1}^{k} g_i e^{x_i} \qquad (7.21)$$

Here θ_{010} is the retrieved volumetric soil moisture at 10cm soil layer. The coefficients $a_i \sim g_i$ (i=1,5) are selected and determined by the program. Therefore, volumetric soil moisture for the simulated region can be computed with equation (7.21), which reflects not only the linear but also the nonlinear relationship between soil moisture and those parameters x_i (i=1,5). As an example, retrieval formula for volumetric soil moisture in the land in the Yangtze River valley is given by equation (7.22).

$$\theta_{010} = -2.213x_2^3 - 2.259x_3^3 - 6.017x_1x_4 + 2.541x_2x_4 - 0.669x_4x_5 + 0.494\log x_3 + 0.599 \qquad (7.22)$$

(2). For the volumetric soil moisture at 100cm, θ_{10-100}, the storage of soil water content η (unit: cm) can be written as,

$$\eta = h \times \theta \qquad (7.23)$$

where h is the depth of soil layer (unit: cm), therefore,

$$\theta_{10-100} = \frac{10\theta_{0-100} - \theta_{010}}{9} \qquad (7.24)$$

where $\theta_{0-100} = \theta_{swi}$. Then θ_{10-100} can be computed from the formula

The heavy rain simulation with remote sensing data retrieved soil moisture

With Pennsylvania State University/National Center for Atmospheric Research (PSU/NCAR)'s fifth generation mesoscale model (MM5; Grell et al., 1994), two sets of initial soil moisture conditions, National Centers for Environmental Prediction (NCEP)/NCAR re-analysis dataset and soil moisture retrieved from SWI at 10cm and 100cm,are used to compare the initial soil water's impact on heavy rainfall simulation integrated from June 1st. SWI retrieved soil moisture has higher resolution of 28km comparing to that of NCEP data with 2.5° resolution, and can reflect more detailed soil moisture distribution in the simulation domain.

The observation showed that heavy rainfall area was located to the south of 30°N in the Yangtze River valley. Rainfall belt is zonal and its intensity is about 100mm, with 100mm isohyet locating between 111°-122°E (Fig. 7.21a).

The zonal distribution of the rainfall area can be simulated well with SWI and NCEP data, but both rainfall belts in the west domain drift southward (Fig. 7.21b and 21c). For NCEP soil moisture, there are two 100mm rainfall centers located at (110-113°E, 27°N) and (121°E, 29.5°N)，which show that the rainfall intensity from NCEP is lower than that of the observation. For SWI, there is a 200mm rainfall center at (112-114°E, 27°N). The 100mm isohyet extends eastward and agrees well with the observation at most part of the rainfall belt except for the lower intensity near 27.5°N between 117.5-119°E.

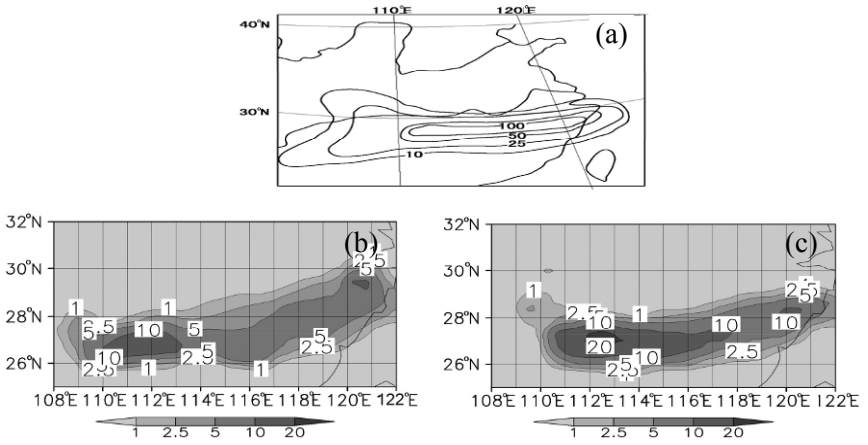

Fig. 7.21 Observational (a, unit: mm) and simulated (b: NCEP; c: SWI, unit: cm) total precipitation from June 13-14.

The analysis above, as well as the simulations to heavy rainfall events in 18-22 June and 21-26 July, 1998 in the Yangtze River valley (not displayed here), show that simulated precipitation with SWI soil moisture is better than that with NCEP one. The rainfall intensity and location from SWI is more close to the observation.

As a result, soil moisture retrieved from scatterometer derived SWI and in situ soil moisture can overcome the difficulty in soil moisture observation in large scale and reflect soil moisture distribution with higher resolution. The retrieval method of soil moisture reflects not only the linear but also the nonlinear relationship between soil moisture and those soil parameters: θ_{swi}, S_{wi}, f_c, t_{wc}, and w_l. Further analysis shows that it is convincible for SWI retrieved soil moisture at 10cm and 100cm on June 1st.

7.4 Relationship between soil moisture and regional climate variation in China

7.4.1 Soil moisture and climatic interannual variability

From south to north three sub-regions (south of 30°N, 30-40°N north of 40°N) in Eastern China are defined to study the relationship of soil moisture and regional climate change (Table 7.3). Detailed division can better depict the characteristics of soil moisture variability in different regions and its relationship with climatic variations.

Table 7.3 Number of gauge stations for each parameter in different regions of eastern China (SM: soil moisture; T: temperature; P: precipitation

	The southern		Middle latitude		The northern	
Parameters	SM	T & P	SM	T & P	SM	T & P
No.	22	14	33	15	43	14

The analysis emphasizes on interannual variations of soil moisture, temperature and precipitation and their relationships in three sub-regions. T Time series for these three parameters are computed and 37 dekads smoothing averages are applied. Interannual variations of precipitation, temperature and soil moisture at different soil layers (0-5cm, 20-30cm, 50-60cm, 90-100cm） in three regions are shown in Fig. 7.22.

In the southern part of southern China

The amplitude of interannual variations of soil moisture decreases with the increasing depth (Fig. 7.22). Only change trend without period can be found at deep layer (80-90cm and 90-100cm). Soil moisture at surface layer significantly depends on the precipitation; however, soil moisture variation has less amplitude. Therefore, interannual variation of soil moisture at surface layer is mainly dominated by that of precipitation. It is worthwhile noticing that soil's been drying in both deep layer and surface layer since 1980s, during which the interannual variability can reach -10.4/9a at deep layer (Table 7.4). And the drying intensity at deep layer is almost three times as that at surface layer. It is obvious that the drying variation in the region is connected with less precipitation (fig7.22-1b) and greater evapotrapiration resulting from rising temperature (Fig. 7.22-1c). However, further analyses are required to understand the mechanism of stronger drying trend at deep soil layer.

Table 7.4 Interannual variabilities of soil moisture, precipitation and temperature (unit of soil moisture: %)

Temperature	Precipitation	Soil moisture			
		0-5cm	40-50cm	80-90cm	90-100cm
0.6°C/5a	-4.8/6a	-2.3/6a	-0.3/7a	-10.4/9a	-10.4/9a

Soil's been drying since 1980s and it's associated with less precipitation and higher temperature. Meanwhile, the drier soil will raise temperature and more latent heat flux can be transported to the atmosphere and increases surface air temperature, which forms negative feedback between soil moisture and surface air temperature. Therefore, the rise of surface air temperature from drying soil accelerated the drying trend, which may leads to the higher surface air temperature and drying trend in the southern of eastern China.

Table 7.5 Maximum and minimum of soil moisture (unit: %), temperature (T, unit: ºC) and precipitation (P, unit: mm)

	P	T	0~5cm	40~50cm	80~90cm	90~100cm
	Max/Min	Max/Min	Max/Min	Max/Min	Max/Min	Max/Min
1	25.9/18.1	12.7/11.6	19.5/16.9	21.4/19.5	22.1/20.5	22.2/20.6
2	23.8/15.4	13.1/12.0	19.1/16.6	20.3/19.2	21.8/20.3	21.7/20.4
3	/19.2	13.3/12.3	/16.7	/18.4	21.3/20.2	21.5/20.2

In middle latitude of eastern China

Soil moisture variation amplitude in the middle latitude is greater than that of the southern for both the surface and deep layers (Fig. 7.22-d-f). interannual variations, which's consist of a 3-4 years cycles at deep layer and two waves with 4-5 cycles at surface layer is obvious. However, the interannual variabilities of precipitation and temperature don't have the same 3-4 year cycle. It is worthwhile noting that interannual variability of soil moisture at 50~60cm layer is characteristic of a decline tendency overlapping a cycle oscillation, which is different from both surface and deep layers. Maximum and minimum of soil moisture, precipitation, surface air temperature are shown in Table 7.5, which show that maximum and minimum of soil moisture decrease with the time excepting that at surface layer. Similar to southern latitude, there also exists drying trend at deep layer, which might be the results of less precipitation (Fig. 7.22e) and stronger evapotranspiration from higher surface air temperature (Fig. 7.22f).

In the Northeast China

Soil moisture gauge stations in north latitude zone mainly locate in the Northeast China. Interannual variations of soil moisture, precipitation don't agree with each other (in Fig. 7.22-3g-3i), except for the extreme dry events in 1982 and 1989. Meanwhile, tendencies for soil moisture at surface and deep layers are opposite, that is, when surface layer is drier soil at deep layer is wetter. Precipitation shows no tendency, and temperature's been rising. As a result, the drying trend in the region is connected with regional warming, which has little affection on soil moisture at deep layer.

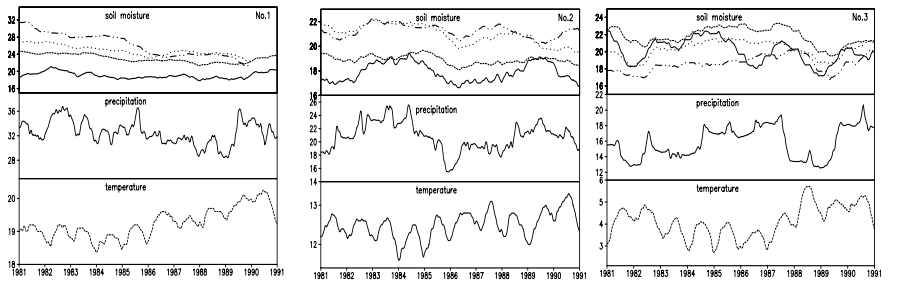

Fig. 7.22 37 dekads smoothing average variation of soil moisture, precipitation and temperature (No.1, No.2, and No.3 represent the southern, middle latitude and the northern separately; four soil moisture layers, solid line: 0-5cm, short line: 20-30cm, dotted line: 50-60cm, dotted short line: 90-100cm; unit: mm)

7.4.2 Correlation between area average soil moisture and climate variation

Lag cross-correlation coefficient

The 37-dekads smoothing average to regional average soil moisture, precipitation and temperature in different regions are computed to illuminate lag cross-correlation at different layers. The smoothing averages of sub-regionally averaged soil moisture, precipitation and temperature are generated, and used to calculate the time lag cross-correlations between precipitation, temperature and soil moisture at different layers.

Results

The relationship between soil moisture and the precipitation

From surface water budget equation, the precipitation is the major source of soil water increasement, which will lead to increase of evapotranspiration from unsaturated soil and provides more water vapor into the atmosphere then increases the precipitation (more water vapor not necessarily leads to more precipitation).

The data used here are 50-dekads (which year to which year) soil moisture and precipitation collected from Southern China (Fig. 7.23a). Positive correlation between precipitation and soil moisture at 0-5cm and 20-30cm are significant (which can pass $\alpha = 0.01$ significance level test ($r_c = 0.135$). It is a notable that time lag cross-correlation coefficients can reach maximum at 20-30cm layer with maximum lag time of 50 dekads and it can pass significance test ($\alpha = 0.01$). The lag cross-correlations between soil moisture and precipitation grow weaker with the increasing depth. And the soil deeper than 50-60cm, largest correlation can only exist when the precipitation proceeds soil moisture for 33 dekads. Therefore, the precipitation is mainly correlated with soil moisture at surface layer in Southern China. The correlation becomes weak when the depth increasing, which means that deeper layer soil moisture can only response to the precipitation and will have little influence on the precipitation.

In the middle latitude (Fig. 7.23b), the lag cross-correlation coefficient is largest between precipitation and soil moisture at 0-5cm with lagging time of 20–dekads, and reaches maximum when no lag is 0. Correlation coefficient decreases with the depth increasing. The correlation between

soil moisture and precipitation in the middle latitude is higher than that of in Southern China, and it passes significant test when soil moisture is 21 dekads prior to precipitation. This means that soil moisture can have effect on the precipitation of half a year later.

In Northern China (Fig. 7.23c), time lag cross-correlation analysis shows that the relationship between precipitation and soil moisture is similar to that in the middle latitude of Eastern China. Analysis also shows that the relationship between deeper soil water content and precipitation is different for 3 sub-regions.

Precipitation and soil moisture are positively correlated; though correlation is weak and lagging time is region and soil depth dependent. The results can be verified by simulation results (Yeh et al., 1984； Retreen and Bolin, 1978).

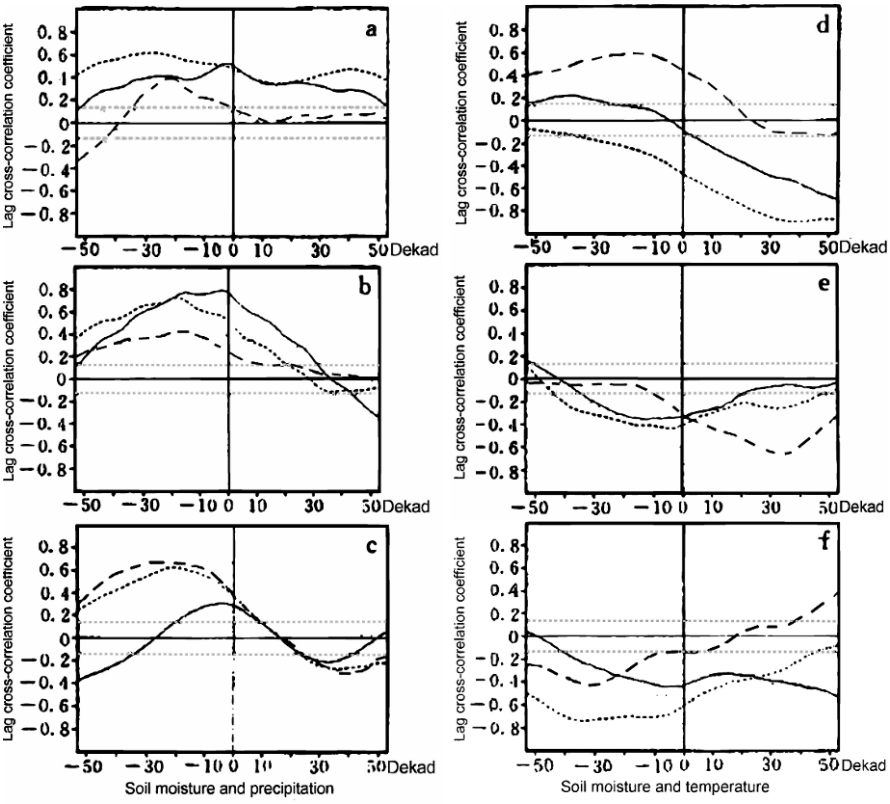

Fig. 7.23 The lag cross-correlation between area average soil moisture and precipitation, temperature

The relationship between soil moisture and surface air temperature

The influence of soil moisture on surface air temperature is realized through energy balance at surface layer by changing soil heat capacity and surface albedo. Unsaturated soil moisture variations can also affect surface evapotranspiration. Therefore, sensible and latent heat flux exchanges between land surface and atmosphere are modified and then mediate climate change. Numerical simulations by Shukla et al (1982) show there are significant difference for latent and sensible heat exchanges between dry and wet soils, which will be discussed in the following with observed soil moisture and temperature.

In Southern China (Fig. 7.23d), there exists obvious difference for soil moisture and surface air temperature between surface (above 20-30cm) and deep layer (the relationships between surface air temperature and soil water are depth dependent.). Negative lag cross-correlation coefficients can be explained from the aspect of energy balance: supposing R_n (net radiation) and G (soil heat flux) are constant. $R_n = H + LE + G$, H (sensible heat flux) decreases with the raised temperature. (T_S =constant), then latent heat flux LE （$= R_n - H - G$） increase and more water vapor is dismissed from the soil which leads to less soil moisture. Preceding soil moisture at 0-5cm and surface air temperature are negatively correlated; and non-significant positive correlation exists between preceding temperature and soil moisture. Soil moisture at deep layer and precipitation are positively correlated for both contemporaneous and time-lag cross correlations. The mechanism of positive feedback between preceding surface air temperature and later soil moisture is not clear.

The relationship between soil moisture and temperature in the middle latitude of eastern China (Fig. 7.23e) shows that above 40-50cm soil layer the time lag cross-correlation coefficient follows a partially distribution with lag time, and to pass significance test, the maximal 23 dekads lag time for positive correlation and maximal 35 lag time dekads for negative correlation are required. The similar distributions for time lag coefficient exist at deep layers. Therefore the proceeding temperature's influence on surface soil moisture would last long, but proceeding soil moisture will not have great impact on surface temperature. The impact of proceeding soil moisture at deeper soil layer on surface temperature is opposite to that of surface soil moisture. It is longer for the impact of former soil moisture to later surface air temperature at deep layer and it is also shorter on the contrary. The impact time of proceeding soil moisture at deeper layer on surface air temperature is up to 67 dekads. It therefore can be concluded that

the effect of surface air temperature on soil moisture mainly limited at surface layer, and soil moisture can greatly influence on air temperature.

The correlations between soil moisture and surface air temperature in Northern China (Fig. 7.23f) show that, for both surface and deep layers, soil moistures are negatively correlated to surface air temperature in both time lag and contemporaneous correlations. There are significant negative correlations between soil moisture and surface air temperature at 0-5cm layer, which can last more than 2 years. Time lag correlation analysis shows that the surface air temperature is significantly connected to deeper layer soil moisture. In general, the relationships between soil moisture and surface air temperature are soil-depth and region dependences among different layers and regions between surface air temperature and soil moisture. In most case there are negative correlations between soil moisture and surface air temperature, and correlation coefficient can pass significance test (α=0.01). However, further research is needed to explain the positive correlation between them at deep layer in the southern of China.

Unlike temperature, precipitation and soil moisture are positive correlated, and correlation coefficients are also soil depth and regional dependent.

7.5 Summary and discussions

There are obvious seasonal variations for soil moisture. It increases significantly in spring in the northern of eastern China due to snow melting. In autumn, soil moisture increases due to less evapotranapiration and reaches its highest value in November. In the mid-latitude of eastern China, the soil water content is lowest in spring and highest in autumn and winter. For the southern of eastern China, in area to the west of 110°E soil is driest in spring and wettest in autumn and winter, while in the area to the east of 100°E soil moisture has opposite seasonal variation. Spatial distribution of soil moisture is highly heterogeneous; the accumulated soil water storage at 100cm ranges from 130mm to 400mm. In general, soil water content increases with the depth; however, in North China the spring soil water has reached its maximum at 10-20cm layer due to snow-melt.

Soil moisture is positively correlated to precipitation and negatively surface air temperature. The correlation coefficients however have significant seasonal variations. The interaction between soil moisture and surface climate is more obvious for drier soil, in the region to the south of 40ºN, interannual variability shows drying trends for both surface and deep layer soil. Analysis indicates that combination of less precipitation and warmer

temperature may cause the drying tendency in soil water, in addition to excessive use of groundwater. Time lag correlation analysis shows that show that the positive correlation between soil moisture and precipitation is significant with lag time exceeds one year. Analysis also shows precipitation has longer influence time on soil moisture and not opposite.

The surface climate is closely connected to soil moisture in both prior and lag correlation analyses. It is obvious that there are close correlations among soil moisture, surface air temperature and the precipitation for both preceding and lagged. Obviously soil moisture is one of essential components in the climate change study, and how to couple soil moisture variations into climate change prediction study requires more efforts.

SRSM is proven to be a reliable and feasible tool to retrieve soil moisture in Eastern China, and the retrieved soil moisture can reproduce the spatial and temporal variations of observed soil moisture.

Remote sensing is another useful way to retrieve soil moisture. SWI is derived from Earth Resources Satellite (ERS) scatterometer observation and can help to reduce the difficulty of lacking soil moisture observation in large scale and high spatial resolution. The retrieved soil moisture can be used as initial conditions in regional climate simulations in Eastern China monsoon regionl, as well as the validation data for land surface model.

The surface climate is closely connected to soil moisture in both prior and lag correlation analyses. It is obvious that there are close correlations among soil moisture, surface air temperature and the precipitation for both preceding and lagged. Obviously soil moisture is one of essential components in the climate change study, and how to couple soil moisture variations into climate change prediction study requires more efforts.

Progresses have been made on the relationship between soil moisture and climate change, still there exists many problems which need further attention, for example, the annual and interannual variations of soil moisture and temperature, and their interactions with regional climate, the design of initial soil moisture scheme in climatic model, soil moisture and temperature anomalies and their impact on regional climate, and the effect of regional drying tendency on climate and environment in middle latitude of Eastern China.

References

Avissar R, Pielke RA (1989) A parameterization of heterogeneous land surfaces for atmospheric numerical models and its impact on regional meteorology. Monthly Weather Review 117: 2113-2136

Avissar R, Chen F (1994) The impact of land-surface wetness heterogeneity on mesoscale heat fluxes. J Applied Meteorology 33:1382-1401

Chang JT, Wetzel PJ (1991) Effect of special variation of soil moisture and vegetation on the evolution of a pre-storm enviroment: A numerical case study. Monthly Weather Review 119:1386-1390

Charney JG (1975) Dynamics of deserts and droughts in the Sahel. Quart J Roy Meteor Soc 101:193-202

Dirmeyer PA, Guo ZC, Gao X (2004) Comparison, validation, and transferability of eight multiyear global soil wetness products. J Hydrometeorology 5:1011-1033

Engman ET, Chauhan N (1995) Status of microwave soil moisture measurements with remote sensing. Remote Sens Environ 51: 189-198

Fennessy MJ, Shukla J (1999) Impact of initial soil wetness on seasonal atmospheric prediction. J. Climate 12: 3167–3180

Grell GA, Dudhia J, Stauffer DR (1994) A description of the Fifth-Generation Penn State / NCAR Model (MM5). NCAR Technical Note, NCAR/TN-398 +STR, pp117

Henderson-Sellers A (1996) Soil moisture: A critical focus for global change studies. Global and Planetary Change 13:3~9

Hollinger SE, Isard SA (1994) A Soil Moisture Climatology of Illinois. J Climate 7: 822–833

Hulme M, Marsh R, Jones PD (1992) Global changes in a humidity index between 1931-60 and 1961-90. Clim Res 2: 1-22

Lanicci JM, Carlon TN, Warner TT (1987) Sensitivity of the great plains severe storm environment to soil moisture distribution. Monthly Weather Review 115: 2660-2673

Liu YQ (1990) The study on the influence to the climate from soil moisture and vegetation. Ph.D thesis, Institute of Atmospheric Sciences, Chinese Academy Sciences (in Chinese)

Ma ZG (1999) The relationship of soil moisture in Eastern China and regional climatic variation and the foundation of a retrieval model for soil moisture. Ph.D thesis, Institute of Atmospheric Sciences, Chinese Academy Sciences (in Chinese)

Ma, ZG, Fu CB (2006) The basic arid situation in the northern from 1951 to 2004. Chinese Science Bulletin, 51(20): 2429-2439

Ma ZG, Wei HL, Fu CB (2000) The relationship between soil moisture and regional climatic variabilityin East China. Acta Meteorologica Sinica 58: 278-287

Mahfouf JF, Richard E, Mascart P (1987) The influence of soil and vegetation on the development of mesoscale circulation. J Applied Meteorology 26:1483-1493

Manabe S (1981) Summer dryness due to an increase of atmospheric co_2 concentration. Climatic Change 3: 347-386

McCumber MC, Pielke RA (1981) Simulation of the effects of Surface fluxes of heat and moisture in a mesoscale numerical model. Part 1: Soil layer. J Geo Res 86: 9929-9938

Moran MS, Hymer DC, Qi J, Sano EE (2000) Soil Moisture evaluation using Synthetic Aperture Radar (SAR) and optical remote sensing in semiarid rangeland. Agricultural and Forest Meteorology 105: 69-80

National Meteorological Administration (1993) The Observational Criterion of Agricultural Meteorological Observation. China Meteorological Press, Beijing, pp151 (in Chinese)

Namias J (1958) Persistence of mid-tropospheric circulations between adjacent months and seasons. Rossby Memorial Volume, Rockfeller Institute Press and Oxford university Press, 240-248

Njoku EG, Entekhabi D (1996) Passive remote sensing of soil moisture. J Hydrology 184: 57– 84

Ookouchi Y, Segal M, Kessler RC, Pielke RA (1984) Evaluation of soil moisture effects on the generation and modification of mesoscale circulation. Monthly Weather Review 112: 2281-2292

Pinty JP, Mascant P, Richard E, Rosset R (1989) An investigation of meso-scale flows induced by vegetation inhomogenerities using an evapotraspiration Model calibrated against HAPEX-MOBILHY data. J Applied Meteorology 28:976-992

Rind D (1982) The influence of ground moisture conditions in North America on summer climate as modeled in the GISS GCM. Monthly Weather Review 110:1487-1494

Robock A, Vinnikov KY, Srinivasan G, Entin JK, Hollinger SE, Speranskaya NA, Liu S, Namkhai A (2000) The Global Soil Moisture Data Bank. Bull Amer Meteorol Soc 81: 1281-1299

Rowntree PR, Bolin JA (1978) Experiment with soil moisture anomalies over Europe, The GARP Programme on Numerical Experimentation: Research Activities in Atmospheric and oceaic modeling. R Asselin (Ed.), GARP Report, No.18, WMO/ICSU, Geneva, August 1978, pp63

Rowntree PR, Bolton JR (1983) Simulation of the atmospheric response to soil moisture anomlies over Europe. Q J R Meteor Soc 109:501-526

Shao YP (1996) A Henderson-sellers. Validation of soil moisture simulation in land－surface parameterization schemes with HAPEX data. Global Planet Change 13:11-46

Shukla J, Mintz Y (1982) The influence of land-surfacee evapotranspiration on Earth's climate. Science 215: 1498-1501

Thornthwaite CW (1948) An approach toward a rational classification of climate. Geogr Rev 38: 55-94

Wang SY (2003) Regional Climate Simulation in East Asia and the study on initial scheme of soil moisture. Ph.D thesis, Institute of Atmospheric Sciences, Chinese Academy Sciences (in Chinese)

Wagner W, Lemoine G, Borgeaud M, Rott H (1999a) A Study of Vegetation Cover Effects on ERS Scatterometer Data. IEEE Trans Geosci Remote Sens 37: 938-948

Wagner W, Lemoine G, Rott, H (1999b) A method for estimating soil moisture from ERS Scatterometer and soil data. Remote Sens Environ 70: 191-207

Wagner W, Scipal K, Pathe C, Gerten D, Lucht W, Rudolf B (2003) Evaluation of the agreement between the first global remotely sensed soil moisture data with model and precipitation data. J Geophys Res-Atmos 108: 4611, doi:10.1029/2003JD003663

Western A, Grayson R, Blöschl G (2002) Scaling of soil moisture: a hydrologic perspective. Ann Rev Earth and Planetary Sci 30: 149–180

Xue Y, Liou KN (1990) Investigation of biogeophysical feedback on the African climate using a two − dimensional model. J Climate 3: 337 − 352

Yeh TC, Wetherald RT, Manabe S (1984) The effect of soil moisture on the short-term climate and hydrology change--A numerical experiment. Monthly Weather Review 112:474-490

Zhang D, Anthes RA (1982) A high-resolution model of the planetary boundary layer-sensitivity tests and comparisons with sesame-79data. J Applied Meteorology 21:1592-1609

Zhao DM, Su BK, Zhao M (2006) Soil moisture retrieved from satellite images and its application to heavy rainfall simulation in Eastern China. Advances in Atmospheric Sciences 26: 299-316

Chapter 8 Climate Extremes and Related Disasters in China

8.1 Introduction

Climate extremes are commonly thought to be in association with rare weather events. To quantify how 'rare' an extreme weather event is, a small percentile (e.g., the 1st) or a large percentile (e.g., the 99th), defined against all weather samples, may be used for statistical analysis. In comparison, an extreme climate event is an average of weather conditions over a certain period that is 'rare' among all climate samples. In the analysis of changes in climate extremes, large percentiles such as the 99th, 95th and 90th or small ones such as the 1st, 5th and 10th may be applied as thresholds for quantifying extremes. If the value of a weather or climate variable exceeds the threshold, it is defined as an extreme. Sometimes, a certain fixed value is also used as a threshold, e.g., 50 mm/day of rainfall for extreme precipitation event and 35℃ of surface air temperature for extreme hot day for certain places (Zhai et al, 2003a). Some events such as droughts are more complex, as these can hardly be defined with a single meteorological variable.

Although extreme events happen with small probability, they have profound impact on society and environment (Karl et al., 1999) and often result in tremendous disasters. The types of climate extremes and related meteorological disasters affecting China are various, in association mainly with rain storm, flood, drought, heat wave, frost, sand storm, typhoon and heavy fog. In addition, climate extremes may induce secondary disasters. For example, heavy rainfall may lead to mudflow or landslide; high temperature and drought enhance chances of forest fires. There is a general spatial / seasonal pattern of climate extremes and disasters over the country. Dust storms occur most frequently in Northwest China in spring. Southeast China is typhoon-prone area with the active season from May to October. Among all the natural disasters, climate and meteorological disasters are the most frequent ones and their influences are enormous with a broad and far-reaching set of impacts. The major impacts are reflected in loss of life, illness, and adaptation costs in transportation, agriculture, energy and in-

frastructure. In China, about 750 km^2 farm lands are hit by climate extremes and meteorological disasters such as droughts, floods and tropical cyclones, about 600 million people are affected each year. On average, the annual economic loss due to meteorological disasters in China is equivalent to 3-6% of Gross Domestic Product (GDP) and it has increased substantially from the 1980s to the 1990s and 2000s (Figure 8.1). Such increase is in association with both the development of social economy and changes in climate extremes.

The study of extreme weather and climate extremes in China has received increasing attention in recent years (Zhai et al., 2005a; Yan and Yang, 2000). This chapter is to introduce some results, especially on changes in temperature and precipitation extremes, tropical cyclones, droughts and dust-storms during recent 50 years.

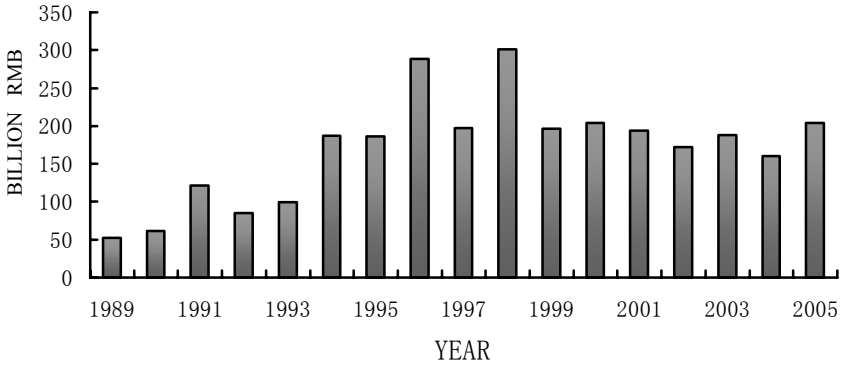

Fig. 8.1 Economic loss resulted from meteorological disasters in China during 1989-2005

8.2 Temperature extremes

Change in the mean temperatures may not well reflect changes in extremes, which are of more direct impacts on human society and environment. According to Yan and Yang (2000), trends in daily temperature extremes were 5-10 times larger than that in mean temperature at most stations in China during recent decades. Alexander et al. (2006) analyzed changes in global temperature and precipitation extremes based on climate extreme indices derived from daily data. Results showed widespread sig-

nificant changes in temperature extremes associated with warming, especially for those indices derived from daily minimum temperature. There are different regional and temporal features of changes in temperature extremes across the vast territory and complex climate in China, however.

Extreme weather fluctuations in temperature such as heat waves and cold surges exert tremendous impacts on the nation. In summer 2003, most areas of southern China were hit by severe heat wave. The maximum temperature in Zhejiang, Jiangsu, Anhui, Jiangxi, Fujian, Guangdong, and Guangxi provinces in summer 2003 claimed the new record since 1951. At Lishui station, Zhejiang province, there were 14 days with maximum temperature exceeding 40℃ and 5 days exceeding 42℃. The extreme heat event caused severe shortage of water and electricity in southern China. In summer 2006, a record heat wave scorched eastern Sichuan province and Chongqing city. In the worst heat spell during the past 56 years, temperatures in Chongqing soared to 40-44℃ and remained unusually high for nearly two months. The excessive heat exacerbated droughts and had left 18.9 million people short of drinking water in Sichuan and Chongqing. In 2005, as heavy frost hit Hunan Province during the Spring Festival (mid-February), the electricity network experienced the worst damage since 1954.

8.2.1 Maximum and minimum temperatures

Increasing trends in the mean maximum temperatures prevailed in northern China, while trivial or slightly decreasing trends occurred in southern China during the past half century (Tang et al., 2005a; Yan and Yang, 2000). The mean minimum temperatures showed consistent significant warming trends throughout the country, more profoundly in northern China (Figure 8.2). The warming trend was stronger for the winter than other seasons (Tang et al., 2005a; Zhai et al., 1999a). The magnitude of the trend in the mean minimum temperature was generally greater than that in the mean maximum temperature, resulting in decreasing diurnal temperature range (DTR) over most China. The most significant decrease in the mean DTR occurred for the winter season over northern China. Decadal and inter-annual variations in the mean maximum and minimum temperatures were quite coherent in general, both showing a noticeable warming trend since the middle of the 1980s.

Warming trends in the extremes of minimum temperature were evident for all the four seasons, with the most significant trend for winter. Trends in the extremes of maximum temperature were more diverse for different seasons than those in the mean maximum temperature. Decreasing trends

were found for summer and autumn, but not statistically significant (Zhai et al., 1999a).

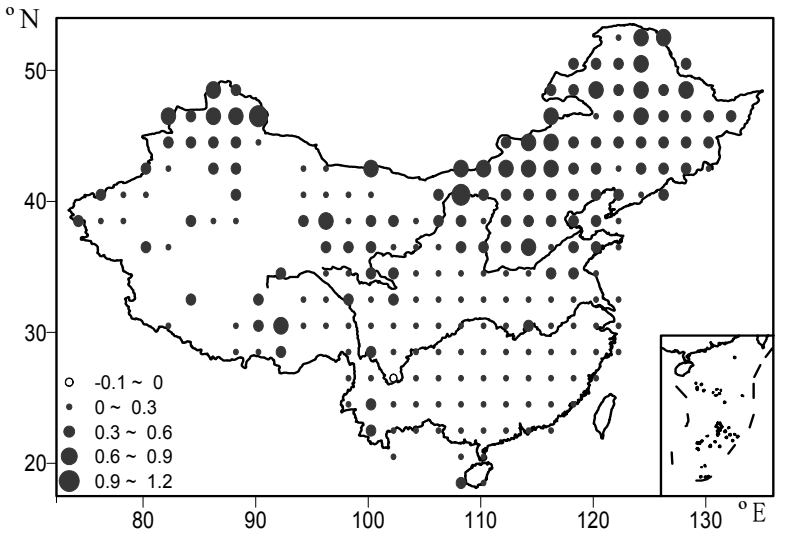

Fig. 8.2 Trends in annual mean minimum temperatures in China during 1951~2002(units:℃/10a)(Tang et al., 2005a)

8.2.2 Warm days and cool days

The development of a suite of climate change indices which primarily focus on extremes provided a useful tool to monitor and detect climate change (Alexander et al., 2006). Temperature indices derived from daily maximum and minimum temperature comprises absolute and percentile-based indices. Percentile-based indices include occurrence of warm days (TX90p), cool days (TX10p), warm nights (TN90p) and cool nights (TN10p) (Table 8.1) (Zhang et al., 2005).

Results showed the warm days in China displayed a slightly decreasing trend prior to the middle of the 1980s, followed by a sharply increasing trend since then (Zhai and Pan, 2003a) (Figure 8.3). The number of warm days slightly increased in northern China and the southeast coast, significantly increased in western China, but decreased in central and southern parts of eastern China.

For China as a whole, the number of cool days displayed a slightly de-

creasing trend of 0.5 day/10a (Zhai and Pan, 2003a). The decreasing trend was especially obvious since the mid-1980s. Although differences exist in defining cool days, a decreasing trend is consistent with those in most Southeast Asian countries as revealed by Manton et al. (2001). Moreover, inter-annual and inter-decadal variability for the number of cool days are also obvious during the past 50 years in China (Figure 8.3). Spatially, the number of cool days displayed significant decreasing trends (about 4 days/10a) in most parts of northern China, but slightly increasing trends in much of southern China.

Table 8.1 Description of six temperature indices derived from daily temperatures (Zhai and Pan, 2003a)

Index	Description
Hot day	Days with Tmax above 35°C
Frost day	Days with Tmin below 0°C
Warm day	Days with Tmax above the 1961-1990 mean 95th percentile of the same day
Cool day	Days with Tmax below the 1961-1990 mean 5th percentile of the same day
Warm night	Days with Tmin above the 1961-1990 mean 95th percentile of the same day
Cool night	Days with Tmin below the 1961-1990 mean 5th percentile of the same day

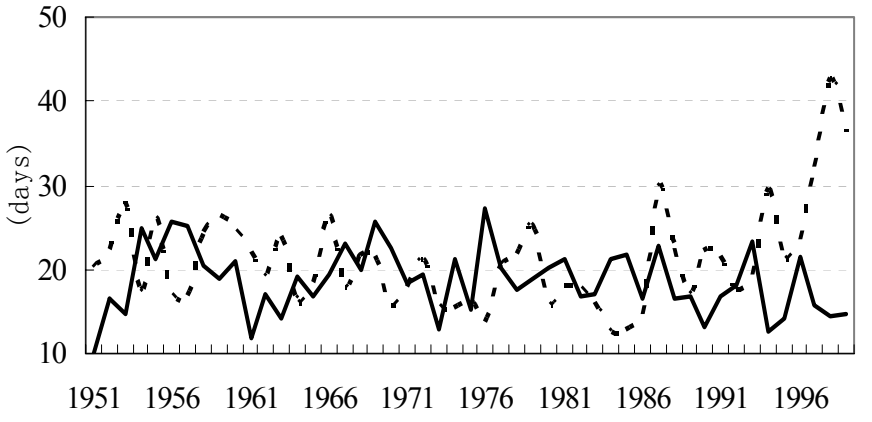

Fig. 8.3 Numbers of warm days (dash lines) and cool days (solid lines) averaged over China during 1951 – 1999. (Zhai and Pan, 2003a)

8.2.3 Warm nights and cool nights

The average number of warm nights in China increased with a rate of 3 day/10a during 1951-1999 (Zhai and Pan, 2003a). Prior to the mid-1980s, there were about 10-20 warm nights per year, compared with 20-40 warm nights per year after the mid-1980s (Figure 8.4). Most China exhibited significant upward trends in warm nights, with the largest increases in parts of southwest China.

Cool nights in China displayed a decreasing trend by about 3 day/10a (Zhai and Pan, 2003a). This rate is more obvious since the mid-1970s (Figure 8.4). Over most regions of the country, cool nights decreased significantly, northern China has greater declines than that in southern China.

The decreasing trends in cold nights are much greater than that in cold days, which is consistent with those of many other countries in SE Asian areas (Alexander et al., 2006) and it also supports the fact that the increase of nighttime temperature is quicker than that of daytime temperature.

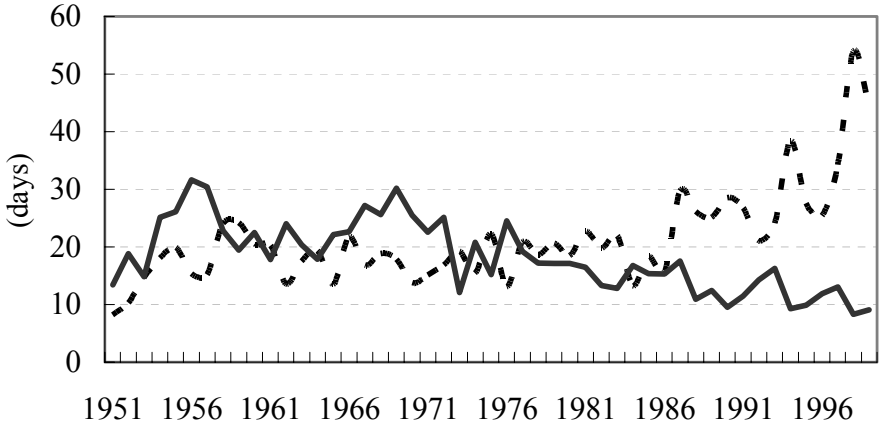

Fig. 8.4 China's averaged numbers of warm nights (dash lines) and cool nights (solid lines) during 1951-1999. (Zhai and Pan, 2003a)

8.2.4 Hot days and frost days

There is a slightly decreasing trend in hot days (Table 8.1) for China as a whole since the 1950s, followed by some increase since the mid-1990's (Zhai and Pan, 2003a). Among different regions, significant deceasing

trends in the number of hot days mainly occurred in the central and southern parts of eastern China. Significant increasing trends were found in some areas in western China. In southern China, although the summer 2003 was declared the hottest during the past half century, it might be considered as an episode in association with interannual variability rather than a reflection of long term trend (Wang et al., 2006).

Frost days (Table 8.1) in China exhibited a large negative change with a rate of 2.4days/10a during 1951-1999. The average number of frost days in the 1990s is about 10 days per year fewer than those in the 1960s. As shown in Figure 8.5, significant decreasing trends in frost days were found in most parts of China. The sharpest decreasing trends occurred in northwestern and eastern China.

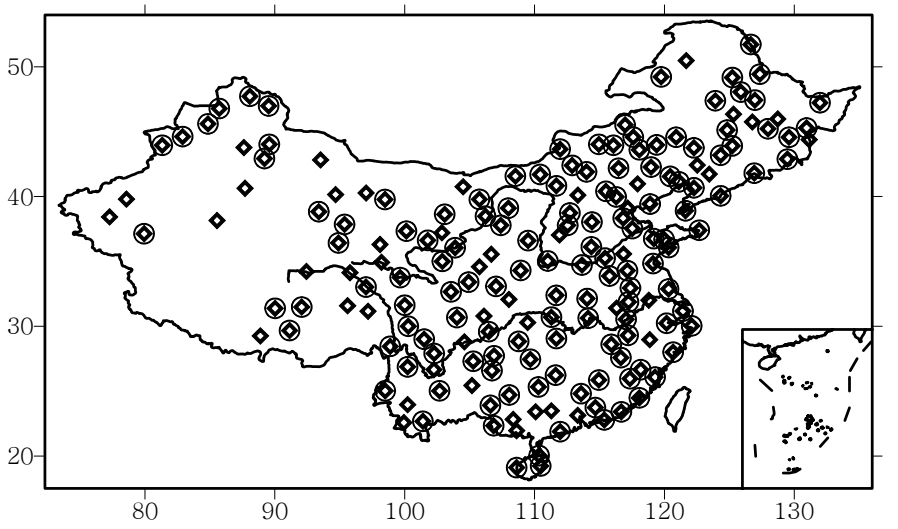

Fig. 8.5 Spatial distribution of trends (diamond signs mean decrease trends and the circle signs indicate statistical significant at 0.05 level) for annual number of frost days in China during 1951-1999. (Zhai and Pan, 2003a)

In summary, for the country as a whole during the last half century, decreasing trends in cold extremes were more profound than increasing trends in warm extremes. This is somehow coherent with the global viewpoint from Alexander et al. (2006): rather than viewing the world as getting hotter it might be more accurate to view it as getting less cold. Similar conclusions were also found in earlier works in China (e.g., Yan and Zhang, 1993; Zhai et al., 1999a; Ma et al., 2003a). Yan et al (2001) analyzed a few long-term daily temperature series in Europe and China with a

wavelet method and concluded that weather-timescale fluctuations tend to be weaker during warmer times for mid-high-latitude areas. The decreases of both hot days and frost days in China during the past half century could partly be resulted from a generally weakening trend in weather fluctuations.

8.3 Precipitation extremes

Trends of climatic extremes, especially precipitation extremes that cause heavy rainfall or flood disasters and result in severe socio-economic losses, have received increasing attention and are seen as an important realm for scientific research in China (Su et al., 2005). Floods in 1998 caused $36 billion economic losses and more than 3000 lives in the Yangtze River valley in southern China and in the Nenjiang-Songhuajiang valley in Northeast China (NCC, 1998). In 2003, because of the high frequency and intensity of precipitation, catastrophic flood occurred in whole areas of the Huaihe River Basin, caused more than 2 million residents to be evacuated, with economic losses of 35 billion yuan (5.4 billion U.S. dollars) in Anhui, Jiangsu and Henan provinces (Wang, 2004).

Changes in total and extreme precipitation have attracted much attention in recent years. The Intergovernmental Panel on Climate Change (IPCC) in its recent Assessment Report (Houghton et al. 2001) presented a global picture of trends in precipitation during different periods. China was a noticeable data-sparse area for that global map, even for the period 1976–99. A few studies dealing with precipitation extremes change in China were carried out in recent years (e.g., Yan and Yang, 2000). Zhai et al. (2005a) used a newly developed higher-quality dataset with much denser network and longer time series, and applied more robust and sounder trend detection techniques. Their results provide a more thorough account and update of changes in annual and seasonal total and extreme precipitation in China over the second half of the twentieth century. Links between changes in total and extreme precipitation were also analyzed.

8.3.1 Total precipitation

The time series of area-weighted annual precipitation anomalies relative to the 1961–90 mean value for China shows strong variability at both interannual and interdecadal scales. For example, the years 1954, 1998, 1973, and 1983 were very wet, while the years 1978 and 1986 were very dry. The period from the 1950s to the early 1960s and the 1990s were generally wet, but the period from the middle 1960s to the 1970s was very dry. The averaged annual total precipitation anomalies show a decreasing trend at a rate

of 1.03 mm per decade.

Figure 8.6 displays the spatial distribution of trends in standardized annual precipitation anomalies. Annual total precipitation has increased by 10% – 20% decade^{-1} at most stations in northwestern China, by 5%–10% decade^{-1} in Tibet, and by 5% or less decade^{-1} at some stations in the southeast coast and the mid lower reaches of the Yangtze River. It has decreased elsewhere, by about 5% decade^{-1}, with the most significant decrease in North China and the Sichuan Basin.

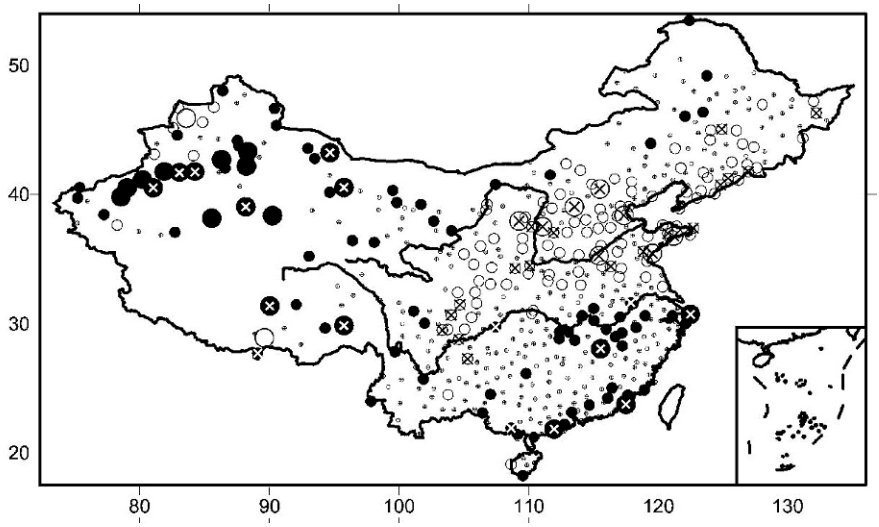

Fig. 8.6 Spatial distribution of trends for annual standardized precipitation anomalies during 1951–2000. The solid (open) circles indicate increasing (decreasing) trends, respectively. Trends that are larger than 7.5% decade-1, between 7.5% and 2.5% decade-1, and less than 2.5% decade-1 are marked by large, middle, and small circles, respectively. Those significant at the 5% level are marked by crosses (×).

8.3.2 Frequency and intensity of precipitation

Except in western China, the number of rain days (Figure 8.7) has significantly decreased. The average daily rain rate has significantly increased over almost the entire country. In most parts of China, while precipitation is getting less frequent, it is more intense. The increase in total precipitation in the mid lower reaches of the Yangtze River and the southeast coast is generally due to the increase of precipitation intensity. The decrease in

total precipitation in northern China is the result of a great decrease in the number of rain days, despite some increase in the average intensity of rainfall. According to Yan and Yang (2000), the significant drying process in northern China during the past half century was featured by (or resulted in) significant decreasing of trivial-rainfall events. In western China, however, the increase in total precipitation over western China is due to increases in both precipitation frequency and average intensity.

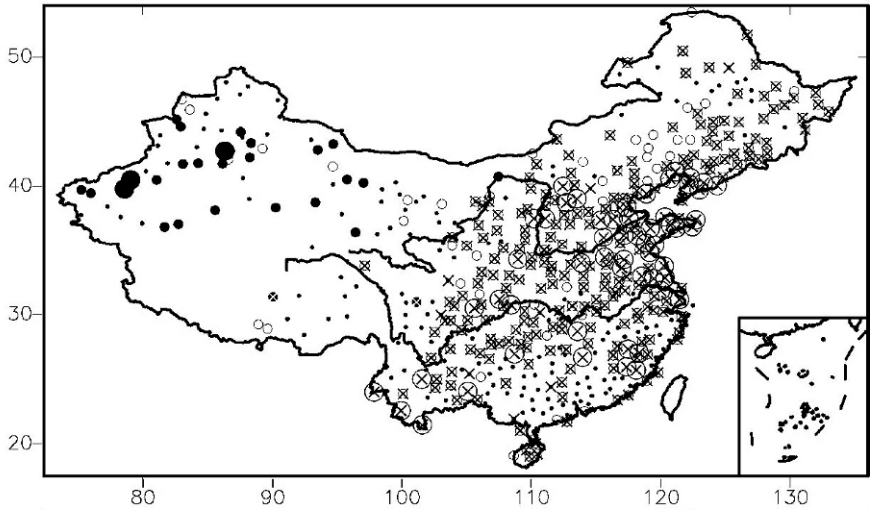

Fig. 8.7 Trends in the annual number of rain days . Units are percentage change over the corresponding 1961–90 averages. Solid (open) circles indicate increasing (decreasing) trends, respectively. Trends larger than 7.5% decade^{-1}, between 7.5% and 2.5% decade^{-1}, and less than 2.5% decade^{-1} are represented by large, middle, and small circles, respectively. Trends significant at the 5% level are marked by crosses (×).

8.3.3 Extreme precipitation

The trends in the annual frequency of extreme precipitation days have similar spatial distribution to that of annual total precipitation (Figure 8.7). Decreasing trends prevail over eastern Northeast and North China, and the Sichuan Basin. Statistically significant decreasing trends are found in both northern China and the Sichuan Basin. Increasing trends are mainly located over western China and the mid–lower reaches of the Yangtze River and some regions to the south. Increasing trends significant at the 5% level occur over the mid lower reaches of the Yangtze River and parts of Southwest China and the south China coastal area.

The geographic distribution of trends in extreme precipitation days for the warm half year resembles the annual case. For the cold half year, there are more stations in southern China with a significant increasing trend.

Zhai et al.(2005a) show that 24% and 19% of mainland China experienced much above-normal occurrence of precipitation extremes during 1998 and 1954, the years with very severe floods in the country. It also seems that an increasing trend in the proportion of China affected by extreme precipitation.

8.3.4 Wet spells

Due to its localized feature, definitions of wet spells vary from region to region. In order to reveal the comparative characteristics of wet spells throughout China, uniform criteria on wet spell have been defined based on previous definitions used in different regions. The detailed definition is described in the following.

(1) In a wet spell, the number of rainy days (daily precipitation $\geqslant$ 0.1mm) should be no less than 4 days, and no dry day (daily precipitation <0.1mm) in the first 3 days.

(2) A wet spell is ceased whenever it occurs 2 consecutive dry days. The duration of a wet spell is defined as the number of days before the two consecutive dry days.

According to this definition, 1 dry day is allowed to occur in a 5-day wet spell, and 2 dry days in the 6-day wet spell, and so on.

Based on the above definition, it is found that in Southwest China and the eastern Tibetan Plateau, the longest wet spell can be up to 60 days, or even 80 days in southernmost Southwest China. In most areas of Northwest China, it is less than 20 days, whereas in North China and Northeast China, it is about 40 days. The spatial distribution pattern of extreme long wet spells shares the similar patterns with that of mean annual number of days in wet spells (Bai et al, 2006).

The maximum mean daily precipitations in wet spells declines from southeastern to northwestern China. In southeast coastal areas, Central China and part of South China, the maximum daily precipitation amounts can be up to 50 mm; whereas in Northeast China, it is only about 30 mm. In the areas to the west of 100ºE, it is less than 20 mm. Obviously, wet spells are relatively weaker in inland China.

The number of days in wet spells has decreased over North China. However, it has slightly increased in part of western China. As for the annual precipitation from wet spells, there are significant negative trends in North China and eastern Northeast China, as well as eastern Southwest

China. But to the south of Yangtze River, wet spell precipitation has increased. In western China except for southern Tibetan Plateau, there are no obvious trends. Obvious regional differences are found in trends of wet spells. The distinct regional difference in trends of annual number of days in wet spell and annual precipitation totals from wet spells over China is particularly clear between the eastern Tibetan Plateau and the mid-lower reaches of the Yellow River. In the mid-lower reaches of the Yellow River, there are significant negative trends; while in the eastern Tibetan Plateau, there are positive trends.

8.4 Cyclones

8.4.1 Tropical cyclones

A tropical cyclone (TC) is a non-frontal synoptic scale cyclone originating over tropical or sub-tropical waters with organized deep convection and a closed surface wind circulation about a well-defined center. Tropical cyclones (TCs) are classified into six main groups: tropical depressions, tropical storms, severe tropical storms, typhoons, severe typhoons and super typhoons in the Northwest Pacific west of the dateline. Tropical storms and severe tropical storms are TCs with maximum sustained winds between 17.2 and 32.6 m/s. Typhoons are defined as TCs with maximum sustained wind speed exceeding 32.7 m/s (China Meteorological Adininistration, 2006). Most of TCs in the western North Pacific (WNP) originally occurred in the sea surface to the west of 170 °E between 5°N and 15°N (Chen et al., 1999). There are three frequent centers over WNP, South China Sea, Philippines and Mariana. Severe TCs often come from the sea surface east to 125°E, especially in Mariana.

East and southeast China are typhoon-prone areas. Tropical storms and typhoons, especially those that make landfall, cause extensive damage every year. For example, Typhoon Rananim made landfall in Wenling city, Zhejiang province in August 2004 with a maximum wind speed near the eyewall of 45 m/s and a minimum central pressure of 950 hPa. It killed 169 people and injured more than 2000, in addition to a direct economic damage of about $2.5 billion (Xu, 2005). In July 2006, severe tropical storm Bilis made landfall at Taiwan and Fujian, influencing Zhejiang, Fujian, Guangdong, Guangxi, Jiangxi and Hunan provinces. With the official death toll of 654 people (Ministry of Civil Affairs of the People's Republic of China), Bilis was claimed as the deadliest in recent decades.

There is considerable inter-decadal variability in the number of TCs over the WNP (Chan and Liu, 2004; Zhang et al., 1995) (Figure 8.8). Ac-

tive years during the latter half of the 20th century were in the mid-1960s and early-1990s. Although there is little to support the hypothesis that typhoons have become more frequent during the past 4 decades (Chan and Liu, 2004), the strengthening and increasing destructiveness of typhoons in the WNP and subtropical East Asia in past 30 years tends to be evident in recent studies (Emanuel, 2005; Wu et al., 2005; Zou et al., 2006). Defining an index of the potential destructiveness of TCs based on the total dissipation of power, integrated over the lifetime of the cyclone, Emanuel (2005) indicated that due to both longer storm lifetimes and greater storm intensities, the index has increased markedly since the mid-1970s over the western North Pacific. Using track data during 1965 to 2003 from the Joint Typhoon Warning Center (JTWC), Wu et al. (2005) showed that two prevailing typhoon tracks in the WNP have shifted westward significantly, thus the subtropical East Asia has experienced increasing typhoon influence. These studies suggest that the influence of tropical storms and typhoons in China has intensified during the past half century. In addition, some studies have shown that the TCs activity over the central South China Sea (south to 20°N) has persistently decreased during the past 4 decades (Wu et al., 2005; Gong and He, 2002a), which was opposite from the increases of TCs activity in the region to the north of 20°N in eastern China.

The WNP subtropical high is one of the most import atmospheric circulation factors to influence summer climate in China. Gong and He (2002a) pointed out the strengthening and southwestward expansion of the WNP subtropical high since the 1980s was closely linked with the increases of TCs activity in the area to the north of 20°N and decreases over the region to the south of 20°N in eastern China. Using historical records from 1949 to 1994, Yang and Shi (1999) found that over the region north to 20°N, west to 140°E in the WNP, increases in sea surface temperature (SST) will likely to lead to more frequent TC activities. Chan et al. (2004) indicated typhoon activity was positively correlated with the mean May-November SST over the equatorial central and eastern Pacific Ocean, with a mean correlation of 0.58 in the Niño-3.4 region (5°S-5°N, 170°-120°W) based on the past 40 yrs record. Such a result suggested that the interannual variations of typhoon activity appear to be closely related to the El Niño-Southern Oscillation (ENSO) (Chan and Liu, 2004; Chan, 2000; He et al., 1999; Li, 1985). The mean annual typhoon activity is generally higher (lower) during an El Niño (La Niña) year (Figure 8.8).

There have been extensive analyses of the influences of TCs on the climate of China. TCs contribute a lot to the rainfall totals in eastern China. Evident downward trends have been found in tropical cyclone precipitation (TCP) amount, the frequency of torrential TCP events and its contribution to total precipitation (Ren et al., 2006; Ren et al., 2002) (Figure 8.9).

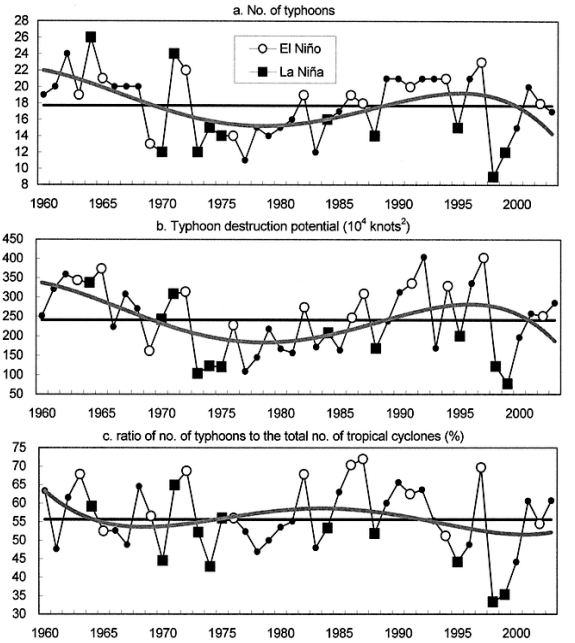

Fig. 8.8 Time series of (a) the number of typhoons (NTY), (b) the typhoon destruction potential (TDP), and (c) the ratio of NTY to the total number of TCs in the period 1960– 2003. Open circles and closed squares indicate the El Niño and La Niña years, respectively. The thick lines and horizontal lines indicate the fourth-order polynomial fits and the 1960–2003 means, respectively. (Chan and Liu., 2004)

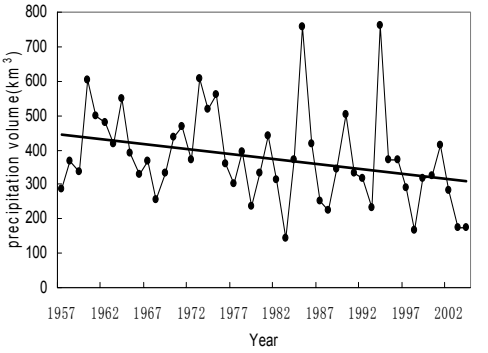

Fig. 8.9 Variations of annual volume of tropical cyclone precipitation for China during 1951-2004 (Ren et al., 2006).

8.4.2 Extra-tropical cyclones

One of the hypothesized effects of global warming from increasing concentrations of greenhouse gases is a change in the frequency and/or intensity of extra-tropical cyclones (McCabe et al., 2001). Extra-tropical cyconles are baroclinic low pressure systems that occur throughout the mid-latitudes of both hemispheres. Their potential for causing property damage, particular as winter storms, is well documented (IPCC, 2001). Severe storms cause tremendous property damage in the country each year. For instance, from November 1995 to April 1996, heavy winter storms ravaged the Tibetan region continuously, 84 people were killed and about 1.5 million livestock died (Chen, 1997). On November 6th, 2003, an overnight blizzard blasted the capital city Beijing. More than 13 million trees were damaged across the city and surrounding suburbs, and heavy economic losses were incurred due to heavy snow and freezing winds (Zou, 2004a). The main interest in studies of severe storms is about wind and wind-generated waves. However, the lack of consistent instrumentation, methodology and exposure makes direct wind speed measurements hardly useful for studying the long-term variations in severe storms. Pressure changes are relatively less sensitive to the site moves and instrumentation changes and hence more reliable to analyze severe storms (IPCC, 2001; Bärring and von Storch, 2004; Alexander et al., 2005). Using ERA-40 SLP reanalysis data during 1958-2001, Wang et al. (2006) improved an algorithm given by Geng and Sugi (2001) based on synoptic definition to detect the extra-tropical cyclone activity over northern East Asia. Their analysis support the notions of McCabe et al. (2001), i.e., a significant decrease in mid-latitude cyclone frequency and an increase in high-latitude in the Northern Hemisphere, suggesting a poleward shift of the storm track (Figure 8.10). Using the 95th and 99th percentiles of absolute mean sea-level pressure (MSLP) changes between two consecutive observations, Zou et al. (2006) discussed the variations of severe storms in China based on 6-hourly pressure change data during 1954-2004. Significant decreases were detected across most northeastern, central and western parts of China (Figure 8.11). Changes of severe storms in winter (DJF) and spring (MAM) contribute the most to these decreasing trends. Also, this is likely to be related to a weakening of the Siberian High during winter. These results are coherent with the analysis of Yan et al (2001), which demonstrated weakening weather fluctuations in the westerlies under a warming trend.

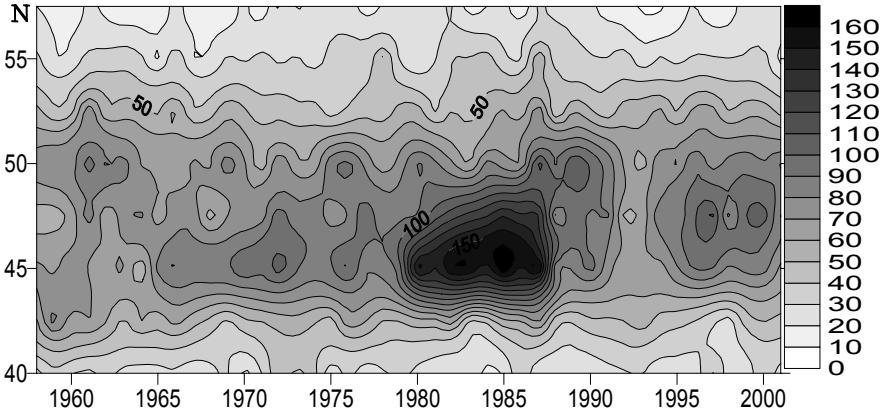

Fig. 8.10 Annual extratropical cyclone frequency for latitudinal bands in northern East Asia.(the region 80°-140°E, 25°-60°N, except the Tibetan Plateau) (Wang and Zhai, 2006)

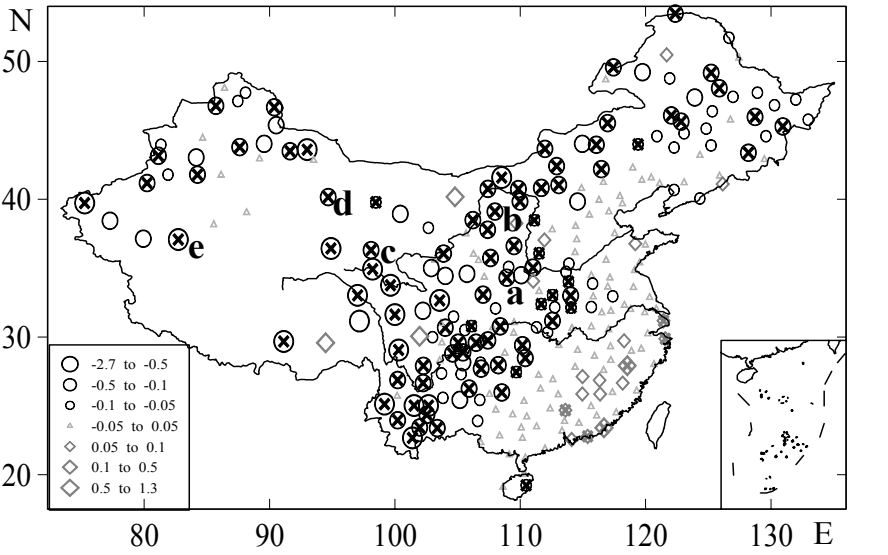

Fig. 8.11 Linear trends (diamond positive; circle negative) of the annual 99th percentile of absolute 6-hourly mean sea-level pressure changes between two observations (hPa/10yr) for 268 stations over China during the period 1954-2004. The crosses indicate where trends are significant at the 5% level using the non-parametric Kendall's tau test.

8.5 Droughts

Meteorological droughts are normally defined as abnormal periods of moisture deficiency relative to the long-term average over a given region (Heddinghaus et al., 1991). It is well known that droughts are one of the most damaging climate-related hazards to impact societies (Woodhouse and Overpeck, 1998). The Palmer Drought Severity Index (PDSI) (Dai et al., 2004) show the global very dry areas (PDSI<-3.0) increased remarkably since the late 1970s due to decreased precipitation and increased temperature over some regions under global warming background. It is suggested that warmer climate would result in longer lasting and more severe drought due to enhanced evaporation (Gregory et al., 1997) if without enough precipitation at the same time. For China as a whole, during the past half century annual precipitation has no significant secular trends, but decreasing trends in the number of rainy days and the longest durations of consecutive rainfall have been detected (Zhai et al., 1999a; 1999b). Also, the spatial distribution of precipitation trends across China is uneven (Zhai et al., 2005a). Decreasing trend has been observed over southern Northeast China, North China, and over the Sichuan Basin, whereas increases occurred in western China, the Yangtze River valley, and southeastern coast.

Using the observations as well as proxy data, Ye et al. (1996) found there were several significant dry or wet phases and abrupt changes of precipitation in the Yangtze River and Yellow River Valleys during recent 100 years. In the 1920s and mid-1960s, there were two climatic jumps from wet to dry in China. The 1960s' drying jump initiated the persistent and aggravating dry conditions in the Yellow River valley and was a part of some larger-scale climate changes involving the well-known drying process in Sahel, North Africa, since the late 1960s (Yan et al., 1990).

The devastating drought conditions in 1997, 1999 to 2002 in many areas of northern China have been a growing concern of both the Chinese government and general public (Zhang et al., 2003; Zou et al., 2005). During 1972-1997, there were 20 years during which the Yellow River experienced seasonal drying-up (zero streamflow) episodes. After the early 1990s, the drying-up happened more frequently than before, with an earlier start time and longer periods. The severe drought of 1997 in northern China resulted in a period of 226 days with no streamflow in the Yellow River, the longest drying-up duration on record. Many studies have examined changes of humid or dry conditions in China during the recent decades. An expanding trend of drought areas in northern China (except western Northwest China) in the latter half of the 20th century has been well documented in many studies (Zou et al., 2005; Wang and Zhai, 2003; Ma

and Fu, 2003b) (Figure 8.12). The successive large increases of dry areas (PDSI<-1.0) since the late 1990s in Northeast, North and eastern Northwest China were unprecedented during the past half century. No obvious trends in drought areas have been found in other regions. There exist large multi-year to decadal variations in drought areas. For example, in the regions of the Yangtze River, quite extensive droughts occurred in the 1960s and late 1970s, while drought stress became relatively small after 1980 (Zhang et al., 2001; Zou et al., 2005). In western part of Northwest China, drought areas have decreased since the late 1980s (Wang et al., 2002; Shi et al., 2002).

Compared with the trend in temperatures over different regions in China, some researchers (Ma et al., 2003c; Xie et al., 2003) attributed the increase of severe droughts over north and northeast China to the regional warming climate. It was noted that risk of droughts had been increased since the late 1970s, as the regional warming not only led to higher temperatures but enhanced drought development (Dai et al., 2004). However, Zhai and Zou (2005b) suggested that variations in regional precipitation were still one of the most influential factor for drought development.

Dry/wet variations in eastern China are mainly governed by the strength of the East Asian monsoon circulation (Guo, 2003; Shi, 1996). In general, weaker summer monsoons lead to less summer precipitation in North China but more in the Middle and Lower Reaches of the Yangtze River (Guo et al, 2003). Guo et al. (2003) and Lu et al. (2004) found that strong summer monsoons existed during the period from 1951 to the mid-1970s, followed by a systematic reduction in the late 1970s, in association with strengthening and southwestward expansion of the WNP subtropical high. This change resulted in more frequent droughts in North China and floods in the middle and lower reaches of the Yangtze River after the 1980s (Gong and He, 2002a; Lu et al., 2004). Gong et al. (2002b) found that a strengthened spring Arctic Oscillation (AO) could trigger a northward movement of rain belt in China, i.e. dryness in the Middle and Lower Reaches of Yangtze River and above-average precipitation in northern China.

The anomalies of precipitation, temperature and other climate variables in many areas might be related to ENSO as well. Gong and Wang (1999) revealed that more precipitation occurred in East China and less in northern China in autumn and winter during El Niño years, while the opposite cases were found during La Niña years. In past El Niño years, northern China often experienced droughts in summer. The time series of ENSO since 1880, established by Wang (1999), showed that in recent decades, the frequency of La Niña events decreased dramatically and that of El Niño events increased. These changes might partly cause the southward move-

ment of rain belt in eastern China since the 1980s (Zhao, 1996). Huang and Yan (1999) found that southerly monsoon currents over eastern China had weakened since the 1960s, leading to the strengthening of droughts in North China and floods in the middle and lower reaches of the Yangtze River in recent decades.

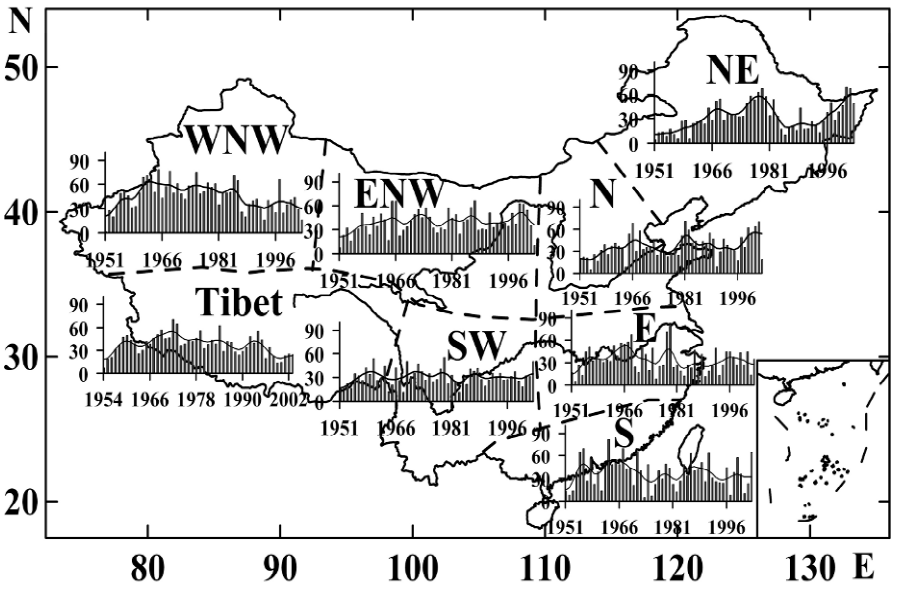

Fig. 8.12 Time series of annual percentage areas (bars) in drought conditions (PDSI<-1.0) over different regions within China during 1951-2003. The smooth curves are generated using an 11-point binomial filter. Due to too few stations in early years, its calculation of drought areas is started from 1954 in Tibet region. (NE: Northeast; N: North; ENW: eastern Northwest; WNW: western Northwest; E: east; S: South China; Tibet: Tibet Plateau) (Zou et al., 2005)

8.6 Dust storms

Dust storm in China is usually classified as dust haze, blowing dust and dust storm. Dust haze consists of aloft dust particles homogeneously suspended in the air and the horizontal visibility may sometimes be reduced to less than 10,000 m. Blowing dust is the state where dust is raised above the ground locally through strong winds and horizontal visibility may be reduced to 1,000-10,000 m. Dust storm is the result of strong turbulent wind systems entraining particles of dust into the air so that the visibility is reduced to 1,000 m or below. Very strong dust storm may cause the horizon-

tal visibility less than 50 m.

China is located in the East Asian monsoon area, with arid and semiarid climate in the northwestern parts. Dust storms often occur in northern China especially in downstream of the deserts and desertification regions in westerlies (Figure 8.13). Dust storms blow away vast amounts of topsoil, destroy crops, grasslands and roads, result in rapid desertification over arid and semiarid regions, and has a negative effect on human health through air pollution. In April 2001, a severe dust storm developed on the Mongolia-China border blanketed vast region of northern China. NOAA news reported that this dust storm moved over the Pacific, and reached as far as the eastern United States (http://www.noaanews.noaa.gov/stories/s624.htm). During April 16–17, 2006, a dust storm made Beijing city coated with as much as 3.3×10^8 kilograms of thick dust.

The annual mean dust storm days are over 10 days in the Tarim Basin, Hexi region and northeastern Tibet and more than 20 days in the Tarim Basin, northeastern Hexi region and Alashan Plateau (Wang et al., 2003; Zhou et al., 2002). Dust storms mostly occur in spring (MAM) and the frequencies in spring take more than half of the annual ones (Zhai and Li, 2003b). The frequency and affecting region of dust storms in April are more than that in other months (Zhai and Li, 2003b; Song et al., 2004).

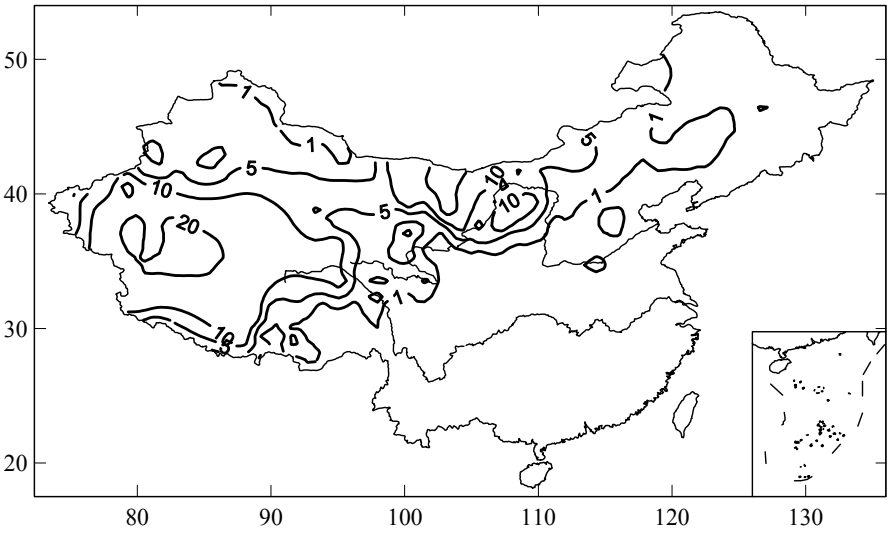

Fig. 8.13 Spatial distribution of annual mean dust storm days for 1971-2000.

Figure 8.14 shows the time series of dust storm days in spring (MAM)

over northern China during 1961-2006. Dust storm days increased from 1961 to the mid 1970s and decreased afterwards. There was a short-term oscillation in the late 1990s and the recent 4 years were the most least persist period. Dust storm days were above normal during 1961-1984 while below normal during 1985-2006 except 2000 and 2001. The highest record was 8.8 dust storm days in 1976 and the lowest was 1.4 days in 2005.

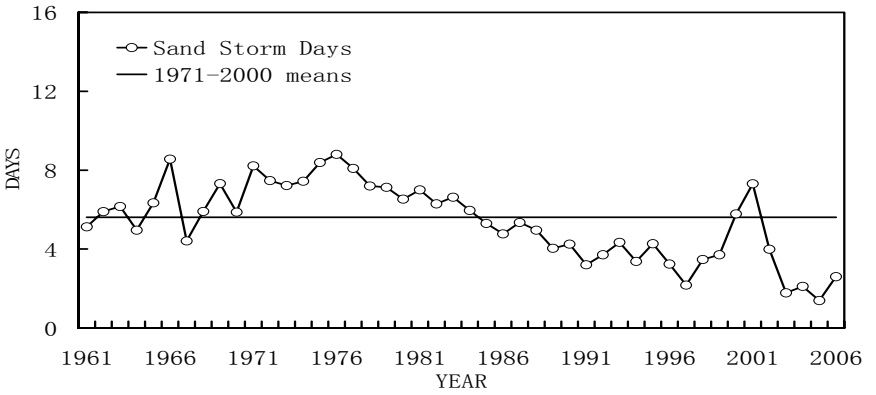

Fig. 8.14 Variation in number of dust storm days in spring (MAM) over northern China during 1961-2006

Decreasing trends in dust storm days were observed in most of northern China. There were more dust storm days in the 1950s and 1970s and fewer in the 1990s (Ding et al., 2003). However, opposite trends occurred in local regions in northern Qinghai and western Xinjiang (Zhou et al., 2002). The frequency of very strong dust storms has decreased since the 1950s, though there were short increases in 2000-2002 (Zhou and Zhang, 2003).

Winds and humidity have great effects on dust storm especially in northwestern China. Strong winds and low humidity lead to more dust storms. There is no doubt that winds have weakened over most of China during the past half century (Yan and Yang, 2000). Surface temperature and snow cover also affect dust weather. There were negative correlations between the frequencies of dust weather in spring and precipitation totals in the previous summer and the correlations were much significant in desert areas (Zhai and Li, 2003). When there is more precipitation in summer, the vegetation grows well and helps consolidate soil, hence reduces dust storms in the next winter/spring seasons. In northern China, vegetations in spring also have negative correlations with dust storms. More (less) vegetation in spring corresponds to fewer (more) dust storms. Zou and Zhai (2004b) suggested that the negative correlation between vegetation and the frequency of dust storms was significant only in the ar-

eas with sufficient vegetation, but not in areas with little vegetation and dry climate such as northwestern China (Figure 8.15). In the late 1990s and early 2000s, especially in 2000 and 2001, dust weather occurred more frequently in northern China, possibly due to the worsening of vegetation conditions in association with the prolonged droughts in these years (Ye et al.，2000; Zou and Zhai, 2004b).

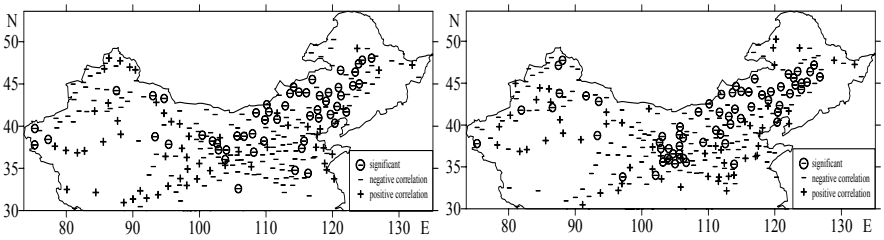

Fig. 8.15 Correlation coefficients between the number of dust storm days in spring (MAM) and the same spring NDVI (left) and previous summer (JJA) NDVI (right) over northern China (minus and plus signs represent negative and positive correlations respectively, minus with circle signs represent significant negative correlations with values less than -0.44, the calculation period is 1982 to 2001)

There were distinctive differences in 500 hPa geopotential heights between the most frequent and the least frequent dust storms years in spring over northern China especially in northwestern China. Positive anomalies were found over the Mt. Ural while negative anomalies were over Siberia and Mongolia when there were more frequent dust storms. During the least frequent dust storm springs, there were negative anomalies over the Mt. Ural and positive anomalies over Europe, Siberia and Mongolia. The previous winter 500 hPa geopotential heights also showed the same characters. This may serve as a precursor for predicting dust storms in the coming spring (Li and Zhai，2003). In the springs of frequent dust storms, the 500 hPa geopotential heights over the inland desert areas were unusually low and the activities of cyclones and cold waves were active. While in the springs of few dust storms, the 500 hPa geopotential heights over desert areas were above normal. When the North Atlantic Oscillation (NAO) is stronger in winter, the frequency of dust storms in the following spring will be smaller than usual (Tang and Zhai，2005b). In years with sparse dust weather, westerlies were weak over northern China and east coast of China, and the East Asian monsoon circulation and cold waves affecting China were also weak (Kang and Wang，2005).

Frequencies of dust weather in spring correlated positively with frequencies of cyclones affecting China and negatively with prior winter

temperatures. Weakening in the activity of cyclones and increasing in prior winter temperatures had direct effect on decreasing in the frequency of dust weather (Qian et al.,2002). In the period with less dust weather, prior winter temperature in China, especially in northwestern and northern China, was above normal and there were more precipitation in the inland desert areas (Kang and Wang，2005).

There were significant correlations between frequencies of dust weather and surface winds in the spring. In recent half century, surface winds and frequencies of dust weather both decreased, prior to a slight increasing in the two time series since 1997. Changes in sea level pressures (SLPs) in spring radically caused the variations in frequencies of dust weather. Decreasing in SLPs over mid-high latitudes and increasing in SLPs over mid-low latitudes led to weakened air pressure gradients and surface winds, and hence weakened dust weather (Wang and Zhai，2004).

8.7 Changes in climate extreme in associated with the mean state

Association between changes in mean and extreme depends on change in variance. Understanding changes in climate variability and climate extremes is made difficult by interactions between the changes in the mean and variability. Nevertheless, Relationship between changes in mean temperature and the corresponding changes in extreme temperature events is the highly non-linear (Meehl, 2000). Small alterations in the mean state can result in a large change in the probabilities of extreme events.

Such association also depends on their statistical distribution of the variables. The distribution of temperatures often resembles a normal distribution where non-stationarity of the distribution implies changes in the mean or variance. If no change in variance, change in the mean will impact on extremes. If variance changes, the relationship between change in mean and extreme becomes complex (As shown in Figure 8.16).

For variables that are not well approximated by normal distributions, such as precipitation, the situation is even more complex. For precipitation, for example, changes in the mean total precipitation can be accompanied by other changes like the frequency of precipitation or the shape of the distribution including its variability. All these changes can affect the various aspects of precipitation extremes including the intensity of precipitation (IPCC 2001).

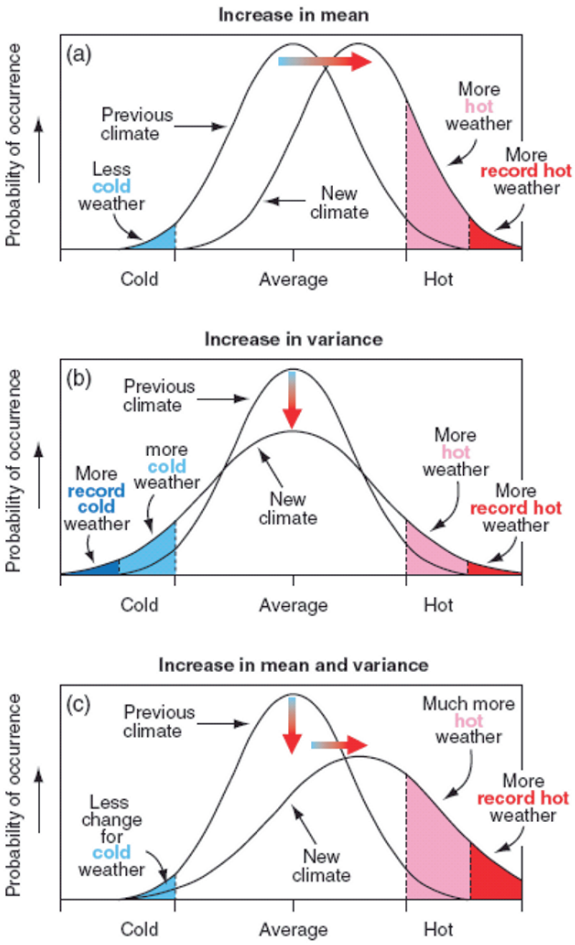

Fig. 8.16 Schematic showing the effect on extreme temperatures when (a) the mean temperature increases, (b) the variance increases, and (c) when both the mean and variance increase for a normal distribution of temperature. (Adapted from IPCC, 2001)

8.7.1 Changes in temperature extremes and mean temperature

Studies on changes in mean temperatures over China are basically consistent with the warming trend in the 20th century of the global one (Wang et al., 2003). During the recent 50 years, especially since late 1980s,

China's temperature obviously increased. The warming trend in the mean surface air temperature is 0.2℃/10a. The warming trend in mean minimum temperature is 0.3℃/10a, which is 2 times higher than that in the mean minimum temperature (the warming trend in the mean maximum temperature is 0.1℃/10a). The trend difference for mean minimum and maximum temperatures in China is larger than that in the USA as given by Karl et al (1991). Zhai and Ren (1997) indicated that China's warming trend in the mean maximum temperature is not obvious based on data in the period 1951-1990. Recent study indicated, however, the mean maximum temperature increased obviously mainly because of the recent warming (Zhai and Pan, 2003a).

Griffith et al (2005) revealed that the changing trends in daily maximum and minimum temperatures, extremes and variance are spatially coherent across the Asia–Pacific region. The majority of stations exhibited significant increases in mean maximum and mean minimum temperature, decreases in cold nights and cool days, and increases in warm nights. Significant decreases were observed in both maximum and minimum temperature standard deviation in China, Korea and some stations in Japan.

8.7.2 Changes in extreme and total precipitation

Overall, there is no apparent trend in total precipitation during the recent 50 years over China, no matter how the averages are computed (Zhai et al, 2005a). This differs from the trend results for many other mid-latitude regions in the Northern Hemisphere. Annual precipitation total in North America increased (Groisman and Easterling, 1994; Zhang et al., 2000) in the 20th Century. However, researches showed there was significant regional difference. Precipitation total has increased in western China, especially in Northwest China. Shi et al. (2002) pointed out there was climate change in Northwest China, from warm-dry climate to warm-wet climate. It was not the case in eastern China, however. In eastern China, precipitation total has decreased in North China, and increased in the Yangtze River (Zhai et al., 1997).

Although without evident trend in precipitation total in China on average, there is a significant decreasing trend in the number of rain days (Zhai et al., 2005a). This suggests that intensity of precipitation may have enhanced, then more flood/drought events occurred (Zhai et al., 1999b).

Recent studies show the frequency and intensity of extreme rainfall in China have increased, especially in 1990s. In North China, annual totals of precipitation decreased, and the intensity and frequency of precipitation also diminished, but the proportion of extreme precipitation to the totals

was still increased relatively. In western part of Northwest China, frequent extreme precipitation events were experienced. In the Yangtze River and other southern regions, the annual totals, totals of extreme precipitation and intensity of extreme rainfall all increased. For warm half year, Zhai et al. (2005a) pointed out that although the extreme precipitation events occurred frequently in both Northwest China and the Yangtze River in recent 50 years, only in the Yangtze River the increasing trend was really significant. This trend was coincident with the increasing trend of floods in the areas since 1980s.

When checking the association of changes in extreme events with the precipitation total in China, Zhai et al (2005a) noticed great similarity exist between the spatial patterns of trends in extreme and total precipitation. The frequency of extreme precipitation is positively correlated with total precipitation at almost all stations across the country.

8.8 Summary

Weather and climate extremes are strongly in associated with natural disasters that cause increasing social and economical losses. In recent years, many studies have suggested that climate change impacts on frequency and characteristics of weather and climate extremes.

For temperature related extremes, cold extremes have decreased while warm extremes have increased in China during the recent 50 years. Stronger warming trends have been detected in the minimum temperature than the maximum one during the past half century, especially in northern China during winter season. This leads to decreasing diurnal temperature range over most China. For the country as whole, the number of the warm nights increased significantly with a rate of 3 day/10a during 1951-1999. And cool nights in China displayed a decreasing trend with the same magnitude. The number of frost days in China during the past half century has been reduced significantly.

Although there is no significant trend in mean annual precipitation for China as whole, there exist distinct regional and seasonal differences. Decreases in annual precipitation were found in southern northeast China, north China, and over the Sichuan Basin, while increases were detected in western China, the Yangtze River valley, and the southeastern coast. The number of rain days has significantly decreased throughout most parts of China with northwest China being an exception. Significant increases in extreme precipitation have been found in western China, the mid-lower reaches of the Yangtze River, and parts of the southwest and south China coastal area.

There is considerable inter-decadal variability in the number of TCs

over the Northwest Pacific, but no evidence to show it has become more frequent for the past 4 decades. Some recent studies suggest that the intensity and destructiveness of typhoons has increased in past 30 years tends to be evident in recent studies. For the influential baroclinic low pressure systems in the mid-latitudes, known as the extra-tropical, significant decreasing trend were detected over most northeastern, central and western parts of China.

An expanding trend of drought areas in northern China (except western Northwest China) in the latter half of the 20th century has been well revealed in many studies. The consecutive large drought areas since the late 1990s in Northeast, North and eastern Northwest China were unprecedented during the past half century.

Decreasing trends in dust storm days were observed in most parts of northern China during the past half century although there exhibited abrupt increases during the period from the late 1990s and early 2000s. The frequency of very strong dust storms has also decreased since the 1950s.

References

Alexander LV, Tett SFB, Jonsson T (2005) Recent observed changes in severe storms over the United Kingdom and Iceland, Geophys. Res. Lett., 32, L13704, doi:10.1029/2005GL022371.

Alexander LV et al (2006) Global observed changes in daily climate extremes of temperature and precipitation, J. of Geophys. Res., 111, D05109, doi:10.1029/2005JD006290.

Bai Aijuan, Panmao Zhai and et al (2006) On Climatology and Trends in Wet Spell of China, Theor. Appl. Climatol., DOI 10.1007/s00704-006-0235-7

Bärring L, H. von Storch (2004) Scandinavian storminess since about 1800. Geophys. Res. Lett., 31, doi:10.1029/2004GL020441.

China Meteorological Administraion (2006) A new classification for tropical cyclones (in Chinese).

Chan JCL, Liu KS (2004) Global warming and western North Pacific typhoon activity from an observational perspective, J. Clim., 17, 4590-4602.

Chan, JCL (2000) Tropical cyclone activity over the Western Northwest Pacific Associated with El Nino and La Nina Events, J. Clim., 13, 2960-2972.

Chen M, Zheng YG, Tao ZY (1999) An analysis on tropical cyclones' climatic feature in the western north pacific for 1949-1996, Journal of tropical meteorology, 15(1), 10-16 (in Chinese).

Chen Y (1997) Cold wave, frost and snowstorm, In: Xu L (ed) Climate Impact Assessment (1996), China Meteorol. Press. Beijing, pp.122 (in Chinese).

Dai AG, Trenberth KE, Qian TT (2004) A Global data set of Palmer Drought Se-

verity Index for 1870-2002: Relationship with soil moisture and effects of surface warming. J. Hydrometeorology, 5, 1117-1130.

Ding Ruiqiang, Wang Shigong, Shang Kezheng et al (2003) Analyses of sandstorm and sand-blowing weather trend and jump in China in recent 45 years. Journal of Desert Research, 23(3):306-310 (in Chinese).

Emanuel, K (2005) Increasing destructiveness of tropical cyclones over the past 30 years, Nature, 436, 686–688, doi: 10.1038/nature 03906.

Geng Q, and Sugi M (2001) Variability of the North Atlantic cyclone activity in winter analyzed from NCEP-NCAR reanalysis data., J. Clim., 14, 3863-3873.

Gong DY, He XZ (2002a) Interdecadal change in Western Pacific subtropical high and climatic effects. Acta Geographica Sinica, 57(2), 185-193 (in Chinese).

Gong DY, Zhu JH, Wang SW (2002b) Significant Relationship between Spring AO and the Summer Rainfall along the Yangtze River. Chinese Science Bulletin, 47(11), 948-951 (in Chinese).

Gong DY, Wang SW (1999) Impact on Global and China's Surface Precipitation of ENSO during Recent 100 Years, Chinese Science Bulletin, 44(3):315-320 (in Chinese).

Gregory JM, Mitchell JFB, Brady AJ (1997), Summer drought in northern midlatitudes in a time-dependent CO2 climate experiment, J. Clim., 10, 662-686.

Griffiths GM, Chambers LE, Haylock MR, Manyon MJ, Nicholls N, Baek HJ, Choi Y, Della-Marta PM, Gosai A, Iga N, Lata R, Laurent V, Maitrepierre L, Nakamigawa H, Ouprasitwong N, Solofa D, Tahani L, Thuy DT, Tibig L, Trewin B, Vediapan K, Zhai P (2005), Change in mean temperature as a predictor of extreme temperature change in the Asia–Pacific Region, Int. J. Climatol. 25: 1301–1330, DOI: 10.1002/joc.1194

Groisman, P.Ya, Easterling D (1994). Variability and trends of total precipitation and snowfall over the United States and Canada. J. Climate, 7:184-205.

Guo QY, Cai JN, Shao XM, Sha WY (2003). Interdecadal Variability of East-Asian Summer Monsoon and Its Impact on the Climate of China. Acta Geographica Sinica, 58(4), 569-576.

He M, Song WL, Chen XF (1999) Relationship between typhoon activity in western North Pacific and ENSO events, Journal of tropical meteorology, 15(1), 17-25 (in Chinese).

Heddinghaus TR, Sabol P (1991) A review of the Palmer Drought Severity Index and where do we go from here? IN Proceedings of the 7th Conference on Applied Climatology, Amer. Meteor. Soc., 242-246.

Huang G, Yan Z (1999) The East Asian Summer Monsoon Circulation Anomaly Index and its interannual variations. Chinese Science Bulletin 44 (14) 1325-1329

IPCC (2001) Climate change (2001), The Science of Climate Change. Contribution of Working Group I to the Third Assessment Report of the Intergovernmental Panel on Climate Change (Houghton, J. T. , Y. Ding, D. J. Griggs, M. Noguer, P. J. van der Linden, X.D, K. Maskell, and . A. Johnson (eds.)). Cambridge University Press, Cambridge, United Kingdom and New York, NY, USA., 156-159.

Karl TR, Easterling DR (1999) Climate Extremes: Selected Review and Future Research Direstions, Climatic Change, 42(10), 309-325.

Karl TR, G Kukla, VN Razuvayev, et al., (1991) Global Warming: Evidence for asymmetric diurnal temperature change, Geophys. Res. Lett., 18, 2253-2256.

Kang Dujuan, Wang Huijun (2005) Analysis on the decadal scale variation of the dust storm in North China. Science in China Series D: Earth Sciences,,48(12):2260-2266

Li CY (1985) El Niño and typhoon in western Pacific, Chinese Science Bulletin, 14, 1087-1989 (in Chinese).

Li Wei, Zhai Panmao (2003) Variability in occurrence of China's spring dust storm and its relationship with atmospheric general circulation. ACTA Meteorological Sinic,17(4):396-405

Lu JM, Ren JZ, Ju JH (2004) The interdecadal variability of East Asia monsoon and its effect on the rainfall over China. Journal of tropical meteorology, 20(1), 73-82 (in Chinese).

Ma ZG (2003a) Trend of annual extreme temperature and its relationship to regional warming in northern China, Acta Geographica Sinica, 58(supplement), 11-20.

Ma ZG, Fu CB (2003b) Interannual characteristics of the surface hydrological variables over the arid and semi-arid areas of northern China, Global and Planetary Change, 37, 189-200, doi:10.1016/S0921-8181(02)00203-5.

Ma ZG, Hua LJ, Ren XB (2003c) The extreme dry/wet events in northern China during recent 100 years, Acta Geographica Sinica, 58(supplement), 75-82 (in Chinese).

Manton MJ, Della-Marta PM, Haylock MR et al. (2001) Trend in extreme daily rainfall and temperature in southeast Asia and the South Pacific: 1961-1998, Int. J. Climatol., 21, 269-284.

Meehl, GA (2000) An introduction to trends in extremes weather and climate events: observations, socioeconomic impact, terrestrial ecological impacts, and model projections, Bull. Am. Meteorol. Soc., 81, 413-416.

McCabe GJ, Clark MP, Serreze MC (2001) Trends in Northern Hemisphere surface cyclone frequency and intensity, J. Clim., 14, 2763-2768.

NCC (National Climate Center) (1998) China's 1998 Severe Flood and Climate Extremes, China's Meteorological Press, 137pp (in Chinese).

Qian Weihong, Quan Lingshen, Shi Shaoyin (2002) Variations of the dust storm in China and its climatic control. J. Climate.,15,1216~1229

Ren, FM et al (2006) Changes in tropical cyclone precipitation over China, Geophys. Res. Let. (Submitted).

Ren FM, Gleason B, Easterling D (2002), Typhoon Impacts on China's Precipitation During 1957~1996, Advances in Atmospheric Sciences, 19(5), 943-952.

Shi YF, Shen YP, Hu RJ (2002) Preliminary Study on Signal, Impact and Foreground of Climatic Shift from Warm-Dry to Warm-Humid in Northwest China. Journal of Glaciology and Geocryology, 24(3), 219-226 (in Chinese).

Shi N, Zhu QG, Wu BG (1996) The East Asian Summer Monsoon in Relation to Summer Large Scale Weather-Climate Anomaly in China for Last 40 Years. Scientic Atmospherica Sinica, 20(5), 575～583 (in Chinese).

Song Lianchun, Han Yongxiang, Zhang Qiang et al (2004) Monthly temporal-spatial distribution of sandstorms in China as well as the origin of Kosa in

Japan and Korea. Chinese Journal of Atmospheric Sciences, 28(6):820-827 (in Chinese).

Su Buda, Xiao B, Zhu D, Jiang T (2005) Trends in frequency of precipitation extremes in the Yantze River basin, China: 1960-2003, Hydrological Sciences-Journal-des Sciences Hydrologiques, 50(3), 479-492.

Tang HY, Zhai PM, Wang ZY (2005a) On changes in mean maximum temperature, minimum temperature and diurnal range in China during 1951-2002, Climatic and Environmental Research, 10(4), 728-735 (in Chinese).

Tang Hongyu, Zhai Panmao (2005b) SVD analysis between northern hemisphere 500hPa heights and spring duststorms over northern China. Journal of Desert Research, 25(4):570-576(in Chinese).

Wang SW, Gong DY, Zhai PM (2002) Climate change, (eds. Wang Shaowu, DongGuanrong) Environmental characteristics and change in West China (ed. Qin Dahe), Assessment on Environment Change in West China (in Chinese), Beijing: Science Press, 1, 29-72 (in Chinese).

Wang SW, Gong DY (2000) Enhancement of the warming trend in China, Geophys. Res. Lett., 27(16), 2581-2584.

Wang SW, Gong DY (1999) ENSO Events and Intensity in the recent 100 years, Meteorological Monthly, 25(1), 9-13 (in Chinese).

Wang Shigong, Wang Jinyan, Zhou Zijiang etal (2003) Regional characteristics of dust events in China. ACTA Geographica Sinica, 58(2):193-200 (in Chinese).

Wang Xiaoling, Zhai Panmao (2004) The spatial and temporal variations of string dust storms in China and its associations with surface winds and sea level pressure. ACTA Meteorologica Sinica, 62(1):96-103 (in Chinese).

Wang XM, Zhai PM (2006) Variation of extratropical cyclone activity in Northern East Asia, Advances in Atmospheric Sciences (submitted).

Wang YW, Zhai PM, Tian H (2006) Extreme high temperatures over South China in 2003 under the background of climate change, Quarterly Journal of Applied Meteorology, 32(10), 27-33 (in Chinese).

Wang YM (2004) Rainstorms and floods, in Climate Impact Assessment (2003) (in Chinese, edited by L. Wang, pp.138, China Meteorol, Press. Beijing.

Wang ZW, Zhai PM (2003) Climate change in drought over northern China during 1950-2000, Acta Geographica Sinica, 58(supplement), 61-68 (in Chinese).

Woodhouse CA, Overpeck JT (1998) 2000 years of drought variability in the central United States, Bull. Amer. Meteor. Soc., 79, 2693-2714.

Wu L, Wang B, Geng S (2005) Growing typhoon influence on east Asia, Geophys. Res. Let., 32, L18703, doi:10.1029/2005GL022937.

Xie A, Sun YG, Bai RH (2003) Arid climate trend over northeastern China and its reponse to global warming, Acta Geographica Sinica, 58(supplement), 75-82 (in Chinese).

Xu L (2005) Typhoon and its impacts, in Climate Impact Assessment (2004), (in Chinese), edited by Q. Zhang, pp.125, China Meteorol. Press. Beijing.

Yan Z, Yang C (2000) Geographic patterns of extreme climate changes in China during 1951-1997. Climatic and Environmental Research, Vol. 5, No. 3, 267-272.

Yan Z, Jones PD, Moberg A, Bergstrom H, Davies TD, Yang C (2001) Recent trends in weather and seasonal cycles, an analysis of daily data from Europe and China. J Geophys Res 106 (D6) p5123-5138.

Yan Z, Zhang M (1993) On the trends of temperature and daily range in China. Chinese Science Bulletin 38: 54-58.

Yan Z, Ji J, Ye D (1990) Northern hemispheric summer climatic jump in the 1960s, part I - rainfall and temperature. Science in China Series B 33: 1092-1101.

Yang G.S, Shi YF (1999) Changes in the frequencies of tropical cyclones and their relationships to sea surface temperature in the Northwestern Pacific, Acta Geographica Sinica, 54(1), 22-29 (in Chinese).

Ye Duzheng, Chou Jifan, Liu Jiyuan et al (2000) Causes of sand-storm weather in northern China and contral measures. ACTA Geographica Sinica, 55(5):513-521.

Ye DZ, Huang RH (1996) Inversigation on Laws and Causes of Droughts and Floods in the Yellow and Yangtze River Valleys of China, Jinan: Shandong Science and Technology Press, 387pp (in Chinese).

Zhai PM, Zhang XB, Pan XH (2005a) Trends in Total Precipitation and Frequency of Daily Precipitation Extremes over China, J. Clim., 18(7), 1096-1108.

Zhai PM, Zou XK (2005b) Changes in temperature and precipitation and their impacts on drought in China since 1951, Advances research in climate change, 1(1), 16-18 (in Chinese).

Zhai PM, Pan XH (2003a) Trends in temperature extremes during 1951-1999 in China, Geophys Res.Lett., 30, doi:10.1029/2003Gl018004.

Zhai Panmao, Li Xiaoyan (2003) On climate background of duststorms over northern China. ACTA Geographica Sinica, ,58(z):125-131(in Chinese).

Zhai PM, Ren FM (1999a) On change of China's maximum and minimum temperatures in 1951–1990. Acta Meteor. Sin., 13 (2), 278–290.

Zhai PM, Sun A, Ren F, Liu X, Gao B, Zhang Q (1999a) Changes of Climate Extremes in China, Climatic Change, 42, 203-218.

Zhai PM, Ren F, Zhang Q (1999b) Detection of Trends in China's Precipitation Extremes, Acta Meteorologica Sinica, 57(2), 208-216 (in Chinese).

Zhai Panmao, Ren Fumin (1997) Change in China's maximum and minimum temperatures in the past 40 years. Acta Meteorologica Sinica,55(4):418-429.

Zhang X, Hegerl G, Zwiers FW, Kenyon J (2005) Avoiding inhomogeneity in percentile-based indices of temperature extremes. J. Clim., 18(11), 1641-1651.

Zhang, X., LA Vincent, WD Mogg. and A. Niitsoo (2000) Temperature and precipitation trends in Canada during the 20th century. Atmos – Ocean, 38, 395-429.

Zhang G.Z, Zhang XG, Wei FY (1995) Characteristics of tropical cyclones frequency in western North Pacific during recent 100 years, Journal of tropical meteorology, 11(4), 315-323 (in Chinese).

Zhang QY, Wei J, Shi SY (2003) The decadal and interannual variations of drought in the northern China and association with the circulations, Climatic and Environmental Reasearch, 8(3), 309-318. (in Chinese)

Zhang Q, Wu GX (2001) The large area flood and drought over Yangtze River valley and its relation to the South Asia High, Acta Meteorologica Sinica, 59(5), 569-577 (in Chinese).

Zhao ZC (1996) Influence of El Nino Phenomenon on General Circulation and China's Precipitation. Atmospheric Science, 4, 422-428.

Zhou Zijiang, Wang Xiwen, Niu Ruoyun (2002) Climate characteristics of sand-storm in China in recent 47 years. Journal of Applied Meteorological Science, 13(2):193-200 (in Chinese).

Zhou Zijiang,Zhang Guocai (2003) Typical severe dust storms in northern China during 1954-2002. China Science Bulletin, 48(21):2366-2370.

Zou X, Alexander L, Parker D, Caesar J (2006) Variations in severe storms over China, Geophys.Res.Lett. 33(17), L17701, doi:10.1029/2006GL026131.

Zou XK, Zhai PM, Zhang Q (2005) Variations in droughts over China: 1951-2003, Geophys.Res.Lett., 32(4), L04707, doi:10.1029/2004GL021853.

Zou X (2004a) Cold wave, frost and snowstorm, In: Wang L (ed) Climate Impact Assessment (2003), China Meteorol. Press. Beijing, pp.138 (in Chinese)

Zou XK, Zhai PM (2004b) Relationship between vegetation coverage and spring dust storms over northern China, J. Geophys. Res., 109, D03104, doi:10.1029/2003JD003913

Chapter 9 Regional Climate Modeling of China and East Asia

9.1 Introduction

Having steadily improved their general performance in simulation of global climate, Coupled Global Climate Models (CGCMs) are now the primary tools to study the climatic processes, natural variability and response to external forcings. However, due to their significant complexity and the climate change community's requirement for long-term integration, the atmospheric components of the most CGCMs usually have their horizontal resolutions limited from 400 km to 125 km, so they are unable to provide reliable climatic information at regional scale, which depends on the treatment of processes at the unresolved scales for CGCMs. In view of the demand to provide integrated assessments of climate change impacts on regional scale, the new challenges are to estimate accurate timing (occurrence) and intensity of regional climate change, analyze its environmental and socio-economic consequences, and provide integrated assessments to society and the environment. Therefore, so called downscaling methods have been developed to generate detailed regional information.

There are two widely used downscaling approaches: the dynamical and empirical downscaling. Dynamical downscaling refers to the methods that derive regional climate information by using high resolution numerical climate models, such as high-resolution Atmosphere-only Global Climate Model (AGCMs) and nested regional climate model (RCM) which use outputs from CGCM or observations as boundary and initial condition.

Currently many research facilities have AGCMs with resolution of 100km and finer; a resolution of 50 km will likely be the normal for AGCMs in the near future (Bengtsson, 1996; May and Roeckner, 2001; Déqué and Gibelin, 2002; Govindaswamy, 2003) (IPCC 2004). Besides uniform high-resolution AGCM, variable-resolution (including stretched-grid) AGCMs are viewed as attractive downscaling approach due to their abilities to increase resolution over interested regions while maintaining a full interaction in other regions of the globe (VRGCM; e.g., Déqué and Piedelievre, 1995; Krinner et al., 1997; Fox-Rabinovitz et al., 2001;

McGregor et al., 2002; Gibelin and Déqué, 2003). The results show that VRGCMs are able to capture finer scale details over the focus regions, and at the same time retain the their global skill (IPCC 2004).

Another dynamic downscaling is to generate realistic regional climate information through regional climate models (RCMs), which are driven by either GCM or observation, which exert correct large circulation through providing boundary and initial conditions. RCMs were first successfully applied in regional climate simulation in late 1980 (Dickinson et al., 1989; Giorgi and Bates, 1989), and coupled with the driving forcings in one-way mode, i.e., there's no feedback from the RCM simulation to the driving GCMs. Not until recently two-way technique has been developed to nest RCM with GCMs (Lorenz and Jacob, 2005), which will allow feedback from the RCM onto the GCM. In addition, more climate components, such as regional ocean and sea ice, hydrology, aerosol, atmospheric chemistry and dynamical land surface process, have been included in RCMs (Gao and Yu, 1998; Xue et al., 2000; Maslanik et al., 2000; D.scher et al., 2002; Rinke et al., 2003; Debernard et al., 2003; Schrum et al., 2003; Meier et al., 2004; Rummukainen et al., 2004). Due to its ability to capture the mesoscale nonlinear effects under perturbed forcing conditions and provide coherent information between multiple climate variables, dynamical downscaling is widely used to reproduce varying climates around the world.

Empirical downscaling refers to the method which predicts future climate change by first establishing a statistic relationship between large scale atmospheric state and regional variables which are derived from historical data, then applying the relationship to model simulation results for future regional climate projection. The methods are computationally inexpensive though they have the drawback that they require long time series of reliable, homogeneous station data and assume that the derived statistical relationships will remain unaltered under perturbed climate.

RCMs have been applied widely in research of current and future climate over United States (Giorgi et al., 1994, 1998; Gutowski et al., 2004), Central America (Giorgi and Mearns, 1996; Anderson et et al., 2003;), West America (Dickinson, 1989; Giorgi, 1990b, 1991; Giorgi et al., 1993c; Anderson et al., 2002), Europe (Giorgi et al., 1990; Giorgi and Marinucci, 1991; Marinucci, 1992; Christensen et et al, 1997; Machenhauer et al, 1996, 1998; Noguer et al., 1998; Pal et al., 2004; Raisanen, 2004), Australia (Walsh and McGregor, 1995), Africa (Sun et al., 1999), Central Asia (Small et al., 1999), North Pole (Rinke et al., 1999; Wei et al., 2002) and East Asia-West Pacific area (Giorgi et al., 1999) etc. RCMs have shown promising performance in reproducing the regional details in surface climate forced by topography, lakes, the costal line, land use distribution and

vegetation coverage, etc.(Christensen et al., 1998; Machenhauer et al., 1998).

The East Asian summer monsoon is characterized by marked variability at seasonal, interannual and interdecadal time scales (Fu and Zheng 1998a). The timing of monsoon onset and the irregular pace of its seasonal, northward progression can influence water availability for agriculture and urban consumption remarkably (Fu et al., 2003; Tao and Chen 1987; Wu and Zhang 1998). Inter-annual variability, such as those linked with the ENSO cycle, affects the frequency of droughts, floods and other weather extremes that occur during the summer monsoon period (Fu and Teng 1993; Ju and Slingo 1995; Fasullo and Webster 2002). On decadal to century time scales, the rapidly growing economy and population of East Asia present anthropogenic influences that may also alter monsoon behavior (Fu and Zheng 1998a; Quan et al. 2003). However coarse resolution climate models generally fail to give satisfactory simulations of the East Asian monsoon (Lau and Yang 1996; Yu et al. 2000).

A series of researchers have used RCMs for simulating the regional climate of East Asia (e.g. Lee, 1992, 2000; Liu et al., 1994, 1996; Hirakuchi et al., 1995; Ji et al., 1997; Qian et al., 1999; Leung et al., 1999; Giorgi et al., 1999; Kato et al., 1999, 2001; Hong, 1999; Gao et al., 2001, 2003; Zhao Zongci et al., 1997, 1999; Fu Congbin et al., 1998; Qiang Yongfu, 1999; Liu Liping, 1999, 2000; Wang Shuyu, 1999; Chen Ming, 2000; Shi Xueli, 2001; Li Qiaoping et al., 2004; Zhang Yinjuan et al, 2005). Many of these studies have shown that RCMs can simulate the spatial detail of monsoon climate better than GCMs (e.g.Liu et al. 1994, 1996; Fu et al. 1998b; Lee and Suh 2000).

Efforts have been made to investigate the role the resolution and topography in East Asian precipitation simulation (Gao et al., 200). The results show that model resolution can significantly influence the simulated East Asian large scale precipitation patterns, and the effect of resolution is more important during the mid to late monsoon months when the precipitation is dominated by smaller scale convection. Other simulations have been carried out to study the impacts of man-made modification of surface character and land cover/land use on regional precipitation. Wu et al. (2006) examined such as the construction of Three Gorges Dam (TGD) on regional climate using the high-resolution Pennsylvania State University-National Center for Atmospheric Research (PSU-NCAR) fifth generation Mesoscale Model (MM5). The numerical simulation indicates that the land use change associated with the TGD construction has increased the precipitation in the region between Daba and Qinling mountains, and reduced the precipitation in the vicinity of the TGD after the TGD water level abruptly rising from 66 to 135 m in June 2003. The results are agreed with inde-

pendent analysis of satellite data sets, i.e., rainfall rate from TRMM (Tropical Rainfall Measuring Mission) and land surface temperature from MODIS (Moderate Resolution Imaging Spectroradiometer).

However, multi-year simulations must be used to identify models' uncertainties in simulating climatology and climatic variations, and systematically evaluate the RCMs' application for Asia. A Regional Climate Model Inter-comparison Project (RMIP) for Asia therefore has been established to study the performance of an ensemble of regional climate models (RCMs) when simulating East Asian climate. Up to ten research groups from the Asia-Pacific area have been participating in the project. One of the objectives of RMIP is to further improve RCM simulations of East Asian climate by evaluating their strengths and weaknesses in a common framework (Fu et al. 2003).

Considering the relatively high degree of uncertainty in regional climate change information of East Asia derived from GCMs, which results from the scenarios construction such as future emission variations and GCMs'modeling of the climate responses to a given scenario, RMIP also try to compare the regional climate scenarios of a set of RCMs and provide multi-RCM ensemble of regional climate change of Asia.

This chapter presents the latest progresses of regional climate modeling of China and East Asia, including mainly (1) the development of a regional integrated environment model system (RIEMS); (2) Simulation of climate of China and East Asia through inter-comparison of a set of regional climate models; and (3) RCM's response to increasing atmospheric greenhouse gases and aerosols and to changing land use/land cover in Asia.

9.2 Development of a regional climate model for Asia (RIEMS) and its validation

9.2.1 Framework of RIEMS

The Asian monsoon system may best be considered as a physical-biological-chemical-social coupled system, which could be named the General Monsoon System, in order to describe the integrated behavior of environmental and human changes in the Asia (Fu, 1997, 2001). Based on above concept, RIEMS (Regional Integrated Environmental Model System) aiming to provide a numerical tool for the integrated study of the Asian monsoon system was developed as a schematic diagram of Fig. 9.1 (Fu et al, 2001).

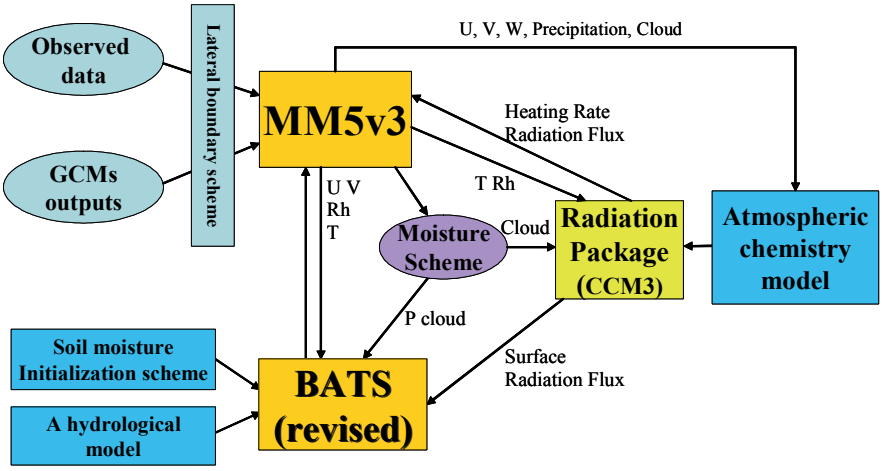

Fig. 9.1 The schematic diagram of RIEMS

Dynamic structure

The atmospheric part of RIEMS is a meso-scale atmospheric model to represent the atmospheric dynamics of the Asian monsoon system. RIEMS applies the MM5V2 in the first version and the MM5V3 in the second version. More detailed description can be found in MM5 users' guide (www.imp-systems.com/downloads/user_guides/MM5u.pdf).

Land surface process

Biosphere and Atmosphere Transfer Scheme (BATS) developed by Dickinson et. al (1993) is used as land surface scheme of RIEMS. The Biosphere Atmosphere Transfer Scheme is designed to provide a realistic representation of hydrometeorology at the atmosphere-land interface for coupling with general circulation models used to describe the role of vegetation in modifying the surface moisture and energy budgets. The earth surface receives and emits various kind of energy. The most important of these from the point view of physical processes include the solar radiation absorbed after undergoing atmospheric absorption and reflection, the infrared radiation emitted from surface, the sensible heat fluxes and the latent heat fluxes.

The presence of vegetation has a strong control over both diurnal and mean fluxes of energy and water. The physical characteristics of vegetation most important are its absorption of solar radiation and consequent shading

of the ground, exchange of latent and sensible heat fluxes with atmosphere and the presence of canopy surface moisture.

Parameterization of radiation

The scheme of radiation parameterization is based on CCM3 radiation package. Comparing with CCM2 scheme, there are following improvement in CCM3: changes to the clear-sky radiation formalism include the incorporation of minor CO_2 bands trace gases (CH4, N_2O, CFC11, CFC12) in the long-wave parameterization, and the incorporation of aerosol in the short-wave parameterization. All-sky changes include improvements to the way in which cloud optical properties are diagnosed, the incorporation of the radiative properties of ice clouds, and a number of minor modifications to the diagnosis of convective and large scale cloud amount.

A hydrological model embedded in BATs

A hydrological model VXM including the heterogeneities of precipitation and infiltration facility is embedded in land surface scheme BATs in RIEMS Version 2.

While some models ignoring the heterogeneity and use uniform soil when calculating infiltration capacity, the Xinanjiang Model (Zhao, 1984), on the other hand, considers the heterogeneity in infiltration capacity mainly due to soil texture, and is also applied to many investigations. VIC model (the Variable Infiltration Capacity Model) was originally developed in the Geophysical Fluid Dynamics Laboratory (GFDL), and coupled with low-spatial resolution GCMs without considering the influences of biosphere.

Combing the parameterizations of VIC Model and Xinganjiang Model, the hydrological model VXM is a one soil-layer model taking surface water budget heterogeneity into consideration. Hence both homogeneous and heterogeneous precipitation as well as runoff, which consisting of surface and ground runoffs, are treated in the model.

RIEMS use BATs as the land surface scheme, which has no description of the hydrological heterogeneity. In addition the treatment of surface hydrological process in BATs is more empirical than physically based, for example, the surface runoff rate in BATs R_s is assumed to be a simple function of the relative saturation of soil water in the surface layer and root zone, and the infiltration rate is calculated the as the difference between soil water and surface runoff. To make the hydrological processes more physically realistic and to improve the description of the hydrological processes at the regional scales, VXM is slightly modified and incorpo-

rated into RIEMS to calculate the surface runoff in BATs. Therefore the incorporated modified VXM along with the original soil moisture scheme and vegetative transpiration scheme in BATs form an integrated two-way coupled hydrological model. As a result RIEMS includes two types of runoff-generation mechanisms, i.e., saturation excess and infiltration excess runoff generations, which can be mainly applied to both wet and arid areas.

In the coupled VXM-BATs-RIEMS system, the water storage W_c varies in the range of 120-160mm with higher values in the arid northern China and lower values in the wet southern China. Besides, the intitial value W_0 corresponds to the initialization scheme in BATs.

Chemical transport model

The concentrations of atmospheric chemical species are controlled by the processes of transportation, source emission, deposition and chemical reaction. For chemical reaction, CBM4 mechanism (Carbon Bond Mechanism IV) (Gery et al. 1989) is adopted in the chemical transport model, which involves 83 reactions among 36 species. Eleven photolysis reactions are included in the gas phase reaction mechanism.

In the chemistry transport model, the dry deposition velocity of gas species are calculated as equal to the reciprocal value of the sum of three characteristic resistances. The time change rate of concentration due to cloud effect includes subgrid scale vertical redistribution, aqueous chemical interactions, and scavenging. The cloud dynamical and microphysical properties are obtained by a one-dimensional diagnostic cloud model. Chemical interactions in the cloud are modeled using a box aqueous chemistry and scavenging submodel. For the sake of complexity of model system and the great cost of calculation, the aqueous chemistry model tries to use less species to simulate the aqueous chemical reactions.

The numerical solution technique used in aqueous chemical model is Quasi-Steady-State-Approximations (QSSA). After the cloud dissipates, the species return to atmosphere. The parameterizations of wet deposition are based on the schemes of Giorgi and Chameides (1986) and Giorgi (1989).

Heterogeneous reaction is the chemical reaction occurring on the surface of aerosol. Though the quality of the interface is far smaller than total value, the effect may be great. For example, the coarse surface of marble can be corroded ore easily by SO2 than smooth surface. SO2 is adsorbed on the surface of aerosol and reacts with OH radical, and the final product is sulfate aerosol, here the rate coefficients of reactions are relative to the component of aerosol. The heterogeneous reaction acting on the surface of aerosol can influence not only the oxidation of SO_2 but also the concentra-

tions of NOx and troposphere ozone. The aforementioned influence can affect troposphere sulfate concentration and finally modify the climate.

Aerosols have a direct radiative forcing because they scatter and absorb solar and infrared radiation in the atmosphere. Aerosols also alter warm, ice and mixed-phase cloud formation processes by increasing droplet number concentrations and ice particle concentrations. They decrease the precipitation efficiency of warm clouds and thereby cause an indirect radiative forcing associated with these changes in cloud properties. Aerosols have most likely made a significant negative contribution to the overall radiative forcing. An important characteristic of aerosols is that they have short atmospheric lifetimes and therefore cannot be considered simply as a long-term offset to the warming influence of greenhouse gases.

Playing an important role in anthropogenic climate change, different kind of aerosol has its characteristic effect to radiation transfer process. In East Asia area, anthropogenic aerosol includes sulfate, black carbon, organic aerosol and so on, and the main natural aerosols include sea salt and mineral dust aerosol. In recent years, as while as the development of society, more and more land has been over-farmed. The dust weather especial heave dust storm has an increasing trend. The radiative and climate effects of mineral dust aerosol are becoming more important than before. On the other hand, due to the rapid development of industrial in Asian countries, more carbon fuel has been combusted and more carbon aerosol is releasing in to the atmosphere. As an important anthropogenic aerosol, black carbon (BC) can absorb solar radiation, which can affect the solar radiative transfer. Based on the relative research (Menon, 2002), BC can take an important role in climate change of East Asia.

In model system, three coupling schemes of RIEMS and chemical model are considered. In every coupling scheme, the chemical model and RIEMS are integral at the same time. The meteorological data which the chemical model needed are generated by RIEMS at every time step, and at one time, the concentration of aerosol computed by the chemical model are transported to RIEMS. In direct coupling scheme, sulfate aerosol, dust and BC aerosol are transported to the CCM3 radiative scheme of RIEMS; In indirect scheme, the concentrations of aerosol are transported to cloud model of RIEMS; In ozone coupling scheme, the ozone concentrations are transported to CCM3 and replace the old constant value with computed value.

A new soil moisture initialization scheme

Soil moisture is one of the most important factors that affect the energy and water exchanges between surface and atmosphere. Accurate initializa-

tion of soil moisture in a climate system models is critical for seasonal-to-interannual climatological and hydrological prediction. The empirical initial soil moisture scheme used in RIEMS Version a, which uses the land cover types and soil type as major inputs, can reproduce the climatology of soil moisture reasonably. However, because of the large variability of soil moisture in both spatial and temporal scales, the method used in RIEMS Version 1 can hardly describe the highly heterogeneity of soil moisture, especially when extreme soil-moisture conditions such as drought and flooding occur.

In RIEMS Version 2, a new scheme MRSM (Model for Retrieving Soil Moisture) is applied to generate initial soil moisture.

MRSM is based on the theoretical and statistical analyses of surface climate, observed soil moisture and the relationship between the. Having precipitation and temperature as inputs, the humid index aiming to represent soil water budget is defined in the scheme, and soil moisture at different depths are thereafter retrieved.

9.2.2 Validation of RIEMS

In order to validate RIEMS, a series of numerical experiments were designed to simulate the climate of China and East Asia.

Xiong Zhe and Wang Shuyu et al. (2003) analyzed the simulated heavy rain over the Yangtze River valley during 11-30 June 1998 using an 18-month (April 1997-September 1998) integration result. Fig.9.2 shows the observed total precipitation, the Westerly jet at 200 hPa, and Low-level jet at 850 hPa during the period of 11-30 June 1998. For the Low-level jet, the observed largest wind speed center is located on the West Pacific Ocean to the southeast of the Japan Islands, with the maximum wind speed of 20 m s^{-1}, and the simulated largest wind speed center is in Southeast China with the maximum wind speed exceeding 30 m s^{-1}. For the Westerly jet, the observed center is located in the east of Xinjiang, however, the simulated Westerly jet center is shifted southeastwards.

The model can reproduce the location of the observed heavy rainfall center to the left of the Low-level jet axis, but on the right side of the Westerly jet axis, however, the simulated heavy rainfall belt with total precipitation over 300 mm is far too westwards nearing the Tibetan Plateau and the northwest part of the upper reaches of the Yangtze River when comparing to the observed position of the heavy rain belt, which is located in the middle and lower reaches of the Yangtze River valley and South China.

The occurrence of this heavy rainfall is accompanied by the Westerly jet

and Low-level jet. Therefore partly because of the southwest shift of the simulated Low-level jet and southeast shift of the simulated Westerly jet, RIEMS' main rain belt drifts to the northwest of the Yangtze River valley.

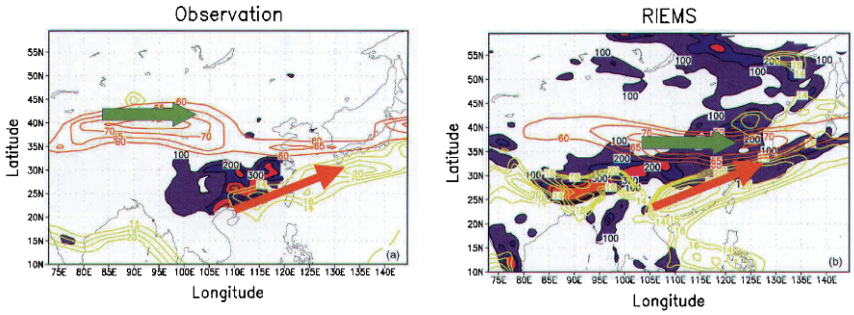

Fig. 9.2 The distribution of total precipitation over 100 mm and the location of the Westerly at 200 hPa and Low-level jet at 850 hPa during the period of 11-30 June 1998. (a) Observation; (b) RIEMS.

The analyses indicate that RIEMS can basically reproduce the major features of seasonal variation of temperature and precipitation over China and East Asia. It has also captured extreme hot summer in 1997 over East China and Asia reasonable well (results not shown here). Comparing to the observed heavy precipitation over the Yangtze River valley in June 1998 and accompanied circulation, RIEMS's simulation has shown following main features: (1) It can reproduce the pattern of heavy precipitation over the Yangtze River valley during 11-30 June 1998, but the simulated heavy rain area is further northwestwards. (2) The simulated West Pacific Subtropical High (WPSH) that controls the East Asia monsoon evolution is stronger than the observation and its location extended westwards, which may be response to the northwestward shift of the heavy rain belt. (3) The westerly jet at 200 hPa and the low-level jet at 850 hPa, both of which are related to the heavy monsoon rainfall, are reasonably reproduced by RIEMS, although their intensities in simulation are stronger than the observation and the location of the westerly jet leans to the southeast, which may produce too much heavy rainfall in the north of the Yangtze River valley in the simulation.

Continuous 10-year simulation in East Asia for the period from 1 January 1987 to 31 December 1996 was conducted by RIEMS using NCEP reanalysis data as driving fields (Xiong Zhe, 2004). The simulated surface air temperature and precipitation are compared with on-site observations from 160 meteorology stations distributed over East Asia as well as NCEP

reanalysis dataset (2.5°×2.5°). RIEMS reproduces reasonably well the spatial pattern and seasonal cycle of surface air temperature and precipitation, and regionally averaged seasonal mean temperature biases were within 1 ~ 2°C. For precipitation, the model tends to give better simulation in winter than in summer, and seasonal precipitation biases are mostly in the range of +3% ~ +50% of observations. The temporal evolution of East Asia summer monsoon rain belt, with steady phases separated by more rapid transitions, was reproduced.

EOF analysis is applied to both RIEMS simulations and observation, in order to further validate the model's capacity in reproducing Asia climate. The main components of both the model climate and observed climate of East Asia are presented in the study (Xiong Zhe, 2004). The results show that RIEMS can capture the spatial distribution in regional scale, annual variation and inter-annual variability of temperature over East Asia; RIEMS can basically reproduce the spatial patterns, annual variation and inter-annual variability of precipitation over East Asia, but the simulated maximum center of annual precipitation is located further north than the observation; and in general, RIEMS's performance in simulating temperature is better than that of precipitation.

9.3 Simulation of climate of China and East Asia through inter-comparison of a set of regional climate models

Although regional climate models have shown promising performance in reproducing the regional detail in surface climate characteristics as forced by regional details, such as topography, lakes, the coastline, and land-use distribution, more systematic and wider application of RCMs to adequately assess their performance and uncertainties in producing the regional climate information is required. To serve this purpose, several inter-comparison projects on regional climate modeling are being conducted (Takle et al. 1999; Curry and Lynch 2002; Anderson et al. 2003). The Regional Climate Model Inter-comparison Project (RMIP) for Asia has been established to study the performance of a group of RCMs when simulating East Asian climate (Fu et al, 2000).

RMIP seeks to improve further RCM simulations of the East Asian climate by evaluating its strengths and weaknesses in a common framework. The specific objectives of RMIP are 1) to assess the current status of East Asian regional climate simulation, 2) to provide a scientific basis for further RCM improvement, and 3) to provide scenarios of East Asian regional climate change in the twenty-first century based on an ensemble of RCMs

that are nested within a GCM.

9.3.1 Project Design

A three-phase simulation program is underway to meet these objectives.

Phase one: This 18-month simulation (March 1997–August 1998) covers a full annual cycle–East Asian drought and heat waves during the summer of 1997, and flooding in Korea, Japan, and the Yangtze and Songhua River valleys of China, during the summer of 1998. Phase-one tasks entail examining model capabilities to reproduce the annual cycle of monsoon climate and to capture extreme climate events. To date, nine models from five countries have contributed to RMIP's phase one (Table 9.1). These include eight limited-area models and one global variable resolution model, the Conformal-Cubic Atmospheric Model (CCAM). Detailed model information is listed in the appendix.

Table 9.1 Properties of participating RMIP models for phase one

Model	RIEMS	DARLAM	CCAM	JSM_BAIM	RegCM	RegCM2a	RegCM2b	ALT.MM5/ LSM	SNU _RCM
Group leader	C. Fu	J. McGregor	J. McGregor	Y. Sato	J. Kim	M. Suh	H. Kato	W. Gutowski	D. Lee
Country	China	Australia	Australia	Japan	South Korea	South Korea	Japan	United States	South Korea
Vertical levels	σ-17 levels	σ-18 levels	σ-18 levels	σ-23 levels	σ-15 levels	σ-15 levels	σ-14 levels	σ-23 levels	σ-23 levels
Dynamic process	Hydrostatic	Hydrostatic	Hydrostatic	Hydrostatic	Hydrostatic	Hydrostatic	Hydrostatic	Non Hydro-static	Non Hydro-static
Lateral boundary condition	Linear re-laxation	Exponential relaxation	Exponential relaxation	ER+spectral coupling	Exponential relaxation	Exponential relaxation	Exponential relaxation	Linear relaxation	Exponential relaxation
Convective scheme	Kuo-Anthes	Arakawa-Gordon	Arakawa-Gordon	Moist con-vective ad-justment	Grell	Kuo-Anthes	Kuo-Anthes	Betts-Miller	Grell
Land surface	BATS	Kowalczyk	Kowalczyk	BAIM	BATS	BATS	NCAR/LS M	NCAR/ LSM	NCAR/LS M
Planetary boundary	Holtslag	Louis	Louis	Yamada level 2 Louis scheme	Holtslag	Holtslag	Holtslag	MRF	MRF
Longwave radiation scheme	CCM3	GFDL	GFDL	Sugi	CCM3	CCM2	CCM3	CCM2	CCM2
Shortwave radiation scheme	CCM3+Aer osol	Lacis and Hansen	Lacis and Hansen	Lacis and Hansen	CCM3+ Aerosol	CCM2	CCM3	CCM2	CCM2

Phase two: This 10-yr simulation (July 1988– December 1998) assesses the models' ability to reproduce statistical behavior of the Asian monsoon

climate.
Phase three: Simulations with RCMs driven by GCM output under different forcing scenarios, including changes of atmospheric CO_2 concentration, sulfate aerosol emissions, and land cover are made.

Phase-three tasks aim at providing improved climate change scenarios and uncertainty estimates for East Asia through an ensemble of model simulations.

9.3.2 Phase one of RMIP

Ten research groups from the Asia–Pacific area are currently participating in the project, and eight of them have contributed their simulation results to RMIP's phase one. Phase one of RMIP for Asia reveals the capacities of regional climate models (RCMs) for simulating the Asian monsoon climate and extreme events as well (Fu et al., 2005).

The Domain of simulation

The simulation domain covers most of Asia and parts of the surrounding ocean waters in order to encompass the Asian monsoon circulation internally. Standard resolution is 60 km, resulting in a grid of 111 (latitude) × 151 (longitude) points. Except for Australia's Commonwealth Scientific and Industrial Research Organization (CSIRO) Division of Atmospheric Research Limited Area Model (DARLAM), which uses a polar stereographic projection, all of the participating RCMs use a Lambert conformal projection with true latitudes at 15° and 55°N. Phases one and two use initial and lateral boundary conditions supplied by the National Centers for Environmental Prediction (NCEP)– National Center for Atmospheric Research (NCAR) reanalysis (Kalney et al. 1996), whereas phase three will use output from simulations produced by CSIRO.

Validation data

A key part of RMIP is a comparison of models with observations. To this end, we have assembled a rich database of 710 observing sites for which 514 have daily records. These sites provide observations of temperature and precipitation. We complement this database with gridded analyses of monthly precipitation from Xie and Arkin (1997), for the areas where station data are either sparse or not available, several fields from the NCEP–NCAR reanalysis (Kalnay et al. 1996), and sea level pressure from the Japan Meteorological Agency.

Assessment of bias in simulation of monsoon climate of China, Korea and Japan

Contour plots over the RMIP domain of seasonal averages in daily mean, maximum, and minimum temperatures (not shown) reveal that all of the models reproduce the observed spatial patterns and annual cycles of these fields. Model temperatures tend to have a cool bias, with a smaller magnitude in the low latitudes. The largest cool biases tend to occur over the arid and semiarid regions of northern China.

Because of their dense station data available for validation, three regions of the mainland part of China, the Japanese islands, and the Korean peninsula (represented by A, B, C, respectively) are chosen to evaluate the models' abilities in simulating the surface climate. No ocean points are included in these three regions.

Fig.9.3a and Fig.9.3b show model-simulated average temperature biases in these three sub-regions. The models generally have a cool bias in winter (December–January–February) of about –4°C, except for the Meteorological Research Institute, Japan (MRI) model, which is 5–6°C over Korea and Japan, and DARLAM, which shows relatively little bias. The models generally have smaller biases over China than Korea and Japan, though this may be a consequence of averaging over a larger region for China. Most models also have a cool bias in summer (June–July–August), ranging from –4 to –1°C. The exceptions are the Regional Integrated Environmental Model System (RIEMS), which is too warm in all three regions (1–3°C), and DARLAM and the MRI model, which are 1–3°C too warm over Japan and Korea.

It is also worth noting that Fig.9.3a and Fig.9.3b presents significant diversity among the models. Some models have biases of less than +1°C, while some models have biases as large as +6°C, which is much greater than the average bias values in Houghton et al. (2001), mentioned in the introduction. This inconsistency suggests the need for further systematic evaluation of RCM performance over different regions and across more models, before making any general conclusions.

Taking the ensemble average of a group of models is one approach for possibly reducing bias. The simple ensemble average, (i.e., arithmetic average) bias of the nine participating models (last row of Fig.9.3a,b) also shows a cold bias in temperature, but less bias than most of the individual models. The mean biases of temperature simulation over China, Korea, and Japan are -2.05, -0.30, and 0.01°C, respectively, for the summer of 1998 and -0.96, -2.99, and -2.81°C, respectively, for the winter of 1997. These values are close to the average value of temperature biases in Houghton et al. (2001).

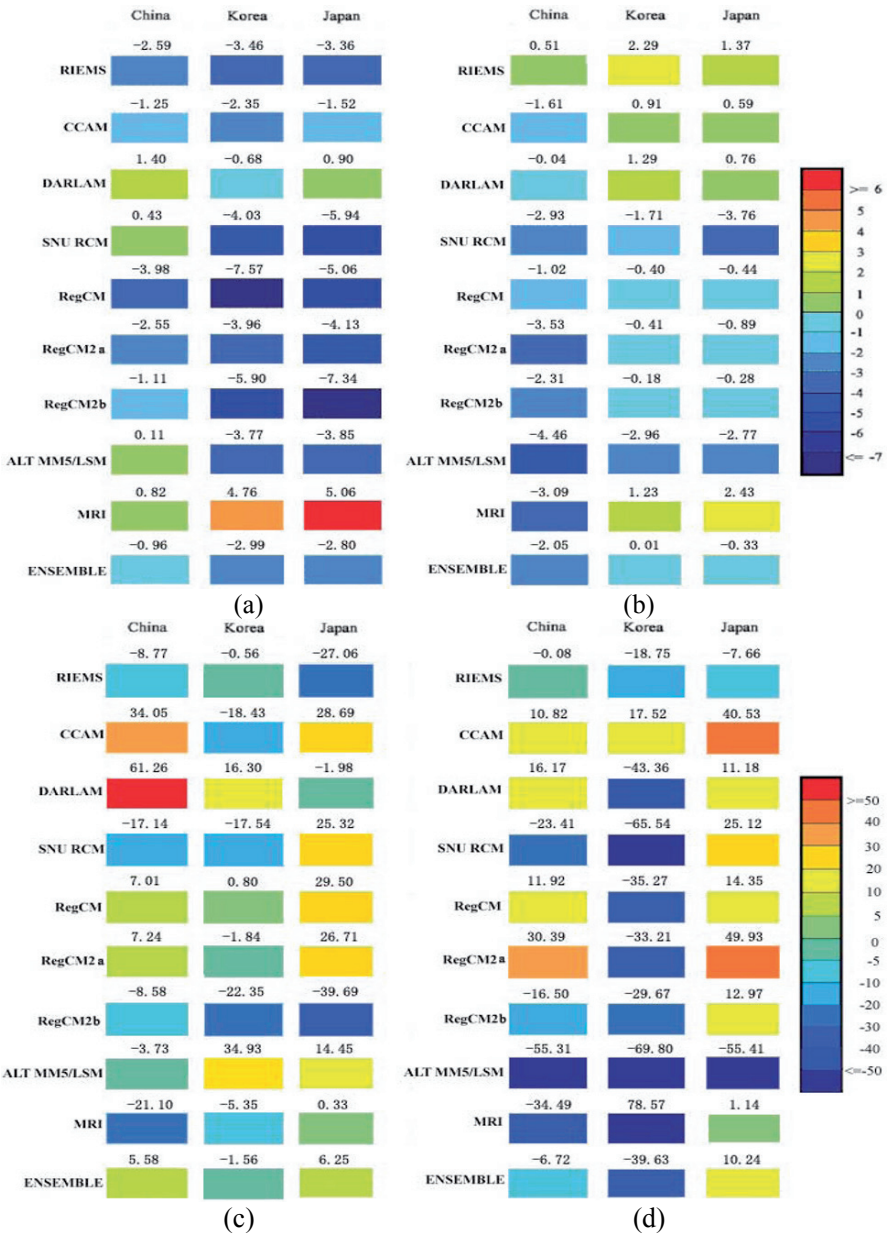

Fig. 9.3 Seasonal averaged surface air temperature bias (°C) in (a) winter 1997 and (b) summer 1998 and Seasonal total precipitation bias (%) in (c) winter 1997 and (d) summer 1998

Model precipitation usually agrees better with observations in winter than in summer (not shown). The models generally produce too much precipitation in high latitudes, but, overall, tend to reproduce the annual cycle across most of China, Korea, and Japan except in the western arid and semiarid regions. As with temperature, the three areas of the China mainland, Japanese islands, and Korean peninsula are chosen for a quantitative assessment of precipitation bias, which is shown in Fig.9.3c and Fig.9.3d. In winter, most models show a bias of less than +30%, while in summer most models show a dry bias in Korea, but a wet bias over Japan. There are mixed positive and negative biases from different models over China: CCAM shows a wet bias, while RIEMS and Alternate (ALT) fifth-generation Pennsylvania State University (PSU)–NCAR Mesoscale Model (MM5)/Bonan (1996) Land Surface Model (LSM) show a dry bias. Compared to most individual models, the ensemble average precipitation bias is relatively small in winter 1997, ranging from –5% to ~ 6%. In the summer of 1998, the ensemble average precipitation bias is up to –30% over the Korean peninsula, which is much larger in magnitude than the bias for China and Japan (–6% and 10%, respectively). The above analyses show that the ensemble average results are better than most of the individual models' performance, which suggests that there is value in using an ensemble of RCMs when projecting future climate to get a mean change and range of possible changes. In order to understand the possible reasons for the bias in the surface climate simulation, the atmospheric circulation in both the lower and higher latitudes has been analyzed further and will be presented in other related papers.

One of RMIP's goals is to examine the capacities of regional models to simulate extreme climatic events. During the RMIP phase-one simulation period, two climatic extremes occurred—the drought in North China in the summer of 1997 and heavy rains that caused severe flooding in the Yangtze River valley and northeast China in the summer of 1998. Most models captured the extreme events of both the summer drought in 1997 and the heavy rainfall in 1998, although the simulated intensities are different from observations. Fig.9.4, for example, compares the nine simulations against observations for the case of heavy rainfall during 11–20 June 1998 in the Yangtze River valley (framed area in Fig.9.4). This period is 15 months into the phase-one simulation period, so model output is strongly a product of model climatology, as opposed to initial conditions. Most models reproduce, to some degree, the heavy rainbelt over the Yangtze valley and its related 850hPa low-level jet. Simulated south-to-north moisture transport at this level (not shown) appears to explain much of the differences between the models' results. Fig.9.4 also is an example of the models' tendency to

produce too much precipitation at higher latitudes.

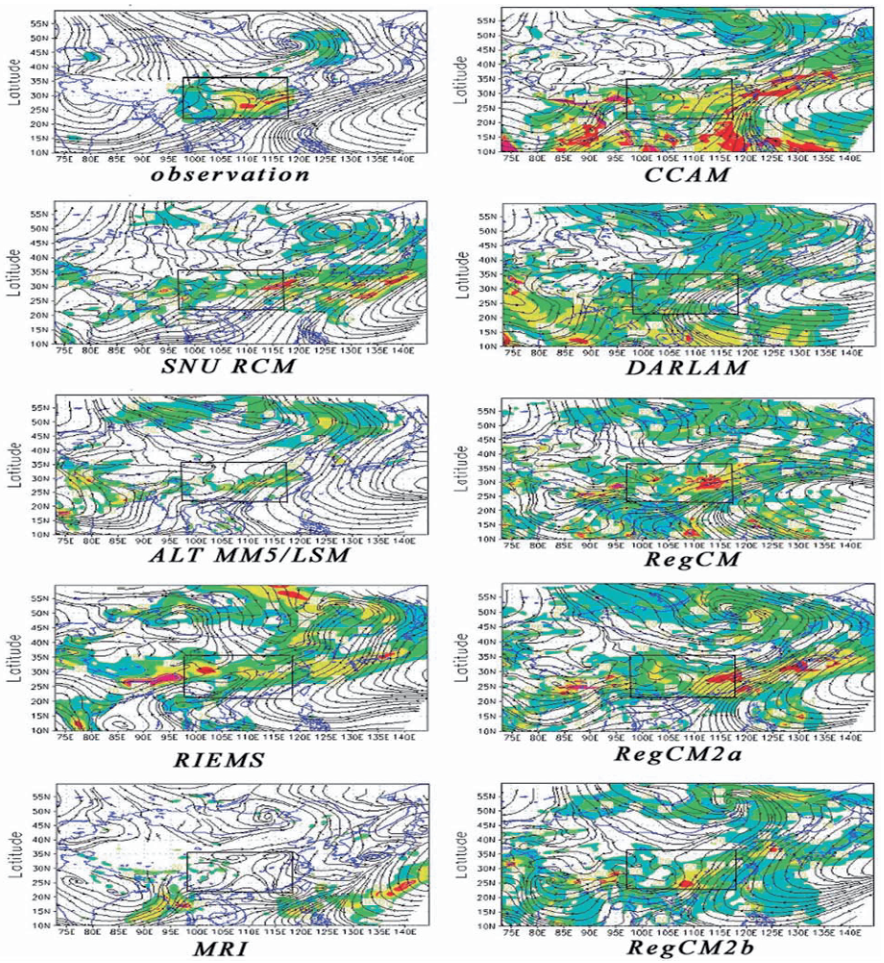

Fig. 9.4 Total precipitation (mm) and 850hPa streamlines for 11–20 Jun 1998

9.3.3 Phase two of RMIP

The objective of phase II is to systemically assess the statistical properties and capacities of the models in simulating Asian monsoon climate, including the mean fields and variability of meteorological elements. Five RCMs and a global variable resolution model participate in a 10-year

simulation of Asian climate. The RCMs include: RIEMS, developed by START Regional Center for Temperate East Asia (Fu et al., 2000; Xiong et al., 2003); NJU RCM, based on MM5v3 and improved by Department of Atmospheric Sciences, Nanjing University, China (Tang, 2004); MRI JSM_BAIM, a Japanese Spectral Model developed by Meteorological Research Institute/JMA (Mabuchi et al., 2002); RegCM2b, based on RegCM2, improved by Department of Atmospheric Science, Central Research Institute of Electric Power Industry, Japan (Kato et al., 2001); SNU RCM, based on MM5v3, improved by the Atmospheric Sciences Program, School of Earth and Environmental Sciences, Seoul National University, Korea (Lee and Kang, 1999). CSIRO CCAM is a global variable resolution model, developed by Commonwealth Scientific and Industrial Research Organization Atmospheric Research, Australia (McGregor, 1996; McGregor and Katzfey, 1998). Table 9.2 shows the basic information and physical processes of the six models.

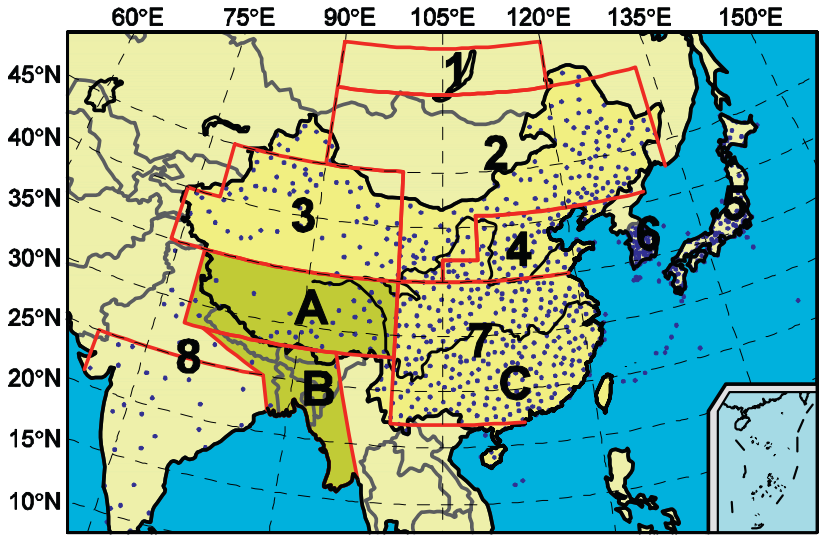

Fig. 9.5 Simulation domain and sub-regions for RMIP. 1.Far East of Russia 2.Northeast China and Mongolia 3.Northwest China 4.North China 5.Japanese Islands 6.Korean Peninsula 7. Southeast China 8.Indian Subcontinent 9.China 10.Continental part of domain A. Tibetan Plateau B. Bay of Bengal C. Changjiang-Huaihe Valley

The experiment domain is the same as phase I, which contains a large part of the Asian continent, western Pacific, Bay of Bengal and the South

China Sea (Fig.9.5). The simulation period is from July 1988 to December 1998. The driving fields come from NCEP-II (National Centers for Environmental Prediction) reanalysis data, with a 15-grid buffer zone. The NCAR (National Center for Atmospheric Research) terrain data are used in the model integration with a horizontal resolution of 0.5°×0.5°, in addition to satellite land surface data supplied by NASA. The same driving field, topography, land surface vegetation, simulation domain and horizontal resolution ensure the comparability of the simulation results.

As the precipitation is most crucial variable of monsoon climate, here only the simulation of precipitation are presented from the RMIP phase II.

Table 9.2 The basic information and physical processes of models in RMIP phase II

Model	RIEMS	NJU MM5	RegCM2b	MRI (JSM_BAIM)	SNU RCM	CSIRO CCAM
Country	China	China	Japan	Japan	Korea	Australia
Vertical levels	σ -17 levels	σ-16 levels	σ-14 levels	σ-23 levels	σ-23 levels	σ- 18 levels
Dynamics	hydrostatic	non-hydrostatic	hydrostatic	hydrostatic	non-hydrostatic	CCAM
LBC	ER	ER	ER	ER+ Spectral coupling	ER	Far-field nudging
Convective scheme	Kuo-Anthes	Grell	Kuo-Anthes	Moist convective adjustment	Grell	Arakawa-Gordon
Land surface	BATS	LSM	LSM	BAIM	LSM	Kowalczyk
PBL scheme	Holtslag	MRF	Holtslag	Yamada Level 2 Louis scheme	MRF	Louis-Holtslag
radiation scheme	CCM3+ aerosol	CCM2	CCM3	Sugi& Lacis+Hansen	CCM2	GFDL

ER: exponential relaxation; LBC: Lateral boundary condition

The data of the observation stations in the domain are used for comparison. There are a total of 903 stations whose monthly precipitation data are available, in which 640 stations are located in China, 155 in Japan, 68 in Korea and 40 in India. At the same time, in the areas where observation stations are scarce, other grid analysis data, such as the precipitation data sets of Xie and Arkin (1997) and CRU (Climatic Research Unit, University of East Anglia) are also used.

The continental area in the simulated domain is divided into 8 subregions in the following analysis (Fig.9.5). Owing to very few observations

and poor simulation results over the Tibetan Plateau (region A) and Bay of Bengal (region B), these areas are excluded in the statistics. In the analysis, region 9 represents China with regions A and region B excluded. Region 10 represents the entire continental region in the simulated domain with regions A and B excluded too. In addition, region C represents the Yangtze-Huaihe Valley. The simulation period is from July 1988 to December 1998. To exclude the spin-up period and for the convenience of statistical analysis, the analysis focus on the period of December 1988 to November 1998, i.e. ten whole years from the winter of 1988 to the fall of 1998.

Mean spatial pattern and seasonal variation in 10-year simulation

In summer, following the onset of the South and East Asia monsoons, the precipitation significantly increases over India, the Bay of Bengal and East Asia. Fig.9.6 illustrates the spatial distribution of 10-year mean summer precipitation (months of June, July and August). With limited space only the observations and three models' simulations are shown in the figures.

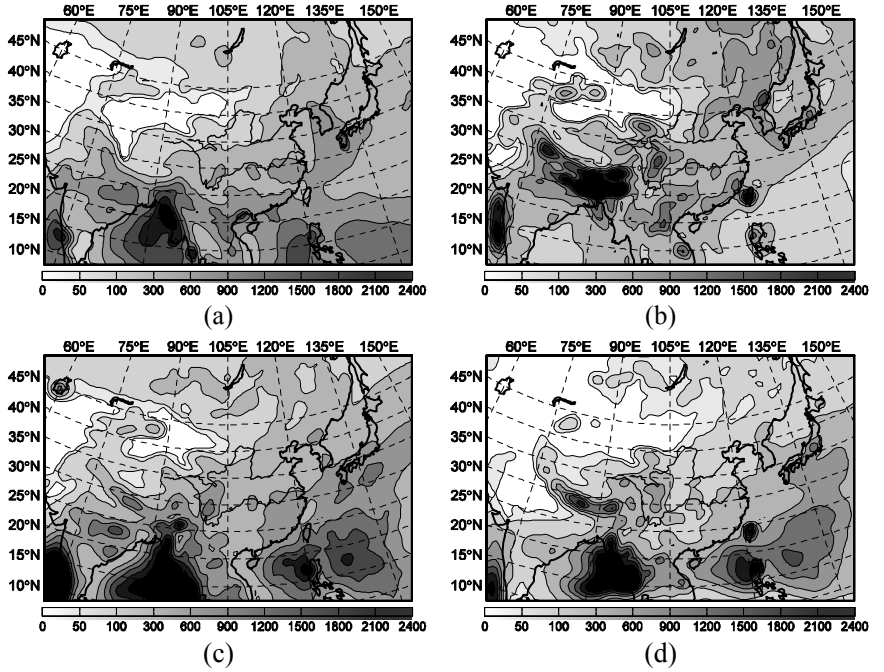

Fig. 9.6 The spatial distribution of 10-year mean summer precipitation (mm). (a) Observation; (b) RIEMS; (c) SNU; (d) MRI

According to the observations, there are three centers of high precipitation along the Yangtze-Huaihe valley, reaching at 600-900 mm. In the Bay of Bengal, the precipitation reaches 2400 mm. All models can basically reproduce the spatial pattern of the precipitation, i.e., more rainfall in the south and southeast and less rainfall in the northwest of East Asia. Unfortunately most models overestimate the precipitation in western China. The main rainbelt over the Yangtze-Huaihe Valley of China, is simulated by almost all of the models, but the details of location and the magnitude among the models are different. RIEMS and SNU overestimate the precipitation in most areas, while MRI underestimates it. As a whole, the distribution of precipitation simulated by NJU MM5 (figure omitted) is similar with SNU because they use the same dynamical frame and physical process parameterization scheme (from Table 9.1). RIEMS and RegCM2b use similar main parameterization schemes except for land surface scheme,, but they show significant difference in simulating precipitation. RIEMS overestimates precipitation in most areas while RegCM2b underestimates. RIEMS and RegCM2b both underestimate the precipitation over the ocean. In addition, CSIRO CCAM significantly overestimates the precipitation in the domain. Therefore, except for MRI and RegCM2b, the precipitation simulated by the other models is more than the observations in continental East Asian, especially to the north of the Tibetan Plateau. In general, SNU simulates the precipitation relatively better than the other models.

Suffering from the inland dry and cold winter wind, most regions in the East Asia have less precipitation in winter. Most of the precipitation is in the south of the Yangtze River and in the Southeast ocean of Japan. It can be seen that all the models can give better simulation of the spatial distribution of winter precipitation and also reproduce the main rainbelt. The simulated precipitation in Northwest China was overestimated. In Southeast China the most models simulated less precipitation except for the CSIRO model, but the simulated rainbelt was similar to the observations. The RIEMS model simulated more precipitation in the east of the Chinese continent and the Northwest Pacific Ocean around Japan. The RegCM2b simulated precipitation was obviously larger than the observations in the arid and semi-arid areas of Northwest China (Figure omitted).

Due to the breakout of the South Sea monsoon, South Asia monsoon and East Asia monsoon, the precipitation distinctly increases over most areas of East Asia from winter to spring. The strong spring precipitation basically appears the zonal distribution from east to west. Three strong precipitation canters lie in South china, the southwest of Japan and the eastern ocean of Japanese island. The model can better simulate the spatial distributions of the spring precipitation, but the simulated precipitation in

Northwest China is larger than the observations. The simulated precipitation canters by RIEMS and CSIRO are stronger over South china and the Pacific Ocean than the observations. The location of the simulated rainbelt in South china stretches to northward and the simulated intensity is weaker than the observations using the MRI model, and the rainbelt over the Pacific Ocean can not be simulated (Figure omitted).

In the fall, main rainbelt locates over southeastern coast and Japanese island due to the South Asia monsoon and East Asia monsoon retreat southward, the precipitation amount reaches 200-400 mm over the Yangtze River. The spatial distributions of the precipitation can be simulated by the model, but the stronger precipitation centre is simulated along southeastern edge of the Tibetan Plateau, the simulated range stretches to northward and westward. The simulated precipitation is smaller than the observations using the RIEMS and RegCM2b model. The spatial distributions of the simulated precipitation from the NJUM model are close to those from the SNU model, but the simulated results over southern ocean from these two models are larger than the observations (Figure omitted).

In areas of steep topography areas and some small islands, many models reproduce numerical point storms (NPSs). This is maybe caused by the process of terrain gradient (Leung et al., 1999). Over the southeast of the Tibetan Plateau, most models simulate a pseudo center of strong precipitation, but this is different from a numerical point storm. It may be related to the topography effect of a large area. Generally, a numerical point storm represents strong precipitation from several grid points, but the area of strong precipitation over the southeast of the Tibetan Plateau is beyond several grid points.

Compared to other seasons, the spatial distribution of simulated precipitation in the summertime is no better than in winter. Most models overestimate the winter and summer precipitation in large part of domain. In terms of precipitation type, the season of winter is dominated by the large-scale precipitation, while the summer is dominated by the convective precipitation. Many factors make the regional climate simulation in summer more complicated than that in winter.

To examining the potential impacts of parameterization schemes, following results are interesting. Noting the difference of the six models, RIEMS and RegCM2b use the cumulus parameterization scheme of Kuo-Anthes, but NJU MM5 and SNU RCM use Grell's. It seems that the Grell scheme generally produces more precipitation than the Kuo-Anthes scheme (Giorgi et al., 1993; Liu, et al., 1996). The further experiments by RIEMS and the results in phase I of RMIP for Asia can also prove this point (Fu et al., 2005). RIEMS and RegCM2b have same parameterization schemes for all physical processes except that RIEMS uses BATS and

RegCM2b uses LSM of land surface processes, but RIEMS produces more precipitation than RegCM2b. It indicates the potential impacts of land surface scheme on the simulation of precipitation. The results in phase I of RMIP for Asia also support such speculation.

In the experiments of the 10-year simulation, the driving fields come from the NCEP-II reanalysis data. The spatial distribution of percentage bias of the summer precipitation in the NCEP-II data and RCM's simulation is analyzed. The spatial distribution of the NCEP-II bias has some similarities with the results of most RCMs over the continental region, such as the positive bias over most areas of Mongolia and the southwest of China, and the negative bias over the north of India, etc. Because of the few observation stations in Northwest China and the Tibetan Plateau, the observed data used to validate the models almost come from the CRU precipitation data, so a larger bias may exist. Hence, the biases of the large-scale forcing fields and the deficiency of the validation data are one of the possible reasons for the biases of the simulation.

The simulated precipitation bias in every sub-region is statistically computed and shown in Fig.9.7. Fig.9.7a and Fig.9.7b respectively denote the bias percentage of the 10-year mean winter and summer precipitation, in which ensemble means the percentage bias of the arithmetical average result of the five RCMs. In most of the regions, especially in the northern regions, the precipitation simulated by most of the models is larger than the observations, while the precipitation produced by MRI is less than the observations in most of the regions, except for a few regions. The percentage bias is largest in Northwest China. In North China, the simulation by most models has a large bias in all seasons except for summer. In the entire continental area, the percentage bias is relatively smaller than that in the other sub-regions. Compared with the other models, CSIRO CCAM and RIEMS have more positive biases.

In total, most models reproduce more precipitation than the observations in northwestern China and less in India; the model simulations usually are better in Japan and Korea than in other areas.

Table 9.3 The bias of 10-year mean annual precipitation on the continent (%)

	Ensemble	RIEMS	RegCM2b	NJU	SNU	MRI	CSIRO
Bias	3.5	35.4	-15.5	9.8	18.6	-30.9	63.2

According to Table 9.3, the bias of the continental average annual precipitation of the different models varies between -30.9 and 35.4% (equivalent to -210–240 mm). The previous research results show that the bias of

precipitation simulated by GCMs is 3-784 mm (Zhao et al., 1998). So the bias of RCMs is much smaller than that of GCMs.

All models can simulate the seasonal cycle of the 10-year mean continental precipitation. However, the precipitation simulated by SNU RCM, RIEMS and CSIRO CCAM is more than the observations; the simulated precipitation of MRI, RegCM2b and NJUM is larger in the winter and less in the summer than the observations. The ensemble result of the RCMs is closer to the observations than that of any single model (Figure omitted).

To understand the atmospheric circulation related to the simulated precipitation, the 850 hPa summer wind fields of the 10-year mean NCEP-II data and simulations are analyzed (Figure omitted). In summer, the southeast and southwest monsoons prevail over the East Asian continent. The strong summer monsoon transports the abundant water vapor northward from the Bay of Bengal and West Pacific, thereby generating a large amount of precipitation in South China, Yangtze-Huaihe valley and later in North China. It can be seen the summer monsoon flow located to the south of 30ºN is underestimated by MRI compared to the NCEP-II data. So the precipitation simulated by MRI is much smaller in summer than other models. The summer monsoon current simulated by RIEMS is much stronger and the region of strong monsoon flow is extended further northward. This is perhaps the main reason that RIEMS simulates much more precipitation in the summer. The summer monsoon flow simulated by SNU is close to NCEP-II and therefore the bias of the simulated precipitation is relatively small.

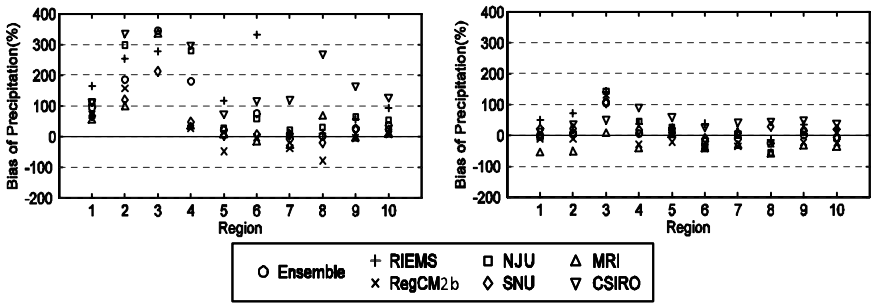

Fig. 9.7 Bias of simulated precipitation in the sub-regions. (a) winter; (b) summer

The inter-annual variability of East Asian monsoon climate

To normalize the variability, here the ratio of standard deviation (SD) of precipitation to the 10-year mean precipitation is used. Fig.9.8 shows the

spatial distribution of interannual variability of July precipitation. The shaded areas in the figure indicate where the differences of the interannual variability between the simulation and the observations are below the significance level of 0.05 in F-test.

As can see from Fig.9.8, over most areas, the difference between the simulation and the observations is not significant, i.e., models can better simulate the interannual variability of precipitation. In northern China, i.e., in the Talimu basin of Xinjiang and Inner Mongolia, the interannual variability of the precipitation is higher than in other areas. Except for RegCM2b, all the models can basically simulate this spatial pattern. In addition, the models can also simulate the center of the high precipitation variability near Pakistan. The interannual variability of the July precipitation simulated by the models is higher than the observations in Western Pacific.

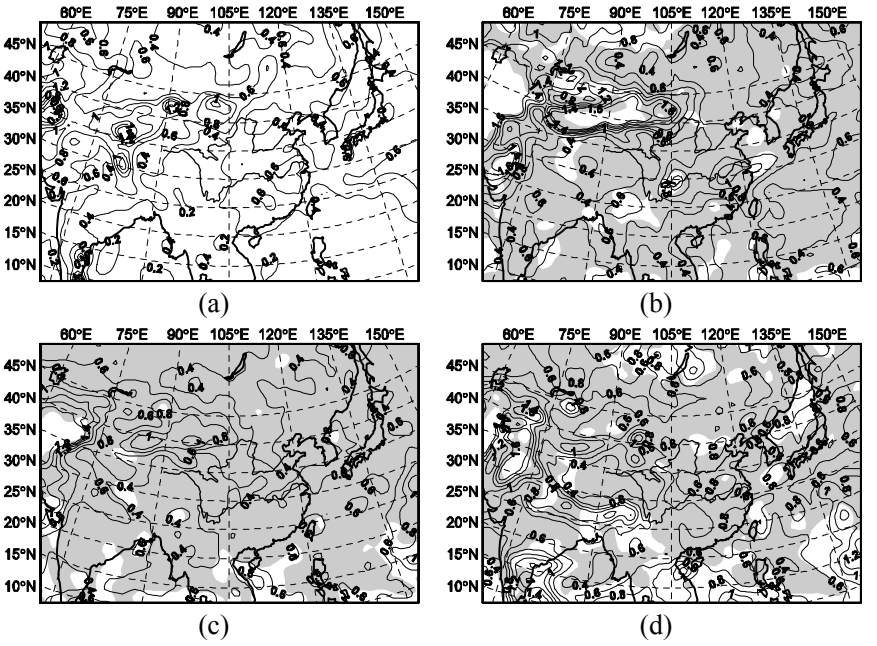

Fig. 9.8 Interannual variability of July precipitation (The shaded areas mean that the difference between the simulation and the observations is not significant) (a) Observations; (b) RIEMS; (c) SNU; (d) MRI

Most of the models can reproduce the interannual variation of winter and summer precipitation in the continental region, but there is a large difference among the models (Figure omitted). Considering the continental

region and all sub-regions, the interannual variation of the precipitation simulated in winter is better than that in summer. The results of the models CSIRO CCAM and MRI are not as good as the other models.

Shift of major rainbelt

The seasonal shift of the monsoon rainbelt is one of the main climatic characteristics in the east of China, which determines the basic pattern of the regional precipitation distribution during China's rainy season.

Fig.9.9 shows the seasonal shift of the 10-year mean rainbelt for eastern China. The longitudinal range selected for averaging the precipitation is 110º-120ºE. The lateral abscissa represents the date. The ensemble represents the results of the arithmetical average of five RCMs. The observations show that the intensive precipitation emerges on the last several days of April, and the rainbelt is located at about 23ºN from early May till early June. Then it shifts northward to 28º-32ºN and remains over the Yangtze-Huaihe valley during early June throughout mid-July. It shifts northward again at the end of July and reaches North China. In mid-August, the rainbelt begins to retreat southward and returns to southern China at the end of August or the beginning of September.

The intensity and the northward shift of the rainbelt can be simulated reasonably well by the models of NJU MM5 and SNU RCM, but they fail to reproduce the southward retreat. The intensity of the rainbelt simulated by RegCM2b and MRI is much weaker than the observations, and therefore, main characteristics of the rainbelt are not simulated. The rainbelt simulated by RIEMS over the Yangtze-Huaihe valley is much stronger than the observations and its northward jump stage is simulated earlier than observation, but the southward retreat is simulated well. In addition, the rainbelt simulated by CSIRO CCAM is much stronger than the observations. In general, the simulated location of the North China rainbelt by the six models is situated further north than the observations. As one expected, the ensemble evolution of rainbelt are relatively closer to the observations than most of individual models.

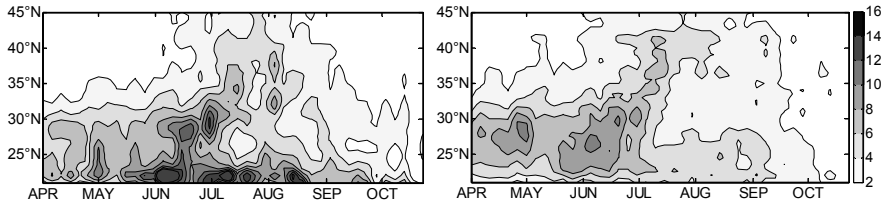

(a) (b)

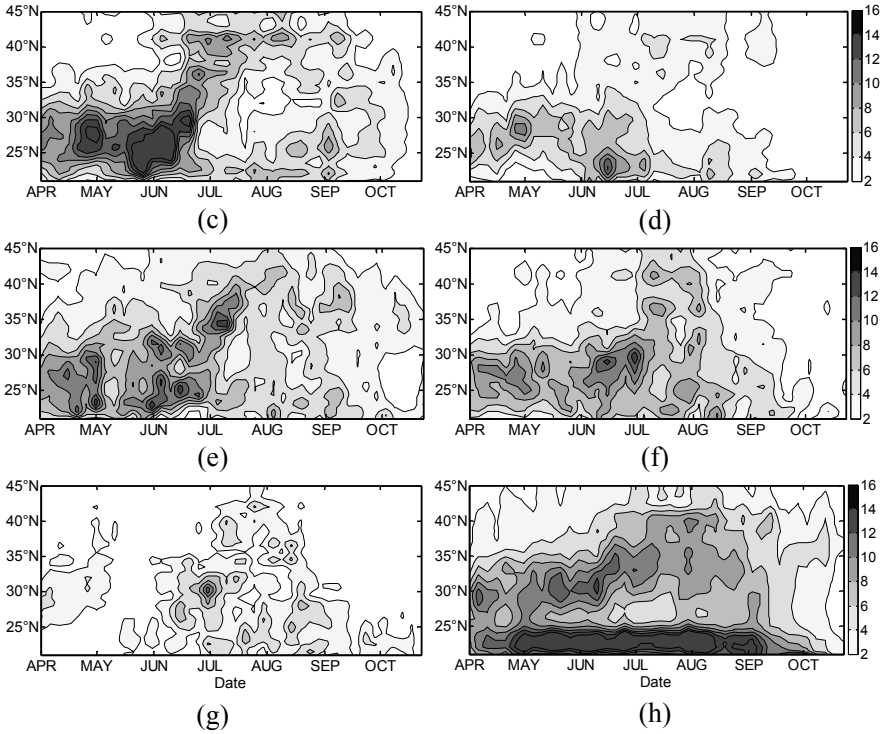

Fig. 9.9 Seasonal shift of 10-year mean rainbelt over eastern China(mm d^{-1}) (a) Observation; (b) Ensemble; (c) RIEMS; (d) RegCM2b; (e) NJUM; (f) SNU RCM; (g) MRI; (h) CSIRO CCAM

Conclusions

(1) Most models can simulate the basic spatial pattern of precipitation, but the location and intensity of the rainbelt show somewhat differences from the observations. Most models overestimate the precipitation in most continental regions. The seasonal variation of precipitation can be simulated, but there are large differences in the regional precipitation among the models.

(2) The biases of the simulated stream fields are important reasons behind the simulation errors of RCMs. The deviation of the large-scale driving fields may also bring biases in the simulation. The schemes of cumulus parameterization and land surface process can also influence on the precipitation simulation. The Grell scheme generally produces more precipitation than the Kuo-Anthes scheme.

(3) Most models can basically reproduce the spatial distribution and time evolution of of the interannual variability of precipitation, but there are significant differences in the magnitude among the models.

(4) The models can reasonably simulate the evolution of the main rainbelt in the East China, i.e., the major rainbelt shifting northward and retreating southward during the rainy season in China, although differences exist among the models.

9.4 Study on multi-RCM ensemble of regional climate simulation for Asia

The performance of climate models are affected by many factors such as the dynamic framework, parameterization scheme of physical processes, initial and driving fields, horizontal and vertical resolution, and so on. So far neither any single global or regional model can be satisfied in every aspects of climate simulation. Since the chaos phenomenon in the atmosphere was discovered by Lorenz (1963), meteorologists have carried on many researches on the forecast uncertainty. Due to the limitation of observation data and assimilation methods, errors in initial data, advantages and disadvantages in different parameterization schemes, the atmosphere state can not be described accurately under current resolution of models. These factors make the model results uncertainty. Some researches have shown that the ensemble of simulation results can reduce the uncertainty of single models and improve the credibility of the results. Therefore the ensemble approach becomes an effective tool to improve climate simulation and prediction.

Currently, ensemble approaches have been widely applied in global models, but few studies for RCMs, because of scarcity of long-term simulation experiments with multi-RCM. The phase II of RMIP for Asia provides a good chance to carry on ensemble research of RCMs. Here four ensemble methods are used to deal with three climatic variables of temperature, precipitation and sea level pressure over Asia from 5 RCMs. The ensemble results of temperature and precipitation are mainly presented.

9.4.1 Ensemble Methods

The principal method of multi-model ensemble is arithmetic mean, i.e. calculating the simple arithmetic average of the simulation results of different models. This method is convenient to perform because it is not necessary to consider the comparison between the models and the observa-

tions. However, generally different models have different simulation capacities, and one variable may be simulated better in one model while worse in another. Taking the different capacities of models into account and using the method of weighted mean by giving different models weighting coefficients, the ensemble results may be closer to the observations than arithmetic mean method. The weighting coefficients need derive from comparison with the observations, thus this method depend on the observations. When applying this method to multi-model ensemble prediction, firstly the weighting coefficients need to be calculated using simulation results of historical climate and observed data through corresponding statistical approach, i.e. data training. At present many ensemble methods are constructed surrounding the problem that how to decide the weighting coefficients. The ensemble method based on multivariate linear regression is widely applied in the ensemble researches. In addition, nonlinear regression and artificial neural network are also applied to the model ensemble gradually.

The ensemble methods used in following analysis are: (1) Arithmetic mean method, (2) Weighted mean method, (3) Multivariate linear regression, (4) Singular value decomposition (SVD)

9.4.2 Mean climate and biases

According to the four ensemble methods, using the 10-year total simulations and observations, the 10-year ensemble results can be calculated (Figure omitted). The precipitations from four ensemble methods can better reflect the spatial distribution of annual total precipitation in Asia. The results of weighted mean, multivariate linear regression and SVD are better than those of arithmetic mean. For the location and extent of the rainbelt in the Yangtze-Huaihe valley and southeast of Japan, the results are close to the observation with the latter three methods. The pseudo precipitation centers appearing in the east of the Tibetan Plateau can be eliminated with the multivariate linear regression and SVD methods.

The spatial distributions of 10-year mean temperature biases from the four ensemble methods are analyzed (Figure omitted). There are cool temperature biases in most regions of mainland using the arithmetic mean method. Using the inverse-distance square weighting and SVD methods, the area of cool biases decreases rapidly, and the biases are very little in India, east China, northern part of the control regions. And the biases using SVD are less than those with weighted mean method. Using multivariate linear regression, the biases, most ranging from -1° C to 1° C, are little in the total domain.

Fig.9.10 shows the spatial distributions of the 10-year mean annual total precipitation biases ratios to the observation, using the four ensemble methods. For the arithmetic mean, the simulated precipitations are overestimated in most part of China except southeast China, while underestimated in Indian region. As to inverse-distance square weighting, except overestimated in the northern part of the Tibetan Plateau and control region, and underestimated in some regions of India, the biases are between -20—20% in most part of the mainland. Using SVD method, the biases in most of the domain are little, between -20—20%, except underestimated in India. Using multivariate linear regression, the biases are much little except several small regions where the precipitation is underestimated.

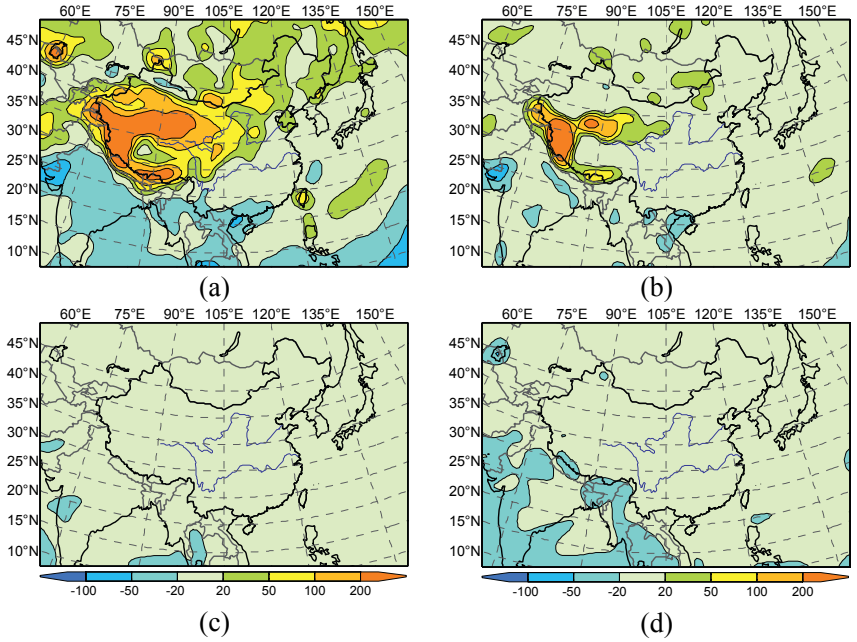

Fig. 9.10 Bias of annual total precipitation of the ensemble results with different methods (%) (a) arithmetic mean, (b) weighted mean, (c) multivariate linear regression, (d) SVD

So we can conclude that multivariate linear regression is the best method in the temperature and precipitation ensemble, the next is SVD and weighted mean, while the method of arithmetic mean is not better than the other three methods.

Correlation coefficient and root mean square error (RMSE) are two

analysis ways to assess the performance of the simulations and the ensemble results. For anomaly correlation coefficient, firstly the seasonal variation information of climatic variables is removed, and then the correlation coefficient is calculated. Root mean square error reflects the total bias of the simulations and the ensemble results to the observations. It is calculated according to the following formula:

$$rmse = \sqrt{\frac{\sum_{i=1}^{N}(M_i - O_i)^2}{N}}$$

Where M is the simulation or the ensemble result, O is the observation, and N is the size of samples.

The anomaly correlation coefficients of temperature, precipitation and sea level pressure between the simulations or ensemble results and the observations are calculated (Figure omitted). As to temperature, the correlation coefficients of the ensemble results are all higher than those of individual simulations, in which the correlation coefficient is highest using multivariate linear regression method. For precipitation, the correlation coefficients vary largely among different models. The correlation coefficients by arithmetic mean and weighted mean are a little lower than the maximum of single models. The correlation coefficients by multivariate linear regression are higher than those by single models and other ensemble methods. As to sea level pressure, correlation coefficients by arithmetic mean, weighted mean and SVD are a little lower than the maximum of single models. The results by multivariate linear regression method are a little higher, but the difference is not significant.

The root mean square errors of temperature, precipitation and sea level pressure using single models and ensemble methods are calculated (Figure omitted). The RMSE calculated by the time series points after regional average, i.e. the sample size N=120. For temperature, the RMSE is lowest using multivariate linear regression, and the next is SVD, weighted mean and arithmetic mean. Except for multivariate linear regression, the RMSEs of the other methods are lager than the minimal RMSE of single models. For precipitation, the RMSEs of the four ensemble methods are lower than those of single models, and the RMSE of multivariate linear regression is the lowest. As to sea level pressure, same as the precipitation, the RMSEs of ensemble results are all lower than those of single models and the RMSE of multivariate linear regression is the lowest.

Table 9.4 shows the decreased percentages of the RMSEs calculated by all spatial and temporal points using ensemble methods compared with the lowest RMSE of single models. The decrease of RMSEs of all variables is largest using multivariate linear regression, 66% decrease for temperature,

45% for precipitation, and 60% for sea level pressure. The next is SVD. For temperature and sea level pressure, inverse-distance square weighting is better than arithmetic mean, and reverse for the precipitation, but the difference is not significant.

Table 9.4 Decreased percentages of RMSEs using ensemble methods compared with the lowest RMSE of single models

Variables	Arithmetic mean	inverse-distance square weighting	Multivariate linear regression	SVD
Temperature	4.0	15.7	65.6	24.6
Precipitation	23.9	20.9	45.3	35.6
Sea level pressure	18.1	24.4	60.2	36.6

Therefore, the ensemble methods can all make some improvements for the climatic variables. The effect of multivariate linear regression is most significant. The improvements are different for different variables with different ensemble methods. The improvements by multivariate linear regression are most significant for temperature, and the next for sea level pressure and precipitation.

9.4.3 Cross validation of ensemble results

In the above ensemble analysis, the ensemble deals with the 10-year simulations to get a 10-year ensemble result, and then it is compared with observations or single models. However, in order to apply the ensemble methods to predict future climate, the best way is to make cross validation using historical data to evaluate the performance of the ensemble methods. Hence, firstly, weighting coefficients are calculated using the simulated and observed data of first 9 years, i.e. data training. Then they are applied into the ensemble results of 1998, to be validated with the observations. For arithmetic mean method, it is only needed to calculate the arithmetic mean of the simulated results, without considering the observations to train data.

Fig.9.11 shows the root mean square errors of temperature, precipitation and sea level pressure in 1998 from the models and the ensemble results. The RMSEs of the three variables from the multivariate linear regression are the least, except for the precipitation. The next is SVD and weighted mean for temperature. The results of arithmetic mean are not good relatively. For precipitation, the RMSE are the largest using SVD, while least using weighted mean, but they differ little with arithmetic mean and multi-

variate linear regression. The RMSE of sea level pressure is the least using multivariate linear regression.

By the cross validation, it is also proved that the ensemble methods can improve the simulations of single models, especially the multivariate linear regression. The method of arithmetic mean is rather simple, without considering the different simulation capacities of different models to different variables, so it is not better than the other methods.

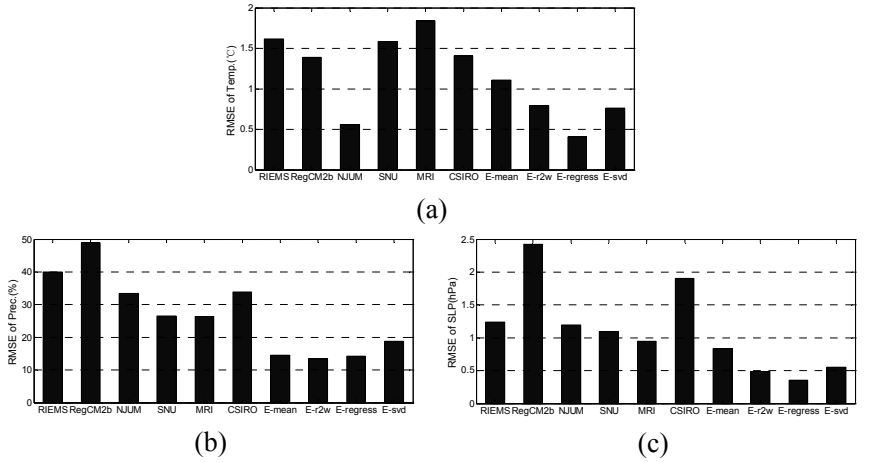

Fig. 9.11 Root mean square errors of models and ensemble results in 1998 E-mean(arithmetic mean), E-r2w(weighted mean), E-regress(multivariate linear regression), E-svd(SVD) (a) temperature, (b) precipitation, (c) sea level pressure

9.4.4 Conclusions

In this session, the principles of the ensemble methods of arithmetic mean, weighted mean, multivariate linear regression and singular value decomposition are discussed firstly. Then the multi-RCM ensemble using the 10-year simulations for Asia are analyzed with the four ensemble methods.

1. Arithmetic mean is a basic method for multi-RCM ensemble. The results of arithmetic mean are better than single models in many aspects. Because the uncertainty of single model can be decreased by arithmetic mean, the results of arithmetic mean agree with the observations better than single models.

2. Considering the spatial distributions of mean states and biases, the

multivariate linear regression is the best ensemble method for the temperature or precipitation. SVD and weighted mean methods are the next and arithmetic mean is not better than the other methods. For spatial distributions of mean climate states, the ensemble result of temperature is better than that of precipitation.

3. According to the analysis of correlation coefficients and root mean square errors, the four methods can all improve the results of temperature, precipitation and sea level pressure, especially the multivariate linear regression.

4. Using the first 9 year data of the 10-year simulations to train data, and the last year data to cross validation, the four ensemble methods present all better than single models. The distributions of root mean square errors are generally consistent with that of ensemble results calculated with all 10 years data. In total, multivariate linear regression based on the minimization of the root mean square errors improves the ensemble results significantly among the four ensemble methods.

9.5 Effects of increasing greenhouse gases and aerosols on regional climate of East Asia

Increasing greenhouse and aerosols induced by human activities is one of the most important global environmental problems.

Climate effects of anthropogenic sulfate aerosol, especially the direct effect, under $2 \times CO_2$ condition were investigated by introducing aerosol distribution into the latest version of RegCM2 (Gao et al., 2003). Two experimental runs, a double CO_2 with no aerosol run and double CO_2 with aerosol distribution run, were integrated for 5 years respectively. Preliminary analysis shows that the direct climate effect of aerosol might cause a decrease of surface air temperature. The decrease might be larger in winter and in South China. The area-averaged monthly precipitation might also decrease at most of the months. The annual mean precipitation might decrease in East and increase in West China. But climate responses of aerosol simulated by the model were much smaller comparing to the greenhouse effects.

Climate change due to greenhouse effects (double CO_2) over China, with focus on Northwest China, is simulated by RegCM2 regional climate model (Gao et al., 2003). The mode is nested to a global coupled ocean-atmosphere model (CSIRO R21L9 AOGCM). Driven by lateral boundary conditions from the GCM, both control ($1 \times CO_2$) and sensitive ($2 \times CO_2$) experiments of the RCM have been run for 5 years respectively. Model

outputs are interpolated in 34 stations in the region for convenience of analysis. Results of control run of the RCM indicated that it has a better capability in reproducing present climate for both China and Northwest China than that of the GCM. It reproduced the fine scale structure of air surface temperature caused by small topography fluctuations, and lowered down the overestimated precipitation by the GCM. The annually averaged spatial correlation coefficient of the monthly mean temperature and precipitation between the RCM simulation and observation are 0.80 and 0.85, respectively. Results of sensitive experiment by the RCM with $2 \times CO_2$ showed a remarkably warming over Northwest China due to greenhouse effect. In Northwest China, mean temperature will increase 2.7 °C, higher than that in the whole China (2.5°C). The warming is higher in winter and spring, about increasing 3.0 °C. Rising of temperature can be noticed in all the 12 months of a year. The summer daily maximum temperature also increases in Northwest China with an average increasing of 3.1 °C, higher than the average over the whole country, 2.0 °C. While the winter daily minimum temperature raises 1.6 °C, close to the average over the whole country, 1.7 °C. More rainfall may also be expected over the region under the greenhouse effect. Increasing rate of annual precipitation is usually greater than 20% in most of Northwest China, and 30% or more in some places. The mean precipitation increase is 25% in Northwest China, much higher than that averaged over the whole China (12%). Increasing rates of precipitation follow the order of winter, spring, autumn and summer. The precipitation increases in all months, except for September, when a slightly decrease appears. The simulated change of temperature and precipitation under $2 \times CO_2$ showed some similarities with observation in the recent years.

A similar research is conducted using the same regional climate model(RegCM2) and global ocean-atmosphere model (CSIRO R21 AOGCM), to study the effect of doubling CO_2 for the middle and lower reaches of the Yangtze River (Gao Xuejie et al., 2004). Results show that under the influence of CO_2 doubling, the temperature in the middle and lower reaches of the Yangtze River would rise obviously, and the increment of the temperature would be generally over 2.3-2.5°C, which is lower than average of whole China. At the same time the precipitation in greater part of the reaches would be increased, especially in winter and summer with percentage increment of 7%, which is still lower than that of whole China. Greenhouse effects will make the daily highest and lowest temperature higher and days with precipitation increase. Increase of precipitation in summer might bring on more flood disasters.

9.5.1 Future climate simulated by RIEMS-GOALS under the scenario of increased CO_2 emission

Zhang Yingjuang (2006) nested the regional climate model RIEMS into the Global Ocean-Atmosphere Coupled Model (referred as GOALS in this chapter) developed by State Key Laboratory of Numerical Modelling for Atmospheric Sciences and Geophysical Fluid Dynamics, IAP/CAS. The future climate over China is simulated and predicted using RIEMS driving by GOALS under the scenario of increased CO_2 emission. Combined with the simulation results from the global model, the scenario prediction is analyzed.

Experiment Design

Two long-term integrations were carried out by GOALS: the control experiment, in which CO_2 concentration is fixed to integrate for 80 years continually; and the sensitive experiment, in which CO_2 concentration increases by 1% annually. The results produce by GOALS thus being used as initial fields and lateral boundary conditions for RIEMS. Three periods of integrations are conducted using RIEMS, that is, 2-11 years (in the 10s of the future), 15-24 years (in the 20s of the future) and 45-54 years (in the 50s of the future). The simulation region contains entire China.

Change of surface air temperature in China due to CO_2 increasing

Change of surface air temperature in China in 10 years, 20 years and 50 years are shown in Fig.9.12. The results of global model indicate that in the first 10 years, there is going to be a slightly increasing trend over most regions of China. The warming trend will increase with the latitude, though the amplitude is not large. However, temperature in coastal area of Southeast China as well as in the western part of Xinjiang region will decrease slightly. Furthermore, from the top right figure of Fig.9.12, we can conclude that the increase amplitude of air temperature simulated by RIEMS is lower than that of GOALS. The averaged temperature increase over most regions of China will be between 0.2~0.2°C, except for the northeastern China, which will reach 0.8°C.

As for the following 20 years, global model simulates a warming trend of up to 1°Cin different areas of China with maximum warming locating in the coastal area of the East China and the Huanghe River valley. RIEMS, however, produces the maximum warming in the Tibetan Plateau, and the air temperature will decrease by 0.4°C in Guangxi in the South of China.

For the 50 years into integration, both results simulated by GOALS and

RIEMS show that the maximum increases of air surface temperature will appear near the Tibetan Plateau, with the maximum increase simulated by GOALS will reach 2.2°C, and RIEMS 0.6°C lower than that of GOALS. The intensity of warming trend will reduce eastward. Over coastal areas of East China the warming trend is less obvious, with intensities produced by GOALS and RIEMS being 0.8°C and 0.2°C respectively.

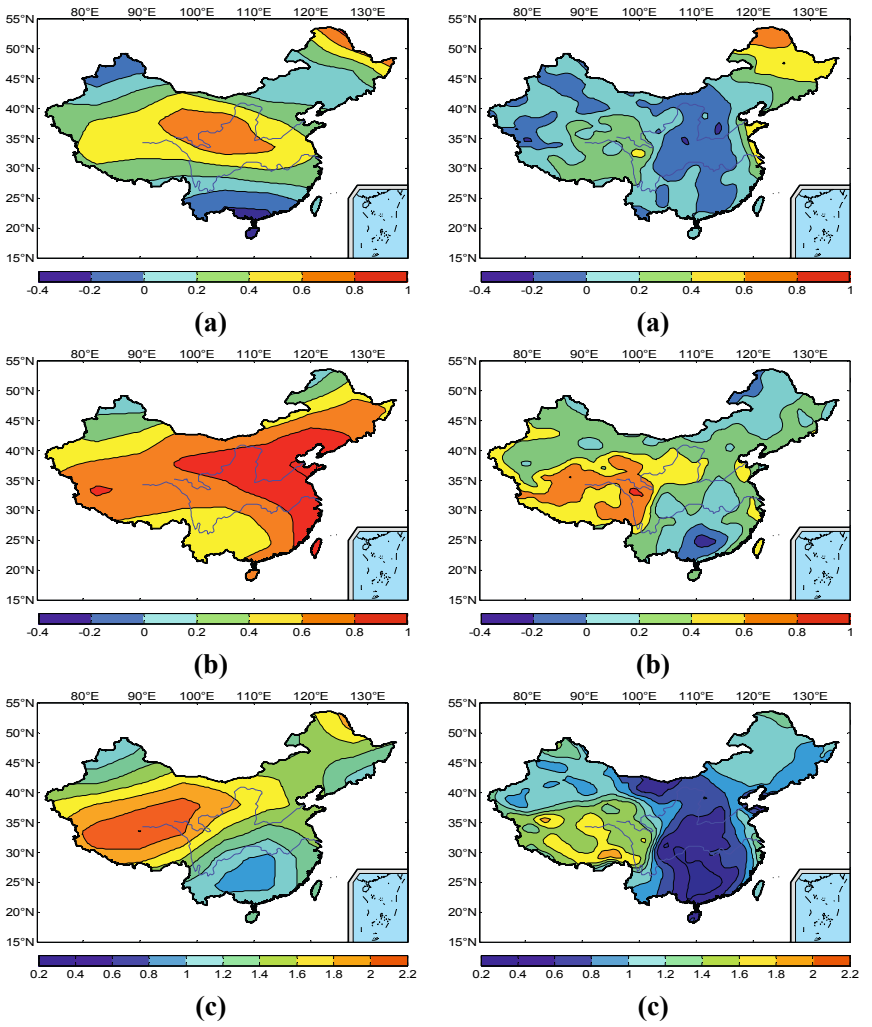

Fig. 9.12 Annual mean surface air temperature change in the future 10 years, 20 years and 50 years over China for the increasing 1% CO_2 per year (units: °C) left：GOALS, right：RIEMS, (a) 10 years, (b) 20 years, (c) 50 years

The projected distribution of precipitation due to the increasing of CO_2 emission in China

The probable distributions of precipitation under the CO_2 increasing scenario in China, simulated by both models, are presented in Fig.9.13. It can be seen that within the starting period of CO_2 increase, RIEMS simulates the increasing trend in precipitation in East China and decreasing trend in West China. But there will be less in Talimu Basin in south of Xinjiang, which may result from the better description of terrain by RIEMS.

The middle left figure in Fig.9.13 indicates that, with the gradually increased CO_2 concentration, precipitation will slightly decrease in northern China and increase to different degree in different regions of Southern China. The increasing trend for precipitation simulated by RIEMS is less obvious than that of GOALS. RIEMS's precipitation will increase by 50% in Tianshan Mountain areas. In the following 50 years, as indicated by the bottom panel of Fig.9.13, the largest increase in precipitation will occur in Talimu Basin, with more than 120% in the center. Over other areas the precipitation trend intensities are within ±20%. Comparing to the following 20 years, the precipitation is generally decreasing for following 50 years.

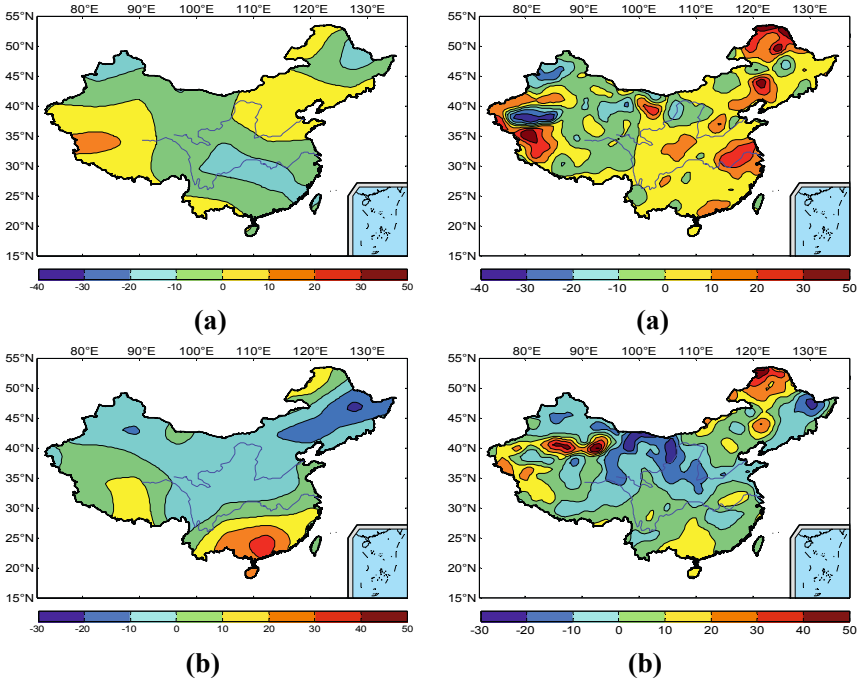

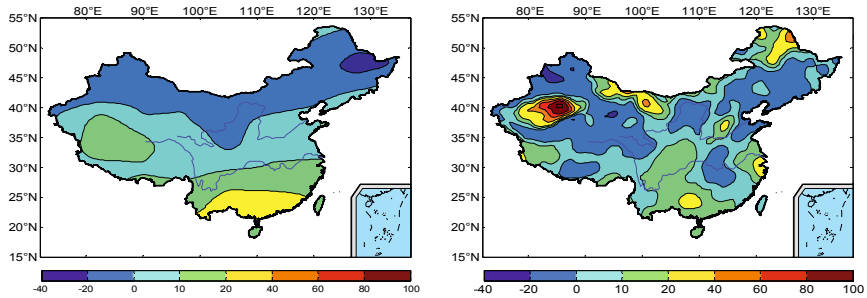

Fig. 9.13 The distribution of annual total precipitation rate difference in the future 10 years, 20years and 50 years over China for the increasing 1% CO_2 per year (units: %) left：GOALS, right：RIEMS, a：10 years, b：20 years, c：50years

9.5.2 Impacts of aerosols on East Asia monsoon climate

Wu Jian (2002) used a coupled regional climate-atmospheric chemistry model to simulate sulfate aerosol and its climate impacts over China area (Wu Jian, 2002). The direct and indirect radiative effects of sulfate aerosol were also explored. The results showed that the sulfate aerosol exerts negative radiative forcing on the top of atmosphere, and reduces the surface air temperature. The study shows that, to improve the model performance, both direct and indirect effects of sulfate aerosol should be taken into consideration in the modeling system. In other work, Wu et al. (2002) investigated-the distribution and the seasonal variation of SO_2 and sulfate aerosol in China. The simulation shows that the total burden of SO_2 in winter and autumn is more than that in spring and summer, and the concentration of the sulfate aerosol reaches maximum in summer. In vertical SO2 concentration follows the monotone distribution of decreasing from the surface to the upper atmosphere. The seasonal variation of sulfate aerosol occurs mainly under the 400 hPa.

Research conducted in 2005 by Wu et al. compared the climatic effects of sulfate aerosol simulated by RegCM2-atmospheric chemistry modeling system and GCM-Atmospheric Chemistry Modeling system. The results show that the coupling simulation system at regional scale obtains more accurate information on the sulfate distribution and radiative responses than that of large scale modeling system. Both online and offline experiments were carried out for two modeling systems. It has been clarified that,

over most regions, the online and offline experiments produce different sulfate burdens, radiative forcings at top of atmosphere (TOA) and surface air temperature. The difference in regional scale modeling system is more obvious than that of large scale.

The coupled Regional Climate-Chemistry Model mentioned above was also used to interactions between climate and troposphere ozone over China (Wu Jian et al., 2002). It has been found that East Asia monsoon circulation is one of the dominant factors that can deeply affect ozone distribution in troposphere. Other controlling factors include complex terrain and pollutant, etc. The radiative forcing at the top of atmosphere in clear sky condition has also been explored with the regional climate-chemical coupled model system.

Preliminary simulation research of direct forcing of mineral dust aerosol over east Asia

To study the direct radiative effect of dust aerosol over the East Asia region, a dust emission scheme, a transport model and a radiative scheme of dust aerosol have been added into the Regional Climate Model Version 3 (RegCM3) (Wu et al., 2005).

For the annual averaged emission rate, main dust sources are in the north-west China and south of Mongolia. The emission rates of Taklimakan and Badan Jilin deserts are more than 30μg/ m^2s, with maximum value of 90-100μg/ m^2s in west part of Taklimakan desert. The Hunshan Dake desert in north of China is also an important source with emission rate of 10μg/ m^2s. Simulated distribution of dust sources is consistent with the observation (MuKai, et al., 2004).

Based on the simulation for the period from March 2001 to February 2002, it has been found that Northwest China and Mongolia are the main dust sources in East Asia, whose emission rates exceed 1μg/(m^2 s) with maximum value of 90μg/(m^2 s). The maximum column burden of dust aerosol is about 5g/m^2, which emerges over the Taklimakan desert and the Qinling Mountains. Fig.9.14 shows the total column burden of mineral dust aerosols for 4 seasons. In spring, mineral dust aerosol covers almost entire Chinese mainland, and there exist three high concentration centers: Taklimakan desert, desert of west part of Inner Mongolia, and Qin Ling Mountain, with maximum values of 2.5g/m^2, 5g/m^2 and 5g/m^2 respectively. The maximum burden in Qin Ling Mountain is due to the blockage effect of complex terrain. The contour line of 1g/m^2 and 0.5g/m^2 cover most of China and most of East Asia respectively, which proves the long-term southward transport of mineral dust from Northwest China in spring can affect most of East Asia area. In summer, the highest mineral dust aerosol

column content is between 35°–45°N, and column burden decreases in the south of simulation domain. The maximum values in Teng Ge Li desert and Badan Jilin desert decrease to 3g/m^2, and so does the dust aerosol content in Qin Ling Mountain. On the other hand, the maximum concentration in Taklimakan desert will increase to 3.5g/m^2, due to the change of general circulation and heavy rainfall in summer. In autumn, aerosols almost condense in northwest China. does it mean that the dust aerosol is basically located in North-west china? and maximum contents of Takalimakan, Teng Ge Li and Badan Jilin deserts are 3.5g/m^2 and 2.5g/m^2; Compare to summer, the contour line of 0.5g/m^2 extends to south-east China, which also indicates the southward transport of mineral dust aerosol. The main high value centers in winter are much like those in autumn, while column burden over Taklimakan desert and Qin Lin Mountain increase to 4g/m^2 and 3/g/m^2, and Teng Ge Li and Badan Jilin desert is 2.5g/m^2. Contour of 0.5g/m^2 extends eastward and covers Tai Wan and Japan. The above conclusions are consistent with some results of ACE-Asia (Gong et al., 2003).

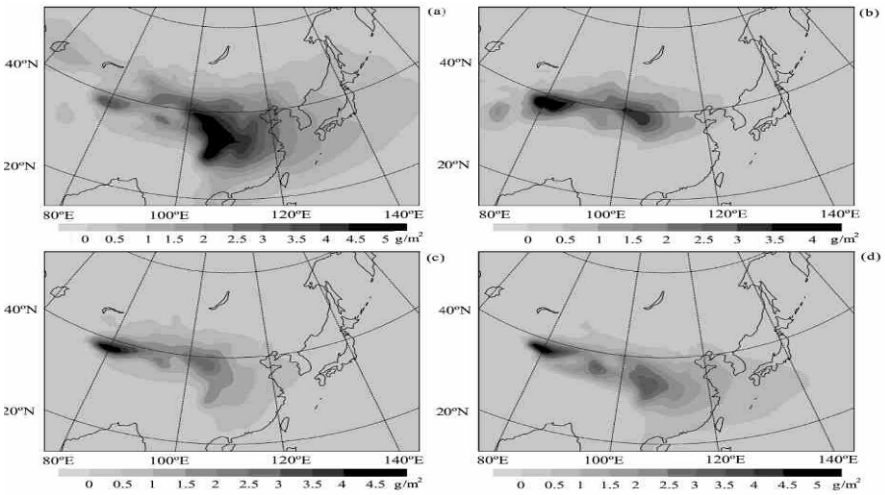

Fig. 9.14 Column burdens of mineral dust aerosol (a) Spring ; (b) Summer ; (c)Autumn ; (d)Winter.

Due to the severe desertification and sandification in northern China, it's easier to reach the threshold for dust lifting and the area becomes the most important dust aerosol source region for Asia. Southern area has relative high load of mineral dust aerosol in winter and spring because the strong southward wind tends to carry the dust to the area. In summer and fall the dust concentration is much lower than that in northern area. For the whole

area, the highest dust load is in spring when dust storms happen frequently in northern China.

The direct radiative forcing at TOA by dust aerosol is positive over land and negative or positive over sea , and its regional average values in Spring, Summer, Autumn , and Winter are 1.08 , 0.88 , 0.37 , 0.40W/m^2 , respectively. The solar radiative forcing is also positive over land and negative or positive over sea, but the infrared radiative forcing is positive in the modeling region. The radiative forcing values at the surface for four seasons are -5.64 , -2.25 , -1.37 , -1.87W/m^2, respectively. Radiative forcing is affected sensitively by the change of single scattering albedo of dust aerosol.

Fig 9.15 presents the daily total radiative forcings of dust aerosol for all 4 seasons. It can be seen that the radiative forcing is largest over northern desert and semidesert areas, which are near the source region of dust aerosol, with maximum values of 12 W/m^2 at Teng Ge Li desert and Badan Jilin desert (MAM), 10-12 W/ m^2 at northern desert area (JJA), 6 W/ m^2 Taklimakan desert (SON) and 2-8 W/m^2 northern deserts to Qin Lin Mountain (DJF) respectively. The radiative forcing over land is basically positive, except in South-East China for winter time, while over the ocean the radiative forcing is negative expect for autumn and much smaller than over land. The negative radiative forcing might be caused by absorption effect being compromised by the scattering effect of mineral dust aerosol in such regions.

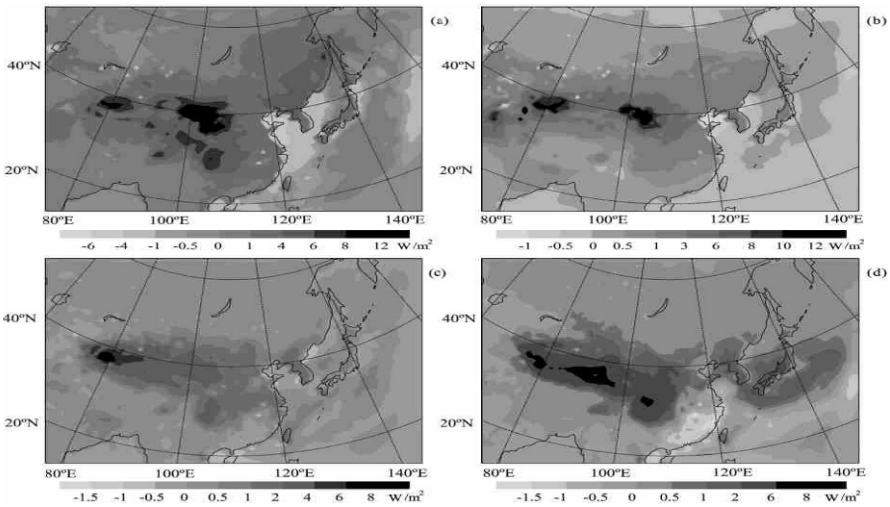

Fig. 9.15 Radiative forcing at the top of atmosphere (a) Spring (MAM) ; (b) Summer (JJA) ; (c)Autumn (SON); (d)Winter (DJF).

Above results give evidence to the fact that dust aerosol can increase incoming solar radiation over lands and decrease it over seas. Main radiative forcing centers lie in band between 35º ~ 40ºN in all seasons, with largest positive forcing locate over Teng Ge Li and Badan Jilin desert. Huang Hai Sea and Dong Hai Sea are negative centers, but it is positive value over north-west Pacific Ocean in all seasons especially 2 W/m^2 in winter. Radiative forcing of mineral dust can be changed by its vertical distribution, surface albedo besides its column burden, and its sign can change with situation.

Simulation Research of Radiative Forcing and Climate Responses of Black Carbon Aerosol in Spring Season Over East Asia Region

The distribution of black carbon (BC) aerosols from anthropogenic emission and biomass burning over East Asia region and their radiative effects with and without climate response during the spring time from year 2000 to 2004 have been simulated.

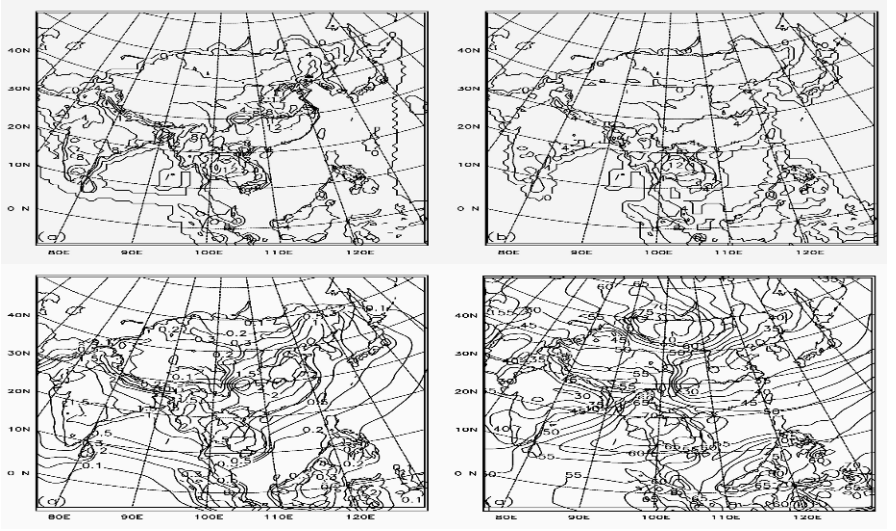

Fig. 9.16 Emission rate of BC (units: ng · m^{-2} · s^{-1}): (a)Anthropogenic and biomass burning emission; (b) Biomass burning emission, and Surface concentration of BC aerosols: (c) Concentration under total emission condition (μg/m^3), (d) Percentage contribution of biomass burning (%)

The emission rate of BC from Streets (2003) has been utilized in the

simulations. The inventory includes anthropogenic and biomass burning emissions, and it does not vary with model time. Fig.9.16a and Fig.9.16b shows the total emission rate (a, unit: ng/m^2s) and biomass burning rate only (b, unit: ng/m^2s). The main emission sources are located in India, Indo-China peninsula and east China, and the maximum value of $16ng/m^2s$ is in the middle of Indo-China peninsula.

The simulated distributions of surface concentration of BC are showed in Fig.9.16c and Fig.9.16d. Panel a plots the BC concentration under total emission condition. Indian peninsula, Indo-China peninsula and east of China apperently are high concentration regions where the concentration exceeds $1\mu g/m^3$. The BC concentrations over north India, Burma, part of Thailand, and east of China are greater than $2\mu g/m^3$. An extreme value of $2.5\mu g/m^3$ can be seen in Bengal, Sichuan basin of China and its adjacent area. On the other hand, there are only $0.2\text{-}1\mu g/m^3$ concentrations in Malaya and Indonesia, lower than $0.3\mu g/m^3$ in west of China, and less than $0.2\mu g/m^3$ in other regions. It is consistent with the averaged value of the observations from Feb. to Apr. in 1995 in Waliguan Mountain (Tang, 1999). The concentration in the north Zhejiang province in China is about $1.5\text{-}2\mu g/m^3$, which is also in the same range as the observation in Lin'an station in July and August 1991(Tang, 1999).

Fig.9.16d depicts the spatial variations of the percentage contributions of the biomass burning to the BC concentration. In East Asia, the contributions are higher in both south and north regions, but lower in east and west regions. The values are about 30%-45% in Indian peninsula, 55%-75% in Indo-China peninsula and 30%-40% in most parts of east China. The maximum value appears in the south of Burma and the north of Thailand. In mainland China, large contribution occurs in regions west of 100ºE, and its maximum is about 60%. In Malaya and Indonesia, the percentage is higher than 60%, even between 80% and 85% for some parts. There exists 55%-85% contribution in Mongolia.

Cloud coverage and cloud water path are two important factors influencing the direct effects of BC aerosols on the radiative forcing. Fig.9.17a and b plot the column averaged variation of cloud coverage and cloud water path for the case with climate response. Fig.9.17a shows that the cloud coverage over India Semi-continent, south of The Yangtze River of China, most of Indo-China peninsula and China south sea decrease. Even small amount of decreasing in the cloud coverage can dramatically change the radiative fluxes. The decreases of cloud coverage in these regions are consistent with the positive radiative forcing regions. Meanwhile, regions with increasing cloud coverage in part of low reaches of the Yangtze River and part of northern China are corresponding to the regions with negative ra-

diative forcing. Changes of cloud water showed in Fig.9.17b are mainly located in regions south of 10ºN and become smaller to the north of 10ºN. Unlike the cloud coverage, the changes of cloud water path show small scale spatial variation. It suggests that BC aerosols change the cloud water path primarily in convective clouds rather than in stratiform clouds. The locations of small centers with high radiative forcing are consistent with the centers of cloud water change in low latitude regions. Regions with increase of the cloud coverage also have increased cloud water path. Both changes of cloud coverage and cloud water path affect the distribution and the values of radiative forcing to the north of 10ºN, but the change of cloud water path has more prominent effects on the small centers of radiative forcing in regions south of 10ºN.

In simulations without the climate response, three main column burden regions, namely the Indian peninsula, the Indo-China peninsula, and the east of China, have been revealed. The column burden over these three regions exceeds 1mg/m^2. Pollutant from Indian peninsula can be transported into China, and affects the region between 25-30ºN in mainland China. Emission from the Indo-China peninsula can contribute to the column burden in south of 25ºN over China. The maximum horizontal flux of BC from Indo-China peninsula emerges in a level between 850-700hPa. BC from the east and north-east of China can pollute Korea peninsula and Japan due to the easterly wind. The inward flux of BC is larger than outward flux over China. It has more significant effect to the west and south of China than to the north due to the emission from other neighbour countries. With the assumption of no climate responses, BC aerosol increases the net downward radiative flux at TOA in both clear and all sky, but decreases it at the surface. The change over the Si Chuan basin area can be 4W/m^2 to the TOA flux, and -5.5W/m^2 to the surface flux.

In the other set of experiments, the climate responses to BC aerosol have been simulated, and the radiative forcing with climate responses and surface temperature change have been analyzed. The distribution patterns and the values of clear sky radiative forcing are similar under the condition of with or without climate responses, but all sky radiative forcing are different due to the variations in the cloud field. Cloud coverage and cloud water path are two important factors influencing the direct effects of BC aerosols to the radiative forcing. The decreased cloud coverage in the India Semi-continent, in the south of the Yangtze River of China, and in most regions of Indo-China peninsula and Chinese South Sea can affect dramatically the radiative fluxes, which results in positive radiative forcing over these regions. On the other hand, the cloud coverage increases over the low reaches of the Yangtze River and part of northern China. Changes of the cloud water path are mainly located to the south of 10ºN. BC aerosols have

more prominent effects on the cloud water path in convective clouds than in stratiform clouds. Changes in the cloud coverage and the cloud water path influence the distribution and the value of the radiative forcing in regions north of 10ºN. Changes in cloud water path are also responsible to the small centers of radiative forcing in regions south of 10ºN. BC aerosols decrease the surface temperature over 0.4K in mainland China except Tibet plateau, and increase it in the east and south of India, Tibet plateau and the Indo-China peninsula. BC aerosols induce excessive absorptions in the atmosphere especially in the low levels, which can lead to the temperature increase in the lower atmosphere. The temperature difference between the surface and lower atmosphere is reduced, so is the net surface sensible heat flux. The main reason of surface temperature decrease, however, is not due to the excessive surface sensible heat flux.

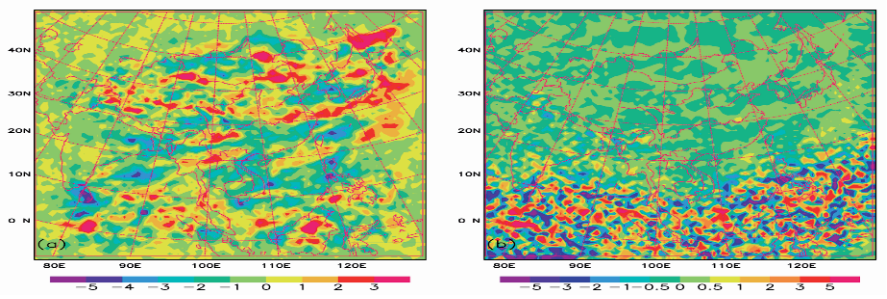

Fig. 9.17 Variation of cloud (a) change of coverage (amplified by 1000); (b) change of cloud water

9.6 Impact of human-induced large-scale land cover changes on the East Asian monsoon climate in RCM simulations

Both observational as well as theoretical studies have proved that human-induced large-scale land-cover changes, such as destructive forest harvesting and over-cultivation or over-grazing of grassland, have been one of the major causes for the deterioration of regional climate and environment (e.g. Charney 1975; Lean and Warrilow 1989; Nobre et al. 1991; Wei and Fu 1998; Pielke 2001c; Pielke et al. 1991; Xue 1996). The interaction between climate and land-cover over the Asia monsoon region is particularly strong in two respects: In terms of natural processes, the

highly variable monsoon climate with regard to precipitation and temperature, forces changes in function and structure of terrestrial ecosystems on various time scales through changing their physiological processes (Fu and Wen 1999). Long-term monsoon climate changes can even alter the biogeographic distributions of the ecosystems (An et al. 1990) and such changes bring about feedback effects on the monsoon climate itself (Xue 1996). On the other hand, the long history of civilization has caused significant changes in land cover over Asia. The human-induced land use and land-cover changes in East Asia, one of the largest regions of anthropogenic activities in the world, is particularly triking: in the past 3000 years, more than 60% of the region has been affected by the conversion of various categories of natural vegetation into farmland, grassland into semi-desert and widespread land degradation. Such human-induced land-cover changes result in significant changes to surface dynamic parameters, such as albedo, surface roughness, leaf area index and fractional vegetation coverage. The variation in the East Asian monsoon presented here is the result of land-cover changes only. It is likely that anthropogenic modification of the monsoon system would occur through changing the surface fluxes of energy, water and greenhouse gases under different land use patterns.

9.6.1 History of land-cover/-use changes over East Asia

The rapid industrialization and urbanization have caused the natural ecosystems in Asia, such as forest, grassland and wetlands, being replaced by farmland and other man-made ecosystems. For example, China was covered by various kinds of natural ecosystems in the early days except for a very narrow band of farmland along the lower reaches of the Yellow River basin. Since the 11th century B.C there has been a significant expansion of farmlands throughout China (Deng et al. 1983) into the upper reaches of the major river basins. Around the late 19th century, the land use pattern was set up much as it is today, although the land cover was continuously changing until recently. Currently nearly 80% of the total terrestrial area in China is covered by man-made ecosystems (Fu, 2003). Such human-induced land-cover changes have been as great in Asia as in any other part of the world, if not greater. To what extent has the monsoon system itself been modified by such changes? In this chapter numerical experiments using a high-resolution regional climate model are presented which examine the most likely response of the Asian monsoon system to human-induced land-cover changes.

9.6.2 Design of the numerical experiments

In East Asia the natural ecosystem has been modified to such a degree that its reconstruction is difficult except by modeling (Fu, 2003). However, it is feasible to give an estimate of the equilibrium land-use condition, by providing potential vegetation (Vp) that could could be obtained by the so-called biome approach (e.g. Prentice et al. 1992; Ojima 2000). Potential vegetation is computed from atmospheric and soil conditions only, and neglects any anthropogenic influence on the biosphere.

The current vegetation used in simulation is derived from ISLSCP Initiative I, also know as International Satellite Land Surface Climatology Project. It produces the global land-cover classification data as part of the global datasets for land-atmosphere models (ISLSCP, see also Sect. C.2.4) (Meeson et al. 1995). Although the current vegetation cover is somewhat different from that for 1987–1988, these differences are relatively smaller than the differences of what with the potential vegetation as described in the previous paragraph. Therefore, we assume that the vegetation cover data (Vc) can be looked upon as approximating the actual current vegetation cover. The human-induced land-cover change is defined as the difference between the potential and current vegetation, as presented by Fig.9.18. More than 80% of the region has been affected by conversion of various categories of natural vegetation into farmland, grassland into semi-desert and widespread land degradation. The most pronounced changes occur in north-west China where the grassland has been changed into semi-desert or desert and in East China where the forest has been replaced by crop lands. There are also significant changes over Japan.

A pair of numerical experiments is performed for the above two land-cover conditions by using the Regional Integrated Environmental Model System (RIEMS) version 1 (Fu et al. 2000). The validation study on the model performance has shown reasonably good results in its capacity to simulate the regional climate in the Asia monsoon region (Fu et al. 1998).

The differential fields of integration by the two vegetation cover datasets (current minus potential vegetation) are used to exemplify the impacts of the change in natural vegetation, since the two simulations are identical to each other for all conditions, including the large-scale driving fields used as the initial and lateral boundary conditions, the parameters of all physical processes, except for the vegetation cover. In order to maintain the linkages between the large-scale environment and the simulated region, a relaxation scheme with ten buffer zones is applied for nesting at the lateral boundary (Wei et al. 1998).

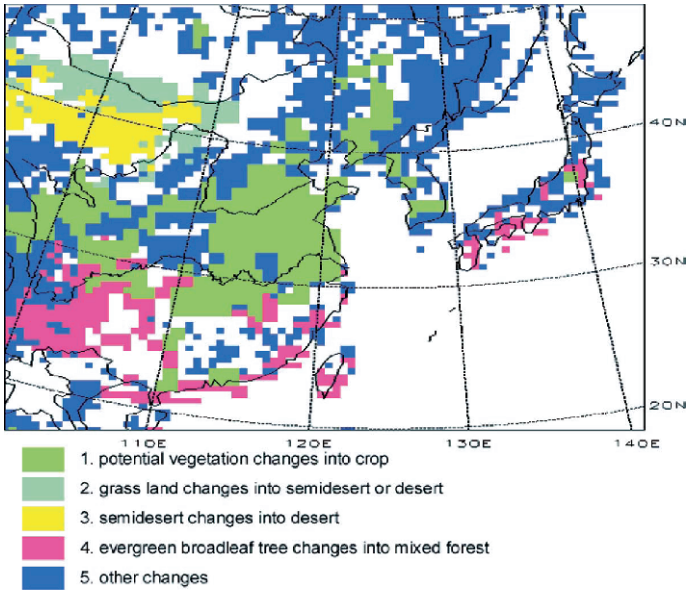

Fig. 9.18 Changes of vegetation cover from potential to current

9.6.3 Changes of surface dynamic parameters under two vegetation coverages

Changes in four main surface parameters, resulting from comparisons from potential to current vegetation distributions, are shown in Fig.9.19: albedo, surface roughness, leaf area index and total vegetation fractional coverage. In those areas where the natural vegetation (mainly forests) have been turned into farmland or where grasslands have been turned into semi-desert or desert (the green area shown in Fig.9.18), the significant decrease in surface roughness and leaf area index is shown in blue (Fig.9.19a,b); increase in albedo is shown in red (Fig.9.19c). The total fractional vegetation coverage is higher in the farmland area than in natural forests (the red area in Fig.9.19d), but is lower in the semi-desert and desert areas in comparison with grassland and in areas of mixed forests in comparison with evergreen broadleaf forests (the blue area in Fig.9.19d). Changes in these surface parameters would certainly modify the exchanges of energy and water between the land surface and the atmosphere and result in the changes in atmospheric circulation as shown in the next section.

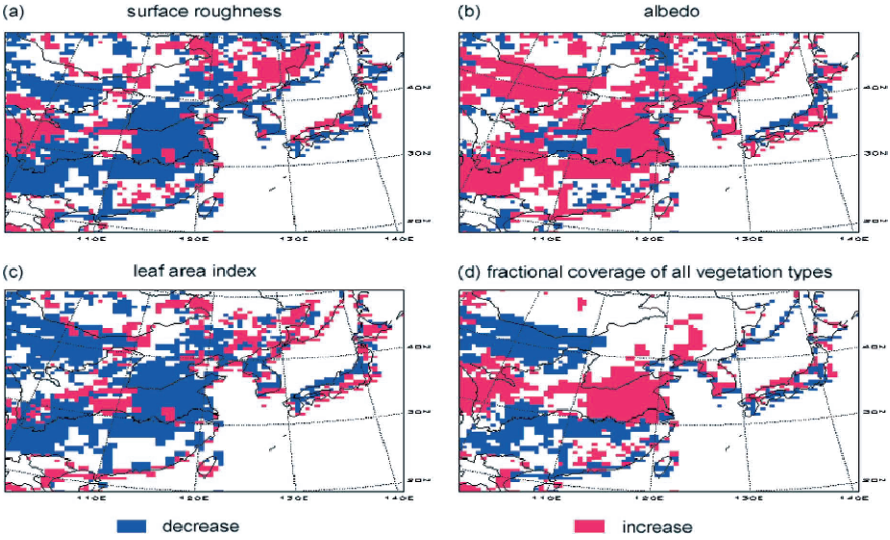

Fig. 9.19 Changes of surface dynamic parameters under two vegetation coverage

9.6.4 Changes of the East Asia monsoon by human-induced land-cover changes

To examine the potential modification of the East Asian monsoon system resulting from land-cover changes, the analyses focus here on the changes in the monsoon circulation and related surface climate. Fig.9.20a presents the mean changes of vector wind and geopotential height in the lower atmosphere in summer. The weakening of the monsoon depression is shown by the positive anomalies in the region to the south of 30°N and the weakening of summer monsoon are shown by the northerly anomalous flow. There is a negative departure in geopotential height over the northern part of the domain, representing the development of a low-pressure system over there, which brings about the anomalous north-west flow.

The changes in mean meridional circulation and zonal circulation are shown in Fig.9.20b, c with major characteristics of the enhancement of descending motion flows over 35–40°N and 100–115°E respectively, which would prevent the development of the summer monsoon circulation. Both these two northerly anomalous flows and the enhancement of descending motion over East Asia would prevent the northward transport of moisture, and the development of convective activities, resulting in more dry conditions in the atmosphere over most of the domain.

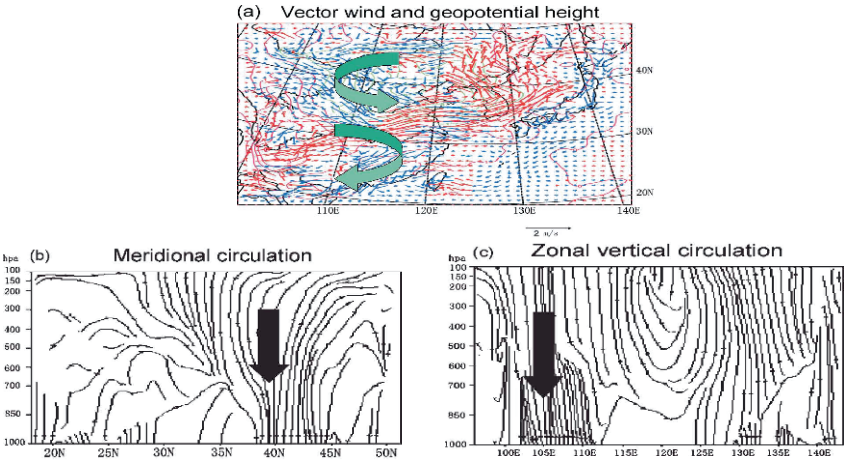

Fig. 9.20 Changes of summer monsoon circulation over East Asia under two vegetation covers (current minus potential) during summer (JJA). (a) vector wind and 850 hPa geopotential height in m (*blue*: north wind, *red*: south wind, pink: positive, *green*: negative); (b) mean meridional circulation along 100–120°E; (c) mean zonal circulation along 25–40°N

Fig.9.21 presents the changes in surface climate related to summer monsoon changes. All components of the surface water cycle, including precipitation (*a*), runoff (*b*) and soil moisture (*c*) are reduced over most of the region. It indicates the weakening of the water cycle through the deterioration of the natural vegetation. There are no significant changes in surface temperature except for a relative warming of an area in the northern China plain (Fig.9.21d), mainly related to the significant reduction in surface evaporation.

In contrast, the winter monsoon over East Asia becomes stronger with the deterioration in the natural vegetation cover, as shown by the strong anomalous northerly flow in the differential fields of vector wind and geopotential height at 850 hPa (Fig.9.22a). This circulation pattern would bring dry and cold air masses from inland down to all regions of East Asia, resulting in changes in the surface climate, for example the reduction of atmospheric humidity (Fig.9.22b) and precipitation (Fig.9.22c), mostly in the southern part of the region, and cold temperatures over almost the whole region (Fig.9.22d).

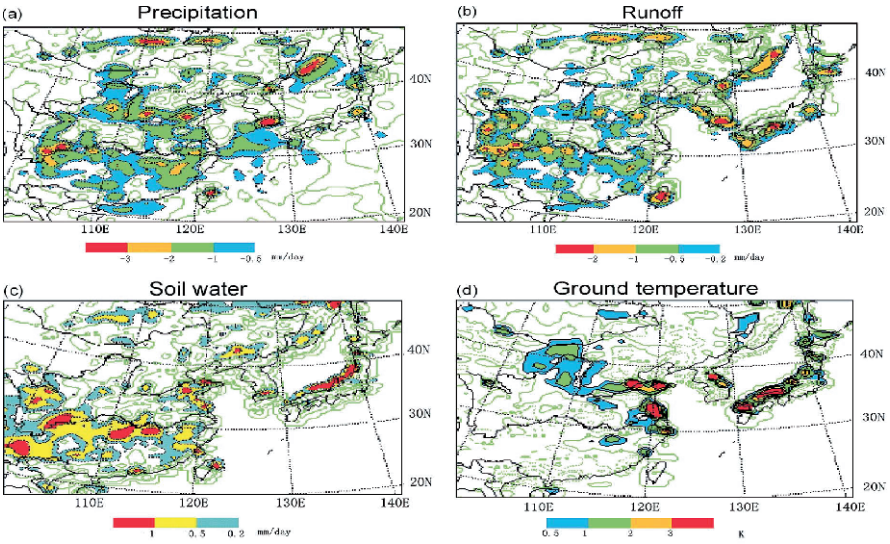

Fig. 9.21 Changes of surface climate over East Asia under two vegetation covers (current minus potential). (a) Precipitation (mm d^{-1}); (b) runoff (mm d^{-1}); (c) soil moisture (mm d^{-1}); (d) ground temperature (K)

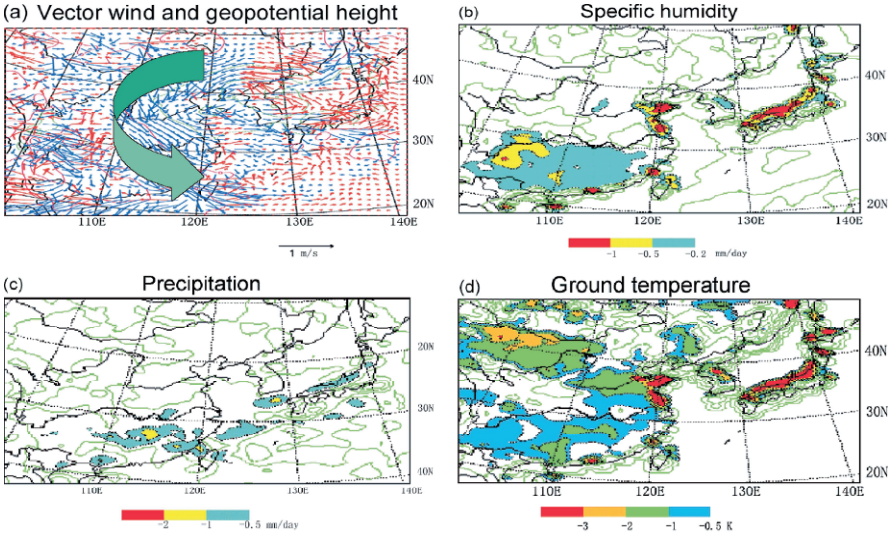

Fig. 9.22 Changes of winter (December, January, February) monsoon circulation and related surface climate. (a) Vector wind and geopotential height at 850 hPa in m (blue: north wind, red: south wind, pink: positive, green: negative); (b) surface humidity (g kg^{-1}); (c) precipitation (mm d^{-1}); (d) ground temperature (K)

9.6.5 Conclusions

According to the above analysis, human-induced land-cover changes have modified the monsoon circulation by the weakening of the summer monsoon and the enhancement of the winter monsoon over East Asia, which result in related changes in the surface climate over the region. The conclusions derived from the numerical experiments have been proven by observations. For example, the time evolution of the aridity index over East China since 1880, showing a significant trend in aridification during the last 120 years, with a 36-year period of oscillation (the Brucker period) superimposed on it (Fu 1994). Since the moisture condition over East China is mainly related to the intensity of the summer monsoon, it is a reflection of the weakening of the summer monsoon during that period. On a longer time scale, a 25 000-year lake level dataset for the Daihai Lake in Inner-Mongolia shows a significant reduction in its level, beginning about 3000 years ago (Wang, S. M., pers. comn.). There is also an indication of an aridification trend over Northern China and therefore the weakening of the summer monsoon since then. Over a much longer period, the proxy datasets of winter and summer monsoon indices from loess deposition show an overall dry trend since 2.5 Myears ago.

It seems that the deterioration in natural vegetation due to development of human society is one of the most important anthropogenic factors superimposed on the natural variability of the monsoon system.

9.7 Summary

RCMs were gradually applied in regional climate simulation over China and East Asia from 1990's. Many research works were conducted so far, such as the effects of vertical and horizontal resolutions, parameterizations of physical processes, effects of greenhouse and aerosol, and land vegetation and desertification, the cause of extreme climate incidents. The results demonstrate that RCM has the ability of simulating circulation and climate in China and East Asia.

RMIP results show that, the simulated temperature is generally lower than the observation and the simulated precipitation of most models is overestimated in most regions. In the view of models and the general average (misleading, models and general average means multi-model average) over continents, the annual temperature bias is -1.2°C (ranges between -2 – 0.6°C), and the annual precipitation bias is 3.5% (ranges between -31 – 35%). There are significant regional differences in simulation biases

of temperature and precipitation, e.g., the temperature and precipitation biases in the arid and semi-arid areas of northwest China are larger than that of other regions. The spatial distribution, interannual variability and the variation trend of temperature and precipitation in winter are better simulated than those in summer.-However the bias percentage of precipitation is larger in winter. The biases in large-scale forcings may be one of the most important reasons for the biases of regional model simulation.

The systematic analysis of 10-year integration in Asia from different regional climate modes (RCMs) shows that RCMs can simulate well the climatology in Asia, especially East Asia. The models can reproduce both climatological means and interannual variabilities of temperature and precipitation, as well as the extreme climate events; but to different degrees the biases exist in the model simulations. The biases of pressure and stream field are important reasons for the simulation errors of RCMs. The multi-models ensemble is one of effective methods to improve the simulated results. Parameterizations of physical processes, initial and boundary fields, horizontal and vertical resolutions, lateral boundary schemes, topography and the configuration of parameters have some influence on the simulation, but the dominant factors are dynamical framework of models, land surface processes and radiation schemes. Compared to GCMs and variable resolution global models, RCMs can improve the regional climate simulation remarkably and have higher reliabilities. But large uncertainties remain in RCM simulations, thus the deep and further study is needed for the improvement of RCMs.

References

An ZS, Xihao W, Yanchou L, De'er Z, Xiangjun S, Guangrong D (1990) A preliminary study on Paleoenvironment change of China during the last 20 000 years. In: Liu (ed) Loess, Quaternary geology, global change. Science Press, Beijing, pp 1–26

Anderson, C. J., and Coauthors (2003) Hydrologic processes in regional climate model simulations of the central United States flood of June–July 1993. *J. Hydrometeor*., 4, 584–598.

Anderson, C.J., R.W. Arritt, E.S. Takle, Z. Pan, W.J. Gutowski, Jr., R. da Silva, D. Caya, J. H. Christensen, D. Luthi, M.A. Gaertenr, C. Gallardo, F. Giorgi, R. Laprise, S.-Y. Hong, C. Jones, H.-M.H. Juang, J.J. Katzfey, J.L. McGregor, W.M. Lapenta, J.W. Larson, J.A. Taylor, G.E., Liston, R.A. Pielke Sr. and J.O. Roads (2003) Hydrological Processes in Regional Climate Model Simulations of the Central United States Flood of June-July 1993. *Journal of Hydrometeorology*, 4, 584-598.

Anthes, R. A. (19770 A cumulus parameterization scheme utilizing a one-dimensional cloud model. *Mon. Wea. Rev.*, 105, 270–286.

Anthes,R.A., and D. Keyser (1979) Tests of a fine-mesh model over Europe and the United States. *Mon. Wea. Rev.*, 107, 963–984.

B. M. Fekete, 2002: Calibration and validation of a regional climate model for pan-Arctic hydrologic simulation. *J. Climate*, 15, 3222–3236.

Betts, A. K., and M. Miller (1993) The Betts-Miller scheme. The Representation of Cumulus Convection in Numerical Models of the Atmosphere, K. A. Emanuel and D. J. Raymond, Eds., Amer. Meteor. Soc., 107–121.

Bonan, G. B. (1996) A land surface model (LSM version 1.0) for ecological, hydrological, and atmospheric studies: Technical description and user's guide. NCAR Tech. Note NCAR/TN-417+STR, 150 pp.

Briegleb, B. P. (1992) Delta-Eddington approximation for solar radiation in the NCAR Community Climate Model. *J. Geophys. Res.*, 97, 7603–7612.

Charney JG (1975) Dynamics of deserts and drought in the Sahel. *Q J Roy Meteor Soc* 101:193–202

Chaves RR, Ross RS, Krishnamurti TN (2005) Weather and seasonal climate prediction for South America using a multi-model superensemble. *Int J Climatol* 25: 1881-1914

Chen Ming, and Fu Congbin (2000) A nest procedure between regional and global climate model and its application in long term climate simulations. *Chinese J. Atmos. Sci.*, **24**(2), 253-262.(in Chinese)

Christensen J. H., B. Machenhauer, R. G. Jones, C. Schar, P. M. Ruti, M. Castro, and G. Visconti (1997) Validation of present-day regional climate simulations over Europe: LAM simulations with observed boundary conditions. *Climate Dyn.*, **13**, 489-506.

Curry, J. A., and A. H. Lynch (2002) Comparing Arctic Regional Climate Models. Eos, Trans. *Amer. Geophys. Union*, 83, 87.

D.scher, R., U. Willen, C. Jones, A. Rutgersson, H. Meier, and U. Hansson (2002) The development of the coupled ocean-atmosphere model RCAO. *Boreal Environmental Research*, 7, 183-192.

Deng JZ, Chuangjun W, Zhikang X (1983) General view of agriculture geography of China. Science Press, 334 pp

Déqué, M., and A. L. Gibelin (2002) High versus variable resolution in climate modelling. Research Déqué, M., and J. P. Piedelievre (1995) High resolution climate simulation over Europe. *Climate Dynamics*, 11, 321-339

Dickinson RE, Errico RM, Giorgi F, Bates GT (1989) A regional climate model for the western United States. *Climate Change* 15: 383-422

Dickinson, R. E., A. Henderson-Sellers, and P. J. Kennedy (1993) Biosphere-Atmosphere Transfer Scheme (BATS) Version 1e as coupled to NCAR Community Climate Model. NCAR Tech. Note 387+STR, 72 pp.

Dickinson, R. E., R. M. Errico, F. Giorgi and G. T. Bates (1989) A regional climate model for western United States. *Climate Change*, 15, 383-422.

Doblas-Reyes FJ, Hagedorn R, Parmer TN (2005) The rationale behind the success of multi-model ensembles in seasonal forecasting – II. Calibration and combination. *Tellus* 57A: 234-252.

Epstein E (1969) Stochastic dynamic prediction. Tellus 21: 739-759

Fasullo, J., and P. J. Webster (2002) Hydrological signatures relating the Asian summer monsoon and ENSO. *J. Climate*, 15, 3082–3095.

Feng J. M, Fu C.B. (2006) Inter-comparison of 10-year precipitation simulated by several RCMs for Asia. *Adv. Atmos. Sci.* 23(4): 531-542

Fox-Rabinovitz, M.S. et al. (2001) A variable-resolution GCM : Regional climate simulation, MWR, v. 129, No. 3, 453-469.

Fu CB (1994) An aridity trend in China in association with global warming. In: Zepp RG (ed) Climate-biosphere Interaction: biogenic emission and environmental effects of climate change. John Wiley & Sons, Chichester

Fu CB, Wei HL, Qian Y (2000) Documentation on a regional integrated environment model system (RIEMS version 1), TEACOM Science Report No.1, START Regional Committee for Temperate East Asia, Beijing, China, pp26

Fu CB, Wen G (1999) Variation of ecosystems over East Asia in association with seasonal, interannual and decadal monsoon climate variability. *Climatic Change* 43:477–494

Fu CB, Zeng ZM (1998) Monsoon regions: The highest rate of precipitation changes observed from global data. *Chin Sci Bull* 43: 662-666

Fu Congbin, Wang Shuyu, Xiong Zhe, and Feng Jinming (2004) Progress Report on Regional Climate Model Intercomparison Project for Asia. *Climatic and Environmental Research*, **9**(2), 225-239. (in Chinese)

Fu Congbin, Wei Helin and Chen Ming (1998) Simulation of the Evolution of Summer Monsoon Rainbelts over Eastern China from Regional Climate Model, *Chinese Journal of Atmospheric Sciences*, **22**(4), 522-534. (in Chinese)

Fu, C. B., and X. L. Teng (1993) Relationship between summer climate in China and the El Niño/Southern Oscillation phenomenon. Frontiers in Atmospheric Sciences, Allerton Press, 166–178.

Fu, C. B., S. Y. Wang, Z. Xiong, W. J. Gutowski, D. K. Lee, J. L. McGregor, Y. Sato, H. Kato, J. W. Kim, and M. S. Suh (2005) Regional climate model intercomparison project for Asia. *Bull. Amer. Meteor. Soc.*, 86, 257-266.

Fu, C.B., and Z. M. Zheng (1998) Monsoon regions: the highest rate of precipitation changes observed from global data. *Chin. Sci. Bull.*, 43, 662–666.

Fu, C.B., H. L. Wei, M. Chen, B. K. Su, and W. Z. Zhen (1998) Evolution of summer monsoon rain-belts over East China in a regional climate model. *Atmos. Sinica*, 22, 522–534.

GAO Xue_Jie , XU Ying , ZHAO Zong-Ci , Jeremy S. PAL, and Filippo GIORGI (2006) Impacts of Horizontal Resolution Simulation of East and Topography on the Numerical Asian Precipitation. *Chinese Journal of Atmospheric Sciences*, 30(2), 185-192.

GAO Xuejie, LIN Yihua, ZHAO Zongci, Filippo Giorgi (2003) Modelling the effects of anthropogenic sulfate in climate change by using a regional climate model. *Journal of Tropical Meteorology*, 19(2), 169-176.

GAO Xuejie, LIN Yihua, ZHAO Zongci, Filippo Giorgi (2004) Influence of greenhouse effect on climate in middle and lower reaches of the Yangtze River: numerical simulation. *Journal of Natural Disasters*, 13(1), 38-43.

GAO Xuejie, ZHAO Zongci, DING Yihui (2003) Climate Change Due to Greenhouse Effects in Northwest China as Simulated by a Regional Climate Model. *Journal of Glaciology and Geocryology*, 25(2), 165-169.

Gao Xuejie, Zhao Zongci, Ding Yihui, Huang Ronghui, and F. Giorgi (2001) Climate change due to greenhouse effects in China as simulated by a regional climate model. *Adv. Atmos. Sci.*, **18(6)**, 1224-1230.

Gao, Q., and M. Yu (1998) A model of regional vegetation dynamics and its application to the study of Northeast China Transect (NECT) responses to global change. *Global Biogeochemical Cycles*, 12(2), 329-344.

Gao, X.J., D.L. Li, Z.C., Zhao, and F. Giorgi (2003a) Climate Change Due to Greenhouse Effects in Qinghai-Xizang Plateau and Along the Qianghai-Tibet Railway. *Plateau Meteorology*, 22(5), 458-463 (in Chinese).

Gao, X.J., Y. Luo, W.T. Lin, Z.C. Zhao, F. Giorgi (2003b) Simulation of effects of landuse change on climate in China by a regional climate model. *Advances in Atmospheric Sciences*, 20, 583-592

Gao, X.J., Z.C. Zhao, Y.H. Ding, R.H. Huang, and F. Giorgi (2001) Climate Change Due to Greenhouse Effects in China as Simulated by a Regional Climate Model. *Advances in Atmospheric Sciences*, 18, 1224-1230.

Gates, W. L. (1992) AMIP: The Atmospheric Model Intercomparison Project. *Bull Amer. Meteor. Soc.*, **73**(12), 1962-1970.

Gibelin, A. L., and Déqué, M. (2003) Anthropogenic climate change over the Mediterranean region simulated by a global variable resolution model. *Clim. Dyn.* 20, 327-339

Giorgi F. (1990) Simulation of regional climate using a limited area model nested in general circulation model. *J. Climates*, **2**(3), 941-963.

Giorgi F., G.T.Bates and M.R.Marinucci (1993) Development of a second generation regional climate model. Part I: boundary layer and radiative transfer process, *Mon.Wea.Rev.*, **121**, 2794-2812.

Giorgi F., M.R.Marinucci and G.T.Bates (1993) Development of a second- generation regional climate model(RegCM2).Part II: Convective processes and assimilation of lateral boundary conditions, *Mon.Wea.Rev.*, **121**(10), 2814-2832.

Giorgi, F. (1990) Simulation of regional climate using a limited area model nested in a general circulation model. *J. Climate*, 3, 941-963.

Giorgi, F. (1991) Sensitivity of simulated summertime precipitation over the western United States to different physics parameterizations. *Mon. Wea. Rev.*, **119,** 2870-2888.

Giorgi, F., and Coauthors (2001) Regional climate change information—Evaluation and projections. Climate Change 2001: The Scientific Basis, J. T. Houghton et al., Eds., Cambridge University Press, 583–638.

Giorgi, F., and G. T. Bates (1989) The climatological skill of a regional model over complex terrain. *Mon. Wea. Rev.*, 117, 2325-2347.

Giorgi, F., and L. Mearns (1991) Approaches to the simulation of regional climate change: A review. *Rev. Geophys.*, **29,** 191-216.

Giorgi, F., and M. R. Marinucci (1991) Validation of a regional atmospheric model over Europe: Sensitivity of wintertime and summertime simulations to se-

lected physics parameterizations and lower boundary conditions. *Quart. J. Roy. Meteor. Soc.*, **117**(502), 1171-1206.

Giorgi, F., and R. Francisco (2000) Evaluating uncertainties in the prediction of regional climate change. *Geophys. Res. Lett.*, 27, 1295–1298.

Giorgi, F., G. T. Bates, and M. R. Marinucci (1993a) Development of a second generation regional climate model(RegCM2). Part I: Boundary layer and radiative transfer processes. *Mon. Wea. Rev.*, **121**, 2794-2813.

Giorgi, F., M. R. Marinucci, and G. T. Bates (1993b) Development of a second-generation regional climate model(RegCM2).Part II: Convective processes and assimilation of lateral boundary conditions. *Mon. Wea. Rev.*, **121**(10), 2814-2832.

Gong S L, Zhang X Y, Zhao T L, et al. (2003) Characterization of soil dust aerosols in China and its transport and distribution during 2001 ACE-Asia: 2. Model simulation and validation. *J. Geophys. Res.*, 108 (D9),4262, doi: 10.1029/2002JD002633

Gong Wei, and Li Weiliang (1997) Simulation of severe storm rainfall event in 1991 over Changjiang-Huaihe River valley with a Chinese regional climate model. *Quarterly Journal of Applied Meteorology*, **8**(3), 325-334. (in Chinese)

Govindasamy, B., K. Caldeira and P.B. Duffy (2003) Geoengineering Earth's radiation balance to mitigate climate change from a quadrupling of CO2. *Global and Planetary Change*, 37(1-2), 157-168.

Grell, G. A. (1993) Prognostic evaluation of assumptions used by cumulus parameterizations. *Mon. Wea. Rev.*, 121, 764–787.

Grell, G. A., J. Dudhia, and D. R. Stauffer (1995) A description of the Fifth-Generation Penn State/NCAR Mesoscale Model (MM5). NCAR Tech. Note NCAR/TN-398+STR, 117 pp. [Available online at www.mmm.ucar.edu/mm5/documents/mm5-desc-doc.html.]

Gutowski, W.J., F.O. Otieno, R.W. Arritt, E.S. Takle and Z. Pan (2004) Diagnosis and Attribution of a Seasonal Precipitation Deficit in a U.S. Regional Climate Simulation. *Journal of Hydrometeorology*, 5(1), 230-242

Houghton, J. T., L. G. Meira Filho, B. A. Callander, N. Harris, A. Kattenberg, and K. Maskell, Eds. (1995) Climate Change 1995: The Science of Climate Change. Cambridge University Press, 572 pp.

Houghton, J. T., Y. Ding, D. J. Griggs, M. Noguer, P. J. van der Linden, X. Dai, K. Maskell, C. A. Johnson, Eds. (2001) Climate Change 2001: THe Scientific Basis. Cambridge University Press, 881 pp.

Hulme, M., T. Wigley, Z. C. Zhao, F. T. Wang, Y. H. Ding, R. Leomans, and A. Markham (1992) Climate change due to greenhouse effect and implication for China. World Wildlife Fund, 57 pp.

Ju, J., and J. Slingo (1995) The Asian summer monsoon and ENSO. *Quart. J. Roy. Meteor. Soc.*, 121, 1133– 1168.

Kalnay, E., and Coauthors (1996) The NCEP/NCAR 40-Year Reanalysis Project. *Bull. Amer. Meteor. Soc.*, 77, 437–471.

Kang IS, Yoo JH (2006) Examination of multi-model ensemble seasonal prediction methods using a simple climate system. *Clim Dyn* 26: 285-294

Kato H, Nishizawa K, Hirakuchi H, et al. (2001) Performance of RegCM2.5/

NCAR-CSM nested system for the simulation of climate change in East Asia caused by global warming. *J Meteor Soc Japan* 79: 99-121

Kato H., H. Hirakuchi, K. Nishizawa, and F. Giorgi (1999) Performance of the NCAR RegCM in the simulations of June and January climates over eastern Asia and the high-resolution effect of the model. *J. Geophys. Res.*, **104**, 6455-6476.

Kato H., K. Nishizawa, H. Hirakuchi, S. Kadokura, N. Oshima, and F. Giorgi (2001) Performance of RegCM2.5/ NCAR-CSM nested system for the simulation of climate change in East Asia caused by global warming. *J. Meteor. Soc., Japan*, **79**, 99-121.

Kharin VV, Zwiers FW (2002) Climate Predictions with Multimodel Ensembles. *J Clim* 15: 793-799

Krinner, G., C. Genthon, Z. Li, and P.L. Van (1997) Studies of the Antarctic climate with a streched-grid general circulation model. *J. Geophys. Res.*, 102, 13,731-13,745.

Krishnamurti TN, Kishtawal CM, LaRow T, Bachiochi D, Zhang Z, Williford CE, Gadgil S, Surendran S (1999) Improved weather and seasonal climate forecasts from multimodel superensemble. *Science* 285: 1548-1550

Krishnamurti TN, Kishtawal CM, Zhang Z, LaRow T, Bachiochi D, Williford E, Gadgil S, Surendran S (2000) Multimodel ensemble forecasts for weather and seasonal climate. *J Clim* 13: 4196-4216

Lau, W., and S. Yang (1996) Seasonal variation, abrupt transition, and intraseasonal variability associated with the Asian summer monsoon in GLA GCM. *J. Climate*, 9, 965–985.

Lean J, Warrilow DA (1989) Simulation of the regional climate impact of Amazon deforestation. *Nature* 342:411–413

Lee D. K, and M. S. Suh (2000) Ten-year East Asian summer monsoon simulation using a regional climate model(RegCM2), *J. Geophys. Res.*, **105**, 29565-29577.

Lee D. K, and Y. Kim (1992) Variability of East Asian summer monsoon during the period of 1980-1989. *Journal. of Korean Meteorological Society*, **28**(3), 315-331.

Lee, D. K., and H. S. Kang (1999) Coupling of the NCAR/LSM into the MM5 and its application for the East Asian summer monsoon. Preprints, Ninth PSU/NCAR Mesoscale Model Users' Workshop, Boulder, CO, NCAR, 198–201.

Leith, CE (1974) Theoretical skill of Monte Carlo forecast. *Mon. Wea. Rev.* 102: 409-418

Leung L. R., S. J. Ghan, Z. C. Zhao, Y. Luo, W. C. Wang, and H. L. Wei (1999) Intercomparison of regional climate simulation of the 1991 summer monsoon in eastern Asia *J. Geophys. Res.*, **104,** 425-454.

Liguang Wu, Qiang Zhang, and Zhihong Jiang, (2006) Three Gorges Dam affects regional precipitation, *Geo. Res. Lett.*, 33, L13806, doi:10.1029/2006GL026780.

Liu Yongqian, and Ding Yihui (1995) A review of the study on simulation of regional climate. *Quarterly Journal of Applied Meteorology*, **6**(2), 228-239. (in

Chinese)
Liu Yongqian, Ding Yihui, and Zhao Zongci (1996) A Regional Climate Simulation of the High Precipitation over the Changjiang-Huaihe Valley in 1991. *Model Study on the Short-term Climate Prediction in China*. China Meteorological Press, Beijing 106-120. (in Chinese)
Liu, Y., F. Giorgi, and W. M. Washington (1994) Simulation of summer monsoon climate over East Asia with an NCAR regional climate model. *Mon. Wea. Rev.*, 122, 52–62.
Liu, Y., R. Avissar, and F. Giorgi (1996) Simulation with the regional climate model RegCM2 of extremely anomalous precipitation during the 1991 East Asia flood: An evaluation study. *J. Geophys. Res.*, 101, 26 199–26 215.
Lorant, V and J-F Roye (2001) Sensitivity of Equatorial Convection to Horizontal Resolution in Aquaplanet Simulations with a Variable-Resolution GCM, MWR, Vol. 129, No. 11, pp. 2730–2745.
Lorenz EN (1963) Deterministic non-periodic flow. J Atmos Sci 20: 130-141
Lorenz, P, and D. Jacob (2005) *Geophys. Res. Lett.*, VOL. 32, L18706, doi:10.1029/2005GL023351, 2005
Lu Er, and Ding Yihui (1997) Nature of precipitation and activity of cumulus convection during the 1991 Meiyu season. *Acta Meteorologica Sinica*, **55**(3), 318-534. (in Chinese)
Luo Yong, and Zhao Zongci (1997) Numerical simulation of East Asian regional climate with NCAR RegCM2. *Quarterly Journal of Applied Meteorology*, **9**(Suppl.), 124-133. (in Chinese)
Luo Yong, Wang Shaowu, Dang Hongyan, and Zhao Zongci (2002) Recent advances in climate models and model intercomparison projects, *Adv. Earth Sciences*, **17**(3), 372-377. (in Chinese)
Mabuchi, K., Y. Sato, and H. Kida (2002) Verification of the climatic features of a regional climate model with BAIM. *J. Meteor. Soc. Japan*, **80**, 621-644.
Mabuchi,K.,Y.Sato, and H. Kida (2002) Verification of the Climatic Features of a Regional Climate Model with BAIM, *J. Meteor. Soc. Japan*, 80, 621-644.
Maslanik, J.A., A.H. Lynch, M.C. Serreze, and W. Wu (2000) A case study of regional climate anomalies in the Arctic: performance requirements for a coupled model. *Journal of Climate*, 13, 383-401.
May, W. and E. Roeckner (2001) A time-slice experiment with the ECHAM4 AGCM at high resolution: The impact of horizontal resolution on annual mean climate Change. *Climate Dynamics*, 17, 407-420.
McAvaney, B. J., and Coauthors (2001) Model evaluation. Climatc Change 2001: The Scientific Basis, J. T. Houghton et al., Eds., Cambridge University Press, 474–526.
McGregor, J. L. (1996) Semi-Lagrangian advection on conformal-cubic grids. *Mon. Wea. Rev.*, 124, 1311-1322.
McGregor, J. L., K. C. Nguyen and J. J. Katzfey (2002) Regional climate simulations using a stretched-grid global model. Research Activities in Atmospheric and Oceanic Modelling. [Ritchie, H. (ed.)]. Report No. 32 WMO/TD- No. 1105, 3.15-16.
McGregor, L. J. (1997) Regional climate modelling. *Meteor. Atmos. Phys.*, 63,

105–117.
McGregor, L. J., and J. J. Katzfey (1998) Simulating typhoon recurvature with a variable resolution conformal-cubic model. Research Activities in Atmospheric and Oceanic Modeling, WMO/TD-No.942, 3.19-3.20.
Mearns, L. O., and Coauthors (2001) Climate scenario development. Climate Change 2001: The Scientific Basis, J. T. Houghton et al., Eds., Cambridge University Press, 741–770.
Meier, H.E.M., R. D.scher and A. Halkka (2004) Simulated distributions of Baltic sea-ice in warming climate and consequences for the winter habitat of the Baltic Sea ringed seal. Ambio, 33, 249-256.
Mizuta, R., T. Uchiyama, K. Kamiguchi, A. Kitoh and A. Noda (2005) Changes in extremes indices over Japan due to global warming projected by a global 20-km-mesh atmospheric model. SOLA, 1 153-156.
Mukai M, Nakajima T, Takemura T. (2004) A study of long-term trends in mineral dust aerosol distributions in Asia using a general circulation model. *J. Geophys. Res*., 109, D19204, doi: 10.1029/2003JD004270
Nobre C, Sellers P, Shukla J (1991) Amazonian deforestation and the regional climate change. *J Climate* 4:957–988
Pal, J. S., F. Giorgi, and Bi Xunqiang (2004) Consistency of recent European summer precipitation trends and extremes with future regional climate projections. *Geophys. Res. Lett*., **31(13)**, L13202(1-4).
Pal, J.S., F. Giorgi and X. Bi (2004) Consistency of recent European summer precipitation trends and extremes with future regional climate projections. *Geophys. Res. Lett*, 31, L13202.
Palmer TN, Alessandri A, Andersen U, et al. (2004) Development of A European Multimodel Ensemble System for Seasonal-to-Interannual Prediction (DEMETER). *Bull Amer Meteor Soc* 85: 853-872
Peng P, Kumar A, van den Dool H (2002) An analysis of multimodel ensemble predictions for seasonal climate anomalies. *J Geophys Res* 107, 4710, doi:10.1029/2002JD002712
Pielke RA, Dalu GA, Snook JS, Lee TJ, Kittel TGF (1991) Nonlinear influence of mesoscale land use on weather and climate. J Climate 4:1053–1069
Quan, X. W., H. F. Diaz, and C. B. Fu, 2003: Interdecadal change in the Asia-Africa summer monsoon and its associated changes in global atmospheric circulation. Global Planet. Change, 37, 171–188.
Rinke, A., R. Gerdes, K. Dethloff, T. Kandlbinder, M. Karcher, F. Kauker, S. Frickenhaus, C. Koeberle, and W. Hiller (2003) A case study of the anomalous Arctic sea ice conditions during 1990: Insights from coupled and uncoupled regional climate model simulations, *Journal of Geophysical Research*, 108, 4275, doi: 10.1029/2002JD003146.
Rummukainen, M., S. Bergstr.m, G. Persson, J. Rodhe and M. Tjernstr.m (2004) The Swedish Regional Climate Modelling Programme, SWECLIM: a review. Ambio, 33, 176-182.
Sasaki, H., Y. Sato, K. Adachi, and H. Kida (2000) Performance and evaluation of the MRI regional climate model with the spectral boundary coupling method. *J. Meteor. Soc. Japan*, 78, 477–489.

Schrum C., Hübner U., Jacob D., Podzun R. (2003) A coupled atmosphere/ice/ocean model for the North Sea and the Baltic Sea. *Climate Dynamics*, 21, 131-151

Shi Xueli, Ding Yihui, and Liu Yiming (2001) Simulation experiments of summer rainbelt in China with the regional climate model. *Climatic and Environmental Research*, **6**(2), 249-254. (in Chinese)

Small, E:, F. Giorgi, and L. C. Sloan (1999) Regional climate model simulation of precipitation in central Asia: Mean and interannual variability, *J. G. R.*, 104, 6563-6582.

Takle E. S., and coauthors (1999) Project to Intercompare Regional Climate Simulations(PIRCS): Description and initial results. *J. Geophys. Res.*, **104,** 443-462.

Takle ES, Gutowski WJ, Arritt RW, et al (1999) Project to Intercompare Regional Climate Simulations (PIRCS): Description and initial results. *J Geophys Res* 104: 19443-19462

Tang Jianping (2004) Regional Climate Model (MM5v3 Coupled with Land Surface Process) and East-Asian Climate Simulation. Doctoral Paper, Department of Atmospheric Sciences, Nanjing University, China, 1-158. (in Chinese)

Tang Jianping, Su Bingkai, Zhao Ming, Zhao Deming (2004) Long term climate change numerical simulation in east Asia. *Acta Meteorologica Sinica* (in Chinese) 62(6): 752-763

Tao, S., and L. Chen (1987) A review of recent research on the East Asian summer monsoon in China. Monsoon Meteorology, C.-P. Chang and T. N. Krishnamurti, Eds., Oxford University Press, 60–92.

Wang Huijun (1997) The Advance of the Atmospheric Model Intercomparison Project(AMIP). *Chinese J. Atmos. Sci.*, **21**(5), 633-637. (in Chinese)

Wang Shaowu, and Zhu Jinhong (1997) Atmospheric Model Intercomparison Project(AMIP). *Quarterly Journal of Applied Meteorology*, **8**(Suppl.), 92-99. (in Chinese)

Wang Shiyu, and Qian Yongfu (2003) Seasonal and Interannual Variation Simulation of the Regional Climate of East Asia by a Nine-Level P-σ Regional Climate Model. *Chinese Journal of Atmospheric Sciences*, 27(5), 798-810. (in Chinese)

Wang Shiyu, and Zhang Yaocun (1999) Simulation of regional climate over eastern China with different regional climate models. *Plateau Meteorology*, **18**(1), 28-38. (in Chinese)

Wei HL, Fu CB, Wang WC (1998) Impacts of lateral boundary condition treatment of a regional climate model on the East Asia summer monsoon precipitation. *Sci. Atmos. Sin.* 22:779–790

Wei, H. L., W. J. Gutowski Jr., C. J. Vorosmarty, and Wu, G. X., and Y. S. Zhang (1998) Tibetan Plateau forcing and the timing of the monsoon onset over South Asian and the South China Sea. *Mon. Wea. Rev.*, 126, 913–927.

Wei, H., W.J. Gutowski, C.J. Vorosmarty, B.M. Fekete (2002) Calibration and validation of a regional climate model for pan-Arctic hydrologic simulation. *Journal of Climate*, 15, 3222-3236

Wu J , Fu C B , Jiang WM, et al. (2005) A preliminary simulation study of direct

radiative forcing of mineral dust aerosol over the East Asia region. *CHINESE JOURNAL OF GEOPHYSICS* (in Chinese), 48 (6), 1250-1260.

WU Jian , WANG Weiguo , XIE Yingqi , GUO Shichang , Chen Xinmei , LUO Yan (2003) Interactive coupling of regional climate model and atmospheric chemistry model over China area. *Journal of Yunnan University,* 25 (1), 41-47.

WU Jian , JIANG Weimei , LIU Hongnian , TANG Jianping (2002) Simulation of the direct and indirect radiative effects of sulfate aerosol. *ACTA SCIENTIAE CIRCUMSTANTIAE*, 22(2), 129-134.

WU Jian , LUO Yan , WANG Weiguo (2005) The comparison of different simulation methods for the climate responses of the radiative forcing of anthropogenic sulfate aerosol over east Asia. *Journal of Yunnan University*, 27(4), 323-331.

WU Jian , WANG Weiguo , GUO Shichang , XIE Yingqi , CHENG Xinmei (2002) The numeric simulation of the dist ribution and t ransportation of SO2 and sulfate aerosol in China area. *Journal of Yunnan University*, 24 (3), 204-210.

Wu Jian, Jiang Weimei et al. (2002) Using Regional Climate Model and Atmosphere Chemical Model to Model Regional Climate and Ozone in Troposphere over China. *Journal of Nanjing University*, 38(4), 572-582. (in Chinese)

Xie, P., and P. A. Arkin (1997) Global precipitation: A 17-year monthly analysis based on gauge observations, satellite estimates, and numerical model output. *Bull. Amer. Meteor. Soc*., 78, 2539–2558.

Xiong Zhe (2004) Evolutionary Character of Climatology over East Asia by RIEMS. *Climatic and Environmental Research*, 9(2), 296-302.

Xiong Zhe (2004) The Multiyear Surface Climatology of RIEMS over East Asia. *Climatic and Environmental Research*, 9(2), 251-260.

Xiong Zhe, Wang Shuyu, Zeng Zhaomei, and Fu Congbin (2003) Analysis of simulated heavy rain over the Yangtze River valley during 11-30 June 1998 using RIEMS. *Adv. Atmos. Sci.*, **20**, 815-824.

Xue Y (1996) The impact of desertification in the Mongolian and Inner Mongolian grassland on the regional climate. *J Climate* 9:2173–2189

Xue, M., K.K. Droegemeier, V. Wong (2000) The Advanced Regional Prediction System (ARPS) - A multi-scale nonhydrostatic atmospheric simulation and prediction model. Part I: Model dynamics and verification. *Meteorology and Atmospheric Physics*, 75(3 – 4), 161-193.

Yu, R., W. Li, X. Zhang, Y. Liu, Y. Yu, H. Liu, and T. Zhou (2000) Climate features related to Eastern China summer rainfall in the NCAR CCM3. *Adv. Atmos. Sci.*, 17, 503–518.

Yun WT, Stefanova L, Krishnamurti TN (2003) Improvement of the multimodel superensemble technique for seasonal forecasts. J Clim 16: 3834-3840

Yun WT, Stefanova L, Mitra AK, Vijaya Kumar TSV, Dewar W, Krishnamurti TN (2005) A Multi-model Superensemble algorithm for Seasonal Climate Prediction using DEMETER Forecasts. *Tellus* 57A: 280-289

Zhao Zongci, and Luo Yong (1997) Simulations of summer monsoon over East Asia: Inter-comparisons of three regional climate models, *Quarterly Journal of Applied Meteorology*, **8**(Suppl.), 116-123. (in Chinese)

Zhao Zongci, Luo yong (1998) Advance on investigations of Regional Climate

Modelling since 1990, Acta Meterologica Sinica, 56(2), 225-246. (in Chinese)
Zhao, Z. C., and F. T. Wang, 1994: Climate change and cropping systems in China. Bull. CNC-IGB, 3, 52–62.
Zheng Yiqun, and Qian Yongfu (2002) Effects of initial/lateral boundary conditions on regional climate simulations. *Chinese J. Atmos. Sci.*, **26**(6), 794-806. (in Chinese)

Chapter 10 Projection of Future Climate in China

10.1 Introduction

Projections of the global climate changes have been studied for the last 20~30 years. Several IPCC scientific assessment reports have provided numerous investigations around the world (IPCC, 1990, 1992, 1996, 2000 and 2001).

Chinese studies on the projected climate changes started at the end of 1980s, which was later than the developed countries. Originally, most studies have concentrated on the future climate change over East Asia and China due to the doubled CO_2 as simulated by the overseas atmospheric general circulation models (AGCMs) with the mixed-layer ocean and sea ice thermodynamic models (AMOGCMs) (Zhao and Kellogg, 1988; Zhao, 1989; Hulme et al., 1992; Wang and Zhao, 1994; Wang and Zhao, 1995). A few studies have used their own AMOGCM provided by the Institute of Atmospheric Physics (IAP) (Wang et al., 1992). During 1991 to 1995, IAP, Chinese Academy of Meteorological Sciences (CAMS), Peking University and National Oceanic Administration took part in a key project on climate change in China due to the human activities held by National Science and Technology Administration of China. Based on the overseas AMOGCMs and regional models, several Chinese research groups have set up a few AMOGCMs and used those global and regional climate models to examine the impacts of human activities on climate change in East Asia and China (Chen and Song, 1996; Chen et al., 1996; Li and Gong, 1996; Wang et al., 1996; Yu et al., 1996). In order to reduce the uncertainties, the multi-model ensembles have been conducted to detect the future climate change in China due to the doubled CO_2 (Zhao et al., 1996). All the studies have pointed out the obvious warming with the different ranges in China due to the doubled CO_2. The precipitation might also change, but the results simulated by the different models have varied greatly (Zhao et al., 2000; Wang et al., 2001).

Based on the climate modeling under 80 various human emission scenarios, more than 10 Chinese research groups have simulated the climate change for the 21^{th} century and the results are summarized in Fig. 10.1,

which shows the annual mean temperature and precipitation anomalies and their upper and lower limits. All of the projections provide a warming of 0.7~7.0℃ by the late periods of the 21st century with the spatial mean as 4.0℃. The predicted precipitation increases in a range of -3~20% with the spatial mean of 11%. The mean lower and upper limits of the temperature change are 2.8℃ and 5.1℃, respectively, while the lower and upper limits of the precipitation change are 7% and 14%, respectively. The projections also indicate that it is unlikely for the temperature change to be lower than 0.7℃ or higher than 7.0℃. It is also unlikely for the precipitation change to be lower than -3% or higher than 20%.

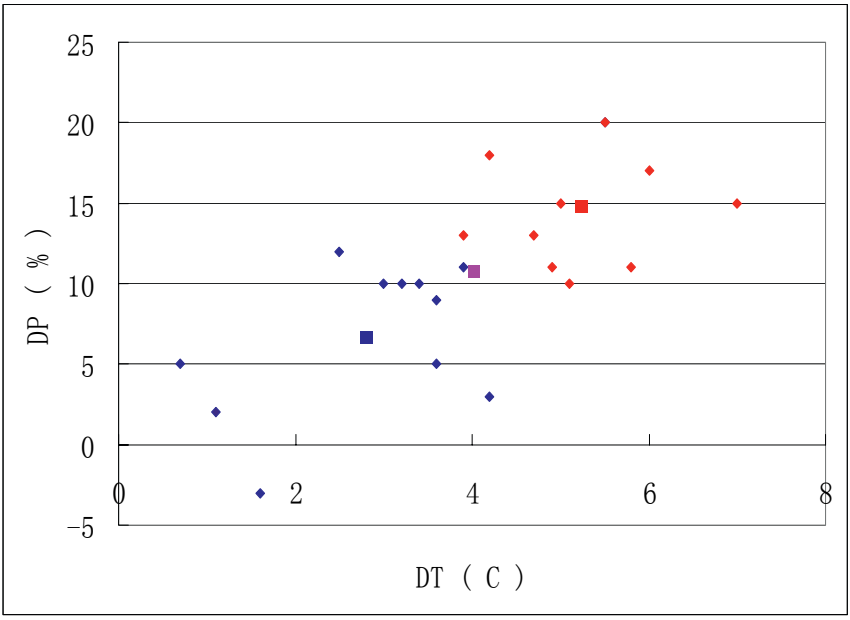

Fig. 10.1 Annual mean temperature and precipitation changes for the late periods of the 21st century relative to the present time, big triangle is the lower limit, big rhombus is the upper limit, big square is total mean. DT represents the departure of temperature, DP is the departure of precipitation (based on Zhao and Li，1997； Zhao et al.，2000；Li and Power，2000；Chen and Fu, 2000; Guo et al.，2001；Gao et al., 2001, 2002, 2003a, 2003b; Zhao and Xu，2002；Shi et al.，2002；Wang et al.，2003；Zhao et al.，2002，2003，2004；Ding et al.，2004)

In order to examine the projected climate change in China, three main

methods have been used by Chinese scientists for the last 10 years. The first is modeling method. Multi global coupled models and climate system models have been chosen, such as the Chinese models named IAP/NCC T63, GOALS, FGOALS-g1.0, BCC_CM1 and the overseas models named CCC, CCSR/NIES, CSIRO, DKRZ, GFDL, HADL and NCAR, as well as IPCC 4th Assessment Report (IPCC AR4) models. Various human emission scenarios are considered: (1) a doubling greenhouse gases, (2) 1% increasing greenhouse gases, (3) IPCC IS92 six scenarios, (4) IPCC Emissions Scenarios of the Special Report on Emissions Scenarios (SRES) A1 (medium-level), (5) A2 (high-level), (6) B1 (low-level), (7) B2 (medium-level), and (8) A1B (medium-level). Most of these research have focused on the climate change in China for both the 20th and 21st centuries (Zhao and Li, 1997; Zhao et al., 2000; Li and Power, 2000; Guo et al., 2001; Zhao and Xu, 2002; Shi et al., 2002; Wang et al., 2003; Zhao et al., 2002, 2003, 2004; Ding et al., 2004; Luo et al., 2005; Xu et al., 2005; Jiang et al., 2008a). Second method is dynamic downscaling. The regional climate models with the high resolutions (20~60km) over China nested with the global climate models have been used to project the future climate change in China and its sub-regions. A doubling greenhouse gases, 1% increasing greenhouse gases and sulfate aerosols, IPCC SRES A2 and B2 have been used in the research (Chen and Fu, 2000; Gao et al., 2001, 2002, 2003a, 2003b; Luo et al., 2005; Xu et al., 2005, 2006). The third method is statistical downscaling. Chinese scientists started to use the statistical downscaling methods later than the dynamic downscaling method. A couple of studies have concentrated on these methods such as correlations and regressions. The predictands are monthly temperature and precipitation in the China sub-regions with SRES A2 and B2 scenarios (Fan et al., 2006).

For the recent two years, using fine resolution global and regional climate dynamic models or statistical downscaling methods, the climate changes in East Asia and China due to the various anthropogenic scenarios have been projected (Luo et al., 2005; Xu et al., 2005; Xu et al., 2005, 2006; Jiang et al., 2008a; Fan et al., 2006). Several modeling groups have joined the IPCC AR4 intercomparison project. These new results are going to be introduced in the following sections.

10.2 Projections of changes in temperature

10.2.1 Global climate modeling

There are two main experiments using global climate models to pro-

ject the future temperature changes over China. The first one is the near-equilibrium or transient experiment, i.e. the equilibrium climate sensitivity derived from doubled CO_2 or the transient climate response at the CO_2 doubling in 1 %/yr or 2%/yr CO_2 increasing experiment. Table 10.1 gives the temperature changes in East Asia due to the doubled CO_2 by Chinese scientists (Li et al, 1995; Chen et al, 1996; and Guo et al, 2001), and it is seen that the annual mean temperature will increase by 1.4~3.6℃, with the average temperature increase of 2.2℃ and the winter temperature increase (2.7℃) is greater than the summer one (1.8℃).

Table 10.1 Annual and seasonal mean temperature changes (℃) over the East Asia region due to the doubled CO_2 (Based on Li et al, 1995; Chen et al, 1996; and Guo et al, 2001, Unit ℃)

Model	DJF	MAM	JJA	SON	YEAR
LASG/CGCM	4.5	3.5	2.5	3.7	3.6
LASG/GOLAS	2.4	2.3	1.7	1.9	2.1
OPYC	2.3	2.0	1.8	2.1	2.0
LSG	2.5	1.6	1.2	1.7	1.7
NCAR	1.4	1.7	0.9	1.5	1.4
GFDL	2.8		2.4		2.6
MEAN	2.7	2.2	1.8	2.2	2.2

Another is the projections of the 21st century climate changes under various IPCC SRES scenarios. Global coupled models and climate system models have been performed to simulate climate changes in China for both the 20th and 21st centuries and the future climate changes in China with IPCC SRES scenarios calculated will be compared relative to the 1961-1990 climate. Table 10.2 summarizes projections of the linear trends of the annual mean temperature over the China with various emission scenarios in the 21st century by Chinese scientists in the past 10 years (Luo et al, 2005; Xu et al, 2005; and Jiang et al, 2008a). The warming trend in the 21st century estimated by various models in the GG (greenhouse gases increasing only) experiments ranges from 3.0℃ to 9.2℃/100yr, with the average of 4.9℃/100yr, while in the GS (both greenhouse gases and sulfate aerosols increasing) experiments, it ranges from 0.0℃ to 6.9℃/100yr, with the average of 2.9℃/100yr. The averaged warming trend for SRES A2 scenario is 5.0℃/100yr, with a range of 2.5~8.9℃/100yr; and it amounts to 4.2℃/100yr and 3.0℃/100yr for A1B and B2 scenarios, respectively, and to 2.7℃/100yr for B1. For the end of the 21st century, for the A2 scenario annual mean temperature change in China from multi global coupled models compared to 1961 to 1990 is 5℃, and for A1B, the mean temperature

change is about 4℃, for B1 and the smallest, about 2.7℃. It is worth noting in Table 10.2 that Jiang et al's results (2008a) are based on the projections of global climate system models provided by the IPCC AR4 Program of Climate Model Diagnosis and Intercomparison (PCMDI); Table 10.3 provides the basic information of the models. The warming trends under the same emission scenario projected by the various IPCC AR4 models are quite consistent, and the ensemble standard deviation of the warming trends is far smaller than that by the previous old models, which suggests that the uncertainty of the projected temperature change over China in the 21st century has been reduced.

Table 10.2 Warming trend (℃/100yr) of annual mean temperature in China in the 21st century under various emission scenarios (* for East Asia)

Source	Model name	GG	GS	A2	A1B	B2	B1
Luo et al, 2005	CCC	9.2	6.9	5.4		2.9	
	CCSR	5.1	3.9	8.9		5.4	
	CSIRO	3.9	3.5	5.1		3.3	
	DKRZ	4.7	0.7				
	GFDL	3.0	2.5	3.8		2.5	4.7
	HADL	4.1	3.1	5.2		2.9	
	NCAR	4.0	-0.3				
	ECHAM4-OPYC			2.5		1.2	
Xu et al, 2005	NCC/IAP T63			5.1*	3.6*		
Above model mean		4.9	2.9	5.2		3.0	
Above model standard deviation		1.9	2.2	1.8		1.2	
Jiang et al, 2008a	CGCM3.1			4.6	3.0		1.7
	CNRM-CM3			5.0	3.8		1.8
	CSIRO-Mk3.0			3.7	3.0		1.8
	GFDL-CM2.0			5.3	4.6		2.5
	GFDL-CM2.1			4.7	4.4		2.2
	GISS-ER			3.9	2.9		1.7
	INM-CM3.0			5.1	3.6		2.4
	IPSL-CM4			5.7	5.1		3.1
	MIROC3.2(medres)			5.4	5.0		3.2
	ECHO-G			6.0	5.6		3.3
	UKMO-HadCM3			5.7	5.0		3.3
	ECHAM5/MPI-OM			5.7	5.5		3.7
	PCM1			3.2	2.7		
	IPCC AR4 model mean			4.9	4.2		2.6
	model standard deviation			0.8	1.0		0.7
Ensemble mean		4.9	2.9	5.0	4.2	3.0	2.7
Ensemble standard deviation		1.9	2.2	1.3	1.0	1.2	0.9

Table 10.3 Basic information for the 13 climate system models of the IPCC AR4

Country, center	Model name	References
Canada, CCCMA	CGCM3.1	Kim et al. (2002)
France ,CNRM	CNRM-CM3	Salas y M´elia et al.(2005)
Australia ,CSIRO	CSIRO-Mk3.0	Gordon et al. (2002)
USA, GFDL(CM2.0)	GFDL-CM2.0	Delworth et al.(2005)
USA, GFDL(CM2.1)	GFDL-CM2.1	Delworth et al. (2005)
USA, GISS	GISS-ER	Schmidt et al. (2005)
Russia, INM	INM-CM3.0	Volodin and Diansky (2004)
France, IPSL	IPSL-CM4	Marti et al. (2005)
Japan,CCSR/NIES/FRCGC(med-res)	MIROC3.2(medres)	K-1 model developers (2004)
Germany / Korea, MIUB(Germany), Institute of KMA (Korea), and Model and Data Group.	ECHO-G	Min et al.(2005)
UK,UKMO(Hadcm3)	UKMO-HadCM3	Gordon et al. (2000)
Germany, MPI	ECHAM5/MPI-OM	Jungclaus et al. (2005)
USA,NCAR(PCM1)	PCM1	Washington et al. (2000)

Based on the projections of the temperature changes for the three marker scenarios (SRES A2, A1B, and B1) by the IPCC AR4 13 models of CGCM3.1, CNRM-CM3, CSIRO-MK3.0, GFDL-CM2.0, GFDL-CM2.1, GISS-ER, INM-CM3.0, IPSL-CM4, MIROC3.2 (medres), ECHO-G, UKMO-HadCM3, ECHAM5/MPI-OM, and PCM1, the multi-model ensemble projections of the annual and seasonal mean temperature changes in different period of the 21st century relative to the period 1961 to 1990 in China are listed in Table 10.4. Differences between the increased ranges of annual and seasonal mean temperatures in the period of 2021-2050 relative to the 1961-1990 under the three marker scenarios are small, and the increases in annual mean temperature under the A2, A1B, B1 scenarios are 1.7℃, 1.8℃, and 1.5℃, respectively. However, the differences become large in the late 21st century (2071-2100), with the largest increase of 4.2℃ for the A2 scenario, and medium and smaller increases of 3.7℃ and 2.7 ℃

for the A1B and B1 scenarios, respectively. Differences among seasonal warming under the three marker scenarios are consistent, with the largest range of warming in the winter, and a lower or almost the same range in the other seasons. It was found in comparison with the previous projections (Luo et al, 2005; Zhao et al, 2000) that the intensity of warming in the IPCC AR4 model projections is slightly reduced, and differences among the seasonal warming are also reduced.

In order to know the geographic distribution of temperature changes in China for the 21st century, Fig. 10.2 displays the mean annual temperature changes of the 13 models for the years 2071 to 2100 relative to the period 1961 to 1990. It can be seen that distributions of warming under the A2 and B1 scenarios are basically consistent, with the maximum warming in the Tibetan plateau, the secondary one in Northeast China, Northwest China, and North China, and a smaller and northwestward consecutive increase in the other regions. Warming in the late 21st century (2071 to 2100) is the largest under the scenario A2, with a 4.6~5.2℃ increase in the Tibetan plateau, about 4.5℃ in Northeast China and North China, and 3.0~4.0℃ in the Yangtze valley and the region south of the Yangtze river, warming is least under the scenario B1, with an increase of 2.8~3.2℃, 2.8℃, and 2.0~2.5℃ in the above corresponding regions; and in-between under the scenario A1B, with warming generally 0.4℃ less than those under the scenario A2. Comparing temperature change patterns for various seasons (not shown) in the late 21st century, it shows that no matter under what marker scenario, except the summer, patterns of seasonal temperature increases are consistent with those of annual temperature changes, i.e. the maximum warming occurs in the Plateau region, Northeast China, and Northwest China, and the warming increases northwestwards in the other regions. However, the large warming area for the summer lies in Northeast China and Northwest China, but it is not evident in the Plateau region. The maximum warming under the three marker scenarios occurs all in the winter, for example under the A2 scenario, warming ranges from 3.0 to 5.8℃ in the winter, from 2.8 to 5.4℃ in the spring, and from 2.8 to 5.0℃ in the summer and the autumn.

Based on the IPCC-DDC model projections, Luo et al. (2005) analyzed temperature changes under various emission scenarios in China for the late 21st century (not shown), and the results indicate that the maximum warming all occurs in Northeast China and Northwest China, which, in comparison with the above results of the IPCC AR4 model projections, suggests the significant enhancement of warming in the Tibetan Plateau in the IPCC AR4 model. Recently, using the observed data, the ERA40 data, and the IPCC AR4 coupled climate model simulations, Duan et al. (2006) investigated the observed warming over the Tibetan Plateau in the past 50 years,

and argued that the impact of accelerated GG emission on climate was more remarkable over the Plateau than other regions in the world. In view of the unique geographic character of the Tibetan Plateau and the sensitivity of climate changes to its treatment, as well as uncertainties in model projections, further studies on projections of future climate changes over the Plateau are required.

Table 10.4 The multi-model ensemble mean projections of annual and seasonal mean temperature changes in China for the years 2021 to 2050, 2071 to 2100 relative to the period 1961 to 1990 (Unit ℃) (multi-model standard deviation in parentheses)

Time period	Annual		
	A2	A1B	B1
2021-2050	1.67 (0.40)	1.81 (0.36)	1.49 (0.36)
2071-2100	4.20 (0.74)	3.74 (0.79)	2.67 (0.60)
	Winter		
	A2	A1B	B1
2021-2050	1.89 (0.59)	2.04 (0.51)	1.63 (0.48)
2071-2100	4.68 (0.95)	4.15 (0.94)	2.98 (0.68)
	Spring		
	A2	A1B	B1
2021-2050	1.61 (0.47)	1.66 (0.44)	1.41 (0.48)
2071-2100	4.03 (0.86)	3.59 (0.87)	2.54 (0.70)
	Summer		
	A2	A1B	B1
2021-2050	1.58 (0.47)	1.76 (0.49)	1.45 (0.42)
2071-2100	4.03 (0.90)	3.56 (0.93)	2.57 (0.67)
	Autumn		
	A2	A1B	B1
2021-2050	1.62 (0.50)	1.79 (0.45)	1.45 (0.43)
2071-2100	4.06 (0.90)	3.67 (0.86)	2.60 (0.66)

10.2.2 Regional climate modeling

For recent years, another two regional climate models with the human emission scenarios have been used by Chinese scientists to project the climate change in China for the 21st century. One is the RegCM2/CN nested inside the CSIRO, which is coupled with the AOGCM. The horizontal resolution of the RegCM2/CN is 60km. First, the model control runs simulate the present for five years. Then, the sensitivity experiments simulate the climate for five years (around year 2070) considering the

greenhouse gases increasing (GG) or both greenhouse gases and sulfate aerosols increasing (GS), respectively (Gao et al., 2001, 2002; Luo et al., 2005). Another regional climate model used in China is the PRECIS. Its horizontal resolution is 50km and is nested within the HadAM3H. The PRECIS runs the present time for 30 years (1961~1990). Then, it projects the future climate change over China with SRES A2 and B2 for 2070~2079 and 2071~2100, respectively. Based on the analyses of linear trends, the climate change over China and the sub-regions for the other periods of the 21st century is also projected by PRECIS (Xu et al., 2005, 2006).

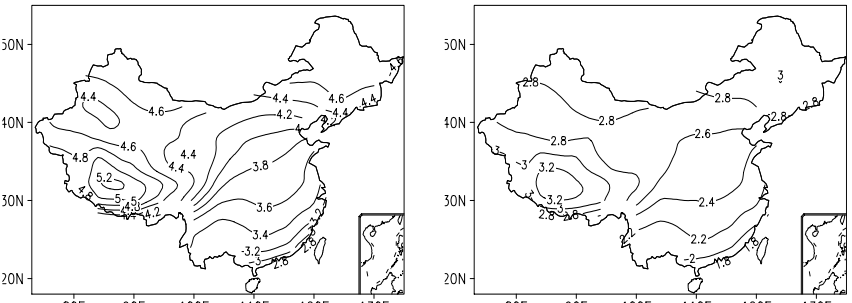

Fig. 10.2 The multi-model ensemble annual mean changes of temperature under (a) the SRES scenarios A2 and (b) the SRES scenarios B1 for the years 2071 to 2100 relative to the period 1961 to 1990. The multi-models include IPCC AR4 13 models of CGCM3.1, CNRM-CM3, CSIRO-MK3.0, GFDL-CM2.0, GFDL-CM2.1, GISS-ER, INM-CM3.0, IPSL-CM4, MIROC3.2(medres), ECHO-G, UKMO-HadCM3, ECHAM5/MPI-OM, and PCM1

Two regional climate models have an agreement to project the obvious warming of 2.6~3.9℃ over China for the late periods of the 21st century relative to 1961~1990. PRECIS projects a warmer climate than RegCM2/CN (see Table 10.5). The warmer values of 3.0~4.5℃ over Northern China (Northeast, Northwest and North China) are more noticeable than 2.0~2.5℃ over Southern China (Central China, Eastern, South and Southwest China). For four seasons comparison, more warming in the winter (DJF) from the RegCM2/CN is shown, especially in Northern China. But PRECIS does not indicate those seasonal change characteristics (see Fig.10.3). Besides, monthly mean temperature changes as projected by RegCM2/CN with GG provide the warmest change in December and less warming in March and September (Figures are not shown).

Zhang Yingjuang et al. (2006) nested the regional climate model RIEMS

into GOALS/LASG，to study the effect of CO_2 gradually increasing on future temperature change over China. The result is demonstrated in 9.5.1

Table 10.5 Projected temperature change over China for the future three periods relative to 1961~1990 by PRECIS with SRES A2 and B2（Xu et al.，2005），and by RegCM2/CN with GG and GS (in the bracket) (Gao et al., 2001) (Unit: ℃）

Periods	A2	B2
2011~2020	1.0	1.2
2041~2050	2.1	2.2
2071~2080	3.9 （GG 2.7）	3.2 （GS 2.6）

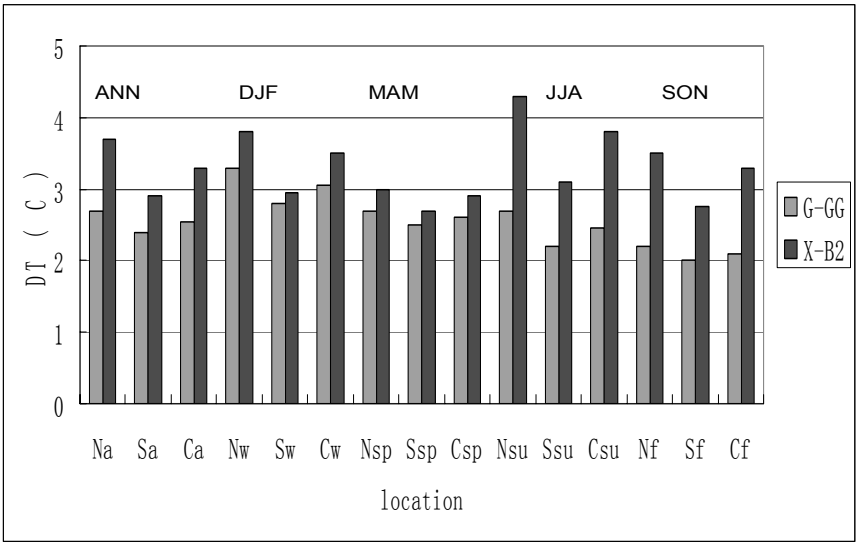

Fig. 10.3 RegCM2/CN and PRECIS projected annual and seasonal mean temperature changes over China (C), Northern China (N) and Southern China (S) for the late periods of the 21st century relative to 1961~1990 (unit: °C), light black is RegCM2/CN (Gao et al., 2001), heavy black is PRECIS (Xu et al., 2005)

10.2.3 Statistical downscaling

There are only a few studies on the application of statistical downscaling technique in China. Fan et al. (2006) first applied statistical downscaling technique to downscale the monthly mean temperatures in Northern China

and at the 562 observational stations in China in January and July (Fan，2006). Due to large area of China, the whole area is divided into seven sub-domains for research, including Northwestern China (I), Northern China (II), Northeastern China (III), Southwestern China (IV), Middle China (V), Eastern China (VI), Southern China (VII)(Figures are not shown). The combination of sea level pressure and 850-hPa temperature is selected as predictors. Statistical downscaling technique based on multiple linear regressions of predictor principal components (PCs) is applied. A stepwise screening procedure is adopted for selecting skilful PCs as predictors used in the regression equation. Finally, the statistical downscaling models are applied to HadCM3 SRES A2 and B2 scenarios to project local future climate change scenarios in China (see Fan 2006 for details).

In January, there is an increase of more than 1 ℃ in the Northern China and less than 1 ℃ in the south during the period of 2021 to 2050 compared to the period of 1961 to 1990. The downscaled temperatures during the period of 2071 to 2099 are significantly warmer than those during the period of 2021-2050 and there is an increase above 1 ℃ in most areas of China, especially above 4 ℃ in some areas of Northwestern China and Northeastern China. There is only a small increase of below 1℃ in most areas in July during the period of 2021 to 2050 relative to 1961 to 1990 and the temperatures in the north of China will become warmer during the period of 2071 to 2099 than those of 2021-2050, while there is a little difference in the south of China between the two periods of 2021 to 2050 and 2071 to 2099. By the comparison of the downscaled results of A2 and B2 scenarios, the downscaled temperatures under A2 scenario will become warmer in most areas than those under B2 scenario, especially in the north of China (Figures are not shown).

Figs 10.4a and 10.4b show that statistically downscaled temperature change in annual mean for the years 2070 to 2099 relative to the period 1961 to 1990 using HadCM3 SRES A2 scenario and B2 scenario. The B2 forcing yields much smaller warming than the A2 forcing, but the spatial patterns of the sensitivities for the two different forcing scenarios are very similar. There is a much more significant warming in the north of China than in the south and a maximum of warming in North Xinjiang, which is much warmer than 3 ℃ under A2 scenario and 2℃ under B2 scenarios. In most areas of Qingzang Plateau and in the south of China, there is a much smaller warming than 1.5 ℃ under A2 scenario and 1.2 ℃ under B2. Especially, there is a minimum of warming in the southwestern and the foremost south of China.

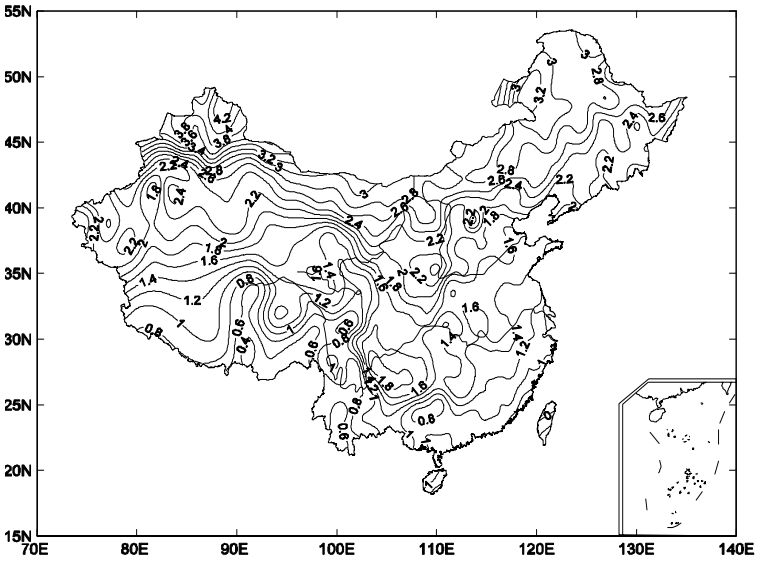

(a)

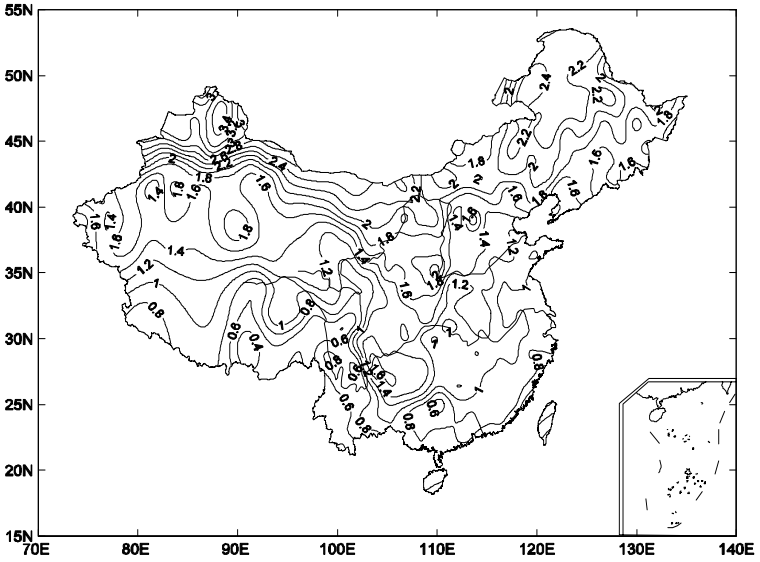

(b)

Fig. 10.4 Downscaled temperature change in annual mean (unit: ^{o}C) for the years 2070 to 2099 relative to the period 1961 to 1990 using HadCM3 （a）SRES A2 scenario and (b) SRES B2 scenario.

A number of statistically downscaled temperature scenarios are presented for 562 locations in China. Based on HadCM3 and CSIRO global climate scenarios, different choices of predictors are taken by employing a technique based on stepwise linear regression of PCs and the choice of predictors varies with different regions. The 30 different temperature scenarios are estimated for each location in Northwestern China and Southwestern China and the 21 scenarios in other areas. The ensemble mean of these scenarios is used as a first order measure of the most likely extrapolation of the current climatic trends. (See Fan 2006 for details).

This analysis brings out a common signal in the various scenarios. The estimated temperatures become warmer under A2 and B2 scenarios in the north than in the south and in January than that in July. In January, the warming trends in the 21st century are 5~6℃/100yr in Northern Xinjiang and Northeastern China and 2~3 ℃/100yr in Northern China, Middle China, Eastern China and Southwestern China under A2 scenario. The warming trends are 3~4℃/100yr and 2~3℃/100yr in most stations in Northeastern China and Northwestern China, respectively, and 1~2℃/100yr in Northern China, Middle China, Eastern China and Southwestern China under B2 scenario. In July, the warmest area is Northeastern China, where the warming trends are 2~2.5℃/100yr under A2 scenario. The warming trends are 1~1.5℃/100yr in Northwestern China, Northern China, Middle China and Eastern China but less than 1℃/100yr in Southwestern China and Southern China under A2 scenario. Under B2 scenario, the warming trends in the north are lower than under A2 scenario by 1℃/100yr, whereas, there is a similar temperature trend between A2 and B2 scenarios in other areas. In January, the standard deviations are by far smaller than the trends, thus, the signal-to-noise ratio is sufficiently high to pick out a common pattern among the various scenarios; In July, the warming trends are weak and the inter-model scatter is of a similar magnitude over Southwestern China and Southern China, making it difficult to identify any common characteristics if they ever exist (Figures are not shown).

10.3 Projections of changes in precipitation

10.3.1 Global climate modeling

The impact of human activities on precipitation in the 21st century is more complicated in comparison with temperature, due to a relatively lower capability of global climate models in simulating precipitation, and there are larger differences in the 21st century precipitation projections in China among different models under various emission scenarios.

However， there are also two main experiments to predict the future precipitation changes by Chinese scientists (Li et al, 1995; Chen et al, 1996; and Guo et al, 2001). Table 10.6 gives the predicted precipitation changes in East Asia at doubled CO_2 scenario. It can be seen that annual rainfall is all projected to increase, with an averaged 9% increase in East Asia. Differences in projected seasonal precipitation changes show that remarkable increase occurs in the spring and the summer in studies before the mid-1990s, but in recently years, researches indicate the increase occurs mainly in the winter.

Table 10.6 Percentage changes in annual and seasonal precipitation in East Asia at doubled CO_2 (Based on Li et al, 1995; Chen et al, 1996; and Guo et al, 2001, Unit %)

Model	DJF	MAM	JJA	SON	YEAR
LASG/CGCM	-1.3	11.2	14.9	7.6	9.8
LASG/GOLAS	22.0	3.3	-2.1	5.5	5.0
OPYC	7.0	20.3	10.5	6.8	11.2
NCAR	4.8	12.3	13.1	6.9	9.3
MEAN	8.1	11.8	9.1	6.7	8.8

Table 10.7 summarizes projections of the linear trend of annual rainfall in East Asia and China in the 21st century by Chinese meteorologists using multiple climate models in the past 10 years (Luo et al, 2005; Xu et al, 2005; and Jiang et al, 2008a). In general, future precipitation projected by most models shows an increasing trend, but differences in the projections by different models are larger, the linear trends of precipitation changes in the 21st century range from -78 to 286 mm/100yr, and the standard deviation of the linear trends under the A2 scenario reaches 80.5 mm/100yr. However, differences in projections of the linear trends by IPCC AR4 models are obviously reduced, and the linear trends range from 4 to 190 mm/100yr, with a centurial average of 95mm/100yr, 86 mm/100yr, and 56 mm/100yr under the A2, A1B, and B1 scenarios, respectively. The maximum standard deviation of the linear trends under various emission scenarios is only 35mm/100yr. All those suggest that uncertainty in precipitation simulation has been improved in the IPCC AR4 models. According to projections of the IPCC AR4 models under the A2 scenario, the increasing trend of precipitation in China is 11%/100yr in the 21st century, and the annual rainfall increases by about 9% in the late 21st century (2071-2100) relative to the period of 1961 to 1990. And under the B1 scenario, the increasing trend is 7%/100yr. Most IPCC AR4 models project that winter rainfall increases remarkably, for example, under the A2 scenario, the rain-

fall in the late 21st century increases by an average 23% in winter, and by 4.9% in summer relative to the period of 1961 to 1990, and under the B1 scenario the rainfall increases by 15.3% and 4.5% in winter and summer, respectively.

Table 10.7 Projections of annual rainfall trends (mm/100yr) and their percentages (the ratio of annual rainfall in China to the long-term (1961–1990) averaged annual rainfall over the same region) (%/100yr; in parentheses) under various emission scenarios in China in the 21st century (for East Asia)

Source	Model name	GG	GS	A2	A1B	B2	B1
Luo et al., 2005	CCC	-78	-72	55		8	
	CCSR	144	84	153		107	88
	CSIRO	36	12	91		75	
	DKRZ	84	48				
	GFDL	72	36	231		115	
	HADL	120	120	286		187	
	NCAR	-48	108				
	ECHAM4-OPYC			-56		-48	
Xu et al., 2005	NCC/IAP T63	24	-60	9.8%*	5.2%*		
Above model mean		47	48	127		74	
Above model SD		77	61	78		53	
Jiang et al., 2008a	CGCM3.1			154 (19)	154 (19)		53 (7)
	CNRM-CM3			85 (9)	87 (9)		40 (4)
	CSIRO-Mk3.0			40 (7)	20 (3)		32 (5)
	GFDL-CM2.0			116 (15)	137 (18)		98 (13)
	GFDL-CM2.1			124 (16)	38 (5)		45 (6)
	GISS-ER			110 (10)			58 (5)
	INM-CM3.0			31 (3)	32 (3)		4 (0)
	IPSL-CM4			44 (6)	68 (9)		52 (7)
	MIROC3.2(medres)				136 (16)		109 (13)
	ECHO-G				62 (9)		41 (13)
	UKMO-HadCM3			190 (22)	162 (19)		132 (16)
	ECHAM5/MPI-OM			41 (5)	58 (7)		7 (1)
	PCM1			53 (6)	77 (9)		
IPCC AR4 model mean				95 (11)	86 (10)		56 (7)
IPCC AR4 model SD				35 (6)	23(6)		26 (5)
Ensemble mean		47	48	103	86	74	58
Ensemble SD		77	61	81	23	53	37

Table 10.8 The multi-model ensemble projections of annual and seasonal precipitation percent changes in China for the years 2021 to 2050, 2071 to 2100 relative to the period 1961 to 1990 (Unit %) (multi-model standard deviation in parentheses)

Time period	Annual		
	A2	A1B	B1
2021-2050	2.8 (6.2)	3.7 (6.3)	3.9 (5.2)
2071-2100	9.0 (10.1)	9.8 (9.6)	7.2 (7.7)
	Winter		
	A2	A1B	B1
2021-2050	11.5 (19.5)	11.9 (19.6)	10.2 (17.3)
2071-2100	22.6 (27.0)	23.2 (26.3)	15.3 (19.1)
	Summer		
	A2	A1B	B1
2021-2050	0.3 (10.8)	1.4 (11.1)	1.3 (9.7)
2071-2100	4.9 (16.5)	6.0 (15.5)	4.5 (12.5)

The geographic distribution of projected precipitation (Fig.10.5) shows that under different emission scenarios the annual rainfall increases remarkably in North China, Northwest China, and Northeast China, but changes a little in the Yangtze River basin and the region south of the Yangtze River. In the late 21st century (2071-2100), the annual rainfall under the A2 scenario will increase 15% to 21% relative to 1961-1990 in North China, Northwest China, the north of Northeast China, and the south fringe of the Tibetan Plateau and by less than 5% in the region south of the Yangtze River; and under the B1 scenario it increases by nearly 15%, 15%, and 10% in North China, Northwest China, and Northeast China, respectively, and by less than 4% in the south of the Yangtze River. With regard to seasonal changes of projected precipitation, the percentages of precipitation increase in the winter are higher than in the summer (not shown). Under the scenario A2 the winter rainfall increases by more than 30% in most areas north of 35^{o}N, by about 10% in the middle-lower reach of the Yangtze River, and decreases in South China and the south fringe of the Tibetan Plateau; and the summer rainfall increases mostly in the south fringe of the Plateau and the north of Northwest China (10%), but slightly (less than 5%) in Eastern China, and reduces by 10% in the east of Northwest China.

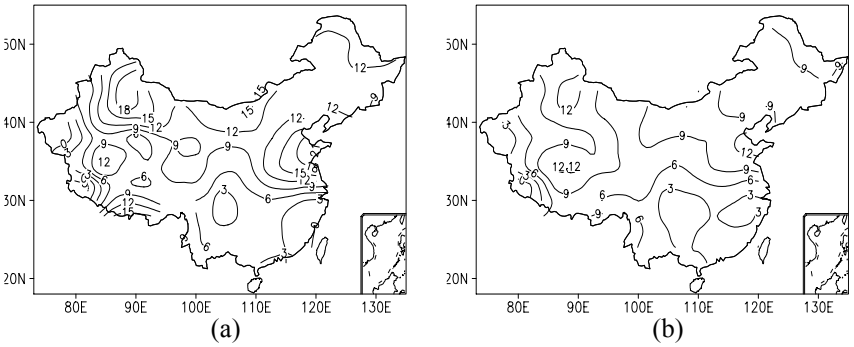

Fig. 10.5 As in Fig. 10.2 except for annual precipitation percentage changes

10.3.2 Regional climate modeling

Similar to the projections of the temperature, two regional climate models RegCM2/CN with GG and GS scenarios and PRECIS with SRES A2 and B2 also have projected the precipitation changes over China and subregions for the 21st century. Both the models have consistently projected an increasing precipitation by about 10~14% in China for the late periods of the 21st century relative to 1961~1990 (see Table 10.9). Generally speaking, RegCM2/CN projects a larger increase in precipitation than that by PRECIS (see Table 10.9). But the patterns of the annual mean precipitation changes projected by the two regional models are quite different. The larger increase in precipitation of 0.5~1.5 mm/day for the late periods of the 21st century relative to 1961~1990 by PRECIS occurs over Southern China, North China and Tibetan Plateau. But RegCM2/CN projects more precipitation of 20~30% over Northwest and Northeast China, as well as some southern parts of South China. The drying regions are also very different, such as Hainan province, some parts of Guangdong, Sichuan and Jilin provinces by PRECIS; Hebei and Liaoning provinces, as well as some parts of Yangtze River valley by RegCM2/CN (Figures are not shown).

For seasonal precipitation changes, the two models have projected the larger increase in precipitation in four seasons of the late periods of the 21st century relative to 1961~1990 over China, North and South China, except for PRECIS over South China in the winter. A remarkable increase in precipitation by about 40~50% in Northwest China for winter might occur as projected by two models. The two models have projected another increase in precipitation by about 10~20% over Southern China in the summer and Northern China in the spring, respectively (see Fig.10.6).

Besides, based on the monthly mean precipitation projections over China by the RegCM2/CN with GG, most months might become wetter by 6~25% for the late periods of the 21st century than 1961~1990, especially for January and August. April and September might become drier by -4 ~ -7% than 1961~1990 (Figures are not shown).

Using the regional climate model RIEMS/GOALS, Zhang Yingjuang et al. (2006) studied the effect of CO_2 gradual increasing on future precipitation change over China. The results can be found in 9.5.1

Table 10.9 PRECIS with SRES A2 and B2 projects the precipitation changes over China for the future three periods relative to 1961~1990（Xu et al., 2005），in the bracket, RegCM2/CN with GG and GS (Gao et al., 2001) (unit: %）

Periods	A2	B2
2011~2020	3	4
2041~2050	7	7
2071~2080	13 (GG 14)	10 (GS 13)

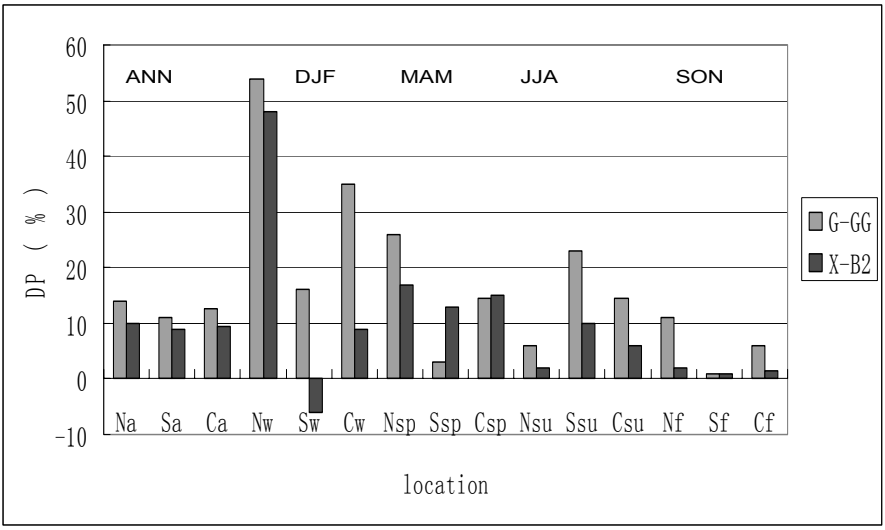

Fig. 10.6 RegCM2/CN and PRECIS project the annual and seasonal mean precipitation changes over China (C), Northern China (N) and Southern China (S) for the late periods of the 21st century relative to 1961~1990 (unit: %), light black is RegCM2/CN (Gao et al., 2001), heavy black is PRECIS (Xu et al., 2005)

10.3.3 Statistical downscaling

Different from temperature in sub-domain division, the regionally-mean monthly mean precipitations are downscaled and Northwestern China is also divided into four sub-domains (Area1. >43°N; Area 2. <90°E ,< 43°N; Area 3. 90～101°E, < 43°N; Area 4. >101°E) and Southwestern China into three sub-domains (Area 1. <100°E; Area 2. >100°E, >28°N; Area 3. >100°E, <28°N) to be studied.

Table 10.10 shows the downscaled mean precipitation change for the years 2071 to 2099 relative to the period 1961 to1990. In January, there is an increase of rainfall in Southern Xinjiang and Northeastern China and a decrease in Southern China under both A2 and B2 scenarios. Rainfall will increase under A2 scenario and decrease under B2 scenario in Northern Xinjiang, Area 4 of Northwestern China, Northern China, Area 2 of Southwestern China, Central China and Eastern China, whereas rainfall will decrease under A2 scenario and increase under B2 scenario in Area 3 of Northwestern China, and Area 1 and 3 of Southwestern China.

In July, there is a decrease of rainfall in the west of China and Southern China and an increase in Central China and Eastern China under both A2 and B2 scenarios. Rainfall will decrease under A2 scenario and increase under B2 scenario in Northern China and Northeastern China.

There is a little more increase of rainfall under B2 scenario than under A2 scenario in Southern Xinjiang and Northeastern China in January and in Middle China and Eastern China in July. There is a little more decrease under B2 scenario than under A2 scenario in the west China and Southern China.

Table 10.10 Downscaled precipitation change for the years 2071 to 2099 relative to the period 1961 to 1990 using HadCM3 A2 and B2 scenarios in January and July (unit: mm/day).

		I1	I2	I3	I4	II	III
Jan	A2	0.8	0.2	-0.5	0.8	0.5	1.5
	B2	-2.0	0.3	0.0	-0.9	-0.4	2.3
Jul	A2	-24.4	-2.5	-21.7	-26.5	-0.4	-10.3
	B2	-19.9	-1.8	-14.7	-15.7	6.8	5.1
		IV1	IV2	IV3	V	VI	VII
Jan	A2	-0.7	1.9	-6.3	8.6	5.8	-18.9
	B2	0.8	-1.1	4.7	-8.9	-1.3	-4.3
Jul	A2	-3.2	-47.7	-51.3	9.5	6.8	-19.4
	B2	-6.8	-26.6	-34.1	14.4	12.5	-12.3

10.4 Projection of extreme events

In the recent years, under the global warming background, changes in extreme weather and climate events have drawn people's increasing attention. With persistent global warming, the extreme climate events associated with temperature have occurred frequently, on the other hand, changes in water cycle due to the warming have led to increase in heavy rain and extreme precipitation events (Trenberth et al, 2003). More data reveal that the exponentially increasing trend of economic losses is resulted from meteorological disasters in the recent 10 years in many areas over the world. According to statistics, the averaged yearly economic loss for meteorological disasters in China since 1995 has exceeded 100 billion yuan, with the highest loss of 200 billion yuan in 2006. Owing to the small spatial and temporal scales of extreme events, the simulation and projection of the events are performed mainly by using the downscaling approaches. On the other hand, a small change in mean climate might induce larger changes in the frequency and intensity of extreme events (Mearns et al, 1984). Therefore, some studies in the recent years have paid attention on how to extract the signals of extreme climate and meanwhile to project their changes by using models.

10.4.1 Extreme temperature

Similar to the projections of the mean temperature, two regional climate models RegCM2/CN with GG and GS scenarios and PRECIS with SRES A2 and B2 also have projected extreme temperature changes over China for the 21st century (Gao et al, 2001, 2002; Luo et al, 2005; and Xu et al., 2005). Results from both the models suggest that future extreme maximum and minimum temperatures will increase remarkably. The experiments of RegCM2/CN indicate that daily maximum and minimum temperatures in China for the late periods of 21st century will remarkably increase, with their annual mean increases being 1.6℃ and 2.1℃ relative to 1961-1990, respectively, thus leading to the reduction in the diurnal range of temperature.

Xu et al. (2005) analyzed the projection characteristics of frequency distributions of daily maximum and minimum temperatures over China in the late 21st century (2071-2100) using the PRECIS regional climate model. Under the Scenario B2 the daily maximum temperature shows a relatively uniform increasing trend over China in the late 21st century (2071-2100) (Fig.10.7a) relative to 1961-1990, the increase range of the maximum temperatures less than 22℃ is small, and their frequencies tend to be re-

duced; and for the maximum temperatures greater than 22℃ the opposite is true. The extreme events with daily maximum temperature greater than 35℃ may increase by 1.5% relative to 1961-1990. The daily minimum temperature also displays an increasing trend (Fig.10.7b), the frequencies of daily minimum temperatures less than 18℃ will be reduced, and those greater than 18℃ remarkably increased. The extreme events with a daily minimum temperature lower than -10℃ are reduced by 2% relative to 1961-1990.

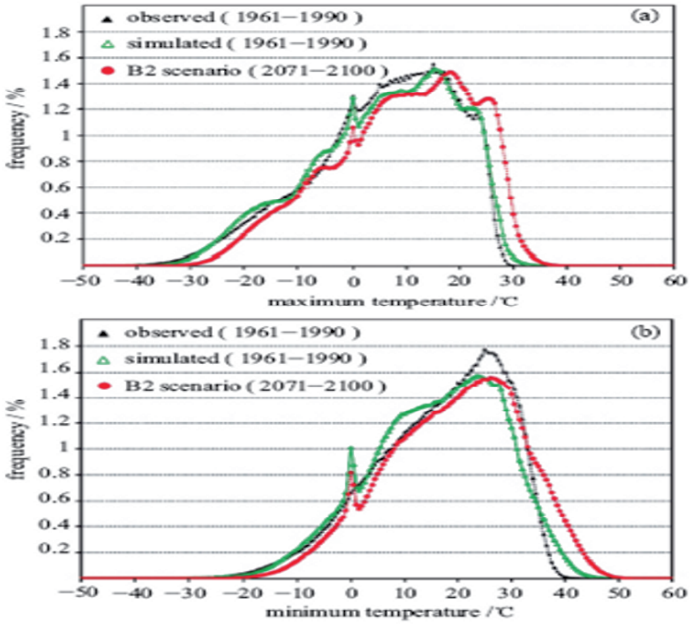

Fig. 10.7 Observed and simulated (B2 scenario) frequency distributions for daily (a) maximum and (b) minimum temperatures at 740 stations in China for 1961-1990 and 2071-2100 (Xu et al., 2005)

Recently, Jiang et al (2008a) analyzed changes in extreme temperatures over China in the 21st century based on projections of daily maximum and minimum temperatures provided by the IPCC AR4 models of GFDL-CM2.0, GFDL-CM2.1, INM-CM3.0, IPSL-CM4, MIROC3.2(medres), MIROC3.2(hires), CNRM_CM3. Table 10.11 exhibits the increase ranges of daily maximum and minimum temperatures in different time periods of the 21st century relative to the period 1961 to 1990 over China, and it is seen that under various emission scenarios the increase range of daily

minimum temperature is always greater than that of daily maximum temperature, suggesting the obvious reduction in the diurnal range of temperature. Especially under the A2 scenario the annual mean daily maximum and minimum temperatures over China will increase by 4.0℃ and 5.0℃, respectively, in the late 21st century, and seasonally the increases of winter daily minimum and summer maximum temperatures may reach 5.5℃ and 3.8℃, respectively.

Table 10.11 The multi-model ensemble projections of annual and seasonal mean daily maximum and minimum temperatures changes in China for the years 2021 to 2050, 2071 to 2100 relative to the period 1961 to 1990 (Jiang et al., 2008a)

Time period	Annual mean daily maximum temperature		
	A2	A1B	B1
2021-2050	1.66	1.64	1.32
2071-2100	3.97	3.34	2.30
	Annual mean daily minimum temperature		
	A2	A1B	B1
2021-2050	2.40	1.87	1.53
2071-2100	4.95	3.71	2.54
	Mean daily maximum temperature in summer		
	A2	A1B	B1
2021-2050	1.57	1.67	1.34
2071-2100	3.77	3.17	2.20
	Mean daily minimum temperature in winter		
	A2	A1B	B1
2021-2050	2.64	1.95	1.58
2071-2100	5.47	4.08	2.78

Fig.10.8 shows distributions of mean change in winter daily minimum temperatures in the late 21st century relative to 1961-1990 by multi-model ensemble. Under various emission scenarios, change patterns of the winter daily minimum temperatures are consistent with those of winter mean temperatures (Fig. not shown), i.e. the largest increases occur in the Tibetan Plateau, Northeast China, and Northwest China, and in the other areas, the mean change of daily minimum temperatures increases generally northwestwards with an increase range greater than that of mean temperature. In comparison with 1961-1990, the winter minimum temperature under the A2/B1 scenario in the late 21st century will increases by 6.5~7.5℃/3.3~4.0℃, 6~7℃/3.0~3.6℃ in the Plateau, Northwest China and Northeast China, and by 3.5~4.5℃/1.8~2.5℃ in the Yangtze River basin and the region south of the river, respectively. Changes in the summer daily maximum temperatures in the late 21st century are also consistent

each other under various emission scenarios (see Fig.10.9), however it is different from the pattern of the change of winter minimum temperatures that the largest increases occur mainly in the Plateau and Northwest China, and in Eastern China, the summer maximum temperature consecutively increases northwards. Under the A2/B1 scenario the summer maximum temperatures in the late 21st century, increase by 4.0~4.8℃/2.4~3.2℃, 4.5~4.8℃/2.6~2.8℃, and 2.7~4℃/1.8~2.2℃ in the Plateau, Northwest China and Eastern China, respectively, suggesting smaller differences in the increase ranges of the temperatures among different regions.

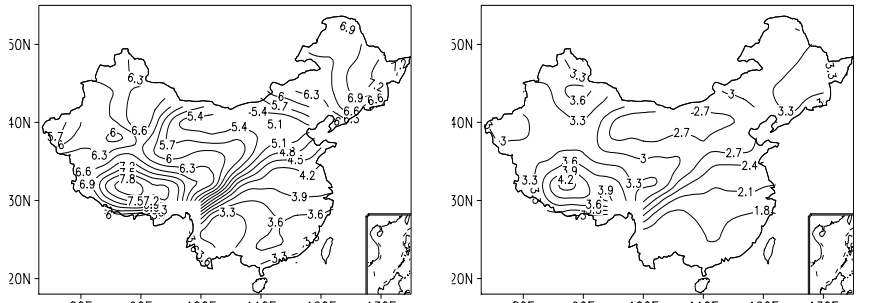

Fig. 10.8 The multi-model ensemble mean changes of winter daily minimum temperatures in China under (a) the SRES scenarios A2 and (b) the SRES scenarios B1 for the years 2071 to 2100 relative to the period 1961 to 1990. The multi-models include IPCC AR4 models of GFDL-CM2.0, GFDL-CM2.1, INM-CM3.0, IPSL-CM4, MIROC3.2(medres), MIROC3.2(hidres), CNRM_CM3 (Jiang et al., 2008a).

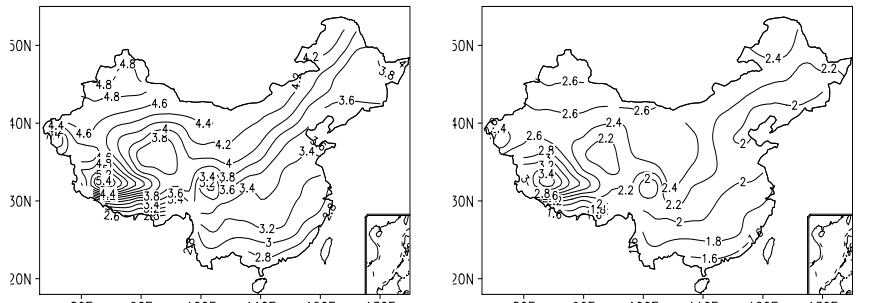

Fig. 10.9 As in Fig.10.8 except for summer daily maximum temperatures (Jiang et al., 2008a)

10.4.2 Rain and heavy rain days

Experiments of CO_2-doubling by the RegCM2 suggest that the enhancement of GG effect increases rainfall in Northern China as well as rain days remarkably. However, rain days are not remarkably increased in central China and Southeast China although rainfall is also increased there (not shown), indicating that the increase in rainfall might result mostly from increase in heavy rain events (not shown). Heavy rain days with daily rainfall greater than 35mm will increase remarkably in Southern China, but sporadically in part of Northern China, suggesting that the enhancement of GG effect may lead to increase in heavy rain events at local or regional scale.

Projections of frequency distributions of future daily rainfalls by regional climate model PRECIS (Xu et al, 2005) show that under the B2 scenario the frequency of daily rainfall greater than 40mm/d obviously increases in the late 21st century relative to 1961-1990, but the frequency of daily rainfall less than 40mm/d remains almost the same, in particular, frequencies of heavy rain and exceptionally heavy rain events increase remarkably.

10.4.3 Extreme climate indicators

Extreme Indicators

To extract signals of changes in extreme climate events from climate changes, the STARDEX program has developed a set of extreme indices. In view of the small spatial/temporal scales, weaker stability of extreme and rare events, and the poor capability of global models in simulating extreme events, Frich (1999) and Frich et al., (2002) put forward 10 less extreme, less noisy, but hopefully more robust indicators, and furthermore IPCC AR4 models have projected changes of the 10 indicators. Based on multi-model projection results, Jiang et al (2008b) analyzed changes in extreme climate events in China for the 21st century.

Table 10.12 lists definitions of the 10 extreme climate indicators (Frich et al., 2002), among them 5 indicators are associated with temperatures, such as Fd measuring the length of frost period in all extra-tropical regions, ETR would span the most extreme high-temperature event of the summer and the most extreme low-temperature event of the winter, GSL would sample spring and autumn anomalies in the higher latitudes, HWDI would sample the daytime maxima throughout the year in most climates, and Tn90 would sam-

ple primarily the warm nights during the year. Another 5 indicators are related with precipitation. Total number of days with precipitation ≥10 mm/d (R10), mean daily precipitation intensity, and the simple daily intensity index (SDII) would similarly summaries the wet period of the year. The greatest 5 d precipitation total of the year (R5d) and the fraction of the annual total greater than or equal to the daily 95th percentile (R95T) would represent some of the more extreme precipitation events of the year. The maximum number of consecutive dry days (CDD) could potentially become a valuable drought indicator for the dry part of the year.

Table 10.12 Definitions of 10 extreme climate indicators (from Frich et al ,2002)

Indicator	Acronym	Definition	Unit
Frost days	Fd	Total number of frost days (days with absolute minimum temperature <0°C) days	days
Intra-annual extreme temperature range	ETR	difference between the highest temperature observation of any given calendar year and the lowest temperature reading of the same calendar year	℃
Growing season length	GSL	Period between when T_{day} >5°C for >5 d and T_{day} < 5°C for >5 d	days
Heat wave duration index	HWDI	Maximum period > 5 consecutive days with T_{max} >5°C above the 1961–1990 daily T_{max} normal	days
Warm night index	Tn90	Percent of time T_{min} > 90th percentile of daily minimum temperature	%
Consecutive dry days	CDD	Maximum number of consecutive dry days (R_{day} < 1 mm)	days
Rain days	R10	Number of days with precipitation ≥10 mm/ d	days
Maximum 5 d rainfall	R5d	Maximum precipitation total in 5 days	mm
Heavy precipitation fraction	R95T	Fraction of annual total precipitation events exceeding the 1961–1990 95th percentile	%
Simple daily intensity index	SDII	Annual total/number of R_{day} ≥ 1 mm/d	mm/d

Projections of changes in extreme temperature indicators

Based on projections of IPCC AR4 models of GFDL-CM2.0, GFDL-CM2.1, INM-CM3.0, IPSL-CM4, MIROC3.2 (medres),

MIROC3.2(hidres), CNRM_CM3, Table 10.13 lists multi-model ensemble mean linear trends of extreme temperature indicators over China in the 21st century. Under various (A2, A1B, B1) scenarios, warm night index (Tn90), heat wave duration index (HWDI), and growing season length (GSL) all increase remarkably, while frost days (Fd) and Intra-annual extreme temperature range (ETR) reduce obviously. For example, under the A2 scenario, the increasing trends of Tn90, HWDI, and GSL in the 21st century are 44.3%/100yr, 90d/100yr and 28d/100yr, respectively, and the Tn90 will increases by 38% in the late 21st century (2071-2100) relative to 1961-1990, the HWDI by 73d, and the GSL by 36d in the region north of the Yangtze River (30°N); and the decreasing trends of Fd and the ETR are 42d/100yr, and 1.7°K/100yr, respectively, and the Fd will reduce by 40d in the late 21st century (2071-2100) relative to 1961-1990, and the ETR by 1.3°C. Under various emission scenarios, comparing changes in various extreme temperature indicators suggests that under the low emission scenario, say B1, changes in extreme temperature indicators are relatively smaller. Further comparing projections of different models indicates that the signs of changing trends are completely the same, only the intensities of trends are different to certain extent. Therefore, above changes in extreme temperature indicators might be associated with the enhancement of GG effect.

Table 10.13 The multi-model ensemble mean projections of the trends in extreme temperature indicators over China in the 21st century and its changes for the years 2071 to 2100 relative to the period 1961 to 1990

	Scenario	HWDI (days)	Tn90(%)	GSL (days)	ETR (°C)	Fd (days)
Linear trend /100yr	A2	90.2	44.3	28.1	-1.7	-42.0
	A1B	74.2	37.6	23.5	-1.2	-37.0
	B1	35.2	25.7	12.4	-0.8	-21.2
Indicator Change 2071-2100	A2	72.9	38.0	36.4	-1.3	-39.8
	A1B	59.3	33.2	33.9	-1.1	-36.8
	B1	32.7	25.3	23.6	-0.8	-25.8

Analyzing the geographic distributions of multi-model ensemble mean change of extreme temperature indicators in the late 21st century relative to the period in 1961-1990, it is found that under various emission scenarios, warm night index (Fig.10.10), heat wave duration (Fig.10.11), and growing season length (not shown) increase consistently over China, and the large increases of warm night and growing season both lie in South-

west China, but the large increases of heat wave duration lie in the Tibetan Plateau. The frost duration (not shown) is reduced over the whole China, with the largest reductions in the Plateau, Northwest China, and Northeast China. The Intra-annual extreme temperature range (not shown) over all regions in China except South China shows a decreasing trend with the reduction centers in the Plateau, Northwest China and Northeast China, which indicates that the rising trend of extreme minimum temperature is greater than that of extreme maximum temperature. The increase of the annual range of extreme temperatures in South China possibly results from that the rising trend of extreme minimum temperature is less than that of extreme maximum temperature.

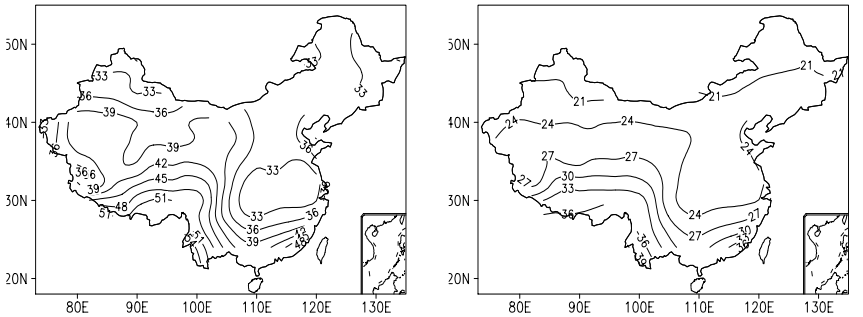

Fig. 10.10 As in Fig.10.8 except for Tn90

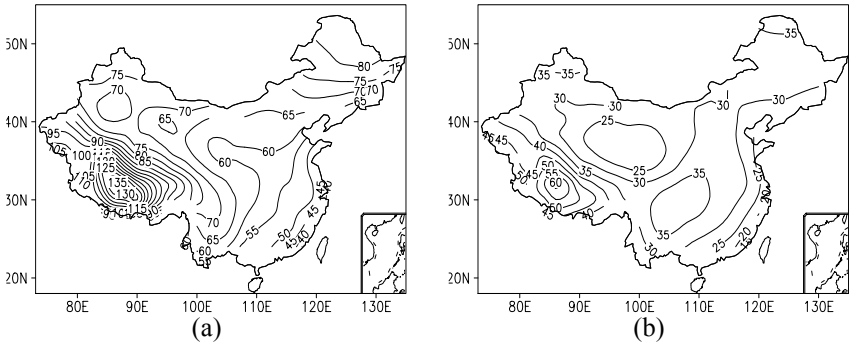

Fig. 10.11 As in Fig. 10.8 except for HWDI

Projections of changes in extreme precipitation indicators

Table 10.14 gives the multi-model ensemble mean projections of changes in extreme precipitation indicators in China in the 21st century provided by the 5 IPCC AR4 models, GFDL-CM2.0, GFDL-CM2.1, INM-CM3.0, IPSL-CM4, MIROC3.2 (medres). Except the CDD under the B1 Scenario, all indicators associated with precipitation under various emission scenarios have an increasing trend in China in the 21st century. For example, under the A2 scenario R5d will increases by 17 mm, R95T by 8%, R10 by 2 days, SDII by 0.6 mm/d, and CDD by 3 days in the late 21st century relative to 1961-1990, indicating that future precipitation events tend to be extremes, and in the late 21st century, the extreme precipitation intensity in China may increases in comparison with 1961-1990, and the droughts will also exacerbate.

Table 10.14 The multi-model ensemble mean projections of the trends in extreme precipitation indicators over China in the 21st century and its changes for the years 2071 to 2100 relative to the period 1961 to 1990

	Scenario	R5d (mm)	R95T （%）	R10 (days)	SDII （mm/d）	CDD (days)
Linear	A2	20.5	8.7	3.4	1.0	2.6
trend	A1B	16.6	7.2	3.0	0.8	1.7
/100yr	B1	9.1	4.0	2.1	0.5	-0.1
Indicator	A2	17.2	7.6	2.0	0.8	2.5
change	A1B	14.9	6.6	2.2	0.7	1.3
2071-2100	B1	10.2	4.7	1.8	0.5	-0.7

From the geographic distributions of multi-model ensemble mean change in the extreme precipitation indicators in the late 21st century relative to 1961-1990, it can be seen that under various emission scenarios the heavy precipitation indicators, R5d (Fig.10.12) and R95T (not shown), and daily precipitation intensity (SDII) (not shown) are basically increasing, and the largest increases occur mainly in Southwest China, the south fringe of the Tibetan Plateau, and the Huaihe River valley. For example, under the A2 scenario the R5d in these regions will increase by 20~30 mm in the late 21st century relative to 1961-1990, R95T by more than 10%, and corresponding SDII by above 1 mm/d. Except for the Yangtze River basin and the region south of the river, R10 increases over the other areas in China, and CDD reduces mainly in Northeast China, inner Mongolia to the north of the Plateau, but increases in the west of Northwest China and the region south of the Yangtze River, such as under the A2 scenario the CDD in the late 21st century will reduces by 6~8 days in Northeast China and the north

of the Plateau, while it will increase by 6~8 days in the region south of the Yangtze River (see Fig.10.13).

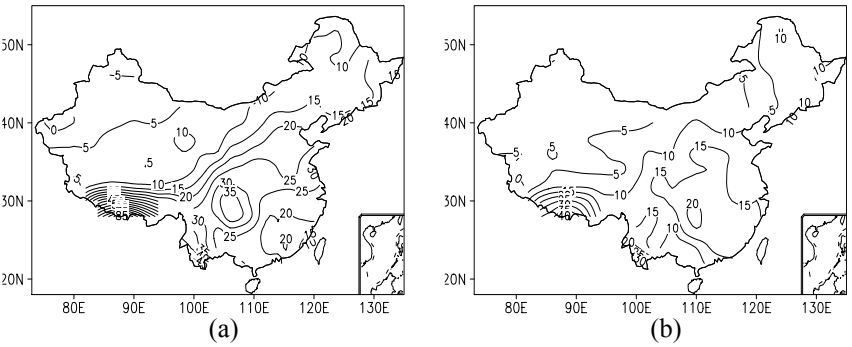

Fig. 10.12 The multi-model ensemble mean changes of R5d in China under (a) the SRES scenarios A2 and (b) the SRES scenarios B1 for the years 2071 to 2100 relative to the period 1961 to 1990. The multi-models include IPCC AR4 models of GFDL-CM2.0, GFDL-CM2.1, INM-CM3.0, IPSL-CM4, MIROC3.2(medres).

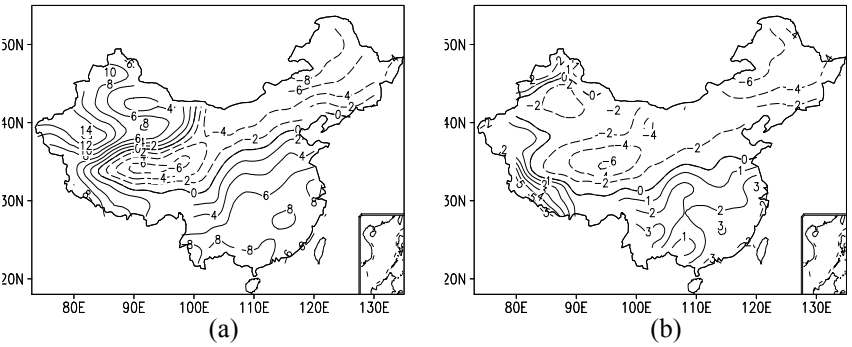

Fig. 10.13 As in Fig.10.12 except for CDD

In combination with the above projections of rainfall, the rainfall does not show evident increase in the Yangtze River basin and the region south of the river, but the rain days are reduced, which lead to the remarkable increase in the precipitation intensity and heavy precipitation; in the west of Northwest China and the south fringe of the Tibetan Plateau, the number of rain days are reduced, but the rainfall and precipitation intensity are both remarkably increased; and in Northeast China and Inner Mongolia to the north of the Plateau rainfall as well as the number of rain days are both in-

creased, but the increase in the intensity of precipitation is not evident. All those suggest that impacts of the enhancement of GG effect on rainfall and extreme precipitation events are complicated. In most areas of China, along with increase in future precipitation, the intensity of precipitation also increases remarkably, even if in the Yangtze River basin and the region south of the river where the increase in rainfall is not obvious, the intensity of precipitation is also increased obviously due to the reduction in the number of rain days; however in Northeast China and Inner Mongolia to the north of the Plateau the increase in rainfall is mainly associated with the increase in the number of rain days, which is obviously favorable to the improvement of arid and semi-arid ecological environment in these areas.

10.4.4 Tropical cyclones

As we know, the projections of typhoon are an intractable and tricky problem. For recent years, several modeling groups focused on the projections of the annual typhoon change over the Northwestern Pacific Ocean for the 21st century. Table 10.15 summaries those main results. It is noticed in Table 10.15 that the number of annual total typhoon over the Northwestern Pacific Ocean for the last 30 years of the 21st century might decrease by -15 ~ -30% relative to 1971~2000, but the number of strong typhoons and their intensities of both wind speeds and rainfall might increase. Some research indicates that the annual total typhoon numbers near by China and their intensities might be enhanced. A few studies find that the locations of the typhoon occurrence might be shifted eastwards and the occurring date of first and last typhoons might become later than the present time.

10.5 Conclusions and discussions

Summarizing the above recent studies, several conclusions and discussions are described as following:

1 New results on the projections of future climate changes in China

Table 10.16 summarized the new results on the projections of future climate change in China for the late periods of the 21st century relative to 1961~1990 due to the human activities. It is noticed in Table 10.16 that based on the projections of the global and regional climate models, as well as statistical downscaling methods, a mean warming of 3.8℃ with mean ranges of 2.3~5.6℃ in China might appear for the late periods of the 21st

century. A warming of both T_{max} and T_{min} might be in a range of 2.0~5.0℃. The days of both warm nights and heat waves might increase. The precipitation in China might increase by 8% with mean ranges of 1~13%. The local heavy rain might increase in some sub-regions and decrease in several other regions. The warming climate of lower than 0.7℃ or higher than 7.0 ℃ in China for the late periods of the 21st century is unlikely. The precipitation change by lower than -5% or higher than 20% in China is also unlikely.

Table 10.15 Projections of annual total tropical cyclones and typhoons numbers over the Northwestern Pacific Ocean for the 21st century by the climate models with the various human emission scenarios (Zhao et al., in press)

Authors (years)	Models and scenarios	Main conclusions
Gao et al.（2002）	RegCM2/CN(60km) with a doubled CO_2	At the doubled CO_2, increasing near China, decreasing over NW Pacific, increasing over South China Sea
Sugi et al.（2002）	JMA-AGCM（T106）with a doubled CO_2	Decreasing over NW Pacific with no obvious change in intensity
Zhao et al.（2004）	CCSR/NIES-AOGCM（T21）with SRES A1, A2, B1, B2	Decreasing by -15 ～ -30％ at the end of the 21st century relative to 1971~2000
Hasegawa, Emori（2005）	CCSR/NIES/FRCGC-AGCM（T106）with a doubled CO_2	Decreasing slightly, intensity increasing
Yoshimura, Sugi（2005） Yoshimura et al.（2006）	MRI-AOGCM（T106）with an increasing greenhouse gases	Decreasing obviously, enhancing intensity of rainfall over the centers
McDonald et al.（2005）	HadCM3-AGCM(2.5X3.75) with an increasing greenhouse gases	Decreasing, enhancing intensity of rainfall
Oocuchi et al.（2005）	MRI-AGCM（20km）with an increasing greenhouse gases	Decreasing by -30％ at the end of the 21st century, wind speeds of strong typhoons enhancing
Wu and Wang（2005）	GFDL-AOGCM with an increasing greenhouse gases	Decreasing over South China Sea, tracks move westwards over NW Pacific
Summary	All models with the human emission scenarios	Decreasing annual total typhoon numbers over NW Pacific, enhancing rainfall and wind speeds of strong typhoons, increasing typhoon numbers near by China

Table 10.16 Climate change in China for the late periods of the 21st century relative to 1961~1990 summarized above the new projections by the models and methods with human activities

Investigators	Methods	Temperature projection	Precipitation projection
Luo et al, 2005a, 2005b	40 global and regional models with $2XCO_2$, 1%, GG, GS, SRES A2, B2	Warming of 0.7~7.0℃, T_{max} and T_{min} warming of 2.0~5.0℃	Wetting by -3~20%
Xu et al., 2005	NCC/IAP T63 with SRES A2 and A1B	Warming of 3.0~6.0℃	Changing by -5~5%
Xu et al., 2005, 2006	PRECIS with SRES A2 and B2	Warming of 3.2~3.9℃	Wetting by 10~13%
Jiang et al., 2008a, 2008b	AR4 13CSMs with SRES A2, A1B and B1	Warming of 3.5℃, increasing days of warm nights and heat waves	Wetting by 9%, increasing local rainfall intensities
Fan et al., 2006	Statistical downscaling	Warming	Wetting
Summaries	Global and regional models and statistical methods	Mean warming of 3.8℃ with mean ranges of 2.3~5.6℃, T_{max} and T_{min} warming of 2.0~5.0℃, increasing days of warm nights and heat waves	Mean wetting by 8%, with mean ranges of 1~13%, local heavy rain might increase or decrease

2 Detection and attribution analyses of climate change in China for the 20th century

The key and common issue is whether we can trust those projections of the future climate change in China for the 21st century and their reliability and dependability. To answer those questions, the detection and attribution analyses of the climate change in China for the 20th century might provide a certain revelation. Table 10.17 gives the anomalous correlation coefficients and linear trends of the annual mean temperature in China between the observations and simulations by three sets of the model simulations for the several periods such as the 20th century, the second half of the 20th century, 1960~1970 and 1980~1999. Three sets of model experiments are 40 climate models with human emission scenarios simulation (E1), 19 earth

system models with the full forcing simulations (included both natural and anthropogenic forcing) (E2) and a coupled model driving by the observed sea surface temperature (SST) and sea ice (SI) (E3). To compare three sets of model simulations with the observation, it is found that E1 and E2 simulate the warming trend in China reasonably well, especially the obvious warming for the last 50 and 20 years. E3 does not simulate the warming trends for the last 50 and 20 years well (see Table 10.17). It also needs to point out that the model control simulations without human emission scenarios do not show the warming trends and significant correlations in China for the 20th century. Their ACC are near 0 and linear trends are the negative values. Based on those detection and attribution analyses, it is very likely that anthropogenic greenhouse gases increases caused most of the observed warming in China for the last 50 years. Therefore, the warming trends in China for the 21st century projected by the models with the human activities have a relatively higher reliability. But the reliability of the projected precipitation change in China for the 21st century is much lower than the reliability of for projected temperature change.

Table 10.17 Anomalous correlation coefficients (ACC) and linear trends (LT) of annual mean temperature in China for the 20th century between observation and simulations by the climate model experiments (linear trends of observations for the 20th century, the last 50 years, 1960~1970 and 1980~1999 are 0.4~0.8℃/100a，0.5~0.9℃/50a，-0.55℃/10a, and 0.53℃/10a, respectively) (Zhou and Zhao, 2006)

	ACC	LT in 20th century	LT in second half of 20th century	LT in 1960~1970	LT in 1980-1999
E1 (40 models with human scenarios)	0.47	0.71℃/100a	0.90℃/50a	-0.07℃/10a	0.38℃/10a
E2 (full forcing)	0.55	0.70℃/100a	0.85℃/50a	-0.06℃/10a	0.24℃/10a
E3 (12 ensembles with observed SST and SI)	0.50	0.33℃/100a	0.01℃/50a	-0.12℃/10a	0.21℃/10a

3 Narrowing the uncertainties in future research

As we know, there are several sources of uncertainties in the climate projections in the world. The major sources of uncertainties are: anthropogenic emission scenarios; parameterizations of climate model schemes; lower resolutions of the models in the regional analyses; understanding of physical, chemical and biological processes in the earth system; dynamic and statistic downscaling methods, the natural climate changes in the fu-

ture. These uncertainties are interrelated.

Further research is required to reduce the uncertainties. For example, NCC is going to use the regional climate model with the 20km resolution to get detailed climate projections in China. TEACOM continues to use both dynamic and statistical downscaling methods to improve the climate projections. Nanjing University of Information Science & Technology is trying to use multi model ensembles to understand the future climate change and to improve the feedback mechanisms of the interrelated processes. It is expected to provide the reliable climate projection for the public and policy-makers.

References

Chen KM, Zhang XH, Jin XZ, Lin WY, Yu YQ, Guo YF (1996) Primary analysis on experiments of increasing greenhouse effects by a coupled atmospheric and oceanic general circulation model. In Collection of Climate Change and Numerical Simulations II, ed. by 85-913-02 project, China Meteorological Press, Beijing, pp.61-84 (in Chinese).

Chen LX, Song YK (1996) Analysis of the simulations by the CCM1 and the intercomparison with other GCMs. In Collection of Climate Change and Numerical Simulations II, ed. by 85-913-02 project, China Meteorological Press, Beijing, pp.241-254 (in Chinese).

Chen M, Fu C (2000) A nest procedure between regional and global climate models and its application in long term regional climate simulation. Chinese J. Atmos. Sci., 24, 233-262 (in Chinese).

Chen QY, Yu YQ, Guo YF (1996) Regional climate change over China induced by a doubled CO_2. In Collection of Climate Change and Numerical Simulations II, ed. by 85-913-02 project, China Meteorological Press, Beijing, pp.156-170 (in Chinese).

Delworth TL, Broccoli AJ, Rosati A et al (2005) GFDLs CM2 global coupled climate models – Part 1: Formulation and simulation characteristics, J.Climate, in press.

Ding Yihui, Xu Ying, Zhao Zongci, Luo Yong and Gao Xuejie (2004) Climate change scenarios over East Asia and China in the future 100 years, Newsletter on Climate Change 2003/2004, 2-4

Duan Anmin, Wu Guoxiong, Zhang Qiong, Liu Yimin (2006) New evidence for the climate warming over the Tibetan plateau resulted from greenhouse gases emission. Chin. Sci. Bull., 51, 989-992

Fan Lijun (2006) Statistical downscaling of local and regional climate scenarios over China, Chinese Academy of Sciences, PhD theses, pp164 (in Chinese)

Frich P (1999) REWARD—A Nordic Collaborative Project Annex. In: CK Folland, EB Horton, and PR Scholefield, Eds, Meeting of the Joint CCl/CLIVAR Task Group on Climate Indices, Bracknell, UK, 2–4 September 1998. World ClimateData and Monitoring Programme, WCDMP-No. 37, WMO-TD No. 930.

Frich P, Alexander LV, Della-Marta P et al (2002) Observed coherent changes in climatic extremes during the second half of the twentieth century. Clim. Res., 19, 193–212

Gao Xuejie, Zhao Zongci, Ding Yihui, Huang Ronghui and Filippo Giorgi (2001) Climate change due to greenhouse effect in China as simulated by a regional climate model, Advances in Atmospheric Sciences, 18, 1224-1230

Gao Xuejie, Zhao Zongci and Filippo Giorgi (2002) Changes of extreme events in regional climate simulations over East Asia, Advances in Atmospheric Sciences, 19, 927-942

Gao Xuejie, Zhao Zongci, Ding Yihui and Huang Ronghui (2003a) Numerical experiments of regional climate changes in China due to the greenhouse gases, Acta meteorological Sinica, 61 (1), 20-28 (in Chinese)

Gao Xuejie, Li Yihua, Zhao Zong-ci, et al. (2003b) Numerical studies of tropical typhoons changes near China caused by the doubled CO_2, Tropical Oceanic Meteorology, 22 (4), 77-83 (in Chinese)

Gordon C, Cooper C, Senior CA et al (2000) The Simulation of SST, sea ice extents and ocean heat transport in a version of the Hadley Centre coupled model without flux adjustments, Climate Dyn., 16, 147–168.

Gordon HB, Rotstayn LD, McGregor JL et al (2002) The CSIRO Mk3 Climate System Model, Tech. Rep. 60, CSIRO Atmospheric Research, Aspendale

Guo Yufu, Yu Yongqiang, Liu Xiying, et al (2001) Simulation of climate change induced by CO_2 increasing for east Asia with IAP/LASG GOALS model, Advances in Atmospheric Sciences, 18, 53-66

Hasegawa A, Emori S (2005) Tropical cyclones and associated precipitation over the western North Pacific in present and doubled CO_2 climates simulated by a T106 atmospheric GCM, SOLA, 1,145-148

Hulme M, Wigley T, Jiang Tao, Zhao Zong-ci, Wang Futang, Ding Yihui, Leemans R, Markham A (1992) Climate Change due to the Greenhouse Effects and its Implications for China, A Banson Production （UK）, pp53; Another booklet in Chinese published in Hong Kong, pp55

IPCC WG1 (1990) Climate change, The IPCC Scientific Assessment, eds by J.T.Houghton et al., Cambridge UK, Cambridge University Press, 365pp

IPCC WG1 (1992) Climate change 1992, The Supplementary report, eds by J.T.Houghton et al., Cambridge UK, Cambridge University Press, 198pp

IPCC WG1 (1996) Climate change 1995, The Science of Climate Change, eds. by J.T.Houghton et al., Cambridge UK, Cambridge University Press, 572pp

IPCC (2000) Emission scenarios, eds. by N.Nakicenovic and R.Swart, Cambridge UK, Cambridge University Press, 570pp

IPCC WG1 (2001) Climate change 2000, The scientific basis, eds. by J.T.Houghton and Ding Yihui et al., Cambridge UK, Cambridge University Press, 881pp

Jiang Zhihong, Zhang Xia and Wang Ji et al (2008a) Projection of climate change in China in the 21st century by IPCC-AR4 Models and their uncertainties, Geographical Research (in Chinese) accepted

Jiang Zhihong, Chen Weilin, Wang Ji (2008b) Projection and Evaluation of the Annual Precipitation Extremes Indices over China Based on Seven IPCC AR4

coupled Climate Models, Chinese Journal of Atmospheric Sciences (in Chinese), accepted

Jungclaus J, Botzet M, Haak H.et al (2006) Ocean circulation and tropical variability in the AOGCM ECHAM5 /MPIOM, J. Climate, 19(16), 3952–3972

K-1 model developers (2004) K-1 coupled model (MIROC) description, Tech. Rep. 1, Center for Climate System Research, University of Tokyo.

Kim SJ, Flato GM, de Boer GJ, McFarlane NA (2002) A coupled climate model simulation of the Last Glacial Maximum, Part 1: transient multi-decadal response, Climate Dyn., 19, 515–537.

Li Qingquan, Power SB (2000) Response of a global CGCM to CO_2 increase, Acta Meteorologica Sinica, 14 (1), 46-60

Li WL, Gong W (1996) Scenarios of regional climate change over China as simulated by a regional climate model, Collection of Climate Change and Numerical Simulations II, ed. by 85-913-02 project, China Meteorological Press, Beijing, pp.255-272 (in Chinese).

Li Xiaodong, Zhao Zong-ci, Wang Shao-wu and Ding Yihui (1995) Evaluation of CGCMs and simulations of regional climate change in East Asia, Acta Meteorologica Sinica (English version), 9, 385-401

Luo Yong, Ding Yihui, Zhao Zong-ci, Gao Xuejie, Xu Ying and Xie Zhiren (2005),Chapter 10, Projections of the future anthropogenic climate change in China, In: Qin Dahe, Ding Yihui, Su Jilan and Wang Sumin (eds) Volume I: Climate and Environment Changes in China and Their Projections, China Science Press, 507－555 (in Chinese)

Luo Yong, Zhao Zongci, Xu Ying, Gao Xuejie and Ding Yihui (2005) Projections of climate change over China for the 21st century, Acta Meteorologica Sinica, 19, 401-406

McDonald RE, G.Bleaken D, Cresswell DR, Pope VD, Senior CA (2005) Tropical storms: representation and diagnosis in climate models and the impacts of climate change, Clim.Dyn., 25,19-36

Marti O et al (2005) The new IPSL climate system model: IPSLCM4,Tech. rep., Institut Pierre Simon Laplace des Sciences del'Environnement Global, IPSL, Case 101, 4 place Jussieu, Paris,France.

Mearns L, Katz R, Schneider S (1984) Extreme high-temperature events: changes in their probabilities with hanges in mean temperature. J. Clim. Appl. Meteor. 23, 1601–1613.

Min SK, Legutke S, Hense A et al (2005) East Asian climate change in the 21st century as simulated by the coupled climate model ECHO-G under IPCC SRES scenarios. Revised, J. Meteorol. Soc. Japan.

Salas y M´elia, Chauvin D, D´equ´e F et al (2005) Description and validation of the CNRM-CM3 global coupled model, Climate Dyn., submitted.

Oocuchi K, Yoshimura J, Yoshimura H, Mizuta R, Noda A (2005) Tropical cyclone climatology in a global-warming climate as simulated in a 20km-mesh global atmospheric model, J.Met.Soc.Japan, 84, 259-276

Schmidt GA et al (2006) Present day atmospheric simulations using GISS ModelE: Comparison to in-situ, satellite and reanalysis data, J. Climate, 19(2), 153–192

Shi Guangyu, Wang Xihong, Zhang Lisheng Huang Xingyo (2002) Impact of

Human Activities on Climate I1. Impact on Climate Variability over East Asia and China, Climatic and Environmental Research, 7 (2), 255-266 (in Chinese)
Sugi M, Noda A, Sato N (2002) Influence of the global warming on tropical cyclone climatology: an experiment with the JMA global model, J. of Met. Soc. Of Japan, 80, 249-272.
Trenberth KE, Dai A, Rasmussen RM, Parsons DB (2003) The changing character of precipitation. Bull. Amer. Meteor. Soc., 84, 1205-1217.
Volodin EM, Diansky NA (2004) El-Ni˜no reproduction in coupled general circulation model of atmosphere and ocean, Russian meteorology and hydrology, 12, 5–14.
Wang Futang and Zhao Zong-ci (1994) Climate change and natural vegetation in China, Acta Meteorologica Sinica (English version), 10, 1-8
Wang Futang, Zhao Zong-ci, Wang Shili and Liu Wenquan, (2003) Impacts of climate change on agriculture and ecosystem, ed. By Qin Dahe, China meteorological Press, pp190 (in Chinese)
Wang HJ, Zeng QC, Zhang XH (1992) Numerical experiments on climate change due to a doubled CO_2. China Science B, 6, 663-672 (in Chinese).
Wang Shao-wu, Zhao Zong-ci (1995) Climate change scenarios for China in the next 50 years, Quar.J.Appl.Meteor. 6, 333-342 (in Chinese)
Wang ZG, Chao JP, Chen YY, Cai Y, Xing RN (1996) Response to the increasing CO_2 as simulated by a coupled A/OGCM, part I: without CO_2 cycle of air and sea. in Collection of Climate Change and Numerical Simulations II, ed. by 85-913-02 project, pp289-299, China Meteorological Press, Beijing, (in Chinese).
Wang ZG, Chao JP, Chen YY, Cai Y, Xing RN (1996) Response to the increasing CO_2 as simulated by a coupled A/OGCM, part II: with CO_2 cycle of air and sea, in Collection of Climate Change and Numerical Simulations II, ed. by 85-913-02 project, pp300-307, China Meteorological Press, Beijing, (in Chinese).
Wang SW (2001) Advances on climatology in the modern times. China Meteorological Press, 550pp (in Chinese).
Washington WM, Weatherly JW, Meehl GA et al (2000) Parallel climate model (PCM) control and transient simulations, Climate Dyn.,16, 755–774.
Wu L, Wang B, (2005) Projection of tropical cyclones over Northwestern Pacific Ocean, J.Clim., 17, 1686-1698
Xu Yinlong, Huang Xiaoying, Zhang Yong, Lin Wantao, Lin Erda (2005) Statistical analyses of climate change scenarios over China in the 21st century, Advance on Climate Change Research, 1 (2), 80-83 (in Chinese)
Xu Yinlong, Lin Yihua, Lin Erda, Lin Wantao, Dong Wenjie, Richard Jones, David Hassell and Simon Wilson (2006) Analyses on the climate change responses over China under SRES B2 scenarios using PRECIS, Chinese Science Bulleting, 51(7), 2068-2074 (in Chinese), 51 (1), 1-8 (in English)
Xu Ying, Zhao Zong-ci, Gao Xuejie, Zhang Zhen (2005) Projections of future climate change over the River valley of the South-North water diversion (East Route), Advances on Climate Change Research, 1（4）， 176－178 (in Chinese)
Xu Ying, Zhao Zongci, Luo Yong, Gao Xuejie (2005) Climate change projections for the 21st century by the NCC/IAP T63 model with SRES scenarios, Acta

Meteorologica Sinica, 19, 407-417
Yoshimura J, Sugi M (2005) Tropical cyclone climatology in a high-resolution AGCM: impacts of SST warming and CO_2 increase, SOLA, 1 133-136
Yoshimura, J. M.Sugi, and A.Noda, 2006, Influence of greenhouse warming on tropical cyclone frequency, J.Met.Soc.Japan, 84, 405-428
Yu YQ, Chen KM, Jin XZ, Guo YF, Zhang XH, 1996: Global climate change induced by the greenhouse effect. in Collection of Climate Change and Numerical Simulations II, ed. by 85-913-02 project, pp123-137, China Meteorological Press, Beijing, (in Chinese)
Zhao Zong-ci, Kellogg WW (1988) Sensitivity of soil moisture to doubling CO_2 in climate model experiments: Part II: The Asian Monsoon region, J. Climate, 1, 367-378
Zhao Zong-ci (1989) Impacts of climatic changes in China induced by greenhouse gases as simulated by the GCMs, J.Meteorology, 3 (in Chinese).
Zhao Zong-ci (1994) Climate change in China, World Resource Review, 6, 125-130.
Zhao Zong-ci (1996) Climate change and sustainable developement in China's semi-arid regions, In: Ribot, Magalhaes AR, Panagides SS (eds) Climate Variability, Climate Change and Social Vulnerability in the Semi-Arid tropics, Cambridge University Press, 92-108.
Zhao Zong-ci, Li Xiaodong (1997) Impacts of global warming on climate change over East Asia as simulated by 15 GCMs, World Resource Review (USA), 10, 17-21.
Zhao Zong-ci, Luo Yong, Gao Xuejie (2000) GCM studies on anthropogenic climate change in China, Acta Meteorologica Sinica, 14, 247-256.
Zhao Zongci, Xu Ying (2002) Detection and scenarios of temperature change in East Asia, World Resource Review (USA), 321-333
Zhao Zong-ci, Akimasa Sumi, Kim JW (2003) Characteristics of climate change in East Asia for several key periods, World Resource Review (USA), 15,3, 289-304.
Zhao Zong-ci, Akimasa Sumi, Chikako Harada, Toru Nozawa (2003) Projections of extreme temperature over East Asia for the 21st century as simulated by the CCSR/NIES2 coupled model, Proceedings of International Symposium on Climate Change, eds by WMO and CMA, WMO/TD No.1172, China Meteorological Press, Beijing, China, 158-164.
Zhao Zong-ci, Akimasa Sumi, Chikako Harada, Toru Nozawa (2004) Detection and projections of floods/droughts over east Asia for the 20th and 21st centuries due to human emission, World Resource Review, 16, 3, 312-329.
Zhao Zong-ci, Gao Xuejie, Xu Ying, Luo Yong, Projections of extreme weather and climate events in China for the 21st century, 'Approaches to the study of Climate Change in China and in the UK, Proceedings of a NERC-NSFC-CMA workshop, Beijing, China Eds. by Ding Yihui and Gerry Lawson, UK Publisher, in press
Zhou Tian-jun, Zhao Zong-ci (2006) Attribution of the climate warming in China for the 20th century, Advances in Climate Change Research, 28-31 (in Chinese)

Chapter 11 Impacts of Climate Change on Water Resources and Agriculture in China

11.1 Introduction

China's freshwater resource ranks the sixth in the world after Brazil, Russia, Canada, United States and Indonesia, but the freshwater resource per capita in China is comparatively low, only equivalent to 21% of the world average. Furthermore, the distribution of freshwater resource in China appears to be uneven. For instance, the climatological annual rainfall is up to 1,600 mm in southeastern China; however, it is less than 200 mm in some parts of northwestern China. Therefore, China has been facing serious water resource problems. Especially under the background of global warming, the increasing extreme weather and climate events strongly affect the water resource and agriculture in China. On the other hand, as reported in Chapter 5, an evident aridity trend has been detected in northern China where is suffering from persistent drought and shortage of water resource. Lin (2005) pointed out that China's water resources issues are facing four challenges: (1) Frequent flood disasters; (2) Severe shortage of water resources; (3) Serious soil erosion, which in turn caused land degradation, land desertification, ecological deterioration and enhancement of sedimentation in rivers and lakes; (4) Water pollution.

China is a developing country with almost 70% agricultural population. The development of agriculture is strongly impacted by the regional climate and water sources. In China the main agricultural issues are: the decrease in cultivable land and water resources, soil degradation and desertification, frequent agricultural meteorological disasters, crop diseases and insect pests, the species and gene resources losses, and so on. In this chapter, the recent studies on the impacts of climate change on water resource and agriculture are summarized briefly.

11.2 Impacts of climate change on water cycle and water resources

Climate change impacts the hydrologic system by changing the hydrologic variables such as rainfall, evaporation, runoff and soil water content. These changes will lead to the spatial-temporal redistribution of the water resources, which in turn influences the supply and demand balance of water.

11.2.1 Impact of climate change on runoff

The volume of climatological annual rainfall in China is 6188.9 billion m^3, of which 45% is turned to surface water and groundwater, 55% is consumed in evaporation. River runoff accounts for about 94.4% of total amount of water resource in China. It is seen that the runoff could be strongly influenced by rainfall in association with climate anomaly.

Wang et al. (2000) investigated the sensitivity of runoff to climate change by using a monthly hydrological model with hypothetical climate change scenarios. Here the Yellow River basin is shown as an example. In analyzing the sensitivity of runoff to climate change, the spatial-temporal distribution of climatic fields was supposed to remain no change when the rainfall and temperature are varied under different climate change scenarios. Table 11.1 shows the response of runoff to the change of rainfall and temperature. It is seen from Table 11.1 that (1) The runoff increases in association with the increase of rainfall, but decreases with the increase of temperature; (2) The response of runoff to rainfall is more sensitive than to temperature; (3) The influence of temperature on runoff appears to be more significant in the cases with more rainfall, while the opposite situation is found in the cases with less rainfall. (4) The dryer basins (Huangfuchuan and Hong River) in the four sub-basins are more sensitive to the climate change, in comparison with the wetter ones (Daxia River and Dongnian River); (5) Among the 15 climate change scenarios, the most disadvantageous one is the case with 2°C increase in temperature associated with 20% decrease in the rainfall. Under this condition, the runoff decreases by 35%~43%.

A macro-scale hydrological model was used to investigate the response of land-surface runoff to various climate change scenarios with considering the effects of CO_2 and aerosols (You et al. 2002). This advanced model included a climate change scenario model, a potential evaporation model and a modified soil water balance model. The effects of rainfall, evaporation, snow storage, snow melting, water supply of soil, and runoff were considered in the model. In the development of future climate change scenarios, the observed temperature and rainfall data were used to adjust the projected temperature and rainfall changes by the general circulation mod-

els (GCM). The Thornthwaite Method developed by Mintz et al (1993) was used in the calculation of potential evaporation. The soil moisture, evaporation and runoff were simulated by the soil water moisture budget model according to the status of climate, vegetation, elevation and character of soil. With the support of geographic information system (GIS), the land-surface runoff in every grid cell was calculated under current climate condition and the future scenario. The monthly average runoff was calculated by the accumulation of runoff in every grid cell (0.5 longitude × 0.5 latitude). The results showed that, under the scenarios of global warming, the land-surface runoff of upper Yangtze River basin decreased in spring but increased in summer, while an opposite situation was found in the lower Yangtze River. Aerosols may also influence the land-surface runoff, but the results were inconsistent under different climate change scenarios.

Table 11.1 Runoff within sub-basins of the Yellow River under different climate change scenarios

change rate of rainfall (ΔP/P)		-20%	-10%	0	+10%	+20%
Daxia River ΔT/°C	0	-32.8	-17.0	0.0	18.8	38.2
	1	-36.1	-28.1	-6.3	11.2	29.5
	2	-38.9	-25.6	-11.4	4.8	22.2
Huangfuchuan ΔT/°C	0	-34.4	-18.0	0.0	19.6	40.8
	1	-37.9	-22.0	-4.5	15.1	35.2
	2	-40.2	-24.8	-7.7	10.8	30.9
Hong River ΔT/°C	0	-36.6	-19.4	0.0	23.1	49.1
	1	-39.8	-23.6	-5.5	15.5	39.6
	2	-42.6	-27.4	-10.1	9.2	31.5
Dongnian River ΔT/°C	0	-31.9	-16.5	0.0	17.6	36.1
	1	-34.3	-19.3	-3.3	13.8	31.8
	2	-36.5	-21.9	-6.3	10.3	27.9

Zhang (2006) evaluated the potential effects of global climate change on the mean annual runoff in the Yellow River Basin under different climate scenarios of HadCM3 GCM based on the evaporation ratio function of the aridity index. Simulations under HadCM3 A2 and B2 scenarios indicated that the changes in annual runoff varied from region to region within the range of -48.0% to more than 203%. In general, the potential changes in annual runoff decreased from east to west. For the Yellow River Basin, the mean annual runoff increased by 5.0%, 11.7%, and 8.1% for the A2

scenario, and the changes were 7.2%, -3.1%, and 2.6% for B2 scenario by the year of 2020, 2050 and 2080, respectively.

11.2.2 Impact of climate change on evaporation

Besides runoff, evaporation is also a major component of water cycle. Its variation is closely related to the climate conditions, such as temperature, wind speed, etc.

Guo et al. (2005) investigated the trend of evaporation in Yellow river-Huaihe river basin and analyzed its possible reasons based on the observed pan evaporation data from 117 observatories during the period of 1956-2000. A significant decrease trend of -50 mm/10a in the evaporation was found in the area. The maximum rate of decrease was up to 80mm/10a over the plain area. The most evident decrease in pan evaporation was observed in the southeastern Haihe basin and the lower Yellow River in spring and Huaihe River basin in summer. The decrease of pan evaporation is likely due to the decreasing sunshine duration, the weakening solar radiation, and the decreasing wind speed. Whereas, the change in vapor pressure deficit (VPD) was not significant.

The author investigated the temporal and spatial distributions of pan evaporation in China by using the pan evaporation (diameter 20 cm) and corresponding meteorological data from 465 stations (Shen, 2005). The influence of energy balance and aerodynamic terms in Penman formula on the evaporation and its changes was analyzed at the same time. The main results are as follows: (1) the average pan evaporation in China was about 1629 mm and exhibited an obvious decreasing trend through all of the four seasons, especially in summer. The trend and amplitude of evaporation variation varied with season and region; (2) It is very likely that the decrease of evaporation resulted from the decrease of solar radiation, temperature diurnal range, wind speed and VPD; (3) Based on the coefficients of partial correlation of the temperature, wind speed, actual vapor pressure and sunshine duration, the rising temperature accounted for the increase of evaporation, while the decrease of wind speed, actual vapor pressure and sunshine duration caused the decrease of evaporation. The influence of the four factors on evaporation varied with the season and region; (4) Analysis of energy balance and aerodynamic terms in Penman formula demonstrated that the decrease of pan evaporation in the eastern region mainly resulted from the significant decrease of energy offered to the evaporation, while the pan evaporation's decrease in the western areas was mainly due to the reducing dynamics offered to the evaporation.

11.2.3 Impact of climate change on water supply-demand balance

Climate anomaly is an important factor influencing the demand of agricultural and industrial water resource. Taking the Nanjing and Hangzhou city located in eastern China as examples, the demand of production water exhibits a moderate positive correlation with the July temperature. In addition, the irrigation water for agriculture is closely correlated with the precipitation in Jiangsu province (Yuan et al. 2000).

Liu (1997) used the output of GCM model with $2 \times CO_2$ concentration (by 2030) as input of the monthly water balance model and the water resources comprehensive assessment model to investigate the possible changes of annual and monthly runoff, the evaporation, and the difference between supply and demand of water resources in 2030. The results showed that in most of the river basins, the influence of climate change on water supply system was confined to the land-surface runoff and water supply of reservoirs due to the characteristics of water supply and demand in China, while the influence on water demand was confined to the agricultural irrigation water which accounts for most of the water consumption. In order to evaluate the influences of climate change on the supply-demand balance of water resource, six issues were addressed within each river basin: the analysis of the present situation on water supply and demand; the projection of water demand in 2030; projection of the available water supply in 2030; the analysis of water supply and demand in 2030 under the condition without considering climate change ($1\times CO_2$); the analysis of water supply and demand in 2030 under the condition with considering climate change ($2\times CO_2$); the water surplus or deficiency caused by climate change. The impact of climate change on the water deficit in some basins was shown in Table 11.2.

The results shown that: (1) The water deficit between normal years and extremely water deficient years caused by the increase of population and the development of social economy by 2030 will be $1.5\times10^9 \sim 3.6\times10^9$ m^3 in Beijing-Tianjin-Tangshan area, $3.6\times10^9 \sim 16.0\times10^9$ m^3 in the Huaihe River basin, $16.4\times10^9 \sim 27.2\times10^9$ m^3 in the Yellow River basin, while the Dongjiang River basin will not lack water; (2) The water deficit caused by the increase of population and the development of social economy under four GCM $2\times CO_2$ scenarios by 2030 will be $1.4\times10^9 \sim 5.0\times10^9$ m^3 in Beijing-Tianjin-Tangshan, $2.840\times10^9 \sim 1.956\times10^{10}$ m^3 in the Huaihe River, and $6.2\times10^9 \sim 27.7\times10^9$ m^3 in the Yellow River; (3) The water deficit caused by the climate change by 2030 will be $-0.2\times10^9 \sim 1.4\times10^9$ m^3 in Beijing-Tianjin-Tangshan area, $-0.4\times10^9 \sim 3.5\times10^9$ m^3 in the Huaihe River basin, and $-0.2\times10^9 \sim 12.1\times10^9$ m^3 in the Yellow River basin, however, the

water deficit will not be obvious in the Dongjiang River basin; (4) The water deficit caused by climate change will be less than that caused by the increase of population and the development of social economy. But in semi-arid years and extra-dry years, the water deficit would be more severe than normal year in the Beijing-Tianjin-Tangshan area, the Yellow River basin, and the Huaihe River basin, which will induce serious problems of social economy.

Table 11.2 Impact of climate change on water deficit (in 10^9 m^3) in some basins

The researched region	Probability of water supply (%)	Current water deficit $1\times CO_2$	Water deficit $2\times CO_2$				Increased water deficit ($2\times CO_2$ - $1\times CO_2$)			
			GISS	LLNL	UKMOH	OSU	GISS	LLNL	UKMOH	OSU
Beijing-Tianjin-Tangshan	50	1.5	2.1	2.6	1.3		0.5	1.1	-0.2	
	75	3.0	3.9	4.3	3.0		0.9	1.3	0.0	
	95	3.6	4.6	5.1	3.8		1.0	1.4	0.2	
the Huaihe River	50	3.6	3.7	4.2	2.8	3.5	0.1	0.6	0.2	-0.1
	75	5.1	5.3	6.3	5.5	5.0	0.2	1.7	0.4	-0.1
	95	15.9	16.5	19.5	17.1	15.5	0.6	3.5	1.2	-0.4
the Yellow River	50	16.3	16.2	23.8	22.0	19.7	-0.2	7.5	5.7	3.4
	75	21.8	24.2	31.3	29.6	27.5	2.4	9.4	7.8	5.7
	95	27.1	33.1	39.3	27.8	36.1	5.9	12.1	10.7	8.9
the Dongjiang River	50						0.7	0.2	0.2	-1.2
	75						0.7	0.2	14.9	-0.1
	95						1.1	0.3	0.3	-1.9

11.3 Impacts of climate change on agriculture

11.3.1 Impact of climate change on cropping system

It is found that the growth season will be longer due to the global warming; while the crop growth period will be shorten. If the temperature rises by 2°C, the growth season will be extended by 8 days in the northeastern China and 32 days in the southern China. The average growing period will be reduced by 14 ~ 15 days for rice, 34 days for wheat. The overwintering

period (<0°C) will be shortened by 8 ~ 18 days. Whereas the mid-summer period (>35°C) will be extended by 1 ~ 11 days.

One of the significant natures of Chinese agriculture is the multiple-cropping system, and the multiple-cropping index is up to 150%. Under the hypothetical condition of double CO_2 concentration and 1°C increase in the average temperature of China, the boundary of triple-cropping area is expected to move from the Yangtze River basin to the Yellow River basin, the northern boundary of double-cropping area move northward from the Qin-Huai area to the southern parts of the Northeastern China and inner Mongolia (Tao et al, 1994). In addition, moisture condition is also play an important role in determining the extension of cropping system of China (Cui, 1992).

Wang (2002) simulated and evaluated the potential effect of global warming on Chinese cropping system by using the vegetation-climate model driven by the outputs of GCM simulation under various climate scenarios in 2050. Results showed that, except for areas of Tibetan Plateau and the northern part of northeastern China, the cropping system of almost the whole country will be changed significantly by 2050 (Table 11.3). The most evident changes will take place in the eastern China where is the most important agricultural production areas in China. While most of the double-cropping areas will be replaced by various assembled triple-cropping areas, the double-cropping areas will move northward to the middle part of the present-time single-cropping areas. The boundary of triple-cropping area will obviously move northward from the Yangtze River basin to the Yellow River basin. Thus, the Chinese agricultural production will be benefit from the global warming to a certain extent, especially in the northeastern China, due to the diverse cropping system and the increasing multiple-cropping index. By the year of 2050, the single-cropping area will be reduced from 62.3% to 39.2%, while the triple-cropping area will increase from 13.5% to 35.9%; however, the area of the double-cropping will remain stable.

Table 11.3 The changes of various cropping systems in China under the climate scenario of 2050

	current (1951~1980)	The year of 2050	Predicted changes (%)
single-cropping area	62.3	39.2	-23.1
double-cropping area	24.2	24.9	+0.7
triple-cropping area	13.5	35.9	+22.4

11.3.2 Impact of climate change on crop potential productivity

Zhang et al. (1995) investigated the effect of climate change on maize potential productivity based on the historical climate data from 72 stations on the Loess Plateau during the period of 1961-1990. The result showed that the temperature within the maize growth period in 1980s decreased, so the photothermal potential productivity of maize in this period was less than that in the 1960s and 1970s, although the annual average temperature of the Loess Plateau was rising in 1980s. Owing to the influence of rainfall changes, climate potential productivity of all the provinces, except Shanxi province, was higher in 1980s than that in the 1960s and 1970s. Li (1993) investigated the potential productivity in Anhui province in the past 40 years and pointed out that the potential productivity in the 1980s appears to be lower than that in the 1940s.

To evaluate the influence of the future climate change on the crop potential productivity, most of studies were carried out by $2\times CO_2$ simulation. Li et al. (1992) pointed out that the potential productivity of wheat and maize in the winter wheat region of northern China will increase in certain degrees due to the furterlization effect of increasing CO_2 concentration. With considering the effects of both climate change and the increasing CO_2 concentration, Jin et al (1994) found that the productivity of winter wheat will raise in northern China, while the wheat productivity in the southern China would not be influenced significantly. The relatively high CO_2 concentration would enhance the photosynthesis and improve the water use efficiency (WUE), so as to enhance the adaptation of crops to the climate and increase the productivity. Under the optimal condition (the mineral elements in soil are abundant), doubled CO_2 concentration would result in 20% increase in the crop productivity (Zhang et al, 2002). Clearly, the crop productivity is strongly affected by the CO_2 concentration.

As a matter of fact, there are considerable uncertainties in the evaluation of the influence of climate change on crop productivity, since the crop productivity is affected by many factors such as temperature, CO_2 concentration, solar radiation, rainfall, evaporation, wind speed, and temperature diurnal range etc. For example, the temperature diurnal range plays an important role in the growth of crops. A small temperature diurnal range means a higher minimum temperature, which results in an enhancement of respiratory consumption, in turn, reduces the dry matter accumulation. As a result, the potential crop productivity decreased and the crop quality declined.

11.3.3 Impact of global warming on crop yield

Based on the 2050 climate scenario simulated by three GCMs (GFDL, MPI, and UKMO-H) (Wang, 2002), the effect of climate change on the crop yield was investigated by using three revised crop models (ORIZA1-rice, CERES-wheat and CERES-maize models) which were more suitable to simulate the influence of climate change on Chinese agriculture. The predicted ranges of crop yield are listed in Table 11.4. It is seen that the yield of three main crops will decrease by 5% ~ 10% by 2050.

Table 11.4 The predicted change of crop yield under the climate scenario of 2050 (%)

Crop type	Yield Range (%)	Average (%)
Rain fed winter wheat	-0.2 ~ -23.3	-7.7
Irrigated winter wheat	-1.6 ~ -2.5	-2.0
Rain fed spring wheat	-19.8~ -54.9	-31.4
Irrigated spring wheat	-7.2 ~ -29.0	-17.7
Early rice	-1.9 ~ -5.2	-3.7
Late rice	-8.8 ~ -12.9	-10.4
Single-cropping rice	-8.0 ~ -13.7	-10.5
Rain fed spring maize	-19.4 ~ +5.3	–
Irrigated spring maize	-8.6 ~ +3.6	–
Rain fed summer maize	-11.6 ~ -0.7	–
Irrigated summer maize	-11.6 ~ +0.7	–

As shown in Table 11.4, the effects of global warming on the crop yield of China will be generally negative except some specific crops. All the yield of early rice, late rice and single-cropping rice will decrease without considering moisture condition. The yield of late rice and single-cropping rice will decrease by more than 8%, whereas the decrease in the yield of early rice will be relatively smaller. The warming climate causes a decreasing trend in the wheat yield. The most evident decrease (up to 30%,) will be the rain fed spring wheat, whereas, the decrease in the yield of irrigated spring wheat, rain fed winter wheat, and irrigated winter wheat will be 17%, 7%, and 2%, respectively. The influences of global warming on maize yield basically appear to be negative. The warming climate will result in decrease of the yield by 2% ~ 7%, 5% ~ 7 %, 2% ~ 6%, 6% ~ 7 %, for the spring maize, the summer maize, the irrigated maize, and the maize without irrigation, respectively. Therefore, the climate change will induce decrease of maize average productivity by 3% ~ 6 % in China. The de-

crease in irrigated maize productivity will be less than that in rain cultivated maize.

The impact of climate change on crop yield will be different from region to region. For instance, the most evident decrease (about 17%) in the single-cropping rice productivity occurs in central northern areas of the North China, while the crop productivity are decreased by 10% ~ 15%, 6% ~ 10%, in middle and lower reaches of the Yellow River, and in Yangtze-Huaihe river basin, respectively. In the southern rice areas to the south of the Yangtze River, the decrease of the late rice productivity are 10% ~ 15%, 7% ~ 10% in the northwestern areas, and in the southeastern areas, respectively.

11.3.4 Severe agrometeorological disasters caused by the climate change

The recent research demonstrated that the trends of frequency and intensity of extreme precipitation events had increased under the background of global warming, especially the ratio of extreme precipitation events in the 1990s. The annual rainfall and the extreme rainfall have increased in the areas of the Yangtze River basin, which are the important agricultural areas in China. Most of the rainfall and water-logging in the middle-lower reaches of the Yangtze River are concentrated in the summer crops growth season during May to July.

The frequency of drought event has been increasing in recent ten years in the northern areas of China, especially the severe drought in North China in recent 30 years. The cropping and pasture transitional zone in the arid and semi-arid region is expanding. If the cropping and pasture transitional zone continue to move southeastward, it will cause the reduction of planting area and southeastward extension of desertification. The over-utilization of the land and the drought are two direct reasons for the desertification. The desertification area of China in the 1960s and 1970s increased by approximately 3.19×10^6 km^2, averagely 1560 km^2 per year (Lin et al. 1990).

As a matter of fact, the intensity and frequency of the drought events have also been increased in the southern China since the beginning of this century. For example, the most serious drought in the past 150 years took place in the south China in 2003. The vast regions of middle-lower reaches of the Yangtze River suffered from severe persistent drought for six months, the rice plants were damaged by the high temperature and the rice productivity reduced seriously because of this event. In some of the areas, the drought lasted from summer to autumn or from autumn to winter. In

2004, severe drought occurred in the South China, the agricultural loss caused by drought in Guangdong province only was up to 1.4 billion Yuan. Moreover, the most serious heat wave event in the past 100 years occurred during mid July to early September in 2006 in the region of Chongqing city and eastern Sichuan province where was struck by the heat waves with persistent high temperature of 41°C ~ 44°C in part of this region. The areas of crop suffered from drought were 3.2 million hectares, the areas with no harvest were 727 thousand hectares, the decreased crop's yields were 5 million ton, and the direct economic loss was 15 billion Yuan.

However, the warming climate may also reduce the damages to the winter crops. The cold injury disasters used to happen every year in the northern winter wheat areas in 1950s, 1960s and the early 1970s. While the frequency and intensity of cold injury has decreased due to the increasing temperature in winter since the 1980s. Especially, no large area of frost injury was observed since the middle of 1980s.

11.3.5 Impact of climate warming on the crop diseases and insect pests

The crop diseases and insect pests have a great influence on the agricultural production. The types of agricultural disease, insects, weeds and rats in China are up to 1400. Among these, serious infectious diseases and migrating insect pests are up to 20 kinds. The outbreak and prevalence of nearly all the widespread and destructive crop diseases and insect pests are closely related to the meteorological conditions.

Ye and Huo (2005) summarized recent researches on the meteorological and environmental causes of the crop diseases and insect pests, including the relationship of crop disease and insect pests with meteorological conditions and its mechanism, the possible impact of climate change on the prevalence of the crop diseases and insect pests, etc. The outbreak, spread and prevalence of some crop diseases and insect pests may be evidently accelerated or restrained by the meteorological factors such as temperature, humidity, rainfall, wind and sunshine. With respect to the crop's diseases, the incubation phase will be shortened with the rising temperature within the range suitable for the diseases. For example, the incubation phase of *Didymella melonis* at 15°C will last for 10 ~ 11 days, but only 3.5 days at 28°C. Also, high temperature is in favor of the prevalence of *Colletotrichum higginsianum Sacc*, which is the main cause of the anthrax. Generally, in the suitable temperature range, there is positive correlation between the development rate of each stage of insects and the temperature.

The rising temperature will shorten the stages of insect development, while the falling temperature will extend the stages.

With the temperature increasing, the insect pests occur earlier than normal year, then the numbers of insect generations in one year will increase, which led to more serious damage on crops. In association with the global warming, the propagation of *Mythimna separata* will be increased by 1 ~ 2 generations one year (Li, 1992). On the other hand, the rising winter temperature is in favor of the overwintering for various kinds of insects, which will result in an increase in overwintering insects, which will cause more damages to agriculture. To protect the crop from the disease and insect pest, the use of pesticide dosage had to be increased by more than 20%, which will lead to more agricultural expenditure and pollution.

Low temperature and cold-dew-wind condition is suitable for the prevalence of panicle rice blast. It will bring rice blast to the northern areas and increase its frequency and intensity if the double cropping rice field moves northward. In addition, the *Rhizoctonia solani* is a crop disease which usually happens in relatively high temperature and humidity environment. When the temperature is in the range of 23° ~ 35°C, accompanied by rainfall or high humidity, the disease may develop into the most widespread and serious crop disease.

The humidity has a close relationship with the survival rate, the amount and the avoirdupois of the insects. It was found that the hatch ability, the *nymphae* survival rate, the generation survival rate, the imago fecundity and longevity, the intrinsic increase capacity and population index of *Sogatella furcifera* bear parabolic relationship with the increase of relative humidity when the relative humidity is in the range of 43% ~ 100% (Ye and Qin, 1992). The migration ability, the avoirdupois changes, the population and the prevalent condition of the insect pests will be also affected by the humidity (Cao et al, 1995).

The insect pest will be aggravated with the rising temperature and the increasing humidity. Rainy and damp weathers are the main causes of crop diseases, which have significant effect on the boost of insect pest. For instance, *Peronospora sp.*, *Phytophthora sp.*, *Puccinia sp.*, *Selerotium sp.* and the bacterium could cause various crop diseases. Rainfall, suitable temperature and high humidity favor the propagation and proliferation of most pathogens. In addition, rainfall is one of the essential condition of infection and prevalence of bacterium (Ye et al. 2005). Recent investigations indicated that it is suitable for the spores of *Ustilago virens* to germinate when the temperature is in the range of 22° to 27°C associated with the relative humidity of 92% ~ 98%, which will accelerate the prevalence of rice false smut (Wang, 1996). Rich rainfall in winter and mid-spring ap-

pear to play important role in promoting the prevalence of wheat powdery mildew within the Yangtze River valley.

There were few research projects in the study of the effect of wind on the outbreak and prevalence of crop diseases and insect pests, and their relationship were still unclear. The investigation about the relations between the insect pests and the wind mainly focused on the effect of wind on the taking-off, moving and landing of migrating insects. The research of migrating motions of insect pests in China started from the end of 1950s, which contained *Nilaparvata lugens*, *Mythimna separata*, Leafroller, *Sogatella furcifera* and so on. The research indicated that the flight altitude of migrating insects such as the *Mythimna separata* and rice planthoppers was 500 ~ 2000m in the air. When the wind speed exceeded 3.5m s^{-1}, the movement of adult insects was mainly driven by the airflow (Ye et al. 2005).

It was found that the wind would not only affect the release and spread of fungal spores, but also produce wounds which would create conditions for fungal infection. The rain accompanied by wind was in favor of the spread and infection of fungi. There was obvious positive correlation between the prevalence of wheat powdery mildew in the Yangtze River valley and the average wind speed of ten days within the growth period of wheat. When the average wind speed of ten days within the growth period exceed that of the same period in normal years, the wheat powdery mildew will be more likely to prevail seriously.

11.3.6 Adaptation to the climate change

The influence of climate change on China agriculture is considerably important. It is necessary to take appropriate measures to adapt climate change influences on the agricultural production. The possible measures are summarized as follows:

1) Adjusting the cropping system to make full use of heat energy resource. It needs to carry out the research of adaptation of fine cultivars to changing climate before introducing them. With regard to the existing cultivars, the sowing period should be suitably adjusted according to the warming climate to settle the main growth period in a better climate condition.

2) Expanding the production of greenhouse crops to ensure the supply of agricultural products in the winter. The greenhouse crops will grow better under the warming climate, thus the risk of cold injury disaster is reduced. In addition, the growth of crops will be sped up in warm greenhouse and the market will be supplied by abundant productions.

3) Improving the forecast of crop diseases and insect pests. The climate conditions of the prevailing crop diseases and insect pests and their mechanism should be studied. The monitoring and predicting technology should be developed. The occurrence and development of crop diseases and insect pests should be traced as soon as possible, and their future development should be forecasted accurately. Statistics of 17 main crop diseases and insect pests such as rice blast, *Rhizoctonia solani*, powdery mildew, corn borer and cotton bollworm should be carried out. The loss is expected to reduce by more than 30% if the years with great prevalence possibility are predicted accurately and the appropriate control techniques are undertaken.

4) Strengthening the field management to develop the water-saving agriculture and to defense drought disasters. The drip irrigation, sprinkler irrigation, subsurface irrigation and micro-irrigation should be used to reduce the ineffective evaporation and leakage, and to enhance the water use efficiency. The plastic mulching technology can also save a large quantity of water. For example, this technology can save 60% water in Hexi corridor region.

5) It's important to breed and select the cultivars with high photosynthetic efficiency and better adaptability to flood, drought and extreme temperature. The crop distribution should be improved by developing winter cropping, double-cropping of wheat and cotton, wheat/maize intercropping, double-cropping of rice and so on, which are effective methods to increase the multi-cropping index and the time of crop photosynthesis.

11.4 Summary and prospect

In China, water resource and agriculture are strongly affected by climate change, especially global warming, through changing the temperature, precipitation, and evaporation etc.

The river runoff will reduce in the northern China while increase in the southern China under the global warming scenario. The evaporation is likely increase by about 15% in the Yellow River basin. Meanwhile, the frequency of flooding and drought disasters will increase, which will induce severe instability and contradiction between the supply and demand of water.

Global warming has positive as well as negative influences on Chinese agriculture. With the increase of annual mean temperature, the growth conditions for winter crops in the northern China will be improved, and the cold injury will reduce. The borderline of the cropping area will move

northward. In the southern China, multi-cropping system could be further developed, and also accompanied by the further increase of the multi-cropping index.

However, more influences appear to be negative. The rising temperature will speed up the growth speed of crops and shorten the growth period of crops. Meanwhile, the decrease of temperature diurnal range will intensify the respiration of crop, reduce the net photosynthesis and dry matter productivity, which results in decrease in the productivity and the yield. If the influence of rising CO_2 concentration on the photosynthesis is considered, the loss of agriculture productivity could be the reduced to a certain extent. Research showed that the productivity of early rice, late rice, single season rice, and wheat productivity will be decreased under the global warming scenario when the moisture condition is neglected. With respect to the influence of global warming on maize productivity, the negative effects are more than the positives ones, but the decrease of maize production is not as obvious as the rice and wheat. The average maize productivity in China will decrease by 3% ~ 6%.

Under the background of global warming, the frequency of extreme weather and climate events will be increasing, which results in more frequent agricultural meteorological disasters. The areas to the south of Yangtze River have been suffering from frequent flooding and water-logging disasters since 1980, resulted in a considerable decrease in the crops productivity. On the other hand, in very recent years, the drought and heat wave also cause considerable loss to agriculture. For example, the heat wave and drought in the Yangtze River basin in 2003, the drought of the South China in 2004, the strongest persistent heat wave and drought in past 100 years in Chongqing City and eastern Sichuan Province in 2006, all caused great damages to the national economy. The drought of 2006 only caused the direct economic loss of 15 billion Yuan.

The frequency of the outbreak of crop diseases and insect pests will also be increased under the global warming scenario. In association with the increasing temperature, the insects could make more generations. The prevailing period of insect pest is to be prolonged, which will cause more damages to agriculture. To protect the crop from the crop disease and insect pest, the pesticide dosage is increased by more than 20%, which will lead to more agricultural expenditure and aggravate agriculture pollution. In recent years, the recurring rice pest *Nilaparvata lugens* significantly reduced the rice productivity in Jiangsu, Zhejiang, Anhui and Jiangxi province. For example, the rice pest *Nilaparvata lugens* happened in 2005 covered 70% of the rice areas of Zhejiang province and causes a 30% reduction of productivity.

It is recommended, the following issues need to be addressed in the future studies

1) The effect of climate change on the land freshwater resources in China and the countermeasures to adapt climate change influence on the vulnerability of water resources need to be bring forward.

2) In the previous studies, the influences of climate change on the runoff and evaporation had been studied; however more attentions should be paid to the water supply and demand, the soil water content and the water cycle.

3) More FACE Experiments should be carried out to study the mechanisms of change of the photosynthesis, respiration and water consumption under the condition of changing climate, which can offer the biological foundation of the crop growth models which is developed to evaluate the influences of climate change on the crops.

4) The research of the climate assessment models for agricultural production should be strengthened, including the effect of climate change on the soil nutrition, chemical processes, the crop diseases and insect pests, the economic assessment, the countermeasures, the technical measures, the agricultural managements and so on.

5) The previous studies mainly are focused on the effect of the average climate change on agricultural production. More attentions should be paid on the influences of climate variability and extreme events on the agricultural production in further studies which is helpful to make scientific countermeasures for agriculture production.

6) The models should be further developed into the integrated model which is suitable for the East Asian region. The model's parameters should be further improved by using remote sensing and GIS techniques so as to improve the performance of model. The agricultural resource information system including the data base, the model library and expert system should be established so as to dynamically monitor the whole agro-ecosystem.

The dynamic response of the agro-ecosystem to natural climate variability and human activity should also be studied by establishing corresponding dynamic regional models, so as to make optimal policy to adapt the climate change.

References

Cao Yazhong, Kui Huang, Guang-bo Li (1995) The Effect of Relative Humidity on Flight Activity of Adult Oriental Armyworm (in Chinese). J of Plant Production, 22(2):134-138

Cui Duchang (1992) The Possible Influence of Climate Getting Warmer on Agricultural Production in China (in Chinese). Chinese Journal of Agrometeorology, (2):16-19

Guo Jun, Guoyu Ren (2005) Recent Change of Pan Evaporation and Possible Climate Factors Over the Huang-Huai-Hai Watershed,China (in Chinese). Advances in Water Science 16(5):666-672

Jin Zhiqing (1994) Prospect to Impacts of Climate Change on Winter Wheat Production in China (in Chinese). Acta Agronomica Sinica 20(2):186-197

Li De (1993) The Possible of Climate Getting Warmer and its influence on Potential Crop Productivity of Anhui province (in Chinese). Chinese Journal of Agrometeorology, (4):33-35

Li Shuhua (1992) Impact of Climate Getting Warmer on Occurrence and Prevalent of Crop's Disease and Insect Pests and Its Trend Prospect in China (in Chinese). Chinese Journal of Agrometeorology 13(2):46-49

Li Yu-e, Houxuan Zhang (1992) Possible Influence of Effects of Greenhouse on Potential Crop Productivity of Winter Wheat in North of China (in Chinese). Chinese Journal of Agrometeorology 13(4):37-39

Lin Xuechun (1990) Climatic Trend in China for the Last 40 years (in Chinese). Meteorology Monthly (10):16-21

Lin Yuan (2005) Four Great Challenge of Chinese Water Resources (in Chinese). Chinese Co-operation Economy (3):57

Liu Chunzhen (1997) Potential Impact of Climate Change on Hydrology and Water Resources in China. Advances in Water Science, 8(3): 220-225

Mintz Y, Walker G K (1993) Global field of soil moisture and land surface evapotranspiration derived from observed precipitation and surface air temperature. Journal of Applied Meteorology , 32 :1 305～1 334

Shen Shuanghe (2005) Temporal and Spatial Changes of Pan Evaporation in China and their Cause in Recent 45 Years. In: Shuanghe Shen (eds) Meteorological Economy and Social Economic Sustainable Development. Meteorological Press, Beijing, p313

Tao Zhan et al (1994) Possible Effects of Climate Change on Chinese Agriculture and the Countermeasures (in Chinese). Agro-environment and Development (3):1-7

Wang Changjin (1996) Climatic Condition and Therapeutic Measures of False Smut's Emergence (in Chinese). Agricultural Meteorology 17(3):41-44

Wang Fu-tang. Advances in Climate Warming Impact Research in China in Recent Ten Years [J]. Quarterly Journal of Applied Meteorology, 2002, 12(6):755-765.

Wang Guoqing, Yunzhang Wang (2000) Analysis on the Sensitivity of Runoff to Climate Change (in Chinese). J Shangdong Meteorology 20(3):17-20

Wang Xicheng, Jianting Xu, Huanbang Wang (2002) On Calculation Method of Amount of Available Surface Water (in Chinese). Hebei Water Resources and Hydropower Engineering (3):44-45

Ye Cailing, Huo Zhiguo, Ding Shengli, Shi Shengjin, Wang suyan Hou Tingting (2005) Advance in Study on Formation of Meteorological Environment Causing crop's Disease and Insect Pests (in Chinese). J Natural Disasters 14:90-97

Ye Zhengxiang, Houguo Qin (1992) Ronghua Huang. On the Experimental Population life Table of White Backed Plant Hopper under Different Humidity Conditions (in Chinese). J of Plant Production 19(4):323-329

You Songcai, Kiyoshi (2002) Takahashi, Yuzuru Matsuoka. Climate Change Impact on Surface Runoff in China. Quaternary Sciences 22(2):148-157

Yuan Ruhua, Taozhen Huang (2000) Impacts of Extraordinary Climate on Water Resources in China (in Chinese). Acta Geograhica Sinica 55:128-134

Zhang Aimin (2002) Study on the Climate Change and Its Influence on Agriculture in Drainage Area of Northern Anhui (in Chinese). J Anhui Agricultural Sciences 30(6):843-846

Zhang Aimin (2002) Study on the Climate Change and Its Influence on Agriculture in Drainage Area of Northern Anhui (in Chinese). J Anhui Agricultural Sciences 30(6):843-846

Zhang Qiang, Xianwei Yang, Chaoyin Huang (1995) Impact of Climatic Variation in Maize Productive Capacity in the Loess Plateau in Recent 30 Years (in Chinese). Agricultural Meteorology (6):19-23

Glossary (Acronyms)

4DDA - Four-dimensional data assimilation models
ACC - Anomalous Correlation Coefficients
AGCM - Atmospheric General Circulation Model
AMOGCM - Atmospheric General Circulation Model with Mixed-layer Ocean and Sea Ice Thermodynamic Models
AO - Antarctic Oscillation
ASM - Asian summer monsoon
BC - black carbon
BCC_CM1 - Beijing Climate Center_climate system model version1
BIOME - a major region of distinctive plant and animal groups well adapted to the physical environment of its distribution area.
BOB - Bay of Bengal
CAMS - Chinese Academy of Meteorological Sciences
CBM4 - Carbon Bond Mechanism IV
CCAM - Conformal-Cubic Atmospheric Model
CCC - Short for CCCMA_CGCM3_1. Third Generation Coupled Global Climate Model of Canadian Centre for
CCM - Community Climate Model
CCSR - Center for Climate System Research, University of Tokyo, Japan
CCSR/NIES - Center for Climate System Research, University of Tokyo, Japan/National Institute for Environmental
CDD - Maximum Number of Consecutive Dry Days (Rday < 1 mm)
CEOP - Coordinate Enhanced Observing Period
CGCM3.1 - Canadian Centre for Climate Modeling & Analysis Coupled Model Version 3.1
CGCMs - Coupled Global Climate Models
CLIMAP - Climate/Long range Investigation, Mapping and Prediction
CLIVAR - Climate Variability and Predictability Programme
CLSDB - Chinese Lake Status Data Base
CMAP - CPC Merged Analysis of Precipitation
CNRM-CM3 - Meteo-France/Centre National de Recherches Meteo-rologiques Coupled Model Version 3

COHMAP - Cooperative Holocene Mapping Project
CON - Control experiment
CRF - Cloud Radiative Forcing
CRU - Climatic Research Unit
CSIRO - Commonwealth Scientific and Industrial Research Organization
CSIRO-MK3.0 - CSIRO Atmospheric Research Coupled Model Version 3.0
CSU - Colorado State University
DARLAM - Research Limited Area Model
DFC - droughts-floods coexistence
DFCI - droughts-floods coexistence index
DJF - December, January and February
DKRZ - Deutsche Klimarechenzentrum (German Climate Computing Centre)
DTR - Diurnal Temperature Range
DWI - Dry and Wet Intensity
EAM - East Asian Monsoon
EAMI - East Asian Monsoon Intensity
EASC - East Asian Summer Climate
EASM - East Asian Summer Monsoon
EASWJ - East Asian Subtropical Westerly Jet
EC - Eddy Covariance
ECHAM4-OPYC - Max Planck Institute for Meteorology, Germany
ECHAM5/MPI-OM - Max Planck Institute for Meteorology Coupled Model
ECHO-G - coupled atmosphere ocean model, atmospheric component ECHAM4 and oceanic component HOPE-G.
ENSO - El Nino and South Oscillation
EOF - Empirical Orthogonal Function
ERS - European Remote Sensing Satellite
ET - Evapotanspiration
ETR - Intra-annual Extreme Temperature Range
FD - Frost Days
FDI - The Flood Drought Index
FGOALS-g1.0 - Global Coupled Ocean- Atmosphere General Circulation Models in LASG/IAP
GCM - General Circulation Model
GDP - Gross Domestic Product
GFDL - Geophysical Fluid Dynamics Laboratory
GFDL-CM2.0 - Geophysical Fluid Dynamics Laboratory Coupled Model, Version 2.0

GFDL-CM2.1 - Geophysical Fluid Dynamics Laboratory Coupled Model, Version 2.1
GG - Greenhouse Gases Increasing only
GIS - geographic information system
GISS-ER - NASA / Goddard Institute for Space Studies Coupled Model
GLP - Global Land Project
GLSDB - Global Lake Status Data Base
GMR - great moisture river
GOALS - global ocean-atmosphere-land system model
GS - Both Greenhouse Gases and Sulfate Aerosols Increasing
GSL - Growing Season Length
GWSP - Global Water System Project
HadCM3 - Hadley Centre Coupled Model, Version 3
HadRM - Hadley Centre regional climate model
HWDI - Heat Wave Duration Index
IAP - Institute of Atmospheric Physics
IAP/NCC T63 - Institute of Atmospheric Physics/National Climate Center Coupled Model
IBIS - the Integrated Biosphere Simulator
ICP - Indo-China Peninsula
IH - Iranian High
IJM - Iranian Plateau jet Mode
iLEAPS - Integrated Land Ecosystem Atmosphere Processes Study
INM-CM3.0 - Institute for Numerical Mathematics Coupled Model, Version 3.0
IOD - Indian Ocean Dipole
IODM - Indian Ocean Dipole Mode
IODMI - Indian Ocean Dipole Mode Index
IOV - Indian Ocean Variability
IPCC - Intergovernmental Panel on Climate Change
IPCC AR4 - IPCC 4th Assessment Report
IPCC IS92 - a set of Emission Scenarios was Presented in IPCC (1992)
IPCC SRES A1 - Medium-level Emission Scenarios
IPCC SRES A1B - Medium-level Emission Scenarios
IPCC SRES A2 - High-level Emission Scenarios
IPCC SRES B1 - Low-level Emission Scenarios
IPCC SRES B2 - Medium-level Emission Scenarios
IPCC-DDC - IPCC Data Distribution Centre
IPSL-CM4 - Institut Pierre Simon Laplace Coupled Model，Version 4
ISCCP - International Satellite Cloud Climatology Project

ISLSCP - International Satellite Land Surface Climatology Project
ISO - Intra-seasonal Oscillation
ITCZ - Intertropical Convergence Zone
JJA - June, July, and August
JJAS - June, July, August, and September
JMA-AGCM(T106) - Japan Meteorological Agency - AGCM
JTWC - Joint Typhoon Warning Center
KOE - Kuroshio/Oyashio Extension
LASG/CGCM - LASG/IAP coupled model
LASG/GOLAS - LASG/IAP coupled model
LatD - Latitudinal Land-sea Distribution
LE - Latent heat flux
LGM - Last Glacial Maximum
LIA - Little Ice Age
LonD - Longitudinal Land-sea Distribution
LPM-2D - Land-Surface Process Model-2D
LSM - Land Surface Model
LT - Linear Trends
MAIRS - Monsoon Asia Integrated Regional Study Program
MAM - March, April, and May
MAR - mass accumulation rate
MC - Maritime Continent
MIROC3.2(hidres) - Center for Climate System Research (The University of Tokyo), National Institute for Environment Studies, and Frontier Research Center for Global Change (JAMSTEC) Coupled Model，Vrsion 3.2，High Resolution
MIROC3.2(medres) - Center for Climate System Research (The University of Tokyo), National Institute for Environment Studies, and Frontier Research Center for Global Change (JAMSTEC) Coupled Model，Version 3.2，Medium Resolution
MIS - Marine Isotope Stage
MLR - Multiple Linear Regression
MLYRV - Mid- and Lower Reaches of the Yangtze River valley
MM5 - PSU-NCAR fifth generation Mesoscale Model
MOD - Monsoon Onset Date
MPI - Max Planck Institute
MRI - Meteorological Research Institute
MRI-AGCM - Meteorological Research Institute, Japan – Atmospheric general circulation model
MRI-AOGCM(T106) - Meteorological Research Institute, Japan – coupled model

MRSM - Model for Retrieving Soil Moisture
MSLP - Mean Sea Level Pressure
MWP - Medieval Warm Period
NAM - Northern Hemisphere annual mode
NAO - North Atlantic Oscillations
NASA - National Aeronautics and Space Administration
NCAR - National Center for Atmospheric Research
NCC - National Climate Center in China
NCEP - National Centers for Environmental Prediction
NDJ - November, December, and January
nDM - negative Dipole Mode
NDVI - Normalized Difference Vegetation Index
NECV - Northeast Cold Vortex
NECVI - Northeast Cold Vortex Index
NH - Northern Hemisphere
nIOD - negative Indian Ocean Dipole event
NPO - North Pacific Oscillation
NPSs - numerical point storms
NSH - No Sensible Heat experiment
NW - Northwest
OLR - Outing Long-wave Radiation
OPYC - Ocean model in isoPYCnal coordinates developed at MPI_M
PAGES - Past Global Changes
PBL - Planetary Boundary Layer
PCM1 - National Center for Atmospheric Research Coupled Model
PCMDI - Program of Climate Model Diagnosis and Intercomparison
PCs - Principal Components
pDM - positive Dipole Mode
PDO - Pacific Decadal Oscillation
PDSI - Palmer Drought Severity Index
pIOD - positive Indian Ocean Dipole event
PMIP - Palaeoclimate Modelling Intercomparison Project
PNA - Pacific/North American (pattern)
PRECIS - Providing Regional Climates for Impacts Studies
PSU - Pennsylvania State University
PSU-NCAR - Pennsylvania State University-National Center for Atmospheric Research
QSSA - Quasi-Steady-State-Approximations
QXPMEX - The first Qinghai-Xizang Plateau (Tibetan Plateau) Meteorological Experiment
R10 - No. of Days with Precipitation $\geqslant$10 mm day^{-1}

R5d - Maximum 5 d Precipitation Total
R95T - Fraction of Annual Total Precipitation due to Events Exceeding the 1961–1990 95th Percentile
RAMS - Regional Atmospheric Modeling System
RCMs - Regional Climate Models
RegCM2 - Regional Climate Model version 2
RegCM2/CN - Regional Climate Model version 2 over China
RegCM3 - Regional Climate Model Version 3
REMO - Regioanl Model developted in MPI-M
RIEMS - Regional Integrated Environment Modeling System
RMIP - Regional Climate Model Inter-comparison Project
RMSE - Root Mean Square Error
SACOL - the Semi-Arid Climate & Environment Observatory of Lanzhou University
SAH - South Asian High
SAM - Southern Hemisphere annual mode
SCC - Summer Climate of China
SCS - South China Sea
SCSMEX - South China Sea Monsoon Experiment
SCSSM - South China Sea Summer monsoon
SDII - Simple Daily Intensity Index
SE Asian - Southeast Asian
SH - Southern Hemisphere
SHAP - Sensible heat driving air-pump
SHI - Soil Humidity Index
SLP - Sea Level Pressure
SMMR - Scanning Multichannel Microwave Radiometer
SO - Southern Oscillation
SODA - Simple Ocean Data Assimilation
SON - September, October, and November
SRES - IPCC Special Report on Emissions Scenarios
SRSM - The Scheme for Retrieving Soil Moisture
SSiB - Simplified Simple Biosphere Model
SST - Sea Surface Temperature
SSTA - Sea Surface Temperature Anomaly
SSTI - Sea Surface Temperature and Sea-ice
STARDEX - STAtistical and Regional Dynamical Downscaling of EXtremes for European Regions
SVD - Singular value decomposition
SWI - Soil Water Index
TBB - Black Body Temperature
TC - Tropical Cyclone

TCP - Tropical Cyclone Precipitation
TCZ - Tropical Convergence Zone
TDP - Typhoon Destruction Potential
TEACOM - Temperate East Asia Center, China
TEMPO - Testing Earth System Models with Paleoenvironmental Observations
TH - Tibetan High
TIPEX - The second Tibetan Plateau Experiment
TJM - Tibetan Plateau Jet mode
TKE - Turbulence Kinetic Energy
Tn90 - Percent of Time Tmin > 90th Percentile of Daily Minimum Temperature
TOA - Top of Atmosphere
TP - Tibetan Plateau
TpC - Tropical Continents
TRMM - Tropical Rainfall Measuring Mission
UGAMP - Universities Global Atmospheric Modeling Programme (UK)
UKMO - United Kingdom Meteorological Office
UKMO-HadCM3 - Hadley Centre for Climate Prediction and Research / Met Office Coupled Model Version 3
Vc - Vegetation cover
VIC - Variable Infiltration Capacity
VIMT - Vertically Integrated Moisture Transport
Vp - Potential Vegetation
VPD - Vapor Pressure Deficit
WNP - Western North Pacific
WPSH - West Pacific subtropical high
WUE - water use efficiency

Subject Index

A

A1 (medium-level), 411
A1B (medium-level), 411
A2 (high-level), 411
abrupt change, 157
abrupt climate change, 51
adaptation, 459
aeolian deposits, 159
agricultural irrigation water, 451
agricultural meteorology stations, 273
agro-ecosystem, 462
air temperature, 105, 380
Aleutian low, 102
annual variations, 278
anthropogenic, 159, 174, 203
anthropogenic sulfate aerosol, 378
Arctic Oscillation, 330
arid, 155, 177
aridity index, 449
aridity trend, 157, 173
Aridity trend, 155, 208
Asian winter monsoon, 161
ASM, 5, 6
atmospheric circulation, 157, 161, 180, 182, 184, 207, 209
atmospheric general circulation, 205
atmospheric heat source/sink, 221, 223, 224

B

B1 (low-level), 411
Bay of Bengal, 127, 132, 134, 137, 146, 148
bimodality of SAH, 250
bimodality of the EAWJ, 255
bimodality of the SAH, 249
Black Carbon Aerosol, 387
BOB, 5, 7, 8, 11, 16, 25, 26

C

CGCMs, 345
chemical transport model, 351
Chinese Lake Status Database, 52
climate model, 57
climate potential productivity, 454
cloud coverage, 388
cloud water path, 388
CO_2 concentration, 453, 454
cold injury, 457, 460
cold summer events, 120, 125, 145
cool PDO phase, 107, 108, 110, 111, 114
CRF, 257, 260, 261
crop diseases, 447, 457, 461, 462
cropping index, 453, 460
cross validation, 376, 377
current vegetation, 392

D

desertification, 447, 456
diabatic heating, 251, 253, 255
diurnal temperature range, 315
drought, 456, 460, 461
drought events, 120, 122, 147
drying-up events, 124
DTR, 315
dust aerosol, 384, 385, 387
dust storms, 155
dynamic downscaling, 346, 411

E

EAM, 234, 236
EAMI, 233, 234
East Asia, 125, 127, 137, 148
East Asian monsoon, 157, 394
East Asian peleo-Monsoon, 156
East-Asian summer monsoon, 159
EASWJ, 221, 253
Emissions Scenarios of the Special Report on Emissions Scenarios (SRES), 411
Empirical downscaling, 346
Ensemble Methods, 372
ENSO, 99, 107, 113, 119, 122, 123, 125, 139, 140, 143, 325, 330
ENSO-related climate anomalies, 107
eolian deposits, 160
eolian sand, 165
evaporation, 450, 451, 460
extreme climate indicators, 432

F

field observation, 159, 185, 194, 195
flood events, 122, 124
flooding, 460

G

GIS, 462
glacial–interglacial oscillations, 165
glacial periods, 157, 166
global soil moisture data set, 298
global warming, 157
GOALS, 227, 380
greenhouse effects, 378
Gross Domestic Product, 314
growth season, 452

H

heavy rainfall simulation, 301
historical climate, 54
historical climate simulation, 56
historical documents, 49
Holocene, 51
Huaihe River, 122, 124, 142
Huaihe River valley, 112
human activity, 198, 199, 201, 202, 210
hydrological model, 350

I

ice cores, 50
IH, 249, 250
IJM, 256
in situ soil moisture, 272, 274, 295, 302
incubation, 457
Indian Ocean dipole, 119, 121, 130, 143
Indian Ocean dipole mode, 121
insect pests, 458
interannual variability, 125, 369
interannual variations, 302
interdecadal, 184, 185
interglacial periods, 166
Intergovernmental Panel on Climate Change, 320
IPCC 4th Assessment Report, 411
IPCC AR4, 411, 413, 414, 415, 422, 429, 432, 433, 436
ISCCP, 257
ISO, 2, 3

J

Japan, 122, 125, 126, 134, 138
Joint Typhoon Warning Center, 325

K

Korea, 122, 126, 127, 134

L

lake sediment, 169
land cover, 158, 178
land surface model, 194, 195, 209

land surface process, 185, 159, 195, 209
land use, 185, 203, 210
land-atmospheric interaction, 185
land-cover changes, 390, 391, 394
land-sea distribution, 232, 234
large-scale orography, 232, 235
Last Glacial Maximum, 53
Little Ice Age, 53
loess, 52, 161, 160, 165
Loess Plateau, 163, 165

M

Maunder Minimum, 59
mean sea-level pressure, 327
mechanical forcing, 259
Meiyu, 120, 126
meridional temperature gradient, 254
mid-Holocene, 71
Mongolian high, 102
monsoon, 53
monsoon period, 231
monsoon rainbelt, 370
MRSM, 353
multi-RCM ensemble, 372
MWP, 51

N

natural vegetation, 392
NCEP/NCAR reanalysis, 139, 252, 260
nimbostratus and altostratus clouds, 257, 259
North Atlantic Oscillation, 334
North Pacific, 103, 114
northern China, 155, 159, 173, 183, 203, 204, 208, 210
NSH, 227, 228, 229, 231

O

optic depth, 65
optical thickness, 257, 259
orbital parameters, 168
oscillation, 181, 182

P

paleoclimate, 49, 51
paleoclimatic modeling, 50
paleomonsoon, 168
Palmer Drought Severity Index, 329
PDO, 97, 98, 99, 113
Penman formula, 450
PJ pattern, 126
PJ-like teleconnection pattern, 146
PMIP, 69
Pollen, 55
potential evaporation, 296
potential evapotranspiration, 288, 289
Poyang Lake, 123
precipitation, 277, 288, 302, 305
Program of Climate Model Diagnosis and Intercomparison, 413
proxy data, 49

Q

Quaternary, 68
QXPMEX, 220
Quaternary, 166

R

radiation parameterization, 350
radiative forcing, 383, 386, 389
RCM, 345, 346, 367
regional climate, 293, 295, 302
retrieve, 288, 290, 299
rice blast, 458
RIEMS, 348, 350, 353, 355, 380
river runoff, 460
RMIP, 355, 357, 358, 361
RMSEs, 375
Rossby wave, 126, 135, 138, 230
runoff, 198, 199, 201, 203, 210, 277, 278, 288

S

SAH, 3, 10, 12, 13, 16, 221, 229, 250, 252, 256
SAH intensity, 248
SCS, 2, 4, 8, 10, 13, 15, 22, 26, 252
SCSMEX, 243
sea level pressures, 335
sea surface temperature, 325
seasonal transition, 230, 231
seasonal variations, 278, 279, 285, 308
semi-arid, 155, 158, 177, 178, 179, 185, 195, 208
SHAP, 226, 228, 229, 230, 232
SLP, 327, 335
snow anomalies, 236
snow cover, 237, 243, 244
snow depth, 237, 238, 239, 240, 242, 244, 246
soil moisture anomaly, 272, 283, 284
soil moisture variability, 302
soil temperature, 278
South Asia High, 247
spring wheat, 455
SRES, 412, 418
SRES A2, 411, 412, 414, 417, 419, 425, 428
SST, 325
stalagmite, 50
statistical downscaling, 411, 418, 419, 438, 441
Stratus, 256
Stratus cloud–climate feedback, 259
sulfate aerosol, 383
summer climate of China, 119, 140, 141, 143, 147
summer monsoon, 165, 166, 174, 178, 183, 184
summer monsoon circulation, 125, 130
summertime rainfall, 105, 120, 122
summertime temperature, 106
surface evaporation, 277
surface layer, 279, 281, 284, 288, 292
surface parameters, 393
SVD, 238, 239, 241, 244

T

TC, 325
TCP, 325
TCs, 324, 325, 326, 338
Teleconnection, 127, 134, 146, 147
TH, 249, 250
Thornthwaite Method, 449
Tibetan Plateau, 50, 74, 219
TIPEX, 220
TJM, 256
TKE, 242
transitive zone, 158
tree-rings, 50
tropical cyclone, 324
tropical cyclone precipitation, 325
typhoon destruction potential, 326
Typhoons, 129

V

validation, 293, 309
vegetation, 55
vertically integrated water vapor transports, 140
volumetric soil moisture, 276, 300

W

warm and drought summer in 1997, 298
warm PDO phase, 108, 110
warm preference, 250, 251
water consumption, 451
water resources, 451, 462
water-logging, 456, 461
western North Pacific, 324
wheat powdery mildew, 459
winter wheat, 457
wintertime precipitation, 105
WNP, 4, 27, 324, 325, 330
WPSH, 2, 3, 13, 22, 38, 103, 126, 128

Y

Yangtze River, 120, 122, 123, 140, 145, 148
Yangtze River valley, 110, 112, 115
Yellow River, 122, 124
Younger Dryas, 51

Z

Zhu Kezhen, 54